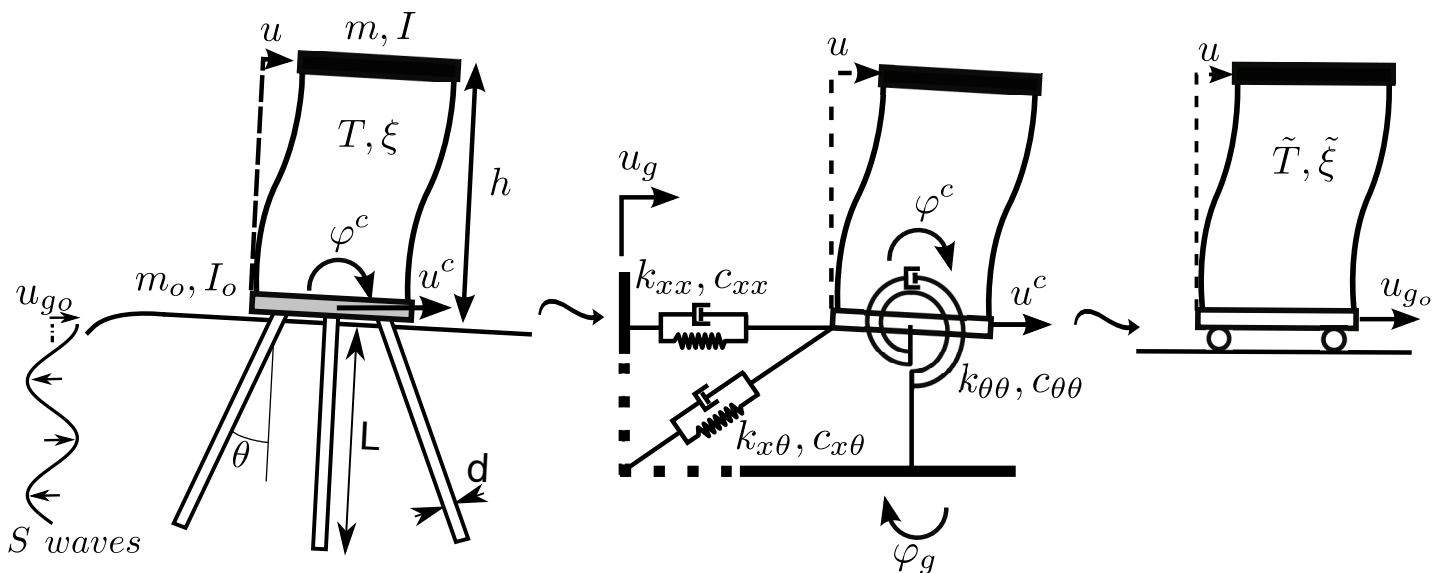


DOCTORAL DISSERTATION

Advances in the study of soil-structure interaction effects on the dynamic response of piled structures



Cristina Medina López

Continuum Mechanics and Structures Division

Las Palmas de Gran Canaria • November 2015



UNIVERSIDAD DE LAS PALMAS DE GRAN CANARIA
Instituto Universitario de Sistemas Inteligentes
y Aplicaciones Numéricas en Ingeniería

EDUARDO RODRÍGUEZ BARRERA, SECRETARIO DEL INSTITUTO
UNIVERSITARIO DE SISTEMAS INTELIGENTES Y APLICACIONES
NUMÉRICAS EN INGENIERÍA (SIANI) DE LA UNIVERSIDAD DE LAS
PALMAS DE GRAN CANARIA,

CERTIFICA

Que el Consejo de Doctores del Instituto Universitario de Sistemas Inteligentes y Aplicaciones Numéricas en Ingeniería (SIANI), en su sesión de fecha 11 de noviembre de 2015, tomó el acuerdo de dar el consentimiento para la tramitación de la Tesis Doctoral titulada “Advances in the study of soil-structure interaction effects on the dynamic response of piled structures (Avances en el estudio de los efectos de interacción suelo-estructura en la respuesta dinámica de estructuras cimentadas con pilotes)”, presentada por el doctorando **D^a. Cristina Medina López**, dirigida por el Dr. D. Juan José Aznarez González, el Dr. D. Orlando Francisco Maeso Fortuny y el Dr. D. Luis Alberto Padrón Hernández, a la vista de la idoneidad y calidad de su contenido, interés y relevancia del tema.

Para que así conste, y a los efectos oportunos se expide el correspondiente certificado a 11 de noviembre de 2015.



Eduardo Rodríguez Barrera



Advances in the study of soil-structure interaction effects on the dynamic response of piled structures

Cristina Medina López

Programa de doctorado:
Sistemas Inteligentes y Aplicaciones Numéricas en Ingeniería
Instituto Universitario SIANI

Director:

Juan J. Aznárez González

Director:

Orlando F. Maeso Fortuny

Director:

Luis A. Padrón Hernández

Las Palmas de Gran Canaria, noviembre 2015

“Science is not only a disciple of reason but, also, one of romance and passion”

Stephen Hawking

*To my parents and to Rayco for
their endless support and for
cheering me up through every
academic and personal endeav-
our in my life.*

Acknowledgments

I am deeply indebted to my supervisors, Prof. Juan José Aznárez, Prof. Orlando Francisco Maeso and Prof. Luis Padrón. I am highly grateful to them for having put at my disposal, from the very first moment, their knowledge, their brilliant ideas, their research talent, their expertise and know-how. This thesis would not have been possible without their invaluable support, help, guidance and dedication. Thank you for giving me the chance to enjoy the privilege of being part of an excellent research group with a great professional and human quality. I will always be grateful for all the resources and opportunities that they have put within my reach.

I also want to extend my appreciation to Prof. Rafael Montenegro, Prof. David Greiner and Prof. Ricardo Aguasca for providing me with their support whenever I have needed it; as well as to Juan Ignacio González for being a loyal ally in the resolution of technical problems present in everyday life, for his positive attitude and for being always willing to help me.

I also wish to thank all the people I have had the pleasure to work with at the Continuum Mechanics and Structures Division. Special thanks to Prof. Fidel García, Fernando García, José María Zarzalejos, Ariel Santana, Jacob Rodríguez, Guillermo Álamo and Lorenzo Baños, for their support and the good times spent together.

I extend my gratitude to Prof. José Manuel Quintana for his wise advice.

I will never forget all the beautiful experiences I shared with my friends and classmates in the engineering school (Escuela Técnica Superior de Ingenieros Industriales) at the University of Las Palmas de Gran Canaria. My regards to Alberto Cuadrado, colleague and friend, with whom I shared wonderful moments.

My sincere thanks also go to my family for their unconditional love and for all the time that I did not spend with them to accomplish this task. I would like to express special thanks to my beloved parents who have always encouraged me to work with passion and enthusiasm to reach my goals, for being a source of motivation, for their faith in me, for supporting me with their endless love and for lighting my way through life. You are my foundation.

It is my privilege to thank Rayco for living with me this adventure, for sharing my dreams, for his encouragement and for believing in me. Without his love, complicity and wholehearted support at all times, nothing would have been the same.

Last but not least, I would like to thank all my friends who directly or indirectly gave me their support. Special thanks to my unforgettable friend Francisco Miguel Sancho. His affection and the sound of his guitar have always accompanied me.

The author, who is a recipient of a fellowship from the Program of predoctoral fellowships of the University of Las Palmas de Gran Canaria (ULPGC), wishes to acknowledge this financial support.

This work was also supported by the Subdirección General de Proyectos de Investigación of the Ministerio de Economía y Competitividad (MINECO) of Spain and FEDER through research project BIA2010-21399-C02-01 and also by the Agencia Canaria de Investigación, Innovación y Sociedad de la Información (ACIISI) of the Government of the Canary Islands and FEDER through research project ProID20100224.

Advances in the study of soil-structure interaction effects on the dynamic response of piled structures

Abstract. My original contribution to knowledge is an analysis of the soil-structure interaction effects on the period and damping of pile-supported structures. For this purpose, an equivalence between the interacting system and a single-degree-of-freedom system which reproduces, as accurately as possible, the coupled system response within the range where the peak response occurs is established. The coupled-system response is obtained by using a substructuring model in which the structure is considered as a single-degree-of-freedom shear structure that represents, from a general point of view, one mode of vibration of multi-storey buildings. In order to determine the dynamic characteristics of this equivalent single-degree-of-freedom system, this Ph. D. thesis addresses the development, implementation and validation of a simple and stable procedure which considers kinematic and inertial interaction effects and takes into account all the elements of the matrix of impedances. A boundary element-finite element coupling formulation is used to compute impedances and kinematic interaction factors of the pile group configurations studied in this thesis. The proposed procedure is applied to perform parametric analyses for the purpose of determining the influence of the main parameters of soil-structure interaction problems on the dynamic response of the superstructure. The scope of this thesis also encompasses the study of deep foundations including battered piles. In this line, the proposed procedure is also used to contribute to clarify whether the use of battered piles has a positive or a negative influence on the dynamic response of superstructures. Ready-to-use graphs are presented for the estimation of flexible-base period and damping in terms of their fixed-base values and the system configuration. These results are used to build modified response spectra that include soil-structure interaction effects. Likewise, the influence of the rake angle of piles on the dynamic response of the foundation itself is also investigated.

Keywords: piled foundations, soil-structure interaction, effective period, effective damping, kinematic interaction, substructure model, inclined piles, seismic response

Avances en el estudio de los efectos de interacción suelo-estructura en la respuesta dinámica de estructuras cimentadas con pilotes

Resumen. La contribución original de este trabajo consiste en un análisis de la influencia de los efectos de interacción suelo-estructura sobre el periodo y el amortiguamiento de estructuras pilotadas. Con este propósito, se establece una equivalencia entre el sistema objeto de estudio y un sistema de un grado de libertad que reproduce, de la forma más precisa posible, la respuesta del sistema acoplado dentro del rango en el que se produce la respuesta máxima. La respuesta del sistema acoplado se obtiene utilizando un modelo de subestructuración en el cual la estructura se considera como una estructura a cortante que representa, desde un punto de vista general, un modo de vibración de edificios de varias plantas. Con el fin de determinar las características dinámicas de dicho sistema equivalente, esta tesis aborda el desarrollo, la implementación y la validación de un procedimiento sencillo y estable que tiene en cuenta todos los términos de la matriz de impedancias así como los efectos de interacción cinemática e inercial. Se ha empleado una formulación acoplada de elementos de contorno y elementos finitos para el cálculo de las impedancias y los factores de interacción cinemática de las configuraciones de grupos de pilotes estudiados en esta tesis. El procedimiento propuesto se aplica a la realización de análisis paramétricos que permiten determinar la influencia de los principales parámetros del problema de interacción suelo-estructura sobre la respuesta dinámica de la superestructura. El ámbito de esta tesis abarca también el estudio de cimentaciones con pilotes inclinados. En esta línea, el procedimiento propuesto se usa con el fin contribuir a esclarecer el efecto beneficioso o perjudicial que el uso de pilotes inclinados tiene sobre la respuesta dinámica de la superestructura. Asimismo, se estudia también la influencia que tiene el ángulo de inclinación de los pilotes sobre la respuesta de la cimentación en sí misma.

Palabras clave: cimentaciones pilotadas, interacción suelo-estructura, periodo efectivo, amortiguamiento efectivo, interacción cinemática, subestructuración, pilotes inclinados, respuesta sísmica



Contents



Contents	iii
List of Figures	vii
List of Tables	xiii
1 Introduction and background	3
1.1 Introduction	3
1.2 Literature review	5
1.3 Aims and objectives	9
1.4 Published works derived from this Ph. D. thesis	10
1.4.1 Contributions in JCR journals	10
1.4.2 Conference contributions	10
1.5 Structure of the dissertation	11
2 Substructuring methodology	15
2.1 Introduction	15
2.2 The three-step approach	15
2.2.1 Direct approach	16
2.2.2 Substructure approach	17
2.3 Problem definition	20
2.4 Substructure model	21
2.4.1 Equations of motion	23
2.5 Main parameters characterizing piles dynamic behaviour	23
2.6 Influence of pile cross-section geometry on the dynamic behaviour of piles	27
2.6.1 Impedance functions	31
2.6.2 Kinematic interaction factors	35
2.7 System equations and dimensionless parameters	38
2.8 Diagonalization of the impedance matrix	41
2.9 Effective period and damping of the soil-foundation-structure coupled system	47
2.10 Implementation	61
2.11 Model validation	65
2.11.1 Shallow foundations. Comparison with Veletsos and Meek	65
2.11.2 Embedded foundations. Comparison with Avilés and Pérez-Rocha	71
3 Boundary elements based models for soil-structure interaction	79
3.1 Introduction	79
3.2 Governing equations of linear elastodynamics	79
3.3 The elastodynamic integral representation	80
3.4 Boundary element method	82
3.5 Boundary element - finite element coupling model	87
4 Numerical computation of impedances and kinematic interaction factors	95
4.1 Introduction	95
4.2 Computation of impedances	95
4.3 Computation of kinematic interaction factors	96
4.4 Problem definition	97



4.5	Pile group configurations consisting of vertical piles	99
4.6	Impedances and kinematic interaction factors for vertical pile groups	101
4.7	Influence of direction and angle of inclination of piles on the kinematic re- sponse of deep foundations	110
4.7.1	Validation of the BEM-FEM coupling formulation	110
4.7.2	Pile group configurations under investigation	112
4.7.3	Translational kinematic interaction factors of single piles	112
4.7.4	Rotational kinematic interaction factors of single piles	113
4.7.5	Translational kinematic interaction factors of pile groups	115
4.7.6	Rotational kinematic interaction factors of pile groups	118
4.7.7	Influence of pile-soil Young's modulus ratio and pile slenderness ratio	124
4.7.8	Influence of rake angle on pile kinematic bending moments	125
4.7.9	Conclusions	126
4.8	Pile group configurations including inclined piles	127
4.9	Impedances and kinematic interaction factors for pile groups comprising in- clined elements	129
5	Seismic behaviour of structures supported on vertical pile groups	139
5.1	Introduction	139
5.2	Configurations under investigation	139
5.3	Influence of foundation-structure mass ratio	140
5.4	Influence of cross-coupled impedances	142
5.5	Influence of structural slenderness ratio and wave parameter	146
5.6	Influence of kinematic interaction factors	149
5.7	Influence of pile slenderness ratio	151
5.8	Influence of embedment ratio	154
5.9	Influence of pile group size	157
5.10	Influence of pile-soil Young's modulus ratio	158
5.11	Influence of fixed-base structure damping ratio	160
5.12	Influence of mass density ratio	161
5.13	Conclusions	162
6	Seismic behaviour of structures supported on battered pile groups	167
6.1	Introduction	167
6.2	Configurations under investigation	167
6.3	Influence of rake angle on the system effective period	168
6.4	Influence of rake angle on the maximum structural shear forces	169
6.5	Influence of rake angle on the elastic response spectra	175
6.6	Conclusions	177
7	Summary, conclusions and future research directions	181
7.1	Summary and conclusions	181
7.2	Future research directions	185
	Appendices	187
A	Summary of the dissertation in Spanish	191

Bibliography

307



List of Figures

2.1	Direct approach.	16
2.2	Step 1. Kinematic interaction.	18
2.3	Step 2. Impedance functions.	18
2.4	Step 3. Inertial interaction.	19
2.5	Problem definition. Single shear structure supported on a piled foundation embedded in a homogeneous half-space under vertically-incident S waves.	20
2.6	Problem definition and substructure model of a one-storey structure.	21
2.7	The three-step approach.	22
2.8	Beam on Dynamic Winkler Foundation.	24
2.9	Piles cross-section.	27
2.10	Pile foundation geometry.	30
2.11	Influence of pile cross-section geometry. Horizontal impedances of 2×2 and 3×3 pile groups.	32
2.12	Influence of pile cross-section geometry. Rocking impedances of 2×2 and 3×3 pile groups.	33
2.13	Influence of pile cross-section geometry. Horizontal-rocking cross-coupled impedances of 2×2 and 3×3 pile groups.	34
2.14	Influence of pile cross-section geometry. Translational kinematic interaction factor of 2×2 and 3×3 pile groups.	36
2.15	Influence of pile cross-section geometry. Rotational kinematic interaction factor of 2×2 and 3×3 pile groups.	37
2.16	Equivalent model with diagonalized impedance matrix.	41
2.17	Substructure model of a one-storey structure and equivalent single-degree-of-freedom oscillator.	47
2.18	Maximum searching strategy (MAX) for obtaining the natural frequency and damping of the equivalent SDOF system.	48
2.19	Root finding strategy (ROOT) for obtaining the natural frequency and damping of the equivalent SDOF system without neglecting second-order damping terms.	49
2.20	Replacement oscillator approach to 3DOF system on a 3×3 pile group with $s/d = 5$ and $L/b = 1$. ROOT strategy.	50
2.21	Replacement oscillator approach to 3DOF system on a 3×3 pile group with $s/d = 5$ and $L/b = 4$. ROOT strategy.	51
2.22	Replacement oscillator approach to 3DOF system on a 3×3 pile group with $s/d = 5$ and $L/b = 2$. EIGEN-S strategy.	53
2.23	Proposed procedure (EIGEN) for obtaining the natural frequency of the equivalent SDOF system by neglecting second-order damping terms, and determining the damping coefficient by considering them.	54
2.24	Replacement oscillator approach to 3DOF system on a 3×3 pile group with $s/d = 5$ and $L/b = 4$. EIGEN vs EIGEN-S.	55
2.25	Influence of neglecting all second-order damping terms. Effective period \tilde{T}/T and damping ratio $\tilde{\xi}$ for 2×2 pile groups with $L/b = 2$	56
2.26	Influence of neglecting all second-order damping terms. Effective period \tilde{T}/T and damping ratio $\tilde{\xi}$ for 4×4 pile groups with $s/d = 3.75$	57



2.27 Influence of neglecting all second-order damping terms. Effective period \tilde{T}/T and damping ratio $\tilde{\xi}$ for 2×2 , 3×3 and 4×4 pile groups with $L/b = 4$ and $L/d = 15$	58
2.28 Strategies for obtaining the natural frequency and damping of the equivalent SDOF system.	59
2.29 Root finding procedure (EIGEN) vs maximum searching algorithm (MAX). Effective period \tilde{T}/T and damping ratio $\tilde{\xi}$ for a 2×2 pile group.	60
2.30 Replacement oscillator approach to 3DOF system on a 2×2 pile group. $L/b = 1, 7.5$, and 15 . Transfer functions, elastic response spectra corresponding to the 1940 El Centro Earthquake and damping ratio ($\tilde{\xi}$) of the equivalent SDOF replacement oscillator.	61
2.31 Problem definition. Single shear structure supported on a shallow foundation at the surface of a homogeneous half-space under vertically-incident S waves.	66
2.32 Dimensionless coefficients in expressions for foundation stiffness and damping.	68
2.33 Comparison between the results obtained with the proposed model and those extracted from the original paper, by Veletsos and Meek.	70
2.34 Comparison between stiffness and damping coefficients given by Veletsos and Meek and those provided by Veletsos and Verbic.	71
2.35 Problem definition. Single shear structure supported on a foundation embedded in a homogeneous half-space under vertically-incident S waves.	72
2.36 Comparison between the results obtained with the proposed model and those digitized from the original paper, by Avilés and Pérez-Rocha.	75
3.1 Strategy for the singularity subtraction. Hemisphere around the collocation point for integration.	82
3.2 Multi-region boundary-element model definitions and BEM mesh.	83
3.3 BEM-FEM model.	88
3.4 Finite element definition	89
3.5 External punctual forces (left) and tractions along the pile-soil interface defined on the generic element	89
4.1 Pile foundation geometry.	98
4.2 Sketches of the different vertical pile group configurations assuming the same diameter $d = cte$ for all cases.	100
4.3 Range of the dimensionless frequency $\omega d/c_s$ for all cases under investigation.	101
4.4 Impedance functions of different 2×2 pile groups. $E_p/E_s = 10^3$ and $\xi_s = 0.05$	102
4.5 Impedance functions of different 3×3 pile groups. $E_p/E_s = 10^3$ and $\xi_s = 0.05$	103
4.6 Impedance functions of different 4×4 pile groups. $E_p/E_s = 10^3$ and $\xi_s = 0.05$	103
4.7 Idealized shape of the kinematic interaction factors of different pile groups embedded in a soil with $E_p/E_s = 10^3$ and $\xi_s = 0.05$	104
4.8 Idealized shape of the kinematic interaction factors of different pile groups with $L/d = 7.5$, $E_p/E_s = 10^3$ and $\xi_s = 0.05$	106
4.9 Idealized shape of the kinematic interaction factors of different pile groups with $L/d = 15$, $E_p/E_s = 10^3$ and $\xi_s = 0.05$	106
4.10 Idealized shape of the kinematic interaction factors of different pile groups with $L/d = 30$, $E_p/E_s = 10^3$ and $\xi_s = 0.05$	107



4.11 Kinematic interaction factors of different 2×2 pile groups, $E_p/E_s = 10^3$ and $\xi_s = 0.05$	107
4.12 Kinematic interaction factors of different 3×3 pile groups. $E_p/E_s = 10^3$ and $\xi_s = 0.05$	108
4.13 Kinematic interaction factors of different 4×4 pile groups. $E_p/E_s = 10^3$ and $\xi_s = 0.05$	108
4.14 Impedance functions of different 2×2 pile groups. $E_p/E_s = 10^2$ and $\xi_s = 0.05$	109
4.15 Kinematic interaction factors of different 2×2 pile groups. $E_p/E_s = 10^2$ and $\xi_s = 0.05$	109
4.16 Kinematic interaction factors, I_u and I_φ , of 2×2 pile groups with different spacing ratios s/d , rake angles θ and stiffness ratios E_p/E_s . Comparison between BEM-BEM and BEM-FEM.	111
4.17 Translational kinematic interaction factor I_u and vertical displacement u_z/u_{g_o} of a single pile for different rake angles θ	113
4.18 Rotational kinematic interaction factor I_φ of a single pile for different rake angles θ	114
4.19 Deformed shape and undeformed shape of simple inclined piles with different rake angles θ considering $ u_{g_o} = 1$. $a_o = 0.3$. $E_p/E_s = 1000$	114
4.20 Translational kinematic interaction factor I_u of a 2×2 pile group with battered piles with different rake angles θ and $s/d = 5$	116
4.21 Translational kinematic interaction factor I_u of a 2×2 pile group with battered piles with different rake angles θ and $s/d = 10$	116
4.22 Translational kinematic interaction factor I_u of a 3×3 pile group with battered piles with different rake angles θ and $s/d = 5$	117
4.23 Translational kinematic interaction factor I_u of a 3×3 pile group with battered piles with different rake angles θ and $s/d = 10$	117
4.24 Rotational kinematic interaction factor I_φ and maximum pile head bending strain ε_p (considering $ u_{g_o} = 1$) of a 2×2 pile group with battered piles with different rake angles θ and $s/d = 5$	119
4.25 Rotational kinematic interaction factor I_φ and maximum pile head bending strain ε_p (considering $ u_{g_o} = 1$) of a 2×2 pile group with battered piles with different rake angles θ and $s/d = 10$	120
4.26 Rotational kinematic interaction factor I_φ of a 3×3 pile group with battered piles with different rake angles θ and $s/d = 5$	121
4.27 Rotational kinematic interaction factor I_φ of a 3×3 pile group with battered piles with different rake angles θ and $s/d = 10$	121
4.28 Deformed shape and undeformed shape of 2×2 pile groups with battered piles with different rake angles θ being $s/d = 5$ considering $ u_{g_o} = 1$. $a_o = 0.3$	122
4.29 Influence of the rake angle on the rocking motion at the pile cap.	123
4.30 Influence of the pile-soil Young's modulus ratio E_p/E_s on the rotational kinematic interaction factor I_φ of 2×2 piles groups with piles inclined parallel to the direction of excitation with different rake angles θ being $s/d = 5$	124
4.31 Influence of the pile slenderness ratio L/d on the rotational kinematic interaction factor I_φ of 2×2 piles groups with piles inclined parallel to the direction of excitation with different rake angles θ being $s/d = 5$	125
4.32 Sketches of the different pile group configurations comprising inclined piles, assuming the same diameter ($d = cte$) for all cases.	128



4.33 Dynamic stiffness functions of different 2×2 pile groups. $E_p/E_s = 1000$ and $\xi_s = 0.05$. $L/d(s/d) = 7.5(3.75), 15(7.5), 30(15)$	130
4.34 Dynamic stiffness functions of different 3×3 pile groups. $E_p/E_s = 1000$ and $\xi_s = 0.05$. $L/d(s/d) = 7.5(2.5), 15(5), 30(10)$	131
4.35 Damping functions of different 2×2 pile groups. $E_p/E_s = 1000$ and $\xi_s = 0.05$. $L/d(s/d) = 7.5(3.75), 15(7.5), 30(15)$	132
4.36 Damping functions of different 3×3 pile groups. $E_p/E_s = 1000$ and $\xi_s = 0.05$. $L/d(s/d) = 7.5(2.5), 15(5), 30(10)$	133
4.37 Kinematic interaction factors of different 2×2 pile groups. $E_p/E_s = 1000$ and $\xi_s = 0.05$. $L/d(s/d) = 7.5(3.75), 15(7.5), 30(15)$	135
4.38 Kinematic interaction factors of different 3×3 pile groups. $E_p/E_s = 1000$ and $\xi_s = 0.05$. $L/d(s/d) = 7.5(2.5), 15(5), 30(10)$	136
5.1 Influence of the foundation-structure mass ratio m_o/m . Maximum structural response value Q_m for 4×4 pile groups with $L/b = 2$ and $E_p/E_s = 10^3$ and $\xi_s = 0.05$	141
5.2 Sketches of the pile group configurations corresponding to the cases analysed in figure 5.1 when considering $d = cte$	142
5.3 Influence of the cross-coupled impedances. Effective period \tilde{T}/T , damping ratio $\tilde{\xi}$ and maximum structural response value Q_m for a 2×2 pile group with $L/b = 2$, $E_p/E_s = 10^3$ and $\xi_s = 0.05$	143
5.4 Sketches of the pile group configurations corresponding to the cases analysed in figure 5.3 when considering $d = cte$	143
5.5 Influence of the cross-coupled impedances. Effective period \tilde{T}/T , damping ratio $\tilde{\xi}$ and maximum structural response value Q_m for a 2×2 pile group with $L/d = 15$, $E_p/E_s = 10^3$ and $\xi_s = 0.05$	144
5.6 Sketches of the pile group configurations corresponding to the cases analysed in figure 5.5 when considering $d = cte$	144
5.7 Influence of the cross-coupled impedances. Effective period \tilde{T}/T , damping ratio $\tilde{\xi}$ and maximum structural response value Q_m for pile groups with $L/d = 15, L/b = 2$, $E_p/E_s = 10^3$ and $\xi_s = 0.05$	145
5.8 Sketches of the pile group configurations corresponding to the cases analysed in figure 5.7 when considering $d = cte$	145
5.9 Influence of the structural slenderness ratio h/b . Effective period \tilde{T}/T for a 4×4 pile group with $s/d = 3.75$, and for a pile group with $L/b = 4$, $L/d = 15$. $E_p/E_s = 10^3$ and $\xi_s = 0.05$	147
5.10 Sketches of the pile group configurations corresponding to the cases analysed in the left column in figure 5.9 when considering $d = cte$	148
5.11 Sketches of the pile group configurations corresponding to the cases analysed in the right column in figure 5.9 when considering $d = cte$	148
5.12 Influence of the kinematic interaction and the size of the pile group. Effective period \tilde{T}/T , damping ratio $\tilde{\xi}$, maximum structural response value Q_m and kinematic interaction factor $ I_u + (h/b)I_\varphi $ for pile groups with $L/b = 4$, $L/d = 15$, $E_p/E_s = 10^3$ and $\xi_s = 0.05$	150
5.13 Sketches of the pile group configurations corresponding to the cases analysed in figure 5.12 when considering $d = cte$	150



5.14 Influence of the pile slenderness ratio L/d . Effective period \tilde{T}/T , damping ratio $\tilde{\xi}$, maximum structural response value Q_m and maximum relative values of the foundation horizontal displacement $ \omega_n^2 u_r^c / \ddot{u}_{g0} $ and rocking $ \omega_n^2 h \varphi_r^c / \ddot{u}_{g0} $ for a 2×2 pile group with $L/b = 2$, $E_p/E_s = 10^3$ and $\xi_s = 0.05$	152
5.15 Sketches of the pile group configurations corresponding to the cases analysed in figures 5.14 and 5.16 when considering $d = cte$	153
5.16 Influence of the pile slenderness ratio L/d . Effective period \tilde{T}/T for 2×2 pile groups with $L/b = 2$, $E_p/E_s = 10^3$ and $\xi_s = 0.05$. $h/b = 0.6$	153
5.17 Influence of the embedment ratio L/b . Effective period \tilde{T}/T , damping ratio $\tilde{\xi}$, maximum structural response value Q_m and maximum relative values of the foundation horizontal displacement $ \omega_n^2 u_r^c / \ddot{u}_{g0} $ and rocking $ \omega_n^2 h \varphi_r^c / \ddot{u}_{g0} $ for a 4×4 pile group with $s/d = 3.75$, $E_p/E_s = 10^3$ and $\xi_s = 0.05$	155
5.18 Sketches of the pile group configurations corresponding to the cases analysed in figures 5.17 and 5.19 when considering $d = cte$	156
5.19 Influence of the embedment ratio L/b . Effective period \tilde{T}/T for 4×4 pile groups with $s/d = 3.75$, $E_p/E_s = 10^3$ and $\xi_s = 0.05$. $h/b = 0.6$	156
5.20 Influence of the kinematic interaction and the size of the pile group. Maximum relative values of the foundation horizontal displacement $ \omega_n^2 u_r^c / \ddot{u}_{g0} $ and rocking $ \omega_n^2 h \varphi_r^c / \ddot{u}_{g0} $ for pile groups with $L/b = 4$, $L/d = 15$, $E_p/E_s = 10^3$ and $\xi_s = 0.05$	157
5.21 Sketches of the pile group configurations corresponding to the cases analysed in figure 5.20 when considering $d = cte$	158
5.22 Influence of the pile-soil Young's modulus ratio E_p/E_s . Effective period \tilde{T}/T , damping ratio $\tilde{\xi}$ and maximum structural response value Q_m for 2×2 pile groups with $L/b = 2$, $\delta = 0.15$, $\xi = 0.05$ and $\xi_s = 0.05$	159
5.23 Sketches of the pile group configurations corresponding to the cases analysed in figure 5.22 when considering $d = cte$	159
5.24 Influence of the fixed-base structure damping ratio ξ . Effective period \tilde{T}/T , damping ratio $\tilde{\xi}$ and maximum structural response value Q_m for a 3×3 pile group with $L/d = 30$, $L/b = 2$, $\delta = 0.15$, $E_p/E_s = 10^3$ and $\xi_s = 0.05$	160
5.25 Influence of the mass density ratio between structure and supporting soil δ . Effective period \tilde{T}/T , damping ratio $\tilde{\xi}$ and maximum structural response value Q_m for a 3×3 pile group with $L/d = 15$, $L/b = 2$, $E_p/E_s = 10^3$ and $\xi_s = 0.05$	161
6.1 Effective period \tilde{T}/T for different 2×2 pile groups. $E_p/E_s = 1000$ and $\xi_s = 0.05$. $L/d (s/d) = 7.5(3.75), 15(7.5), 30(15)$. $h/b = 1, 2, 5, 10$	168
6.2 Effective period \tilde{T}/T for different 3×3 pile groups. $E_p/E_s = 1000$ and $\xi_s = 0.05$. $L/d (s/d) = 7.5(2.5), 15(5), 30(10)$. $h/b = 1, 2, 5, 10$	169
6.3 Maximum structural response value Q_m for different 2×2 pile groups. $E_p/E_s = 1000$ and $\xi_s = 0.05$. $L/d (s/d) = 7.5(3.75), 15(7.5), 30(15)$. $h/b = 1, 2, 5, 10$	170
6.4 Maximum structural response value Q_m for different 3×3 pile groups. $E_p/E_s = 1000$ and $\xi_s = 0.05$. $L/d (s/d) = 7.5(2.5), 15(5), 30(10)$. $h/b = 1, 2, 5, 10$	171
6.5 Maximum structural response value Q_m for different 2×2 pile groups. $E_p/E_s = 1000$ and $\xi_s = 0.05$. $L/d (s/d) = 7.5(3.75), 15(7.5), 30(15)$. $h/b = 1, 2, 5, 10$	172
6.6 Maximum structural response value Q_m for different 3×3 pile groups. $E_p/E_s = 1000$ and $\xi_s = 0.05$. $L/d (s/d) = 7.5(2.5), 15(5), 30(10)$. $h/b = 1, 2, 5, 10$	172
6.7 Center of stiffness \mathcal{D} and height of the geometric point h_p	173



6.8 Evolution of h_p/d (h_p : height above the cap of the geometric point where pile axes meet) and evolution of ratio \mathcal{D}/d (\mathcal{D} : center of stiffness) at $a_o = 0$ and $a_o = a_o(\text{Max}|Q_m|)$ for 2×2 pile groups ($b = s$) with different rake angles. . . . 174

6.9 Evolution of the structural maximum response of a structure with $h/b = 2$ supported on 2×2 pile groups ($b = s$) with different rake angles when h/h_p varies from $h/h_p > 1$ to $h/h_p < 1$. $s/d = 7.5$, $E_p/E_s = 1000$ and $\xi_s = 0.05$ 174

6.10 Elastic response spectra corresponding to the 1940 El Centro Earthquake for different 2×2 pile groups with piles inclined $\theta = 10^\circ$, $E_p/E_s = 1000$ and $\xi_s = 0.05$. L/d (s/d) = 7.5(3.75), 30(15) and $h/b = 1, 2, 5, 10$. SDOF vs 3DOF. 175

6.11 Elastic response spectra corresponding to the 1940 El Centro Earthquake for different 2×2 pile groups. $E_p/E_s = 1000$ and $\xi_s = 0.05$. $L/d = 7.5, 15, 30$ and $h/b = 1, 2, 3$ 176

6.12 Elastic response spectra of the motion of the mass corresponding to the 1940 El Centro Earthquake a 2×2 pile group with $s/d = 3.75$ being $T = 0.44 s$. $E_p/E_s = 1000$ and $\xi_s = 0.05$ 177



List of Tables

2.1	Values adopted for the parameters characterizing the SSI problem.	28
2.2	Model solid circular cross-section geometry and equivalent material properties.	29
2.3	Actual annular cross-section geometry and material properties.	29
2.4	Percentage error for impedance functions yielding from modelling a hollow pile by an equivalent solid pile.	31
2.5	Percentage error for kinematic interaction factors yielding from modelling a hollow pile by an equivalent solid pile.	35
2.6	Numerical coefficients in equations (2.111) to (2.114).	69
3.1	Quadratic triangular and quadrilateral element types.	84
4.1	Pile group configurations consisting of vertical piles.	99
4.2	Pile group configurations for the analysis of the influence of rake angle of piles on the kinematic interaction factors of deep foundations.	112
4.3	Configurations of pile groups comprising inclined piles.	129
5.1	Vertical pile group configurations.	140
6.1	Configurations of pile groups comprising inclined piles.	167



1. INTRODUCTION AND BACKGROUND

- 1.1 Introduction
- 1.2 Literature review
- 1.3 Aims and objectives
- 1.4 Published works derived from this Ph. D. thesis
- 1.5 Structure of the dissertation



1.1 Introduction

Pile foundations are deep foundations consisting of either a single long, slender, columnar element or a group of them whose heads are often connected by a reinforced concrete block named pile cap. A pile cap transfers and distributes the loads from the superstructure to the foundation and also provides lateral restraint to the tops of the piles when necessary. Piles are typically made from steel, reinforced concrete, pre-stressed concrete and sometimes timber.

The use of piles and pile foundations dates back to prehistoric times. The inhabitants of the Alpine region during the Neolithic and the Bronze Age built their homes on wooden piles driven in the soft bottoms of shallow lakes. This type of construction was also used in different places all over the world as Oceania, Africa and South America. Venice stands on wooden piles since the 9th century. Over a million of wooden piles were dug underwater in order to build Santa Maria della Salute church in Venice in the 17th century. The use of steel piles began in the 19th century and that of concrete piles in the 20th century. Today, pile foundations are frequently used to support high rise structures, nuclear reactor buildings, bridge piers, offshore platforms and marine structures.

Pile foundations are commonly used to transfer the loads from a structure above ground through soft, weak underlying surface soil, or even through swelling or collapsing soils, to deeper strata with higher bearing capacity and stability. They are also adopted to transmit uplift loads gradually by side shear, in those cases in which competent layers are not found within an acceptable depth, as well as to resist large horizontal loads by using vertical piles subjected to bending and shear or inclined piles. This type of foundation is also advisable in situations where the underlying soil is not adequate to prevent excessive settlement. With regard to the seismic behaviour of structures, the use of pile foundations can improve their seismic response by reducing the seismic input and, at the same time, increasing the system damping.

Conventional methods used in the analysis and design of structures usually assume a fixed-base condition. This implies that the foundation-soil system underlying the structure is rigid and soil-structure interaction (SSI) effects are neglected. The dynamic soil-structure interaction consists of inertial interaction and kinematic interaction. Inertial interaction results from the inertial forces transmitted by the mass of the superstructure to the compliant soil. Kinematic interaction arises as a result of the inability of the foundation to conform to the distortions of the soil generated by the incident earthquake waves. The study of the behaviour of structures during earthquake events has revealed that the soil-structure interaction can affect the dynamic response of buildings, especially in the case of stiff structures founded on relatively soft soils.

In view of the foregoing, an adequate assessment of the structural dynamic response requires the development of models that rigorously incorporate the interaction between the structure and the soil on which it is founded. The methodologies used for seismic analyses considering soil-structure interaction can be classified into direct and substructuring approaches.

A three step or substructure approach is commonly used to analyse the seismic behaviour of structures including SSI effects arising when fixed-base conditions are not assumed for the structure. This methodology consists in breaking the solution of the problem into three parts. The first part addresses the determination of the foundation motion when subjected to the seismic waves and considering that both the structure

and the foundation are massless. The next part consists in obtaining the foundation impedances which represent the stiffness of the foundation support and the damping associated with foundation-soil interaction. Finally, the last part is the computation of the response, at each frequency, of the structure supported on springs and dashpots, characterized by the foundation impedance matrix, and subjected to the motion computed in the first part. This methodology provides accurate results for the kind of problems tackled in this dissertation and, at the same time, is easy to implement. This approach is particularly appropriate for conducting parametric analysis to determine the influence of the main parameters of the SSI problem on the final response with an affordable computational effort. Another important advantage of this approach is that symmetry or cylindrical conditions can be applied to reduce the size of the model, without loss of accuracy, if the foundation meets these requirements, even if the superstructure does not. In addition, the analysis of each part (superstructure, foundation and soil) of the whole system can be performed by using the most suitable method in each case.

On the other hand, direct approaches model in a single step the soil, foundation and structure and consider mutual interaction in a more rigorous manner. The main shortcoming of these approaches is their relative computational cost, due to the complexity of models with a larger number of degrees of freedom. In fact, few parametric studies are normally performed with direct approaches, since variations in the properties of any part of the system entail a complete new analysis. Even so, these methods are specially competitive in the analysis of interaction phenomena among nearby structures, and in problems involving nonlinearities.

The use of substructuring methodologies in the analysis of the dynamic response of structures supported by shallow or embedded foundations has been the subject of much research. However, the study of the dynamic behaviour of pile-supported structures has received less research attention. Aiming at contributing to fill this gap, this work exploits the advantages of the substructure methodology in order to develop a simple and stable procedure for the estimation of periods and dampings of pile-supported shear structures, in the linear range, including soil-structure interaction. For this purpose, an equivalence between the interacting system and a single-degree-of-freedom (SDOF) system which reproduces, as accurately as possible, the coupled system response within the range where the peak response occurs is established. The coupled system response is obtained by using a substructuring model in which the structure is considered as a SDOF shear structure that represents, from a general point of view, one mode of vibration of multi-storey buildings. Both, dynamic and kinematic interaction effects are included in the analysis of this coupled system and all the elements of the impedance matrix are taken into account. Impedances and kinematic interaction factors of the pile group configurations investigated are calculated using a three-dimensional boundary element - finite element methodology. The structure is analysed as founded on an elastic homogeneous half-space and excited by vertically incident S waves.

Once the model is formulated, implemented and validated, it has been applied to pile foundations comprising vertical and battered piles. Inclined piles are frequently used in foundations that are expected to resist important lateral loads. Vertical piles transmit these loads only through shear and bending. However, raked piles have the ability of transmitting them primarily in axial compression and/or tension, which implies an increase of their lateral stiffness. Thus, when subjected to lateral loading, batter piles present generally smaller deformations and offer larger bearing capacity than vertical

piles of the same material and dimensions. Until 1990s, inclined piles were frequently used in seismic design of bridges as well as in design of marginal wharfs and other port and harbour structures. However, the use of inclined piles became highly discouraged after the unsatisfactory seismic performance that deep foundations with battered piles showed during a series of earthquakes. In fact, the specification of batter piles as foundation systems in seismically active regions is generally avoided, due also to the lack of understanding regarding the seismic response of batter piles and pile foundations with inclined elements and, in the European case, to the note in part 5 of Eurocode 8 stating that the use of inclined piles for transmitting lateral loads to the soil is not recommended when designing for earthquake resistance. Indeed, the need for more research on all facets of this problem is apparent from the lack of information available in the literature and in the different building codes. In recent years, inclined piles have recovered their popularity. Indeed, several studies have shown the beneficial role of battered piles on the seismic response of the structure. However, further research is needed to be able to elucidate in which cases the presence of raked piles is beneficial or detrimental. The kinematic interaction factors of pile foundations with inclined elements is one of the aspects that have not received enough attention. Moreover, the influence of pile rake angle on the seismic response of the superstructure is another aspect that still needs more research. These two aspects are investigated in this work.

An analysis of the influence of SSI effects on the dynamic response of slender and non-slender structures supported on several configurations of 2×2 , 3×3 and 4×4 pile groups is accomplished in this work through a procedure based on a substructure model. The relevance and main trends observed in the influence of the variation of the main parameters of the problem on the dynamic response of the structure are inferred from the presented results.

This document includes ready-to-use graphs for the estimation of flexible-base period and damping, in terms of their fixed-base values, for several system configurations. Maximum shear forces together with base displacement and rocking peak response are also provided. Moreover, modified response spectra considering soil–structure interaction effects are obtained for different rake angles.

1.2 Literature review

The seismic design of Nuclear Power Plants in the 60s and 70s brought with it a growing interest in seismic soil-structure interaction. The research works undertaken by Parmelee [1], Parmelee *et al.* [2], Perelman *et al.* [3] and Sarrazin *et al.* [4] were pioneers in the investigation of the influence of the compliance of the supporting soil on the dynamic response of one-storey-shear-structures. A review of the research developed in the early stages of seismic soil-structure interaction can be found in [5].

When analysing the seismic behaviour of structures, kinematic and inertial effects associated to soil-structure interaction affect the dynamic characteristics of the interacting system and influence the ground motion around the foundation. Thus, it is important to assess the variations of the system period associated with the soil stiffness, as well as the variations of the modal damping associated with the material damping in the soil and especially with the radiation effects.

The effects of SSI on the dynamic characteristics of soil-structure systems have been widely studied both for shallow foundations [6–11] and for embedded foundations, using both 3D models [12–15] and 2D models [16, 17]. The papers by Jennings and Bielak [6], Veletsos and Meek [7], Luco [10], Wolf [11] or Bielak [12], all introduce the analogy of a fixed-base replacement SDOF oscillator whose period and damping can represent the dynamic behaviour of the structure-foundation system. In all these pioneering works, some simplifying assumptions were used in order to obtain results or expressions for the effective system period and damping: the influence of the coupled terms of the soil-impedance matrix was neglected and, for embedded foundations, the kinematic effects of the incident wave were not considered, using as base excitation a horizontal harmonic motion with constant amplitude. In contrast, Kausel and Roësset [18], and later Kausel *et al.* [19], use a three-step or substructure approach that makes it possible to break the solution of the soil-structure interaction problem into three steps, considering kinematic interaction. The effects of the foundation embedment considering both kinematic and inertial interaction were taken into account by Avilés and Pérez-Rocha [14] (for 3D rectangular foundations), by Avilés and Suárez [20] (for axisymmetrical embedded foundations in a layer), and by Todorovska [16] and Todorovska and Trifunac [17, 21] who presented a 2D model with analytical solutions for impedances and kinematic effects for very long buildings founded on rigid cylindrical foundations. Also, Todorovska and Trifunac [17, 21] and Avilés *et al.* [15] for problems with square embedded foundations, studied the effects of the type of waves and their angle of incidence on the system frequency and damping.

Regarding pile-supported buildings, there are few studies in the scientific literature examining the effects of SSI on their dynamic characteristics [22–30]. Rainer [22] used a substructuring methodology to analyse the modal damping of a superstructure supported on piles. Kaynia and Mahzooni [23] used a three-dimensional Green's functions-based formulation, for the pile foundation, and a single-degree-of-freedom (SDOF) model for the structure, in order to calculate the seismic shear forces in the piles during the seismic kinematic and inertial interaction phases for different pile foundations. On the other hand, Aguilar and Avilés [26] analysed piled foundations by extending the Avilés and Pérez-Rocha's [14] procedure for embedded foundations and thus they studied the SSI effects on the system period and damping for a specific configuration of 8×8 piles neglecting kinematic interaction effects. For the purpose of obtaining manageable approximated expressions for the period and damping of the interacting system, Avilés and Pérez-Rocha [14] adopted a simplification which consists in neglecting the cross-coupled horizontal-rocking terms of the impedance matrix and then also the high-order terms involving products of damping coefficients in the resulting expressions. Such assumption has been extensively used by many authors [6–13, 31]. However, neglecting the cross-coupled horizontal-rocking stiffness and damping terms is not acceptable for pile foundations, not even for certain configurations of embedded foundations. Therefore, in order to consider crossed-coupled impedances, some authors [27, 32] propose to condense the soil-foundation interaction to a point at a certain virtual depth such that the impedance matrix becomes diagonal. Maravas *et al.* [27] presented a simple methodology in order to study SSI effects on single-pile supported one-storey shear structures by obtaining its period and damping. However, there are no parametric studies of this nature for piled foundations consisting of a variable number of piles, with different embedment and spacing between them.

In regard to pile groups including battered elements, until today, it has not been clarified whether the use of inclined piles has a detrimental or beneficial effect on the response of the superstructure or the foundation itself when submitted to seismic loads. Related studies have been conducted in order to identify the drawbacks and advantages of battered piles. Pioneering works in this line are those presented by Banerjee and Driscoll [33] and Poulos and Davis [34], which suggest that further research needs to be undertaken to better understand the behaviour of this type of foundations. Some authors [35–37] developed numerical analyses that point to the larger axial loads along the pile shaft, as well as to the increasing bending moment at the pile head, as arguments to use vertical piles instead of inclined piles for seismic loads. Other results discouraging the use of inclined piles in seismic areas are those provided by Neely [38] and Ravazi *et al.* [39]. Conversely, field evidence of the beneficial role of battered piles has been found both for the structure they support and for the piles themselves [40, 41]. These conclusions are in line with those inferred from different numerical analyses [42–44]. This fact, explains why the research on the topic has boosted in the last years (see, for instance, [45–55]). However, only Gerolymos *et al.* [44] and Giannakou *et al.* [48] have analysed the influence of using deep foundations with inclined piles on the dynamic response of the supported structures.

Impedances and kinematic interaction factors are key and non-trivial aspects of the soil-structure interaction problem. They can be used to analyse SSI effects on structures making use of substructure approaches as done in [23, 24, 56] for pile-supported structures. Different expressions and graphs are available in the literature for certain configurations. However, in general, obtaining accurate values for a particular case requires the use of sophisticated numerical models that allow incorporating the foundation-soil interaction in a rigorous manner.

A large number of works address the computation of impedance functions (dynamic stiffness) of piles and pile groups. For example, analytical expressions for single floating piles are reported by Gazetas [57], while Dobry and Gazetas [58] present expressions for pile groups using group factors that are an extension of those obtained for static problems by Poulos [59]. Other researches related to impedance expressions have been carried out by Konagai *et al.* [60], Taherzadeh *et al.* [61] or Dai and Roësset [62]. Different numerical techniques have also been used to determine the dynamic stiffness of pile foundations. For example, a computational procedure based on a finite element model is used by Wolf *et al.* [63] to obtain frequency-dependent dynamic stiffness of single piles and foundations with 2×2 and 10×10 piles embedded in stratified soils. Kaynia [64] obtained dynamic stiffnesses and kinematic interaction factors for several configurations of pile groups embedded in a homogeneous half-space by using a formulation based on Green's functions. Velez *et al.* [65] used a finite element formulation to compute the dynamic stiffness and damping of single piles. Dynamic stiffnesses and dampings of single piles as well as those corresponding to 2×2 and 4×4 pile groups were computed by Miura *et al.* [66] through a 3D formulation based on Green's functions. Horizontal and rocking impedances for 5×5 pile groups were computed by Kaynia and Mahzooni [23] through a formulation previously proposed by Kaynia and Kausel [67]. A boundary element code presented by Aznárez [68] was used by Vinciprova *et al.* [69] and Maeso *et al.* [70] to obtain impedances of piles and pile groups embedded in viscoelastic and poroelastic soils. Padrón *et al.* [71] provided impedance functions corresponding to several

configurations of pile groups, computed by using a three-dimensional boundary element (BEM)- finite element (FEM) coupling model.

With regard to inclined piles, Mamoon *et al.* [72] presented dynamic stiffnesses for a specific configuration of 3×3 pile group. Later, Giannakou *et al.* [46] used a 3-D finite-element model to obtain impedance functions of a single pile embedded in a homogeneous or non-homogeneous soil. Impedance functions for several configurations of 2×2 and 3×3 pile groups including inclined piles were presented by Padrón *et al.* [49].

In regard to kinematic interaction factors, and with respect to numerical research, several studies have also been carried out for piled foundations using only vertical piles. Gazetas [73] provided kinematic interaction factors for end-bearing single piles embedded in different soils and subjected to vertically incident S-waves. Mamoon and Ahmad [74], as well as Mamoon and Benerjee [75], presented pioneer works in which the response of single piles and pile foundations subjected to vertically and obliquely incident waves is analysed in terms of kinematic interaction factors. This problem was studied also for Rayleigh waves by Makris and Badoni [76]. One of the most comprehensive analyses were addressed by Kaynia and Novak [77], in which kinematic interaction factors corresponding to several pile group configurations subjected either to obliquely incident body waves or to Rayleigh waves were obtained. Other works providing kinematic interaction factors for pile foundations are, for instance, those presented by Kaynia [64], Fan *et al.* [78], Gazetas *et al.* [79], Kavvadas and Gazetas [80] and Padrón [81].

Although other authors have accomplished analyses of the kinematic response of battered piles (*e.g.* [37, 82]), kinematic interaction factors of inclined piles have been presented only by Giannakou [47] for groups of 2×1 piles. Therefore, it is apparent that further research is needed in this aspect.

The research work presented in this Ph. D. thesis is inscribed in a research line that has been developed, for about the last 20 years, at the Continuum Mechanics and Structures Division of the University Institute of Intelligent Systems and Numerical Applications in Engineering (SIANI) at the University of Las Palmas de Gran Canaria. This line started in the late 1970s, in the research group led by Professor José Domínguez at the University of Seville, with the pioneering works developed by Domínguez [83] and Domínguez and Alarcón [84]. These cited works address the application of the direct boundary element method to elastodynamic problems. In subsequent years, this group developed several relevant works in this line (see, for instance, [85–88]). A detailed compendium of the work done in this research line at the University of Seville until 1993 can be found in [89]. A three-dimensional multidomain boundary element code in the frequency domain [90–92], developed by Professors Orlando Maeso and José Domínguez, resulted from the fruitful collaboration between the University of Seville and the University of Las Palmas de Gran Canaria. Following this line, a boundary element code that allows analysing the seismic response of arch dams with porous sediments [93–96], as well as computing impedances of piles and pile groups in viscoelastic and poroelastic soils [69, 70], was presented in the Ph. D. thesis of Juan J. Aznárez [68]. In order to simplify this methodology, and also to reduce its computational cost without losing rigour, the Ph. D. thesis of Luis A. Padrón [81] dealt with the formulation and implementation of a model in which piles are modelled using finite elements as beams according to the Bernoulli hypothesis, while soil is modelled using boundary elements. This three-dimensional harmonic coupling model allows the study of the dynamic behaviour of pile foundations [71]. Later, it has been extended to address the dynamic analysis of pile

foundations including battered elements [49]. Moreover, it has also been used to tackle the study of the dynamic response of the superstructure, as well as to analyse the interaction phenomena between nearby structures [97]. Subsequently, this code has been used to analyse how the type of seismic body wave and its angle of incidence influence bending moments at cap level of single piles and 3×3 pile groups [98].

1.3 Aims and objectives

This research work aims to take advantage of the BEM-FEM coupling model developed by Padrón *et al.* for the purpose of computing impedances and kinematic interaction factors for several configurations of pile foundations, in order to perform parametric studies using substructuring techniques. As it is true that numerous references deal with the use of substructuring methodologies in the analysis of the dynamic response of structures supported by shallow or embedded foundations, it is likewise so that the literature is sparse on the study of the dynamic behaviour of pile-supported structures. Therefore, following the reference works for shallow and embedded foundations systems, the main objective of this Ph. D. thesis is to develop a procedure, based on a substructure model, which allows us to evaluate the influence of SSI on the dynamic behaviour of shear structures founded on square pile groups.

The effective period and damping of the interacting system [7, 12–14, 21] represent the dynamic parameters of an equivalent viscously damped SDOF system excited by the free-field ground motion. This replacement oscillator should reproduce, as accurately as possible, the coupled system response within the range where the peak response occurs. This work aims at developing a simple and stable procedure, in the frequency domain, for the estimation of periods and dampings of shear buildings supported on piles, taking into account both kinematic and inertial interaction effects. To this end, a comparative review of the different strategies used in the literature for establishing this equivalence and calculating the parameters of the above-mentioned SDOF system must be performed in order to identify those that best suit to the problem under study. Furthermore, the simplifications adopted for shallow and embedded foundations by many authors [6–13, 31] should be analysed to determine if they are applicable to pile foundations and how they affect the accuracy of the results. In this line, the influence of considering the cross-coupled impedances and the kinematic interaction factors, for the case of pile group configurations, must also be studied.

The accuracy of the proposed procedure will be assessed through comparisons with the solution obtained from the iterative resolution of a complex-valued system of equations, which represents the equation of motion of the interacting system.

Once the model is formulated and validated, the objective is to perform parametric analyses, considering a set of configurations of pile groups, for the purpose of studying the influence of SSI on the seismic response of the superstructure. The idea is to express all equations in terms of the main dimensionless parameters of the problem, in order to facilitate the analysis of their influence on the system dynamic response.

The scope of this work also encompasses the study of deep foundations including battered piles. Thus, the analysis of the influence of the rake angle of piles on the dynamic behaviour of the superstructure will be accomplished, aiming at clarifying the beneficial or detrimental role of foundations comprising inclined piles.

1.4 Published works derived from this Ph. D. thesis

Published works derived from this Ph. D. thesis

The procedure proposed in this dissertation, as well as part of the results, have been previously presented in different journals and conferences [54, 55, 99–105]. Details concerning these research works are presented below.

1.4.1 Contributions in JCR journals

- Medina, C., Aznárez, J. J., Padrón, L. A. and Maeso, O. (2013) Effects of soil-structure interaction on the dynamic properties and seismic response of piled structures. *Soil Dynamics and Earthquake Engineering*, **53**, 160–175.
- Medina, C., Padrón, L. A. , Aznárez, J. J. , Santana, A. and Maeso, O. (2014) Kinematic interaction factors of deep foundations with inclined piles. *Earthquake Engineering and Structural Dynamics*, **43**, 2035–2050.
- Medina, C., Padrón, L. A. , Aznárez, J. J. and Maeso, O. (2015) Influence of pile inclination angle on the dynamic properties and seismic response of piled structures. *Soil Dynamics and Earthquake Engineering*, **69**, 196–206.

1.4.2 Conference contributions

- Medina, C., Padrón, L. A., Aznárez, J. J. and Maeso, O. (2011) Influencia de los fenómenos de interacción en las propiedades dinámicas de estructuras de edificación pilotadas. *Proceedings of the Congress on Numerical Methods in Engineering 2011*, Coimbra, Portugal, pp. 96–115.
- Medina, C., Aznárez, J. J., Padrón, L. A. and Maeso, O. (2013) A procedure for evaluating the soil-structure interaction effects on the system period and damping of pile-supported structures. *Proceedings of 4th ECCOMAS Thematic Conference on Computational Methods in Structural Dynamics and Earthquake Engineering, COMPDYN 2013*, Kos Island, Greece, pp. 4463–4487.
- Medina, C., Aznárez, J. J., Padrón, L. A. and Maeso, O. (2014) Influence of pile rake angle on the seismic response of pile foundations and piled structures. *Proceedings of the 9th International Conference on Structural Dynamics, EURODDYN 2014*, Porto, Portugal, pp. 733–740.
- Medina, C., Aznárez, J. J., Padrón, L. A. and Maeso, O. (2014) Seismic response of deep foundations and piled structures considering inclined piles. *Proceedings of the jointly organized 11th World Congress on Computational Mechanics (WCCM XI) and 5th European Congress on Computational Mechanics (ECCM V)*, Barcelona, Spain, pp. 453–463.
- Medina, C., Padrón, L. A., Aznárez, J. J. and Maeso, O. (2015) Respuesta sísmica de estructuras de edificación cimentadas sobre pilotes inclinados. *Proceedings of the Congress on Numerical Methods in Engineering*, Lisbon, Portugal, no. 237.

- Padrón, L. A., Medina, C., Álamo, G. M., Aznárez, J. J., Santana, A., Maeso, O., García, F. and Chirino, F. (2015) Pilotes inclinados: situación normativa y ventajas e inconvenientes de su uso en proyectos de edificación en zonas con riesgo sísmico. *Proceedings of the 19th International Congress on Project Management and Engineering*, Granada, Spain.

1.5 Structure of the dissertation

The present dissertation has been structured in 7 chapters. The core of the dissertation is addressed in chapter 2 and consists in the development of a simple and stable procedure for the estimation of the effective period and damping of linear shear structures supported on piles. The chapter begins outlining the basic concepts needed to understand the three-step or substructure approach used to model the problem in hand. Once the problem under investigation is defined in detail, the corresponding equations of motion are written. A semi-analytical model is used to identify the main dimensionless parameters characterizing the dynamic response of pile foundations. Then, given that hollow piles have been modelled in this work by equivalent solid piles, the accuracy of this approach is assessed. Afterwards, the different steps of the procedure followed to express the system equations of motion in terms of a set of dimensionless parameters, covering the main features of SSI problems, are explained. This considerably facilitates the analysis of the influence of each parameter on the system dynamic response. Then, the estimation of the dynamic characteristics of a SDOF system reproducing, in an accurate manner, the response of the coupled system within the range where the peak response occurs, is tackled. For this purpose, the different strategies previously proposed by other authors to establish this equivalence and determining the dynamic characteristics of the replacement oscillator are analysed and compared. In this line, the harmonic response spectra corresponding to the resulting SDOF systems, obtained by applying the different strategies to the case of pile foundations, are compared with the harmonic response spectrum of the interacting system in order to determine if the simplifying assumptions adopted in each one of them are suitable for pile-supported structures. Then, a modified strategy, yielding accurate results for structures supported by shallow, embedded or pile foundations, is proposed including cross-coupled horizontal-rocking impedances. Afterwards, the implementation in a code of the proposed procedure is explained. Finally, the validation of the proposed model is completed by comparing the obtained results with those previously provided by other authors for shallow and embedded foundations.

The boundary element (BEM)- finite element (FEM) coupling model used to compute the impedances and kinematic interaction factors of piled foundations is outlined in chapter 3. Likewise, the boundary element formulation that will be used in a later chapter to assess the accuracy of the BEM-FEM formulation, applied to the determination of kinematic interaction factors for deep foundations including inclined piles, is described.

The analysis of the influence of SSI on the dynamic behaviour of the superstructure through a procedure based on a substructure model, as that explained in chapter 2, requires that impedance functions and kinematic interaction factors are previously obtained. In this line, chapter 4 addresses the numerical computation of the impedance functions and kinematic interaction factors of pile foundations through the formulation

described in chapter 3. The geometrical configuration of the pile groups considered in this research are described, and the material properties corresponding to piles and soil are also defined at the beginning of this chapter. Then, the set of vertical pile group configurations considered in this study is defined. The corresponding impedance functions and kinematic interaction factors are provided in plots. Subsequently, impedances and kinematic interaction factors corresponding to several configurations comprising inclined piles are represented. These values are needed to accomplish substructuring analyses that allow determining how the variations of the rake angle of piles affect the dynamic response of the superstructure when considering SSI. The main trends observed in the dynamic behaviour of the soil-foundation system are analysed, both for vertical pile groups and for those including inclined elements.

Chapter 5 deals with the analysis of the effects of SSI on the dynamic properties and the seismic response of structures supported on vertical piles. The geometrical configuration, as well as the material properties of the cases under investigation, are presented at the beginning of the chapter. The values obtained in chapter 4 for impedance functions and kinematic interaction factors are used herein to perform several parametric analyses by using the procedure previously developed and validated in chapter 2. This way, a study of the influence of the main parameters of SSI problems on the dynamic response of the superstructure is accomplished. Results for 21 different configurations of 2×2 , 3×3 and 4×4 pile groups are analysed. Ready-to-use graphs are presented for the estimation of flexible-base period and damping in terms of their fixed-base values and the system configuration. Subsequently, this has allowed obtaining modified response spectra including SSI effects. Maximum shear forces together with base displacement and rocking peak response are also provided in plots. Furthermore, the importance of considering cross-coupled impedances and kinematic interaction factors is also investigated. This chapter finishes with the main conclusions drawn from the obtained results.

Chapter 6 investigates whether battered piles play a beneficial or detrimental role when submitted to dynamic loads, which still remains an open question. In this line, the contribution of this chapter focuses on the influence of pile rake angle on the seismic response of shear structures founded on square pile groups. To this end, results for several configurations of 2×2 and 3×3 pile groups including battered elements are obtained. As done in chapter 5 for vertical piles, results in terms of effective period and damping, and maximum shear force at the base of the structure, are depicted and analysed. Likewise, modified response spectra are built for different values of the rake angle. At the end of this chapter, the main conclusions drawn from the analysis of the results obtained for the cases under investigation are summarised.

Finally, the most relevant conclusions extracted from this work are summarised in chapter 7. The document finishes proposing future research developments that could follow this dissertation.



2. SUBSTRUCTURING METHODOLOGY

- 2.1 Introduction
- 2.2 The three-step approach
- 2.3 Problem definition
- 2.4 Substructure model
- 2.5 Main parameters characterizing piles dynamic behaviour
- 2.6 Influence of pile cross-section geometry on the dynamic behaviour of piles
- 2.7 System equations and dimensionless parameters
- 2.8 Diagonalization of the impedance matrix
- 2.9 Effective period and damping of the soil-foundation-structure coupled system
- 2.10 Implementation
- 2.11 Model validation

2.1 Introduction

Soil-structure interaction involves kinematic and inertial effects that affect the dynamic behaviour of the structures. Thus, a proper assessment of their dynamic response requires the development of models that incorporate, in a rigorous manner, the interaction between the structure and the soil on which it is founded. These interaction phenomena depend on factors such as: the foundation type, its geometry and embedment depth, the soil type, as well as the characteristics of the structure. In line with other authors' studies for shallow [7] and embedded foundations [14], a simple substructuring model of soil-structure interaction in the frequency domain is proposed in this chapter to evaluate the influence of the above-mentioned factors on the dynamic response of structures founded on pile groups and subjected to seismic loads.

Firstly, the substructuring methodology used herein is outlined in section 2.2. Afterwards, the problem under investigation is defined in section 2.3. Then, the substructure model used in this work is presented in section 2.4. A simple semi-analytical model is used in section 2.5 in order to determine the main dimensionless parameters characterizing the dynamic behaviour of pile groups. Then, in order to validate a simplification used in this investigation consisting in modelling the annular cross-section of piles by using an equivalent solid circular section, the accuracy of the results in terms of impedances and kinematic interaction factors is assessed in section 2.6. Afterwards, the dimensionless equations of motion of the system are expressed in terms of a set of parameters characterizing the SSI problem. These parameters are defined in section 2.7. Subsequently, section 2.8 addresses the diagonalization of the impedance matrix which allows obtaining manageable expressions for the shear force at the base of the structure. The strategies previously proposed by other authors for establishing an equivalence between the interacting system and a SDOF replacement oscillator, and determining its dynamic characteristics, are analysed in section 2.9. Then, in this section, a simple and stable procedure is proposed for the estimation of periods and dampings of pile shear buildings, taking SSI into account and considering crossed impedances as well as all damping terms. Section 2.10 deals with the implementation of this procedure. Finally, the validation of the proposed model is addressed in section 2.11, through comparison against results obtained by other authors for shallow and embedded foundations.

2.2 The three-step approach

In this section, a basic problem of structural dynamics, sketched in figure 2.1, is used to explain the substructure approach employed in this work to tackle the soil-structure-interaction problem. As indicated in this figure, the soil and the structure are represented by monodimensional elements subjected to bending. These elements, which are assumed to be axially inextensible, are connected by an infinitely rigid slab representing the foundation. The foundation mass m_o is presumed to be uniformly distributed over a square area. The moment of inertia of this slab is denoted by I_o . The mass matrices corresponding to the soil and the structure are represented by \mathbf{M}^s and \mathbf{M}^{str} , respectively. In this case, vertical displacement and rocking are restricted at the base, and the whole system is subjected to a horizontal displacement at the base denoted by δ_1 .

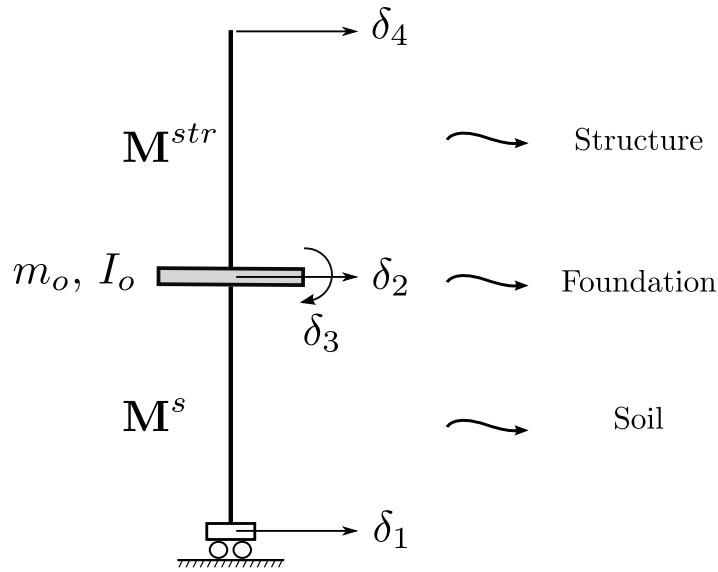


FIGURE 2.1: Direct approach.

2.2.1 Direct approach

The behaviour of the system represented in figure 2.1 may be approximated by that of a three-degree-of-freedom (3DOF) system, defined by the foundation horizontal displacement δ_2 and rocking δ_3 , together with the horizontal displacement at the top of the structure δ_4 . The equation of motion corresponding to the lower element can be written as

$$\begin{bmatrix} K_{22}^s & K_{23}^s \\ K_{32}^s & K_{33}^s \end{bmatrix} \cdot \begin{bmatrix} \delta_2 - \delta_1 \\ \delta_3 \end{bmatrix} - \omega^2 \begin{bmatrix} m_{21}^s & m_{22}^s & m_{23}^s \\ m_{31}^s & m_{32}^s & m_{33}^s \end{bmatrix} \cdot \begin{bmatrix} \delta_1 \\ \delta_2 \\ \delta_3 \end{bmatrix} = \begin{bmatrix} f_2^s \\ f_3^s \end{bmatrix} \quad (2.1)$$

Likewise, the equation of motion of the upper element can be expressed as

$$\begin{bmatrix} K_{22}^{str} & K_{23}^{str} & K_{24}^{str} \\ K_{32}^{str} & K_{33}^{str} & K_{34}^{str} \\ K_{42}^{str} & K_{43}^{str} & K_{44}^{str} \end{bmatrix} \cdot \begin{bmatrix} \delta_2 \\ \delta_3 \\ \delta_4 \end{bmatrix} - \omega^2 \begin{bmatrix} m_{22}^{str} & m_{23}^{str} & m_{24}^{str} \\ m_{32}^{str} & m_{33}^{str} & m_{34}^{str} \\ m_{42}^{str} & m_{43}^{str} & m_{44}^{str} \end{bmatrix} \cdot \begin{bmatrix} \delta_2 \\ \delta_3 \\ \delta_4 \end{bmatrix} = \begin{bmatrix} f_2^{str} \\ f_3^{str} \end{bmatrix} \quad (2.2)$$

Finally, the system equation of motion can be obtained by adding equations (2.1) and (2.2), incorporating the foundation rotational inertia I_o as well as the foundation mass m_o , yielding the following equation:

$$\begin{aligned}
 & \left\{ \begin{bmatrix} K_{22}^s + K_{22}^{str} & K_{23}^s + K_{23}^{str} & K_{24}^{str} \\ K_{32}^s + K_{32}^{str} & K_{33}^s + K_{33}^{str} & K_{34}^{str} \\ K_{42}^{str} & K_{43}^{str} & K_{44}^{str} \end{bmatrix} \right. \\
 & \left. - \omega^2 \begin{bmatrix} m_{22}^s + m_{22}^{str} + m_o & m_{23}^s + m_{23}^{str} & m_{24}^{str} \\ m_{32}^s + m_{32}^{str} & m_{33}^s + m_{33}^{str} + I_o & m_{34}^{str} \\ m_{42}^{str} & m_{43}^{str} & m_{44}^{str} \end{bmatrix} \right\} \cdot \begin{bmatrix} \delta_2 \\ \delta_3 \\ \delta_4 \end{bmatrix} \\
 & = \begin{bmatrix} K_{22}^s \\ K_{32}^s \\ 0 \end{bmatrix} \cdot \delta_1 + \omega^2 \begin{bmatrix} m_{21}^s \\ m_{31}^s \\ 0 \end{bmatrix} \cdot \delta_1
 \end{aligned} \tag{2.3}$$

or, alternatively, as

$$\begin{aligned}
 & \left\{ \begin{bmatrix} K_{22}^s & K_{23}^s & 0 \\ K_{32}^s & K_{33}^s & 0 \\ 0 & 0 & 0 \end{bmatrix} - \omega^2 \begin{bmatrix} m_{22}^s & m_{23}^s & 0 \\ m_{32}^s & m_{33}^s & 0 \\ 0 & 0 & 0 \end{bmatrix} \right\} \cdot \begin{bmatrix} \delta_2 \\ \delta_3 \\ \delta_4 \end{bmatrix} \\
 & + \left\{ \begin{bmatrix} K_{22}^{str} & K_{23}^{str} & K_{24}^{str} \\ K_{32}^{str} & K_{33}^{str} & K_{34}^{str} \\ K_{42}^{str} & K_{43}^{str} & K_{44}^{str} \end{bmatrix} - \omega^2 \begin{bmatrix} m_{22}^{str} + m_o & m_{23}^{str} & m_{24}^{str} \\ m_{32}^{str} & m_{33}^{str} + I_o & m_{34}^{str} \\ m_{42}^{str} & m_{43}^{str} & m_{44}^{str} \end{bmatrix} \right\} \cdot \begin{bmatrix} \delta_2 \\ \delta_3 \\ \delta_4 \end{bmatrix} \\
 & = \begin{bmatrix} K_{22}^s \\ K_{32}^s \\ 0 \end{bmatrix} \cdot \delta_1 + \omega^2 \begin{bmatrix} m_{21}^s \\ m_{31}^s \\ 0 \end{bmatrix} \cdot \delta_1
 \end{aligned} \tag{2.4}$$

2.2.2 Substructure approach

The problem depicted in figure 2.1 can be alternatively addressed through a substructure approach. According to Kausel and Roësset [18], the solution can be broken into three steps.

In the first step, as shown in figure 2.2, the horizontal displacement δ_2^{KI} and rocking δ_3^{KI} of the massless rigid slab, when subjected to the input motion δ_1 , is determined. Assuming that $f_2^s = 0$ and $f_3^s = 0$, yields

$$\begin{bmatrix} K_{22}^s & K_{23}^s \\ K_{32}^s & K_{33}^s \end{bmatrix} \cdot \begin{bmatrix} \delta_2^{KI} - \delta_1 \\ \delta_3^{KI} \end{bmatrix} - \omega^2 \begin{bmatrix} m_{21}^s & m_{22}^s & m_{23}^s \\ m_{31}^s & m_{32}^s & m_{33}^s \end{bmatrix} \cdot \begin{bmatrix} \delta_1 \\ \delta_2^{KI} \\ \delta_3^{KI} \end{bmatrix} = \begin{bmatrix} 0 \\ 0 \end{bmatrix} \tag{2.5}$$

or

$$\left\{ \begin{bmatrix} K_{22}^s & K_{23}^s \\ K_{32}^s & K_{33}^s \end{bmatrix} - \omega^2 \begin{bmatrix} m_{22}^s & m_{23}^s \\ m_{32}^s & m_{33}^s \end{bmatrix} \right\} \cdot \begin{bmatrix} \delta_2^{KI} \\ \delta_3^{KI} \end{bmatrix} = \left\{ \begin{bmatrix} K_{22}^s \\ K_{32}^s \end{bmatrix} + \omega^2 \begin{bmatrix} m_{21}^s \\ m_{31}^s \end{bmatrix} \right\} \delta_1 \quad (2.6)$$

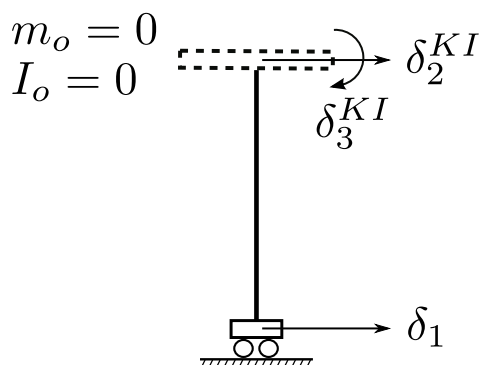


FIGURE 2.2: Step 1. Kinematic interaction.

The second step consists in computing the stiffness and damping of the lower element in the horizontal (K_{22}^s), rocking (K_{33}^s) and cross-coupled horizontal-rocking (K_{23}^s and K_{32}^s) vibration modes. For this purpose, all motions are restricted at the bottom of the lower element and a unitary displacement or rocking is applied at the top. The problem solved in this step is sketched in figure 2.3.

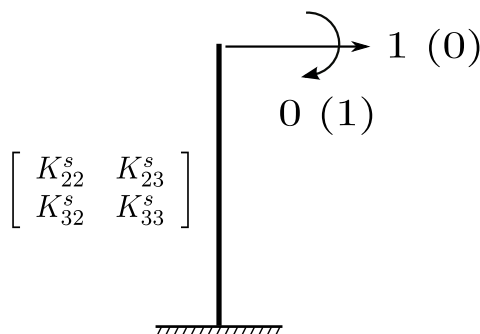


FIGURE 2.3: Step 2. Impedance functions.

The equation of motion corresponding to this step can be written as

$$\left\{ \begin{bmatrix} K_{22}^s & K_{23}^s \\ K_{32}^s & K_{33}^s \end{bmatrix} - \omega^2 \begin{bmatrix} m_{22}^s & m_{23}^s \\ m_{32}^s & m_{33}^s \end{bmatrix} \right\} \cdot \begin{bmatrix} \delta_2 \\ \delta_3 \end{bmatrix} = \begin{bmatrix} f_2^s \\ f_3^s \end{bmatrix} \quad (2.7)$$

Finally, as depicted in figure 2.4, the inertial interaction is considered by assuming the upper element supported on springs and subjected to the motion computed in the first step, which results from kinematic interaction.

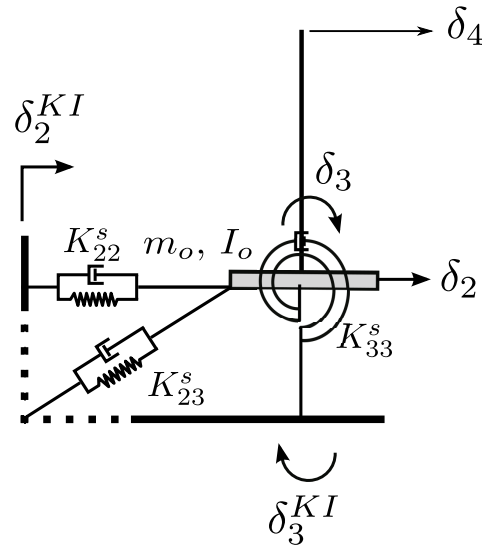


FIGURE 2.4: Step 3. Inertial interaction.

The equation of motion of the upper element was already written in equation (2.2). On the other hand, the equation corresponding to the lower part of the system shown in figure 2.4 can be expressed as

$$\left\{ \begin{bmatrix} K_{22}^s & K_{23}^s \\ K_{32}^s & K_{33}^s \end{bmatrix} - \omega^2 \begin{bmatrix} m_{22}^s & m_{23}^s \\ m_{32}^s & m_{33}^s \end{bmatrix} \right\} \cdot \begin{bmatrix} \delta_2 - \delta_2^{KI} \\ \delta_3 - \delta_3^{KI} \end{bmatrix} = \begin{bmatrix} f_2^s \\ f_3^s \end{bmatrix} \quad (2.8)$$

By adding equations (2.2) and (2.8), and incorporating the foundation rotational inertia I_o as well as the foundation mass m_o , the following equation is obtained:

$$\begin{aligned} & \left\{ \begin{bmatrix} K_{22}^s & K_{23}^s & 0 \\ K_{32}^s & K_{33}^s & 0 \\ 0 & 0 & 0 \end{bmatrix} - \omega^2 \begin{bmatrix} m_{22}^s & m_{23}^s & 0 \\ m_{32}^s & m_{33}^s & 0 \\ 0 & 0 & 0 \end{bmatrix} \right\} \cdot \begin{bmatrix} \delta_2 \\ \delta_3 \\ \delta_4 \end{bmatrix} \\ + & \left\{ \begin{bmatrix} K_{22}^{str} & K_{23}^{str} & K_{24}^{str} \\ K_{32}^{str} & K_{33}^{str} & K_{34}^{str} \\ K_{42}^{str} & K_{43}^{str} & K_{44}^{str} \end{bmatrix} - \omega^2 \begin{bmatrix} m_{22}^{str} + m_o & m_{23}^{str} & m_{24}^{str} \\ m_{32}^{str} & m_{33}^{str} + I_o & m_{34}^{str} \\ m_{42}^{str} & m_{43}^{str} & m_{44}^{str} \end{bmatrix} \right\} \cdot \begin{bmatrix} \delta_2 \\ \delta_3 \\ \delta_4 \end{bmatrix} \\ = & \left\{ \begin{bmatrix} K_{22}^s & K_{23}^s \\ K_{32}^s & K_{33}^s \end{bmatrix} - \omega^2 \begin{bmatrix} m_{22}^s & m_{23}^s \\ m_{32}^s & m_{33}^s \end{bmatrix} \right\} \cdot \begin{bmatrix} \delta_2^{KI} \\ \delta_3^{KI} \end{bmatrix} \end{aligned} \quad (2.9)$$

The left-hand side of equation (2.9) matches that of equation (2.4). According to equation (2.6), the right-hand side of equation (2.9) and that of equation (2.4) are equivalent. Thus, the simple problem analysed in this section allows us to prove that the direct approach and the three-step approach lead to identical system equations of motion.

2.3 Problem definition

The dynamic response of pile-supported shear structures in the linear range is investigated in this work making use of a single-degree-of-freedom system in its fixed-base condition, as the one depicted in figure 2.5, that may represent either one-storey structures or one mode of vibration of multi-storey buildings. The superstructure can be defined by its fixed-base period T , its mass m , the structural stiffness k , the height h of the resultant of the inertia forces for the mode, the moment of inertia of the vibrating mass I , and the viscous damping ratio ξ . The structure is considered to be founded on a square pile group embedded in a homogeneous, viscoelastic and isotropic half-space, as depicted in figure 2.5. It is assumed that the pile heads are constrained by a rigid pile cap, considered as a rigid square plate of negligible thickness, which is not in contact with the half-space. The moment of inertia of this pile cap is denoted by I_o . All piles have identical geometrical properties defined by length L and sectional diameter d . Several configurations of pile groups have been considered in this study. Each one of them is defined by number of piles, foundation halfwidth b , centre-to-centre spacing between adjacent piles s and rake angle of piles θ . The columns of the structure are assumed to be massless and axially inextensible. Both the foundation mass and the mass of the structure are presumed to be uniformly distributed over identical square areas. This model of the foundation-structure system is an enhancement of that which appears to have been first used by Parmelee [1] in 1967 for shallow foundations and, according to Veletsos and Meek [7], has formed the basis of most subsequent investigations.

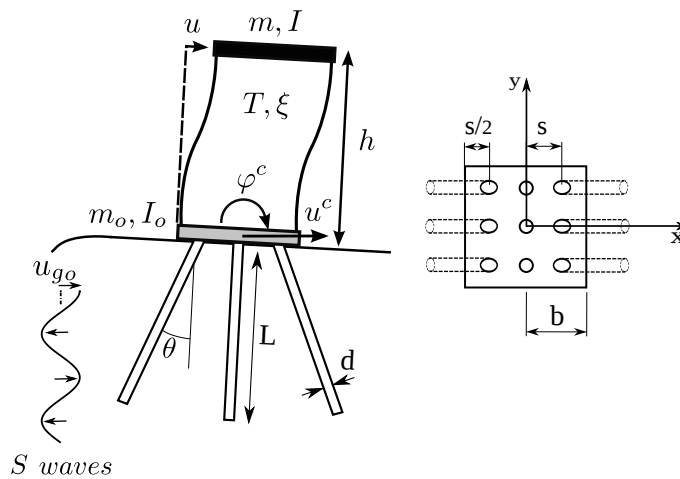


FIGURE 2.5: Problem definition. Single shear structure supported on a piled foundation embedded in a homogeneous half-space under vertically-incident S waves.

If SSI is taken into account, the system behaviour can be approximated by that of a three-degree-of-freedom (3DOF) system, defined by the foundation horizontal displacement u^c and rocking φ^c , together with the structural horizontal deflection u . (Note that rocking of pile cap and structure are identical). The system is subjected to vertically-incident plane S waves. Because of the characteristics of the structural model and the wave excitation, the vertical and torsional motions are neglected in this study.

2.4 Substructure model

The problem described in section 2.3 can be studied using a substructure approach, in which the system is subdivided into *building-cap* superstructure and *soil-foundation* stiffness and damping, represented by means of springs and dashpots, as shown in figure 2.6 (b).

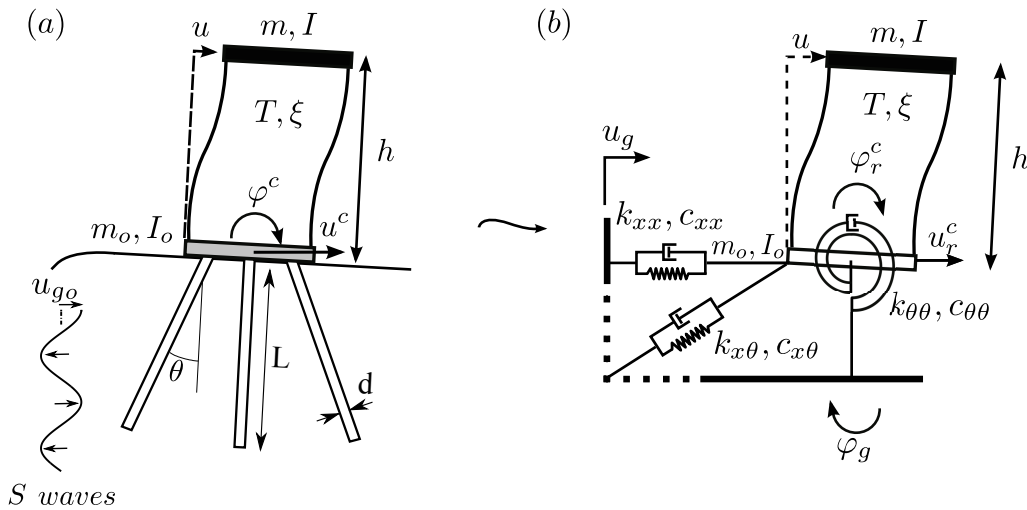


FIGURE 2.6: (a) Problem definition. (b) Substructure model of a one-storey structure.

According to Kausel and Roësset [18], the solution can be broken into three steps. This substructure approach was explained in section 2.2 for the case of a simple problem of structural dynamics depicted on the left side of figure 2.7. This figure illustrates the analogy between that problem and the SSI problem addressed in this work.

1. **Kinematic interaction.** In the present case, the first step consists in the determination of the motion of the massless pile cap when subjected to the same input motion as the total solution. Even for vertically-incident harmonic plane S waves (in which the free-field displacement at the ground surface is exclusively horizontal), this frequency dependent kinematic interaction factors are represented by horizontal (u_g) and rocking (φ_g) motions at the pile cap.
2. **Impedance functions.** The second step is to determine the impedances, which are complex-valued frequency-dependent functions (k_{xx}, c_{xx}), ($k_{\theta\theta}, c_{\theta\theta}$) and ($k_{x\theta}, c_{x\theta}$) that represent the stiffness and damping of the soil in the horizontal, rocking and cross-coupled horizontal-rocking vibration modes, respectively. The mathematical representation of impedance functions is $K_{ij} = k_{ij} + ia_o c_{ij}$, where $a_o = \omega b/c_s$; being i the imaginary unit $i = \sqrt{-1}$, ω the excitation circular frequency, $c_s = \sqrt{\mu_s/\rho_s}$ the speed of propagation of shear waves in the halfspace, and μ_s and ρ_s the soil shear modulus of elasticity and mass density, respectively.
3. **Inertial interaction.** Finally, the last step consists in the computation of the response at each frequency of the structure supported on springs and subjected to the motion computed in the first step.

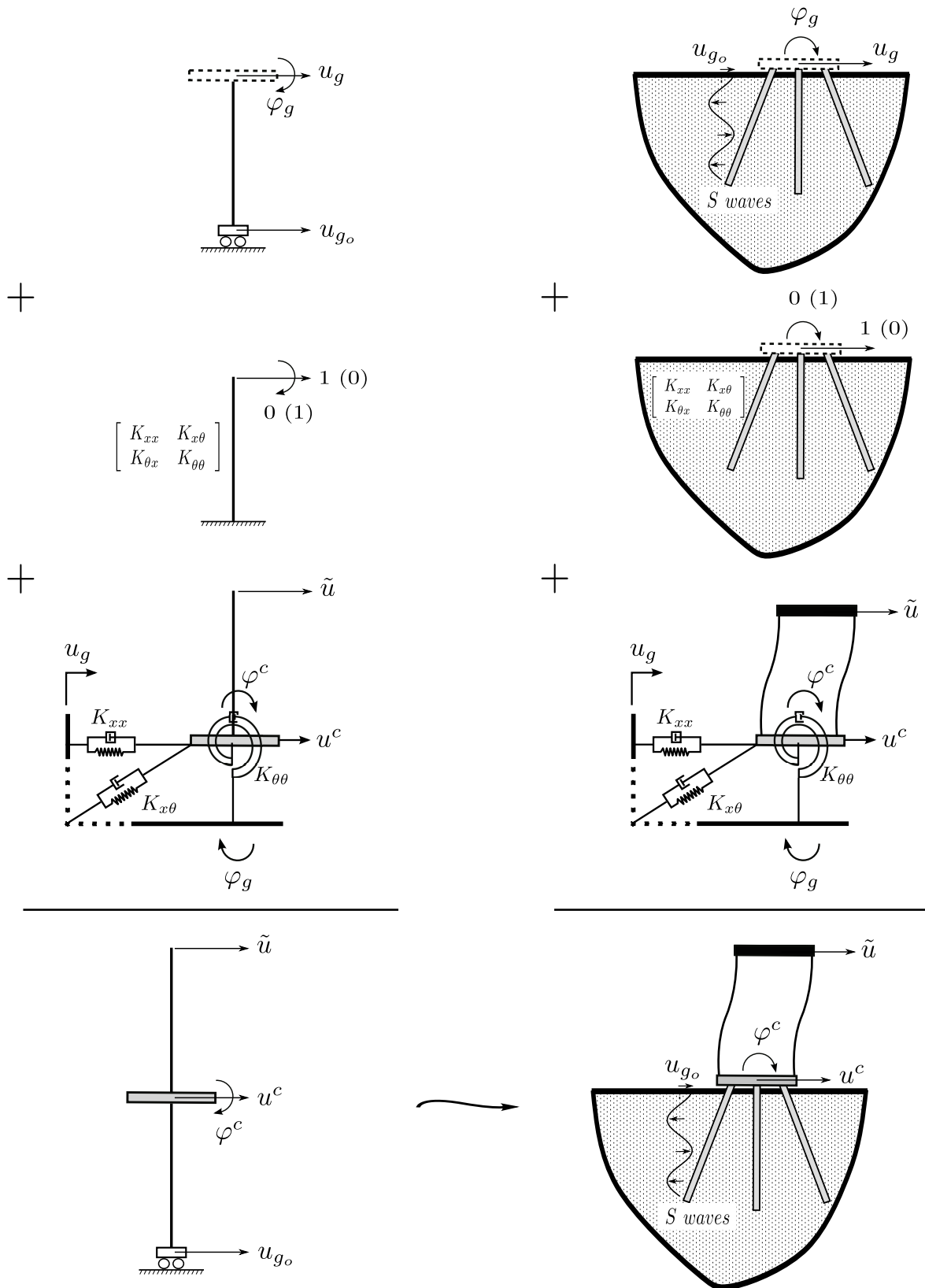


FIGURE 2.7: The three-step approach.

2.4.1 Equations of motion

The equations of motion of the system shown in figure 2.6(b), assuming small displacements, can be written in terms of relative motions, $u_r^c = u^c - u_g$ and $\varphi_r^c = \varphi^c - \varphi_g$, as

$$m \cdot [\ddot{u} + \ddot{u}_r^c + \ddot{u}_g + h(\ddot{\varphi}_r^c + \ddot{\varphi}_g)] + K \cdot u = 0 \quad (2.10)$$

$$m_o \cdot [\ddot{u}_r^c + \ddot{u}_g] + K_{xx} \cdot u_r^c + K_{x\theta} \cdot \varphi_r^c - K \cdot u = 0 \quad (2.11)$$

$$m \cdot h[\ddot{u} + \ddot{u}_r^c + \ddot{u}_g + h(\ddot{\varphi}_r^c + \ddot{\varphi}_g)] + I(\ddot{\varphi}_r^c + \ddot{\varphi}_g) + K_{\theta x} \cdot u_r^c + K_{\theta\theta} \cdot \varphi_r^c + I_o(\ddot{\varphi}_r^c + \ddot{\varphi}_g) = 0 \quad (2.12)$$

where equation (2.10) represents the horizontal force equilibrium of the vibrating mass, equation (2.11) the horizontal force equilibrium of the *soil-foundation* system and equation (2.12) the moment equilibrium of the *structure-foundation* system about the centre of gravity of the pile cap. Dots indicate time derivatives. In the frequency domain (with time dependance $e^{i\omega t}$), this set of equations can be expressed in a matrix form as

$$\left\{ \left[\begin{array}{ccc} K & 0 & 0 \\ -K & K_{xx} & K_{x\theta} \\ 0 & K_{\theta x} & K_{\theta\theta} \end{array} \right] - \omega^2 \left[\begin{array}{ccc} m & m & mh \\ 0 & m_o & 0 \\ mh & mh & I_T \end{array} \right] \right\} \cdot \left[\begin{array}{c} u \\ u_r^c \\ \varphi_r^c \end{array} \right] = \omega^2 \left\{ \left[\begin{array}{c} m \\ m_o \\ mh \end{array} \right] u_g + \left[\begin{array}{c} mh \\ 0 \\ I_T \end{array} \right] \varphi_g \right\} \quad (2.13)$$

where $I_T = m h^2 + I_o + I$ and $K = k + i2\omega_n m \xi \omega$, being $\omega_n = 2\pi/T$ the fixed-base natural frequency of the superstructure. Once the foundation input motion is computed and the right-hand vector and the coefficient matrix are known, the structural deflection and foundation relative motions can be computed in the frequency range of interest.

2.5 Main parameters characterizing piles dynamic behaviour

This section outlines the procedure followed in identifying the main dimensionless parameters characterizing the dynamic behaviour of a single pile when considering soil-structure interaction. This will make it possible to express the system equations of motion in equation (2.13) as a function of these parameters, which in turn allows performing parametric analyses in order to determine how the variations of each one of them affect the system dynamic response.

Figure 2.8 shows a simplified model based on the Winkler approach for embedded beams, which is used in this section to identify the parameters on which depends the pile dynamic response. This type of models have been previously used by other authors to obtain impedance functions and kinematic interaction factors of piled foundations [79, 80, 106–113]. In this model, the soil is represented by means of springs and

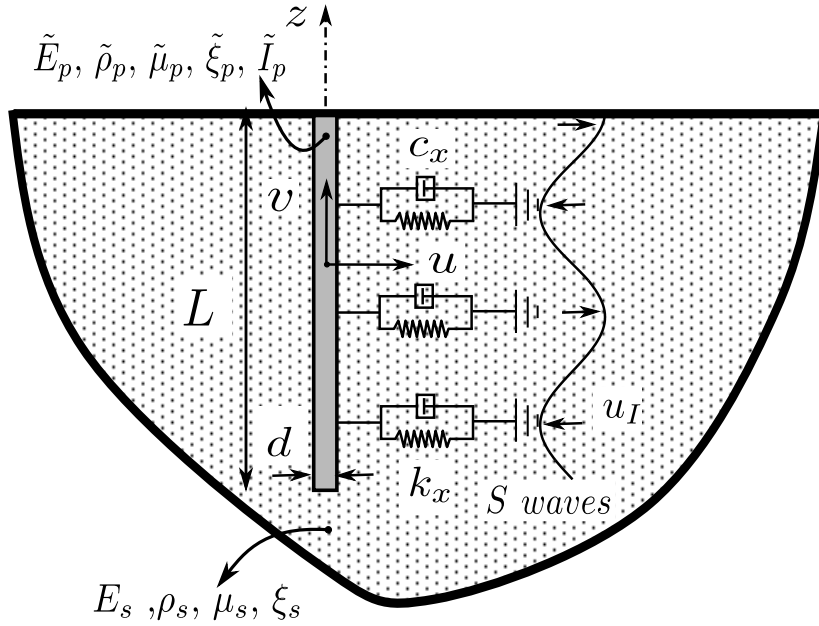


FIGURE 2.8: Beam on Dynamic Winkler Foundation.

dashpots continually distributed along the pile length and characterized by impedances which oppose horizontal displacement $K_x = k_x + i\omega c_x$. k_x and c_x represent, respectively, the soil stiffness and damping, $i = \sqrt{-1}$ is the imaginary unit and ω is the excitation circular frequency. The soil material properties are: Young's module E_s , mass density ρ_s , shear modulus of elasticity μ_s and damping coefficient ξ_s . On the other hand, the pile is modelled as an Euler-Bernoulli beam subjected to a vertically incident SH wave field denoted by u_I . The pile geometry is defined by the pile length L and external diameter d , and its cross-section is characterized by its area \tilde{A}_p and rotational inertia \tilde{I}_p . The pile material properties are: Young's module \tilde{E}_p , mass density $\tilde{\rho}_p$, shear modulus of elasticity $\tilde{\mu}_p$, and damping coefficient $\tilde{\xi}_p$. Finally, $u = u(\omega, z)$ and $v = v(\omega, z)$ represent, respectively, the horizontal and vertical displacements at any point of the pile.

Considering as external forces acting on the section, the inertia forces and those caused by an incident wave field acting on springs and dashpots, the dynamic equilibrium equation for a differential portion of the pile subjected to bending can be expressed as

$$\tilde{E}_p \tilde{I}_p \frac{\partial^4 u}{\partial z^4} + (K_x - \tilde{\rho}_p \tilde{A}_p \omega^2) u = K_x u_I \quad (2.14)$$

where the vertically incident SH waves field u_I has the following expression:

$$u_I = \frac{1}{2} \left(e^{-i\kappa(z-z_s)} + e^{i\kappa(z-z_s)} \right) \quad (2.15)$$

being $\kappa = \omega/c_s$ the angular wave-number and z_s the free-surface coordinate.

A vertical pile, as that shown in figure 2.8, is subjected to bending. However, the more inclined the more the pile works axially according to the following equation:

$$\tilde{\mu}_p \tilde{A}_p \frac{\partial^2 v}{\partial z^2} + (K_z - \tilde{\rho}_p \tilde{A}_p \omega^2) v = K_z v_I \quad (2.16)$$

where $K_z = k_z + i\omega c_z$ represents the impedance that oppose the displacement and v_I is the component of the incident field in the direction of the pile longitudinal axis.

The solution of these equations is the sum of the solution of the homogeneous equation v_H and u_H , respectively, and any particular solution v_P and u_P , in each case, that satisfies the corresponding equation. Thus $v = v_H + v_P$ and $u = u_H + u_P$.

The respective homogeneous solutions satisfy the following equations:

$$\frac{\partial^4 u}{\partial z^4} + \lambda_u^4 u = 0 \quad ; \quad \frac{\partial^2 v}{\partial x^2} + \lambda_v^2 v = 0 \quad (2.17)$$

being

$$\lambda_u^4 = \frac{K_x - \tilde{\rho}_p \tilde{A}_p \omega^2}{\tilde{E}_p \tilde{I}_p} \quad ; \quad \lambda_v^2 = \frac{K_z - \tilde{\rho}_p \tilde{A}_p \omega^2}{\tilde{\mu}_p \tilde{A}_p} \quad (2.18)$$

Given that their solution is of the type $e^{\alpha z}$, the characteristic equations can be written, respectively, as follows:

$$\alpha_u^4 + \lambda_u^4 = 0 \quad ; \quad \alpha_v^2 + \lambda_v^2 = 0 \quad (2.19)$$

thus

$$\alpha_u^4 = -\frac{K_x - \tilde{\rho}_p \tilde{A}_p \omega^2}{\tilde{E}_p \tilde{I}_p} \quad ; \quad \alpha_v^2 = -\frac{K_z - \tilde{\rho}_p \tilde{A}_p \omega^2}{\tilde{\mu}_p \tilde{A}_p} \quad (2.20)$$

which have complex solutions that can be written, respectively, as

$$\alpha_u^j = \sqrt[4]{M_u} e^{i(\theta_u/4 + (j-1)\pi/2)} \quad \text{being} \quad j = 1, 2, 3, 4 \quad (2.21)$$

$$\alpha_v^j = \sqrt{M_v} e^{i(\theta_v/2 + (j-1)\pi)} \quad \text{being} \quad j = 1, 2 \quad (2.22)$$

where M_u and M_v are the modules, and θ_u and θ_v are the phases of the complex numbers α_u^4 and α_v^2 , respectively. In this way,

$$u_H = \sum_{j=1}^{j=4} D_j e^{\alpha_u^j z} \quad \text{and} \quad v_H = \sum_{j=1}^{j=2} \tilde{D}_j e^{\alpha_v^j z} \quad (2.23)$$

The homogeneous solution at the pile top depends then on the following parameters:

$$(\alpha_u L)^4 = \frac{K_x L^4}{\tilde{E}_p \tilde{I}_p} \left(1 - \frac{\tilde{\rho}_p \tilde{A}_p \omega^2}{K_x} \right) \quad (2.24)$$

$$(\alpha_v L)^2 = \frac{K_z L^2}{\tilde{\mu}_p \tilde{A}_p} \left(1 - \frac{\tilde{\rho}_p \tilde{A}_p \omega^2}{K_z} \right) \quad (2.25)$$

where K_x can be expressed as $n_x E_s$, and K_z as $n_z E_s$, being n_x and n_z proportionality constants, and $E_s = 2(1 + \nu_s) c_s^2 \rho_s$. This yields the expressions below.

$$(\alpha_u L)^4 = n_x \frac{E_s L^4}{\tilde{E}_p \tilde{I}_p} \left(1 - \frac{\tilde{\rho}_p \tilde{A}_p \omega^2}{\rho_s c_s^2} \frac{1}{n_x 2(1 + \nu_s)} \right) \quad (2.26)$$

$$(\alpha_v L)^2 = n_z \frac{E_s L^2}{\tilde{E}_p \tilde{A}_p} \left(1 - \frac{\tilde{\rho}_p \tilde{A}_p \omega^2}{\rho_s c_s^2} \frac{1}{n_z 2(1 + \nu_s)} \right) \quad (2.27)$$

Moreover, when introducing the incident field, the particular solutions at the pile top depend also on the parameter κL .

At this point, the dimensionless parameters characterizing the pile dynamic behaviour can be identified from equations (2.26) and (2.27). On the one hand, it can be seen that both expressions depend on

$$\frac{\tilde{\rho}_p \tilde{A}_p \omega^2}{\rho_s c_s^2} \quad (2.28)$$

On the other hand, equations (2.26) and (2.27) depend, respectively, on

$$\frac{\tilde{E}_p \tilde{I}_p}{E_s L^4} \quad (2.29)$$

and

$$\frac{\tilde{E}_p \tilde{A}_p}{E_s L^2} \quad (2.30)$$

Performing some basic algebraic operations, from equation (2.29):

$$\frac{\tilde{E}_p \tilde{I}_p}{E_s L^4} = \frac{\tilde{E}_p \tilde{I}_p I_p}{E_s I_p L^4} = \frac{E_p \pi}{E_s 64} \left(\frac{d}{L} \right)^4 \quad (2.31)$$

where $I_p = \pi d^4/64$ is the rotational inertia corresponding to a solid circular pile cross-section whose diameter coincide with the external diameter of its actual annular cross-section. Besides, $E_p = \tilde{E}_p \tilde{I}_p / I_p$ represents the Young's module of an equivalent solid pile that could model the dynamic behaviour of the actual hollow pile.

Similarly, from equation (2.30):

$$\frac{\tilde{E}_p \tilde{A}_p}{E_s L^2} = \frac{\tilde{E}_p \tilde{I}_p I_p \tilde{A}_p}{E_s I_p \tilde{I}_p L^2} = \frac{E_p I_p L^2}{E_s L^4 \tilde{i}_p^2} = \frac{E_p \pi}{E_s 64} \left(\frac{d}{L} \right)^4 \left(\frac{L}{\tilde{i}_p} \right)^2 \quad (2.32)$$

being $A_p = \pi d^2/4$ the area of a solid circular cross-section of diameter d .

Finally, from equation (2.28):

$$\frac{\tilde{\rho}_p \tilde{A}_p \omega^2}{\rho_s c_s^2} = \frac{\tilde{A}_p \tilde{\rho}_p A_p \omega^2}{A_p \rho_s c_s^2} = \frac{\rho_p}{\rho_s} \left(\frac{\omega d}{c_s} \right)^2 \frac{\pi}{4} \quad (2.33)$$

being $\rho_p = \tilde{\rho}_p \tilde{A}_p / A_p$ the mass density corresponding to the above-mentioned equivalent solid pile, and $\tilde{i}_p^2 = \tilde{I}_p / \tilde{A}_p$ the radius of gyration of the actual pile cross-section.

Thus, the main parameters of the problem can be written as follows:

$$\frac{E_p}{E_s} \quad ; \quad \frac{L}{d} \quad ; \quad \frac{L}{\tilde{i}_p} \quad ; \quad \frac{\rho_p}{\rho_s} \quad ; \quad \frac{\omega d}{c_s} \quad ; \quad \nu_s \quad ; \quad \frac{s}{d} \quad (2.34)$$

where s/d represents the pile spacing ratio for pile groups.

Identical dynamic behaviour is expected for all cases in which these dimensionless parameters have the same values. In order to test this hypothesis, the dynamic response of a set of different pile group configurations with identical values of these parameters is analysed in section 2.6.

2.6 Influence of pile cross-section geometry on the dynamic behaviour of piles

The set of dimensionless parameters characterizing the dynamic behaviour of piles when considering SSI has been identified in section 2.5. For most of the results reported in this document, it is assumed that $E_p/E_s = 10^3$ and $\rho_s/\rho_p = 0.7$. When using steel piles, an annular cross-section, as that shown on the right side of figure 2.9, is the pile cross-section geometry which would correspond to real cases with such values of the pile-soil Young's modulus ratio E_p/E_s and the soil-pile densities ratio ρ_s/ρ_p .

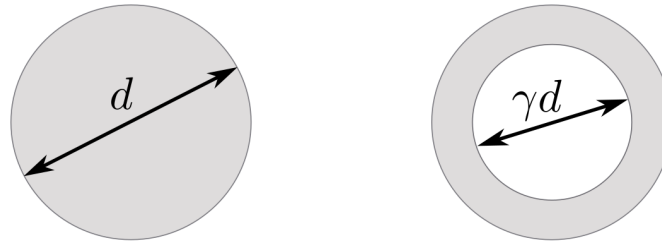


FIGURE 2.9: Piles cross-section.

In this figure, the value of the parameter γ represents the ratio between the internal and the external diameter of the pile section, and takes values into the range $0 \leq \gamma < 1$. Thus, the area of the annular cross-section can be expressed as

$$\tilde{A}_p = \frac{\pi d^2}{4}(1 - \gamma^2) \quad (2.35)$$

Likewise, its rotational inertia can be written as

$$\tilde{I}_p = \frac{\pi d^4}{64}(1 - \gamma^4) \quad (2.36)$$

However, the impedance functions and the kinematic interaction factors, corresponding to the different pile group configurations under study in this work, are computed by considering a solid circular pile cross-section, as that depicted on the left side of figure 2.9. The area and rotational inertia of a solid circular cross-section ($\gamma = 0$), are denoted by A_p and I_p , respectively. According to equations (2.35) and (2.36), when $\gamma = 0$,

$$A_p = \tilde{A}_p(\gamma = 0) = \frac{\pi d^2}{4} \quad (2.37)$$

and

$$I_p = \tilde{I}_p(\gamma = 0) = \frac{\pi d^4}{64} \quad (2.38)$$

Thus, the radius of gyration of a solid circular cross-section i_p can be defined as

$$i_p = \tilde{i}_p(\gamma = 0) = \sqrt{\frac{I_p}{A_p}} = \frac{d}{4} \quad (2.39)$$

Therefore, when considering a solid circular pile cross-section, the dimensionless parameter L/\tilde{i}_p depends only on the pile slenderness ratio L/d , which implies that the dynamic behaviour of piles can be characterized by the following six parameters:

$$\frac{E_p}{E_s} \quad ; \quad \frac{L}{d} \quad ; \quad \frac{\rho_p}{\rho_s} \quad ; \quad \frac{\omega d}{c_s} \quad ; \quad \nu_s \quad ; \quad \frac{s}{d} \quad (2.40)$$

Firstly, this section aims at verifying that, as expected, identical results are obtained for impedances and kinematic interaction factors corresponding to all cases in which the dimensionless parameters characterizing the SSI problem have the same values. For this purpose, a pile model with the same solid circular cross-section ($\tilde{A}_p = A_p = \text{cte}$ and $\tilde{I}_p = I_p = \text{cte}$) is used herein to represent several annular pile cross-sections with different thickness, according to the value of γ in each case. The values of the properties assigned to the solid circular cross-section in order to model the actual annular cross-section, E_p and ρ_p , vary with γ according to equations (2.41) and (2.42).

$$E_p = \tilde{E}_p \frac{\tilde{I}_p}{I_p} = \tilde{E}_p(1 - \gamma^4) \quad (2.41)$$

$$\rho_p = \tilde{\rho}_p \frac{\tilde{A}_p}{A_p} = \tilde{\rho}_p(1 - \gamma^2) \quad (2.42)$$

where the Young's module and density of the pile material are denoted by \tilde{E}_p and $\tilde{\rho}_p$, respectively.

In this study, the properties of pile material are considered to be $\tilde{E}_p = 2.8 \cdot 10^3 \text{ Pa}$ and $\tilde{\rho}_p = 1 \text{ kg/m}^3$. It is assumed that the pile external diameter is $d = 2$ and the pile length is considered to be $L = 30$. The values adopted for the dimensionless parameters characterizing the dynamic behaviour of pile groups are indicated in table 2.1. Each row in table 2.2 lists the properties corresponding to the model of each annular section under study. It can be seen that the parameter L/\tilde{i}_p keeps constant for all values of γ , given that it depends only on L/d when the pile cross-section has a solid circular geometry.

TABLE 2.1: Values adopted for the dimensionless parameters characterizing the SSI problem.

E_p/E_s	L/d	ρ_s/ρ_p	$\omega d/c_s$	ν_s	s/d
10^3	15	0.7	0 – 1	0.4	5, 10

On the other hand, the accuracy of modelling a hollow pile by assuming a solid circular cross-section is assessed by obtaining impedance functions and kinematic interaction factors considering the actual annular geometry of the pile cross-section in each case. Table 2.3 lists the properties corresponding to each annular section under investigation. The same values of the dimensionless parameters considered for all the cases reported in table 2.2 have been assumed for those reported in table 2.3. Now the objective is to compare the results corresponding to each row in table 2.3, representing the actual annular cross-section geometry, with those obtained for the same row in table 2.2, corresponding to an equivalent solid circular cross-section in each case. This allows elucidating whether the approach that consists in modelling hollow piles as solid piles yields accurate results or not.

TABLE 2.2: Model solid circular cross-section geometry and equivalent material properties.

γ	A_p	I_p	L/\tilde{i}_p	E_p	E_s	ρ_p	ρ_s
0.00	3.1416	0.7854	60.00	$2.800 \cdot 10^3$	2.800	1.000	0.700
0.50	3.1416	0.7854	60.00	$2.625 \cdot 10^3$	2.625	0.750	0.525
0.80	3.1416	0.7854	60.00	$1.653 \cdot 10^3$	1.653	0.360	0.252
0.90	3.1416	0.7854	60.00	$0.962 \cdot 10^3$	0.962	0.190	0.133
0.95	3.1416	0.7854	60.00	$0.519 \cdot 10^3$	0.519	0.098	0.068

TABLE 2.3: Actual annular cross-section geometry and material properties.

γ	\tilde{A}_p	\tilde{I}_p	L/\tilde{i}_p	\tilde{E}_p	E_s	$\tilde{\rho}_p$	ρ_s	$\frac{\tilde{E}_p \tilde{I}_p}{E_s L^4} \cdot 10^4$	$\frac{\tilde{E}_p \tilde{A}_p}{E_s L^2}$
0.00	3.1416	0.7854	60.00	2,800	2.800	1.000	0.700	9.6963	3.4907
0.50	2.3562	0.7363	53.67	2,800	2.625	1.000	0.525	9.6963	2.7929
0.80	1.1310	0.4637	46.85	2,800	1.653	1.000	0.252	9.6963	2.1283
0.90	0.5969	0.2701	44.60	2,800	0.962	1.000	0.133	9.6963	1.9287
0.95	0.3063	0.1457	43.50	2,800	0.519	1.000	0.068	9.6963	1.8347

The radius of gyration of the annular cross-section \tilde{i}_p can be expressed as a function of that corresponding to a solid circular cross-section i_p with the same diameter as follows:

$$\tilde{i}_p = \sqrt{\frac{\tilde{I}_p}{\tilde{A}_p}} = i_p \sqrt{\frac{1 - \gamma^4}{1 - \gamma^2}} \quad (2.43)$$

Thus, the parameter L/\tilde{i}_p can be written as

$$\frac{L}{\tilde{i}_p} = 4 \frac{L}{d} \frac{i_p}{\tilde{i}_p} \quad (2.44)$$

Therefore, the column corresponding to L/\tilde{i}_p in table 2.3 shows the relation between the radius of gyration of the actual annular pile cross-section \tilde{i}_p and that corresponding to the virtual equivalent solid cross-section i_p used in the approach of table 2.2.

It should be noted that the ninth column in table 2.3 contains the values of a parameter that influences the behaviour of piles when subjected to bending (see equation (2.26)). Likewise, the tenth column in table 2.3 reflects the values of a parameter that affects the response of piles when subjected to axil (see equation (2.27)). It can be observed that the variations of L/\tilde{i}_p only affect the last column associated to axil. In fact, this parameter has no influence when the pile is only subjected to bending (see equations (2.31) and (2.32)), and only appears when the pile works axially. Thus, the ninth column in table 2.3, which is associated to bending, remains constant. The more inclined, the more the pile works axially. Therefore, modelling piles of annular cross-section by solid piles yields less accurate results as the rake angle increases.

In order to illustrate the accuracy of this approach, impedances and kinematic interaction factors, corresponding to several pile group configurations including vertical and battered piles, have been computed, through a BEM-FEM methodology developed by Padrón *et al.* [71] and outlined in section 3.5, for the different annular pile cross-sections reported in table 2.3 as well as for the corresponding solid circular section in table 2.2.

Different 2×2 and 3×3 pile group configurations, with pile spacing ratios $s/d = 5$ and 10, are analysed. All of them follow the pattern represented in figure 2.10. Configurations containing vertical piles and piles inclined in the direction of excitation, with three different rake angles $\theta = 10^\circ, 20^\circ$ and 30° , are considered.

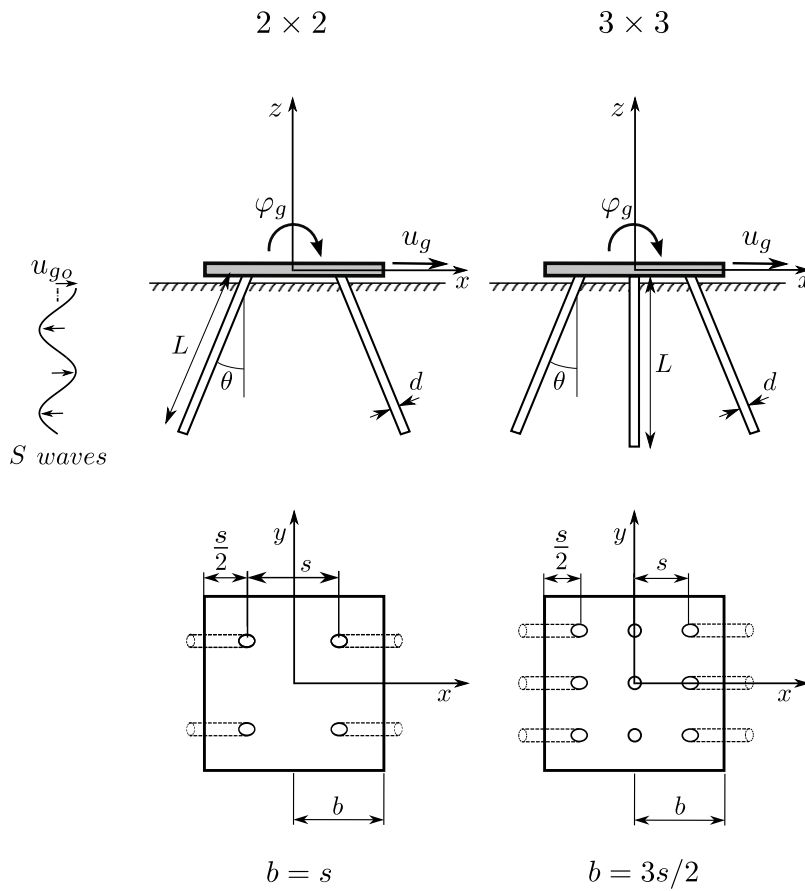


FIGURE 2.10: Pile foundation geometry.

The hypothesis of the first part of the analysis was verified, given that all rows in table 2.2, corresponding to the same solid circular section ($\tilde{A}_p = A_p = cte$ and $\tilde{I}_p = I_p = cte$) with different values of E_p and ρ_p but with the same values of the main parameters of the problem ($E_p/E_s, L/d, L/\tilde{i}_p, \rho_p/\rho_s, \nu_s$), lead to identical results for all the pile group configurations under study. Thus, the black line corresponding to $\gamma = 0$ in all the figures in sections 2.6.1 and 2.6.2 represents, at the same time, the results for all rows in table 2.2.

The accuracy of the results obtained by modelling hollow piles as solid ones is analysed below from the results obtained in terms of impedances and kinematic interaction factors.

2.6.1 Impedance functions

Figures from 2.11 to 2.13 show impedance functions, for all the configurations under investigation, corresponding to the horizontal, rocking and cross-coupled horizontal-rocking vibration modes, respectively. Although four different rake angles have been considered in this study, aiming at providing the reader with concise information that can be easily interpreted, only those results corresponding to the rake angles $\theta = 0^\circ$ (vertical piles) and $\theta = 30^\circ$ are shown herein to illustrate the conclusions of this analysis. Each column of these figures corresponds to a particular pile group configuration.

It can be observed that the variation of γ does not yield great differences in terms of impedances, which implies that modelling the annular cross-section of piles ($\gamma > 0$) as a solid cross-section ($\gamma = 0$) allows obtaining results accurate enough to represent the stiffness and damping of the *soil-foundation* system. However, in these figures, it can be observed that modelling hollow piles as solid piles yields less accurate results as the rake angle increases.

For the purpose of assessing more precisely the accuracy of this simplification concerning the pile cross-section geometry, the percentage error in terms of the area under the curves of stiffness and damping, yielding from assuming a solid cross-section instead of an actual annular cross-section with $\gamma = 0.9$, has been calculated in the frequency range of interest for seismic loading ($0 \leq \omega d/c_s \leq 0.5$) according to Gazetas *et al.* [79]. In this line, table 2.4 reflects data for several configurations of piles comprising vertical or inclined piles with a rake angle $\theta = 30^\circ$.

TABLE 2.4: Percentage error for impedance functions yielding from modelling a hollow pile with $\gamma = 0.9$ by an equivalent solid pile. $0 \leq \omega d/c_s \leq 0.5$.

s/d	2×2				3×3			
	5		10		5		10	
θ	0°	30°	0°	30°	0°	30°	0°	30°
$k_{xx}/(\mu_s d)$	1.88	1.06	1.11	3.51	2.57	0.14	1.07	2.88
$c_{xx}/(\mu_s d)$	0.49	3.93	0.23	5.05	0.59	2.53	0.21	3.50
$k_{\theta\theta}/(\mu_s d^3)$	5.71	1.40	5.55	4.73	0.45	0.80	6.42	5.34
$c_{\theta\theta}/(\mu_s d^3)$	10.71	6.12	11.28	9.13	6.65	6.38	10.92	9.39
$k_{\theta x}/(\mu_s d^2)$	2.02	0.06	1.42	16.36	4.06	2.25	1.46	14.04
$c_{\theta x}/(\mu_s d^2)$	0.19	27.43	0.90	20.42	1.96	19.11	0.38	18.45

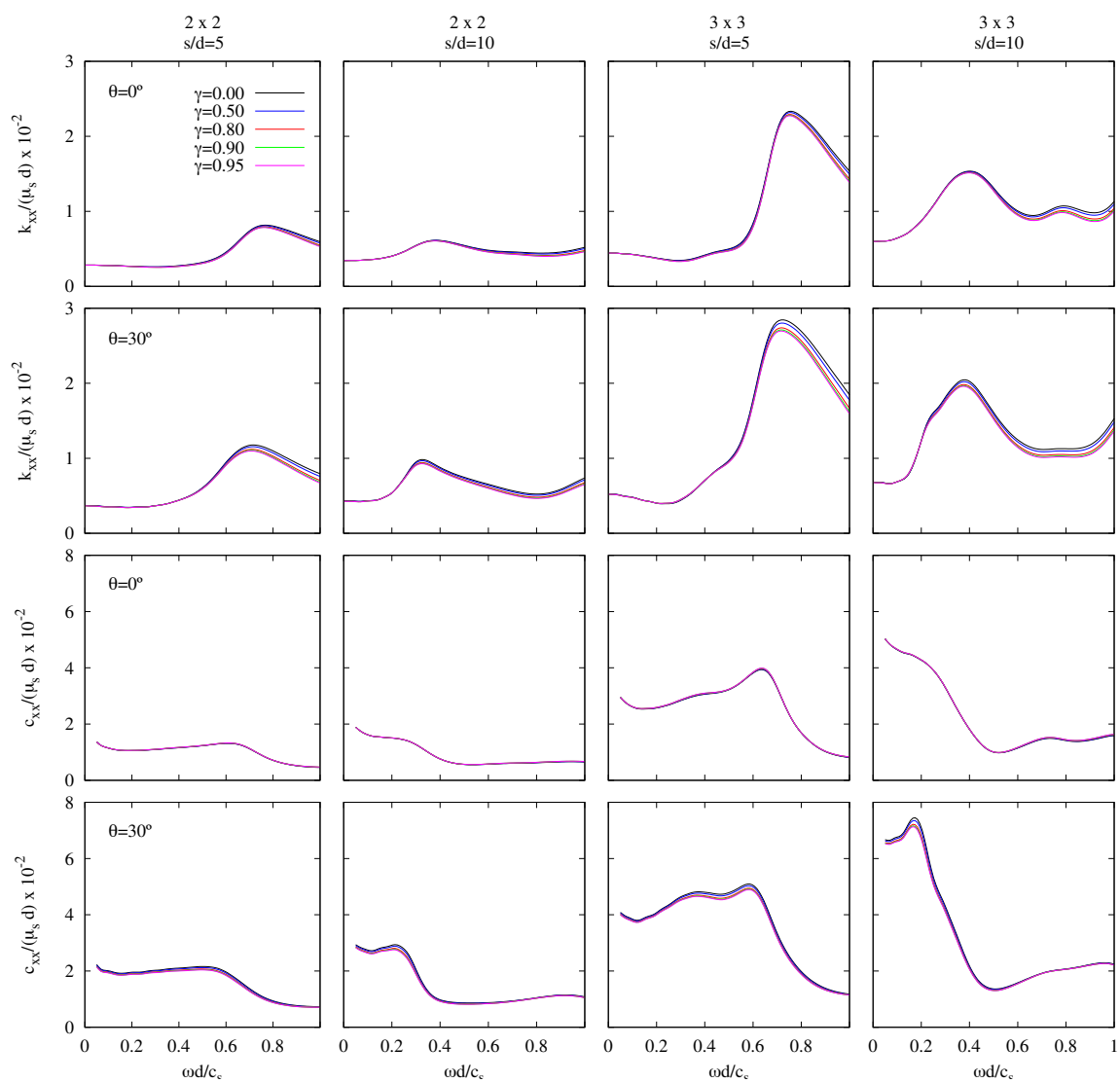


FIGURE 2.11: Influence of pile cross-section geometry. Horizontal impedances of different 2×2 and 3×3 pile groups with vertical ($\theta = 0^\circ$) or inclined elements ($\theta = 30^\circ$). $E_p/E_s = 1000$ and $\xi_s = 0.05$.

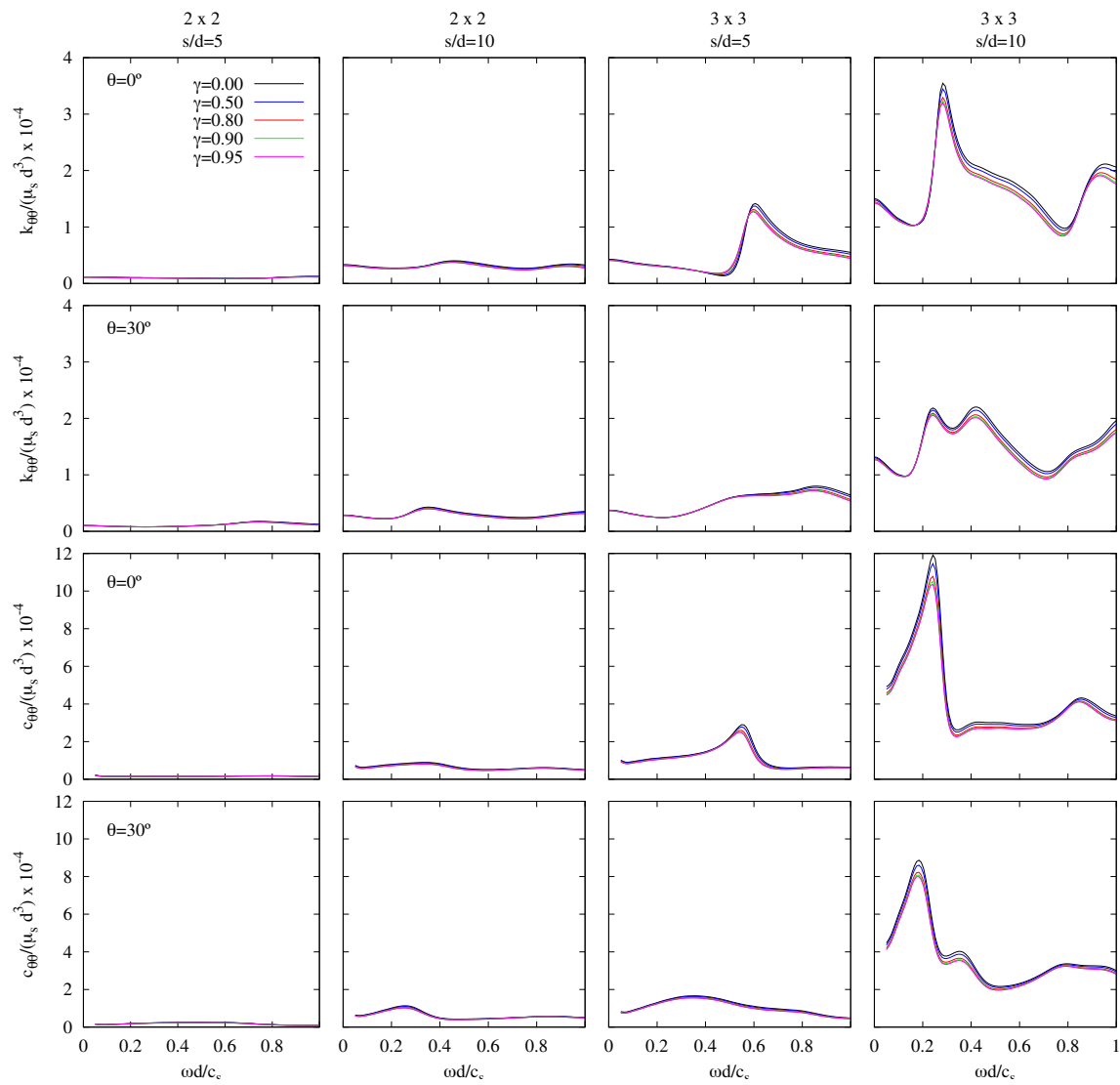


FIGURE 2.12: Influence of pile cross-section geometry. Rocking impedances of different 2×2 and 3×3 pile groups with vertical ($\theta = 0^\circ$) or inclined elements ($\theta = 30^\circ$). $E_p/E_s = 1000$ and $\xi_s = 0.05$.

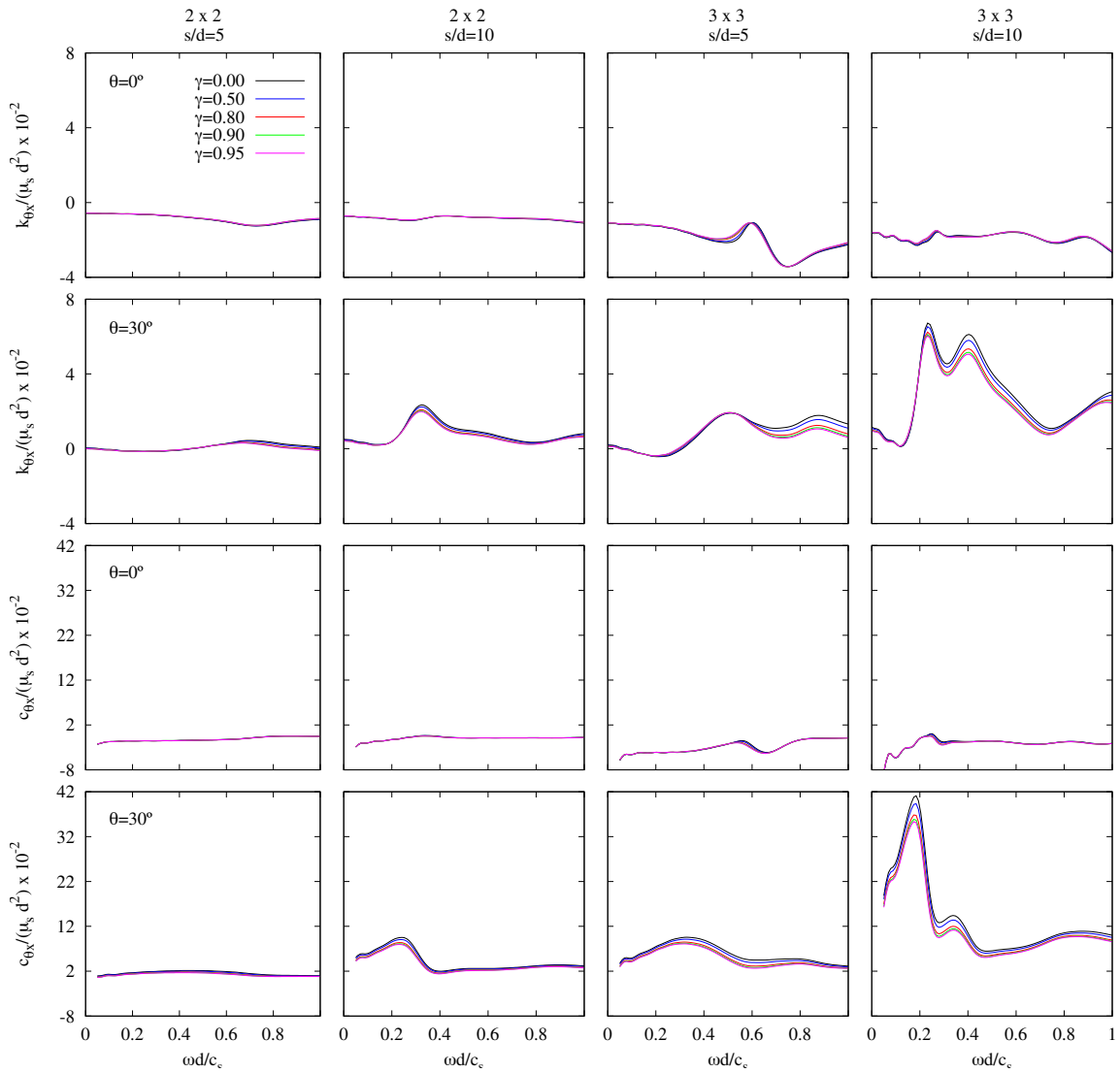


FIGURE 2.13: Influence of pile cross-section geometry. Horizontal-rocking cross-coupled impedances of different 2×2 and 3×3 pile groups with vertical ($\theta = 0^\circ$) or inclined elements ($\theta = 30^\circ$). $E_p/E_s = 1000$ and $\xi_s = 0.05$.

2.6.2 Kinematic interaction factors

This section intends to illustrate the extent to which the kinematic interaction factors of pile groups consisting of piles with annular cross-section ($\gamma > 0$) can be approximated by those of an equivalent group of piles with an equivalent solid circular cross-section ($\gamma = 0$). For this purpose, figures 2.14 and 2.15 present, respectively, translational and rotational kinematic interaction factors for different configurations of 2×2 and 3×3 pile groups. In these figures, the first and the third row correspond to vertical pile groups, while the second and the fourth row correspond to pile groups including battered elements with a rake angle $\theta = 30^\circ$. As mentioned before, results obtained for rake angles $\theta = 10^\circ$ and 20° are not shown in these figures in order to provide the reader with an information that can be easily interpreted.

No major differences have been observed in the kinematic interaction factors obtained for different values of γ . This allows us to conclude that the simplification of the pile cross-section geometry that has been adopted in this work provide results accurate enough for the configurations under investigation.

In order to assess more precisely the accuracy of this simplification that affects the pile cross-section geometry, the percentage error in terms the area under the curves of the kinematic interaction factors, yielding from assuming an equivalent solid cross-section instead of an actual annular cross-section with $\gamma = 0.9$ has been calculated in the frequency range of interest for seismic loading ($0 \leq \omega d/c_s \leq 0.5$) according to Gazetas *et al.* [79]. In this line, table 2.5 provides data for several configurations of piles with vertical or inclined piles with a rake angle $\theta = 30^\circ$.

TABLE 2.5: Percentage error for kinematic interaction factors yielding from modelling a hollow pile with $\gamma = 0.9$ by an equivalent solid pile. $0 \leq \omega d/c_s \leq 0.5$.

s/d	2×2				3×3			
	5		10		5		10	
θ	0°	30°	0°	30°	0°	30°	0°	30°
$\text{Re}[I_u]$	1.91	3.13	0.93	1.73	1.99	2.82	0.80	1.34
$\text{Im}[I_u]$	2.92	0.03	2.78	1.47	2.87	1.58	3.02	2.19
$\text{Re}[I_\varphi]$	7.70	0.67	7.65	2.00	3.60	0.51	7.37	1.86
$\text{Im}[I_\varphi]$	11.03	3.22	4.75	0.27	6.83	8.51	4.67	2.21

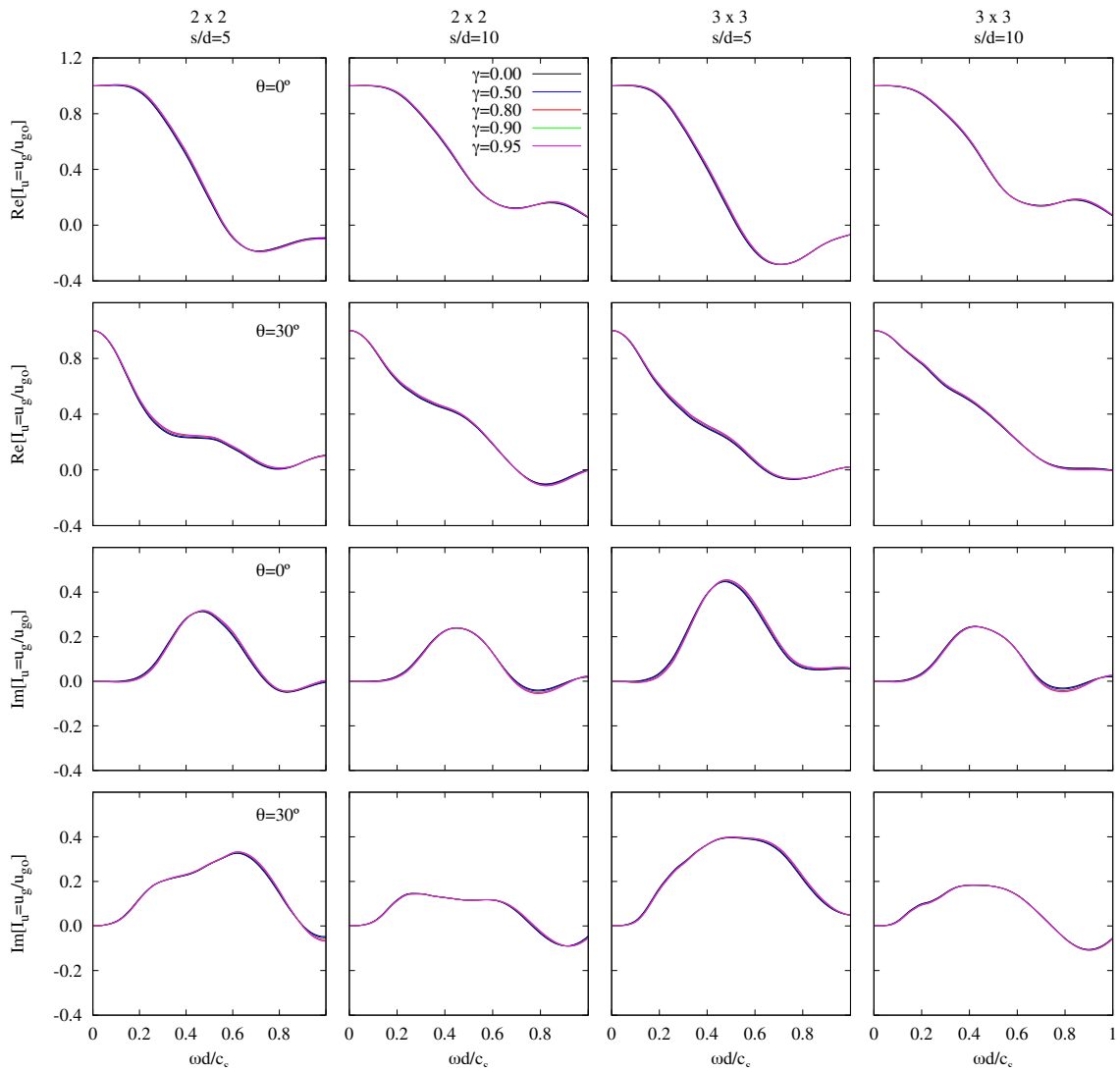


FIGURE 2.14: Influence of pile cross-section geometry. Translational kinematic interaction factor I_u of different 2×2 and 3×3 pile groups with vertical ($\theta = 0^\circ$) or inclined elements ($\theta = 30^\circ$). $E_p/E_s = 1000$ and $\xi_s = 0.05$.

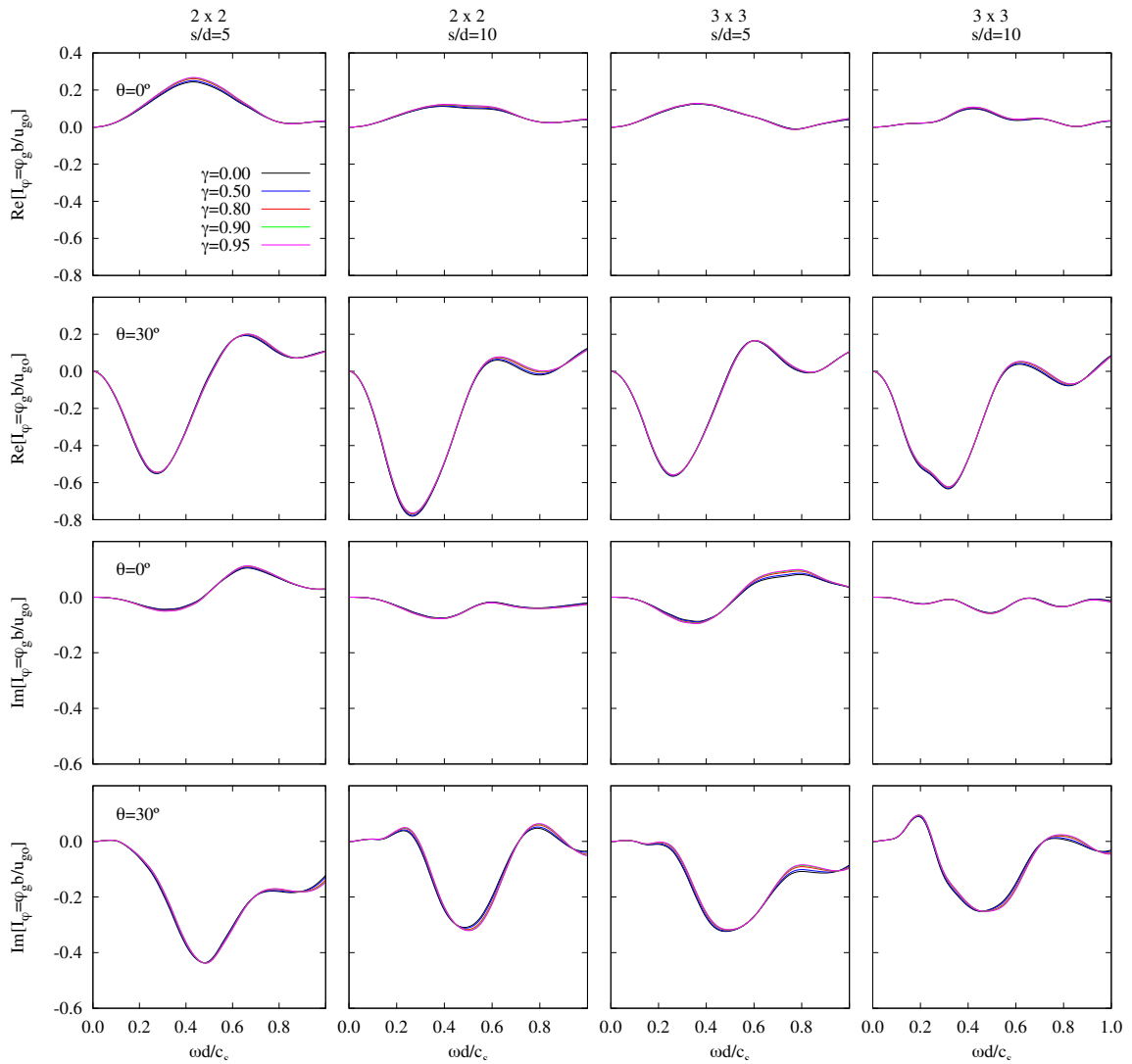


FIGURE 2.15: Influence of pile cross-section geometry. Rotational kinematic interaction factor I_φ of different 2×2 and 3×3 pile groups with vertical ($\theta = 0^\circ$) or inclined elements ($\theta = 30^\circ$). $E_p/E_s = 1000$ and $\xi_s = 0.05$.

2.7 System equations and dimensionless parameters

A set of dimensionless parameters, covering the main features of SSI problems, has been repeatedly used in the related literature to perform parametric analyses [7, 8, 13, 14]. Following these authors, the parameters used in this work to characterize the soil-foundation-structure system are:

1. Wave parameter $\sigma = c_s T/h$, that measures the soil-structure relative stiffness.
2. Slenderness ratio h/b .
3. Mass density ratio $\delta = m/(\rho_s A_b h)$ between structure and supporting soil, being A_b the area of the base of the structure. Thus, in the case of square foundations $A_b = 4b^2$ and, consequently, $\delta = m/(4\rho_s b^2 h)$.
4. Foundation-structure mass ratio m_o/m .
5. Fixed-base structure damping ratio ξ .
6. Dimensionless fixed-base natural frequency of the structure $\lambda = \omega_n/\omega$.
7. Dimensionless excitation frequency $a_o = \omega b/c_s = (b/d)(\omega d/c_s)$.

A hysteretic damping model of the type $\mu_s = \text{Re}[\mu_s](1 + 2i\xi_s)$ is considered in this work for the soil material, being ξ_s the corresponding damping coefficient.

Regarding the pile foundation, the main dimensionless parameters characterizing its dynamic behaviour, which were identified in section 2.5, are considered:

1. Pile spacing ratio s/d .
2. Embedment ratio L/b .
3. Pile-soil Young's modulus ratio E_p/E_s .
4. Dimensionless frequency a_o .
5. Soil-pile densities ratio ρ_s/ρ_p .
6. Pile slenderness ratio L/d .
7. Rake angle of piles θ .
8. Poisson's ratio of the soil ν_s .

By performing basic algebraic operations, the equation of motion of the system (2.13) can be expressed as a function of the dimensionless parameters defined above, in order to facilitate the analysis of their influence on the system dynamic response. Such operations are described below:

1. After adding the first two rows, the second row represents the horizontal equilibrium of the whole.

$$\left\{ \begin{bmatrix} K & 0 & 0 \\ 0 & K_{xx} & K_{x\theta} \\ 0 & K_{\theta x} & K_{\theta\theta} \end{bmatrix} - \omega^2 \begin{bmatrix} m & m & mh \\ m & m+m_o & mh \\ mh & mh & I_T \end{bmatrix} \right\} \cdot \begin{bmatrix} u \\ u_r^c \\ \varphi_r^c \end{bmatrix} = \omega^2 \left\{ \begin{bmatrix} m \\ m+m_o \\ mh \end{bmatrix} u_g + \begin{bmatrix} mh \\ mh \\ I_T \end{bmatrix} \varphi_g \right\} \quad (2.45)$$

2. By introducing the structural stiffness and damping expressions, $k = \omega_n^2 m$ and $c = 2m\omega_n \xi \omega / a_o$, into equation (2.45), and dividing the whole equation by the free-field motion at the surface \ddot{u}_{g_o} , leads to equation (2.46).

$$\left\{ \begin{bmatrix} \omega_n^2 m + i2\omega_n m \xi \omega & 0 & 0 \\ 0 & K_{xx} & K_{x\theta} \\ 0 & K_{\theta x} & K_{\theta\theta} \end{bmatrix} - \omega^2 \begin{bmatrix} m & m & mh \\ m & m+m_o & mh \\ mh & mh & I_T \end{bmatrix} \right\} \cdot \begin{bmatrix} u/\ddot{u}_{g_o} \\ u_r^c/\ddot{u}_{g_o} \\ \varphi_r^c/\ddot{u}_{g_o} \end{bmatrix} = - \left\{ \begin{bmatrix} m \\ m+m_o \\ mh \end{bmatrix} I_u + \frac{1}{b} \begin{bmatrix} mh \\ mh \\ I_T \end{bmatrix} I_\varphi \right\} \quad (2.46)$$

where $I_u = u_g/u_{g_o}$ and $I_\varphi = \varphi_g b/u_{g_o}$ are the normalized kinematic interaction factors, which are both functions of the dimensionless frequency a_o .

3. The ratio ω^2/ω_n^2 can be extracted as a common factor from the first term of equation (2.46). On the other hand, the structural mass m can be extracted as a common factor from both sides of this equation which leads to equation (2.47).

$$\frac{1}{\lambda^2} \cdot \left\{ \begin{bmatrix} \lambda^2 + 2\lambda \xi i & 0 & 0 \\ 0 & \frac{K_{xx}}{\omega_n^2 m} & \frac{K_{x\theta}}{\omega_n^2 m} \\ 0 & \frac{K_{\theta x}}{\omega_n^2 m} & \frac{K_{\theta\theta}}{\omega_n^2 m} \end{bmatrix} - \begin{bmatrix} 1 & 1 & h \\ 1 & 1 + \frac{m_o}{m} & h \\ h & h & \frac{I_T}{m} \end{bmatrix} \right\} \cdot \begin{bmatrix} \omega_n^2 u/\ddot{u}_{g_o} \\ \omega_n^2 u_r^c/\ddot{u}_{g_o} \\ \omega_n^2 \varphi_r^c/\ddot{u}_{g_o} \end{bmatrix} = - \left\{ \begin{bmatrix} 1 \\ 1 + \frac{m_o}{m} \\ h \end{bmatrix} I_u + \frac{1}{b} \begin{bmatrix} h \\ h \\ \frac{I_T}{m} \end{bmatrix} I_\varphi \right\} \quad (2.47)$$

4. Dividing by h the third row of the equation and the third column of the system matrix, and replacing the rotational inertias I_o and I by their expressions $I_o = m_o b^2/3$ and $I = m b^2/3$, respectively, equation (2.47) results in equation (2.48).

$$\frac{1}{\lambda^2} \cdot \left\{ \begin{bmatrix} \lambda^2 + 2\lambda\xi i & 0 & 0 \\ 0 & \frac{K_{xx}}{\omega^2 m} & \frac{K_{x\theta}}{\omega^2 m h} \\ 0 & \frac{K_{\theta x}}{\omega^2 m h} & \frac{K_{\theta\theta}}{\omega^2 m h^2} \end{bmatrix} - \begin{bmatrix} 1 & 1 & 1 \\ 1 & 1 + \frac{m_o}{m} & 1 \\ 1 & 1 & 1 + \frac{b^2}{3h^2} \left(1 + \frac{m_o}{m}\right) \end{bmatrix} \right\} \cdot \begin{bmatrix} \omega_n^2 u / \ddot{u}_{g_o} \\ \omega_n^2 u_r^c / \ddot{u}_{g_o} \\ \omega_n^2 \varphi_r^c / \ddot{u}_{g_o} \end{bmatrix} = - \left\{ \begin{bmatrix} 1 \\ 1 + \frac{m_o}{m} \\ 1 \end{bmatrix} I_u + \frac{1}{b} \begin{bmatrix} h \\ h \\ h + \frac{b^2}{3h} \left(1 + \frac{m_o}{m}\right) \end{bmatrix} I_\varphi \right\} \quad (2.48)$$

5. The terms of the system equation of motion that depend on impedances can be also expressed as a function of the dimensionless parameters already defined, as indicated below. It is worth mentioning that $K_{\theta x} = K_{x\theta}$ as a consequence of reciprocity theorems.

$$\frac{K_{xx}}{\omega^2 m} = \frac{\mu_s b \tilde{K}_{xx}}{\omega^2 m} = \frac{(c_s^2 \rho_s) b \tilde{K}_{xx}}{\omega^2 m} = \left(\frac{\sigma h}{T}\right)^2 \frac{m}{4\delta b^2 h} \frac{b \tilde{K}_{xx}}{\omega^2 m} = \frac{\lambda^2 \sigma^2 h}{16\pi^2 \delta} \frac{1}{b} \tilde{K}_{xx} \quad (2.49)$$

$$\frac{K_{x\theta}}{\omega^2 m h} = \frac{\mu_s b^2 \tilde{K}_{x\theta}}{\omega^2 m h} = \frac{(c_s^2 \rho_s) b^2 \tilde{K}_{x\theta}}{\omega^2 m h} = \left(\frac{\sigma h}{T}\right)^2 \frac{m}{4\delta b^2 h} \frac{b^2 \tilde{K}_{x\theta}}{m h \omega^2} = \frac{\lambda^2 \sigma^2}{16\pi^2 \delta} \frac{1}{h} \tilde{K}_{x\theta} \quad (2.50)$$

$$\frac{K_{\theta\theta}}{\omega^2 m h^2} = \frac{\mu_s b^3 \tilde{K}_{\theta\theta}}{\omega^2 m h^2} = \frac{(c_s^2 \rho_s) b^3 \tilde{K}_{\theta\theta}}{\omega^2 m h^2} = \left(\frac{\sigma h}{T}\right)^2 \frac{m}{4\delta b^2 h} \frac{b^3 \tilde{K}_{\theta\theta}}{m h^2 \omega^2} = \frac{\lambda^2 \sigma^2}{16\pi^2 \delta} \frac{1}{h} \tilde{K}_{\theta\theta} \quad (2.51)$$

Thus, the equation of motion of the system can be written as follows:

$$\left\{ \begin{bmatrix} \lambda^2 + 2\lambda\xi i & 0 & 0 \\ 0 & \lambda^2 \sigma^2 \frac{1}{16\pi^2} \frac{h}{b} \frac{1}{\delta} \tilde{K}_{xx} & \lambda^2 \sigma^2 \frac{1}{\delta} \frac{1}{16\pi^2} \tilde{K}_{x\theta} \\ 0 & \lambda^2 \sigma^2 \frac{1}{\delta} \frac{1}{16\pi^2} \tilde{K}_{\theta x} & \lambda^2 \sigma^2 \frac{1}{16\pi^2} \frac{b}{h} \frac{1}{\delta} \tilde{K}_{\theta\theta} \end{bmatrix} - \begin{bmatrix} 1 & 1 & 1 \\ 1 & 1 + \frac{m_o}{m} & 1 \\ 1 & 1 & 1 + \frac{b^2}{3h^2} \left(1 + \frac{m_o}{m}\right) \end{bmatrix} \right\} \begin{bmatrix} \omega_n^2 u / \ddot{u}_{g_o} \\ \omega_n^2 u_r^c / \ddot{u}_{g_o} \\ \omega_n^2 h \varphi_r^c / \ddot{u}_{g_o} \end{bmatrix} = - \lambda^2 \left\{ \begin{bmatrix} 1 \\ 1 + \frac{m_o}{m} \\ 1 \end{bmatrix} I_u + \frac{h}{b} \begin{bmatrix} 1 \\ 1 \\ 1 + \frac{b^2}{3h^2} \left(1 + \frac{m_o}{m}\right) \end{bmatrix} I_\varphi \right\} \quad (2.52)$$

where the rotational inertias have been replaced by the expressions $I = mb^2/3$ and $I_o = m_o b^2/3$, respectively, given that pile cap and structure mass are assumed to be uniformly distributed over square areas. The impedance functions are normalized as follows: $\tilde{K}_{xx} = K_{xx}/(\mu_s b)$, $\tilde{K}_{\theta\theta} = K_{\theta\theta}/(\mu_s b^3)$ and $\tilde{K}_{x\theta} = K_{x\theta}/(\mu_s b^2)$, and the kinematic interaction factors are normalized with the free-field motion at the surface u_{g_o} , being $I_u = u_g/u_{g_o}$ and $I_\varphi = \varphi_g b/u_{g_o}$, both functions of the dimensionless frequency a_o .

2.8 Diagonalization of the impedance matrix

The dynamic response of the interacting system can be expressed in terms of the shear force at the base of the structure per effective earthquake force unit [7, 114] defined as

$$Q = \left| \frac{\omega_n^2 u}{\ddot{u}_{g_0}} \right| \tag{2.53}$$

Thus, Q can be obtained by solving, at each frequency, the complex system of algebraic equations given in (2.52) for $\omega_n^2 u / \ddot{u}_{g_0}$.

The usefulness of presenting the seismic response of the structure in these terms, lies in the fact that the product of this value with the structural mass and the corresponding free-field horizontal acceleration at ground surface level results in the amplitude of the shear force at the base of the structure.

In order to obtain manageable approximated expressions for Q , while keeping the crossed-coupled impedances, it is necessary to condense the soil-foundation interaction to a point at a certain virtual depth $D(\omega) = -K_{x\theta} / K_{xx}$ (see figure 2.16) such that the impedance matrix becomes diagonal, as some authors propose [27, 32].

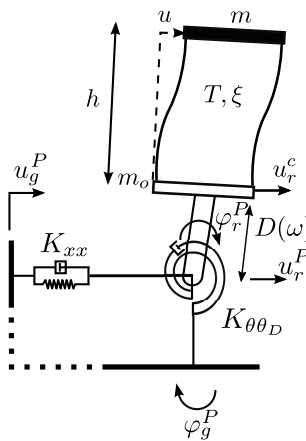


FIGURE 2.16: Equivalent model with diagonalized impedance matrix.

Considering the system shown in figure 2.16, the foundation equation of motion can be written as follows:

$$\begin{bmatrix} F \\ M \end{bmatrix} = \begin{bmatrix} K_{xx} & K_{x\theta} \\ K_{\theta x} & K_{\theta\theta} \end{bmatrix} \cdot \begin{bmatrix} u_r^c \\ \varphi_r^c \end{bmatrix} \tag{2.54}$$

Condensing the soil-foundation interaction to a point at a certain virtual depth $D(\omega)$, the equation of motion of the foundation can be expressed as

$$\begin{bmatrix} F^P \\ M^P - F^P D \end{bmatrix} = \begin{bmatrix} K_{xx} & K_{x\theta} \\ K_{\theta x} & K_{\theta\theta} \end{bmatrix} \cdot \begin{bmatrix} u_r^P + \varphi_r^P D \\ \varphi_r^P \end{bmatrix} \quad (2.55)$$

where $F^P = F$, $M^P - F^P D = M$, $u_r^P = u_r^c - \varphi_r^P D$ and $\varphi_r^P = \varphi_r^c$.

Thus, equation (2.55) can also be written as

$$\begin{bmatrix} F^P \\ M^P \end{bmatrix} = \begin{bmatrix} K_{xx} & K_{x\theta} + K_{xx} D \\ K_{\theta x} + K_{xx} D & K_{\theta\theta} + 2K_{x\theta} D + K_{xx} D^2 \end{bmatrix} \cdot \begin{bmatrix} u_r^P \\ \varphi_r^P \end{bmatrix} \quad (2.56)$$

It can be seen that to obtain a diagonal impedance matrix the pile cap pole must be displaced a distance $D(\omega) = -K_{\theta x}/K_{xx}$, which leads to the equation below. Note that, as mentioned before, $K_{\theta x} = K_{x\theta}$ as a consequence of reciprocity theorems.

$$\begin{bmatrix} F^P \\ M^P \end{bmatrix} = \begin{bmatrix} K_{xx} & 0 \\ 0 & K_{\theta\theta} - \frac{K_{\theta x}^2}{K_{xx}} \end{bmatrix} \cdot \begin{bmatrix} u_r^P \\ \varphi_r^P \end{bmatrix} \quad (2.57)$$

being $K_{\theta\theta} - K_{\theta x}^2/K_{xx} = K_{\theta\theta D}$.

Hence, the equations of motion of the interacting system written in equations (2.10), (2.11) and (2.12) can be now expressed, referred to that point located at a virtual depth D , as

$$m \cdot [\ddot{u} + \ddot{u}_r^P + \ddot{u}_g^P + (h + D) \cdot (\ddot{\varphi}_r^P + \ddot{\varphi}_g^P)] + K \cdot u = 0 \quad (2.58)$$

$$m_o \cdot [\ddot{u}_r^P + \ddot{u}_g^P + (\ddot{\varphi}_r^P + \ddot{\varphi}_g^P) \cdot D] + K_{xx} \cdot u_r^P - K \cdot u = 0 \quad (2.59)$$

$$m \cdot (h + D) [\ddot{u} + \ddot{u}_r^P + \ddot{u}_g^P + (h + D) \cdot (\ddot{\varphi}_r^P + \ddot{\varphi}_g^P)] + I \cdot (\ddot{\varphi}_r^P + \ddot{\varphi}_g^P) + m_o \cdot D [\ddot{u}_r^P + \ddot{u}_g^P + (\ddot{\varphi}_r^P + \ddot{\varphi}_g^P) \cdot D] + I_o \cdot (\ddot{\varphi}_r^P + \ddot{\varphi}_g^P) + K_{\theta\theta D} \cdot \varphi_r^P = 0 \quad (2.60)$$

where equation (2.58) represents the horizontal force equilibrium of the structure, equation (2.59) the horizontal force equilibrium of the structure-foundation system, and equation (2.60) the moment equilibrium of the structure-foundation system about the point located at a virtual depth D to which the soil-foundation interaction has been condensed.

In the frequency domain (with time dependence $e^{i\omega t}$), this set of equations can be expressed in a matrix form as

$$\left\{ \begin{array}{l} \left[\begin{array}{ccc} K & 0 & 0 \\ -K & K_{xx} & 0 \\ 0 & 0 & K_{\theta\theta_D} \end{array} \right] \\ -\omega^2 \left[\begin{array}{ccc} m & m & m(h+D) \\ 0 & m_o & m_o D \\ m(h+D) & m(h+D) + m_o D & I_T \end{array} \right] \end{array} \right\} \cdot \begin{bmatrix} u \\ u_r^P \\ \varphi_r^P \end{bmatrix} = \quad (2.61)$$

$$\omega^2 \left\{ \begin{array}{l} \left[\begin{array}{c} m \\ m_o \\ m(h+D) + m_o D \end{array} \right] u_g^P + \left[\begin{array}{c} m(h+D) \\ m_o D \\ I_T \end{array} \right] \varphi_g^P \end{array} \right\}$$

where $I_T = m(h+D)^2 + m_o D^2 + I_o + I$, $K = k + ia_o c$, and motions have been assumed to be time-harmonic of the type $u(t) = u e^{i\omega t}$.

It should be noted that, after this transformation explained above, the equations of motion of the interacting system are written in terms of the horizontal and rocking input motions at the point to which the soil-foundation interaction has been condensed, u_g^P and φ_g^P , whereas equation (2.13) was expressed in terms of the horizontal and rocking input motions at the pile cap, u_g and φ_g . Moreover, equation (2.61) is written in terms of the relative horizontal displacement and rocking at the point mentioned before, u_r^P and φ_r^P , instead of being expressed in terms of the foundation relative horizontal displacement and rocking at the pile cap level, u_r^c and φ_r^c .

A similar procedure to that described in section 2.7 is followed, in order to express the system equations of motion in the frequency domain as a function of the dimensionless parameters already defined. In this line, the algebraic operations performed for this purpose are explained in detail below:

1. The first step consists in adding the two first rows of the equation. Thus, the second row will represent the horizontal equilibrium of the whole.

2. Then, by introducing the structural stiffness and damping expressions, $k = \omega_n^2 m$ and $c = 2m\omega_n \xi \omega / a_o$, in equation (2.61), and dividing the equation by the free-field motion at the surface \ddot{u}_{g_o} leads to equation (2.62).

$$\begin{aligned}
 & \left\{ \begin{bmatrix} \omega_n^2 m + i2\omega_n m \xi \omega & 0 & 0 \\ 0 & K_{xx} & 0 \\ 0 & 0 & K_{\theta\theta D} \end{bmatrix} - \right. \\
 & \omega^2 \left. \begin{bmatrix} m & m & m(h+D) \\ m & m+m_o & m(h+D) + m_o D \\ m(h+D) & m(h+D) + m_o D & I_T \end{bmatrix} \right\} \begin{bmatrix} u/\ddot{u}_{g_o} \\ u_r^P/\ddot{u}_{g_o} \\ \varphi_r^P/\ddot{u}_{g_o} \end{bmatrix} \quad (2.62) \\
 & = \omega^2 \left\{ \begin{bmatrix} m \\ m+m_o \\ m(h+D) + m_o D \end{bmatrix} \frac{u_g^P}{\ddot{u}_{g_o}} + \begin{bmatrix} m(h+D) \\ m(h+D) + m_o D \\ I_T \end{bmatrix} \frac{\varphi_g^P}{\ddot{u}_{g_o}} \right\}
 \end{aligned}$$

3. The ratio ω^2/ω_n^2 can be extracted as a common factor from the first term of the equation above. On the other hand the structural mass m can be extracted as a common factor from both sides of this equation which leads to

$$\begin{aligned}
 & \frac{1}{\lambda^2} \left\{ \begin{bmatrix} \lambda^2 + 2\lambda\xi i & 0 & 0 \\ 0 & \frac{K_{xx}}{\omega^2 m} & 0 \\ 0 & 0 & \frac{K_{\theta\theta D}}{\omega^2 m} \end{bmatrix} - \right. \\
 & \left. \begin{bmatrix} 1 & 1 & h+D \\ 1 & 1 + \frac{m_o}{m} & h+D + \frac{m_o}{m} D \\ h+D & h+D + \frac{m_o}{m} D & \frac{I_T}{m} \end{bmatrix} \right\} \begin{bmatrix} \omega_n^2 u/\ddot{u}_{g_o} \\ \omega_n^2 u_r^P/\ddot{u}_{g_o} \\ \omega_n^2 \varphi_r^P/\ddot{u}_{g_o} \end{bmatrix} \quad (2.63) \\
 & = \omega^2 \left\{ \begin{bmatrix} 1 \\ 1 + \frac{m_o}{m} \\ h+D + \frac{m_o}{m} D \end{bmatrix} \frac{u_g^P}{\ddot{u}_{g_o}} + \begin{bmatrix} h+D \\ h+D + \frac{m_o}{m} D \\ \frac{I_T}{m} \end{bmatrix} \frac{\varphi_g^P}{\ddot{u}_{g_o}} \right\}
 \end{aligned}$$

4. By dividing by $(h+D)$ the third row of the equation and the third column of the system matrix, equation (2.63) can be written as follows:

$$\begin{aligned}
 & \frac{1}{\lambda^2} \left\{ \begin{bmatrix} \lambda^2 + 2\lambda\xi i & 0 & 0 \\ 0 & \frac{K_{xx}}{\omega^2 m} & 0 \\ 0 & 0 & \frac{K_{\theta\theta D}}{\omega^2 m (h+D)^2} \end{bmatrix} - \right. \\
 & \left. \begin{bmatrix} 1 & 1 & 1 \\ 1 & 1 + \frac{m_o}{m} & 1 + \frac{m_o}{m} \frac{D}{h+D} \\ 1 & 1 + \frac{m_o}{m} \frac{D}{h+D} & 1 + \frac{b^2}{3(h+D)^2} \left(1 + \frac{m_o}{m} \right) + \frac{m_o}{m} \frac{D^2}{(h+D)^2} \end{bmatrix} \right\} \begin{bmatrix} \omega_n^2 u/\ddot{u}_{g_o} \\ \omega_n^2 u_r^P/\ddot{u}_{g_o} \\ \omega_n^2 (h+D) \varphi_r^P/\ddot{u}_{g_o} \end{bmatrix} \quad (2.64) \\
 & = \omega^2 \left\{ \begin{bmatrix} 1 \\ 1 + \frac{m_o}{m} \\ 1 + \frac{m_o}{m} \frac{D}{h+D} \end{bmatrix} \frac{u_g^P}{\ddot{u}_{g_o}} + \begin{bmatrix} h+D \\ h+D + \frac{m_o}{m} D \\ h+D + \frac{b^2}{3(h+D)} \left(1 + \frac{m_o}{m} \right) + \frac{m_o}{m} \frac{D^2}{(h+D)} \end{bmatrix} \frac{\varphi_g^P}{\ddot{u}_{g_o}} \right\}
 \end{aligned}$$

5. The terms of the system matrix where there are impedance expressions can be also expressed as a function of the dimensionless parameters already defined, as indicated below:

$$\frac{K_{xx}}{\omega^2 m} = \frac{\mu_s b \tilde{K}_{xx}}{\omega^2 m} = \frac{(c_s^2 \rho_s) b \tilde{K}_{xx}}{\omega^2 m} = \left(\frac{\sigma h}{T}\right)^2 \frac{m}{4 \delta b^2 h} \frac{b \tilde{K}_{xx}}{\omega^2 m} = \frac{\lambda^2 \sigma^2 h}{16 \pi^2} \frac{1}{b \delta} \tilde{K}_{xx} \quad (2.65)$$

$$\begin{aligned} \frac{K_{\theta\theta D}}{\omega^2 m (h+D)^2} &= \frac{\mu_s b^3 \tilde{K}_{\theta\theta D}}{\omega^2 m (h+D)^2} = \frac{(c_s^2 \rho_s) b^3 \tilde{K}_{\theta\theta D}}{\omega^2 m (h+D)^2} = \\ &= \left(\frac{\sigma h}{T}\right)^2 \frac{m}{4 \delta b^2 h} \frac{b^3 \tilde{K}_{\theta\theta D}}{m (h+D)^2 \omega^2} = \frac{\lambda^2 \sigma^2 h}{16 \pi^2} \frac{1}{\delta} \frac{b^2}{b (h+D)^2} \tilde{K}_{\theta\theta D} \end{aligned} \quad (2.66)$$

It is worth mentioning that the rocking input motion at the point to which the soil-foundation interaction has been condensed matches that at the pile cap ($\varphi_g^P = \varphi_g$). Likewise, the relative rocking motion at that point coincide with the foundation relative rocking motion ($\varphi_r^P = \varphi_r^c$). Considering these equivalences, and given that $u_g^P = u_g - \varphi_g D$, equation (2.64) can be written as

$$\begin{aligned} &\left\{ \begin{bmatrix} \lambda^2 + 2\lambda\xi i & 0 & 0 \\ 0 & \lambda^2 \sigma^2 \frac{1}{16\pi^2} \frac{h}{b} \frac{1}{\delta} \tilde{K}_{xx} & 0 \\ 0 & 0 & \lambda^2 \sigma^2 \frac{1}{16\pi^2} \frac{1}{\delta} \frac{h}{b} \frac{b^2}{(h+D)^2} \tilde{K}_{\theta\theta D} \end{bmatrix} \right. \\ &- \left. \begin{bmatrix} 1 & 1 & 1 \\ 1 & 1 + \frac{m_o}{m} & 1 + \frac{m_o}{m} \frac{D}{h+D} \\ 1 & 1 + \frac{m_o}{m} \frac{D}{h+D} & 1 + \frac{1}{3} \frac{b^2}{(h+D)^2} \left(1 + \frac{m_o}{m}\right) + \frac{m_o}{m} \frac{D^2}{(h+D)^2} \end{bmatrix} \right\} \cdot \begin{bmatrix} \omega_n^2 u / \ddot{u}_{g_o} \\ \omega_n^2 u_r^P / \ddot{u}_{g_o} \\ \omega_n^2 (h+D) \varphi_r^c \ddot{u}_{g_o} \end{bmatrix} \\ &= -\lambda^2 \left\{ \begin{bmatrix} 1 \\ 1 + \frac{m_o}{m} \\ 1 + \frac{m_o}{m} \frac{D}{h+D} \end{bmatrix} I_u + \frac{h}{b} \begin{bmatrix} 1 & 1 \\ 1 + \frac{1}{3} \frac{b}{h} \frac{b}{3(h+D)} \left(1 + \frac{m_o}{m}\right) \end{bmatrix} I_\varphi \right\} \end{aligned} \quad (2.67)$$

or, alternatively, as

$$\begin{aligned} &\left\{ \lambda^2 \begin{bmatrix} (1+i2\xi') & 0 & 0 \\ 0 & \alpha_{xx}^2 (1+i2\xi_{xx}) & 0 \\ 0 & 0 & \alpha_{\theta\theta}^2 (1+i2\xi_{\theta\theta}) \end{bmatrix} \right. \\ &- \left. \begin{bmatrix} 1 & 1 & 1 \\ 1 & 1 + \frac{m_o}{m} & 1 + \frac{m_o}{m} \frac{D}{h+D} \\ 1 & 1 + \frac{m_o}{m} \frac{D}{h+D} & 1 + \frac{1}{3} \frac{b^2}{(h+D)^2} \left(1 + \frac{m_o}{m}\right) + \frac{m_o}{m} \frac{D^2}{(h+D)^2} \end{bmatrix} \right\} \cdot \begin{bmatrix} \omega_n^2 u / \ddot{u}_{g_o} \\ \omega_n^2 u_r^P / \ddot{u}_{g_o} \\ \omega_n^2 (h+D) \varphi_r^c / \ddot{u}_{g_o} \end{bmatrix} \\ &= -\lambda^2 \left\{ \begin{bmatrix} 1 \\ 1 + \frac{m_o}{m} \\ 1 + \frac{m_o}{m} \frac{D}{h+D} \end{bmatrix} I_u + \frac{h}{b} \begin{bmatrix} 1 & 1 \\ 1 + \frac{1}{3} \frac{b}{h} \frac{b}{(h+D)} \left(1 + \frac{m_o}{m}\right) \end{bmatrix} I_\varphi \right\} \end{aligned} \quad (2.68)$$

where,

$$\xi' = \frac{1}{\lambda} \xi \quad (2.69)$$

$$\alpha_{xx}^2 = \sigma^2 \frac{1}{16\pi^2} \frac{h}{b} \frac{1}{\delta} \tilde{k}_{xx} \quad (2.70)$$

$$\xi_{xx} = \frac{\tilde{c}_{xx}}{2\tilde{k}_{xx}} \quad (2.71)$$

$$\alpha_{\theta\theta}^2 = \sigma^2 \frac{1}{16\pi^2} \frac{h}{b} \frac{1}{\delta} \operatorname{Re} \left[\frac{b^2}{(h+D)^2} \tilde{K}_{\theta\theta D} \right] \quad (2.72)$$

$$\xi_{\theta\theta} = \frac{\operatorname{Im} \left[\frac{b^2}{(h+D)^2} \tilde{K}_{\theta\theta D} \right]}{2\operatorname{Re} \left[\frac{b^2}{(h+D)^2} \tilde{K}_{\theta\theta D} \right]} \quad (2.73)$$

being $\tilde{K}_{xx} = \tilde{k}_{xx} + i\tilde{c}_{xx}$ and

$$\tilde{K}_{\theta\theta D} = \frac{1}{\mu_s b^3} \left(K_{\theta\theta} - \frac{K_{\theta x}^2}{K_{xx}} \right) \quad (2.74)$$

$$\frac{b^2}{(h+D)^2} = \left(\left(\frac{h}{b} \right)^2 - 2 \left(\frac{h}{b} \right) \frac{\tilde{K}_{\theta x}}{\tilde{K}_{xx}} + \left(\frac{\tilde{K}_{\theta x}}{\tilde{K}_{xx}} \right)^2 \right)^{-1} \quad (2.75)$$

$$\frac{D}{h+D} = \frac{\tilde{K}_{\theta x}}{\tilde{K}_{xx}} \left(\frac{\tilde{K}_{\theta x}}{\tilde{K}_{xx}} - \frac{h}{b} \right)^{-1} \quad (2.76)$$

Finally, neglecting m_o , I and I_o , as usual (see, for instance [6, 12, 14]), yields

$$\left\{ \lambda^2 \begin{bmatrix} (1+i2\xi') & 0 & 0 \\ 0 & \alpha_{xx}^2(1+i2\xi_{xx}) & 0 \\ 0 & 0 & \alpha_{\theta\theta}^2(1+i2\xi_{\theta\theta}) \end{bmatrix} - \begin{bmatrix} 1 & 1 & 1 \\ 1 & 1 & 1 \\ 1 & 1 & 1 \end{bmatrix} \right\} \cdot \begin{bmatrix} \omega_n^2 u / \ddot{u}_{g_o} \\ \omega_n^2 u_r^P / \ddot{u}_{g_o} \\ \omega_n^2 (h+D) \varphi_r^c / \ddot{u}_{g_o} \end{bmatrix} = -\lambda^2 \left(I_u + \frac{h}{b} I_\varphi \right) \begin{bmatrix} 1 \\ 1 \\ 1 \end{bmatrix} \quad (2.77)$$

Solving the complex system of algebraic equations given in (2.77) for $\omega_n^2 u / \ddot{u}_{g_o}$ yields the following expression for the shear force at the base of the structure per effective earthquake force unit Q :

$$\left| \frac{\omega_n^2 u}{\ddot{u}_{g_o}} \right| = Q(\lambda) = \left| \frac{I_u(\lambda) + \frac{h}{b} I_\varphi(\lambda)}{A(\lambda) + iB(\lambda)} \right| \quad (2.78)$$

where

$$A(\lambda) = 1 - \frac{1}{\lambda^2} - \frac{1 + 4\xi_{xx}\xi'}{\lambda^2\alpha_{xx}^2(1+4\xi_{xx}^2)} - \frac{1 + 4\xi_{\theta\theta}\xi'}{\lambda^2\alpha_{\theta\theta}^2(1+4\xi_{\theta\theta}^2)} \quad (2.79)$$

$$B(\lambda) = 2 \left[\xi' - \frac{\xi' - \xi_{xx}}{\lambda^2\alpha_{xx}^2(1+4\xi_{xx}^2)} - \frac{\xi' - \xi_{\theta\theta}}{\lambda^2\alpha_{\theta\theta}^2(1+4\xi_{\theta\theta}^2)} \right] \quad (2.80)$$

2.9 Effective period and damping of the soil-foundation-structure coupled system

The objective of this section is to find the dynamic characteristics of a viscously damped single-degree-of-freedom (SDOF) oscillator (figure 2.17 (b)) able to reproduce, as accurately as possible, the response of the coupled system shown in figure 2.17 (a).

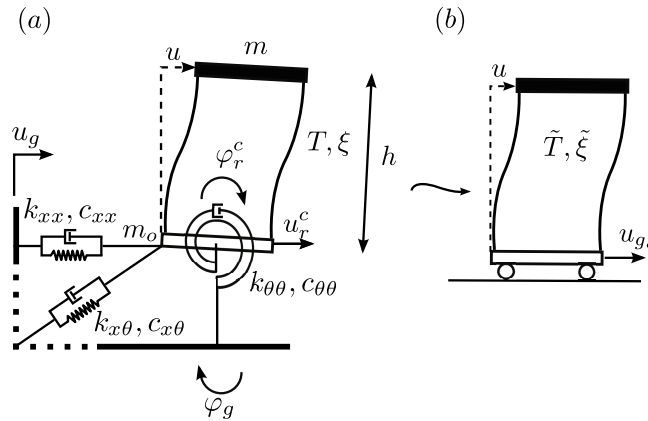


FIGURE 2.17: (a) Substructure model of a one-storey structure. (b) Equivalent single-degree-of-freedom oscillator.

This equivalent SDOF system can be defined by its undamped natural period \tilde{T} and its damping ratio $\tilde{\xi}$, so that its equation of motion can be written as

$$\frac{\tilde{\omega}_n^2 u}{\ddot{u}_{g_o}} = \frac{1}{\left(\frac{\omega^2}{\tilde{\omega}_n^2} - 1\right) - i 2\tilde{\xi}\frac{\omega}{\tilde{\omega}_n}} \quad (2.81)$$

being $\tilde{\omega}_n = 2\pi/\tilde{T}$ and

$$\tilde{Q} = \left| \frac{\tilde{\omega}_n^2 u}{\ddot{u}_{g_o}} \right| \quad (2.82)$$

the transfer-function used to establish this equivalence, which is the most appropriate from an operational point of view since it represents the ratio of the shear force at the base of the structure to the effective earthquake force [114].

It is not possible to find a SDOF system with constant impedances that exactly reproduces the harmonic response curve of a three-degrees-of-freedom (3DOF) system with

either constant or frequency-dependent impedances. Therefore, the aim is to reproduce the 3DOF system response within the range where the peak response occurs. As the definition of a SDOF system needs only two parameters, the strategies used to determine its dynamic characteristics are based on taking one common point between the target response of the 3DOF system and that of a SDOF system that best approximates it.

From an engineering point of view, the most intuitive strategy consists in taking as common point the one corresponding to the maximum value Q_m of the response spectra (see MAX in figure 2.18) as some authors such as Todorovska [16] or Avilés and Pérez-Rocha [14] do. This point can be determined in this case by the iterative resolution of the system of equations (2.52), which allows finding the peak-response period T_m and the corresponding maximum value Q_m . Then, assuming that the damping mechanism of the equivalent SDOF oscillator is of viscous nature, it is well-known [115] that its damping ratio can be found as

$$\tilde{\xi} = \frac{1}{\sqrt{2}} \left(1 - \sqrt{\frac{Q_m^2 - 1}{Q_m^2}} \right)^{\frac{1}{2}} \quad (2.83)$$

which is obtained from the expression for Q_m in figure 2.18. Now, the natural period of the equivalent oscillator \tilde{T} can be computed as

$$\tilde{T} = \sqrt{1 - 2\tilde{\xi}^2} T_m \quad (2.84)$$

which is applicable only for damping values smaller than $1/\sqrt{2}$ [115].

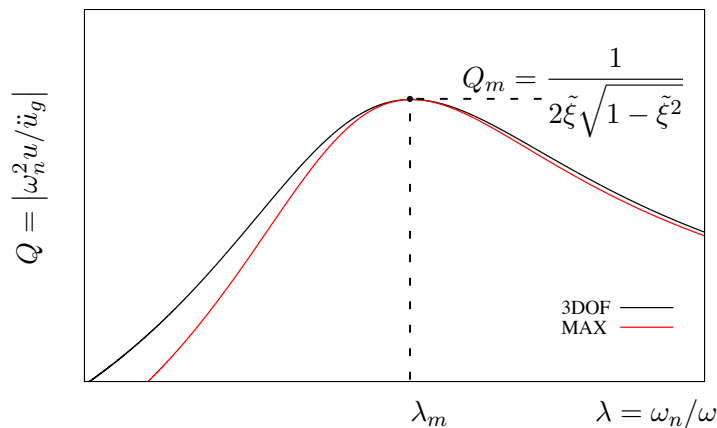


FIGURE 2.18: Maximum searching strategy (MAX) for obtaining the natural frequency and damping of the equivalent SDOF system.

Nevertheless, this strategy leads to unreliable natural frequencies in highly damped systems, in which the peak-response frequency becomes rather undefined. In these cases, the harmonic response spectra become flatter which makes it more difficult to find the frequency value associated with the maximum response value. In order to avoid this drawback, other approach based on finding the eigenvalue λ of the 3DOF system can be used.

The identification of the equations of motion of the coupled system (equations (2.78), (2.79), (2.80)), obtained after the diagonalization of the impedance matrix performed in section 2.8, and that corresponding to the SDOF system (equation (2.82)) at resonance allows obtaining the effective period by finding the root of equation (2.79). Obviously, the 3DOF system has more than one vibration mode and hence equation (2.79) has more than one root. However, in most cases of interest, the maximum response corresponds to the first mode. For this reason, from now on, the procedure focuses on that first solution λ' , despite being aware that there are more. Thus, the system damping ratio can be determined as $\xi = 1/(2Q(\lambda'))$.

Note that using the root λ' of equation (2.79) leads to a SDOF system whose peak response does not always lead to an acceptable approximation for the 3DOF system peak response (see ROOT in figure 2.19). In fact, this approach loses accuracy as $1/\sigma$ or L/b increase, as well as for decreasing structural slenderness ratios h/b . In order to illustrate these effects, figures 2.20 and 2.21 depict the response of the target coupled system (3DOF) together with the response of a SDOF equivalent system whose dynamics characteristics are computed by using this strategy. The results provided in these figures correspond to structures with $h/b = 1, 2$ and 5 , supported by 3×3 pile groups with $s/d = 5$ and $L/b = 1$ and 4 .

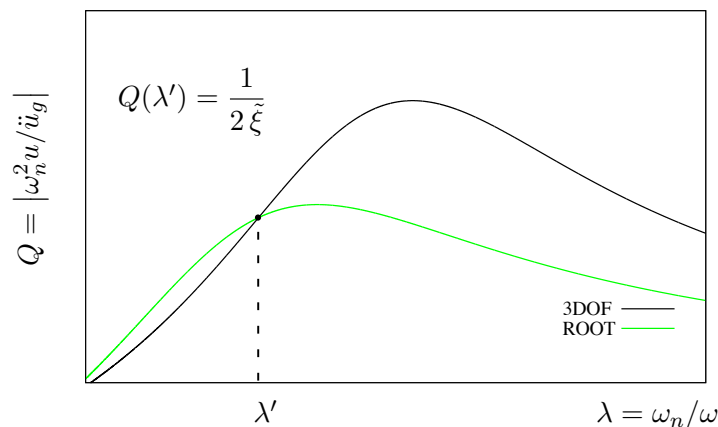


FIGURE 2.19: Root finding strategy (ROOT) for obtaining the natural frequency and damping of the equivalent SDOF system without neglecting second-order damping terms.

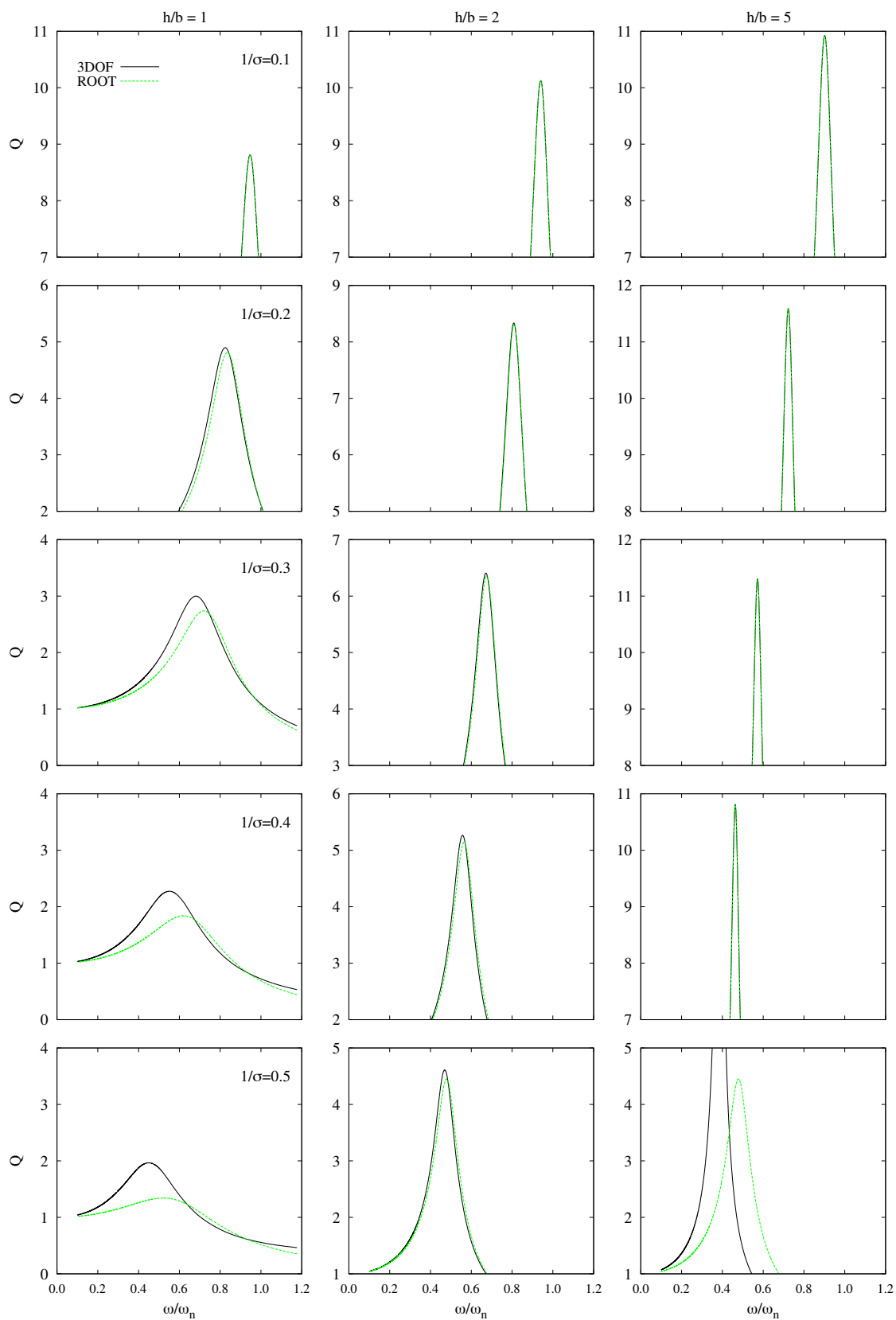


FIGURE 2.20: Replacement oscillator approach to 3DOF system on a 3×3 pile group with $s/d = 5$ and $L/b = 1$. $E_p/E_s = 10^3$ and $\xi_s = 0.05$. ROOT strategy.

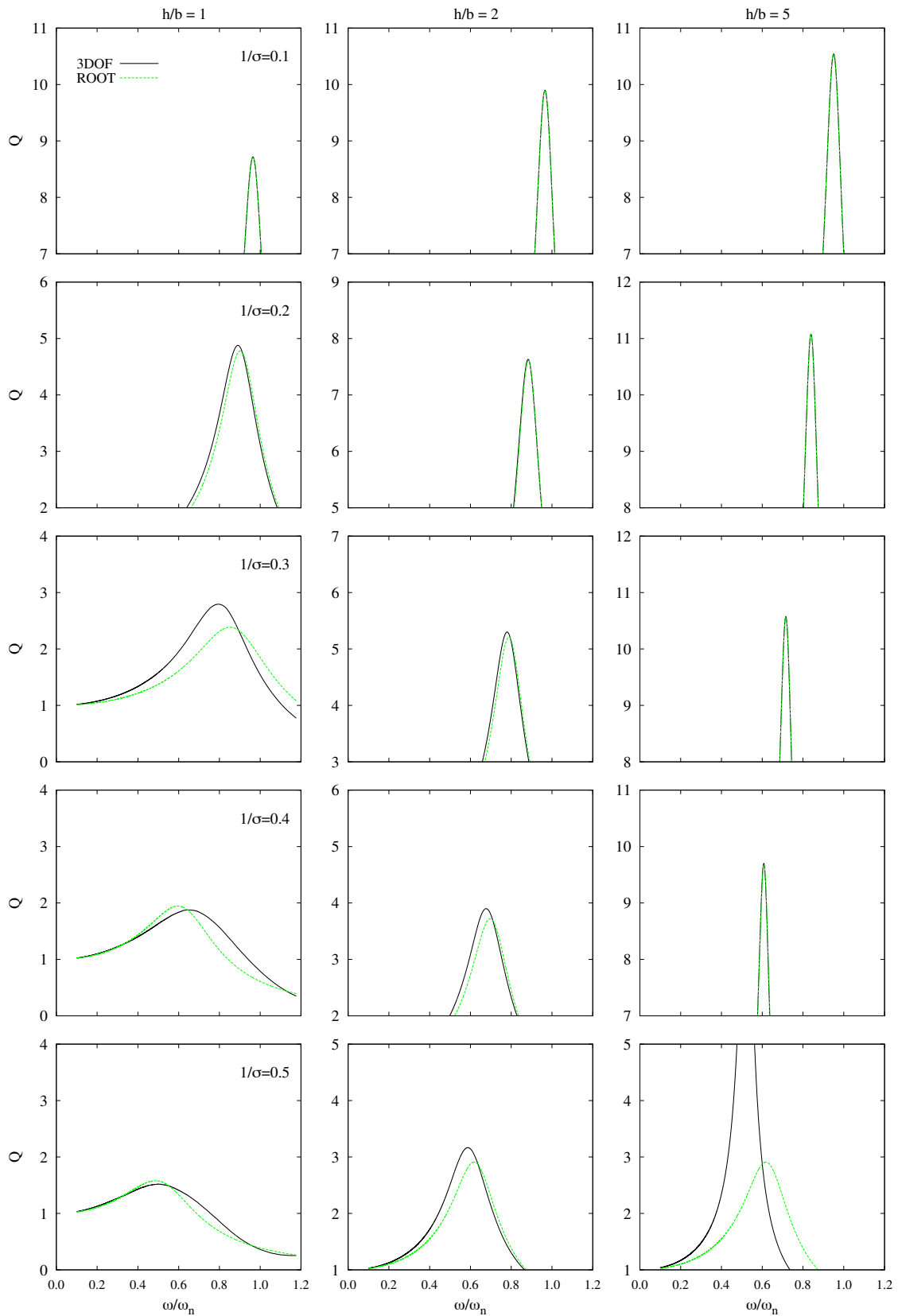


FIGURE 2.21: Replacement oscillator approach to 3DOF system on a 3×3 pile group with $s/d = 5$ and $L/b = 4$. $E_p/E_s = 10^3$ and $\xi_s = 0.05$. ROOT strategy.

On the other hand, neglecting (as Avilés and Pérez-Rocha [14] do) all second-order damping terms, leads to the following approximate expressions for A and B :

$$A(\lambda) = 1 - \frac{1}{\lambda^2} - \frac{1}{\lambda^2 \alpha_{xx}^2} - \frac{1}{\lambda^2 \alpha_{\theta\theta}^2} \quad (2.85)$$

$$B(\lambda) = 2 \left[\xi' - \frac{\xi' - \xi_{xx}}{\lambda^2 \alpha_{xx}^2} - \frac{\xi' - \xi_{\theta\theta}}{\lambda^2 \alpha_{\theta\theta}^2} \right] \quad (2.86)$$

The dimensionless undamped natural frequency of the SDOF system $\tilde{\lambda} = \omega_n / \tilde{\omega}_n$ can be found as the root of equation (2.85). This is equivalent to the resolution of the eigenvalue problem from equation (2.77), without considering damping.

As, in this case, $\tilde{\xi} = 1/(2Q(\tilde{\lambda}))$, and taking the approximate expression for $Q(\tilde{\lambda})$ obtained from taking equations (2.85) and (2.86) as values of A and B , one can write the system damping ratio as

$$\tilde{\xi} = \left| \left(I_u + \frac{h}{b} I_\varphi \right)^{-1} \frac{1}{\tilde{\lambda}^2} \left(\xi' + \frac{\xi_{xx}}{\alpha_{xx}^2} + \frac{\xi_{\theta\theta}}{\alpha_{\theta\theta}^2} \right) \right| \quad (2.87)$$

However, this approach does not always provide a good approximation for the 3DOF system peak response as shown in figure 2.22, where results obtained by using this strategy (EIGEN-S) are represented for structures supported on a 3×3 pile group with $s/d = 5$ and $L/b = 2$.

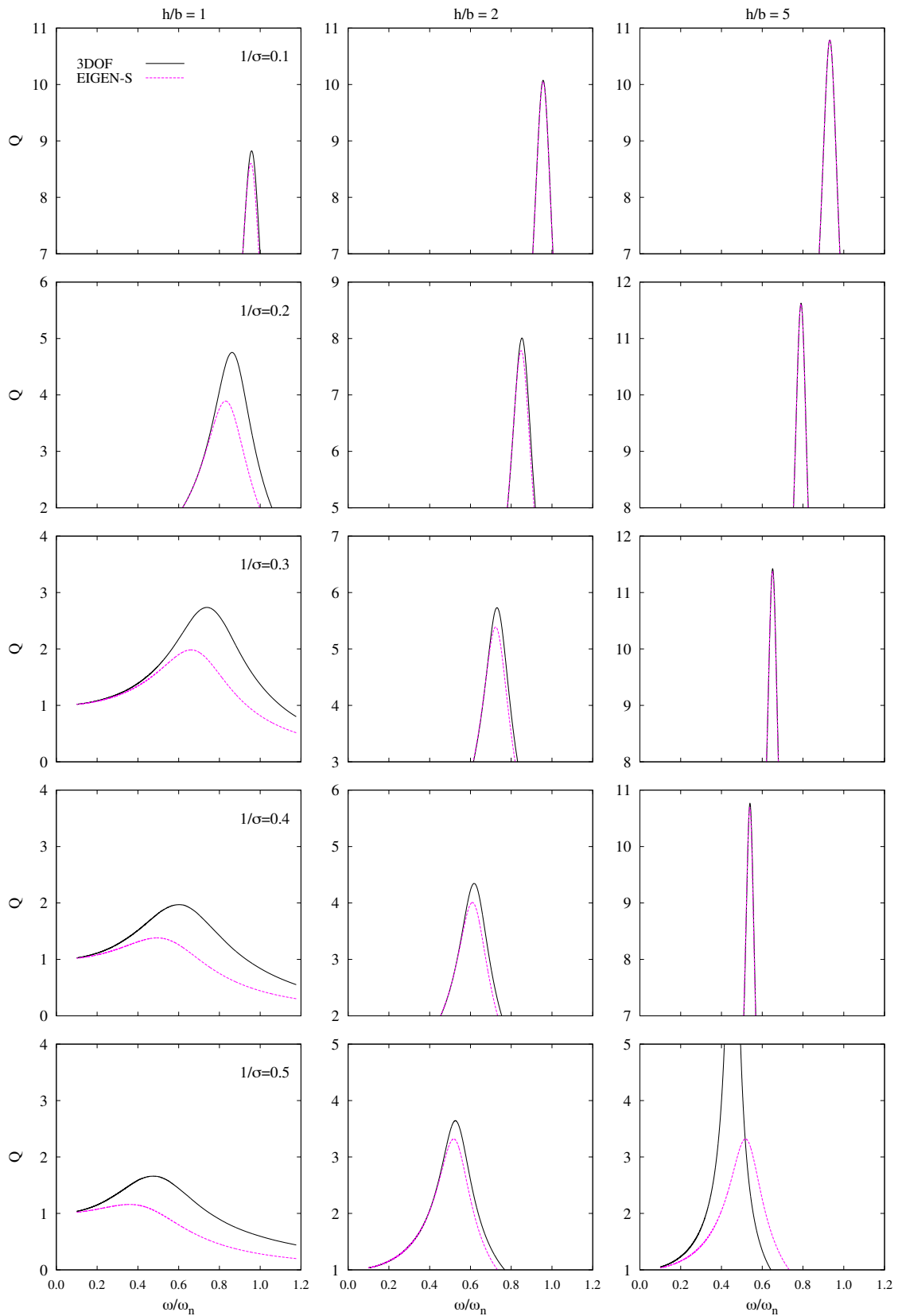


FIGURE 2.22: Replacement oscillator approach to 3DOF system on a 3×3 pile group with $s/d = 5$ and $L/b = 2$. $E_p/E_s = 10^3$ and $\xi_s = 0.05$. EIGEN-S strategy.

Consequently, the proposed procedure (EIGEN in figure 2.23) computes the dimensionless undamped natural frequency of the SDOF system $\tilde{\lambda}$ as the root of equation (2.85) but, unlike what Avilés and Pérez-Rocha [14] do, this procedure calculates $\tilde{\xi}$ from equations (2.79) and (2.80) for the values of A and B instead of equations (2.85) and (2.86), which yields the following expression:

$$\tilde{\xi} = \left| \left(I_u + \frac{h}{b} I_\varphi \right)^{-1} \left[\frac{\xi'}{\tilde{\lambda}^2} + \frac{1}{\tilde{\lambda}^2} \left(\frac{\xi_{xx}}{\alpha_{xx}^2 (1 + i2\xi_{xx})} + \frac{\xi_{\theta\theta}}{\alpha_{\theta\theta}^2 (1 + i2\xi_{\theta\theta})} \right) \right] \right| \quad (2.88)$$

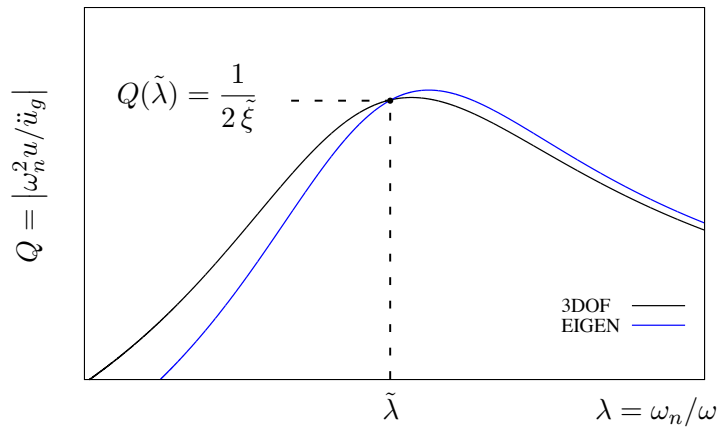


FIGURE 2.23: Proposed procedure (EIGEN) for obtaining the natural frequency of the equivalent SDOF system by neglecting second-order damping terms, and determining the damping coefficient by considering them.

Figure 2.24 shows that considering second-order damping terms when computing the SDOF effective damping $\tilde{\xi}$ (EIGEN) yields a better approximation for the 3DOF system peak than neglecting them (EIGEN-S). For this purpose, results corresponding to both approaches are plotted together with the dynamic response of the target coupled system (3DOF) for structures supported on a 3×3 pile group with $s/d = 5$ and $L/b = 4$.

Figures 2.25, 2.26 and 2.27 allow analysing how the pile group configuration affects the influence that neglecting all second-order terms has on the dynamic characteristics of the equivalent system. For this purpose, results in terms of the system effective period \tilde{T}/T and damping $\tilde{\xi}$ are depicted in these figures for several configurations of pile groups. The influence of adopting this simplification increases with decreasing values of the pile slenderness ratio L/d (see figure 2.25), the structural slenderness ratio h/b and the wave parameter σ , as well as with increasing values of the embedment ratio L/b (see figure 2.26), and the group size (see figure 2.27). Indeed, this assumption may lead to significant differences on the system period and damping values when $h/b \leq 2$.

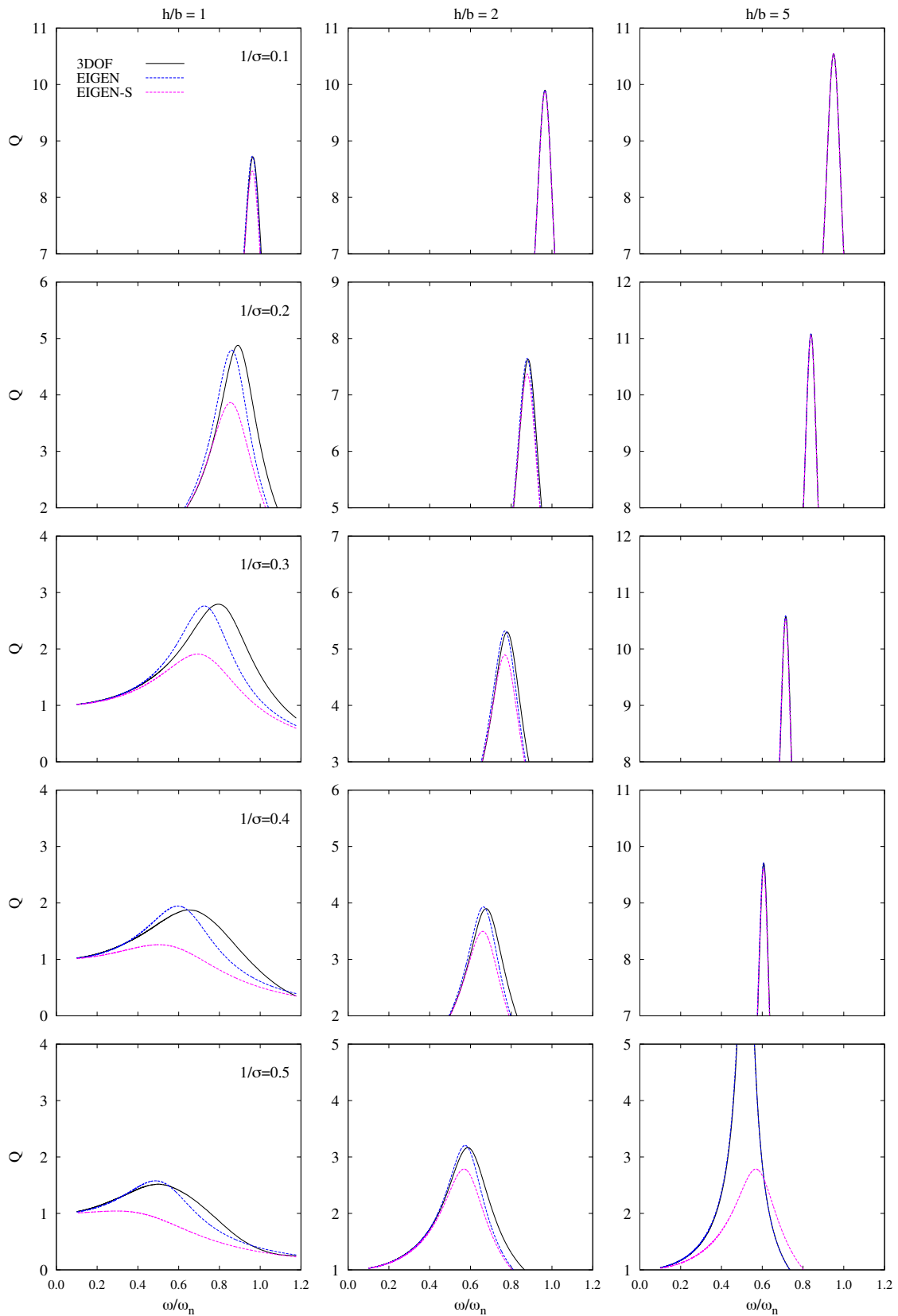


FIGURE 2.24: Replacement oscillator approach to 3DOF system on a 3×3 pile group with $s/d = 5$ and $L/b = 4$. $E_p/E_s = 10^3$ and $\xi_s = 0.05$. EIGEN vs EIGEN-S.

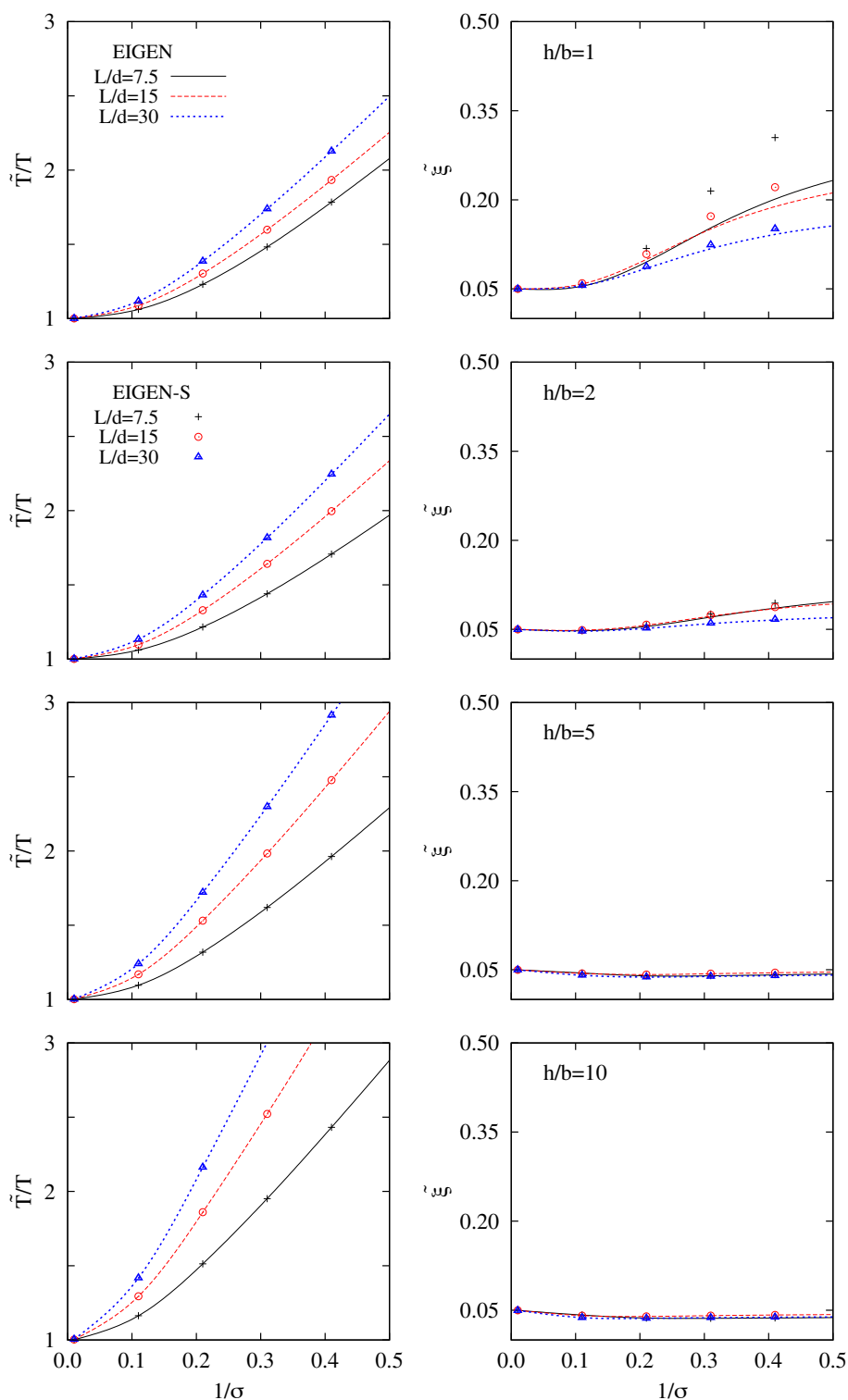


FIGURE 2.25: Influence of neglecting all second-order damping terms. Root finding procedure (EIGEN) vs simplified root finding procedure (EIGEN-S). Effective period \tilde{T}/T and damping ratio $\tilde{\xi}$ for a 4×4 pile group with $L/b = 2$, $E_p/E_s = 10^3$ and $\xi_s = 0.05$.

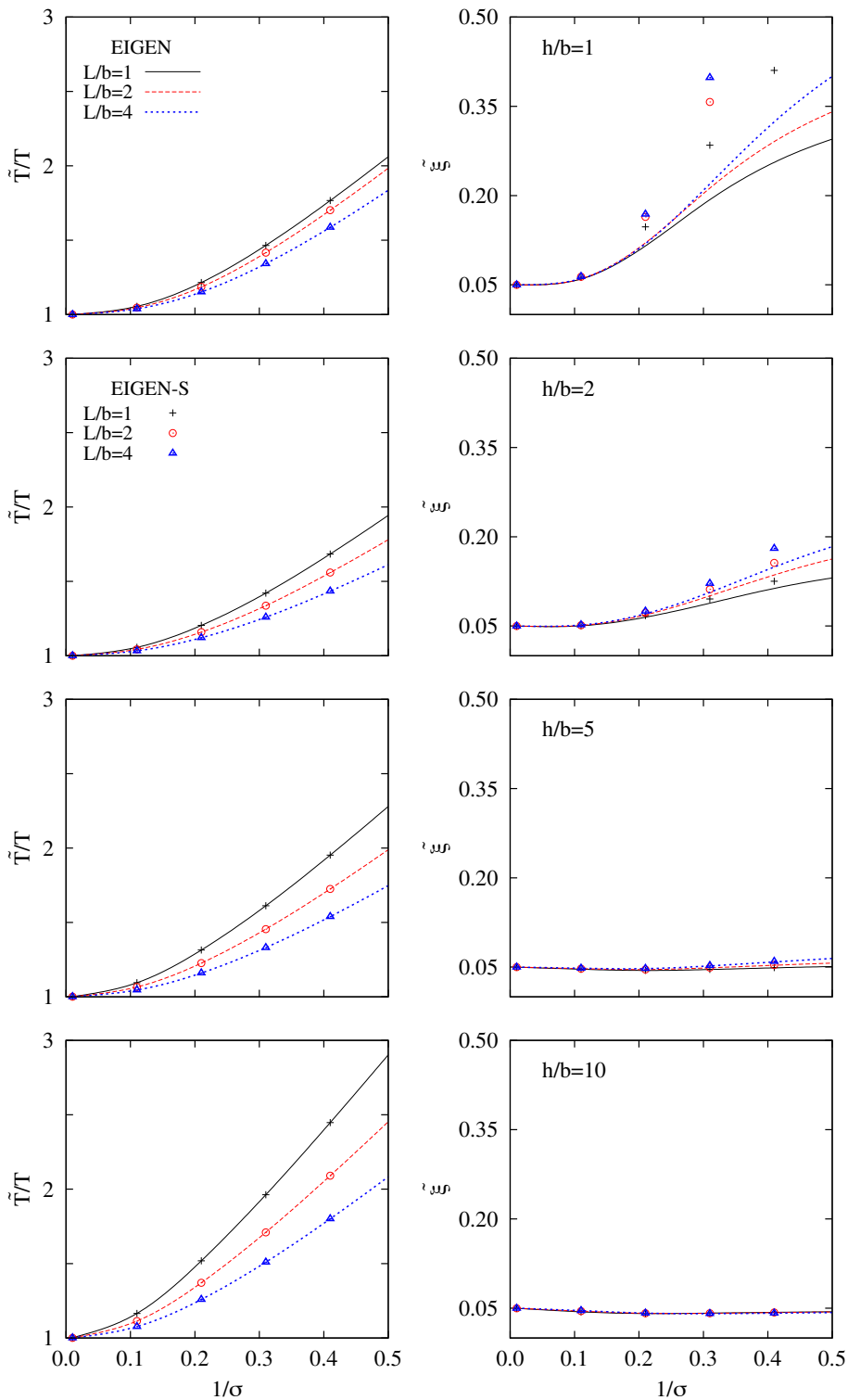


FIGURE 2.26: Influence of neglecting all second-order damping terms. Root finding procedure (EIGEN) vs simplified root finding procedure (EIGEN-S). Effective period \tilde{T}/T and damping ratio $\tilde{\xi}$ for a 4×4 pile group with $s/d = 3.75$, $E_p/E_s = 10^3$ and $\xi_s = 0.05$.

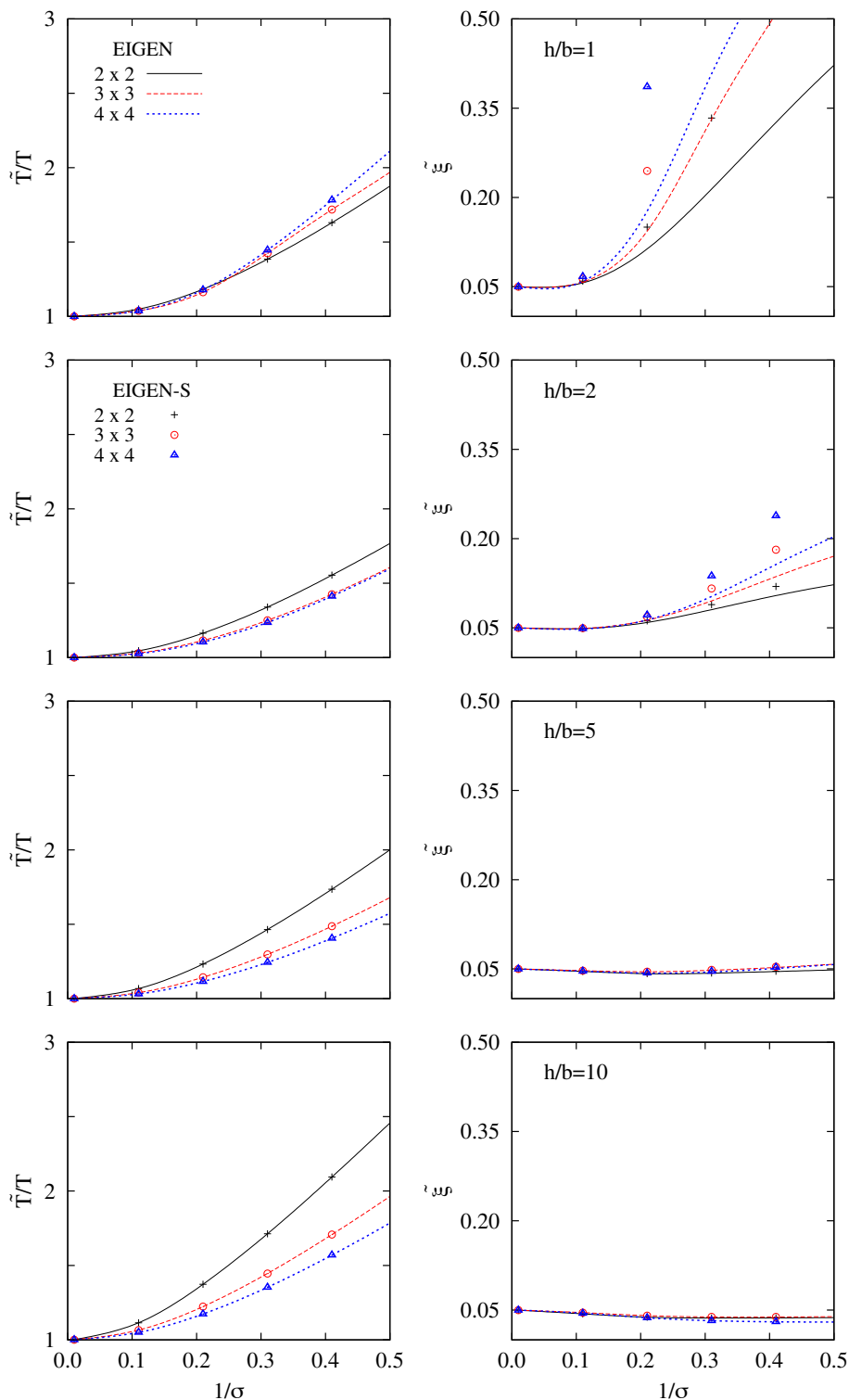


FIGURE 2.27: Influence of neglecting all second-order damping terms. Root finding procedure (EIGEN) vs simplified root finding procedure (EIGEN-S). Effective period \tilde{T}/T and damping ratio $\tilde{\xi}$ for 2×2 , 3×3 and 4×4 pile groups with $L/b = 4$, $L/d = 15$, $E_p/E_s = 10^3$ and $\xi_s = 0.05$.

In order to illustrate the different strategies used to determine the dynamic characteristics of an equivalent SDOF system, figure 2.28 shows a schematic representation of the response of the target coupled system (3DOF) together with that of the different equivalent SDOF models described along this section. Differences have been exaggerated in the figure to highlight the characteristics of these strategies, and show that none of these approaches reproduces exactly the response of the coupled system, having each one of them its own advantages and disadvantages.

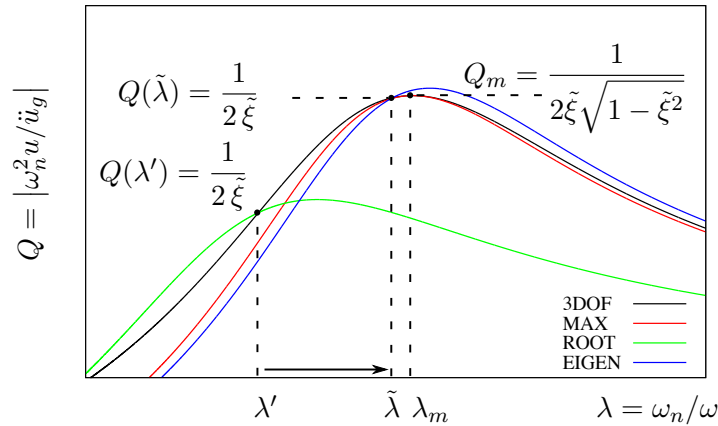


FIGURE 2.28: Strategies for obtaining the natural frequency and damping of the equivalent SDOF system.

When $\tilde{\xi} < 0.2$, effective period and damping results obtained either from the root finding procedure (EIGEN) proposed in this thesis, or by the iterative solution of the system of equations given in equation (2.52) to find the maximum response value (MAX), are almost coincident. Figure 2.29 illustrates this fact for one particular case. However, although both procedures lead to good results in most cases, it is important to point out that, contrary to what occurs with the maximum searching algorithm (MAX), the root finding procedure (EIGEN) will show, in all cases, a stable behaviour whose reliability is not affected by increasing values of the equivalent system damping ($\tilde{\xi} > 0.2$). For this reason, the simplified procedure (EIGEN) is the strategy employed forward, being also true that, as discussed below, the equivalent SDOF system is not always applicable as a simplified methodology for highly damped systems.

Finally, after having described the numerical procedure to be used for defining the parameters of the equivalent single-degree-of-freedom system, and keeping in mind that the response of such SDOF replacement oscillator does not match exactly that of the complete 3DOF system, it is necessary to establish a practical range of validity which, as generally assumed, will depend on the problem characteristics. Avilés and Suárez [20] drew the conclusion that the equivalent SDOF approach is not adequate for highly damped systems ($\tilde{\xi} > 0.2$), which usually corresponds to very short structures ($h/b \leq 1$) on soft soils ($1/\sigma > 0.2$). The results obtained for a significant number of the configurations analysed in the present work agree with such conclusion and suggest a limit value of the parameter $1/\sigma$ between 0.2 and 0.3, depending on the configuration. However, in many other cases, the replacement SDOF oscillator yields excellent results even for high damping ratios ($\tilde{\xi} > 0.2$). On the other hand, the pile group configuration is another

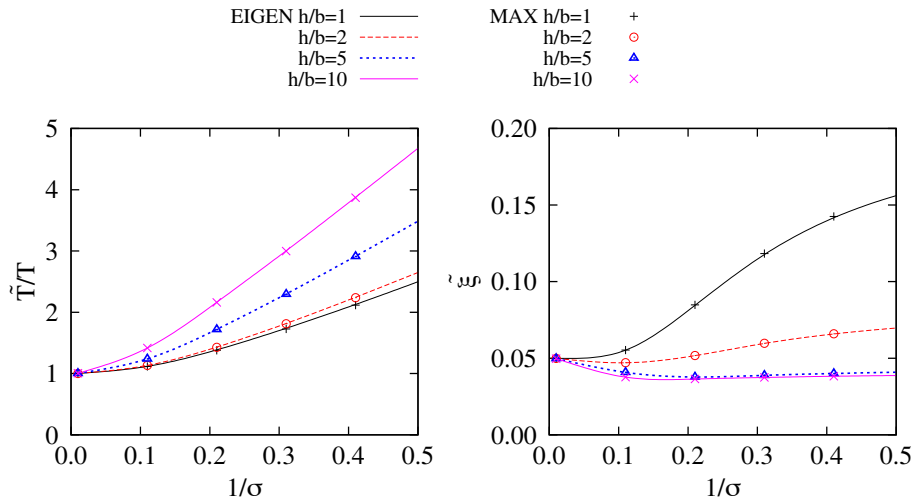


FIGURE 2.29: Root finding procedure (EIGEN) *vs* maximum searching algorithm (MAX). Effective period \tilde{T}/T and damping ratio $\tilde{\xi}$ for a 2×2 pile group. $E_p/E_s = 10^3$, $s/d = 15$, $h/b = 2, 5, 10$, $L/b = 2$, $L/d = 30$ and $\xi_s = 0.05$.

important parameter in the range of validity of the approach. In order to illustrate this fact, figure 2.30 presents frequency response functions and elastic response spectra (corresponding to the N-S component of the 1940 El Centro Earthquake [114]) both obtained keeping $1/\sigma$ constant as in [7], for the case of a 2×2 pile group with embedment and slenderness ratios of $L/b = 2$ and $L/d = 7.5$ and 15 , respectively. In both cases, for $h/b = 1$, the equivalent damping ratio $\tilde{\xi}$ is very similar (see right plots in the same figure). However, while the SDOF replacement oscillator is able to approximate very closely the frequency response functions of the complete system when $L/d = 15$, the same does not hold when $L/d = 7.5$. As a consequence, the elastic response spectra obtained from the equivalent SDOF system are very close to those obtained using the response of the complete 3DOF system for $L/d = 15$ and all values of $1/\sigma$. However, discrepancies are very important for $L/d = 7.5$, even for $1/\sigma = 0.1$. Therefore, it is important to point out that the equivalent single-degree-of-freedom approach shows a finite range of validity that should be taken into account before its practical application.

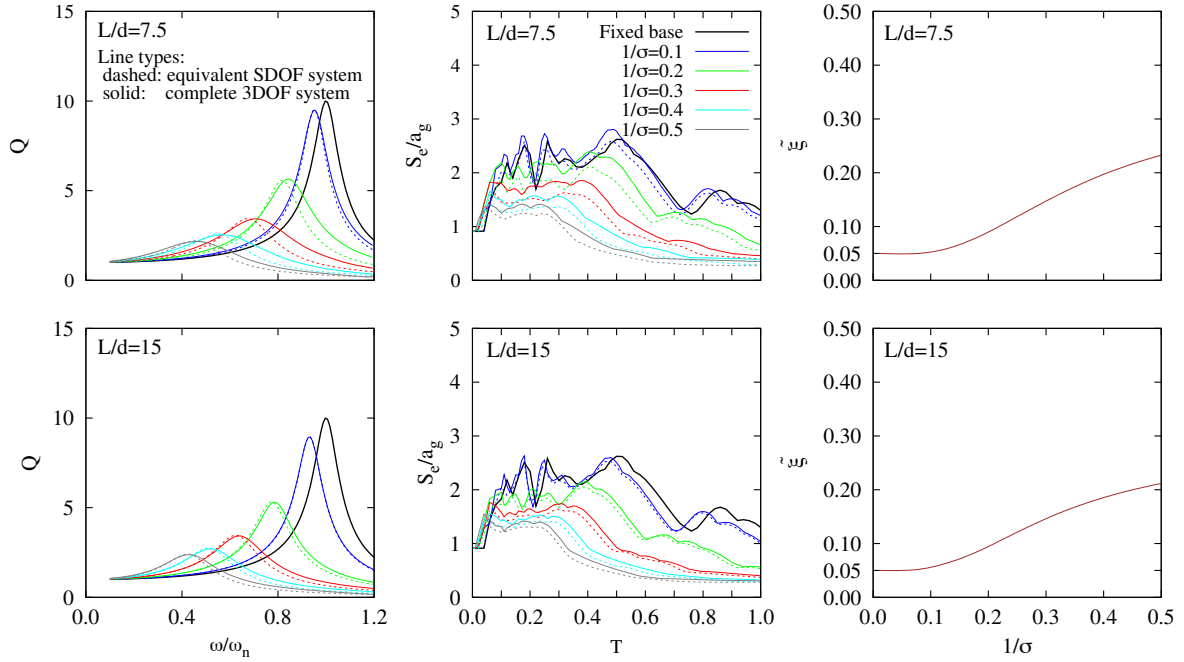


FIGURE 2.30: Replacement oscillator approach to 3DOF system on a 2×2 pile group. $L/b = 1$, $L/d = 7.5$ (top) and $L/d = 15$ (bottom). Transfer functions (left column), elastic response spectra corresponding to the 1940 El Centro Earthquake (central column), and damping ratio ($\tilde{\xi}$) of the equivalent SDOF replacement oscillator (right column).

2.10 Implementation

For the purpose of illustrating the practical implementation of the strategies explained in section 2.9 in a code, algorithms 2.1 and 2.2 show, respectively, pseudocodes for the computation of the system effective period \tilde{T}/T and damping $\tilde{\xi}$ through a maximum finding strategy (MAX), as well as by using root finding procedures (ROOT, EIGEN or EIGEN-S).

The maximum finding algorithm consists in an iterative procedure that searches the maximum of the harmonic spectrum for different values of the wave parameter σ . As shown in algorithm 2.1, this procedure starts in $\sigma = \sigma_{max}$, where $1/\sigma_{max}$ takes a value close to zero which corresponds to very soft structures or very hard soils. This implies that the system period in flexible base tends to the value corresponding to fixed-base condition $\tilde{T} \rightarrow T$ and, consequently, the system effective period \tilde{T}/T tends to the unit value $\tilde{T}/T \rightarrow 1$. Thus, with the assumption of $\lambda^{(i)} = 1$, values of the shear force at the base of the structure per effective earthquake force unit Q are computed at $\lambda^{(i)} - \Delta\lambda$, $\lambda^{(i)}$ and $\lambda^{(i)} + \Delta\lambda$, being $\Delta\lambda \rightarrow 0$, through the expression in equation (2.78), where $A^{(i)}$ and $B^{(i)}$ are obtained from equations (2.79) and (2.80), respectively. Given that these curves are known to be smooth, the search point is displaced in the direction of increasing Q until a maximum is reached, moment in which the corresponding $\lambda^{(i)}$ is stored as the period $(T_m/T)^{(i)}$ corresponding to the maximum response Q_m for this value of σ . Afterwards, the effective damping ratio $\tilde{\xi}^{(i)}$ is determined by introducing the obtained value for $Q_m^{(i)}$

in equation (2.83). Finally, the effective period of the equivalent oscillator $(\tilde{T}/T)^{(i)}$ is computed from equation (2.84). Then, the iterative procedure is repeated for decreasing values of σ until $\sigma = \sigma_{min}$, this time starting at the last computed value of λ , being $\lambda^{(i)} = \lambda^{(i-1)}$.

On the other hand, algorithm 2.2 outlines the implementation of the procedure proposed in this work (EIGEN), as well as that of other strategies (ROOT and EIGEN-S), also based on root finding algorithms. It is worth mentioning that the same algorithm can be used to obtain results corresponding to each one of these strategies only by modifying the expressions used to compute the real (A) and imaginary (B) parts of the denominator of the shear force at the base of the structure per effective earthquake force unit Q , and that used to determine the system effective damping $\tilde{\xi}$. This algorithm is an iterative procedure that searches the root of the real part A of the denominator of Q . In the case of the procedure named ROOT, A is defined in equation (2.79). However, for strategies EIGEN and EIGEN-S all second-order damping terms are neglected and, consequently, A is computed from equation (2.85). This iterative procedure starts in $\sigma = \sigma_{max}$, where $1/\sigma_{max} \rightarrow 0$ which implies that $\tilde{T}/T \rightarrow 1$, as explained above. Thus, with the assumption of $\lambda^{(i)} = 1$, values of A are computed at $\lambda^{(i)}$ and $\lambda^{(i)} + \Delta\lambda$, being $\Delta\lambda \rightarrow 0$. These two points are moved until the sign of A experiences a change, moment in which the value of λ which leads to the lower absolute value of $A^{(i)}$ is stored as the system effective period $(\tilde{T}/T)^{(i)}$. Then, $Q^{(i)}$ is computed from equation (2.78), being $A^{(i)}$ and $B^{(i)}$ obtained either from equations (2.79) and (2.80), when second order damping terms are considered (ROOT and EIGEN), or from equations (2.85) and (2.86), when these terms are neglected (EIGEN-S). Finally, the system effective damping $\tilde{\xi}^{(i)}$ is determined either from equation (2.88) (ROOT and EIGEN) or from its approximate expression in equation (2.87) (EIGEN-S). Afterwards, the iterative procedure is repeated for decreasing values of σ until $\sigma = \sigma_{min}$, this time starting at the last computed value of λ , being $\lambda^{(i)} = \lambda^{(i-1)}$.

Algorithm 2.1 Pseudocode for the computation of $\tilde{T}/T = \mathcal{F}(\sigma)$ and $\tilde{\xi} = \mathcal{G}(\sigma)$ using the maximum finding algorithm (MAX)

INPUT: Set of parameters defining the system: h/b , δ , ξ , foundation impedances (\tilde{K}_{xx} , $\tilde{K}_{\theta x}$ and $\tilde{K}_{\theta\theta}$) and kinematic interaction factors (I_u and I_φ); and algorithm parameters σ_{min} , σ_{max} , $\Delta\sigma$, and $\Delta\lambda$.

$Q^{(i)}$ is obtained from equation (2.78), being $A^{(i)}$ and $B^{(i)}$ obtained, respectively, from equations (2.79) and (2.80).

for $\sigma^{(i)} = \sigma_{max}$ to σ_{min} , in steps of $\Delta\sigma$ **do**

if $\sigma^{(i)} = \sigma_{max}$ **then**

$\lambda^{(i)} \leftarrow 1$

else

$\lambda^{(i)} \leftarrow \lambda^{(i-1)}$

end if

$Q_1^{(i)} = Q(\lambda^{(i)} - \Delta\lambda)$

$Q_2^{(i)} = Q(\lambda^{(i)})$

$Q_3^{(i)} = Q(\lambda^{(i)} + \Delta\lambda)$

do

if $Q_3^{(i)} \geq Q_2^{(i)}$ **then**

$\lambda^{(i)} \leftarrow \lambda^{(i)} + \Delta\lambda$

$Q_1^{(i)} \leftarrow Q_2^{(i)}$

$Q_2^{(i)} \leftarrow Q_3^{(i)}$

$Q_3^{(i)} = Q(\lambda^{(i)} + \Delta\lambda)$

else if $Q_1^{(i)} \geq Q_2^{(i)}$ **then**

$\lambda^{(i)} \leftarrow \lambda^{(i)} - \Delta\lambda$

$Q_3^{(i)} \leftarrow Q_2^{(i)}$

$Q_2^{(i)} \leftarrow Q_1^{(i)}$

$Q_1^{(i)} = Q(\lambda^{(i)} - \Delta\lambda)$

end if

while ($Q_1^{(i)} \geq Q_2^{(i)}$).OR. ($Q_3^{(i)} \geq Q_2^{(i)}$)

$(T_m/T)^{(i)} \leftarrow \lambda^{(i)}$

$Q^{(i)} \leftarrow Q_2^{(i)}$

compute $\tilde{\xi}^{(i)}$ from Eq. (2.83)

compute $(\tilde{T}/T)^{(i)}$ from Eq.(2.84)

end for

OUTPUT: $\sigma^{(i)}$, $(\tilde{T}/T)^{(i)}$, $\tilde{\xi}^{(i)}$

Algorithm 2.2 Pseudocode for the computation of $\tilde{T}/T = \mathcal{F}(\sigma)$ and $\tilde{\xi} = \mathcal{G}(\sigma)$ using root finding algorithms (ROOT, EIGEN or EIGEN-S)

INPUT: Set of parameters defining the system: h/b , δ , ξ , foundation impedances (\tilde{K}_{xx} , $\tilde{K}_{\theta x}$ and $\tilde{K}_{\theta\theta}$) and kinematic interaction factors (I_u and I_φ); and algorithm parameters σ_{min} , σ_{max} , $\Delta\sigma$, and $\Delta\lambda$.

$A^{(i)}$ is obtained from equation (2.79) (ROOT) or from equation (2.85) (EIGEN and EIGEN-S).

for $\sigma^{(i)} = \sigma_{max}$ to σ_{min} , in steps of $\Delta\sigma$ **do**

if $\sigma^{(i)} = \sigma_{max}$ **then**

$\lambda^{(i)} \leftarrow 1$

else

$\lambda^{(i)} \leftarrow (\tilde{T}/T)^{(i-1)}$

end if

$A_1^{(i)} = A(\lambda^{(i)})$

$A_2^{(i)} = A(\lambda^{(i)} + \Delta\lambda)$

do

if ($A_1^{(i)} > 0$.AND. $A_2^{(i)} > 0$) .OR. ($A_1^{(i)} < 0$.AND. $A_2^{(i)} < 0$) **then**

$\lambda^{(i)} \leftarrow \lambda^{(i)} + \Delta\lambda$

$A_1^{(i)} \leftarrow A_2^{(i)}$

$A_2^{(i)} = A(\lambda^{(i)} + \Delta\lambda)$

else

if $|A_1^{(i)}| > |A_2^{(i)}|$ **then**

$(\tilde{T}/T)^{(i)} \leftarrow \lambda^{(i)} - \Delta\lambda$

else

$(\tilde{T}/T)^{(i)} \leftarrow \lambda^{(i)}$

end if

end if

while ($A_1^{(i)} > 0$.AND. $A_2^{(i)} > 0$) .OR. ($A_1^{(i)} < 0$.AND. $A_2^{(i)} < 0$)

compute $Q^{(i)}$ from equation (2.78), being $A^{(i)}$ and $B^{(i)}$ obtained, respectively, either from equations (2.79) and (2.80) (ROOT and EIGEN), or from equations (2.85) and (2.86) (EIGEN-S).

compute $\tilde{\xi}^{(i)}$ from equation (2.88) (ROOT and EIGEN) or from equation (2.87) (EIGEN-S).

end for

OUTPUT: $\sigma^{(i)}$, $(\tilde{T}/T)^{(i)}$, $\tilde{\xi}^{(i)}$

2.11 Model validation

In order to complete the validation of the proposed model, the results obtained from the system dimensionless equations of motion are validated in this section through comparison against results provided by Veletsos and Meek [7] for shallow foundations, paper in which impedance functions come from Bielak [12] and Verbic and Veletsos [116]. Moreover, results computed for embedded foundations are compared with those obtained by Avilés and Pérez-Rocha [14].

2.11.1 Shallow foundations. Comparison with Veletsos and Meek [7]

The system equations of motion (equation (2.68)) obtained in section 2.8 for pile foundations applies as well to shallow foundations. Nevertheless, in this case, the cross-coupled impedances are cancelled ($K_{\theta x} = 0$) yielding $D = 0$, which implies that $u_r^P = u_r^c$. Moreover, the foundation input motion coincides with the free-field motion at the ground surface, which is exclusively horizontal ($u_g = u_{g_o}$ and $\varphi_g = 0$). Therefore, the kinematic interaction factor associated with rotation is cancelled $I_\varphi = 0$, whereas that associated with translation is equal to the unit $I_u = 1$. Thus, equation (2.68) can be written for shallow foundations as

$$\left\{ \begin{array}{l} \lambda^2 \left[\begin{array}{ccc} (1+i2\xi') & 0 & 0 \\ 0 & \alpha_{xx}^2(1+i2\xi_{xx}) & 0 \\ 0 & 0 & \alpha_{\theta\theta}^2(1+i2\xi_{\theta\theta}) \end{array} \right] - \\ \left[\begin{array}{ccc} 1 & 1 & 1 \\ 1 & 1+\frac{m_o}{m} & 1 \\ 1 & 1 & 1+\frac{b^2}{3h^2} \left(1+\frac{m_o}{m}\right) \end{array} \right] \end{array} \right\} \cdot \left[\begin{array}{c} \omega_n^2 u / \ddot{u}_{g_o} \\ \omega_n^2 u_r^c / \ddot{u}_{g_o} \\ \omega_n^2 h \varphi_r^c / \ddot{u}_{g_o} \end{array} \right] \quad (2.89)$$

$$= -\lambda^2 \left[\begin{array}{c} 1 \\ 1+\frac{m_o}{m} \\ 1 \end{array} \right]$$

where,

$$\xi' = \frac{1}{\lambda} \xi \quad (2.90)$$

$$\alpha_{xx}^2 = \sigma^2 \frac{1}{16\pi^2} \frac{h}{b} \frac{1}{\delta} \tilde{k}_{xx} \quad (2.91)$$

$$\xi_{xx} = \frac{\tilde{c}_{xx}}{2\tilde{k}_{xx}} \quad (2.92)$$

$$\alpha_{\theta\theta}^2 = \sigma^2 \frac{1}{16\pi^2} \frac{b}{h} \frac{1}{\delta} \tilde{k}_{\theta\theta} \quad (2.93)$$

$$\xi_{\theta\theta} = \frac{\tilde{c}_{\theta\theta}}{2\tilde{k}_{\theta\theta}} \quad (2.94)$$

being $\tilde{K}_{xx} = \tilde{k}_{xx} + i\tilde{c}_{xx}$ and $\tilde{K}_{\theta\theta} = \tilde{k}_{\theta\theta} + i\tilde{c}_{\theta\theta}$.

In the case of shear structures supported by shallow foundations consisting of a rigid circular plate of negligible thickness, as those studied by Veletsos and Meek [7], the problem under study corresponds to the sketch depicted in figure 2.31. In this figure, the parameters defining the superstructure are the same as those mentioned in section 2.3 for the case of pile foundations. In that section, the foundation mass m_o and the mass of the structure m were supposed to be uniformly distributed over square areas, whereas Veletsos and Meek presume that they are uniformly distributed over circular areas. Notice that the rotational inertias have, in this case, the expressions $I_o = m_o r^2/4$ and $I = m r^2/4$, respectively, being r the radius of these circular areas. Likewise, the structural slenderness ratio is now defined as h/r . Furthermore, this change in the foundation geometry also entails a variation in the expression that relates mass density ratio δ to soil density ρ_s . This relation can be written, for circular foundations, as $\delta = m/(\rho_s \pi r^2)h$. In addition, impedances are normalized, in this case, with respect to r as follows: $\tilde{K}_{xx} = K_{xx}/(\mu_s r)$ and $\tilde{K}_{\theta\theta} = K_{\theta\theta}/(\mu_s r^3)$. Finally, the dimensionless frequency is here defined as $a_o = \omega r/c_s$.

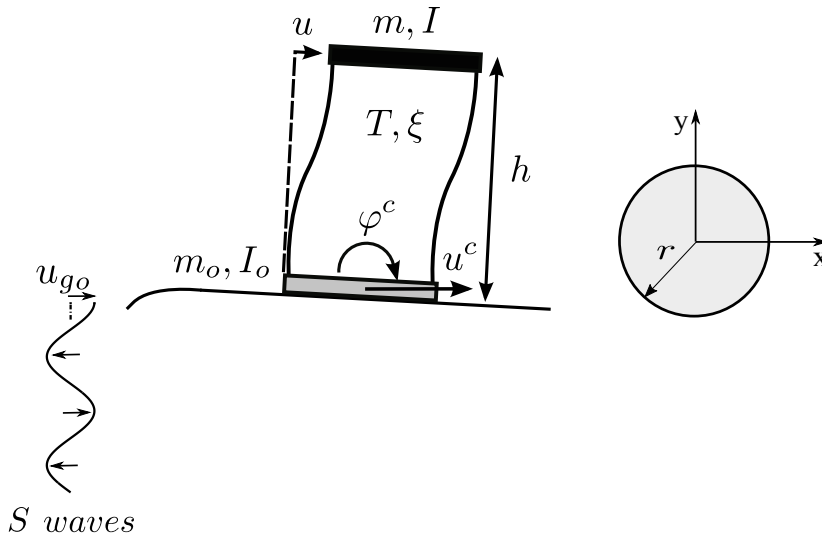


FIGURE 2.31: Problem definition. Single shear structure supported on a shallow foundation at the surface of a homogeneous half-space under vertically-incident S waves.

A dimensionless system equation of motion, analogous to that provided above for square foundations (equation (2.89)), can be obtained for circular foundations from equation (2.13) by considering the above-mentioned changes in the procedure already described in section 2.7, which leads to the following expression:

$$\begin{aligned}
 & \left\{ \lambda^2 \begin{bmatrix} (1+i2\xi') & 0 & 0 \\ 0 & \alpha_{xx}^2(1+i2\xi_{xx}) & 0 \\ 0 & 0 & \alpha_{\theta\theta}^2(1+i2\xi_{\theta\theta}) \end{bmatrix} - \right. \\
 & \left. \begin{bmatrix} 1 & 1 & 1 \\ 1 & 1+\frac{m_o}{m} & 1 \\ 1 & 1 & 1+\frac{r^2}{4h^2} \left(1+\frac{m_o}{m}\right) \end{bmatrix} \right\} \cdot \begin{bmatrix} \omega_n^2 u / \ddot{u}_{g_o} \\ \omega_n^2 u_r^c / \ddot{u}_{g_o} \\ \omega_n^2 h \varphi_r^c / \ddot{u}_{g_o} \end{bmatrix} \\
 & = -\lambda^2 \begin{bmatrix} 1 \\ 1+\frac{m_o}{m} \\ 1 \end{bmatrix}
 \end{aligned} \tag{2.95}$$

where,

$$\xi' = \frac{1}{\lambda} \xi \tag{2.96}$$

$$\alpha_{xx}^2 = \sigma^2 \frac{1}{4\pi^3} \frac{h}{r} \frac{1}{\delta} \tilde{k}_{xx} \tag{2.97}$$

$$\xi_{xx} = \frac{\tilde{c}_{xx}}{2\tilde{k}_{xx}} \tag{2.98}$$

$$\alpha_{\theta\theta}^2 = \sigma^2 \frac{1}{4\pi^3} \frac{r}{h} \frac{1}{\delta} \tilde{k}_{\theta\theta} \tag{2.99}$$

$$\xi_{\theta\theta} = \frac{\tilde{c}_{\theta\theta}}{2\tilde{k}_{\theta\theta}} \tag{2.100}$$

being $\tilde{K}_{xx} = \tilde{k}_{xx} + i\tilde{c}_{xx}$ and $\tilde{K}_{\theta\theta} = \tilde{k}_{\theta\theta} + i\tilde{c}_{\theta\theta}$.

It should be noted that the results presented herein have been obtained considering the following parameters: $m_o/m = 0$, $I_o = 0$, $\nu_s = 0.45$, $\xi = 0.02$ and $\delta = 0.15$, as Veletsos and Meek do.

With regard to the impedances of the foundation mat, Veletsos and Meek [7] give a set of simple expressions for horizontal and rocking impedance functions which depend on a series of dimensionless parameters (α_x , α_θ , β_x and β_θ). These expressions can be written as follows:

$$K_{xx} = k_{xx}^s \left(\hat{k}_{xx} + i a_o \hat{c}_{xx} \right) \tag{2.101}$$

$$K_{\theta\theta} = k_{\theta\theta}^s \left(\hat{k}_{\theta\theta} + i a_o \hat{c}_{\theta\theta} \right) \tag{2.102}$$

where

$$k_{xx}^s = \frac{8}{2 - \nu_s} \mu_s r \tag{2.103}$$

$$\hat{k}_{xx} = \alpha_x \tag{2.104}$$

$$\hat{c}_{xx} = \beta_x \tag{2.105}$$

$$k_{\theta\theta}^s = \frac{8}{2 - \nu_s} \mu_s r \tag{2.106}$$

$$\hat{k}_{\theta\theta} = \alpha_\theta \tag{2.107}$$

$$\hat{c}_{\theta\theta} = \beta_\theta \tag{2.108}$$

The values for the dimensionless parameters α_x , α_θ , β_x and β_θ , corresponding to a supporting soil with a Poisson's ratio $\nu_s = 0.45$, have been digitized from the cited work and are depicted in figure 2.32. Plots for other values of ν_s can be found in [117].

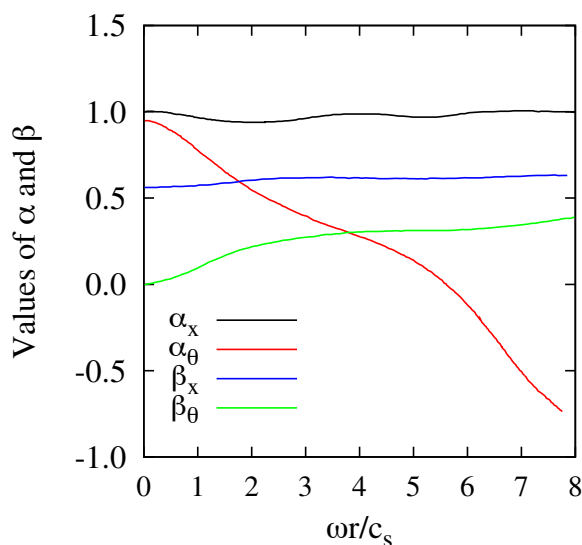


FIGURE 2.32: Dimensionless coefficients in expressions for foundation stiffness and damping (after Veletsos and Meek [7]).

It may be noticed that the expression proposed for the static stiffness in the rocking vibration mode (equation (2.106)) does not allow expressing the system equation of motion in terms of the dimensionless parameters defined in section 2.7. Indeed, a mismatch can be detected through a comparison against that extracted from a paper by Veletsos and Verbic [118], which was previously extracted from a report by Verbic and Veletsos [116]. In order to clarify this point, the approximate expressions provided by

Verbic and Veletsos for impedance functions are written below using the same mathematical representation written in equations (2.101) and (2.102).

$$k_{xx}^s = \frac{8}{2 - \nu_s} \mu_s r \quad (2.109)$$

$$\hat{k}_{xx} = 1 \quad (2.110)$$

$$\hat{c}_{xx} = a_1 \quad (2.111)$$

$$k_{\theta\theta}^s = \frac{8}{3(1 - \nu_s)} \mu_s r^3 \quad (2.112)$$

$$\hat{k}_{\theta\theta} = 1 - \frac{b_1 (b_2 a_o)^2}{1 + (b_2 a_o)^2} - b_3 a_o^2 \quad (2.113)$$

$$\hat{c}_{\theta\theta} = \frac{b_1 b_2 (b_2 a_o)^2}{1 + (b_2 a_o)^2} \quad (2.114)$$

where a_1 , b_1 , b_2 and b_3 are numerical coefficients which depend on ν_s , as shown in table 2.6.

TABLE 2.6: Numerical coefficients in equations (2.111) to (2.114) (after Veletsos and Verbic [118]).

Quantity	ν_s			
	0	1/3	0.45	0.5
a_1	0.775	0.65	0.60	0.60
b_1	0.525	0.5	0.45	0.4
b_2	0.8	0.8	0.8	0.8
b_3	0	0	0.023	0.027

Moreover, results obtained for the harmonic response spectra by using the expressions proposed by Veletsos and Meek for the impedances does not coincide with those extracted from the plots provided in the same work. By contrast, the expressions provided by Veletsos and Verbic, allow obtaining these curves. Consequently, for the results shown in this section, the impedance functions have been extracted from the aforementioned paper by Veletsos and Verbic.

For the purpose of validating the proposed model, figure 2.33 allows comparing the results obtained with the proposed model against those provided by Veletsos and Meek, in terms of system effective frequency T/\tilde{T} and damping $\tilde{\xi}$ for structural slenderness ratios $h/r = 1, 2$ and 5 . As pointed out by Veletsos and Meek, some relevant conclusions can be drawn from these results:

- The system effective frequency T/\tilde{T} decreases with the wave parameter σ , as well as for increasing values of the structural slenderness ratio h/r .

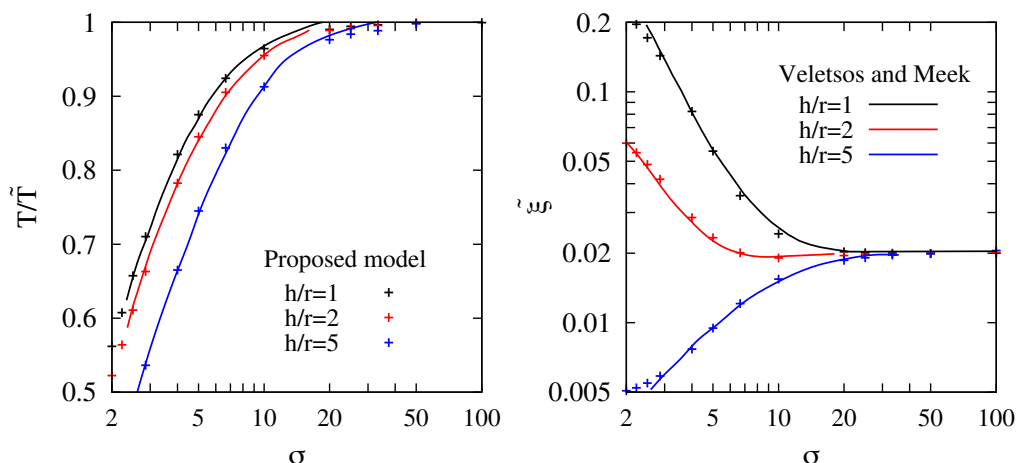


FIGURE 2.33: Comparison between the results obtained with the proposed model and those extracted from the original paper, by Veletsos and Meek [7].

- The influence of SSI on the system effective damping $\tilde{\xi}$ increases for decreasing values of σ . The system damping may reach greater or lower values than that corresponding to fixed-base condition depending on h/r . Veletsos and Meek explain this fact as the result of two opposite effects: as the soil-structure relative stiffness σ decreases, the effective damping ratio $\tilde{\xi}$ tends to increase as a consequence of an increment of the energy dissipated into the soil; however, a diminution of σ leads also to an increase of the foundation rocking, yielding higher inertia forces at the structural mass m , which in turn results in an increment of the structural response. This latter effect is more important as the slenderness ratio increases h/r , leading to smaller values of the effective damping $\tilde{\xi}$. On the contrary, the former effect is the controlling one for non-slender structures, which explains an increment of $\tilde{\xi}$ as h/r decreases.

Negligible differences are obtained when comparing the results computed through the proposed procedure with those provided by Veletsos and Meek. It is worth mentioning that the slight differences that can be observed in the effective damping are due to small discrepancies between the expressions provided by Veletsos and Verbic and those proposed by Veletsos and Meek for stiffness and damping coefficients, as shown in figure 2.34.

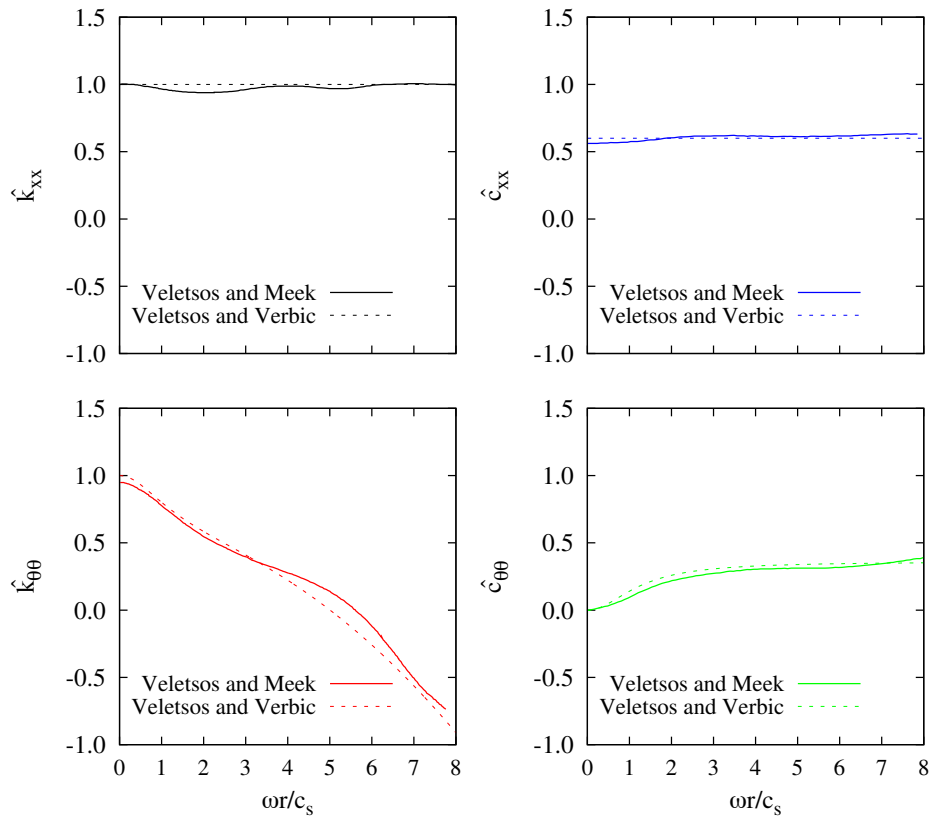


FIGURE 2.34: Comparison between stiffness and damping coefficients given by Veletsos and Meek [7] and those provided by Veletsos and Verbic [118].

2.11.2 Embedded foundations. Comparison with Avilés and Pérez-Rocha [14]

The procedure proposed in this work is also applicable for embedded foundations as that shown in figure 2.35. In this figure, the parameters characterizing the superstructure are the same as those defined in section 2.3 for the case of pile foundations. Nevertheless, it should be noticed that, in this case, D_e represents the embedment depth. The foundation horizontal displacement u^c and rocking φ^c , as well as the horizontal u_g and rocking φ_g input motions are defined, in this case, at the bottom of the foundation. Furthermore, the foundation mass m_o is presumed to be located at half the depth of embedment.

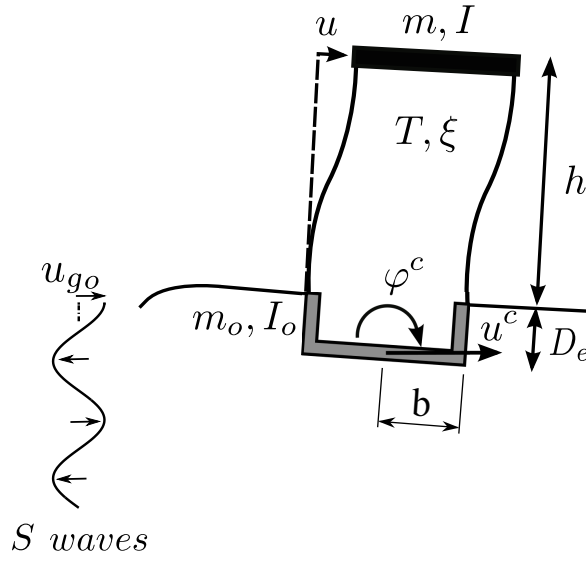


FIGURE 2.35: Problem definition. Single shear structure supported on a foundation embedded in a homogeneous half-space under vertically-incident S waves.

Thus, the equations of motion of the system sketched in figure 2.35 can be written, in terms of relative motions $u_r^c = u^c - u_g$ and $\varphi_r^c = \varphi^c - \varphi_g$, as

$$m \cdot [\ddot{u} + \ddot{u}_r^c + \ddot{u}_g + (h + D_e)(\ddot{\varphi}_r^c + \ddot{\varphi}_g)] + K \cdot u = 0 \quad (2.115)$$

$$m_o \cdot [\ddot{u}_r^c + \ddot{u}_g + \frac{D_e}{2}(\ddot{\varphi}_r^c + \ddot{\varphi}_g)] + K_{xx} \cdot u_r^c + K_{x\theta} \cdot \varphi_r^c - K \cdot u = 0 \quad (2.116)$$

$$m \cdot (h + D_e)[\ddot{u} + \ddot{u}_r^c + \ddot{u}_g + (h + D_e)(\ddot{\varphi}_r^c + \ddot{\varphi}_g)] + I(\ddot{\varphi}_r^c + \ddot{\varphi}_g) + K_{\theta x} \cdot u_r^c + K_{\theta\theta} \cdot \varphi_r^c + m_o \frac{D_e}{2}[\ddot{u}_r^c + \ddot{u}_g + \frac{D_e}{2}(\ddot{\varphi}_r^c + \ddot{\varphi}_g)] + I_o(\ddot{\varphi}_r^c + \ddot{\varphi}_g) = 0 \quad (2.117)$$

where equation (2.115) represents the equilibrium of forces acting on the building, equation (2.116) the horizontal force equilibrium of the soil-foundation system and equation (2.117) the moment equilibrium of the structure-foundation system about the centre of the base.

It can be observed that for $D_e = 0$ equations (2.115), (2.116) and (2.117) coincide, respectively, with those written in section 2.4.1 for pile foundations (equations (2.10), (2.11) and (2.12)). Likewise, by following an analogous procedure to that described in section 2.7, these equations can be written in the frequency domain (with time dependance $e^{i\omega t}$), in terms of the dimensionless parameters defined in that section. Furthermore, as it was explained in section 2.8, the soil-foundation interaction is condensed to a point at a certain virtual depth $D(\omega) = -K_{x\theta}/K_{xx}$, in order to diagonalize the impedance matrix. Thus, the system equations of motion can be expressed as

$$\left\{ \lambda^2 \begin{bmatrix} (1+i2\xi') & 0 & 0 \\ 0 & \alpha_{xx}^2(1+i2\xi_{xx}) & 0 \\ 0 & 0 & \alpha_{\theta\theta}^2(1+i2\xi_{\theta\theta}) \end{bmatrix} - \begin{bmatrix} 1 & 1 & 1 \\ 1 & 1 + \frac{m_o}{m} & 1 + \frac{m_o}{m} \frac{D_e+2D}{2(h+D+D_e)} \\ 1 & 1 + \frac{m_o}{m} \frac{D_e+2D}{2(h+D+D_e)} & 1 + \frac{b^2}{3(h+D+D_e)^2} \left(1 + \frac{m_o}{m}\right) + \frac{m_o}{m} \frac{(D_e+2D)^2}{4(h+D+D_e)^2} \end{bmatrix} \right\} \quad (2.118)$$

$$\begin{bmatrix} \omega_n^2 u / \ddot{u}_{g_o} \\ \omega_n^2 u_r^P / \ddot{u}_{g_o} \\ \omega_n^2 (h+D+D_e) \varphi_r^c / \ddot{u}_{g_o} \end{bmatrix} = -\lambda^2 \left\{ \begin{bmatrix} 1 \\ 1 + \frac{m_o}{m} \\ 1 + \frac{m_o}{m} \frac{D_e+2D}{2(h+D+D_e)} \end{bmatrix} I_u + \left(\frac{h}{b} + \frac{D_e}{b} \right) \begin{bmatrix} 1 \\ 1 + \frac{m_o}{m} \frac{D_e}{2(h+D_e)} \\ 1 + \frac{b^2}{3(h+D_e)(h+D+D_e)} \left(1 + \frac{m_o}{m}\right) + \frac{m_o}{m} \frac{D_e(D_e+2D)}{4(h+D_e)(h+D+D_e)} \end{bmatrix} I_\varphi \right\}$$

where $u_g^P = u_g - \varphi_g D$ and

$$\xi' = \frac{1}{\lambda} \xi \quad (2.119)$$

$$\alpha_{xx}^2 = \sigma^2 \frac{1}{16\pi^2} \frac{h}{b} \frac{1}{\delta} \tilde{k}_{xx} \quad (2.120)$$

$$\xi_{xx} = \frac{\tilde{c}_{xx}}{2\tilde{k}_{xx}} \quad (2.121)$$

$$\alpha_{\theta\theta}^2 = \sigma^2 \frac{1}{16\pi^2} \frac{h}{b} \frac{1}{\delta} \operatorname{Re} \left[\frac{b^2}{(h+D+D_e)^2} \tilde{K}_{\theta\theta D} \right] \quad (2.122)$$

$$\xi_{\theta\theta} = \frac{\operatorname{Im} \left[\frac{b^2}{(h+D+D_e)^2} \tilde{K}_{\theta\theta D} \right]}{2\operatorname{Re} \left[\frac{b^2}{(h+D+D_e)^2} \tilde{K}_{\theta\theta D} \right]} \quad (2.123)$$

being $\tilde{K}_{xx} = \tilde{k}_{xx} + i\tilde{c}_{xx}$ and

$$\tilde{K}_{\theta\theta D} = \frac{1}{\mu_s b^3} \left(K_{\theta\theta} - \frac{K_{\theta x}^2}{K_{xx}} \right) \quad (2.124)$$

$$\frac{b^2}{(h+D+D_e)^2} = \left(\frac{h}{b} + \frac{D_e}{b} - \frac{\tilde{K}_{\theta x}}{\tilde{K}_{xx}} \right)^{-2} \quad (2.125)$$

$$\frac{D_e+2D}{h+D+D_e} = \left(\frac{D_e}{b} - 2 \frac{\tilde{K}_{\theta x}}{\tilde{K}_{xx}} \right) \left(\frac{h}{b} + \frac{D_e}{b} - \frac{\tilde{K}_{\theta x}}{\tilde{K}_{xx}} \right)^{-1} \quad (2.126)$$

$$\frac{b}{h + D_e} = \left(\frac{h}{b} + \frac{D_e}{b} \right)^{-1} \quad (2.127)$$

$$\frac{D_e}{h + D_e} = \frac{D_e}{b} \left(\frac{h}{b} + \frac{D_e}{b} \right)^{-1} \quad (2.128)$$

Finally, neglecting m_o , I and I_o , as usual (see, for instance [6, 12, 14]), yields

$$\left\{ \lambda^2 \begin{bmatrix} (1+i2\xi') & 0 & 0 \\ 0 & \alpha_{xx}^2(1+i2\xi_{xx}) & 0 \\ 0 & 0 & \alpha_{\theta\theta}^2(1+i2\xi_{\theta\theta}) \end{bmatrix} - \begin{bmatrix} 1 & 1 & 1 \\ 1 & 1 & 1 \\ 1 & 1 & 1 \end{bmatrix} \right\} \begin{bmatrix} \omega_n^2 u / \ddot{u}_{g_o} \\ \omega_n^2 u_r^P / \ddot{u}_{g_o} \\ \omega_n^2 (h + D + D_e) \varphi_r^c / \ddot{u}_{g_o} \end{bmatrix} = -\lambda^2 \left(I_u + \left(\frac{h}{b} + \frac{D_e}{b} \right) I_\varphi \right) \begin{bmatrix} 1 \\ 1 \\ 1 \end{bmatrix} \quad (2.129)$$

Solving the complex system of algebraic equations given in equation (2.129) for $\omega_n^2 u / \ddot{u}_{g_o}$ yields the following expression for the shear force at the base of the structure per effective earthquake force unit Q :

$$\left| \frac{\omega_n^2 u}{\ddot{u}_{g_o}} \right| = Q(\lambda) = \left| \frac{I_u(\lambda) + \left(\frac{h}{b} + \frac{D_e}{b} \right) I_\varphi(\lambda)}{A(\lambda) + iB(\lambda)} \right| \quad (2.130)$$

where

$$A(\lambda) = 1 - \frac{1}{\lambda^2} - \frac{1 + 4\xi_{xx}\xi'}{\lambda^2 \alpha_{xx}^2 (1 + 4\xi_{xx}^2)} - \frac{1 + 4\xi_{\theta\theta}\xi'}{\lambda^2 \alpha_{\theta\theta}^2 (1 + 4\xi_{\theta\theta}^2)} \quad (2.131)$$

$$B(\lambda) = 2 \left[\xi' - \frac{\xi' - \xi_{xx}}{\lambda^2 \alpha_{xx}^2 (1 + 4\xi_{xx}^2)} - \frac{\xi' - \xi_{\theta\theta}}{\lambda^2 \alpha_{\theta\theta}^2 (1 + 4\xi_{\theta\theta}^2)} \right] \quad (2.132)$$

It should be noticed that, when the embedment depth is cancelled $D_e = 0$, equations (2.118) and (2.129) coincide with those written for pile foundations in equations (2.68) and (2.77), respectively. Likewise, the expression of the shear force at the base of the structure per effective earthquake force unit Q for embedded foundations (equation (2.130)) matches that obtained for pile foundations (equation (2.78)) when $D_e = 0$.

In order to validate the proposed model, figure 2.36 depicts the results provided by Avilés and Pérez-Rocha [14] for embedded foundations, in terms of system effective period \tilde{T}/T and damping $\tilde{\xi}$, together with those obtained by using the procedure proposed in this Ph. D. thesis. In this figure, each column show results corresponding to a different embedment ratio: $D_e/b = 0$ (left column), 0.5 (central column) and 1.5 (right column). Likewise, each chart provide results for two structural slenderness ratios: $h/b = 1$, corresponding to non-slender structures, and $h/b = 3$, corresponding to slender structures. Note further that results obtained when considering kinematic and inertial interaction are represented together with those computed without considering kinematic interaction. All these results are obtained making use of the impedance functions and input

motions provided, in tabular form, by Mita and Luco [119] for the soil hysteretic damping ratios for S and P waves $\xi_S = 0.001$ and $\xi_P = 0.0005$, respectively. In addition, it is assumed that $\nu_s = 1/3$, $\xi = 0.05$ and $\delta = 0.15$. It is worth mentioning that cross-coupled impedances and all second-order damping terms have been considered.

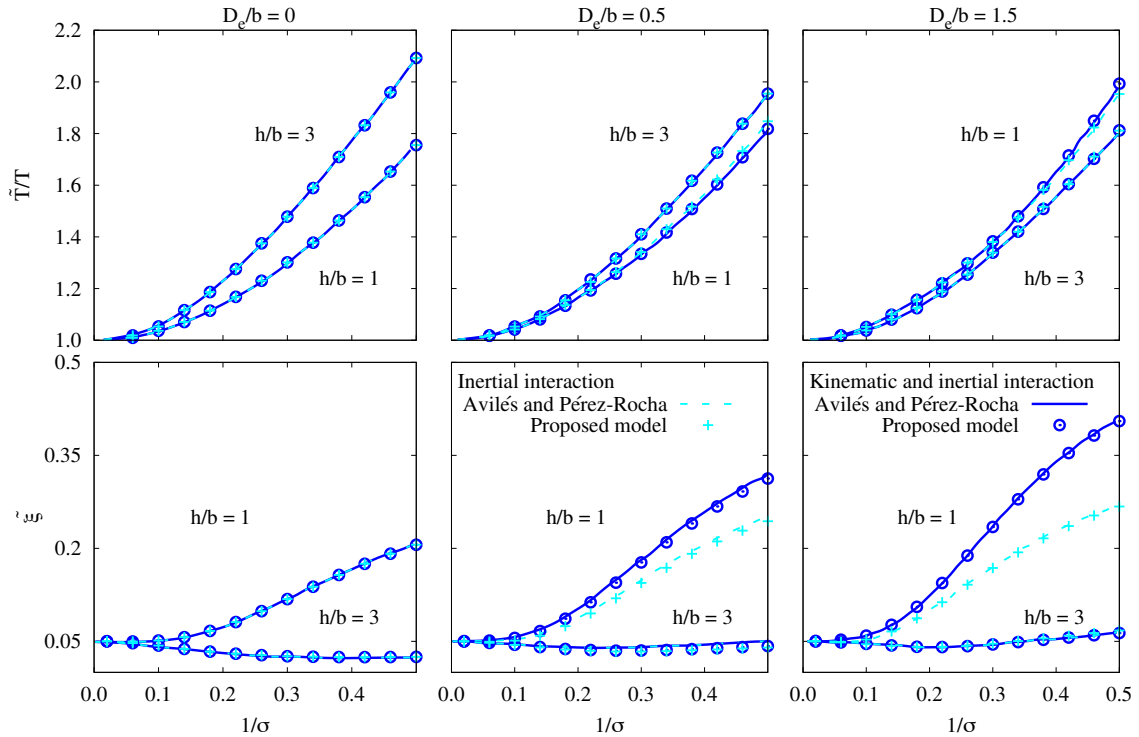



FIGURE 2.36: Comparison between the results obtained with the proposed model and those digitized from the original paper, by Avilés and Pérez-Rocha [14].

As already pointed out by Avilés and Pérez-Rocha, the following trends are worthy of note in figure 2.36:

- The system effective period \tilde{T}/T grows as the wave parameter σ decreases. For non-slender structures ($h/b = 1$), it increases with the embedment ratio D_e/b . On the contrary, in the case of slender structures ($h/b = 3$), \tilde{T}/T experiences a reduction as D_e/b grows. It should be noted that the system effective period increases with the structural slenderness ratio h/b , except for $D_e/b = 1.5$. Besides, it can be observed that the system period is not affected by the consideration of kinematic interaction.
- With regard to the system effective damping $\tilde{\xi}$, it can be seen that it experiences a reduction as h/b grows. For non-slender structures ($h/b = 1$), $\tilde{\xi}$ is always over that corresponding to fixed-base condition and it increases for decreasing values of σ , whereas in the case of slender structures ($h/b = 3$), the effects of SSI on $\tilde{\xi}$ depends on the value of σ . Moreover, when kinematic interaction is considered, a significant increment of the effective damping is observed in the case of non-slender structures ($h/b = 1$). However, for slender structures ($h/b = 3$), only slight reductions or increments of $\tilde{\xi}$ result from considering kinematic interaction.

2 Substructuring methodology

Finally, it should be noted that the results obtained through the proposed procedure show a strong agreement with those extracted directly from the cited paper written by Avilés and Pérez-Rocha.

A decorative graphic consisting of several overlapping, dashed lines in a light gray color, forming a curved, abstract shape that resembles a stylized 'S' or a series of connected arcs. It is positioned in the background, partially behind the title box and extending towards the right side of the page.

3. BOUNDARY ELEMENTS BASED MODELS FOR SOIL-STRUCTURE INTERACTION

- 3.1 Introduction
- 3.2 Governing equations of linear elastodynamics
- 3.3 The elastodynamic integral representation
- 3.4 Boundary element method
- 3.5 Boundary element - finite element coupling model

3.1 Introduction

In this work, impedances and kinematic interaction factors are numerically obtained by means of a boundary element (BEM) - finite element (FEM) coupling formulation, developed by Padrón *et al.* [49, 54, 71, 120], which allows dealing with the dynamic analysis of piles and pile groups. This formulation was implemented in a previously existent multi-region BEM code [69, 70]. This 3D multi-region boundary element formulation, in which both soil and piles are modelled as continuum isotropic homogeneous linear viscoelastic regions with their actual geometries, is more rigorous and versatile than the simplified BEM-FEM formulation used in this work. However, it involves a greater number of degrees of freedom due to the fact that the pile-soil interface must also be discretized. In this work, this BEM formulation is used to address the validation of the BEM-FEM coupling formulation (as well as its implementation), in terms of the kinematic interaction factors of pile group configurations including battered piles.

This chapter begins by setting the basic governing equations of the elastodynamic problem in section 3.2. Afterwards, the elastodynamic integral representation of the problem is presented in section 3.3. Such representation allows the formulation of the boundary element method outlined in section 3.4. Finally, the chapter ends in section 3.5 with a description of the BEM-FEM coupling formulation, used in this work to determine the dynamic behaviour of 3D pile foundations embedded in viscoelastic soils.

3.2 Governing equations of linear elastodynamics

The governing equations of motion of an elastic, homogeneous, isotropic, linear body can be obtained from the combination of kinematic relations, equilibrium equations and constitutive law, ruling the dynamic behaviour of elastic solids. These equations can be expressed as

$$\mu \nabla^2 \mathbf{u} + (\lambda + \mu) \nabla (\nabla \cdot \mathbf{u}) + \rho \mathbf{b} = \rho \ddot{\mathbf{u}} \quad (3.1)$$

which are the Navier's equations, that represent the governing equations of motion in terms of the displacement vector \mathbf{u} at time t of a point in a body Ω whose position vector with respect to a system of fixed rectangular Cartesian coordinates is \mathbf{x} . Here, dots indicate time derivatives, ρ is the mass density and \mathbf{b} is the vector of body forces per unit mass. λ and μ are the Lamé's constants, which are related to the Young's modulus E and the Poisson's ratio ν as

$$\mu = \frac{E}{2(1 + \nu)} \quad ; \quad \lambda = \frac{\nu E}{(1 + \nu)(1 - 2\nu)} \quad (3.2)$$

being μ the shear modulus.

As a differential equation, the solution of equation (3.1) requires the establishment of a set of boundary conditions, in this case, applied in terms of known tractions and/or displacements on the boundary Γ of the body Ω , as well as time initial conditions $\forall \mathbf{x} \in \Omega$.

In order to obtain a set of simpler differential wave equations, elastodynamic problems can be formulated in terms of the dilatation $e = \nabla \cdot \mathbf{u}$ and rotation $\omega = \nabla \times \mathbf{u}$

vectors. Taking the divergence and the curl of equation (3.1) one obtains, respectively, the following two wave equations:

$$c_p^2 \nabla^2 \mathbf{e} + \nabla \cdot \mathbf{b} = \ddot{\mathbf{e}} \quad (3.3)$$

$$c_s^2 \nabla^2 \boldsymbol{\omega} + \nabla \times \mathbf{b} = \ddot{\boldsymbol{\omega}} \quad (3.4)$$

where

$$c_p^2 = \frac{\lambda + 2\mu}{\rho} \quad \text{and} \quad c_s^2 = \frac{\mu}{\rho} \quad (3.5)$$

Equations (3.3) and (3.4) represent the decoupled formulation of Navier's equations in terms of the dilatation and the three components of the rotation vector. Equation (3.3) is a scalar wave equation with propagation velocity c_p , while equation (3.4) is a vector wave equation with propagation velocity c_s . Therefore, waves within the elastic body can be classified as irrotational and equivoluminal waves, also called compressional (or primary) and shear (or secondary) waves (P and S waves), respectively. The *primary* and *secondary* names come from the field of seismology, because $c_p > c_s$ and, consequently, the former kind reaches first the seismological station in case of an earthquake.

3.3 The elastodynamic integral representation

The boundary element formulation of the problem is obtained from the transformation of the differential equations governing the dynamic behaviour of an elastic, homogeneous, isotropic, linear body into integral expressions.

The elastodynamic formulation used in this work considers time-harmonic body forces and boundary conditions, with angular frequency ω . In this case, it is possible to define two distinct elastodynamic states in the frequency domain as $\mathcal{S}_\omega(\mathbf{u}, \boldsymbol{\sigma}, \mathbf{b}; \omega, \Omega)$ and $\mathcal{S}_\omega^*(\mathbf{u}^*, \boldsymbol{\sigma}^*, \mathbf{b}^*; \omega, \Omega)$. \mathcal{S}_ω^* will be a known reference solution used to solve the problem and obtain the unknown state \mathcal{S}_ω . Assuming zero initial conditions, the dynamic reciprocal theorem can be written as

$$\int_{\Gamma} \mathbf{p}\mathbf{u}^* d\Gamma + \rho \int_{\Omega} \mathbf{b}\mathbf{u}^* d\Omega = \int_{\Gamma} \mathbf{p}^*\mathbf{u} d\Gamma + \rho \int_{\Omega} \mathbf{b}^*\mathbf{u} d\Omega \quad (3.6)$$

where \mathbf{u} and \mathbf{u}^* are the displacement vectors of any point of the domain; while \mathbf{p} and \mathbf{p}^* are the traction vectors on Γ , in equilibrium with the corresponding stress tensors $\boldsymbol{\sigma}$ and $\boldsymbol{\sigma}^*$, for states \mathcal{S}_ω and \mathcal{S}_ω^* , respectively.

The reference state \mathcal{S}_ω^* , usually called *fundamental solution*, used in the present work corresponds to the complete space because there is no closed form expression for the half-space fundamental solution. Therefore, the soil free surface should be discretized. In practice, however, only a small region around the analysis area has to be included in the model to reach accurate results.

The *fundamental solution* used in the present work is that representing the response, in terms of displacements and tractions, of an unbounded linear, elastic, homogeneous, isotropic domain to a harmonic concentrated unit load of the form

$$\rho b_k^* = \delta(\mathbf{t}) \delta_{lk} e^{i\omega t} \quad (3.7)$$

applied at the source point ι in the direction l , being δ_{lk} the Kronecker delta and $\delta(\iota)$ the Dirac delta, defined as

$$\int_{\Omega} \delta(\iota) d\Omega = \begin{cases} 1, & \text{if } \iota \in \Omega \\ 0, & \text{if } \iota \notin \Omega \end{cases} \quad (3.8)$$

The elastodynamic fundamental solution, that gives the displacement in a k direction at the field point \mathbf{x} due to the load applied at the source point ι in the direction l , is written in equation (3.9). In turn, equation (3.11) represents the k component of tractions associated to a plane with exterior unit normal \mathbf{n} at the field point \mathbf{x} .

$$u_{lk}^*(\mathbf{x}, \iota, \omega) = \frac{1}{4\pi\mu} [\psi\delta_{lk} - \chi r_{,k}r_{,l}] \quad (3.9)$$

$$p_{lk}^*(\mathbf{x}, \iota, \omega) = \frac{1}{4\pi} \left[\left(\frac{\partial\psi}{\partial r} - \frac{\chi}{r} \right) \left(\delta_{kl} \frac{\partial r}{\partial \mathbf{n}} + r_{,k}n_l \right) - \frac{2}{r} \chi \left(n_k r_{,l} - 2 r_{,k}r_{,l} \frac{\partial r}{\partial \mathbf{n}} \right) - 2 \frac{\partial\chi}{\partial r} r_{,k}r_{,l} \frac{\partial r}{\partial \mathbf{n}} + \left(\frac{c_p^2}{c_s^2} - 2 \right) \left(\frac{\partial\psi}{\partial r} - \frac{\partial\chi}{\partial r} - \frac{2}{r} \chi \right) r_{,l}n_k \right] \quad (3.10)$$

where $r = |\mathbf{x} - \iota|$ and

$$\begin{aligned} \psi &= - \left(\frac{c_s}{c_p} \right)^2 \left(\frac{1}{z_p^2 r^2} - \frac{1}{z_p r} \right) \frac{e^{z_p r}}{r} + \left(\frac{1}{z_s^2 r^2} - \frac{1}{z_s r} + 1 \right) \frac{e^{z_s r}}{r} \\ \chi &= - \left(\frac{c_s}{c_p} \right)^2 \left(\frac{3}{z_p^2 r^2} - \frac{3}{z_p r} + 1 \right) \frac{e^{z_p r}}{r} + \left(\frac{3}{z_s^2 r^2} - \frac{3}{z_s r} + 1 \right) \frac{e^{z_s r}}{r} \end{aligned} \quad (3.11)$$

being

$$z_p = -\frac{i\omega}{c_p} \quad ; \quad z_s = -\frac{i\omega}{c_s} \quad (3.12)$$

Hereafter, equations will be written representing a set of three equations arising from the collocation of the unit load in the three directions of space, so that vectors \mathbf{u}^* , \mathbf{p}^* and \mathbf{b}^* will be arranged into 3×3 matrices \mathbf{u}^* , \mathbf{p}^* and \mathbf{b}^* . When the fundamental solution defined above is considered, and taking equation (3.7) into account, the last term of equation (3.6) becomes

$$\rho \int_{\Omega} \mathbf{b}^* \mathbf{u} d\Omega = \int_{\Omega} \delta(\iota) \mathbf{u} d\Omega = \mathbf{u}^{\iota} \quad (3.13)$$

Thus, the integral representation of the displacements field of the harmonic elastodynamic problem when the point load is applied at $\iota \in \Omega$ can be written as

$$\mathbf{u}^{\iota} + \int_{\Gamma} \mathbf{p}^* \mathbf{u} d\Gamma = \int_{\Gamma} \mathbf{u}^* \mathbf{p} d\Gamma + \rho \int_{\Omega} \mathbf{u}^* \mathbf{b} d\Omega \quad (3.14)$$

where \mathbf{u} and \mathbf{p} are the displacement and traction vectors, while \mathbf{u}^* and \mathbf{p}^* are the fundamental solution tensors, which in matrix form can be written as

$$\mathbf{u} = \begin{bmatrix} u_1 \\ u_2 \\ u_3 \end{bmatrix} ; \quad \mathbf{u}^* = \begin{bmatrix} u_{11}^* & u_{12}^* & u_{13}^* \\ u_{21}^* & u_{22}^* & u_{23}^* \\ u_{31}^* & u_{32}^* & u_{33}^* \end{bmatrix} \quad (3.15)$$

$$\mathbf{p} = \begin{bmatrix} p_1 \\ p_2 \\ p_3 \end{bmatrix}; \quad \mathbf{p}^* = \begin{bmatrix} p_{11}^* & p_{12}^* & p_{13}^* \\ p_{21}^* & p_{22}^* & p_{23}^* \\ p_{31}^* & p_{32}^* & p_{33}^* \end{bmatrix} \quad (3.16)$$

The integral formulation of the problem in equation (3.14) allows the computation of displacements at internal points of Ω when displacements and tractions are known on Γ . For the purpose of obtaining an integral equation written in terms only of variables on Γ the unit load must be applied on the boundary ($\iota \in \Gamma$). In this case, a strategy that consists in slightly modifying Γ is used in order to subtract the singularity of the fundamental solution when $r \rightarrow 0$. As depicted in figure 3.1, the approximate boundary considered is made up by the boundary Γ of the domain Ω itself but augmented by a semisphere Γ_ε of radius $\varepsilon \rightarrow 0$ whose centre is the collocation point ι . This strategy allows the decomposition of the boundary integrals into another two extended over $\Gamma - \Gamma_\varepsilon$ and Γ_ε , respectively. Integrals extended over $\Gamma - \Gamma_\varepsilon$ do not contain the singularity, and for $\varepsilon \rightarrow 0$ they represent the Cauchy principal value of the original integral. On the other hand, integrals extended over Γ_ε are defined in the limit. This way, the boundary integral representation of the problem can be expressed as

$$\mathbf{c}^t \mathbf{u}^t + \int_{\Gamma} \mathbf{p}^* \mathbf{u} \, d\Gamma = \int_{\Gamma} \mathbf{u}^* \mathbf{p} \, d\Gamma + \rho \int_{\Omega} \mathbf{u}^* \mathbf{b} \, d\Omega \quad (3.17)$$

where all integrals are Cauchy principal value integrals and \mathbf{c}^t is the *free term*. In the three-dimensional case, if the boundary is smooth at ι , then $\mathbf{c}^t = 1/2 \mathbf{I}$, while $\mathbf{c}^t = \mathbf{I}$ at internal points, \mathbf{I} being the unit 3×3 diagonal matrix.

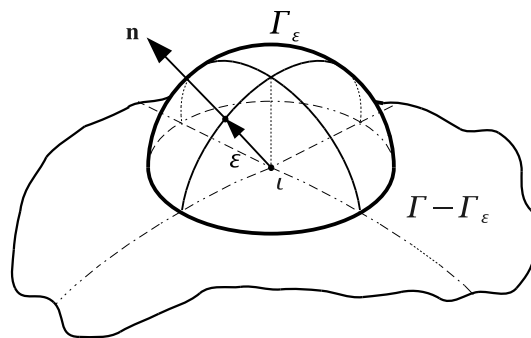


FIGURE 3.1: Strategy for the singularity subtraction. Semisphere around the collocation point for integration.

3.4 Boundary element method

The boundary integral representation of the displacements in each region (soil and each pile) can be written, from equation (3.17) assuming zero body forces, as

$$\mathbf{c}^t \mathbf{u}^t + \int_{\Gamma} \mathbf{p}^* \mathbf{u} \, d\Gamma = \int_{\Gamma} \mathbf{u}^* \mathbf{p} \, d\Gamma \quad (3.18)$$

The numerical solution of equation (3.18) requires, first, the discretization of the boundary surface into \mathcal{N}_e elements Γ_j and \mathcal{N}_n nodes so that

$$\Gamma \simeq \bigcup_{j=1}^{\mathcal{N}_e} \Gamma_j \quad (3.19)$$

where each element is defined by \mathcal{N}_n^j nodes. Over each element j , displacement \mathbf{u} and traction \mathbf{p} fields are approximated in terms of their values at nodal points making use of a set of polynomial interpolation functions $\Phi(\boldsymbol{\xi})$ expressed as a matrix of dimensions $3 \times 3\mathcal{N}_n^j$ of the form

$$\Phi(\boldsymbol{\xi}) = \begin{bmatrix} \phi_1 & 0 & 0 & \phi_2 & 0 & 0 & \cdots & \phi_{\mathcal{N}_n^j} & 0 & 0 \\ 0 & \phi_1 & 0 & 0 & \phi_2 & 0 & \cdots & 0 & \phi_{\mathcal{N}_n^j} & 0 \\ 0 & 0 & \phi_1 & 0 & 0 & \phi_2 & \cdots & 0 & 0 & \phi_{\mathcal{N}_n^j} \end{bmatrix} \quad (3.20)$$

containing the specific polynomial interpolation functions for the element. $\boldsymbol{\xi}$ represents the set of natural coordinates used to define a point in the reference element.

This way, the fields $\mathbf{u}(\boldsymbol{\xi})$ and $\mathbf{p}(\boldsymbol{\xi})$ within an element are approximated as

$$\mathbf{u}(\boldsymbol{\xi}) = \Phi(\boldsymbol{\xi}) \mathbf{u}^j \quad ; \quad \mathbf{p}(\boldsymbol{\xi}) = \Phi(\boldsymbol{\xi}) \mathbf{p}^j \quad (3.21)$$

where \mathbf{u}^j and \mathbf{p}^j are vectors containing the element nodal displacements and tractions.

In this work, all boundaries are discretized into a finite number of isoparametric quadratic elements of triangular and quadrilateral shapes with six and nine nodes, respectively. These elements, together with their approximation functions, which are written in terms of natural coordinates ξ_1 and ξ_2 , are defined in table 3.1. Only one quarter of the geometry needs to be discretized due to the problem symmetries (see figure 3.2).

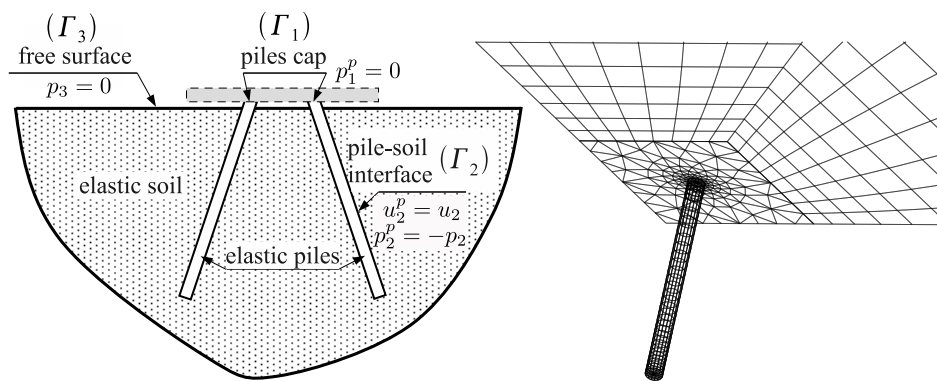


FIGURE 3.2: Multi-region boundary-element model definitions and BEM mesh.

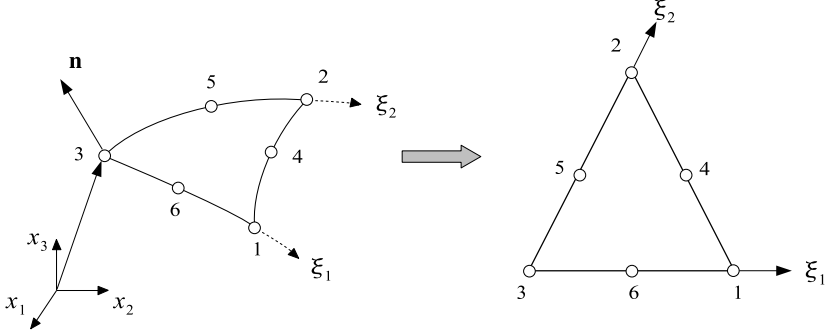
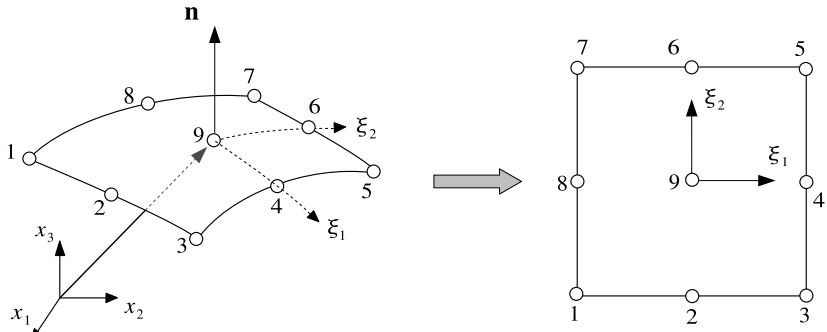
 $\begin{aligned} \phi_1 &= \xi_1(2\xi_1 - 1) & ; & & \phi_4 &= 4\xi_1\xi_2 \\ \phi_2 &= \xi_2(2\xi_2 - 1) & ; & & \phi_5 &= 4\xi_2\xi_3 \\ \phi_3 &= \xi_3(2\xi_3 - 1) & ; & & \phi_6 &= 4\xi_1\xi_3 \\ \xi_3 &= 1 - \xi_1 - \xi_2 & ; & & 0 \leq \xi_1 \leq 1 & ; & 0 \leq \xi_2 \leq 1 \end{aligned}$
 $\begin{aligned} \phi_1 &= \frac{1}{4}\xi_1(\xi_1 - 1)\xi_2(\xi_2 - 1) & ; & & \phi_2 &= \frac{1}{2}(1 - \xi_1^2)\xi_2(\xi_2 - 1) \\ \phi_3 &= \frac{1}{4}\xi_1(\xi_1 + 1)\xi_2(\xi_2 - 1) & ; & & \phi_4 &= \frac{1}{2}(1 + \xi_1)\xi_2(1 - \xi_2^2) \\ \phi_5 &= \frac{1}{4}\xi_1(\xi_1 + 1)\xi_2(\xi_2 + 1) & ; & & \phi_6 &= \frac{1}{2}(1 - \xi_1^2)\xi_2(\xi_2 + 1) \\ \phi_7 &= \frac{1}{4}\xi_1(\xi_1 - 1)\xi_2(\xi_2 + 1) & ; & & \phi_8 &= \frac{1}{2}(\xi_1 - 1)\xi_2(1 - \xi_2^2) \\ \phi_9 &= (1 - \xi_1^2)(1 - \xi_2^2) \\ & & & & -1 \leq \xi_1 \leq 1 & ; & -1 \leq \xi_2 \leq 1 \end{aligned}$

TABLE 3.1: Quadratic triangular and quadrilateral element types.

Once all boundaries have been discretized, equation (3.18) can be written, in a matrix form, as

$$\sum_{m=1}^{N_n} \mathbf{H}^{um} \mathbf{u}^m = \sum_{m=1}^{N_n} \mathbf{G}^{um} \mathbf{p}^m \quad (3.22)$$

being

$$\mathbf{H}^{\iota m} = \begin{cases} \hat{\mathbf{H}}^{\iota m} & , \text{ if } \iota \neq m \\ \mathbf{c}^{\iota} + \hat{\mathbf{H}}^{\iota m} & , \text{ if } \iota = m \end{cases} \quad (3.23)$$

$$\hat{\mathbf{H}}^{\iota m} = \sum_{e_m} \int_{\Gamma_{e_m}} \mathbf{p}^* \phi_k d\Gamma \quad (3.24)$$

$$\mathbf{G}^{\iota m} = \sum_{e_m} \int_{\Gamma_{e_m}} \mathbf{u}^* \phi_k d\Gamma \quad (3.25)$$

and vectors \mathbf{u}^m and \mathbf{p}^m , of dimensions 3×1 , represent the three nodal components of displacements and tractions at node m . Matrices $\hat{\mathbf{H}}^{\iota m}$ and $\mathbf{G}^{\iota m}$, of dimensions 3×3 , represent the response at node m due to the harmonic unit load at collocation point ι .

Note that different values of tractions may exist at the same point when this belongs to more than one element with non-parallel exterior normals. This situation is solved by considering more than one node at the same point. When both tractions are unknown, the system matrix becomes singular because the equations associated to the duplicated nodes are equal one to another. In this case, known as the *corner problem*, a non-nodal collocation strategy is carried out. This procedure was studied in depth by Aznárez [68].

Finally, writing equation (3.22) for every single node, a system of equations of the type

$$\mathbf{H}\bar{\mathbf{u}} = \mathbf{G}\bar{\mathbf{p}} \quad (3.26)$$

is obtained, where $\bar{\mathbf{u}}$ and $\bar{\mathbf{p}}$ are vectors of dimensions $3N_n \times 1$ containing the problem nodal values, and where matrices \mathbf{H} and \mathbf{G} are composed by submatrices $\mathbf{H}^{\iota m}$ and $\mathbf{G}^{\iota m}$.

Applying boundary conditions and rearranging the columns so that all unknowns are grouped in a vector $\bar{\mathbf{x}}$, a square system of linear independent algebraic equations of the form

$$\mathbf{A}\bar{\mathbf{x}} = \bar{\mathbf{f}} \quad (3.27)$$

can be written, where $\bar{\mathbf{f}}$ is the known vector arising from the application of the boundary conditions and the subsequent rearrangement of equations.

A detailed explanation of the numerical evaluation of integrals and other numerical aspects of the boundary element method can be found in [68, 89].

In order to illustrate the application of this methodology to the problem at hand, a particular example will be developed in the next few lines. For the specific case of a single floating pile embedded in a viscoelastic half-space the boundary element equations for each region (pile and soil) in partitioned form are

$$\mathbf{H}_1^p \bar{\mathbf{u}}_1^p + \mathbf{H}_2^p \bar{\mathbf{u}}_2^p = \mathbf{G}_1^p \bar{\mathbf{p}}_1^p + \mathbf{G}_2^p \bar{\mathbf{p}}_2^p \quad (3.28)$$

$$\begin{bmatrix} \mathbf{H}_2^{pp} & \mathbf{H}_2^{ps} \\ \mathbf{H}_3^{sp} & \mathbf{H}_3^{ss} \end{bmatrix} \begin{bmatrix} \bar{\mathbf{u}}_2 \\ \bar{\mathbf{u}}_3 \end{bmatrix} = \begin{bmatrix} \mathbf{G}_2^{pp} & \mathbf{G}_2^{ps} \\ \mathbf{G}_3^{sp} & \mathbf{G}_3^{ss} \end{bmatrix} \begin{bmatrix} \bar{\mathbf{p}}_2 \\ \bar{\mathbf{p}}_3 \end{bmatrix} \quad (3.29)$$

Imposing external boundary conditions ($\bar{\mathbf{u}}_1^p = \hat{\mathbf{u}}$ and $\bar{\mathbf{p}}_3 = 0$) together with compatibility ($\bar{\mathbf{u}}_2^p = \bar{\mathbf{u}}_2$) and equilibrium ($\bar{\mathbf{p}}_2^p = -\bar{\mathbf{p}}_2$) along the pile-soil interfaces, the combined equations for the coupled impedance problem can be written as

$$\begin{bmatrix} -\mathbf{G}_1^p & \mathbf{H}_2^p & \mathbf{G}_2^p & \mathbf{0} \\ \mathbf{0} & \mathbf{H}_2^{pp} & -\mathbf{G}_2^{pp} & \mathbf{H}_2^{ps} \\ \mathbf{0} & \mathbf{H}_3^{sp} & -\mathbf{G}_3^{sp} & \mathbf{H}_3^{ss} \end{bmatrix} \begin{bmatrix} \bar{\mathbf{p}}_1^p \\ \bar{\mathbf{u}}_2 \\ \bar{\mathbf{p}}_2 \\ \bar{\mathbf{u}}_3 \end{bmatrix} = \begin{bmatrix} -\mathbf{H}_1^p \hat{\mathbf{u}} \\ 0 \\ 0 \\ 0 \end{bmatrix} \quad (3.30)$$

When this single floating pile is embedded in a viscoelastic half-space subjected to a seismic excitation, writing equation (3.22) for each node of each region, yields the following matrix equations for pile and soil regions:

$$\mathbf{H}_1^p \bar{\mathbf{u}}_{1s}^p + \mathbf{H}_2^p \bar{\mathbf{u}}_{2s}^p = \mathbf{G}_1^p \bar{\mathbf{p}}_{1s}^p + \mathbf{G}_2^p \bar{\mathbf{p}}_{2s}^p \quad (3.31)$$

$$\begin{bmatrix} \mathbf{H}_2^{pp} & \mathbf{H}_2^{ps} \\ \mathbf{H}_3^{sp} & \mathbf{H}_3^{ss} \end{bmatrix} \begin{bmatrix} \bar{\mathbf{u}}_{2s} \\ \bar{\mathbf{u}}_{3s} \end{bmatrix} = \begin{bmatrix} \mathbf{G}_2^{pp} & \mathbf{G}_2^{ps} \\ \mathbf{G}_3^{sp} & \mathbf{G}_3^{ss} \end{bmatrix} \begin{bmatrix} \bar{\mathbf{p}}_{2s} \\ \bar{\mathbf{p}}_{3s} \end{bmatrix} \quad (3.32)$$

where the sub-indexes 1 – 3 correspond, respectively, to the pile connection with the rigid cap where tractions are null (Γ_1), to the pile-soil interface (Γ_2), and to the soil free-traction ground surface (Γ_3). The sub-index s indicates that the equations are written for the *scattered field*.

When seismic waves impinge on the site under study, reflection and refraction phenomena take place, and the arising wave field modifies the incident wave train. In this work, the seismic excitation is assumed to be a harmonic plane S wave impinging the model from a far source. The wave field in the halfspace discretization ($\bar{\mathbf{u}}$) consists of two parts: the known *incident field* ($\bar{\mathbf{u}}_I$) and the unknown *scattered field* ($\bar{\mathbf{u}}_S$). The resulting displacement can be obtained by superposition as $\bar{\mathbf{u}} = \bar{\mathbf{u}}_I + \bar{\mathbf{u}}_S$. Likewise, the resulting traction field can be expressed as $\bar{\mathbf{p}} = \bar{\mathbf{p}}_I + \bar{\mathbf{p}}_S$. Thus, equations (3.31) and (3.32) can be expressed as follows:

$$\mathbf{H}_1^p \bar{\mathbf{u}}_1^p + \mathbf{H}_2^p \bar{\mathbf{u}}_2^p - \mathbf{G}_1^p \bar{\mathbf{p}}_1^p - \mathbf{G}_2^p \bar{\mathbf{p}}_2^p = \mathbf{H}_1^p \bar{\mathbf{u}}_{1I}^p + \mathbf{H}_2^p \bar{\mathbf{u}}_{2I}^p - \mathbf{G}_1^p \bar{\mathbf{p}}_{1I}^p - \mathbf{G}_2^p \bar{\mathbf{p}}_{2I}^p \quad (3.33)$$

$$\begin{bmatrix} \mathbf{H}_2^{pp} & -\mathbf{G}_2^{pp} & \mathbf{H}_2^{ps} & -\mathbf{G}_2^{ps} \\ \mathbf{H}_3^{sp} & -\mathbf{G}_3^{sp} & \mathbf{H}_3^{ss} & -\mathbf{G}_3^{ss} \end{bmatrix} \begin{bmatrix} \bar{\mathbf{u}}_2 \\ \bar{\mathbf{p}}_2 \\ \bar{\mathbf{u}}_3 \\ \bar{\mathbf{p}}_3 \end{bmatrix} = \begin{bmatrix} \mathbf{H}_2^{pp} & -\mathbf{G}_2^{pp} & \mathbf{H}_2^{ps} & -\mathbf{G}_2^{ps} \\ \mathbf{H}_3^{sp} & -\mathbf{G}_3^{sp} & \mathbf{H}_3^{ss} & -\mathbf{G}_3^{ss} \end{bmatrix} \begin{bmatrix} \bar{\mathbf{u}}_{2I} \\ \bar{\mathbf{p}}_{2I} \\ \bar{\mathbf{u}}_{3I} \\ \bar{\mathbf{p}}_{3I} \end{bmatrix} \quad (3.34)$$

Imposing external boundary conditions ($\bar{\mathbf{p}}_1^p = 0$ and $\bar{\mathbf{p}}_3 = 0$) together with compatibility ($\bar{\mathbf{u}}_2^p = \bar{\mathbf{u}}_2$) and equilibrium ($\bar{\mathbf{p}}_2^p = -\bar{\mathbf{p}}_2$) along the pile-soil interfaces, the combined equations for the kinematic interaction factors problem can be written as

$$\begin{bmatrix} \mathbf{H}_1^p & \mathbf{H}_2^p & \mathbf{G}_2^p & \mathbf{0} \\ \mathbf{0} & \mathbf{H}_2^{pp} & -\mathbf{G}_2^{pp} & \mathbf{H}_2^{ps} \\ \mathbf{0} & \mathbf{H}_3^{sp} & -\mathbf{G}_3^{sp} & \mathbf{H}_3^{ss} \end{bmatrix} \begin{bmatrix} \bar{\mathbf{u}}_1^p \\ \bar{\mathbf{u}}_2 \\ \bar{\mathbf{p}}_2 \\ \bar{\mathbf{u}}_3 \end{bmatrix} = \begin{bmatrix} \mathbf{H}_1^p & \mathbf{H}_2^p & \mathbf{G}_2^p & \mathbf{0} \\ \mathbf{0} & \mathbf{H}_2^{pp} & -\mathbf{G}_2^{pp} & \mathbf{H}_2^{ps} \\ \mathbf{0} & \mathbf{H}_3^{sp} & -\mathbf{G}_3^{sp} & \mathbf{H}_3^{ss} \end{bmatrix} \begin{bmatrix} \bar{\mathbf{u}}_{1I}^p \\ \bar{\mathbf{u}}_{2I} \\ \bar{\mathbf{p}}_{2I} \\ \bar{\mathbf{u}}_{3I} \end{bmatrix} \quad (3.35)$$

Regarding material damping, in this work, it has been included in the model by considering BEM regions to be linear viscoelastic materials. The constitutive relation that describes the time-harmonic behaviour of linear, homogeneous, isotropic, viscoelastic media is identical to that corresponding to linear elastic problems, except for the fact that the constitutive material parameters are complex-valued and frequency-dependent, as shown in equation (3.36).

$$\sigma_{ij} = \lambda(\omega) \delta_{ij} \varepsilon_{kk} + 2\mu(\omega) \varepsilon_{ij} \quad (3.36)$$

being

$$\mu(\omega) = \text{Re}[\mu](1 + i2\beta_\mu(\omega)) \quad (3.37a)$$

$$\lambda(\omega) = \text{Re}[\lambda](1 + i2\beta_\lambda(\omega)) \quad (3.37b)$$

where β_μ and β_λ are usually set to the same value β .

When considering the specific problem of plane elastic waves propagating in a certain direction defined by a unit vector \mathbf{s} , in the steady-state harmonic case, resulting displacements of a point \mathbf{x} are of the form

$$\bar{\mathbf{u}} = A e^{i(\omega t - \kappa \mathbf{s} \cdot \mathbf{x})} \mathbf{d} \quad (3.38)$$

where A is the amplitude of the motion, $i = \sqrt{-1}$ and $\kappa = \omega/c$ is the wave number, being c the wave velocity. As λ and μ are complex values in case of viscoelastic materials, c_s , c_p and wave numbers κ will also have an imaginary part. Therefore, according to equation (3.38), the wave motion will be multiplied by an exponentially decreasing function, arising from the imaginary part of κ , in such a way that, as distance in the propagation direction grows, the amplitude of the motion decays, being this phenomenon produced by material damping.

A linear hysteretic viscoelastic damping model, where the Lamé's constants are of the form

$$\mu = \text{Re}[\mu](1 + i2\beta) \quad (3.39a)$$

$$\lambda = \text{Re}[\lambda](1 + i2\beta) \quad (3.39b)$$

and β is frequency independent, is considered to represent the dynamic behaviour of materials included in the analysis performed in this work.

3.5 Boundary element - finite element coupling model

The model developed by Padrón *et al.* [71] for piled foundations is along the lines of those proposed by other authors [23, 64, 66]. The dynamic response of the soil region is modelled by using a BEM formulation which considers the tractions at pile-soil interfaces as body forces acting within the domain. The stiffness of piles is introduced by longitudinal finite elements linking the internal nodes of the soil. The whole approach is depicted in figure 3.3. The main advantage of this approach is that, being able to produce accurate results, it assumes that soil continuity is not altered by the presence of piles and, consequently, it is not necessary to discretize the pile-soil interfaces by boundary

elements, which considerably reduces the number of degrees of freedom in comparison with a pure multi-region boundary element approach. Due to the problem symmetries, only one quarter of the geometry needs to be discretized. Moreover, the pile discretization is independent of the soil mesh which allows using the same boundary mesh for all the pile group configurations under investigation.

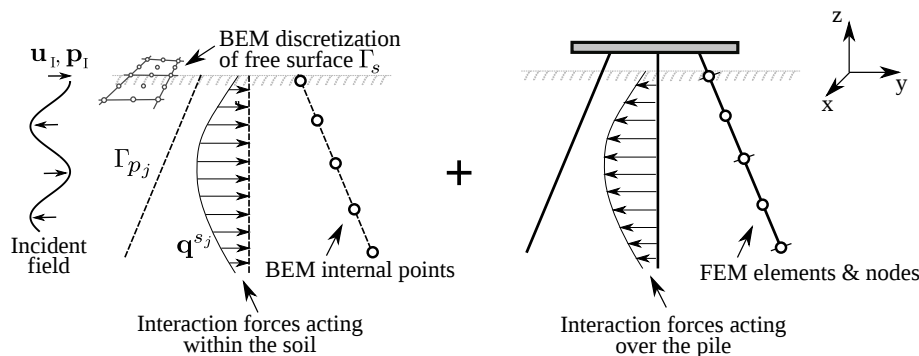


FIGURE 3.3: BEM-FEM model.

The piles are modelled by FEM according to the Euler-Bernoulli hypothesis and are discretized into three-node beam elements, shown in figure 3.4, in which the displacements along the element are approximated by the following interpolation functions:

$$u_i = \varphi_1 u_{k_i} + \varphi_2 \theta_{k_i} + \varphi_3 u_{l_i} + \varphi_4 u_{m_i} + \varphi_5 \theta_{m_i} \quad ; \quad i = 1, 2 \quad (3.40a)$$

$$u_3 = \phi_1 u_{k_3} + \phi_2 u_{l_3} + \phi_3 u_{m_3} \quad (3.40b)$$

where

$$\begin{aligned} \varphi_1 &= \xi \left(-\frac{3}{4} + \xi + \frac{1}{4} \xi^2 - \frac{1}{2} \xi^3 \right) \\ \varphi_2 &= \frac{1}{4} \xi (-1 + \xi + \xi^2 - \xi^3) \\ \varphi_3 &= 1 - 2\xi^2 + \xi^4 \\ \varphi_4 &= \xi \left(\frac{3}{4} + \xi - \frac{1}{4} \xi^2 - \frac{1}{2} \xi^3 \right) \\ \varphi_5 &= \frac{1}{4} \xi (-1 - \xi + \xi^2 + \xi^3) \end{aligned} \quad (3.41)$$

and

$$\begin{aligned} \phi_1 &= \frac{1}{2} \xi (\xi - 1) \\ \phi_2 &= 1 - \xi^2 \\ \phi_3 &= \frac{1}{2} \xi (\xi + 1) \end{aligned} \quad (3.42)$$

being ξ the elemental dimensionless coordinate varying from $\xi = -1$ to $\xi = +1$.

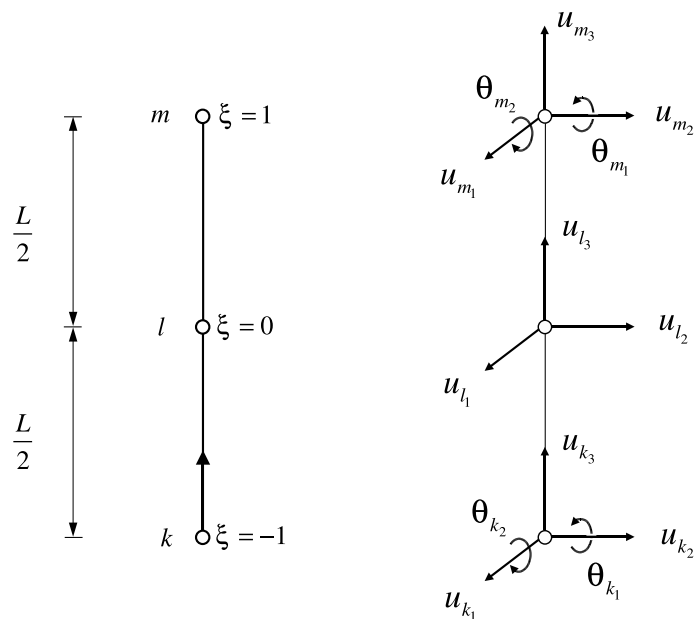


FIGURE 3.4: Finite element definition

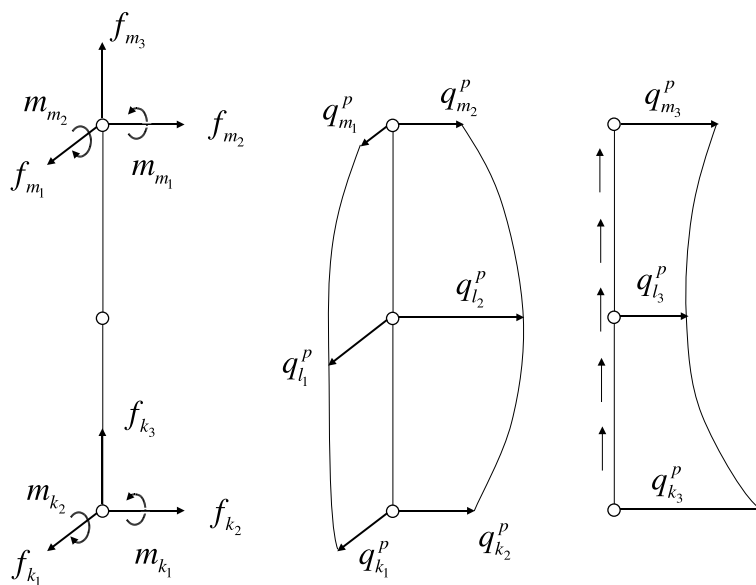


FIGURE 3.5: External punctual forces (left) and tractions along the pile-soil interface defined on the generic element

The external forces defined over the generic element are schematized in figure 3.5. The tractions along the pile-soil interface are approximated by

$$q_i = \phi_1 q_{k_i} + \phi_2 q_{l_i} + \phi_3 q_{m_i} \quad ; \quad i = 1, 2, 3 \quad (3.43)$$

using the set of shape functions defined in equation (3.42).

The principle of virtual displacements is used to obtain the mass and stiffness matrices (\mathbf{M}_j and \mathbf{K}_j) for the described element type [115], and also the matrix \mathbf{Q}_j that transforms nodal tractions $\bar{\mathbf{q}}^{p_j}$ into equivalent nodal forces. Thus, the dynamic behaviour of pile j in a finite element sense, can be described as

$$(\mathbf{K}_j - \omega^2 \mathbf{M}_j) \bar{\mathbf{u}}_j^p = \mathbf{F}_j^{ext} + \mathbf{Q}_j \bar{\mathbf{q}}^{p_j} \quad (3.44)$$

where $\bar{\mathbf{u}}_j^p$ is the vector of nodal translation and rotation amplitudes along the pile, \mathbf{F}_j^{ext} represents the punctual forces acting at the top and the tip of the pile and ω is the frequency of excitation.

The soil is modelled by the BEM as a linear, homogeneous, isotropic, viscoelastic unbounded region with complex valued shear modulus μ of the type $\mu = Re[\mu](1 + 2i\beta)$, where β is the damping coefficient. The boundary integral equation for a time-harmonic elastodynamic state defined in a domain Ω with boundary Γ can be written in a condensed form as

$$\mathbf{c}' \mathbf{u}' + \int_{\Gamma} \mathbf{p}^* \mathbf{u} d\Gamma = \int_{\Gamma} \mathbf{u}^* \mathbf{p} d\Gamma + \sum_{j=1}^{n_p} \left[\int_{\Gamma_{p_j}} \mathbf{u}^* \mathbf{q}^{s_j} d\Gamma_{p_j} - \delta_j \Upsilon_l^j F_{p_j} \right] \quad (3.45)$$

where \mathbf{c}' is the local free term matrix at collocation point \mathbf{x}' ; Γ_{p_j} is the pile-soil interface along the load-line j ; \mathbf{u} and \mathbf{p} are the displacement and traction vectors, and \mathbf{u}^* and \mathbf{p}^* are the elastodynamic fundamental solution tensors representing the response of an unbounded region to a harmonic concentrated unit load with a time variation $e^{i\omega t}$ applied at a point \mathbf{x}' ; n_p is the total number of load-lines; \mathbf{q}^{s_j} denotes the distribution of interaction loads along the pile shaft applied on a line defined by the pile axis; and Υ_l^j is a three-component vector that represents the contribution of the axial force F_{p_j} at the tip of the j^{th} load-line.

The boundary surface Γ is discretized into quadratic elements of triangular and quadrilateral shapes with six and nine nodes, respectively. The displacement and traction fields \mathbf{u} and \mathbf{p} , over each boundary element, is approximated in terms of their values at nodal points ($\bar{\mathbf{u}}$ and $\bar{\mathbf{p}}$) making use of the polynomial interpolation functions. Thus, equation (3.45) can be written for all nodes in Γ as a matrix equation of the type

$$\mathbf{H}^{ss} \bar{\mathbf{u}} - \mathbf{G}^{ss} \bar{\mathbf{p}} - \sum_{j=1}^{n_p} \mathbf{G}^{sp_j} \bar{\mathbf{q}}^{s_j} + \sum_{j=1}^{n_p} \Upsilon^{s_j} F_{p_j} = 0 \quad (3.46)$$

where $\bar{\mathbf{u}}$ and $\bar{\mathbf{p}}$ are the vectors of nodal displacements and tractions of boundary elements; $\bar{\mathbf{q}}^{s_j}$ is the vector of tractions defined at a series of internal nodes; \mathbf{H}^{ss} and \mathbf{G}^{ss} are coefficient matrices obtained by numerical integration over the boundary elements of the fundamental solution times the corresponding shape functions; and \mathbf{G}^{sp_j} is the coefficient matrix obtained by numerical integration over load-line j of the fundamental solution times the interpolation functions (3.42), when the unit load is applied on Γ .

Moreover, equation (3.45) can be written for all internal nodes in load-line Γ_{p_i} which results in the matrix equation below:

$$\mathbf{C}\bar{\mathbf{u}}^{p_i} + \mathbf{H}^{p_i s}\bar{\mathbf{u}} - \mathbf{G}^{p_i s}\bar{\mathbf{p}} - \sum_{j=1}^{n_p} \mathbf{G}^{p_i p_j}\bar{\mathbf{q}}^{s_j} + \sum_{j=1}^{n_p} \Upsilon_j^{p_i} F_{p_j} = 0 \quad (3.47)$$

where $\bar{\mathbf{u}}^{p_i}$ is the vector of nodal displacements along load-line i , which is multiplied by the diagonal matrix \mathbf{C} , whose non-zero terms are valued $1/2$ in positions corresponding to pile nodes placed on a smooth surface (as *e.g.* pile heads) and unity at the internal points.

The axial punctual force F_{p_j} considered at the tip of a floating pile j adds a new unknown per pile, in such a way that an extra equation needs to be written. To do so, the unit load must be applied in the vertical direction at any non-nodal point. The point with elemental dimensionless coordinate $\xi = -1/2$ in the bottom element of the pile has been chosen because of its nearness to the tip. The third row (corresponding to the application of the unit load in the vertical direction) of equation (3.48) written for a non-nodal point placed between the two bottom nodes of the pile yields a suitable additional equation for this purpose.

$$\Phi\bar{\mathbf{u}}_k^{p_i} + \mathbf{H}^{p_i s}\bar{\mathbf{u}} - \mathbf{G}^{p_i s}\bar{\mathbf{p}} - \sum_{j=1}^{n_p} \mathbf{G}^{p_i p_j}\bar{\mathbf{q}}^{s_j} + \sum_{j=1}^{n_p} \Upsilon_j^{p_i} F_{p_j} = 0 \quad (3.48)$$

where $\bar{\mathbf{u}}_k^{p_i}$ is the vector of nodal displacement of element Γ_k and Φ is the matrix of shape functions specified at the collocation point.

As explained in section 3.4, when the soil-foundation system is subjected to a seismic excitation, the resulting displacements and traction fields can be obtained by superposition as follows:

$$\bar{\mathbf{u}} = \bar{\mathbf{u}}_I + \bar{\mathbf{u}}_S \quad (3.49)$$

$$\bar{\mathbf{p}} = \bar{\mathbf{p}}_I + \bar{\mathbf{p}}_S \quad (3.50)$$

where the sub-indexes I and S correspond, respectively, to incident and scattered fields.

In this case, equation (3.46) can be written, in terms of the total field, as

$$\mathbf{H}^{ss}\bar{\mathbf{u}} - \mathbf{G}^{ss}\bar{\mathbf{p}} - \sum_{j=1}^{n_p} \mathbf{G}^{sp_j}\bar{\mathbf{q}}^{s_j} + \sum_{j=1}^{n_p} \Upsilon_j^{s_j} F_{p_j} = 0 \quad (3.51)$$

On the other hand, equation (3.46) can also be written in terms of the incident field as

$$\mathbf{H}^{ss}\bar{\mathbf{u}}_I + \mathbf{G}^{ss}\bar{\mathbf{p}}_I = 0 \quad (3.52)$$

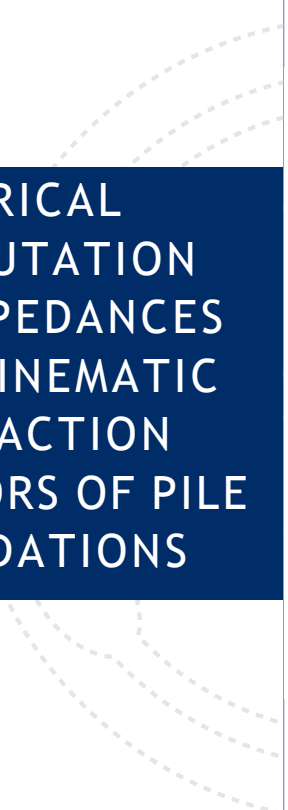
where tractions along the pile-soil interface and forces at piles tip are not present because they only exist in the scattered fields. The subtraction of equation (3.52) from equation (3.51) yields

$$\mathbf{H}^{ss}\bar{\mathbf{u}} - \mathbf{G}^{ss}\bar{\mathbf{p}} - \sum_{j=1}^{n_p} \mathbf{G}^{sp_j}\bar{\mathbf{q}}^{s_j} + \sum_{j=1}^{n_p} \Upsilon_j^{s_j} F_{p_j} = \mathbf{H}^{ss}\bar{\mathbf{u}}_I + \mathbf{G}^{ss}\bar{\mathbf{p}}_I \quad (3.53)$$

The same procedure can be followed to obtain the boundary element equations (3.47) and (3.48) for load-lines. It should be noticed that the pile finite elements equation (3.44) contains variables existing only in the scattered field, and consequently does not need to be rewritten.

Imposing additional equations of equilibrium and compatibility by correlating BEM load lines and FEM piles, equations (3.44), (3.46), (3.47) and (3.48) can be rearranged in a system of equations representing the soil-pile foundation problem.

A more detailed explanation of this formulation as well as the numerical evaluation of integrals over load lines can be found in [81].



4. NUMERICAL COMPUTATION OF IMPEDANCES AND KINEMATIC INTERACTION FACTORS OF PILE FOUNDATIONS

- 4.1 Introduction
- 4.2 Computation of impedances
- 4.3 Computation of kinematic interaction factors
- 4.4 Problem definition
- 4.5 Pile group configurations consisting of vertical piles
- 4.6 Impedances and kinematic interaction factors for vertical pile groups
- 4.7 Influence of direction and angle of inclination of piles on the kinematic response of deep foundations
- 4.8 Pile group configurations including inclined piles
- 4.9 Impedances and kinematic interaction factors for pile groups comprising inclined elements

4.1 Introduction

The present chapter deals with the numerical computation of the impedance functions and kinematic interaction factors corresponding to all the pile group configurations under investigation. As explained in chapter 2, their computation is a key aspect of the substructuring methodology, which is the base of the procedure proposed in this dissertation to determine the influence of the main parameters of the soil-structure-interaction problem on the dynamic behaviour of shear structures in the linear range. In this work, impedances and kinematic interaction factors are numerically obtained by means of a BEM-FEM coupling formulation, developed by Padrón *et al.* [49, 54, 71, 120] and outlined in section 3.5, which allows dealing with the dynamic analysis of piles and pile groups. This formulation was implemented in a previously existent multi-region BEM code [69, 70] that is explained in section 3.4. In this work, this BEM formulation is used to address the validation of the BEM-FEM coupling formulation (as well as its implementation), in terms of the kinematic interaction factors of configurations including battered piles.

Sections 4.2 and 4.3 address the concepts of dynamic stiffness and kinematic interaction factors, respectively. The geometrical characteristics, as well as the material properties, of the pile group configurations studied in this research work are defined in section 4.4. Afterwards, the values of the parameters defining the set of pile group configurations under investigation consisting of vertical piles are defined in section 4.5. The impedance functions and the kinematic interaction factors corresponding to each one of these configurations are presented in section 4.6. These values will be used in chapter 5 in order to perform parametric analyses that allow studying the influence of the main parameters of the SSI problem on the dynamic behaviour of the structure supported on these piled foundations. On the other hand, section 4.7 addresses the analysis of the influence of rake angle and direction of inclination of piles on the kinematic interaction factors of deep foundations. This section intend to contribute to clarify the beneficial or detrimental role of battered piles when submitted to dynamic loads, as well as to provide the scientific and engineering communities with the kinematic interaction factors corresponding to the different pile group configurations analysed in terms of impedance functions by Padrón *et al.* [49]. Then, section 4.8 gives the values of the parameters that characterize the set of pile group configurations that will be used in chapter 6 for the purpose of analysing the influence of the rake angle of piles on the dynamic response of shear structures founded on pile groups comprising inclined piles. The impedance functions and kinematic interaction factors corresponding to these configurations are represented and analysed in section 4.9. Results are given in ready-to-use dimensionless graphs in order to facilitate their use in soil-structure interaction studies. All plots are presented as a function of the dimensionless frequency.

4.2 Computation of impedances

Impedances are complex-valued frequency-dependent functions (k_{xx}, c_{xx}) , $(k_{\theta\theta}, c_{\theta\theta})$ and $(k_{x\theta}, c_{x\theta})$ that represent the stiffness and damping of the soil-foundation system in the horizontal, rocking and cross-coupled horizontal-rocking vibration modes, respectively. In order to compute them, pile heads are subjected to forced vibration in each of

the oscillation modes. Then, the ratio between each component of the vector of forces (and moments) applied at the pile top and the corresponding term of the resulting vector of displacements (and rotations) at the same point yields the dynamic stiffness matrix K_{ij} of the foundation. For pile groups, the impedances are obtained from the proper combination of the contributions of each pile.

The mathematical representation of dynamic stiffness, as complex-valued functions of the excitation circular frequency ω , can be written as

$$K_{ij} = k_{ij} + ia_0c_{ij} \quad (4.1)$$

where k_{ij} and c_{ij} are the frequency dependent dynamic stiffness and damping coefficients, respectively, $i = \sqrt{-1}$ is the imaginary unit, a_0 is the dimensionless frequency expressed as

$$a_0 = \frac{\omega b}{c_s} \quad (4.2)$$

being b the foundation halfwidth and c_s the speed of propagation of shear waves in the half-space which can be expressed as

$$c_s = \sqrt{\frac{\mu_s}{\rho_s}} \quad (4.3)$$

where μ_s and ρ_s are the soil shear modulus of elasticity and mass density, respectively.

As the coupled BEM-FEM formulation used to determine the impedances of several pile groups embedded in a viscoelastic half-space is implemented in a software that incorporates symmetry properties and due to the problem symmetries, only a quarter of the total geometry of the problem has to be discretized. A sensitivity analysis was performed to establish the extension and topology of the optimal meshes. Quadratic boundary elements of quadrilateral shape are used to discretize the soil as a linear, homogeneous, isotropic and viscoelastic half-space. The length of free surface that has been discretized is, approximately, four times the pile length. The criterion used in the choice of the element size consist in keeping its main dimension always shorter than the half of the wave length. The total number of nodes and elements resulting from such discretization is 5407 and 1320, respectively. On the other hand, three-node beam elements have been used to discretize piles by finite elements according to the Euler-Bernoulli hypothesis. The number of elements used in this case depends on the pile length.

4.3 Computation of kinematic interaction factors

Kinematic interaction refers to the behaviour of the foundation, which due to its geometry and stiffness filters the seismic input. Thus, kinematic interaction leads to a foundation input motion different than the free-field ground motion.

In order to consider kinematic interaction effects, the motion of the massless pile cap when subjected to the same input motion as the total solution is computed. Even for vertically-incident harmonic plane S waves (in which the free-field displacement at the ground surface is exclusively horizontal), this frequency dependent kinematic interaction factors are represented by horizontal (u_g) and rocking (φ_g) motions at the pile cap.

The kinematic interaction factors are functions of the dimensionless frequency a_o that can be normalized with the free-field motion at the surface u_{g_o} as follows:

$$I_u = \frac{u_g}{u_{g_o}} \quad (4.4)$$

$$I_\varphi = \frac{\varphi_g b}{u_{g_o}} \quad (4.5)$$

As explained before for the case of impedances, a BEM-FEM coupling formulation has been used to compute kinematic interaction factors for different configurations of pile groups.

4.4 Problem definition

All the configurations under study consist of piles arranged in square regular groups which are symmetrical with respect to planes xz and yz (see figure 4.1). These pile groups are considered to be embedded in a homogeneous, viscoelastic and isotropic half-space and subjected to vertically-incident S waves. Pile heads are constrained (through fixed-head connection conditions) by a rigid mass-less pile cap which is assumed to be free of contact with the soil. Free-head single piles are also studied. Welded boundary contact conditions at the pile-soil interfaces are assumed. All piles have identical material and geometrical properties.

Figure 4.1 illustrates the main geometrical parameters of the system: piles length (L) and diameter (d), spacing between centers of adjacent pile heads (s), and rake angle between the vertical and the pile axis (θ). The foundation halfwidth is defined as $b = d$ for single piles, $b = s$ for 2×2 pile groups, $b = 3s/2$ for 3×3 pile groups and $b = 2s$ for 4×4 pile groups. It is worth noting that some vertical piles are included in 3×3 pile groups for the purpose of maintaining symmetry with respect to planes xz and yz . Those configurations with 4×4 piles are only used in this work for vertical piles ($\theta = 0$).

When analysing the dynamic behaviour of piles it is necessary to consider their geometrical characteristics as well as the material properties. As explained in section 2.5, the main dimensionless parameters characterizing piles dynamic behaviour are:

- The pile-soil Young's modulus ratio E_p/E_s .
- The pile slenderness ratio defined as L/d .
- The soil-pile densities ratio ρ_s/ρ_p .
- The dimensionless excitation frequency $a_o = \omega d/c_s$.
- The Poisson's ratio ν_s .

Moreover, the dynamic response of pile groups depends also on the following dimensionless parameters related to the foundation geometry:

- The pile spacing ratio s/d .
- The foundation embedment ratio L/b .

The equations of motion of the substructuring model described in section 2.4.1 are expressed in terms of these dimensionless parameters, which considerably facilitates the analysis of their influence on the system dynamic response by performing parametric studies. The main advantage of using dimensionless parameters is that the conclusions drawn from the obtained results are applicable to all those different real cases with the same values of these parameters.

In this work, the following properties are considered: soil internal hysteretic damping coefficient $\beta_s = 0.05$, soil Poisson's ratio $\nu_s = 0.4$, soil-pile density ratio $\rho_s/\rho_p = 0.7$, and pile-soil modulus ratios $E_p/E_s = 10^3$ (soft soil) and $E_p/E_s = 10^2$ (stiff soil).

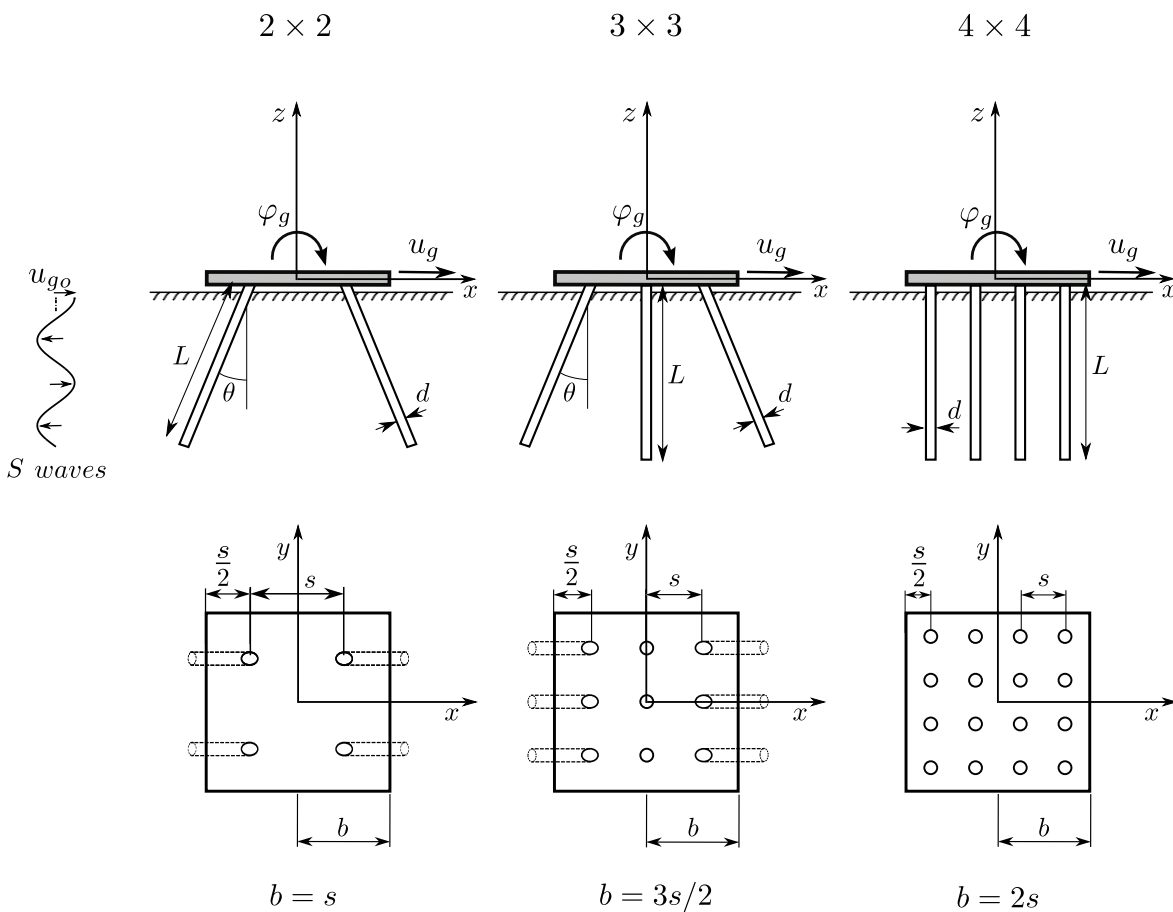


FIGURE 4.1: Pile foundation geometry.

4.5 Pile group configurations consisting of vertical piles

Table 4.1 lists the values of the main dimensionless parameters governing the SSI problem corresponding to the different configurations of vertical pile groups analysed in this work. The dynamic response of several groups of 2×2 , 3×3 and 4×4 piles is studied herein.

TABLE 4.1: Pile group configurations consisting of vertical piles.

L/b	L/d	s/d		
		2×2	3×3	4×4
1	7.5	7.5	5	3.75
	15	15	10	7.5
2	7.5	3.75	2.5	1.875
	15	7.5	5	3.75
	30	15	10	7.5
4	15	3.75	2.5	1.875
	30	7.5	5	3.75

The varying values of the pile spacing ratio s/d are chosen in order to make the different results more comparable among each other by keeping the foundation halfwidth b constant for configurations with different number of piles. In order to facilitate the interpretation of the results, figure 4.2 depicts a sketch of the different configurations when considering the same pile diameter ($d = \text{cte}$) for all cases. It can be observed that the same value of b corresponds to all configurations in the same row. In turn, three different values are chosen for the pile slenderness ratio ($L/d = 7.5, 15, \text{ and } 30$) as well as for the foundation embedment ratio ($L/b = 1, 2, \text{ and } 4$), in order to analyse the effects of the variation of these parameters on the dynamic behaviour of the pile foundation. All configurations follow the pattern represented in figure 4.1 and correspond to the description exposed in section 4.4.

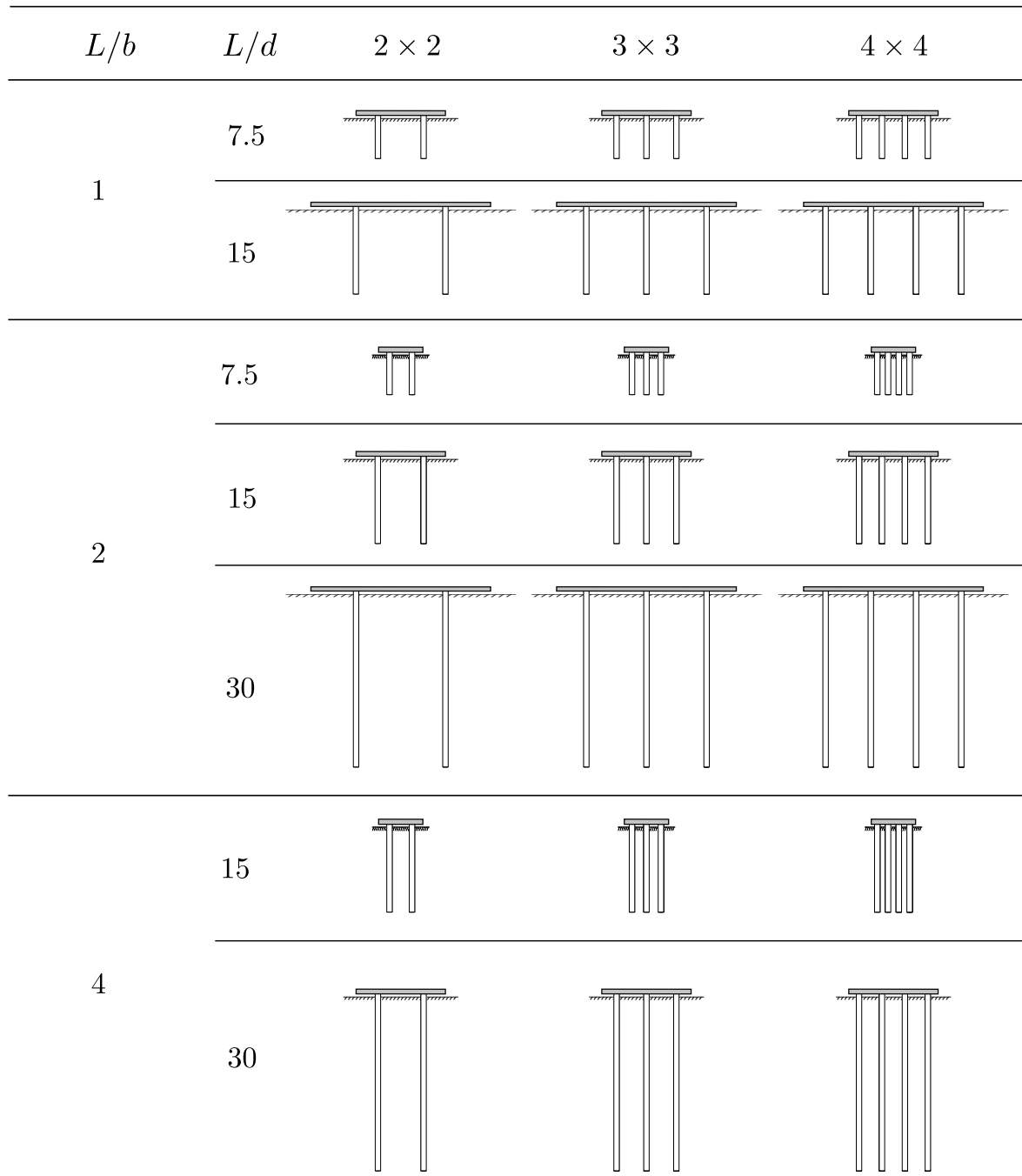


FIGURE 4.2: Sketches of the different vertical pile group configurations assuming the same diameter $d = cte$ for all cases.

All the pile group configurations are analysed in the frequency range of interest for seismic loading ($\omega d/c_s < 0.5$, according to Gazetas *et al.* [79]). For the purpose of verifying that this range of frequencies is appropriate for the research work presented in this document, figure 4.3 depicts, for all of the 21 configurations under study and for 4 different values of the structural slenderness ratio h/b , the value of the dimensionless excitation frequency $\omega d/c_s$ which corresponds to the effective period \tilde{T}/T of an SDOF equivalent system which reproduces the coupled system response within the range where the peak response occurs. The dynamic behaviour of each one of these different configurations has been studied within a range of values of the wave parameter such that $1/\sigma \leq 0.5$. It is assumed that $\xi_s = 0.05$, $\nu_s = 0.4$, $E_p/E_s = 10^3$ and $\rho_s/\rho_p = 0.7$. The vertical axis represents the maximum value reached for the dimensionless excitation frequency within all the analysed range of $1/\sigma$. The horizontal axis represents the structural slenderness ratio. Each cross in the plot area represents one of the 84 different cases analysed. As it can be observed in this figure, it has been found that the value of $\omega d/c_s$ is always below 0.5.

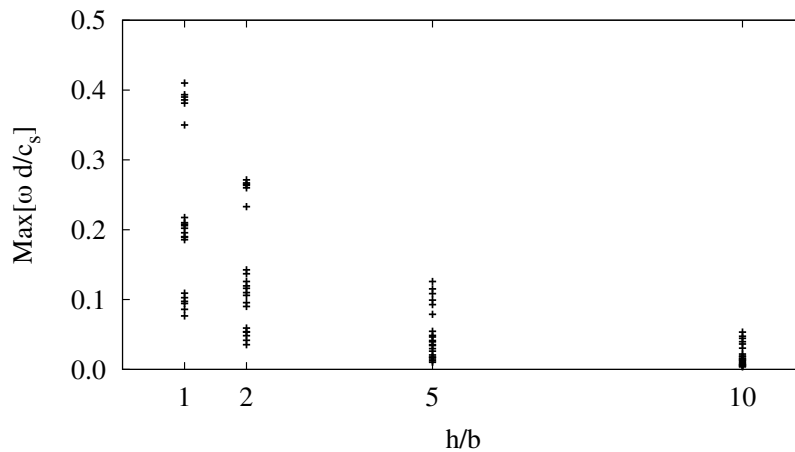


FIGURE 4.3: Range of the dimensionless frequency $\omega d/c_s$ for all cases under investigation.

4.6 Impedances and kinematic interaction factors for vertical pile groups

Figures 4.4, 4.5 and 4.6 show, respectively, the impedances of the 2×2 , 3×3 and 4×4 pile group configurations under investigation (see table 4.1), in the range of the dimensionless excitation frequency $a_o = \omega d/c_s$ needed to obtain all the results presented in chapter 5. In each figure, the first and the second row represent, respectively, the frequency dependent dynamic stiffness and damping coefficients. The different columns correspond, from left to right to the horizontal, rocking and cross-coupled horizontal-rocking vibration modes, respectively. Impedance values are represented herein normalized with the soil shear modulus of elasticity μ_s and the pile diameter d as follows: $k_{xx}/\mu_s d$, $c_{xx}/\mu_s d$, $k_{\theta\theta}/\mu_s d^3$, $c_{\theta\theta}/\mu_s d^3$, $k_{x\theta}/\mu_s d^2$ and $c_{x\theta}/\mu_s d^2$. Each curve in a plot area cor-

responds to a particular pile group configuration, characterized by the pile spacing ratio s/d and the embedment ratio L/b .

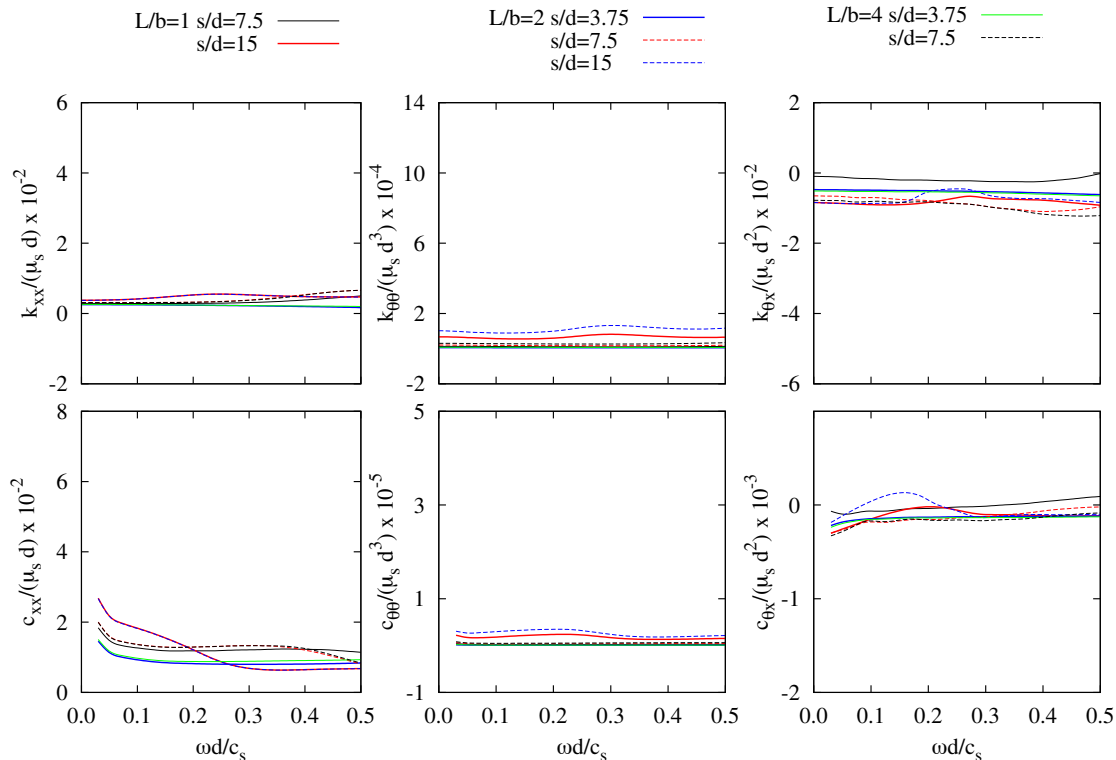


FIGURE 4.4: Impedance functions of different 2×2 pile groups. $E_p/E_s = 10^3$ and $\xi_s = 0.05$.

All the results represented in terms of impedance functions have a dimensionless character, thus their physical interpretation must be carefully done and requires a specific data processing, taking into account the influence of every dimensionless parameter. Although these results could be interpreted in different ways, let's consider for example that all configurations are embedded in the same soil ($c_s = \text{cte}$) and that all piles have the same diameter ($d = \text{cte}$). When analysing only the results corresponding to configurations with the same value of the embedment ratio L/b and the same number of piles, it can be observed that the soil-foundation horizontal stiffness k_{xx} and damping c_{xx} generally increases with the distance between adjacent piles s . Looking at figure 4.2 it can be noticed that an increment of s implies, in these cases, greater values of the pile length L as well as an increase of the foundation halfwidth b . Moreover, the variation of k_{xx} and c_{xx} with the excitation frequency ω increases with the pile spacing ratio s/d , reaching greater values as ω grows. With regard to the soil-foundation rocking stiffness $k_{\theta\theta}$ and damping $c_{\theta\theta}$, it can be seen that they increase with the pile spacing ratio s/d . With respect to the stiffness $k_{x\theta}$ for the cross-couple vibration mode, it generally increases for greater values of the distance between adjacent piles s . However, the damping coefficient $c_{x\theta}$ does not show a clear trend within the analysed range of frequencies.

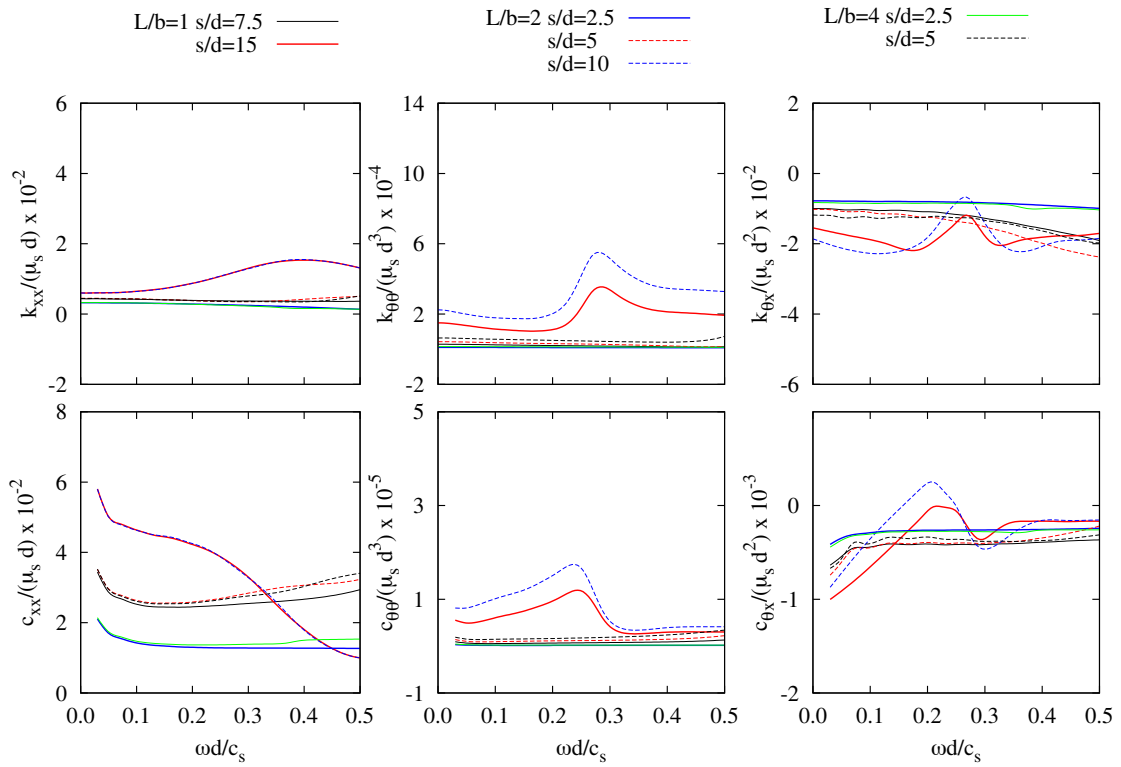


FIGURE 4.5: Impedance functions of different 3×3 pile groups. $E_p/E_s = 10^3$ and $\xi_s = 0.05$.

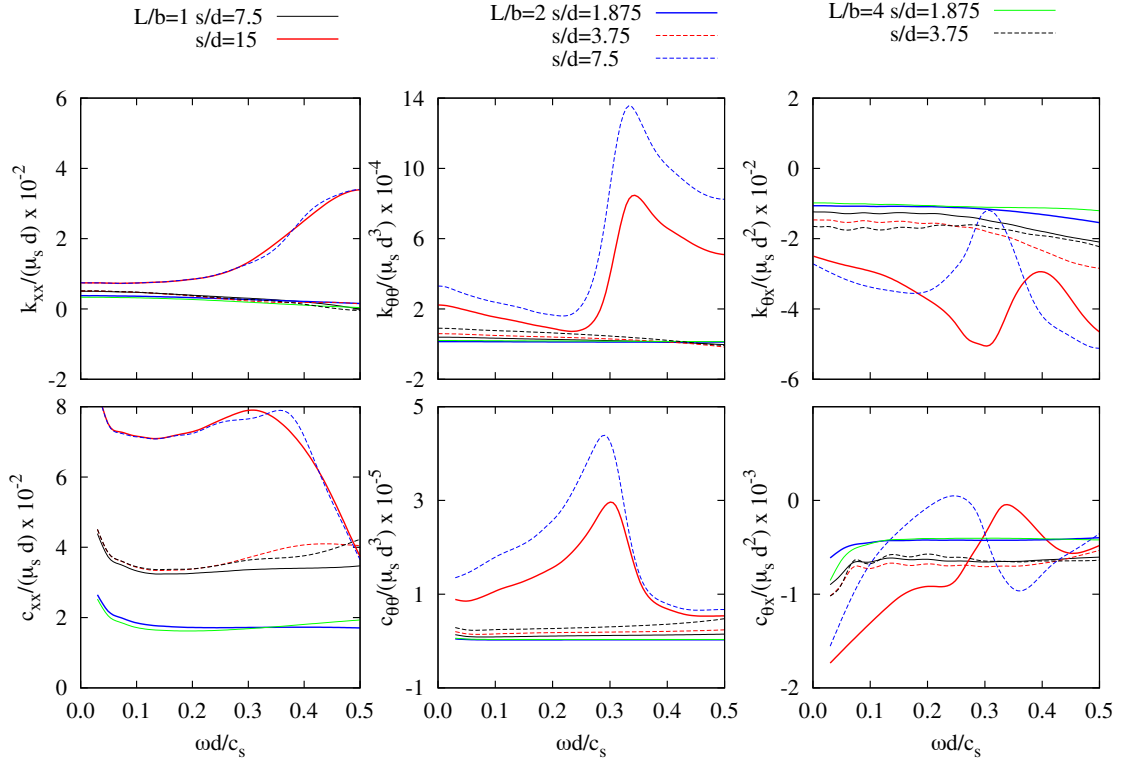


FIGURE 4.6: Impedance functions of different 4×4 pile groups. $E_p/E_s = 10^3$ and $\xi_s = 0.05$.

On the other hand, figures 4.7 to 4.13 depict the kinematic interaction factors, in a dimensionless form, for all the configurations under investigation. In each figure, the first and the second row represent, respectively, the effective seismic pile-cap horizontal and rocking motions normalized with the free-field ground-surface motion. In each row, the plot area on the left side shows the real part of the kinematic interaction factor, whereas that on the right shows the values corresponding to its imaginary part. The horizontal axis represents the dimensionless excitation frequency.

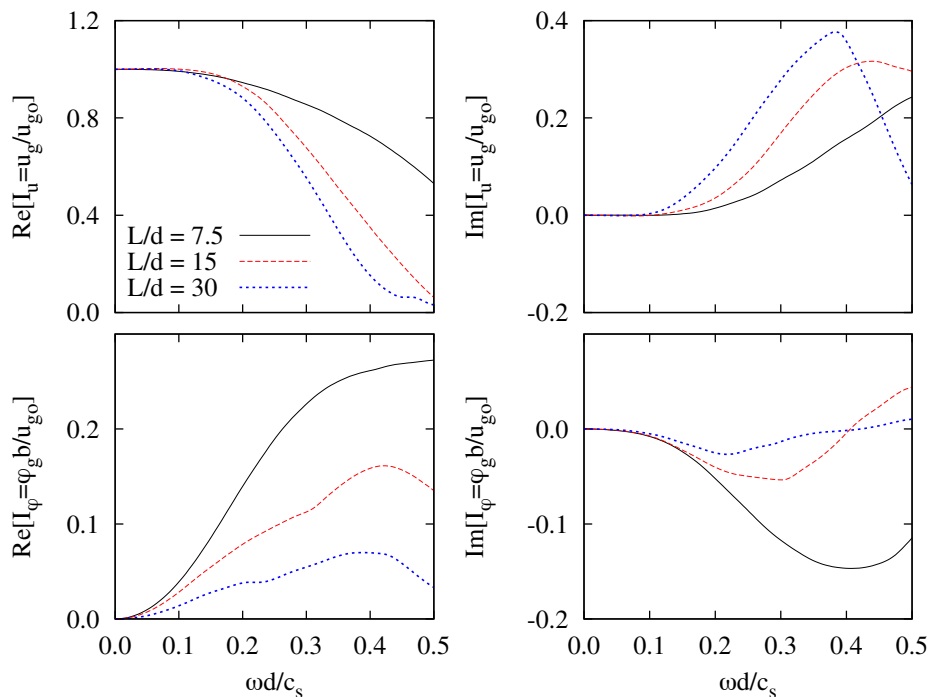


FIGURE 4.7: Idealized shape of the kinematic interaction factors of pile groups with different s/d , L/b and number of piles embedded in a soil with $E_p/E_s = 10^3$ and $\xi_s = 0.05$.

Figure 4.7 presents the kinematic interaction factors in terms of an idealized general shape [79] for each L/d . This shape is the midline of a band which contains all the curves obtained for the different configurations studied for this value of L/d . For the purpose of illustrating how this idealized shape is determined, figures 4.8, 4.9 and 4.10 depict, for each value of L/d , the curves corresponding to the kinematic interaction factors of the different configurations under study, the band that they define, as well as the midline whose values can be adopted as an approach of the kinematic interaction factors for all these configurations. With regard to the shape of the translational kinematic interaction factor I_u as a function of frequency, in the frequency range of interest for earthquake loading ($a_o < 0.5$), it can be observed that there exist a low-frequency range in which I_u takes values close to the unity, an intermediate-frequency range where I_u decreases monotonically with frequency and a small high-frequency range where its values fluctuates with frequency. On the other hand, the rotational kinematic interaction factor I_φ increases with the dimensionless frequency $\omega d/c_s$. It should be noticed that

both the translational and the rotational kinematic interaction factors experience a decrease when considering greater values of the pile slenderness ratio L/d , which implies also increasing values of the pile spacing ratio s/d for the configurations under study.

A sensitivity analysis was performed in order to assess the accuracy of approaching the kinematic interaction factors by the idealized shape described above. Firstly, the idealized shape, obtained as previously shown in figures 4.8, 4.9 and 4.10, was used to compute the maximum value of the shear force at the base of the structure per effective earthquake force unit Q_m , through the procedure proposed in chapter 2, for different values of the structural slenderness ratio $h/b = 1, 2, 5$ and 10 . The obtained results were compared against those obtained by using the exact values of the kinematic interaction factors for each pile group configuration (see figures 4.11 to 4.13). It was found that by using the idealized kinematic interaction factors for a given value of L/d (see figure 4.7), the mean relative error within the range of the wave parameter $1/\sigma \leq 0.5$ committed in terms of Q_m , taking as a reference the response obtained with their exact values, is always lower than 14% for all the pile group configurations under study. It should be noted that this error decreases for increasing values of h/b . Thus, when $h/b = 10$ the relative error reaches a 4% for the most unfavourable configuration. However, when $h/b = 1$ the relative error reaches a maximum value near 22%.

On the other hand, an analogous comparison was made between the results obtained for Q_m by using the exact values of the kinematic interaction factors for each configuration and those obtained by approaching these values by an idealized shape representing each set of configurations, not only with the same value of the pile slenderness ratio L/d but also with the same value of the foundation embedment ratio L/b . As expected, the mean relative error committed by using this approach reaches values slightly lower than those obtained when considering the same idealized shape for configurations with different values of L/b . In fact, the mean relative error committed is always lower than 11% for all the pile group configurations under study, and the maximum value of the relative error is near 19%.

Fan *et al.* [78] performed a parametric analysis for the purpose of investigating the kinematic behaviour of typical pile-group configurations embedded in three idealized soil profiles, one of which was a homogeneous half-space. They shown that the kinematic interaction factor associated with translation I_u depends mainly on L/d and it is not significantly influenced by the pile-group configuration, number of piles in the group, and relative spacing between piles. However, they showed that this conclusion is not so valid for I_φ as these factors are usually important for pile-cap rotations. Therefore, although the idealized shape of I_u and I_φ for each value of L/d is presented, all results presented in this chapter have been obtained with the exact kinematic interaction functions depicted in figures 4.11 to 4.13.

In order to determine the influence of the pile-soil Young's modulus ratio on the dynamic behaviour of the superstructure, an additional value of E_p/E_s has been considered. In this line, figures 4.14 and Figure 4.15 show, respectively, impedance functions and kinematic interaction factors for 2×2 pile groups embedded in a homogeneous soil such that $E_p/E_s = 10^2$. Results for three different values of the pile slenderness ratio ($L/d = 7.5, 15$ and 30) are represented. Comparing this results against those obtained for $E_p/E_s = 10^3$, it can be observed that the influence of the variation of L/d is more remarkable as the pile-soil Young's modulus ratio increases.

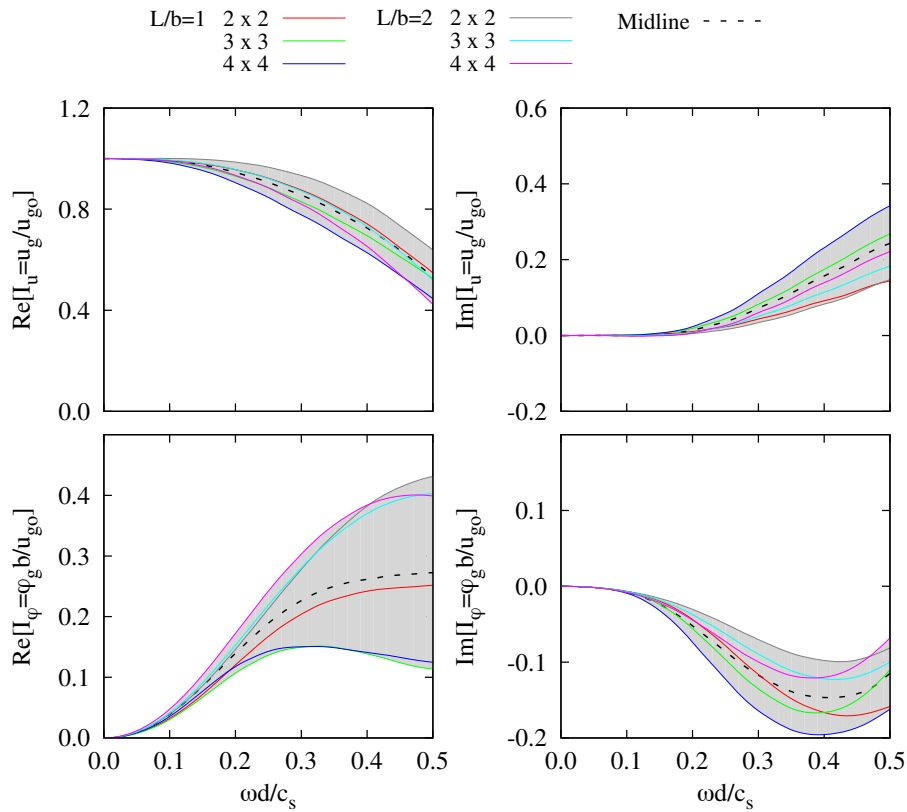


FIGURE 4.8: Idealized shape of the kinematic interaction factors of different pile groups with $L/d = 7.5$, $E_p/E_s = 10^3$ and $\xi_s = 0.05$.

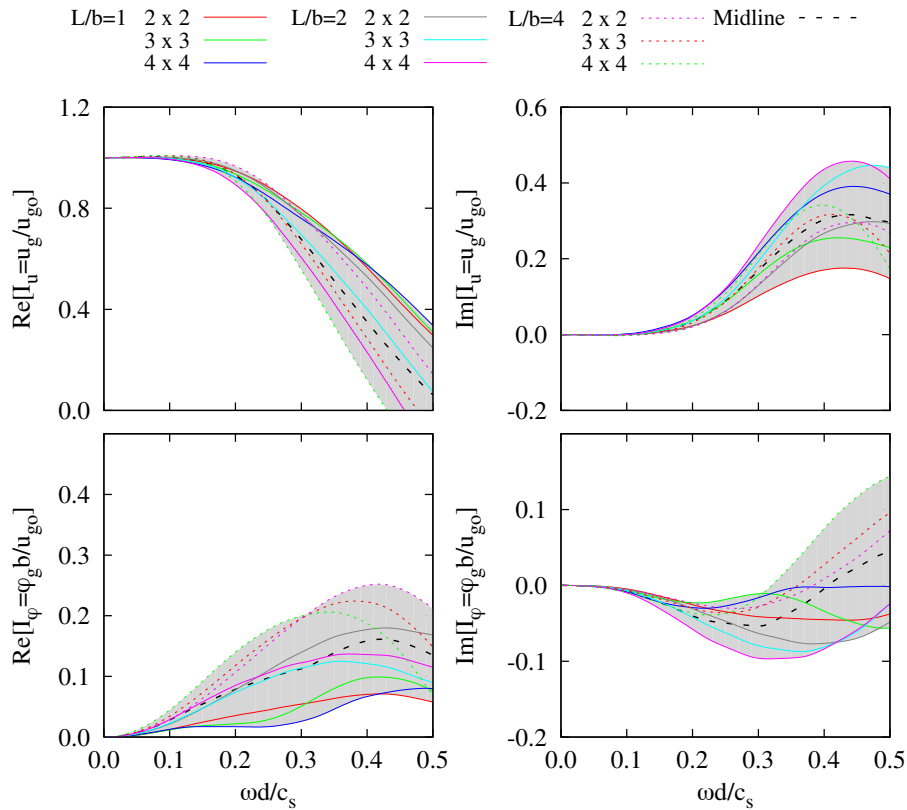


FIGURE 4.9: Idealized shape of the kinematic interaction factors of different pile groups with $L/d = 15$, $E_p/E_s = 10^3$ and $\xi_s = 0.05$.

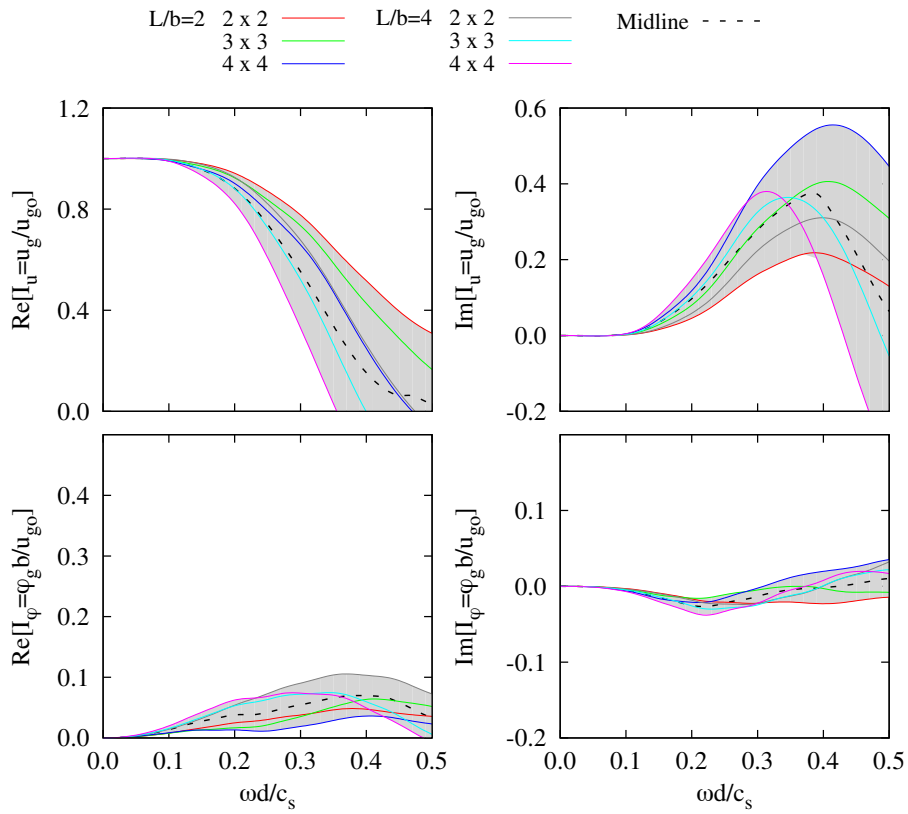


FIGURE 4.10: Idealized shape of the kinematic interaction factors of different pile groups with $L/d = 30$, $E_p/E_s = 10^3$ and $\xi_s = 0.05$.

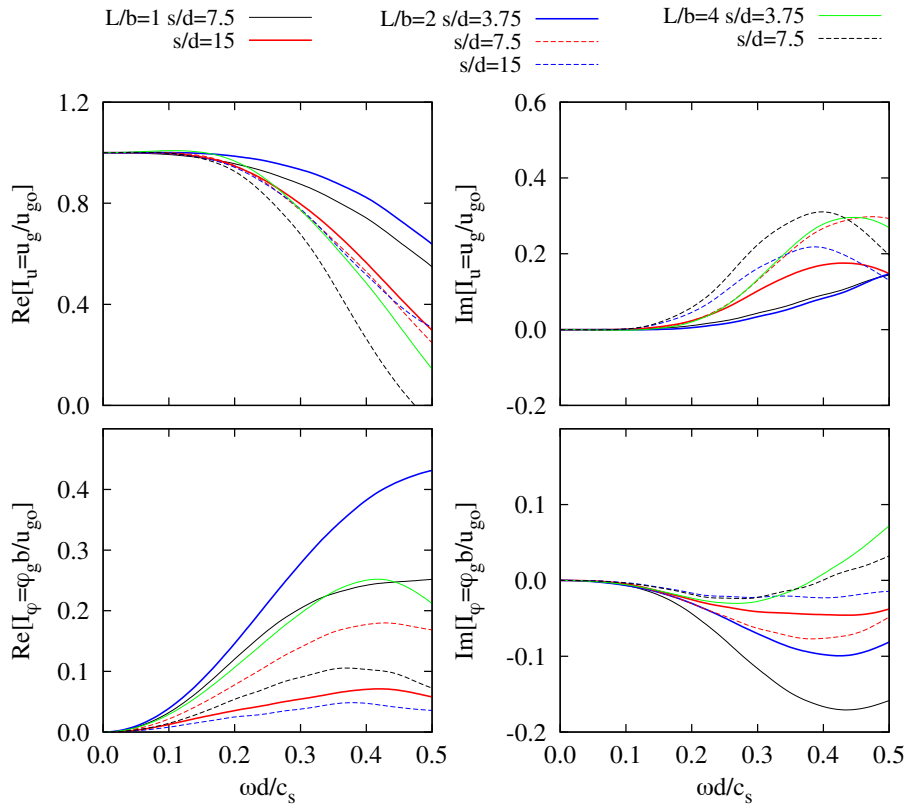


FIGURE 4.11: Kinematic interaction factors of different 2×2 pile groups, $E_p/E_s = 10^3$ and $\xi_s = 0.05$.

4  Numerical computation of impedances and kinematic interaction factors

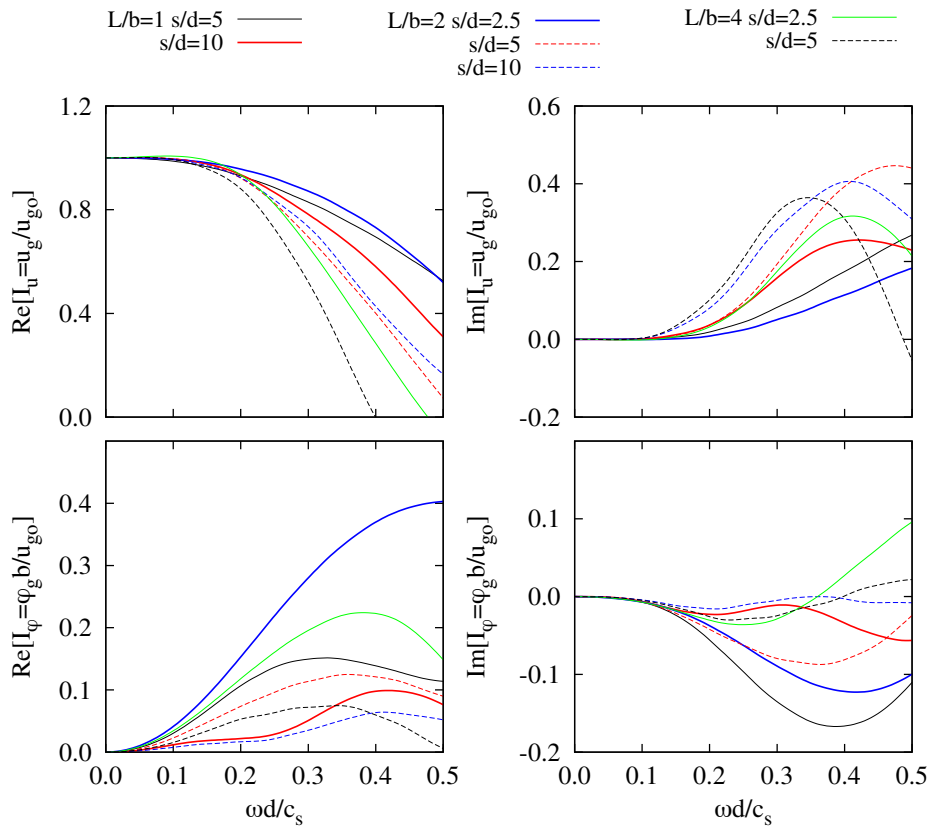


FIGURE 4.12: Kinematic interaction factors of different 3×3 pile groups. $E_p/E_s = 10^3$ and $\xi_s = 0.05$.

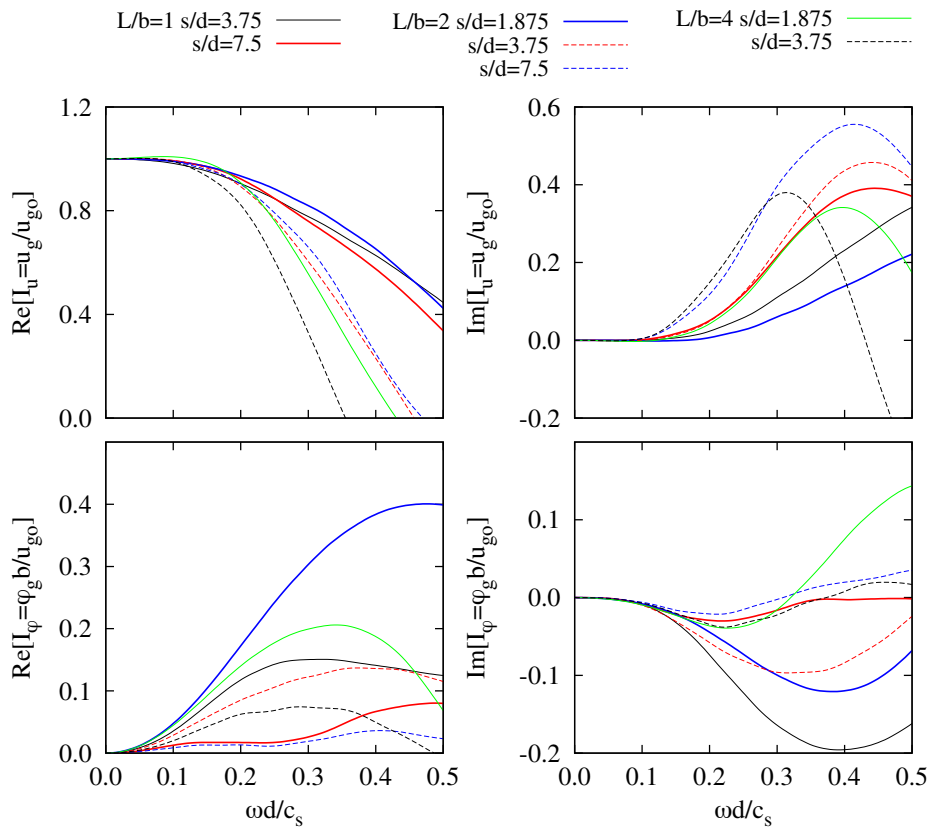


FIGURE 4.13: Kinematic interaction factors of different 4×4 pile groups. $E_p/E_s = 10^3$ and $\xi_s = 0.05$.

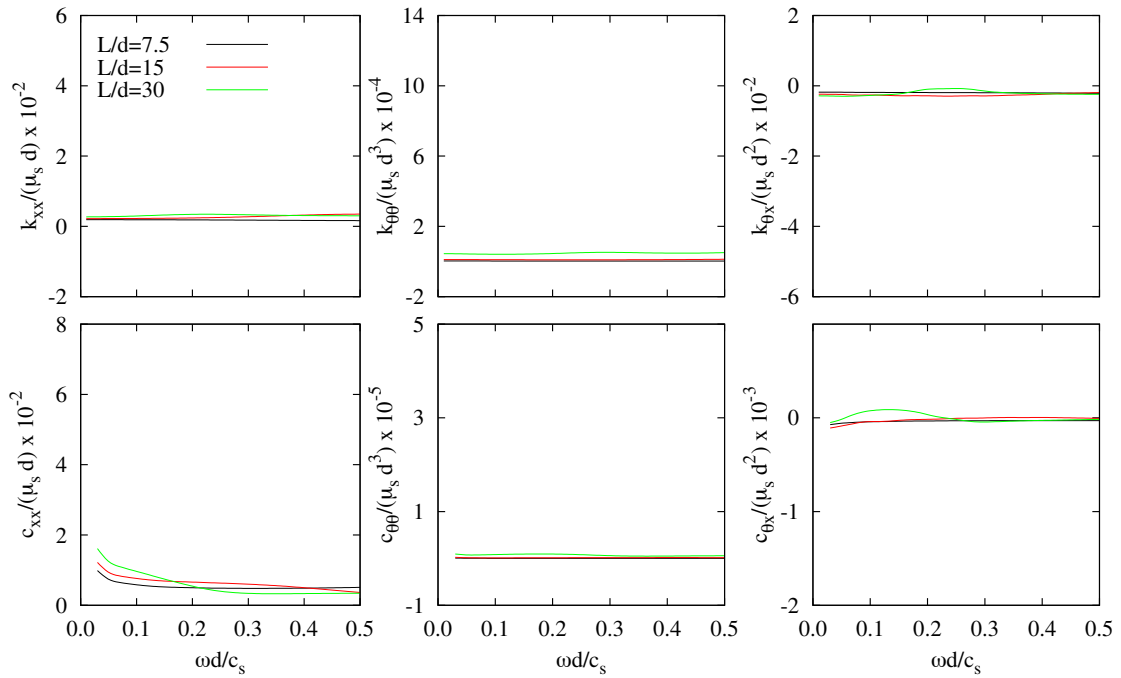


FIGURE 4.14: Impedance functions of different 2×2 pile groups. $E_p/E_s = 10^2$ and $\xi_s = 0.05$.

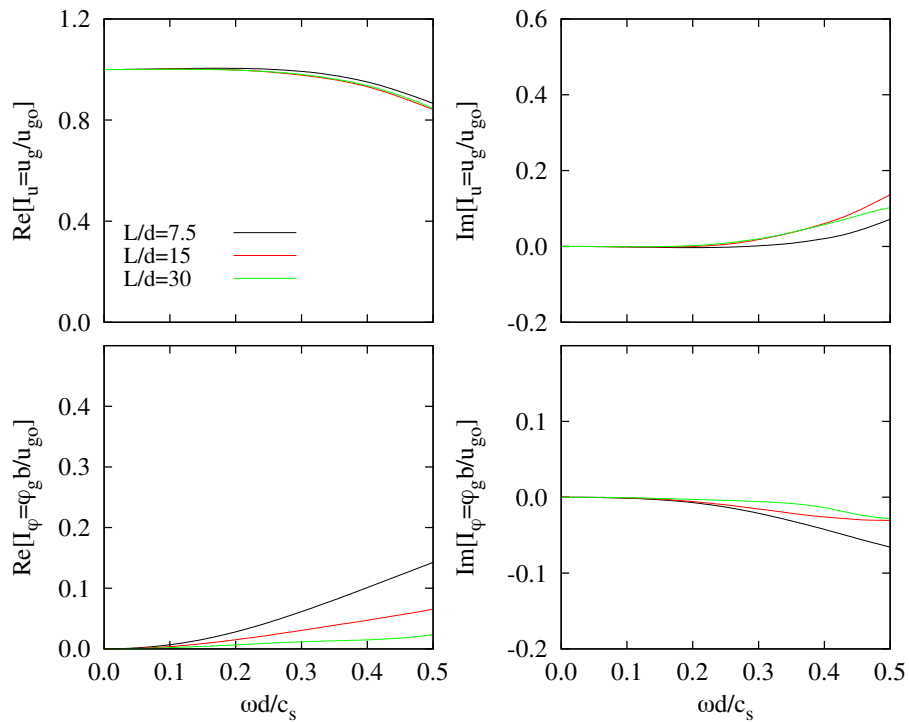


FIGURE 4.15: Kinematic interaction factors of different 2×2 pile groups. $E_p/E_s = 10^2$ and $\xi_s = 0.05$.

4.7 Influence of direction and angle of inclination of piles on the kinematic response of deep foundations

The beneficial or detrimental role of battered piles on the dynamic response of piled foundations has not been yet fully elucidated. In order to shed more light on this aspect, kinematic interaction factors of single inclined piles, as well as those of 2×2 and 3×3 pile groups with raked elements, embedded in a viscoelastic half-space and subjected to vertically incident plane shear S waves, are presented in this section. These results have been computed through the BEM-FEM formulation described in section 3.5. This formulation was implemented in a previously existent multi-region BEM FORTRAN code [69, 70] outlined in section 3.4. Its validity for obtaining kinematic interaction functions of vertical piles has been already checked. For example, Padrón *et al.* [81] compare the obtained results with those provided by Kaynia and Novak [77] for a single pile, as well as for 3×3 groups of piles under vertically incident S waves. Herein, the validation of the BEM-FEM coupling formulation (as well as its implementation) for configurations including battered piles is addressed. Afterwards, the relevance and main trends observed in the influence of the rake angle and the direction of inclination of piles on the kinematic interaction factors of the analysed foundations are inferred from the presented results.

4.7.1 Validation of the BEM-FEM coupling formulation

In order to assess the accuracy of the BEM-FEM formulation, described in section 3.5, when applied to the determination of kinematic interaction factors corresponding to configurations including battered piles, results computed with this model are compared with those corresponding to the multi-region boundary element code outlined in section 3.4.

Figure 4.16 presents comparison results for several configurations of 2×2 inclined pile groups according to the geometrical parameters and material properties defined in section 4.4 and subjected to vertically incident S waves that, at free-field ground surface, causes motions in the direction of the x axis. The first and the second rows of the plots correspond to a pile spacing ratio of $s/d = 5$ and piles inclined, with a rake angle of $\theta = 10^\circ$, parallel and perpendicular to the direction of the excitation, respectively. The third row shows the results corresponding to a pile spacing ratio of $s/d = 10$ and piles inclined symmetrically along the cap diagonals with a rake angle of $\theta = 20^\circ$. Finally, the fourth and fifth rows, present the results for a pile spacing ratio of $s/d = 10$ and piles inclined, with a rake angle of $\theta = 30^\circ$, parallel and perpendicular to the direction of the excitation, respectively. In all cases, results are obtained for two different pile-soil stiffness ratios.

The results corresponding to the BEM-FEM coupling formulation are in strong agreement with those obtained from the more rigorous multi-domain boundary element (BEM-BEM) code. The resulting relative errors, for a dimensionless frequency value $a_o = 0.25$, for instance, are below 8% in terms of rotational kinematic interaction function I_φ , and below 3% in terms of translational kinematic interaction function I_u . Therefore, the BEM-FEM formulation is the preferred method to carry out parametric studies, since it is more cost-effective.

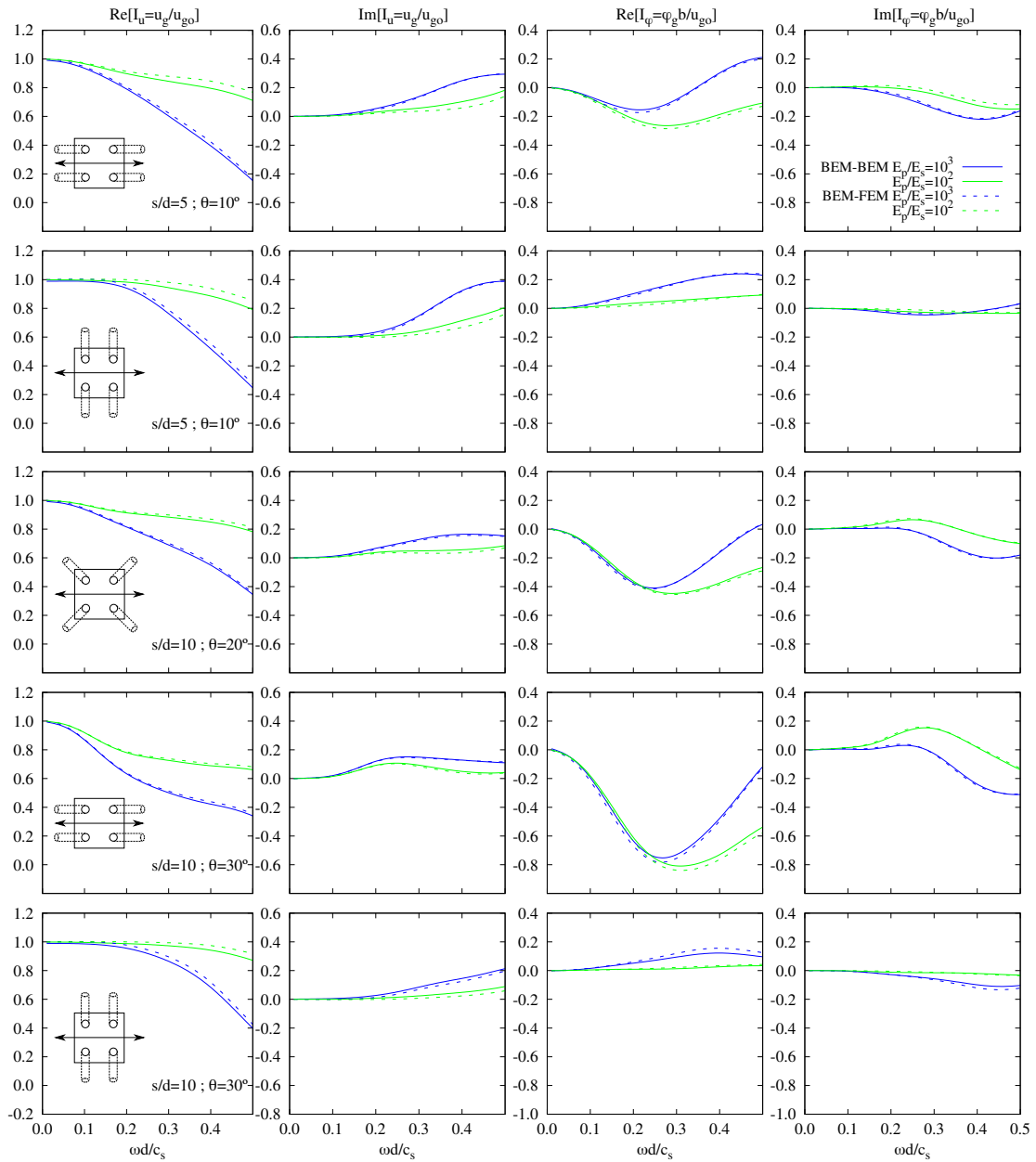


FIGURE 4.16: Kinematic interaction factors, I_u and I_φ , of 2×2 pile groups with different spacing ratios s/d , rake angles θ and stiffness ratios E_p/E_s . Comparison between BEM-BEM and BEM-FEM.

4.7.2 Pile group configurations under investigation

This section provides kinematic interaction factors of single inclined piles, and 2×2 and 3×3 pile groups with battered elements according to the geometrical parameters and material properties defined in section 4.4 and subjected to vertically-incident plane shear S waves. The values of the dimensionless parameters for the pile group configurations analysed in this section are listed in table 4.2.

TABLE 4.2: Pile group configurations for the analysis of the influence of rake angle of piles on the kinematic interaction factors of deep foundations.

L/d	s/d	L/b	
		2×2	3×3
15	5	3	2
	10	1.5	1

This study includes results corresponding to different pile group configurations with piles inclined perpendicular or parallel to the direction of excitation as well as symmetrically along the cap diagonals. Four different rake angles have been considered: $\theta = 0^\circ$ (vertical piles), 10° , 20° and 30° . Some vertical piles are included in 3×3 pile groups in order to maintain symmetry with respect to planes xz and yz . Results corresponding to pile-soil stiffness ratios $E_p/E_s = 1000$ (soft soil) and 100 (stiff soil) are presented. Stability and convergence analyses of the meshes have been performed in order to ensure the accuracy of the obtained results.

The configurations analysed herein coincide with those whose impedance functions were provided by Padrón *et al.* [49]. An analogous study is performed in this work, and this section intends to provide the scientific and engineering communities with complementary data in terms of kinematic interaction factors needed to accomplish substructuring analyses. This is why the same configurations are chosen for the study accomplished in this section.

4.7.3 Translational kinematic interaction factors of single piles

Figure 4.17 presents the translational kinematic interaction factors I_u corresponding to free-head single inclined piles, together with the relative vertical displacements produced at the pile top by the incident field. When the pile is inclined parallel to the direction of the excitation (central column), I_u decreases for increasing rake angles up to $a_o = 0.5$ for $E_p/E_s = 1000$, and up to $a_o = 0.8$ for $E_p/E_s = 100$. However, inclining the pile perpendicular to the direction of excitation (left column) has no beneficial effects in the low-frequency range and even shows a detrimental behaviour in the intermediate-frequency region as it leads to increasing values of the horizontal motion. For low values of a_o , I_u increases for increasing pile-soil modulus ratios. The opposite occurs for high values of the dimensionless frequency. As expected, vertical displacements also grow for increasing rake angles, reaching displacements up to 60% of the horizontal free-field ground motion at $a_o = 0.3$.

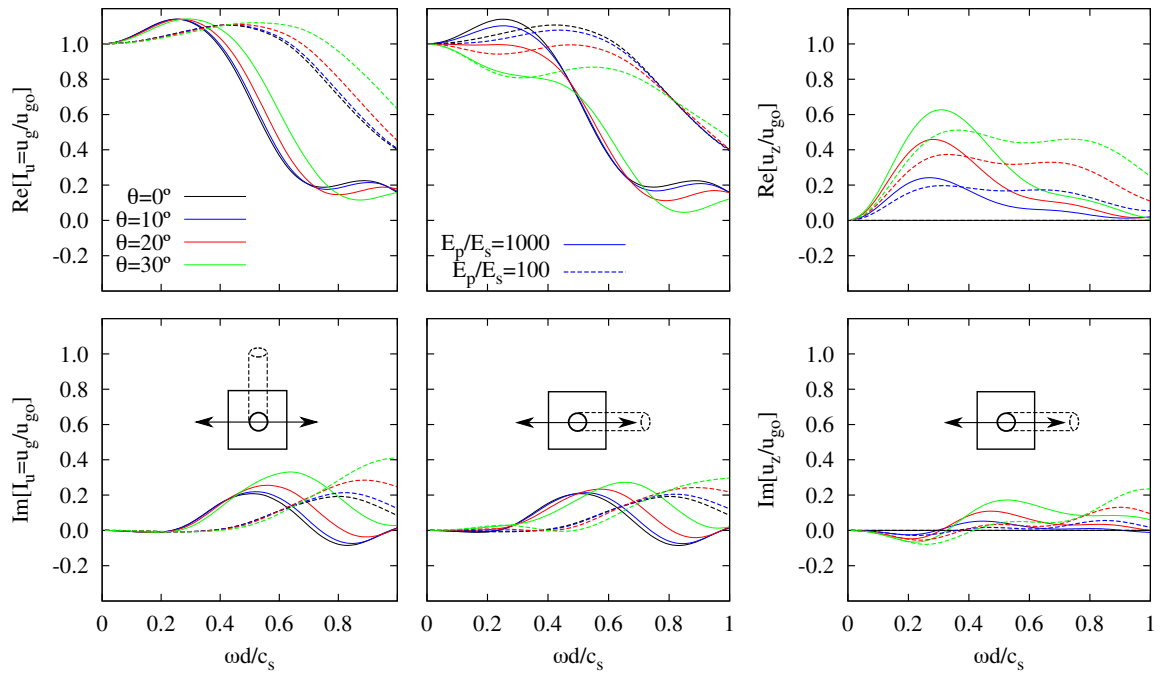


FIGURE 4.17: Translational kinematic interaction factor I_u and vertical displacement u_z/u_{g0} of a single pile for different rake angles θ .

4.7.4 Rotational kinematic interaction factors of single piles

Figure 4.18 depicts the rotational kinematic interaction functions I_φ for the cases defined above. For increasing rake angles, rotation slightly decreases for low-to-mid frequencies, and slightly increases for mid-to-high frequencies. Contrary to what could have been expected, the rotation is almost independent of the direction of inclination. In order to look into this fact, the deformed shapes of single piles, inclined in both directions, at $a_o = 0.3$ are represented in figure 4.19. It can be seen that the direction of inclination does influence significantly the pile behaviour as a whole, although the comparison between the undeformed and deformed shapes shows similar rotations in both configurations.

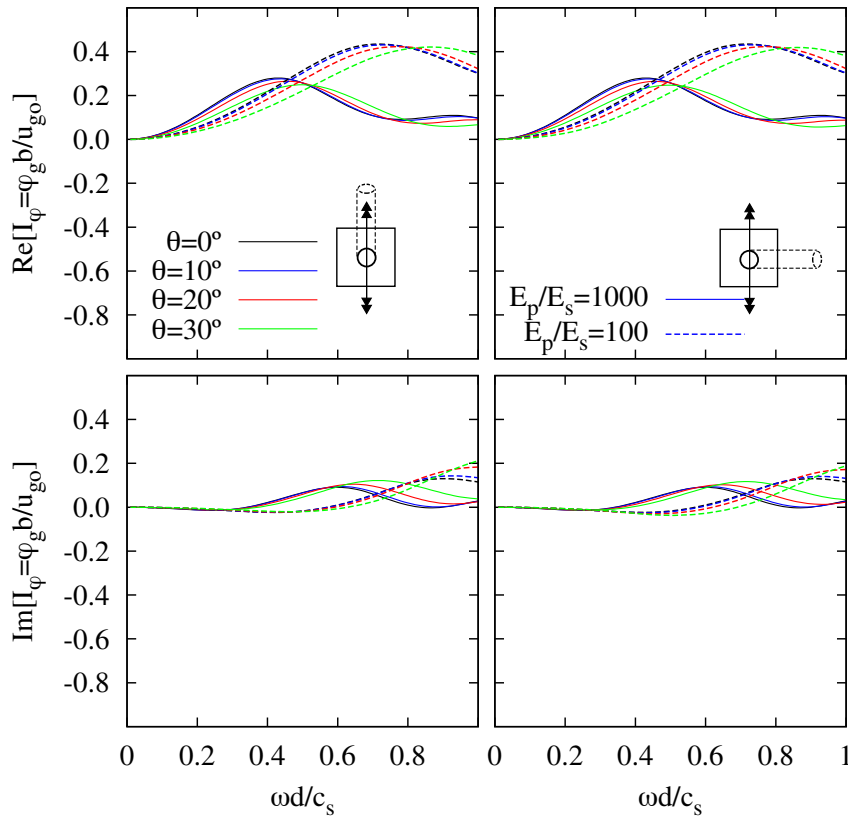


FIGURE 4.18: Rotational kinematic interaction factor I_φ of a single pile for different rake angles θ .

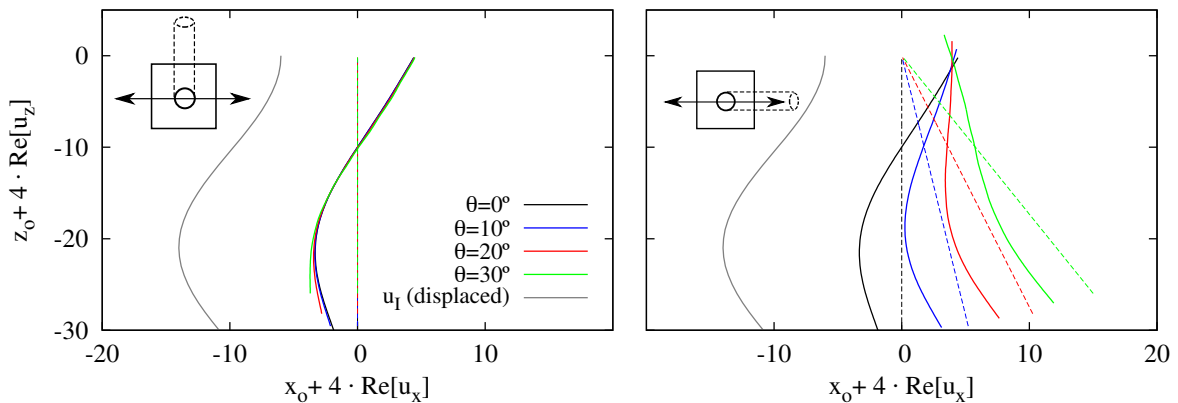


FIGURE 4.19: Deformed shape (solid line) and undeformed shape (dash line) of simple inclined piles with different rake angles θ considering $|u_{g_o}| = 1$ (u_I displaced 10 units to the left only for illustration purposes). $a_o = 0.3$. $E_p/E_s = 1000$.



4.7.5 Translational kinematic interaction factors of pile groups

Figures 4.20, 4.21, 4.22 and 4.23 show the influence of rake angle on the translational kinematic interaction functions of four different configurations of pile groups. The low frequency region in which I_u increases with frequency for single piles does not appear in the translational kinematic interaction function of pile groups, case in which $|I_u| \leq 1$ for all ω . Inclining piles perpendicular to the direction of the excitation (left column) leads generally to higher values of I_u in comparison with those obtained with vertical piles. Conversely, the use of piles inclined symmetrically along the cap diagonals (central column) generally results in a reduction of this motion in the low-to-mid frequency range. A stronger filtering of the seismic excitation can be achieved by inclining piles parallel to the direction of excitation (right column). The kinematic response of pile groups including battered piles is less sensitive to variations of the rake angle as the pile spacing ratio s/d and the number of piles increase. In all cases, I_u decreases for higher pile-soil modulus ratios for low-to-mid frequencies.

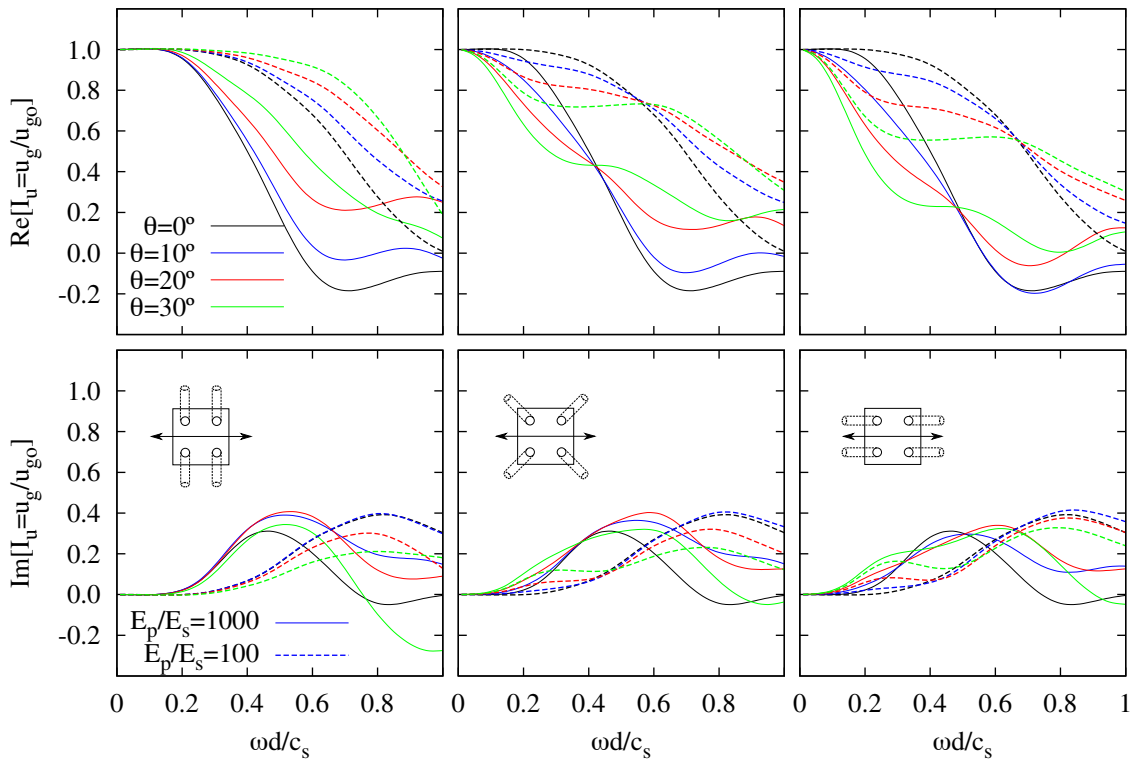


FIGURE 4.20: Translational kinematic interaction factor I_u of a 2×2 pile group with battered piles with different rake angles θ and $s/d = 5$.

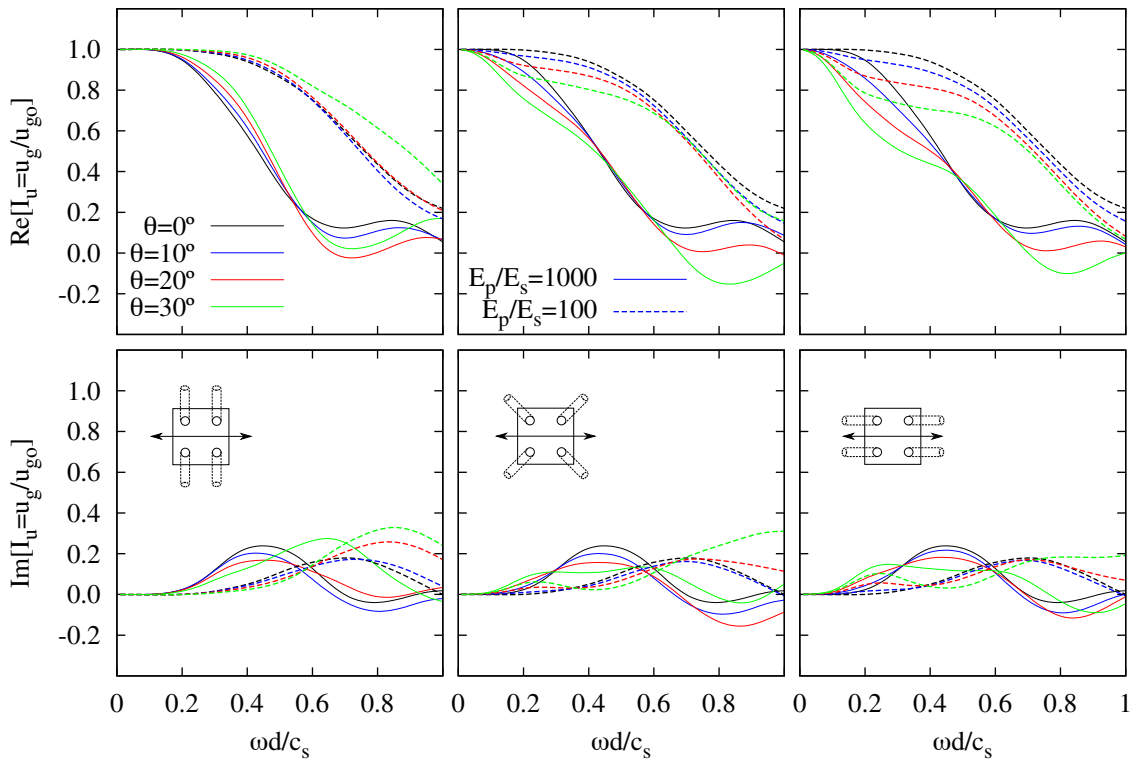


FIGURE 4.21: Translational kinematic interaction factor I_u of a 2×2 pile group with battered piles with different rake angles θ and $s/d = 10$.

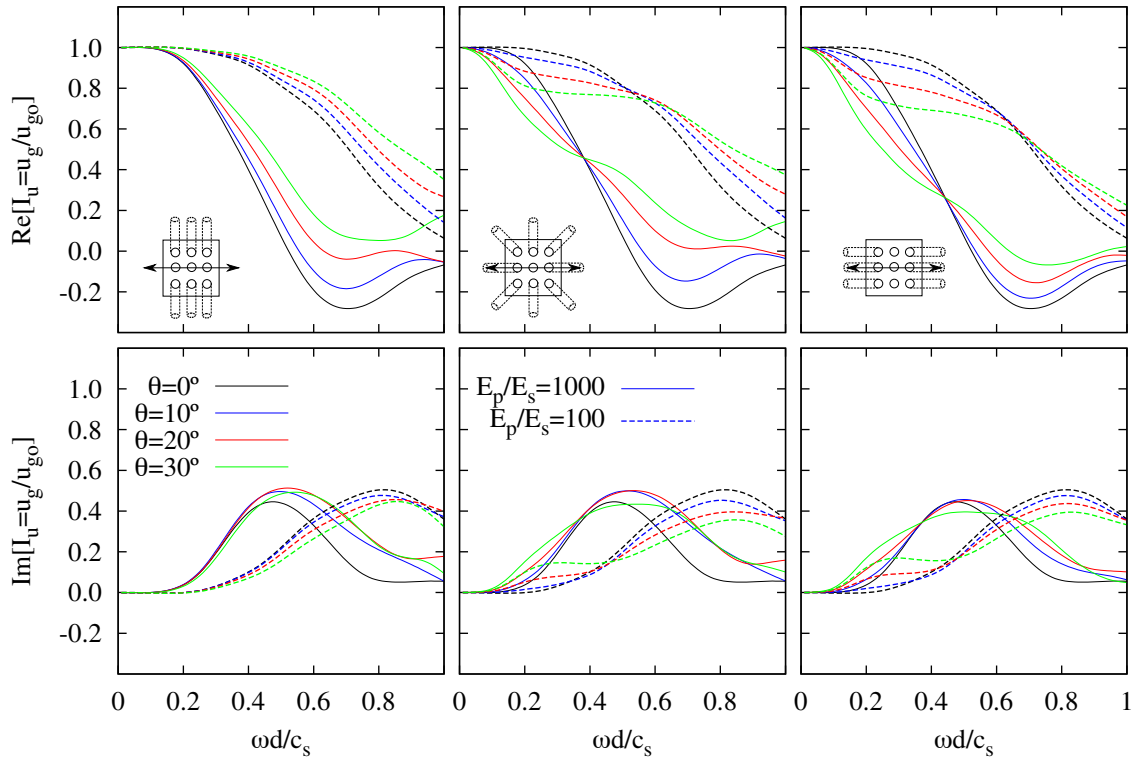


FIGURE 4.22: Translational kinematic interaction factor I_u of a 3×3 pile group with battered piles with different rake angles θ and $s/d = 5$.

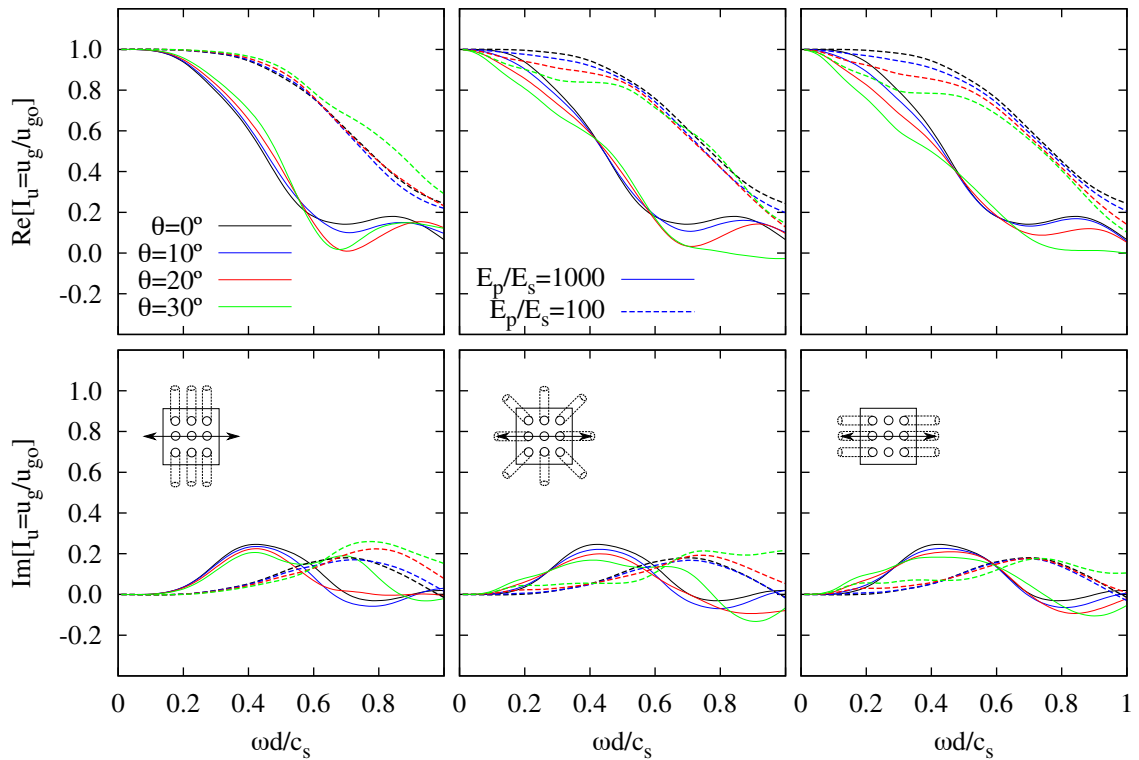


FIGURE 4.23: Translational kinematic interaction factor I_u of a 3×3 pile group with battered piles with different rake angles θ and $s/d = 10$.

4.7.6 Rotational kinematic interaction factors of pile groups

Figures 4.24, 4.25, 4.26 and 4.27 present the rotational kinematic interaction factors for the pile groups under study in order to illustrate how the use of pile groups including battered piles influences the rocking motion at the pile cap. Higher pile spacing ratios s/d or larger number of piles result in less cap rotation, though generally, this rotation increases with the rake angle. This effect is more pronounced when piles are inclined parallel to the direction of excitation. The more inclined, the more the pile works axially, that causes an axial displacement which in turn produces higher cap rotation. In fact, the maximum value of this rotation occurs at $a_o \approx 0.3$, which is the dimensionless frequency corresponding to the maximum value of the vertical displacement at the top of vertical single inclined piles (see right column of figure 4.17). However, no relevant effects can be appreciated when inclining piles perpendicular to the direction of excitation. The dependence on the direction of inclination does not exist for single piles (see figure 4.18), which suggests that it is the constraint imposed by the rigid pile cap which leads to changes in the dynamic behaviour of the foundation. Note that b (used for the normalization of I_φ) changes for every configuration. When taking this into account, the absolute cap rotation strongly decreases with larger pile separations or number of piles.

Contrary to what occurs for vertical piles and even for single inclined piles, cap rotation and horizontal free-field ground motion become out of phase when inclining piles parallel to the direction of excitation or symmetrically along the cap diagonals. This can be observed in the first row of figures 4.24, 4.25, 4.26 and 4.27. For the purpose of illustrating this effect, figure 4.28 shows the deformed shape at $a_o = 0.3$ of 2×2 pile groups containing piles inclined parallel to the direction of excitation with four different rake angles (solid color lines), together with the undeformed shapes (dashed lines), and the deformed shape of the incident field u_{g_o} (grey solid line). The response is qualitatively independent of the pile spacing ratio s/d . The lower the E_p/E_s ratio, the better the pile compliance with the free-field motion.

The figures discussed above show a trend consisting in a monotonic increase of cap rotation at low-to-mid frequencies for higher rake angles. However, the observed change of phase suggests that this does not need to be the case. In order to analyse more closely the effects of rake angle on the rocking motion at the pile cap, figure 4.29 shows the real part and the modulus of the rotational kinematic interaction factor of four different configurations with piles inclined parallel to the direction of excitation. Five different rake angles have been considered: $\theta = 0^\circ$ (vertical piles), 1° , 3° , 5° , and 10° . It is worth to notice that the use of configurations with piles inclined a small rake angle (e.g. $\theta = 1^\circ$, $\theta = 3^\circ$) leads to a minimum rocking motion at the pile cap. This might represent a beneficial effect on the dynamic behaviour of slender structures, case in which the determination of an optimum rake angle for a minimum rocking input motion could be interesting.

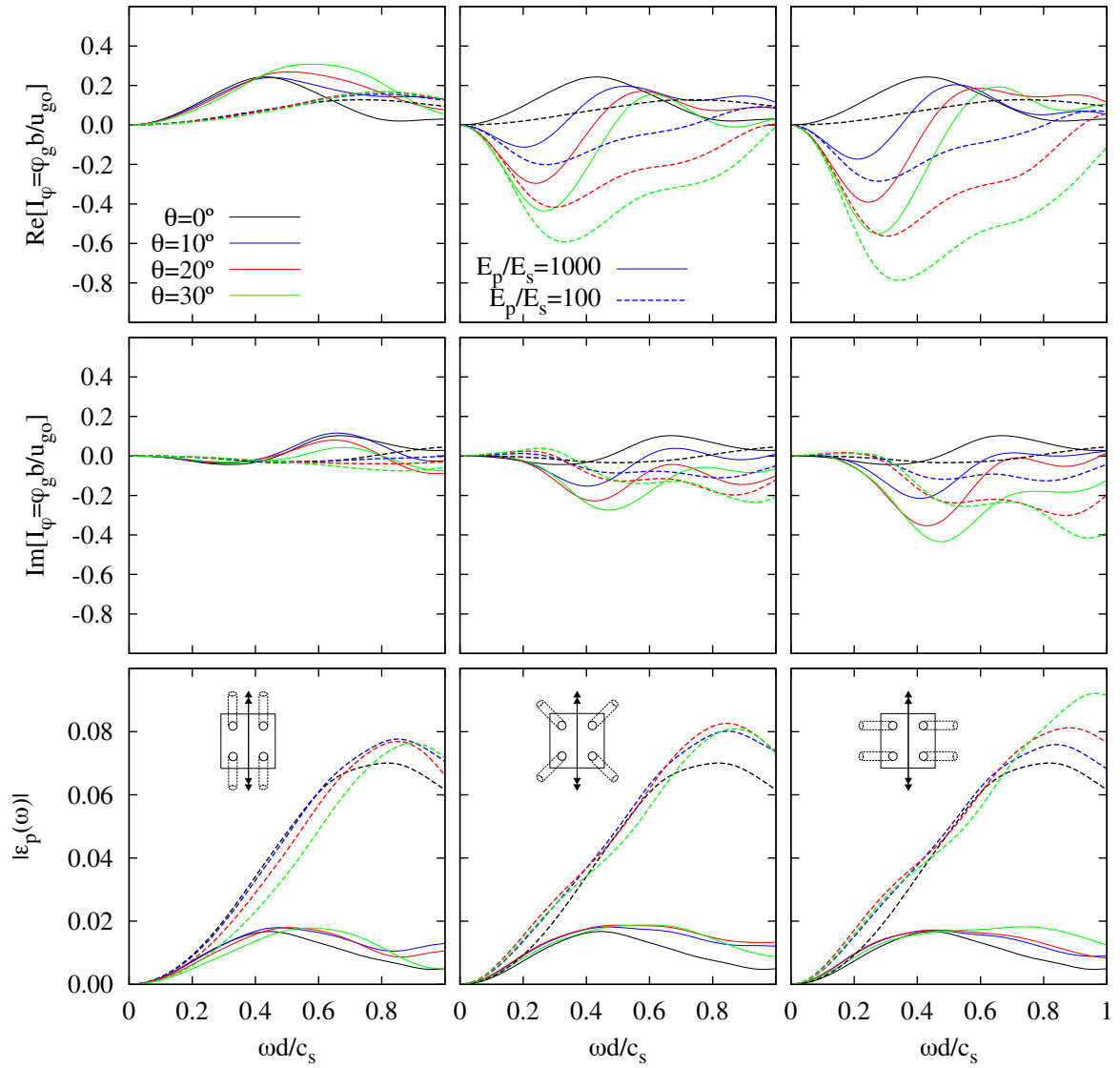


FIGURE 4.24: Rotational kinematic interaction factor I_φ and maximum pile head bending strain ε_p (considering $|u_{g0}| = 1$) of a 2×2 pile group with battered piles with different rake angles θ and $s/d = 5$.

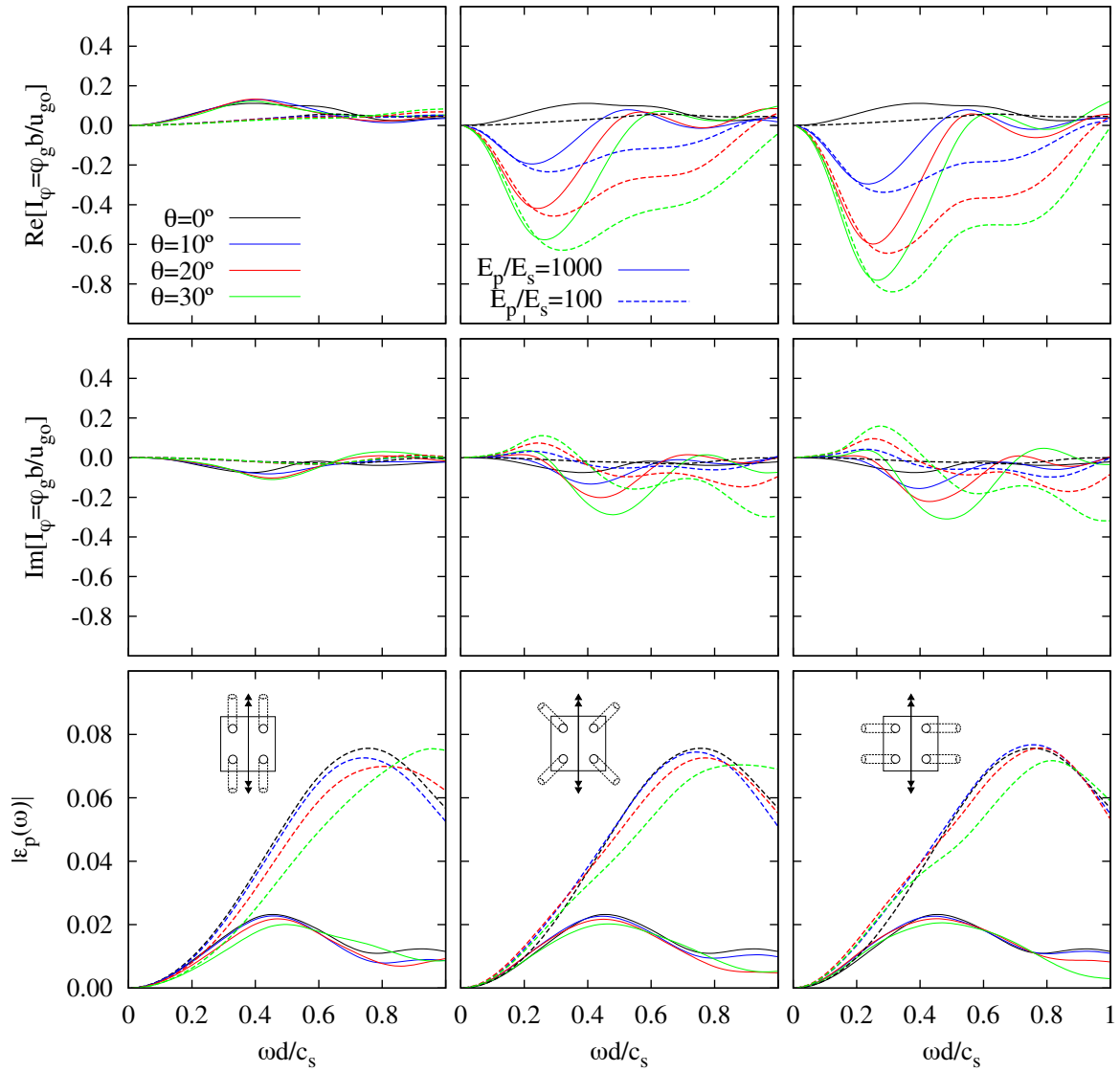


FIGURE 4.25: Rotational kinematic interaction factor I_φ and maximum pile head bending strain ε_p (considering $|u_{g_0}| = 1$) of a 2×2 pile group with battered piles with different rake angles θ and $s/d = 10$.

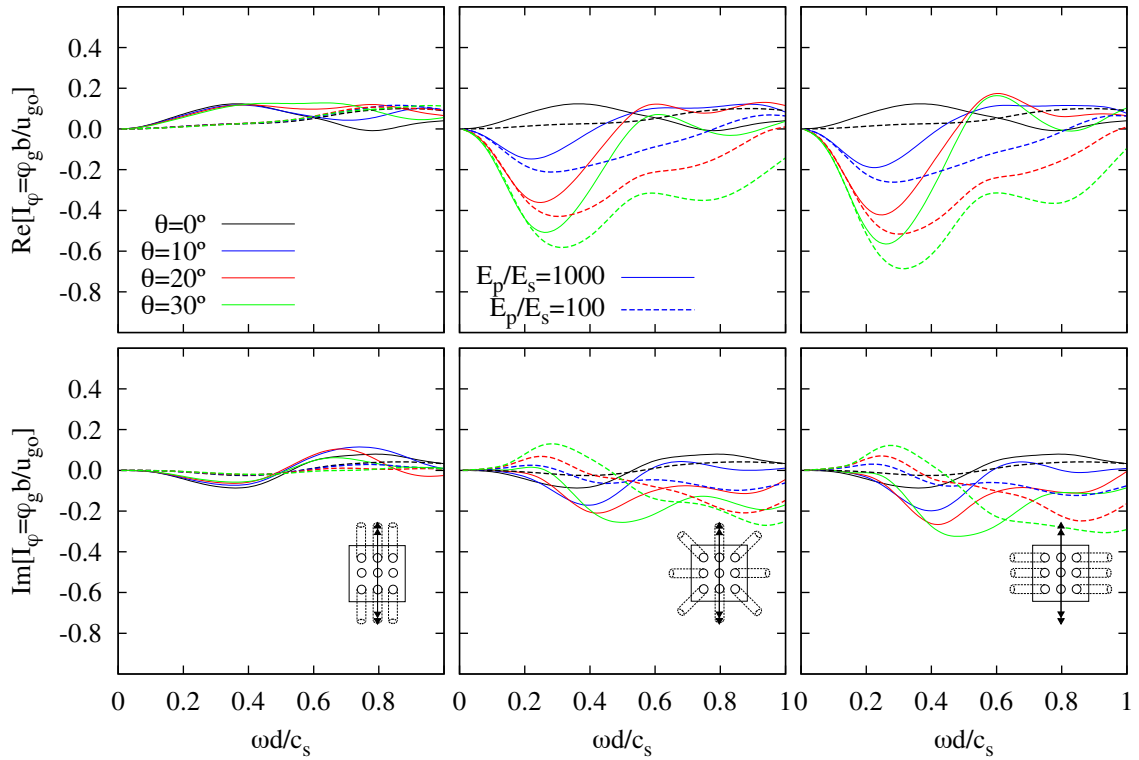


FIGURE 4.26: Rotational kinematic interaction factor I_φ of a 3×3 pile group with battered piles with different rake angles θ and $s/d = 5$.

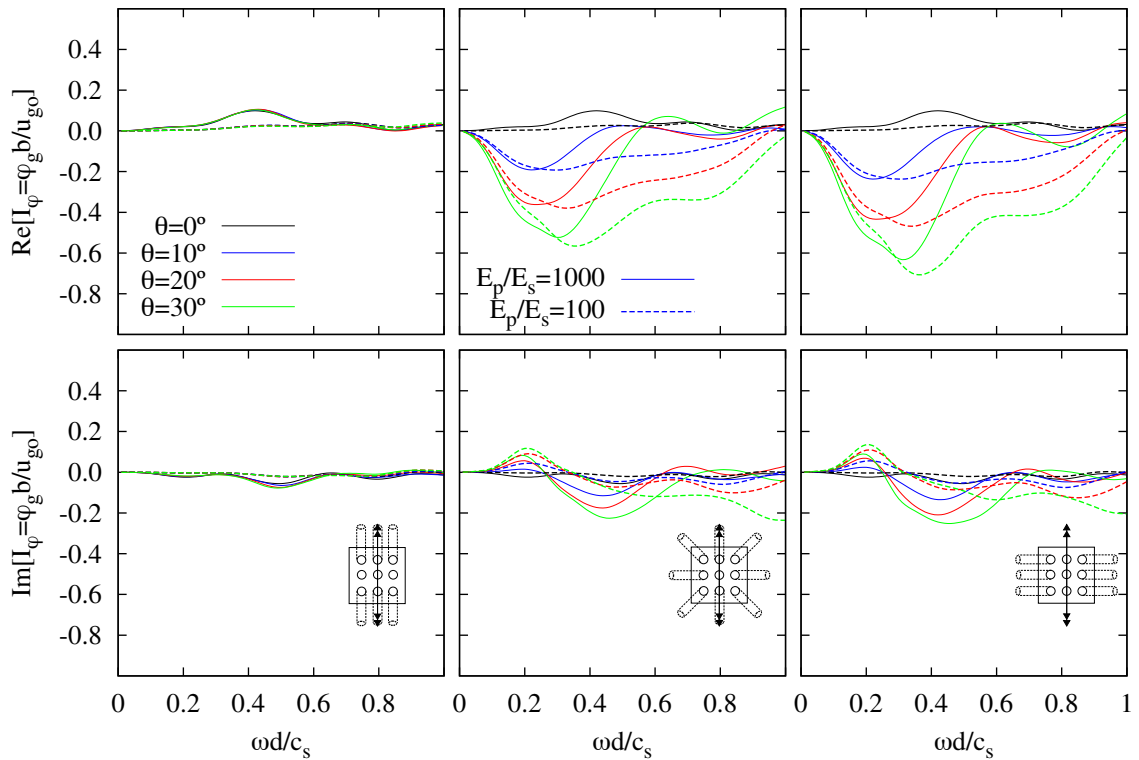


FIGURE 4.27: Rotational kinematic interaction factor I_φ of a 3×3 pile group with battered piles with different rake angles θ and $s/d = 10$.

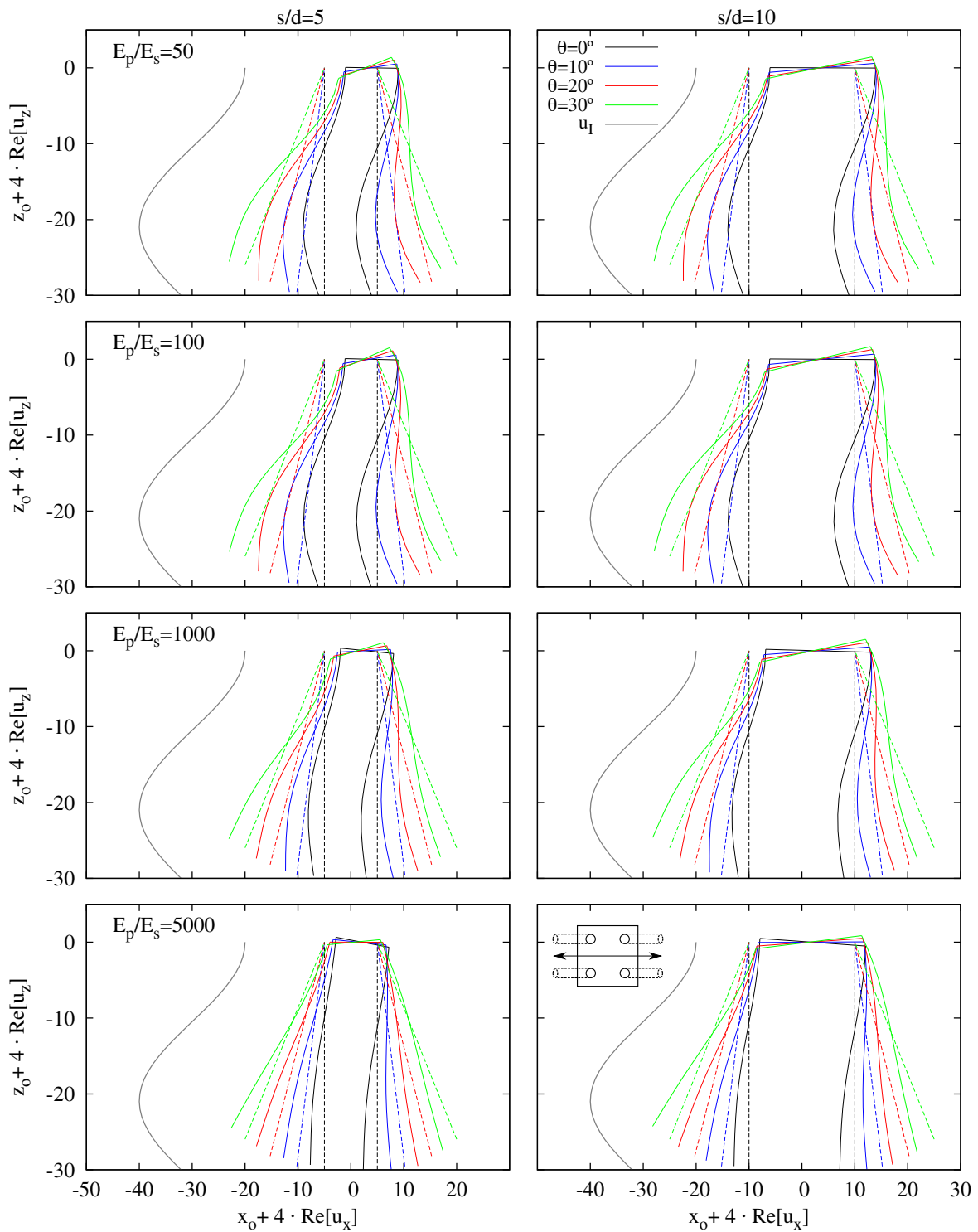


FIGURE 4.28: Deformed shape (solid line) and undeformed shape (dash line) of 2×2 pile groups with battered piles with different rake angles θ being $s/d = 5$ considering $|u_{g_o}| = 1$ (u_I displaced 30 units to the left only for illustration purposes). $a_o = 0.3$.

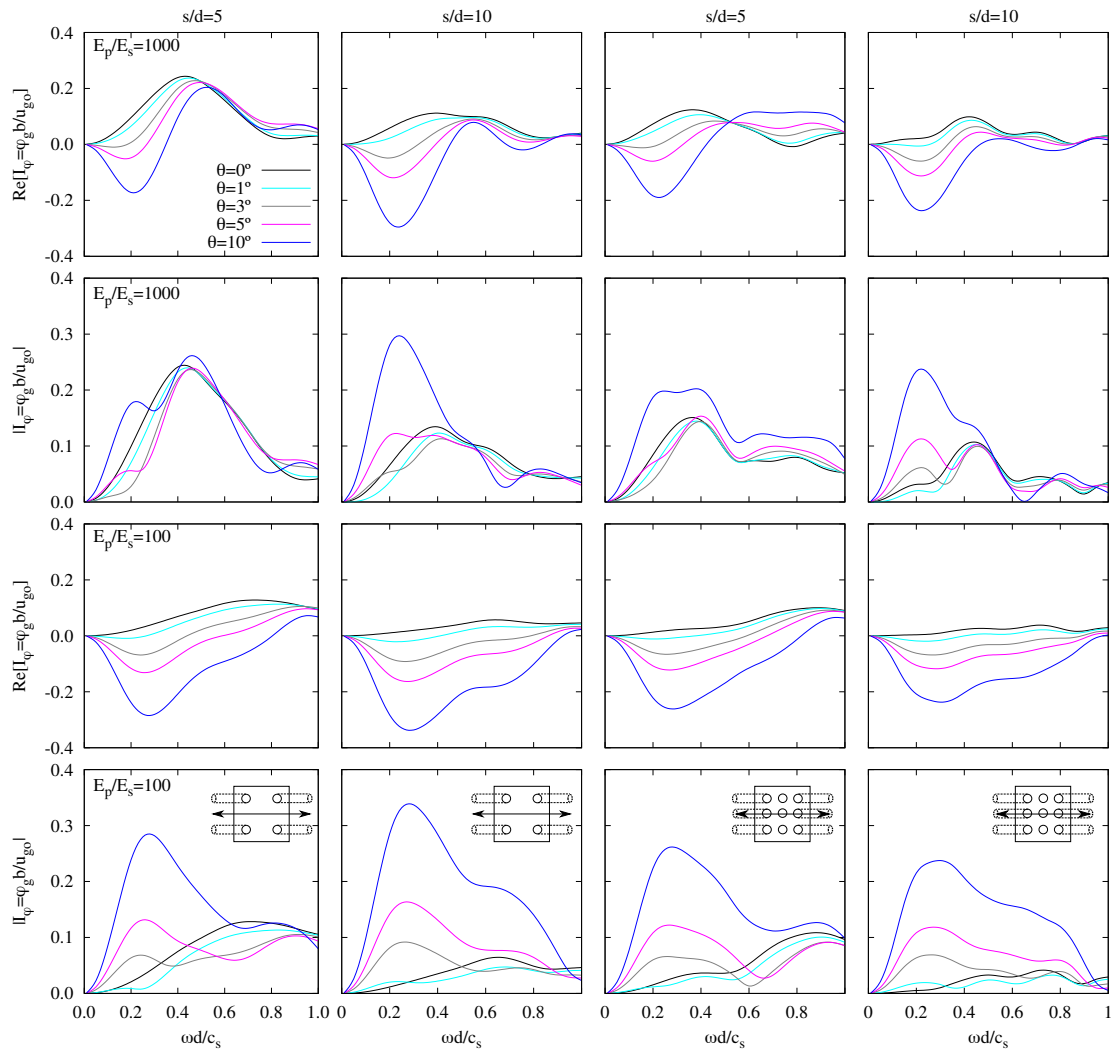


FIGURE 4.29: Influence of the rake angle on the rocking motion at the pile cap.

4.7.7 Influence of pile-soil Young's modulus ratio and pile slenderness ratio

The influence of pile-soil Young's modulus ratio E_p/E_s and pile slenderness ratio L/d on the rotational kinematic interaction factors of configurations including battered piles has also been studied. Additional L/d and E_p/E_s ratios have been studied for configurations with piles inclined parallel to the direction of excitation.

Figure 4.30 depicts, the rotational kinematic interaction factors corresponding to 2×2 pile groups with pile spacing ratio $s/d = 5$ and piles inclined in the direction of excitation. Results for four different values of the pile-soil Young's modulus ratio ($E_p/E_s = 50, 100, 1000$ and 5000) have been represented. Each one the columns corresponds to a different value of the pile rake angle θ . It can be observed that, contrary to what occurs for vertical piles, lower stiffness ratios E_p/E_s (stiffer soils) lead to larger cap rotations. On the other hand, higher stiffness ratios (softer soils) result in an increase of the rake angle at which cap rotation and horizontal free-field ground surface motion become out of phase at low-to-mid frequencies. For instance, such an angle can reach values over 10° for $E_p/E_s = 5000$ (see figure 4.28).

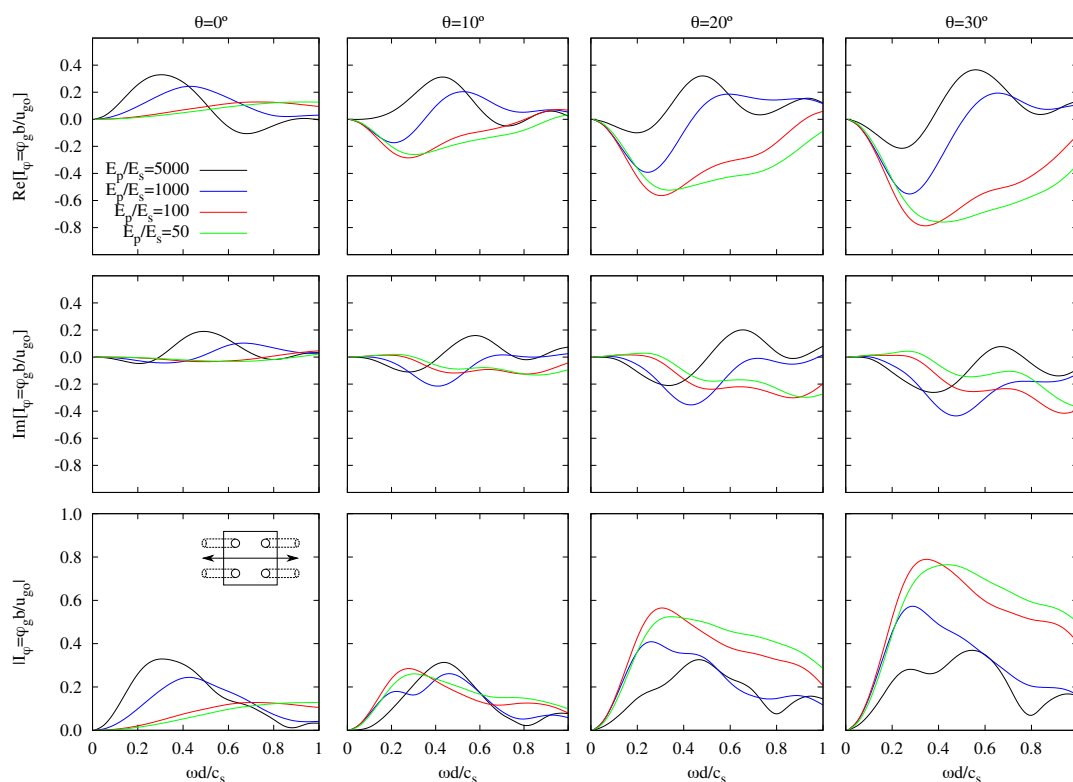


FIGURE 4.30: Influence of the pile-soil Young's modulus ratio E_p/E_s on the rotational kinematic interaction factor I_φ of 2×2 piles groups with piles inclined parallel to the direction of excitation with different rake angles θ being $s/d = 5$.

Finally, it is worth noting that, when considering configurations with piles inclined parallel to the direction of excitation, higher pile slenderness ratios yield increasing rock-

ing motions at the pile cap in a low frequency range, contrary to what occurs for vertical piles. For the purpose of illustrating this effect, figure 4.31 shows the rotational kinematic interaction factors of 2×2 pile groups with pile spacing ratio $s/d = 5$ and piles inclined in the direction of excitation. Results for three different values of the pile slenderness ratio ($L/d = 10, 15,$ and 20) have been represented.

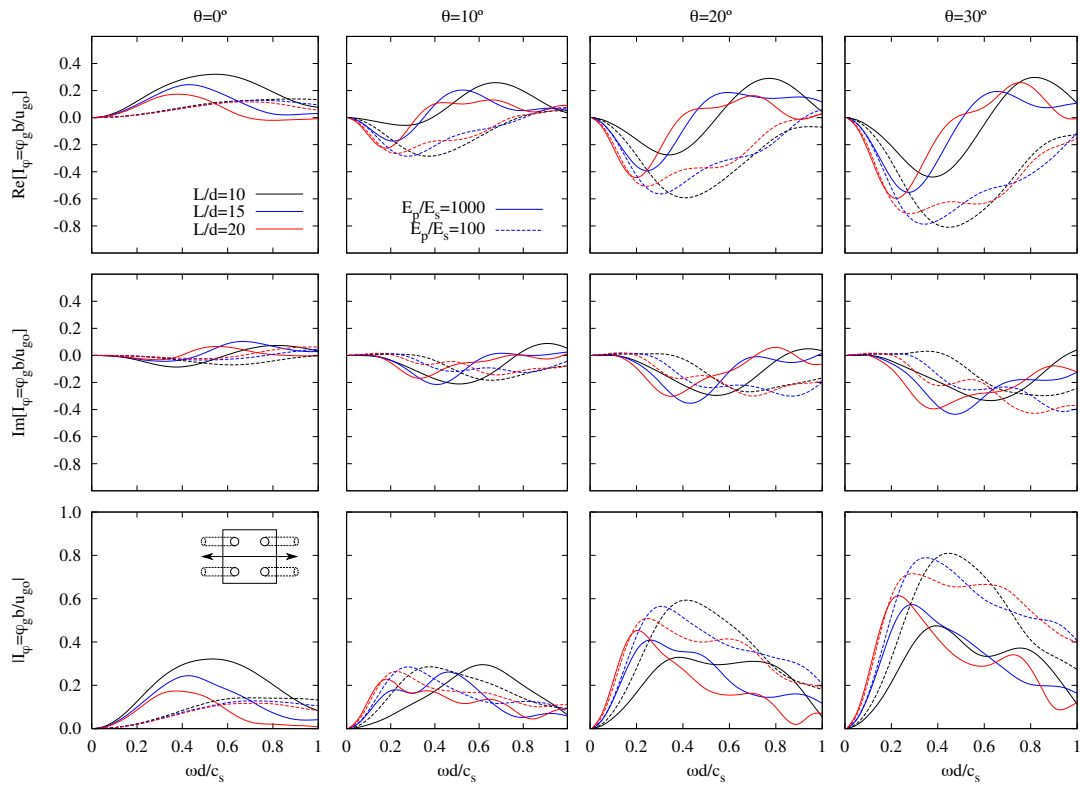


FIGURE 4.31: Influence of the pile slenderness ratio L/d on the rotational kinematic interaction factor I_φ of 2×2 piles groups with piles inclined parallel to the direction of excitation with different rake angles θ being $s/d = 5$.

4.7.8 Influence of rake angle on pile kinematic bending moments

Besides kinematic interaction factors, the influence of rake angle on pile kinematic interaction forces is an important issue in the study of inclined piles subjected to SH waves. This is because the possibility of the development of large kinematic bending moments and shear forces when inclining the piles has resulted in a negative attitude towards batter piles (see [44]). In order to look also into this aspect of the problem, kinematic bending moments M at pile heads are presented, for some configurations and vertically-incident S waves producing unitary horizontal free-field motion at the ground surface, in terms of the pile maximum bending strain ε_p . Note that the axis around which such bending moments are measured is depicted in the corresponding figures. In [121], Mylonakis *et al.* point out the convenience of representing the pile maximum bending

strain ε_p instead of the kinematic bending moment M . The use of this deformation-related quantity has advantages such as its dimensionless nature, as well as the fact that it can be directly measured experimentally and used to quantify damage. Moreover, common structural materials such as concrete or steel have similar values of the ultimate bending strain.

The relation between the pile maximum bending strain ε_p and the kinematic bending moment M can be expressed as follows:

$$\varepsilon_p = \frac{M}{E_p I_p} \frac{d}{2} \quad (4.6)$$

being I_p the pile cross-sectional moment of inertia.

The third row of figures 4.24 and 4.25, illustrates how the variations of the rake angle affect the maximum bending strain of piles in configurations of 2×2 pile groups. When piles are inclined parallel to the direction of excitation (right column) or symmetrically along the cap diagonals (central column), the maximum bending strain increases with the rake angle for both low and high frequencies (in terms of the frequency range presented in the figures) when $s/d = 5$, reaching an increment of up to 60% in the low frequency range (when $E_p/E_s = 100$) with respect to the values corresponding to vertical piles. Nevertheless, for intermediate frequencies the rake angle does not have a significant influence on the maximum bending strain. In those cases in which $E_p/E_s = 1000$, the maximum bending strain reaches increments of up to 16% in the low frequency range. When $s/d = 10$, maximum bending strain tends to increase with rake angle at mid-to-low frequencies but decreases at higher frequencies. On the other hand, in those cases in which piles are inclined perpendicular to the direction of excitation (left column), the maximum pile bending strain decreases as the rake angle increases for low-to-mid frequencies in all configurations. In short, in the mid-to-low frequency range maximum pile bending strains at pile heads tend to increase when piles are inclined parallel to the direction of the shaking; but tend to decrease when the piles are inclined perpendicular to such direction.

4.7.9 Conclusions

This section provides kinematic interaction factors of single inclined piles, and 2×2 and 3×3 pile groups including battered elements embedded in a homogeneous viscoelastic half-space and subjected to vertically-incident plane shear S waves. In order to study the effect of rake angle on kinematic bending moments, maximum pile bending strain at pile heads are also presented for some cases. A boundary element-finite element formulation has been used to obtain numerical results for different soil properties, rake angles and configurations.

The main conclusions drawn from the analysis of the results obtained for the cases under study are summarised below:

- The ability of a deep foundation to filter the seismic input increases significantly if all or some of its members are inclined in the direction of shaking.
- The beneficial role of the pile inclination disappears at high frequencies.

- Both kinematic interaction factors strongly depends on the direction of inclination of piles. Deep foundations including piles inclined perpendicular to the direction of excitation generally have a detrimental role in terms of horizontal motion.
- The rotational kinematic interaction factor I_φ of battered single piles is almost independent of the rake angle.
- Cap rotation and horizontal free-field ground motion become out of phase when inclining piles parallel to the direction of excitation or symmetrically along the cap diagonals. This effect depend on the rake angle, as well as on the pile-soil Young's modulus ratio.
- There exists an optimum rake angle (usually small) for which a minimum rotational motion at pile cap is obtained in the low-to-mid frequency range. This phenomenon could be used in order to minimize the seismic input of a structure submitted to seismic loads although, in some cases, the realization of the optimum small rake angles could not be feasible. A monotonic trend of increasing cap rotation for increasing rake angles is observed for larger angles.
- Higher stiffness ratios (softer soils) result in an increase of the rake angle at which cap rotation and horizontal free-field ground surface motion become out of phase at low-to-mid frequencies.
- The kinematic response of pile groups including battered piles is less sensitive to variations of the rake angle as the pile spacing ratio s/d or the number of piles increase.
- Lower stiffness ratios E_p/E_s (stiffer soils) lead to higher cap rocking motions.
- Contrary to what occurs for vertical piles, a reduction of the pile slenderness ratio L/d leads to decreasing values of the rocking motion at the pile cap, at least in a low frequency range, when considering configurations with piles inclined parallel to the direction of excitation.
- In the mid-to-low frequency range (usually the most important in the seismic design of deep foundations), maximum pile bending strains at pile heads tend to increase when piles are inclined parallel to the direction of the shaking; but tend to decrease when the piles are inclined perpendicular to such direction.

4.8 Pile group configurations including inclined piles

Table 4.3 lists the values of the dimensionless parameters characterizing the set of pile group configurations considered in this work to perform an analysis of the influence of the rake angle of piles θ on the dynamic behaviour of the structure they support, in the frequency range of interest for seismic loading ($\omega d/c_s < 0.5$, according to Gazetas et al. [79]). The dynamic response of several groups of 2×2 and 3×3 piles has been studied. The criterion adopted for the choice of the different values of the pile spacing ratio s/d consist in keeping the foundation halfwidth b constant for configurations with different number of piles, as done for vertical pile groups in section 4.5. Thus, the results

corresponding to different configurations are more comparable among each other. For the purpose of facilitating the interpretation of the results, figure 4.32 depicts a sketch of the different configurations considering $d = cte$ for all cases. Four different rake angles have been considered: $\theta = 0^\circ$ (vertical piles), 10° , 20° and 30° . The results presented hereinafter correspond to pile group configurations in which piles are inclined parallel to the direction of excitation. It is worth noting that some vertical piles are included in 3×3 pile groups in order to maintain symmetry with respect to planes xz and yz . In the light of previous studies [101], an intermediate value of the embedment ratio $L/b = 2$ has been chosen as representative in this work. In turn, three different values are chosen for the pile slenderness ratio ($L/d = 7.5, 15, \text{ and } 30$). It is assumed that $\xi_s = 0.05$, $\nu_s = 0.4$, $E_p/E_s = 10^3$ and $\rho_s/\rho_p = 0.7$. All configurations follow the pattern represented in figure 4.1 and correspond to the description exposed in section 4.4.

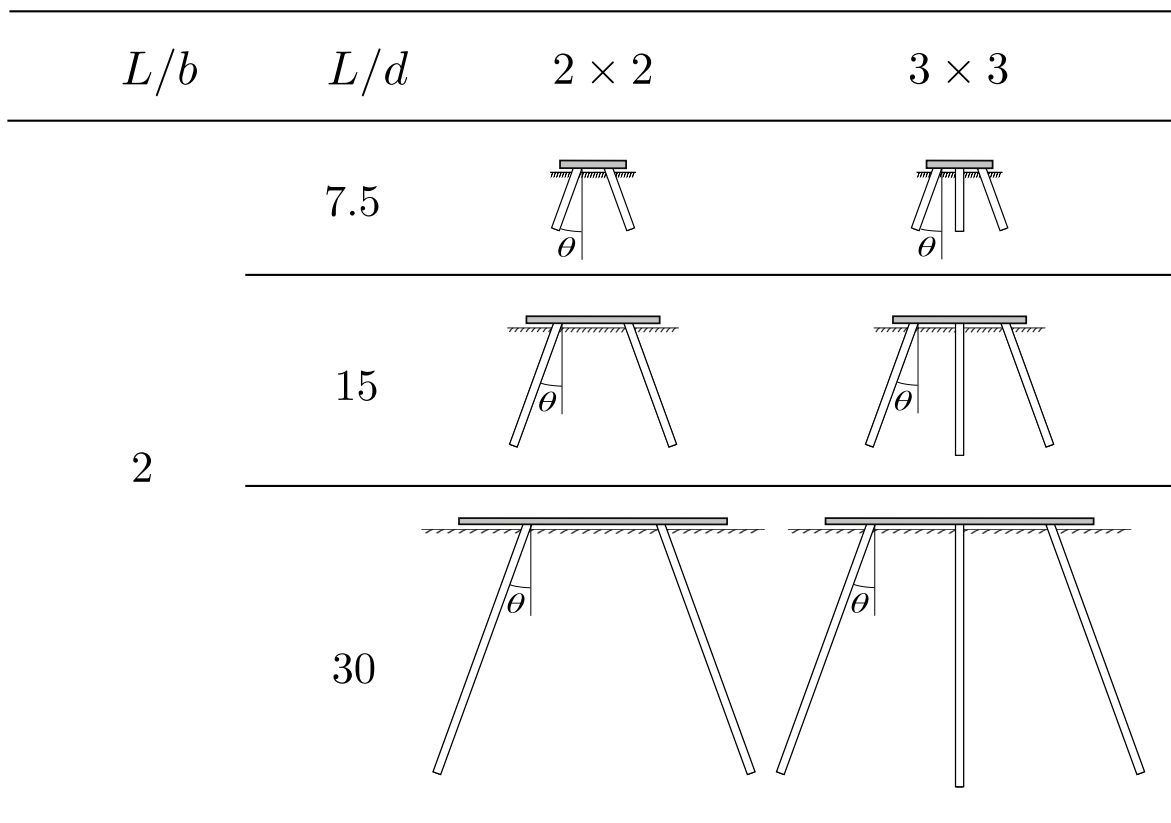


FIGURE 4.32: Sketches of the different pile group configurations comprising inclined piles, assuming the same diameter ($d = cte$) for all cases.

TABLE 4.3: Configurations of pile groups comprising inclined piles.

L/b	L/d	s/d	
		2×2	3×3
	7.5	3.75	2.5
2	15	7.5	5
	30	15	10

4.9 Impedances and kinematic interaction factors for pile groups comprising inclined elements

This section presents impedance functions and kinematic interaction factors corresponding to the pile group configurations defined in section 4.8, and addresses an analysis of the main trends observed in the obtained results. The configurations analysed in this section consist of square pile groups comprising inclined elements embedded in a viscoelastic homogeneous half-space.

Figures 4.33 and 4.34 provide dynamic stiffness coefficients k_{ij} corresponding to different 2×2 and 3×3 pile group configurations, respectively. On the other hand, figures 4.35 and 4.36 depict the corresponding damping coefficients c_{ij} for the same configurations. In all these figures, each column presents results for a different value of the pile slenderness ratio: $L/d = 7.5$ (left column), $L/d = 15$ (central column) and $L/d = 30$ (right column). In turn, the different rows present the stiffness values of the soil-foundation systems in the horizontal, rocking, and cross-coupled horizontal-rocking vibration modes, respectively. Finally, in each plot, the results for the different values of the rake angle considered in this study ($\theta = 0^\circ$ (vertical piles), 10° , 20° and 30°) are represented with solid lines of different colors. Dashed lines to be read on right axis provide a zoomed view in those cases in which it is necessary. All plots are presented as a function of the dimensionless frequency $\omega d/c_s$.

Focusing firstly on the dynamic stiffness, the following aspects are worthy of comment. In general, the horizontal stiffness increases significantly with the rake angle in all the frequency range under investigation due to the contribution of the pile axial stiffness to withstand the lateral loads. However, when analysing, in figure 4.34, the 3×3 pile group configuration with a slenderness ratio $L/d = 7.5$ ($s/d = 2.5$) it can be observed that this trend is reversed for $\omega d/c_s > 0.3$, which implies that the horizontal stiffness decreases as the rake angle grows. It is worth noting that when $\omega d/c_s \approx 0.3$ the variation of θ has no influence on the horizontal stiffness. A similar effect can be observed in the case of the 3×3 pile group with $L/d = 15$ ($s/d = 5$). In this case, there is a mid-frequency range in which lower values of the horizontal stiffness are reached when inclining piles 10° or 20° . The group effect associated to the horizontal vibration is not significantly modified when inclining the piles, although the peak moves slightly to lower frequencies.

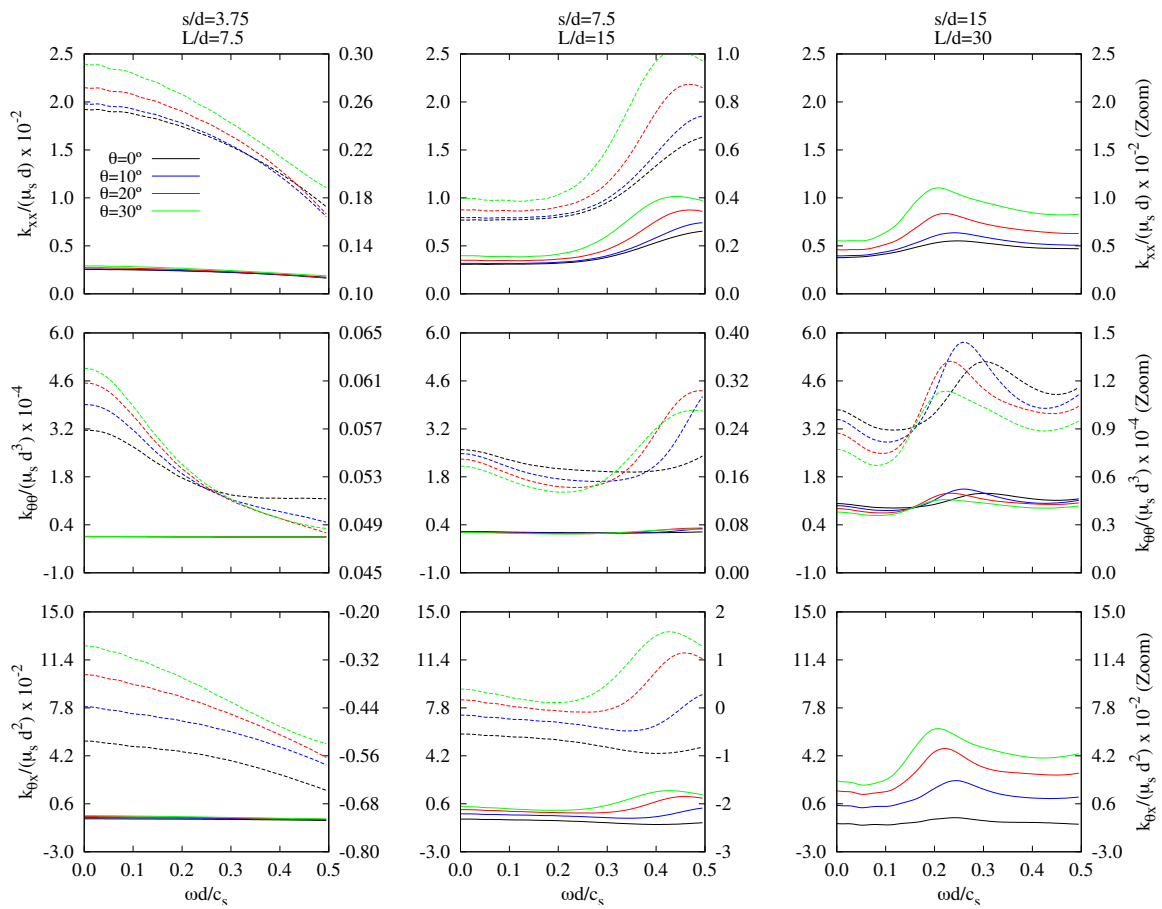


FIGURE 4.33: Dynamic stiffness of different 2×2 pile groups. $E_p/E_s = 1000$ and $\xi_s = 0.05$. $L/d(s/d) = 7.5(3.75), 15(7.5), 30(15)$. Solid lines to be read on left axis. Dashed lines to be read on right axis provide a zoomed view.

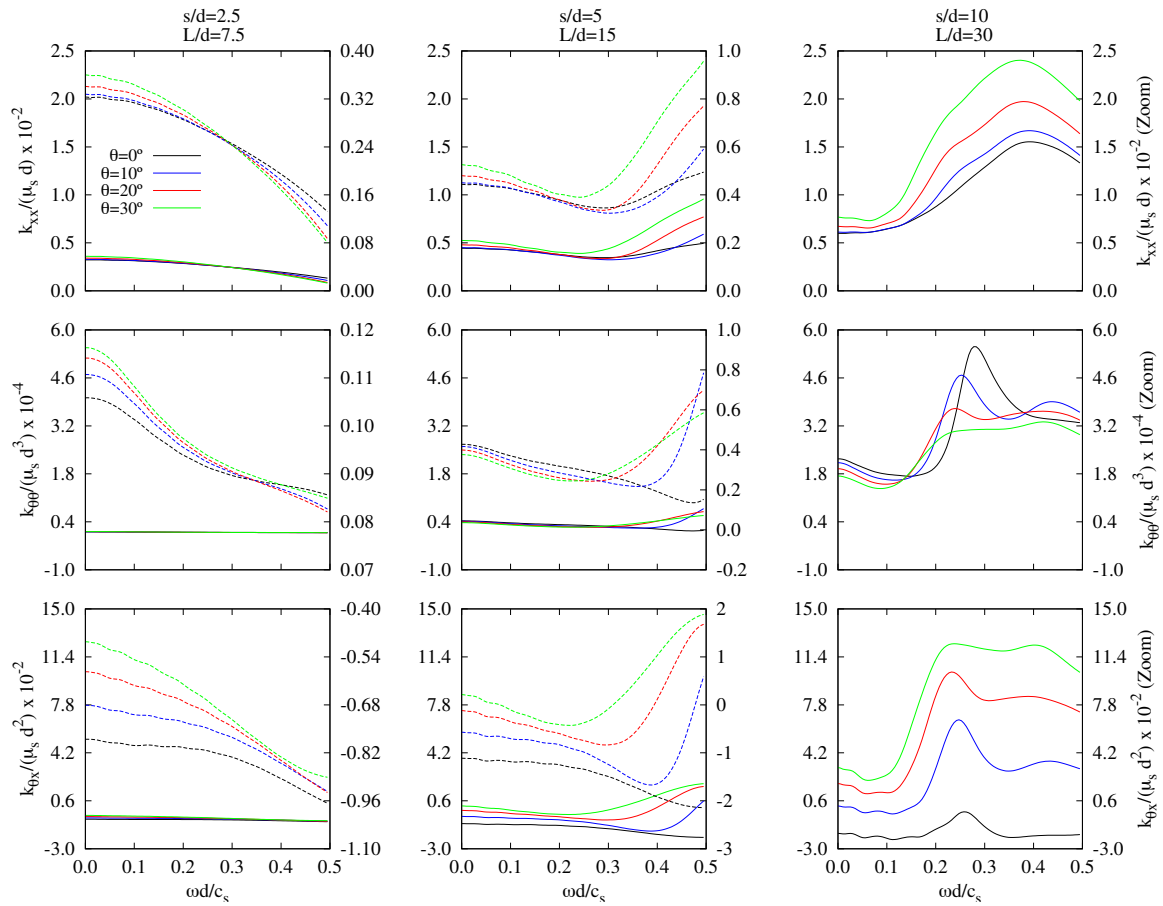


FIGURE 4.34: Dynamic stiffness functions of different 3×3 pile groups. $E_p/E_s = 1000$ and $\xi_s = 0.05$. $L/d(s/d) = 7.5(2.5), 15(5), 30(10)$. Solid lines to be read on left axis. Dashed lines to be read on right axis provide a zoomed view.

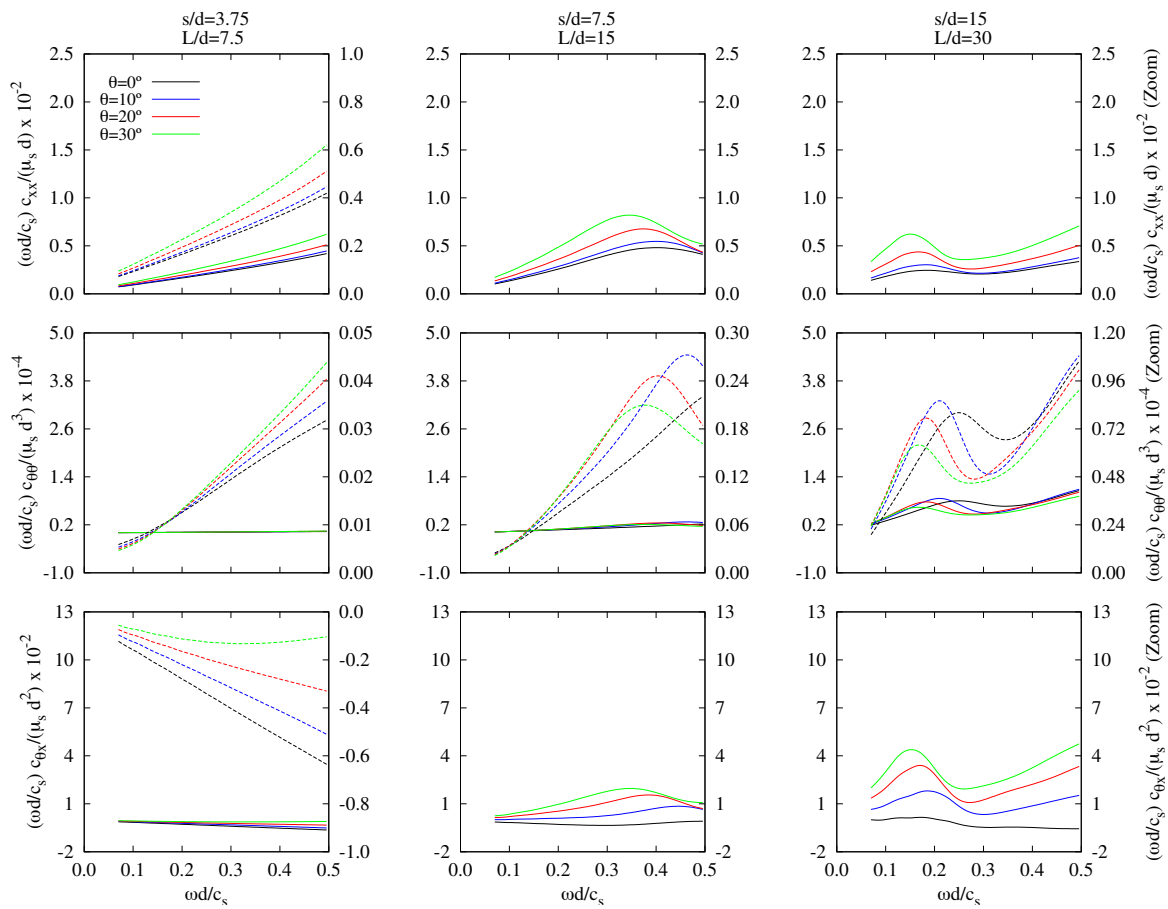


FIGURE 4.35: Damping functions of different 2×2 pile groups. $E_p/E_s = 1000$ and $\xi_s = 0.05$. $L/d(s/d) = 7.5(3.75), 15(7.5), 30(15)$. Solid lines to be read on left axis. Dashed lines to be read on right axis provide a zoomed view.

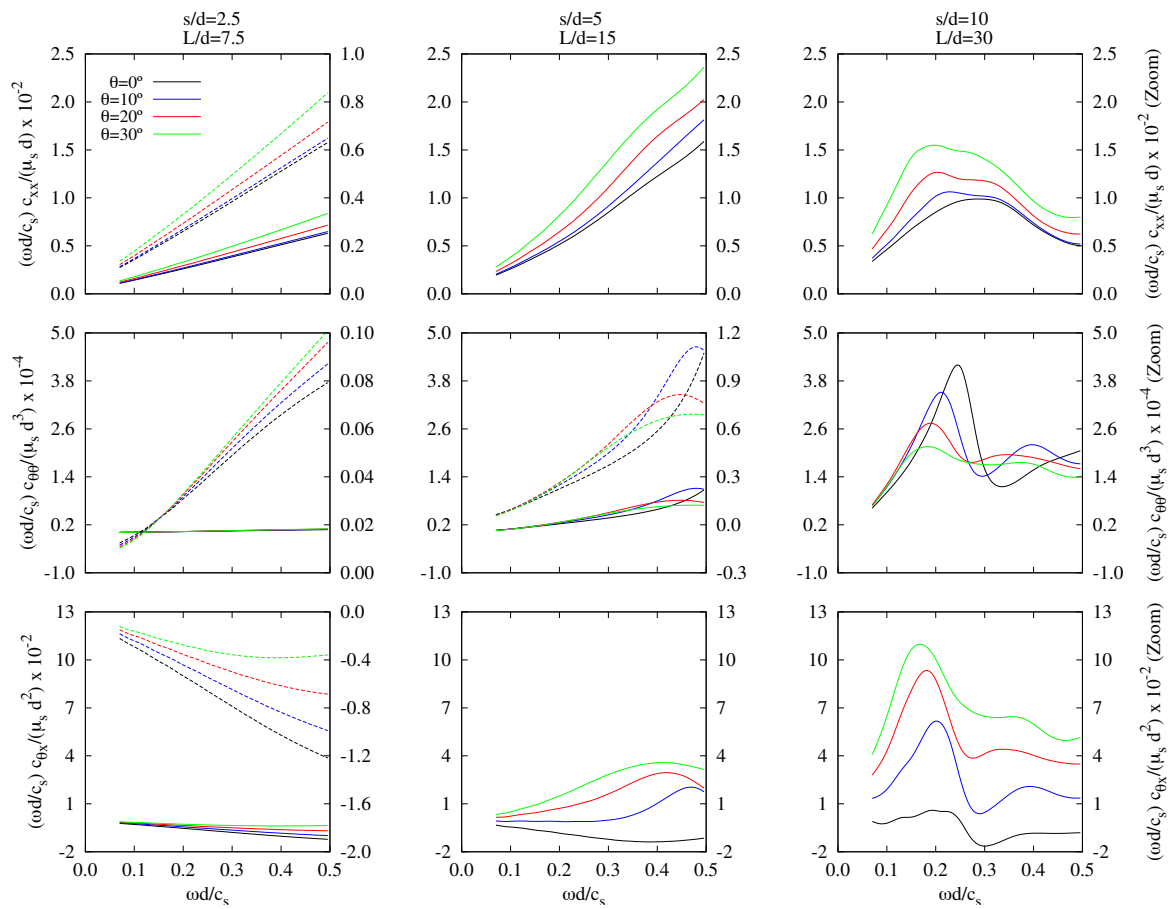


FIGURE 4.36: Damping functions of different 3×3 pile groups. $E_p/E_s = 1000$ and $\xi_s = 0.05$. $L/d (s/d) = 7.5(2.5), 15(5), 30(10)$. Solid lines to be read on left axis. Dashed lines to be read on right axis provide a zoomed view.

Similar to what happens with the stiffness functions, horizontal damping coefficients increase also with rake angle (even doubling for $\theta = 30^\circ$ in some cases), in all the frequency range under investigation (see figures 4.35 and 4.36). This conclusion is applicable to both 2×2 and 3×3 pile groups and to the s/d values considered in this study.

Although it has been shown that the rocking impedance of a single inclined pile is independent of the rake angle [49], the rocking impedance of pile groups is highly dependent on θ since, in this case, rocking and vertical modes are coupled in each pile. Due to the decrease in vertical stiffness of individual inclined piles with respect to the vertical case, rocking stiffness coefficients of pile groups decrease with rake angle for mid-to-low frequencies. Exceptionally, in those cases with little spacing between adjacent piles (left column in figures 4.33 and 4.34), the pile-soil-pile interaction effect takes predominance over that of inclination and the vertical impedance of each pile increases with the rake angle since the distance between the pile tips widens with depth. On the other hand, it can be observed that for mid-to high frequencies greater values of the rocking stiffness can be reached by inclining piles. In general, the increment or decrease of stiffness with the rake angle is, mainly for $L/d = 30$, extraordinary dependent on $\omega d/c_s$.

A very important influence of pile inclination can be appreciated in the horizontal-rocking cross-coupled impedance. Both dynamic stiffness and damping functions significantly increases with rake angle for all the configurations under investigation. It is worth mentioning that not only their magnitude may change, but also their sign may even change for different rake angles leading to significant differences in the dynamic behaviour of the superstructure.

Figures 4.37 and 4.38 provide the kinematic interaction factors of 2×2 and 3×3 pile group configurations, respectively. In these figures, each column depicts results for a different value of the pile slenderness ratio: $L/d = 7.5$ (left column), $L/d = 15$ (central column) and $L/d = 30$ (right column). The real part and magnitude of translational and rotational kinematic interaction factors for vertically-incident shear waves are plotted in the upper and the lower parts of the figures, respectively.

Translational kinematic interaction factors I_u show that batter piles allow the foundation to filter part of the seismic input motion even at very low frequencies. Such filtering can reach 20% for $\theta = 20^\circ$, and 40% for $\theta = 30^\circ$.

The rotational kinematic interaction factors I_φ show a consistent and significant increase in the rotational input motion to the superstructure for increasing rake angles. This increase is really significant when comparing rake angles $\theta \geq 20^\circ$ with the vertical case, in which the magnitude of I_φ can be multiplied by a factor of 30 (low frequency of 2×2 case).

The effects of inclining piles on the kinematic interaction factors of pile foundations were discussed in greater detail in section 4.7.

In short, it is shown that, apart from the well known larger horizontal stiffness, inclined piles provide a significantly larger capacity to dissipate energy and to filter the horizontal input motion to the superstructure when the direction of the excitation coincides with that of the inclination of the piles, which might make them useful for non-slender structures. On the other hand, the larger rotational input motions and rocking damping but smaller rocking stiffness makes it difficult to make a general prediction of the seismic response of slender structures, which will be studied in detail in chapter 6.

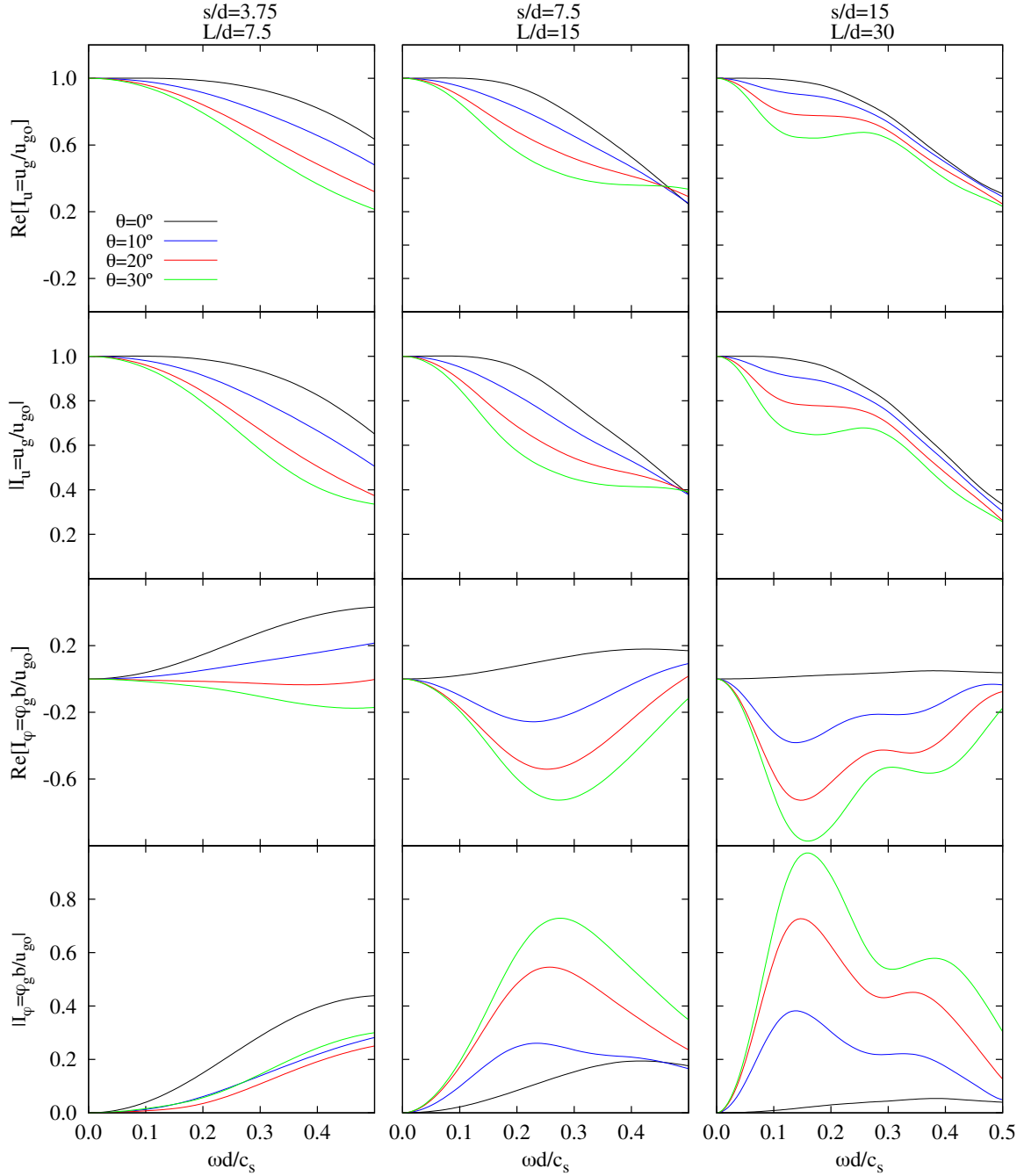


FIGURE 4.37: Kinematic interaction factors of different 2×2 pile groups. $E_p/E_s = 1000$ and $\xi_s = 0.05$. $L/d (s/d) = 7.5(3.75), 15(7.5), 30(15)$.

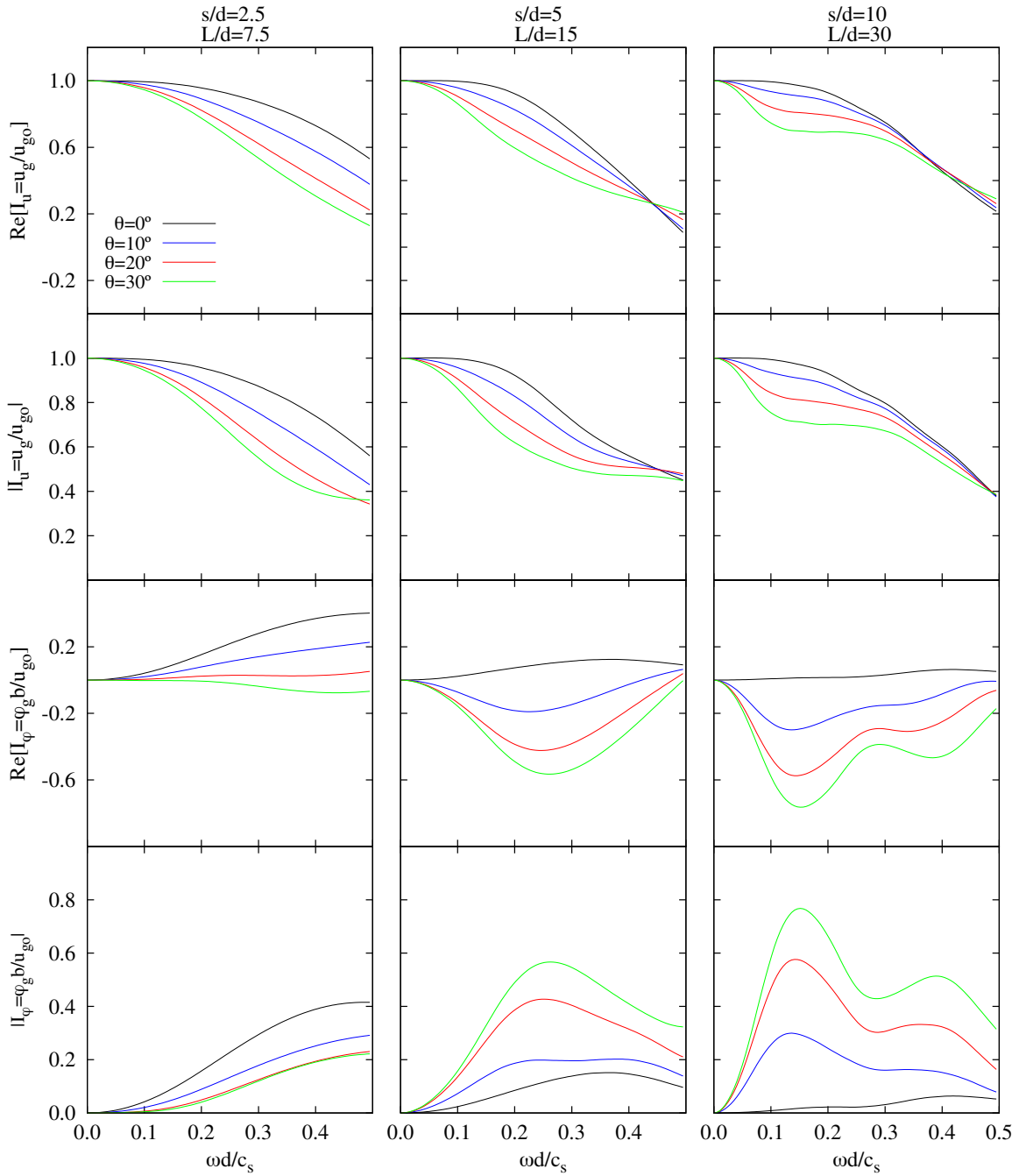



FIGURE 4.38: Kinematic interaction factors of different 3×3 pile groups. $E_p/E_s = 1000$ and $\xi_s = 0.05$. L/d (s/d) = 7.5(2.5), 15(5), 30(10).



5. SEISMIC BEHAVIOUR OF STRUCTURES SUPPORTED ON VERTICAL PILE GROUPS

- 5.1 Introduction
- 5.2 Configurations under investigation
- 5.3 Influence of foundation-structure mass ratio
- 5.4 Influence of cross-coupled impedances
- 5.5 Influence of structural slenderness ratio and wave parameter
- 5.6 Influence of kinematic interaction factors
- 5.7 Influence of pile slenderness ratio
- 5.8 Influence of embedment ratio
- 5.9 Influence of pile group size
- 5.10 Influence of pile-soil Young's modulus ratio
- 5.11 Influence of fixed-base structure damping ratio
- 5.12 Influence of mass density ratio
- 5.13 Conclusions

5.1 Introduction

This chapter addresses an analysis of the dynamic response of linear shear structures supported on square groups of vertical piles embedded in a homogeneous, viscoelastic and isotropic half-space and subjected to vertically-incident S waves. A detailed description of the problem can be found in section 2.3. The procedure proposed in chapter 2 is used herein to study the influence of SSI on the response of pile-supported structures, in terms of maximum shear force at the base of the structure per effective earthquake force unit Q_m and effective system period \tilde{T}/T and damping $\tilde{\xi}$. These two last parameters represent the dynamic characteristics of an equivalent viscously damped SDOF system [7, 12–14, 21]. This equivalent system reproduce, as accurately as possible, the coupled system response within the range where the peak response occurs. The corresponding foundation horizontal displacement and rocking, as well as the kinematic interaction factors, will also be shown for different cases. Even though it is not a comprehensive analysis, several interesting conclusions can be drawn from studying how the SSI effects, that affect the system dynamic behaviour, are influenced by the variation of parameters such as the foundation-structure mass ratio m_o/m , the structural slenderness ratio h/b , the wave parameter σ , the spacing between adjacent piles s/d , the embedment ratio L/b , the pile slenderness ratio L/d , the number of piles, the pile-soil Young's modulus ratio E_p/E_s , the fixed-base structure damping ratio ξ and the mass density ratio δ . Moreover, the influence of considering or not the cross-coupled impedances and the kinematic interaction factors is also studied for the configurations of pile foundations under investigation.

Firstly, the cases under investigation are defined in section 5.2. In sections 5.3 to 5.12 several parametric analyses are performed, in order to determine the influence on the system dynamic response of the main parameters of the problem. Figures that allow comparing results obtained for several pile group configurations are provided. In order to facilitate the comprehension of these results, each one of these figures is followed by sketches corresponding to the pile group configurations considered in each case. Finally, the conclusions that can be drawn from these analyses are given in section 5.13.

5.2 Configurations under investigation

The dynamic response of structures supported on several groups of 2×2 , 3×3 and 4×4 piles is studied in this chapter. Four different values of the structural slenderness ratio ($h/b = 1, 2, 5, 10$) have been considered. The geometrical characteristics, as well as the material properties, of the pile group configurations considered in the analyses addressed in this chapter were already defined in section 4.5. The values of the dimensionless parameters that define the geometry of these configurations are listed in table 5.1.

Unless otherwise specified, for the results presented in this chapter, it is assumed that $\delta = 0.15$; $m_o/m = 0$; $0 < 1/\sigma < 0.5$; $\xi = 0.05$; $\xi_s = 0.05$ and $\nu_s = 0.4$. These values are representative for typical buildings and soils [14, 122]. Moreover, $E_p/E_s = 10^3$ or 10^2 and $\rho_s/\rho_p = 0.7$.

TABLE 5.1: Vertical pile group configurations.

L/b	L/d	s/d		
		2×2	3×3	4×4
1	7.5	7.5	5	3.75
	15	15	10	7.5
2	7.5	3.75	2.5	1.875
	15	7.5	5	3.75
	30	15	10	7.5
4	15	3.75	2.5	1.875
	30	7.5	5	3.75

The range of values used in this study for $1/\sigma$ encompasses most real cases as can be seen in Stewart *et al.* [122], where empirical results for SSI effects are provided for 57 building sites that cover a wide range of real structural and geotechnical conditions. Most of those cases show values of $1/\sigma$ between 0 and 0.3.

The impedance functions and the kinematic interaction factors corresponding to all the pile group configurations involved in this study were computed by using a BEM-FEM methodology outlined in section 3.5. Their values were represented and analysed in section 4.6.

As explained in section 2.6, piles have been modelled by equivalent solid piles although the values obtained for impedances and kinematic interaction factors are also used herein to represent the dynamic behaviour of pile group configurations consisting of hollow piles. The accuracy of this simplification of the pile section geometry was assessed in section 2.6 in terms of impedances and kinematic interaction factors. However, given that these values are used in this section to determine the dynamic response of the superstructure, it is worth analysing how the simplification consisting in assuming a solid circular pile cross-section affects the dynamic behaviour of the superstructure in terms of effective system period \tilde{T}/T and maximum shear force at the base of the structure per effective earthquake force unit Q_m . The mean percentage error in terms of \tilde{T}/T and Q_m , yielding from modelling a hollow pile with $\gamma = 0.9$ by an equivalent solid pile, is always below 5% for all the configurations analysed in section 2.6 when considering a range for the wave parameter such that $0 < 1/\sigma \leq 0.5$.

5.3 Influence of foundation-structure mass ratio

The assumption consisting in neglecting the foundation mass m_o is extensively adopted by many authors (see, for instance, [6, 7, 9, 11, 13, 14]). For the purpose of evaluating how this simplification affects the dynamic response of the superstructure, figure 5.1 depicts, for five different values of the foundation-structure mass ratio ($m_o/m = 0, 0.25, 0.50, 0.75$ and 1), the maximum shear force at the base of the structure per effective earthquake force unit Q_m corresponding to several linear shear structures supported on 4×4 verti-

cal pile groups with embedment ratio $L/b = 2$. Each column shows results for structural slenderness ratios $h/b = 1, 2, 5$ and 10 , respectively. In turn, each row represents results corresponding to pile slenderness ratios $L/d = 7.5, 15$ and 30 . Sketches of these pile group configurations, considering $d = \text{cte}$, are depicted in figure 5.2. All plots are presented as a function of $1/\sigma$, being σ the wave parameter.

In all the configurations studied in this work, the relative error in terms of Q_m , committed by assuming $m_o/m = 0$ when $m_o/m = 0.5$, reaches a maximum value of 8%. However, the mean relative error is always below 5%. Thus, the variation of the foundation-structure mass ratio m_o/m in the range between 0 and 0.5 does not yield significant differences in terms of Q_m . This conclusion support the simplification usually assumed.

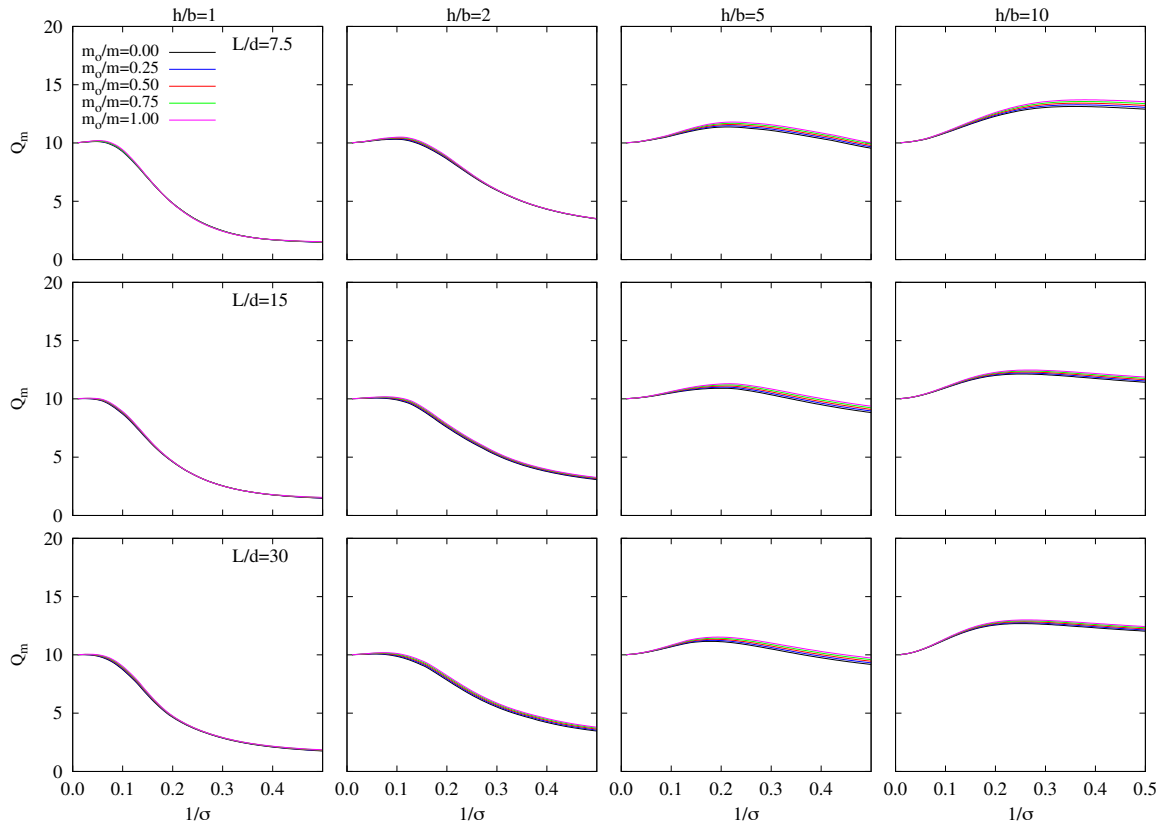


FIGURE 5.1: Influence of the foundation-structure mass ratio m_o/m . Maximum structural response value Q_m for 4×4 pile groups with $L/b = 2$ and $E_p/E_s = 10^3$ and $\xi_s = 0.05$.

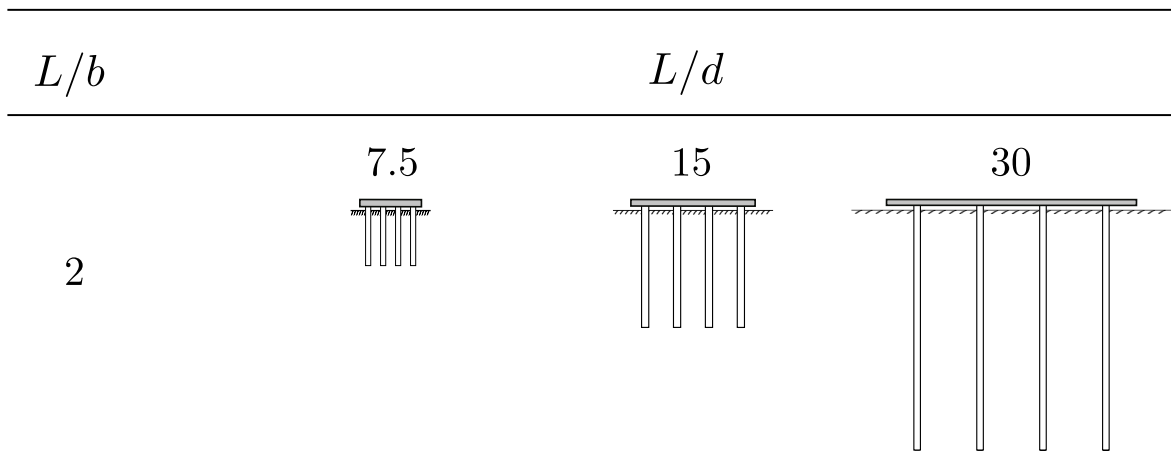


FIGURE 5.2: Sketches of the pile group configurations corresponding to the cases analysed in figure 5.1 when considering $d = cte$.

5.4 Influence of cross-coupled impedances

All the results presented in this work are obtained considering all the elements of the matrix of impedances. Although many authors neglect the cross-coupled stiffness and damping terms [7, 8, 12, 13], this is not acceptable for pile foundations, not even for certain configurations of embedded foundations. Therefore, a comparative analysis to determine the influence of cross-coupled impedances on the system dynamic response has been addressed.

Figures 5.3, 5.5 and 5.7 show the extent to which neglecting the cross-coupled impedances influences the dynamic response of the system. At the same time, these figures allow analysing how this influence is affected by the variation of the main parameters of the problem. In turn, figures 5.4, 5.6 and 5.8 provide, respectively, sketches of the pile group configurations considered in each case. Results obtained neglecting cross-coupled impedances, as well as those computed taking them into account, are represented in terms of \tilde{T} , $\tilde{\xi}$ and Q_m . These figures show that the influence of considering cross-coupled impedances generally decreases as h/b or σ grows. Likewise, as shown in figure 5.3, this influence becomes more remarkable as L/d decrease. On the other hand, in figure 5.5, a greater influence is observed for increasing values of L/b . Finally, figure 5.7 depicts how the size of the pile group modifies the influence of the cross-coupled impedances on the system dynamic response. It can be seen that this influence slightly decreases for those configurations with a greater number of piles.

In a significant number of cases, the system damping $\tilde{\xi}$ decreases when considering the cross-coupled impedances, which implies that the system dynamic response is subestimated when neglecting them. On the other hand, the system natural period \tilde{T} increases, in all cases, when the cross-coupled impedances are taken into account.

For the configurations studied herein, the relative error in terms of Q_m , committed by neglecting the cross-coupled impedances, reaches a maximum value of 40%. However, the mean relative error is below 16%.

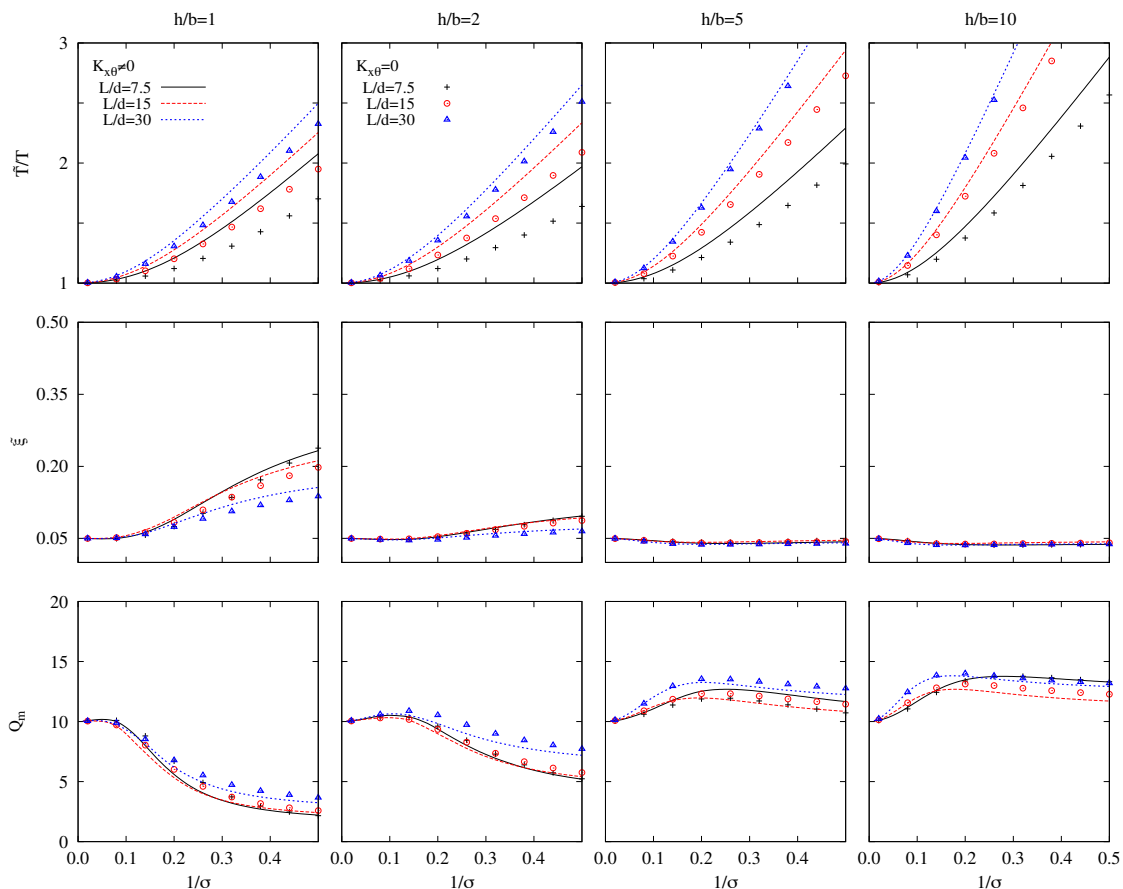


FIGURE 5.3: Influence of the cross-coupled impedances. Effective period \tilde{T}/T , damping ratio $\tilde{\xi}$ and maximum structural response value Q_m for a 2×2 pile group with $L/b = 2$, $E_p/E_s = 10^3$ and $\xi_s = 0.05$.

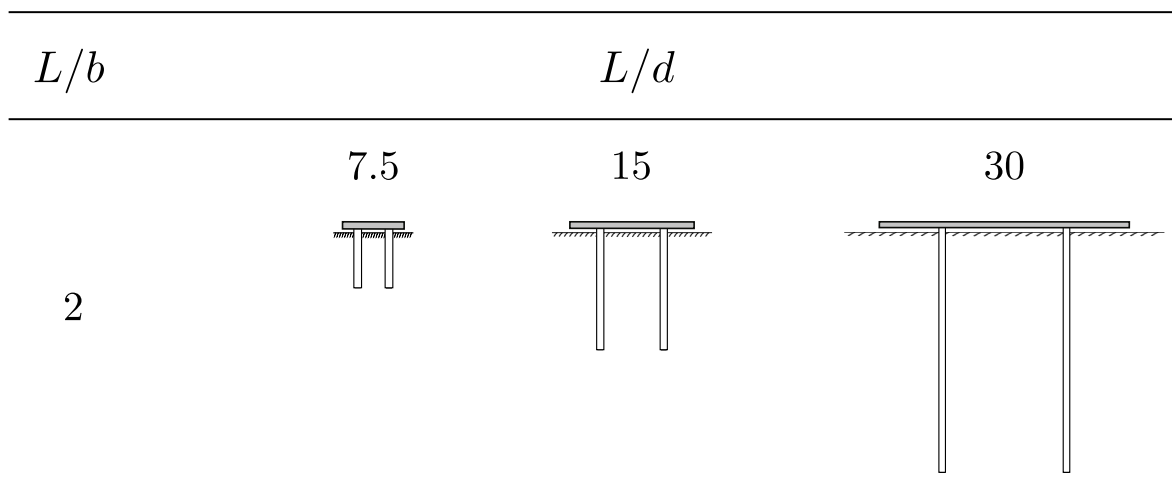


FIGURE 5.4: Sketches of the pile group configurations corresponding to the cases analysed in figure 5.3 when considering $d = cte$.

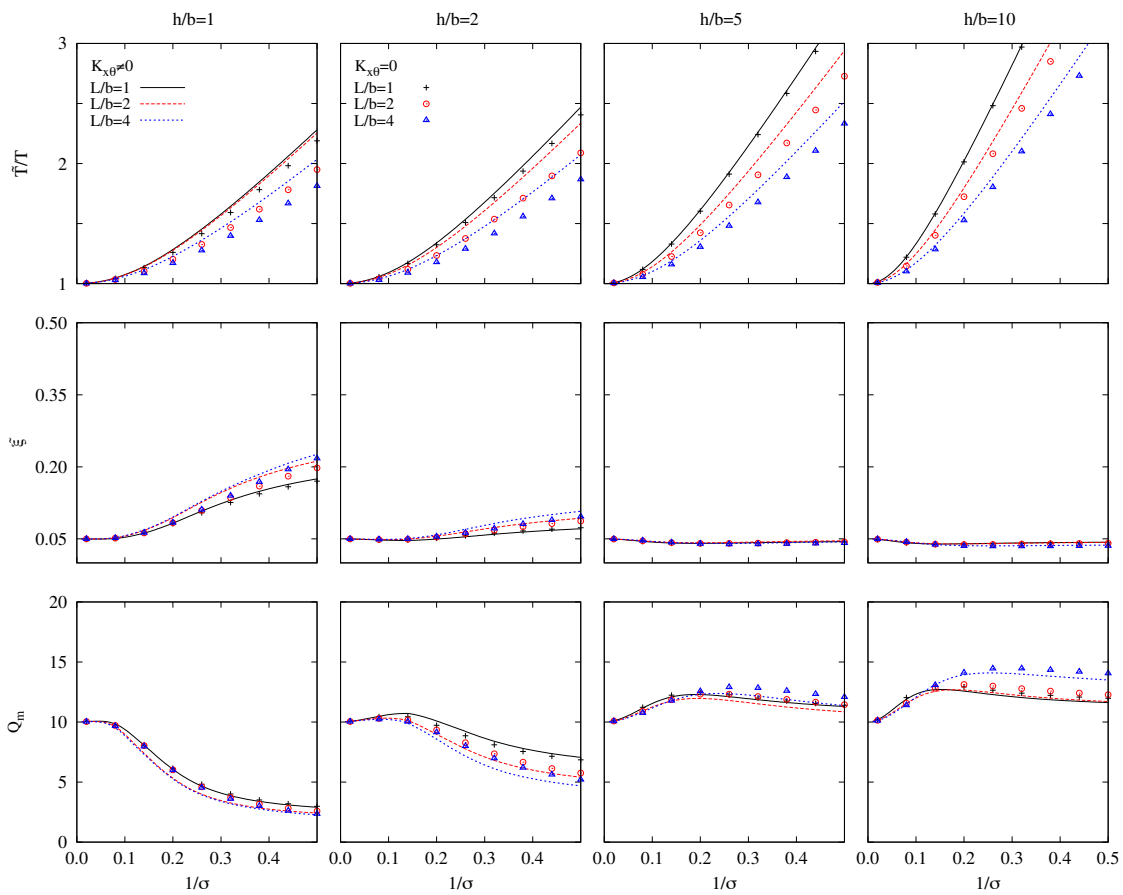


FIGURE 5.5: Influence of the cross-coupled impedances. Effective period \tilde{T}/T , damping ratio $\tilde{\xi}$ and maximum structural response value Q_m for a 2×2 pile group with $L/d = 15$, $E_p/E_s = 10^3$ and $\xi_s = 0.05$.

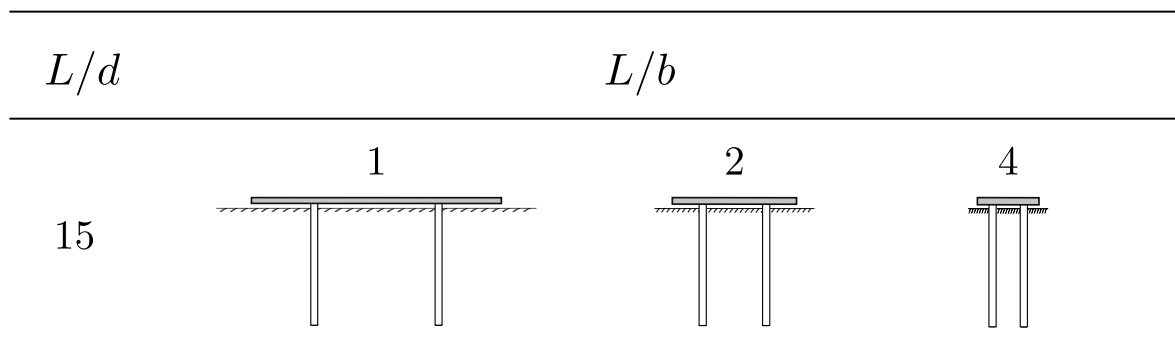


FIGURE 5.6: Sketches of the pile group configurations corresponding to the cases analysed in figure 5.5 when considering $d = cte$.

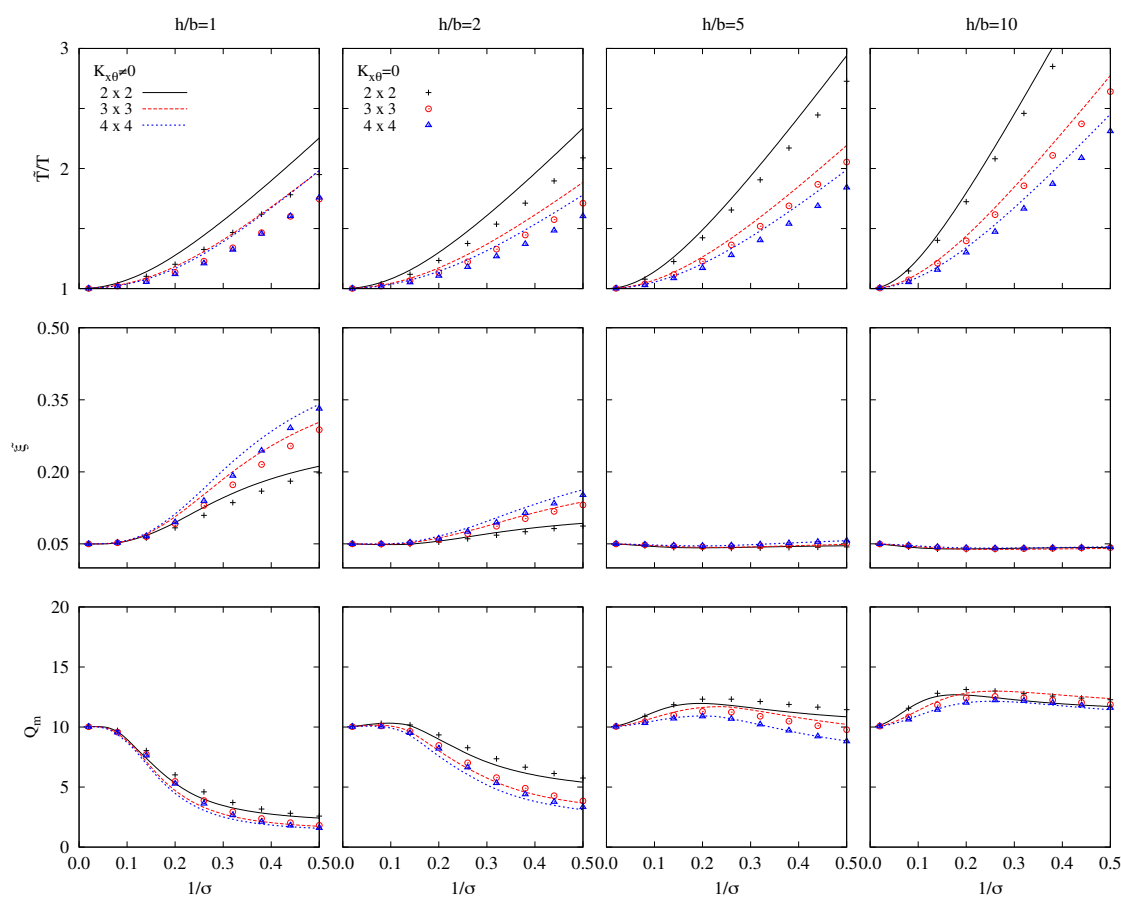


FIGURE 5.7: Influence of the cross-coupled impedances. Effective period \tilde{T}/T , damping ratio $\tilde{\xi}$ and maximum structural response value Q_m for pile groups with $L/d = 15, L/b = 2, E_p/E_s = 10^3$ and $\xi_s = 0.05$.

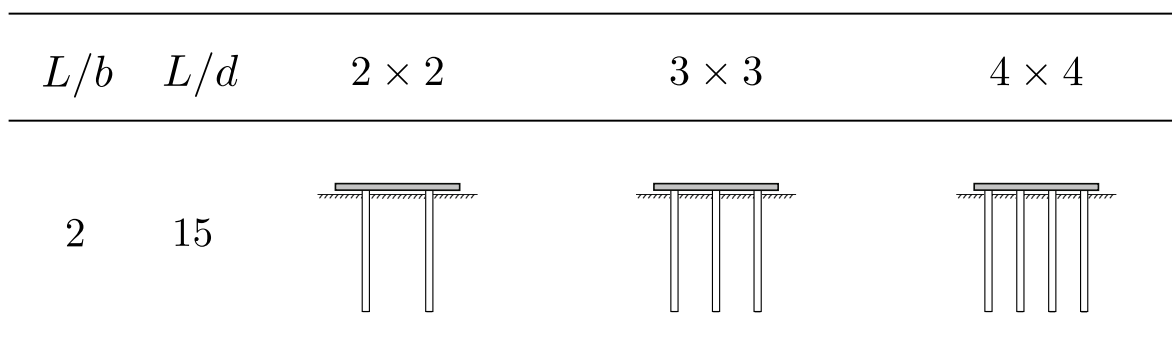


FIGURE 5.8: Sketches of the pile group configurations corresponding to the cases analysed in figure 5.7 when considering $d = cte$.

5.5 Influence of structural slenderness ratio and wave parameter

The influence of the structural slenderness ratio h/b and the wave parameter σ is examined from figures 5.9, 5.12, 5.14 and 5.17. Figures 5.12 to 5.17 will also be used for comparative analyses in next sections. First, figure 5.9 shows the system effective period \tilde{T}/T for structures with $h/b = 1, 2, 5$ and 10, and several pile configurations. Sketches of the configurations whose results are represented in the left column are depicted in figure 5.10. In turn, figure 5.11 provides sketches for those considered in the right column. On the other hand, figures 5.12, 5.14 and 5.17 depict results in terms of effective period \tilde{T}/T and damping $\tilde{\xi}$ and maximum shear force at the base of the structure per effective earthquake force unit Q_m for several pile group configurations whose sketches are provided in figures 5.13, 5.15 and 5.18, respectively. All plots are presented as a function of $1/\sigma$ being σ the wave parameter.

As expected, the system effective period \tilde{T}/T increases for decreasing values of σ , which implies lower soil stiffness. Generally, lower values of h/b lead to a reduction of \tilde{T}/T . However, this trend can change for $h/b \leq 1$ (see figure 5.9). In all cases, SSI implies an increase of the system period ($\tilde{T} > T$). On the contrary, the value of the effective damping ratio $\tilde{\xi}$ can be greater or lower than that corresponding to the fixed-base structure depending mainly on h/b (see figures 5.12, 5.14 or 5.17). For buildings with $h/b < 5$, it increases with $1/\sigma$ and shows values over the fixed-base structural damping ratio. By contrast, for buildings with $h/b \geq 5$ it is almost independent of $1/\sigma$ so it stands at around the fixed-base structural damping ratio. Similar conclusions have been extracted from studies in the same line for structures founded on shallow [7] and embedded foundations [14].

Again from figures 5.12, 5.14 or 5.17, it should be noted that, for short and squat buildings with $h/b \leq 2$, the value of Q_m decreases as $1/\sigma$ increases. However, for high buildings with $h/b \geq 3$, Q_m is moderately dependent on $1/\sigma$ and it can reach values over that corresponding to fixed-base condition. Furthermore, the maximum value of Q_m occurs for greater values of $1/\sigma$ (in most cases between 0.1 and 0.3), as h/b increases. Indeed, in the cases analysed in this work, the maximum value obtained for Q_m when considering SSI effects is 67% greater than that corresponding to fixed-base condition. This is the case of the maximum value of Q_m reached for a superstructure with $h/b = 10$ supported on a 4×4 pile group with embedment ratio $L/b = 4$ and pile slenderness ratio $L/d = 15$ (see figure 5.12).

The foundation horizontal displacement expressed as $|\omega_n^2 u_r^c / \ddot{u}_{g_o}|$ (see figures 5.14 and 5.17) increases with $1/\sigma$ for all cases under study. Its dependence on the structural slenderness ratio h/b is related with the configuration corresponding to each particular case. Besides, the foundation rocking expressed as $|\omega_n^2 h \varphi_r^c / \ddot{u}_{g_o}|$ increases with $1/\sigma$, being this effect more pronounced for greater values of the ratio h/b .

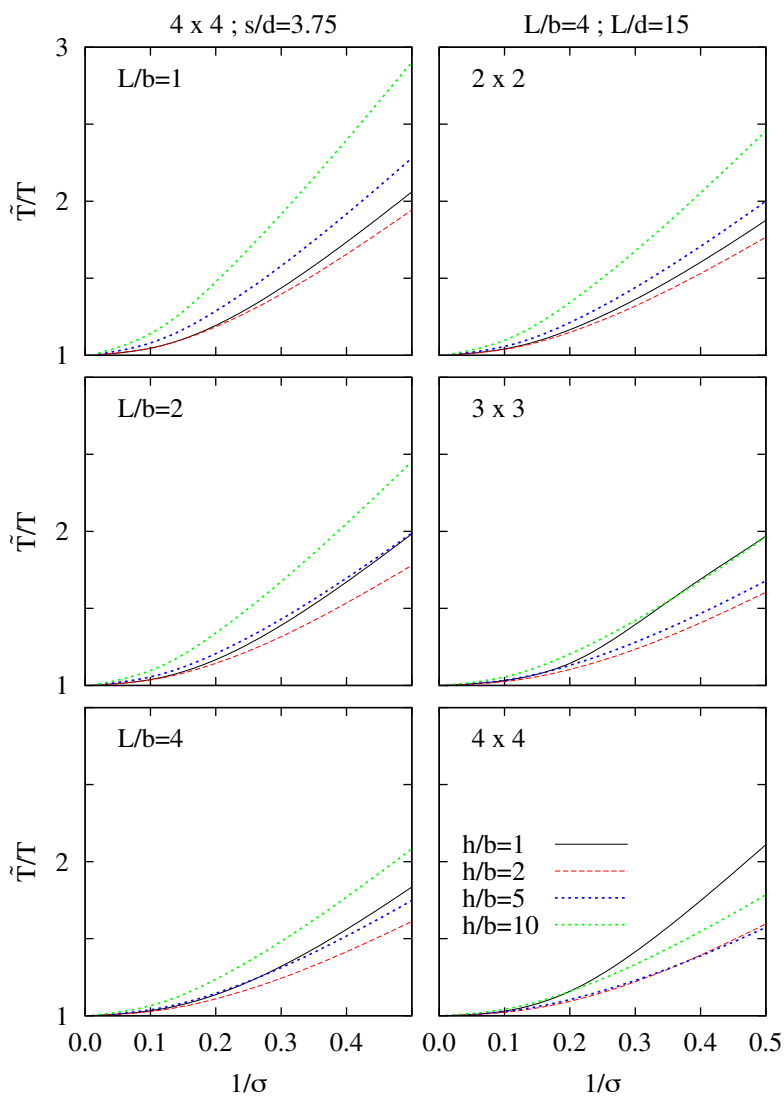


FIGURE 5.9: Influence of the structural slenderness ratio h/b . Effective period \tilde{T}/T for a 4×4 pile group with $s/d = 3.75$ (left column) and for a pile group with $L/b = 4$, $L/d = 15$ (right column). $E_p/E_s = 10^3$ and $\xi_s = 0.05$.

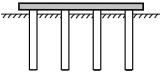
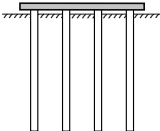
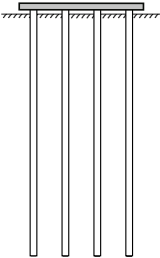
L/b	1	2	4
L/d	7.5	15	30
			

FIGURE 5.10: Sketches of the pile group configurations corresponding to the cases analysed in the left column in figure 5.9 when considering $d = cte$.

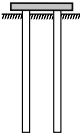
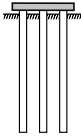
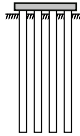
L/b	L/d	2×2	3×3	4×4
4	15			

FIGURE 5.11: Sketches of the pile group configurations corresponding to the cases analysed in the right column in figure 5.9 when considering $d = cte$.

5.6 Influence of kinematic interaction factors

Figure 5.12 shows the extent to which kinematic interaction influences the dynamic characteristics of the system. To this end, this figure depicts \tilde{T} , $\tilde{\xi}$ and Q_m functions involving total soil-structure interaction (both kinematic and inertial interaction) or only inertial interaction for different pile groups (2×2 , 3×3 and 4×4) with the same pile slenderness (L/d) and mechanical properties (E_p/E_s). Sketches of these pile group configurations are provided in figure 5.13. Kinematic interaction is also assessed in this case through the function $|I_u + (h/b)I_\varphi|$.

Obviously, as the natural frequency of the system does not depend on the excitation, the system effective period is insensitive to kinematic interaction. However, in most cases, the effective damping decreases when these factors are taken into account ($|I_u + (h/b)I_\varphi| > 1$). On the contrary, this trend could be reversed for non-slender structures ($h/b \leq 1$) on soft soils ($1/\sigma \geq 0.2$) (i.e. $|I_u + (h/b)I_\varphi| < 1$) which implies that greater values of $\tilde{\xi}$ can be reached when considering kinematic interaction. This effect becomes more noticeable as the group size increases (stiffer foundation). Consequently, the results obtained without considering the kinematic interaction effects are not on the side of safety except for those corresponding to non-slender structures $h/b \leq 1$. Similar conclusions were drawn by Avilés and Pérez-Rocha [14] for embedded foundations.

It should be noted that, for those cases where the kinematic interaction effects are relevant, their influence becomes more noticeable as the wave parameter σ decreases. With respect to the damping ratio, the influence of the kinematic interaction effects decreases and even disappears for decreasing values of foundation stiffness, and the same happens for increasing values of the slenderness ratio of the structure h/b .

The relative error, in terms of maximum shear force at the base of the structure Q_m , committed by ignoring the kinematic interaction factors, reaches a 55% for the most unfavourable configuration of those analysed. This occurs for non-slender structures $h/b = 1$ in which the maximum structural response value is below that corresponding to the fixed-base condition. However, the relative error is below 10% for buildings with $h/b = 10$.

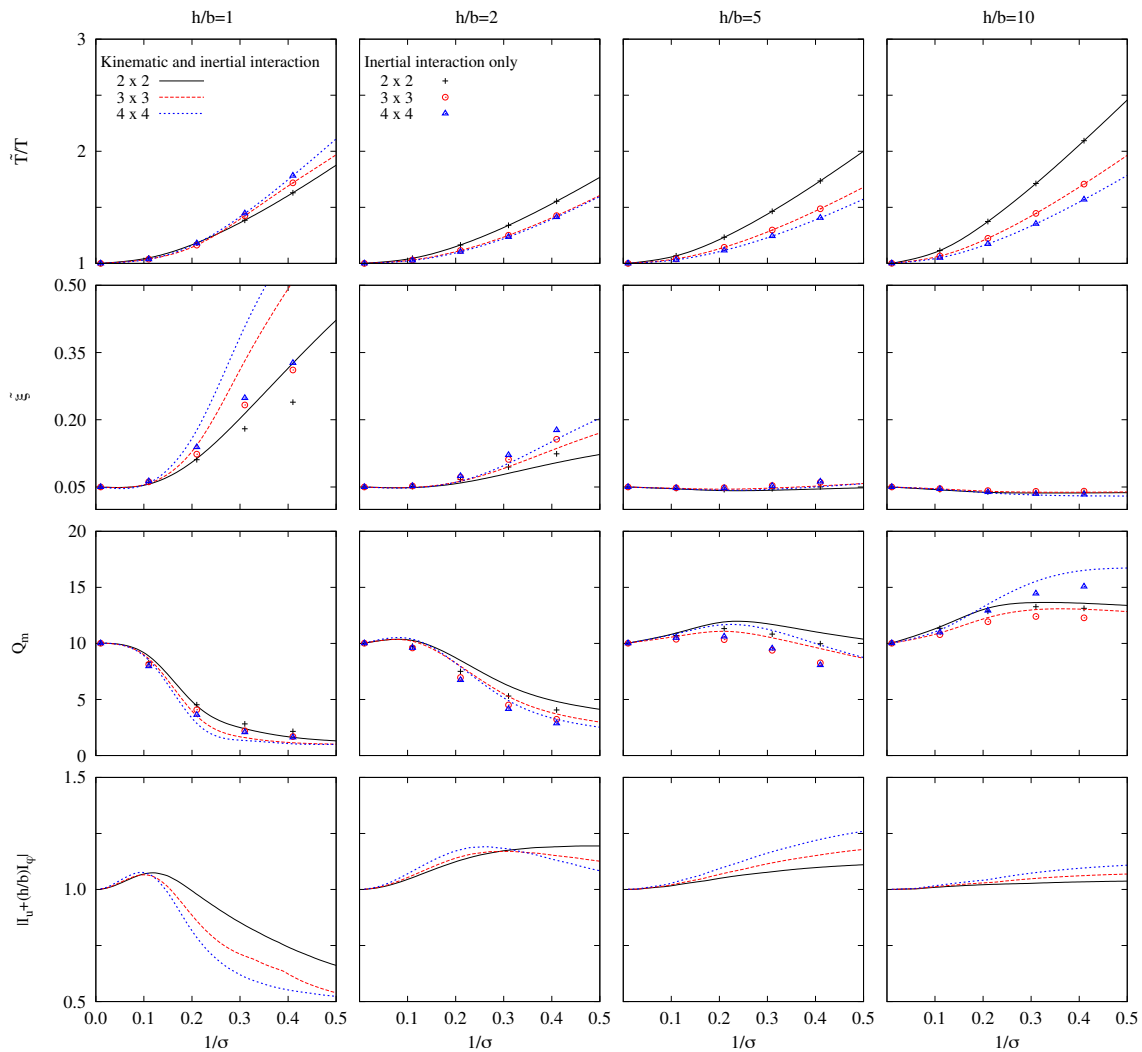


FIGURE 5.12: Influence of the kinematic interaction and the size of the pile group. Effective period \tilde{T}/T , damping ratio $\tilde{\xi}$, maximum structural response value Q_m and kinematic interaction factor $|I_u + (h/b)I_\varphi|$ for pile groups with $L/b = 4$, $L/d = 15$, $E_p/E_s = 10^3$ and $\xi_s = 0.05$.

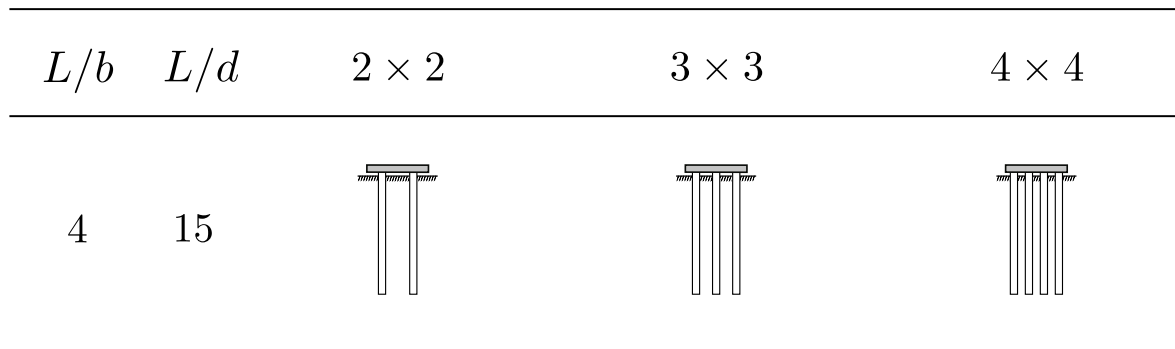


FIGURE 5.13: Sketches of the pile group configurations corresponding to the cases analysed in figure 5.12 when considering $d = cte$.

5.7 Influence of pile slenderness ratio

As shown in figure 5.14, for piled foundations with the same embedment ratio L/b , increasing values of L/d (more slender piles) imply a reduction of the effective length of piles, and consequently a diminution of the system stiffness, which results in an increase of the effective period. This effect increases as the soil stiffness decreases (lower values of σ). These differences are smaller for short and squat structures (lower values of h/b); although this trend is even reversed for very low values of this parameter. In order to illustrate this effect, figure 5.16 shows results in terms of effective period \tilde{T}/T for the same pile groups configurations considered in figure 5.14 but considering a superstructure with a slenderness ratio $h/b = 0.6$. In this case, it can be observed that, for values of the wave parameter such that $1/\sigma > 0.25$, the values of \tilde{T}/T reached for $L/d = 7.5$ are greater than those obtained for $L/d = 15$.

In regard to the damping ratio, generally, the increase of L/d reduces the system damping. This effect becomes less appreciable for slender structures (greater values of h/b). It should be noted that for $h/b \geq 5$ the system damping $\tilde{\xi}$ is close to the structural damping ξ and it is not too sensitive to L/d variations. Furthermore, it can be seen that there are not significant differences between the results for the damping ratio for $L/d = 7.5$ and $L/d = 15$, respectively.

The results for the system maximum response Q_m are affected by the trends explained above regarding the damping ratio $\tilde{\xi}$. Thus, it should be noticed that when $h/b \leq 2$, Q_m reaches greater values for $L/d = 30$ than for lower values of L/d ; and there are not significant differences between the results obtained for $L/d = 7.5$ and $L/d = 15$, respectively. However, a change of trend can be observed when $h/b \geq 5$, which consists in an increment of the system maximum response corresponding to the configuration with $L/d = 7.5$ with respect to that obtained when considering $L/b = 15$ or even $L/b = 30$. This is the case of slender structures with $h/b = 10$ when considering $1/\sigma > 0.2$.

Concerning the foundation horizontal displacement and rocking, it can be seen that both increase for greater values of the pile slenderness ratio L/d .

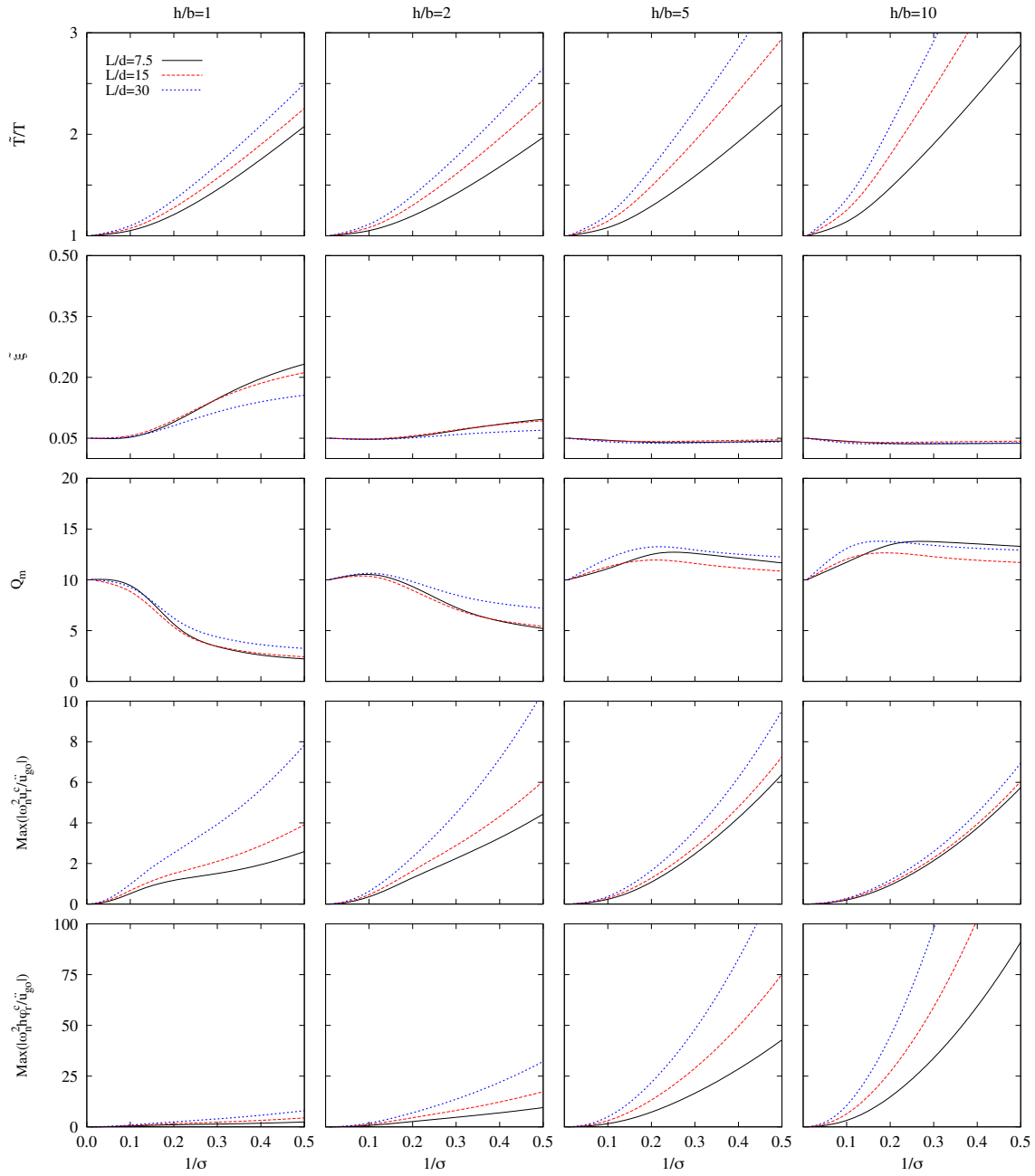


FIGURE 5.14: Influence of the pile slenderness ratio L/d . Effective period \tilde{T}/T , damping ratio $\tilde{\xi}$, maximum structural response value Q_m and maximum relative values of the foundation horizontal displacement $|\omega_n^2 u_r^c / \ddot{u}_{g0}|$ and rocking $|\omega_n^2 h \varphi_r^c / \ddot{u}_{g0}|$ for a 2×2 pile group with $L/b = 2$, $E_p/E_s = 10^3$ and $\xi_s = 0.05$.

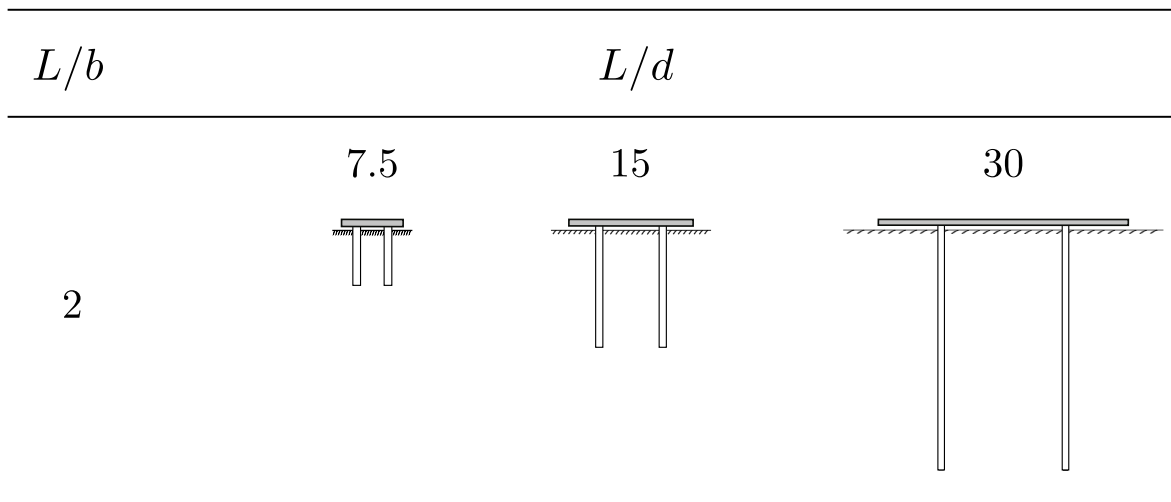


FIGURE 5.15: Sketches of the pile group configurations corresponding to the cases analysed in figures 5.14 and 5.16 when considering $d = cte$.

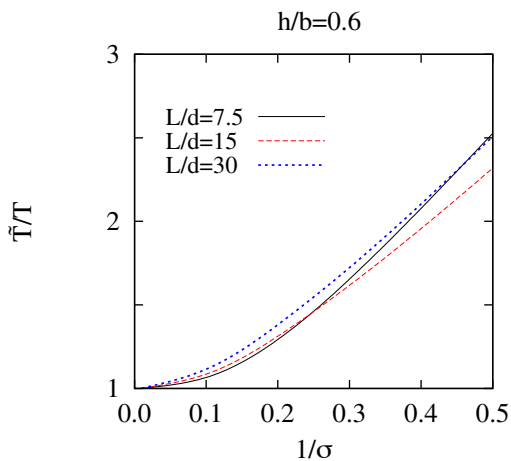


FIGURE 5.16: Influence of the pile slenderness ratio L/d . Effective period \tilde{T}/T for 2×2 pile groups with $L/b = 2$, $E_p/E_s = 10^3$ and $\xi_s = 0.05$. $h/b = 0.6$.

5.8 Influence of embedment ratio

As shown in figure 5.17, for piled foundations with the same spacing between adjacent piles s/d , keeping the foundation half-width b constant, decreasing values of L/b reduce the length of piles L (see figure 5.18), and consequently the system stiffness, which results in an increase of the effective period. This effect is less appreciable for low values of h/b ; and this trend is reversed for very low values of this parameter. In order to illustrate this effect, figure 5.19 shows results in terms of effective period \tilde{T}/T for the same pile groups configurations considered in figure 5.17 but considering a superstructure with a slenderness ratio $h/b = 0.6$. In this case, it can be observed that \tilde{T}/T reaches values for $L/b = 2$ greater than those obtained for $L/b = 1$.

In regard to the effective damping ratio, although it is not affected by L/b variations for $1/\sigma < 0.2$, in all cases, the decrease of L/b results in a reduction of the system damping for higher values of $1/\sigma$. This effect is more remarkable as h/b decreases. It should be noted that for $h/b \geq 5$ the system damping $\tilde{\xi}$ is close to the structural damping ξ , and it is not sensitive to L/b variations.

Regarding the effect of the embedment ratio on the maximum structural response Q_m , the same figure shows that it experiences an increase for decreasing values of the embedment ratio L/b . Generally, this effect is more remarkable for $h/b = 2$ and 5; however, a change of trend can be observed between the results corresponding to $h/b = 5$ and $h/b = 10$, respectively, where this effect is not so appreciable. Something similar occurs with the foundation horizontal displacement expressed as $|\omega_n^2 u_r^c / \ddot{u}_{g_0}|$. The foundation rocking $|\omega_n^2 h \varphi_r^c / \ddot{u}_{g_0}|$, on the other hand, grows for decreasing values of L/b , being this effect more noticeable as h/b increases.

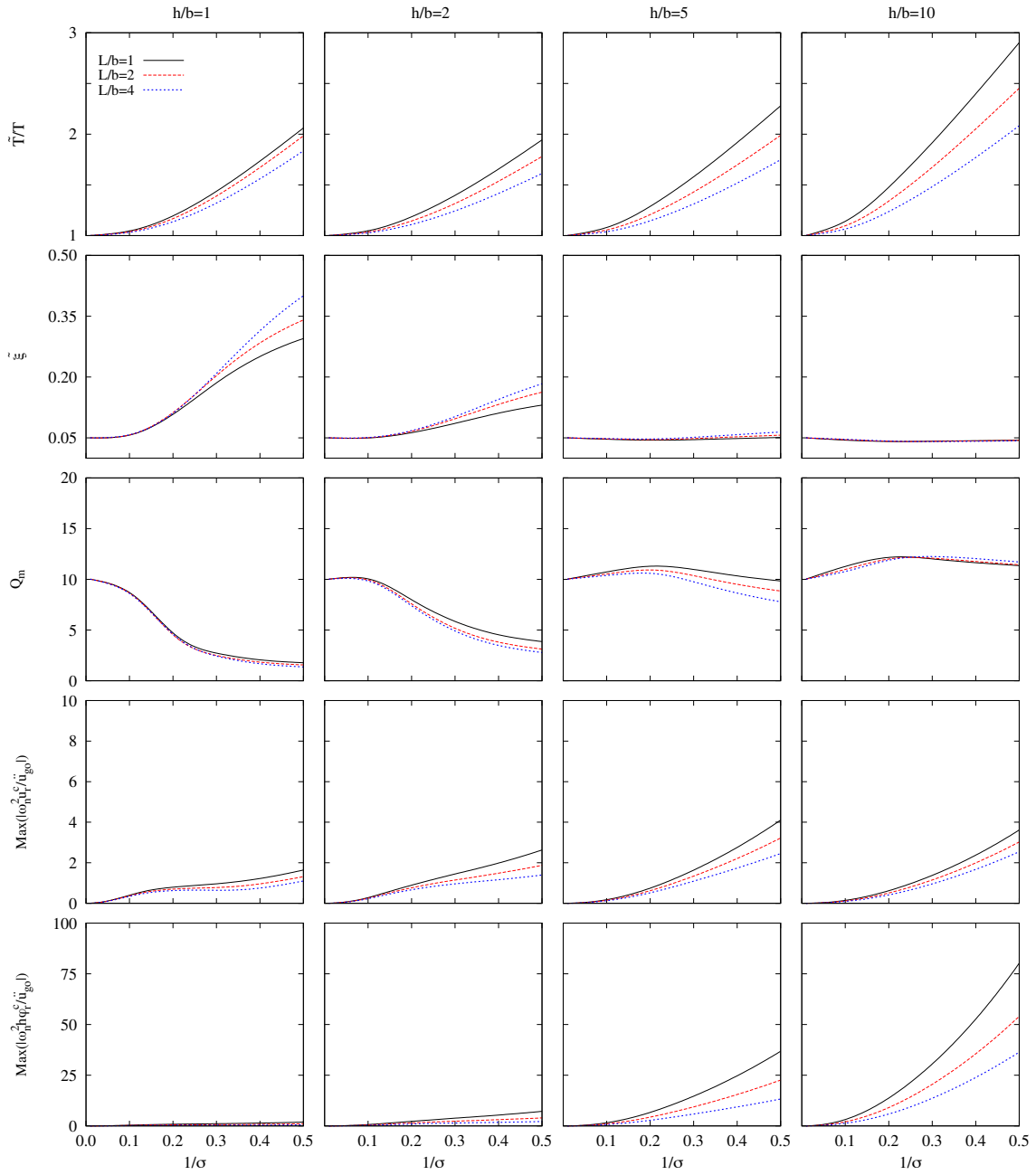


FIGURE 5.17: Influence of the embedment ratio L/b . Effective period \tilde{T}/T , damping ratio $\tilde{\xi}$, maximum structural response value Q_m and maximum relative values of the foundation horizontal displacement $|\omega_n^2 u_r^c / \ddot{u}_{g0}|$ and rocking $|\omega_n^2 h \varphi_r^c / \ddot{u}_{g0}|$ for a 4×4 pile group with $s/d = 3.75$, $E_p/E_s = 10^3$ and $\xi_s = 0.05$.

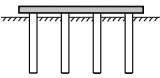
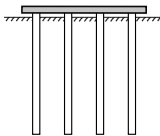
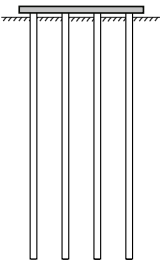
L/b	1	2	4
L/d	7.5	15	30
			

FIGURE 5.18: Sketches of the pile group configurations corresponding to the cases analysed in figures 5.17 and 5.19 when considering $d = cte$.

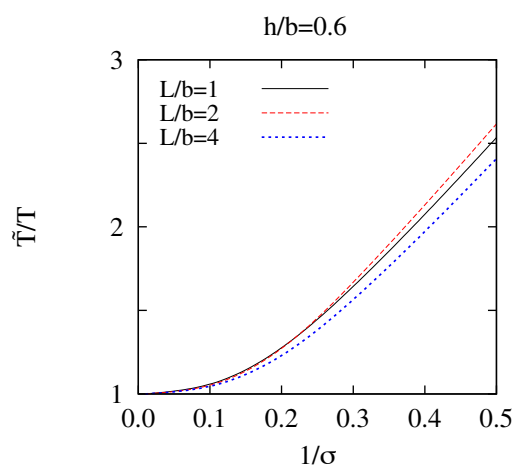


FIGURE 5.19: Influence of the embedment ratio L/b . Effective period \tilde{T}/T for 4×4 pile groups with $s/d = 3.75$, $E_p/E_s = 10^3$ and $\xi_s = 0.05$. $h/b = 0.6$.

5.9 Influence of pile group size

As shown in figure 5.12, for piled foundations with high h/b and the same embedment ratio L/b and pile slenderness ratio L/d , fewer piles lead to a reduction of the system stiffness, which results in an increase of the effective period. However, the magnitude of this trend decreases for decreasing values of h/b , and tends to be the opposite for non-slender structures. On the other hand, a larger pile group leads to greater values of the system effective damping and, consequently, smaller maxima Q_m in the response, when $h/b < 5$, while no clear trends are observed for higher slendernesses. For high buildings ($h/b = 5$ and 10) the value obtained for Q_m when considering SSI exceeds that corresponding to fixed-base condition. Also, the maximum value of Q_m occurs for $1/\sigma = 0.2$ when $h/b = 5$ and increases with $1/\sigma$ for $h/b = 10$, approaching (in the depicted range) an asymptotic value that increases with the number of piles.

Regarding the foundation horizontal displacement and rocking, both increase for smaller pile groups, being this effect more remarkable for slender structures as shown in figure 5.20.

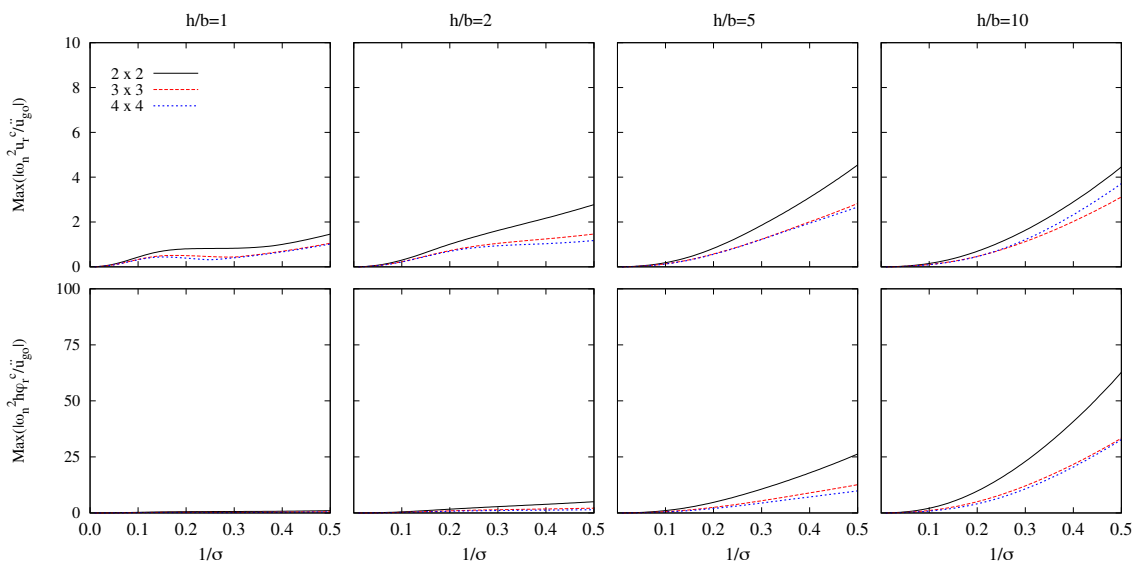


FIGURE 5.20: Influence of the kinematic interaction and the size of the pile group. Maximum relative values of the foundation horizontal displacement $|\omega_n^2 u_r^c / \ddot{u}_{g_o}|$ and rocking $|\omega_n^2 h \varphi_r^c / \ddot{u}_{g_o}|$ for pile groups with $L/b = 4$, $L/d = 15$, $E_p/E_s = 10^3$ and $\xi_s = 0.05$.

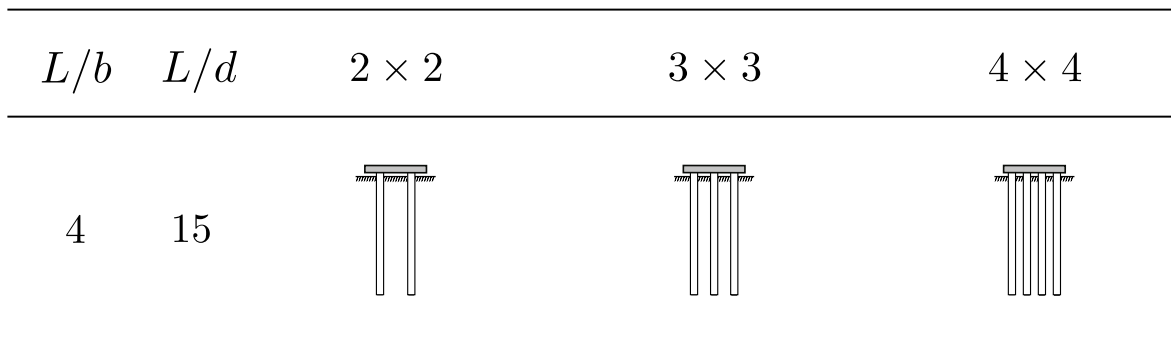


FIGURE 5.21: Sketches of the pile group configurations corresponding to the cases analysed in figure 5.20 when considering $d = cte$.

5.10 Influence of pile-soil Young's modulus ratio

The variations of the pile-soil Young's modulus ratio E_p/E_s affect the impedance functions and kinematic interaction factors of the soil-foundation system. Consequently, SSI effects on the system dynamic response are also influenced by these variations. In order to analyse this influence, figure 5.22 depicts in columns the dynamic response corresponding to structures with slenderness ratios $h/b = 1, 2, 5$ and 10 , respectively, supported on square groups of 2×2 vertical piles embedded in a homogeneous, viscoelastic and isotropic half-space such that $E_p/E_s = 100$ or 1000 . Each plot area shows results for three different values of the pile slenderness ratio: $L/d = 7.5, 15$ and 30 . All plots are presented as a function of $1/\sigma$, being σ the wave parameter. Results in terms of effective period \tilde{T}/T , damping $\tilde{\xi}$ and maximum shear force at the base of the structure per effective earthquake force unit Q_m are depicted in the upper, central and lower part of this figure, respectively. In turn, figure 5.23 provides sketches of the different pile group configurations considered in figure 5.22.

Assuming constant properties for the material of piles, lower values of E_p/E_s imply an increase of the soil stiffness which leads to greater values of the system effective period \tilde{T}/T and lower values of the effective damping $\tilde{\xi}$. Consequently, higher values of Q_m are reached. This effect is more remarkable for greater values of the pile slenderness ratio L/d and as $1/\sigma$ grows.

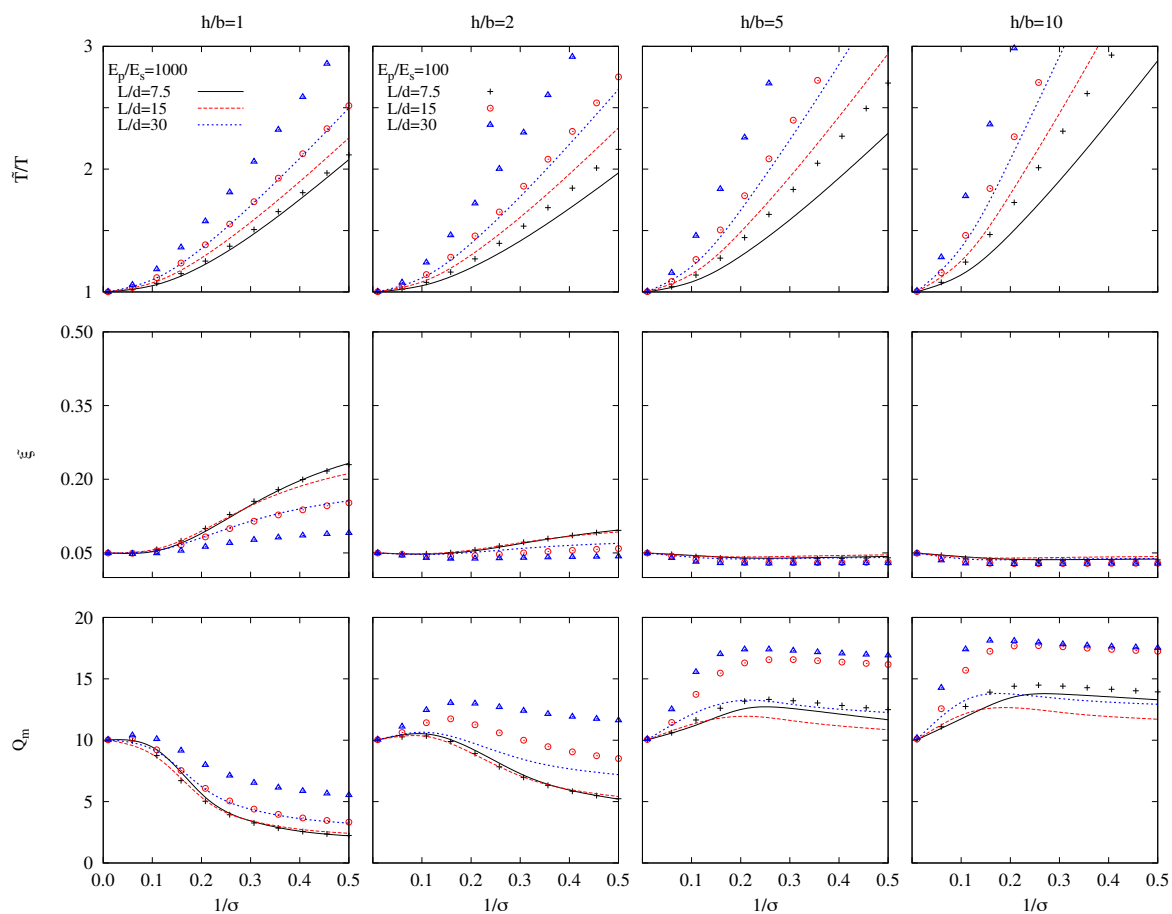


FIGURE 5.22: Influence of the pile-soil Young's modulus ratio E_p/E_s . Effective period \tilde{T}/T , damping ratio $\tilde{\xi}$ and maximum structural response value Q_m for 2×2 pile groups with $L/b = 2$, $\delta = 0.15$, $\xi = 0.05$ and $\xi_s = 0.05$.

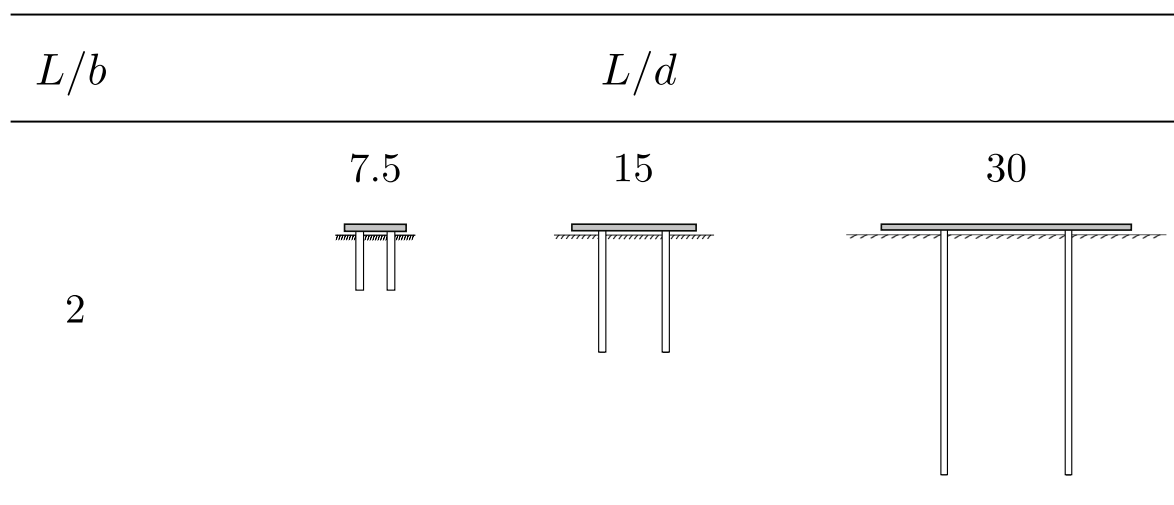


FIGURE 5.23: Sketches of the pile group configurations corresponding to the cases analysed in figure 5.22 when considering $d = cte$.

5.11 Influence of fixed-base structure damping ratio

Figure 5.24 shows how the variation of the fixed-base structure damping ratio influences the effects of SSI on the system dynamic response. It can be observed that this parameter has no influence on the system effective period \tilde{T}/T . However, as expected, it affects the system effective damping $\tilde{\xi}$, that reaches greater values as ξ increases. This effect becomes more remarkable for greater values of the wave parameter σ . By contrast, its influence is negligible when $1/\sigma \geq 0.4$. These variations of the system effective damping lead to increasing values of Q_m as the fixed-base structure damping ratio ξ decreases. Furthermore, greater values of the structural slenderness ratio h/b imply a wider range of the parameter σ where the variation of ξ has a significant influence.

For the results provided in this work, it is assumed that $\xi = 0.05$ because this value is representative for typical buildings and it has been used in previous works (*e.g.* [7, 14]).

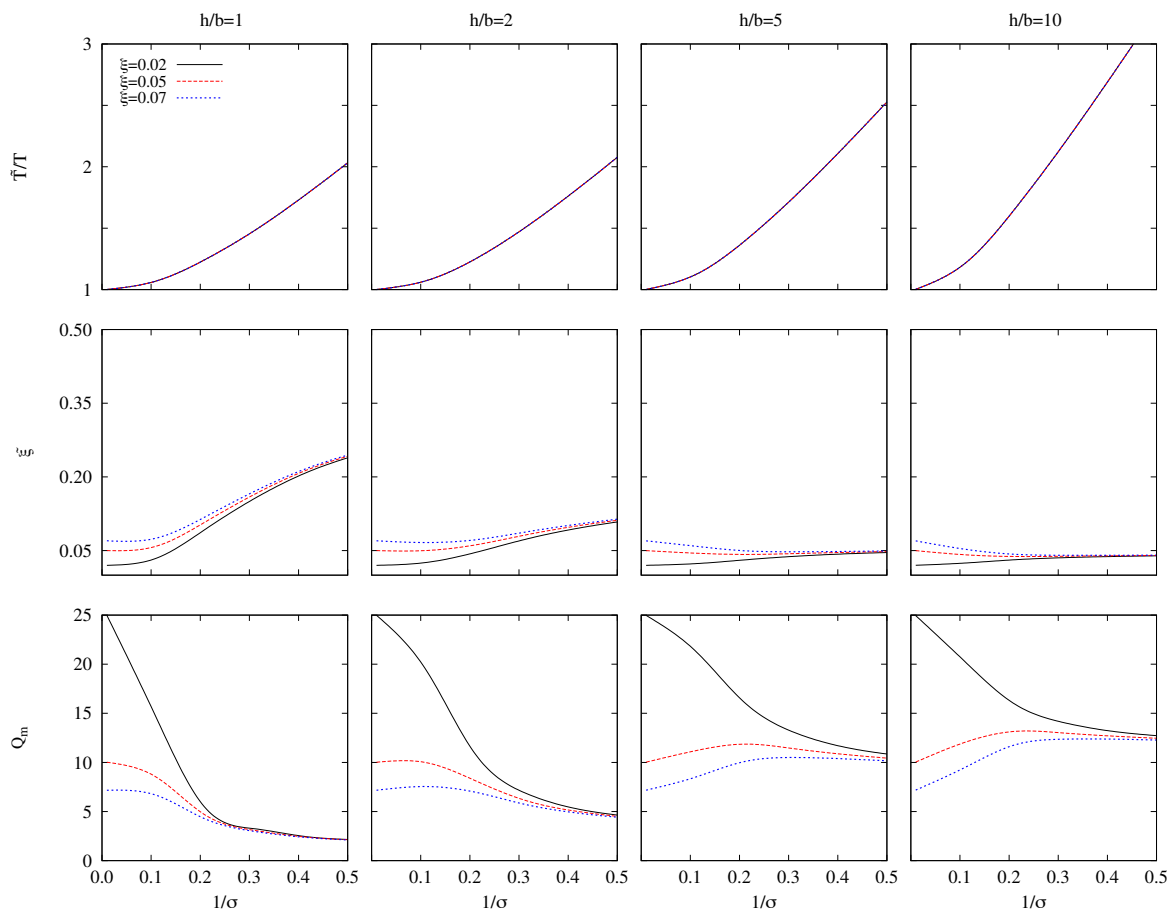


FIGURE 5.24: Influence of the fixed-base structure damping ratio ξ . Effective period \tilde{T}/T , damping ratio $\tilde{\xi}$ and maximum structural response value Q_m for a 3×3 pile group with $L/d = 30$, $L/b = 2$, $\delta = 0.15$, $E_p/E_s = 10^3$ and $\xi_s = 0.05$.

5.12 Influence of mass density ratio

With regard to the mass density ratio between structure and supporting soil δ , it should be mentioned that this is a parameter which has a relevant influence on the system response. Figure 5.25 shows that the decrease of δ implies an increase of the system stiffness, which leads to lower values of effective period \tilde{T}/T and damping $\tilde{\xi}$ and, consequently, higher values of Q_m are reached. The effects associated to SSI become more remarkable as the structural slenderness ratio h/b increases. Nevertheless, as mentioned before, the value considered herein ($\delta = 0.15$) is representative for typical buildings and soils and it has been adopted in previous works by other authors such as Avilés and Pérez-Rocha [14] or Veletsos and Meek [7].

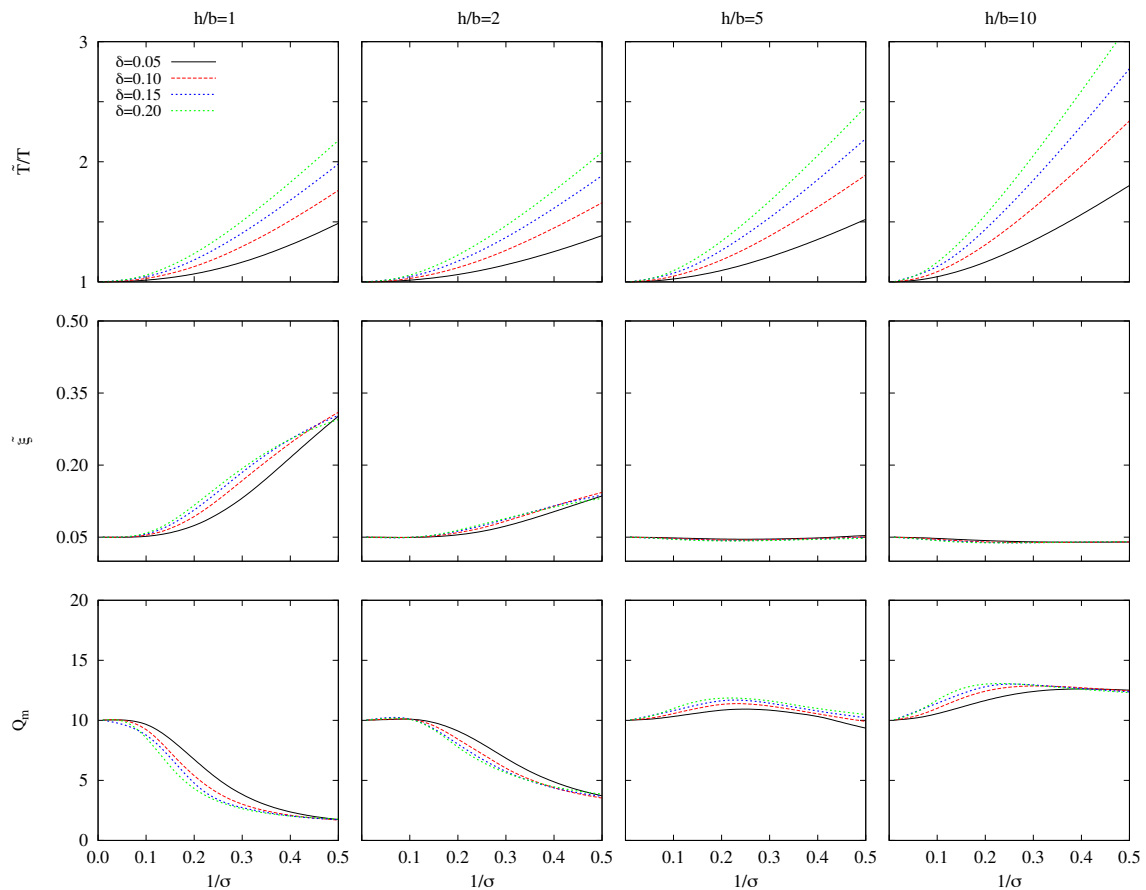


FIGURE 5.25: Influence of the mass density ratio between structure and supporting soil δ . Effective period \tilde{T}/T , damping ratio $\tilde{\xi}$ and maximum structural response value Q_m for a 3×3 pile group with $L/d = 15$, $L/b = 2$, $E_p/E_s = 10^3$ and $\xi_s = 0.05$.

5.13 Conclusions

In this chapter, an analysis of the SSI effects on the period and damping of pile-supported structures is accomplished. For this purpose, the simplified and stable procedure presented in chapter 2 has been used to determine the dynamic properties of a SDOF system which reproduces, as accurately as possible, the coupled system response within the range where the peak response occurs. The coupled-system response is obtained by using a substructuring model in which the structure is considered as a SDOF shear structure that represents, from a general point of view, one mode of vibration of multi-storey buildings. Both, dynamic and kinematic interaction effects are included in the analysis of this coupled system. Impedances and kinematic interaction factors of the pile group configurations studied in this work, are calculated using a BEM-FEM methodology outlined in section 3.5.

Results for 21 different configurations of pile groups are obtained in order to accomplish an analysis of the influence of the main parameters of the problem for these cases. All the results obtained herein have a dimensionless character, thus their physical interpretation must be carefully done and requires a specific data processing taking into account the influence of every dimensionless parameter.

The conclusions extracted from the analysis are detailed in sections 5.4 to 5.12, and they are consistent with those drawn in relevant literature for embedded foundations. The main conclusions are summarised below:

- Piles configurations which imply stiffer foundations yield a reduction on the effective period of the coupled system: larger number of piles (figure 5.12) or embedment ratio (Figure 5.17), and lower pile slenderness ratio (figure 5.14). The obtained results show that this conclusion is not applicable for short and squat buildings, case in which the opposite occurs.
- The effective damping increases with the foundation stiffness (see figures 5.12, 5.14 and 5.17).
- Slender buildings as well as soft soils magnify the SSI effects for a particular configuration. This trend can be reversed for very stiff foundations or very short and squat buildings (see figure 5.9).
- The effective damping for slender buildings is close to that corresponding to fixed-base condition or lower. For short or medium-height buildings ($h/b < 5$), the effective damping increases as σ decreases and this effect becomes more relevant for stiffer piles configurations (see *e.g.* figures 5.12 and 5.17).
- As the influence of the SSI effects increases, the maximum shear force at the base of the structure remains lower than that corresponding to fixed-base condition for buildings with $h/b \leq 2$ in all configurations studied. For larger values of the structural slenderness ratio, the maximum shear force increases when these effects are considered (see *e.g.* figure 5.14). Stiffer foundations yield lower shear forces if $h/b < 5$ (see *e.g.* figure 5.12). However, for greater slenderness, the results show variations in the trend that depend on the parameter analysed.



- The foundation horizontal displacement and rocking increase for softer soils as well as for more flexible geometric configurations (see *e.g.* figures 5.14 or 5.17).
- Lower values of the pile-soil Young's modulus ratio E_p/E_s result in an increase of the foundation stiffness which leads to lower values of the effective period and greater values of the effective damping.
- An increase of the mass density ratio δ implies greater values of the system effective period and damping.
- The effective period is not affected by variations of the fixed-base structure damping ratio ξ . However, the influence of this variation on the effective damping is more important as the wave parameter increases.
- In a significant number of cases, the system dynamic response is subestimated when neglecting the cross-coupled impedances.
- The results computed without considering the kinematic interaction effects are not on the side of safety except for those corresponding to non-slender structures $h/b \leq 1$.

Results in terms of period \tilde{T}/T and damping $\tilde{\xi}$ for different pile configurations are provided in ready-to-use graphs that can be used to build modified response spectra that include SSI effects.



6. SEISMIC BEHAVIOUR OF STRUCTURES SUPPORTED ON BATTERED PILE GROUPS

- 6.1 Introduction
- 6.2 Configurations under investigation
- 6.3 Influence of rake angle on the system effective period
- 6.4 Influence of rake angle on the maximum structural shear forces
- 6.5 Influence of rake angle on the elastic response spectra
- 6.6 Conclusions

6.1 Introduction

The procedure explained in section 2.9 is applied herein to clarify whether the use of battered piles has a positive or a negative influence on the seismic response of the superstructure. In this line, the dynamic response of linear shear structures founded on square pile groups comprising inclined piles embedded in homogeneous viscoelastic half-spaces and subjected to vertically incident S waves is evaluated. Such influence is measured here in terms of the effective system period \tilde{T}/T and the maximum shear force at the base of the structure per effective earthquake force unit Q_m [7, 114]. Moreover, results in terms of effective period and damping are used to build modified response spectra for different values of the rake angle. Results for different soil-foundation-structure systems as that described in section 2.3, are studied in this chapter.

Firstly, the cases under investigation are defined in section 6.2. Then, in section 6.3, the influence of the rake angle θ on the system effective period \tilde{T}/T is studied. Afterwards, section 6.4 addresses an analysis on how the variation of the rake angle affects the maximum shear force at the base of the structure per effective earthquake force unit Q_m . The influence of inclining piles on the dynamic response of the superstructure is analysed in section 6.5 from modified response spectra which consider SSI. Finally, the main conclusions drawn from the analysis of the results obtained for the cases under investigation are summarised in section 6.6.

6.2 Configurations under investigation

The square pile group configurations considered in the study addressed in this chapter were defined in section 4.8. The dimensionless parameters characterizing the geometry of these configurations are listed in table 6.1.

TABLE 6.1: Configurations of pile groups comprising inclined piles.

L/b	L/d	s/d	
		2×2	3×3
	7.5	3.75	2.5
2	15	7.5	5
	30	15	10

A boundary element (BEM)- finite element (FEM) coupling formulation [49, 71, 120], outlined in section 3.5, has been used to obtain numerically impedances and kinematic interaction factors for all the pile group configurations under investigation. The obtained results are depicted and analysed in section 4.9.

As done in chapter 5 for the case of vertical piles, it is assumed that $\delta = 0.15$; $m_o/m = 0$; $0 < 1/\sigma < 0.5$; $h/b = 1, 2, 5, 10$; $\xi = 0.05$; $\xi_s = 0.05$ and $\nu_s = 0.4$. These values are representative for typical buildings and soils [14, 122]. Moreover, $E_p/E_s = 10^3$ and $\rho_s/\rho_p = 0.7$.

The range of values considered in this study for $1/\sigma$ covers most real cases as shown by Stewart *et al.* [122], who provide empirical results for SSI effects for 57 building sites

covering a wide range of real structural and geotechnical conditions. Most of those cases show values of $1/\sigma$ between 0 and 0.3.

6.3 Influence of rake angle on the system effective period

Figures 6.1 and 6.2 present \tilde{T}/T as a function of $1/\sigma$ for different rake angles θ , which illustrates the influence of the rake angle on the system effective period for the different configurations of 2×2 and 3×3 pile groups under study. Discrete points to be read on the right axis provide a zoomed view in those cases in which it is necessary.

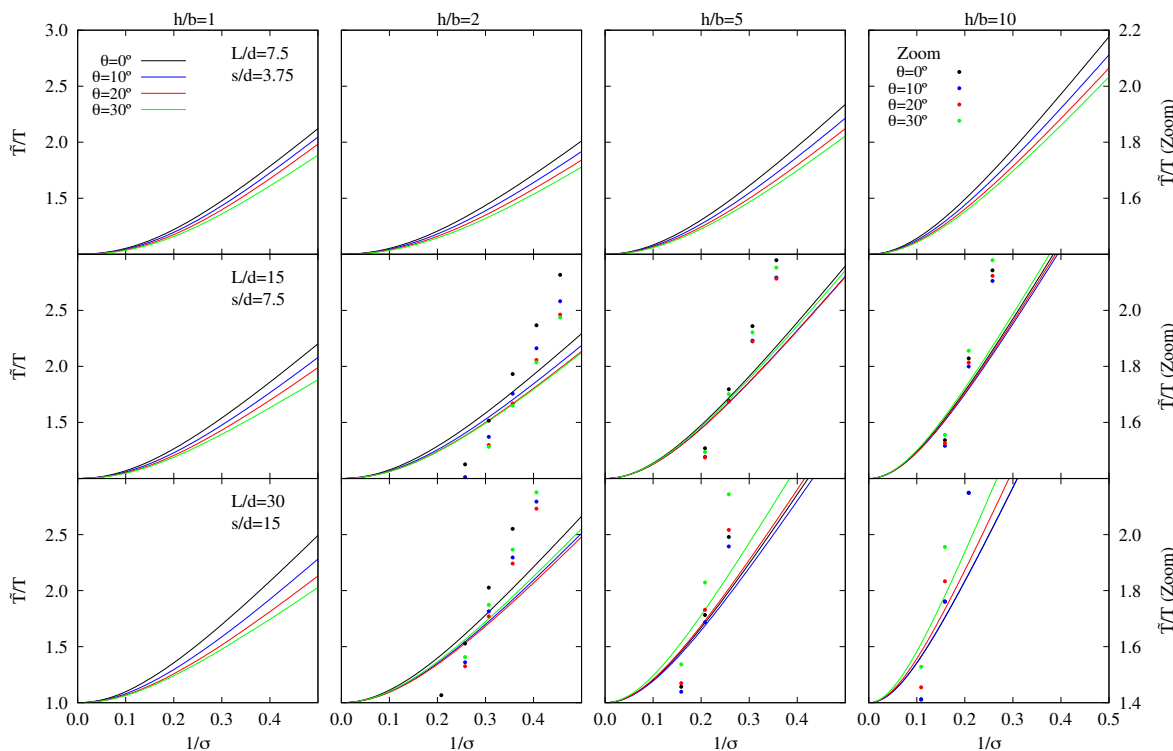


FIGURE 6.1: Effective period \tilde{T}/T for different 2×2 pile groups. $E_p/E_s = 1000$ and $\xi_s = 0.05$. $L/d(s/d) = 7.5(3.75), 15(7.5), 30(15)$. $h/b = 1, 2, 5, 10$. Solid lines to be read on left axis. Dotted lines to be read on right axis when a zoomed view is needed.

For short and squat buildings ($h/b = 1$), in which the horizontal displacement is the controlling factor, the system period decreases for higher rake angles. This is because an increment of the rake angle leads to an increase of the horizontal stiffness due to the contribution of the pile axial stiffness to withstand the lateral loads. This effect can be observed in figures 4.33 and 4.34 which depict, impedances of three different 2×2 and 3×3 pile groups, respectively, with $L/d = 7.5, 15$ and 30 .

In the case of slender structures ($h/b = 10$), the effect of the rake angle on the system period depends on the variation of the rocking stiffness as well. An increment of the rake angle generally leads to a decrease of the rocking impedance (second row in fig-

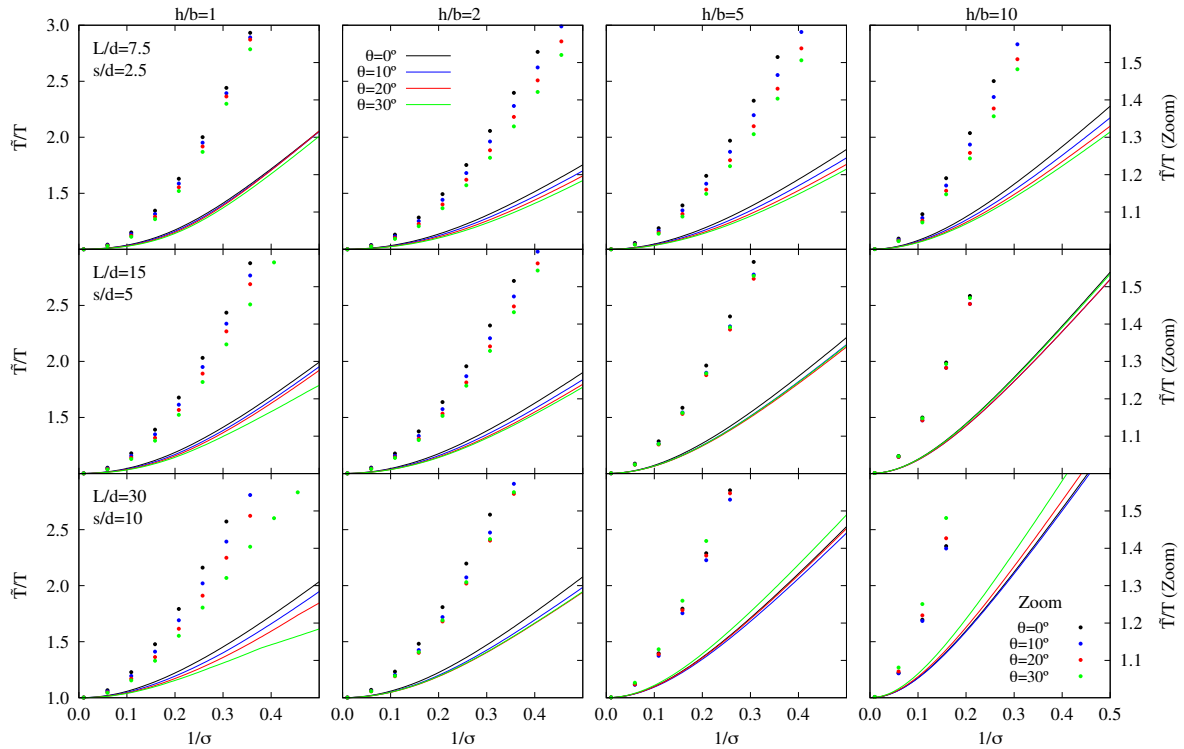


FIGURE 6.2: Effective period \tilde{T}/T for different 3×3 pile groups. $E_p/E_s = 1000$ and $\xi_s = 0.05$. $L/d(s/d) = 7.5(2.5), 15(5), 30(10)$. $h/b = 1, 2, 5, 10$. Solid lines to be read on left axis. Dotted lines to be read on right axis when a zoomed view is needed.

ure 4.33). This results from the fact that vertical impedance of single piles experiences a reduction when piles are inclined. Exceptionally, in those cases with little spacing between adjacent piles (left column in figure 4.33) the pile-soil-pile interaction effect takes predominance over that of inclination and the vertical impedance of each pile increases with the rake angle since the distance between the pile tips widens with depth. Thus, in those cases in which the increase of the rake angle leads to a reduction of the rocking stiffness ($L/d = 15$ and $L/d = 30$), the system period experiences an increase with θ . Accordingly, a reduction of the system period results from the increase of the rake angle when $L/d = 7.5$ since the rocking stiffness increases in this case.

6.4 Influence of rake angle on the maximum structural shear forces

Figures 6.3 and 6.4 depict the system response of structures founded on 2×2 and 3×3 pile groups, in terms of the maximum shear force at the base of the structure per effective earthquake force unit Q_m . Dotted lines to be read on the right axis provide a zoomed view in those cases in which it is necessary.

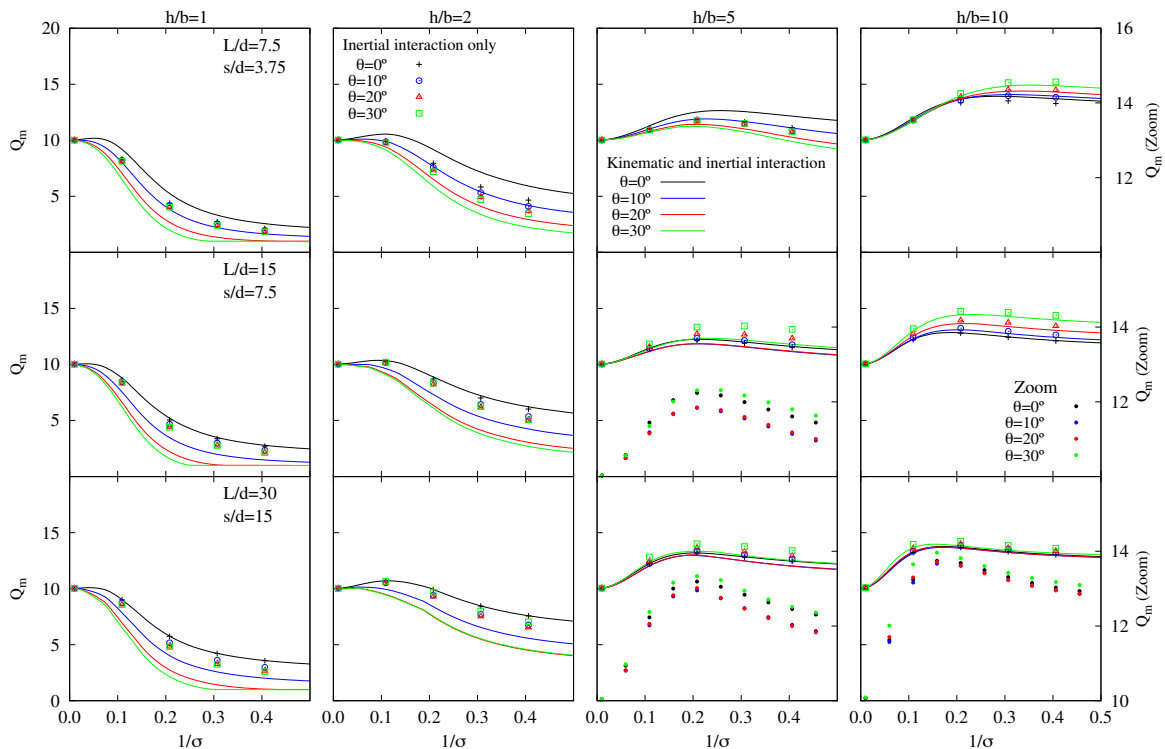


FIGURE 6.3: Maximum structural response value Q_m for different 2×2 pile groups. $E_p/E_s = 1000$ and $\xi_s = 0.05$. $L/d(s/d) = 7.5(3.75), 15(7.5), 30(15)$. $h/b = 1, 2, 5, 10$. Dotted lines to be read on right axis provide a zoomed view.

For short and squat buildings ($h/b = 1$ and $h/b = 2$), the increment of the rake angle results in lower values of the maximum shear force at the base of the structure. This effect is due to several concurrent factors: a) an increase of the horizontal damping c_{xx} (see figure 4.35); b) an increase in the horizontal stiffness of the foundation which leads to a reduction of the effective period and, consequently, an increment of the dissipated energy which contributes to reduce Q_m ; and c) a reduction of the translational kinematic interaction factor (which predominates for non-slender structures). Such reduction can be observed in figure 4.37, that presents kinematic interaction factors for three different 2×2 pile groups with $L/d = 7.5, 15$ and 30 .

In the case of slender structures ($h/b = 10$), an increase of the rake angle leads to slightly greater values of Q_m due to the reduction of the rocking damping $c_{\theta\theta}$ and to the increment of the overturning moment, which is the controlling factor in these cases.

Figure 6.3 shows the extent to which kinematic interaction influences the system dynamic response. To this end, results involving both kinematic and inertial interaction or only inertial interaction are represented. It can be seen that the ability of the foundation to filter the seismic input has significant effects on the variation of Q_m . All configurations under study show a reduction of the translational kinematic interaction factor I_u for higher rake angles, as illustrated in figure 4.37. Generally, I_φ increases significantly with θ for large pile-to-pile separation ratios such as $s/d = 5, 7.5, 10, 15$, except for small

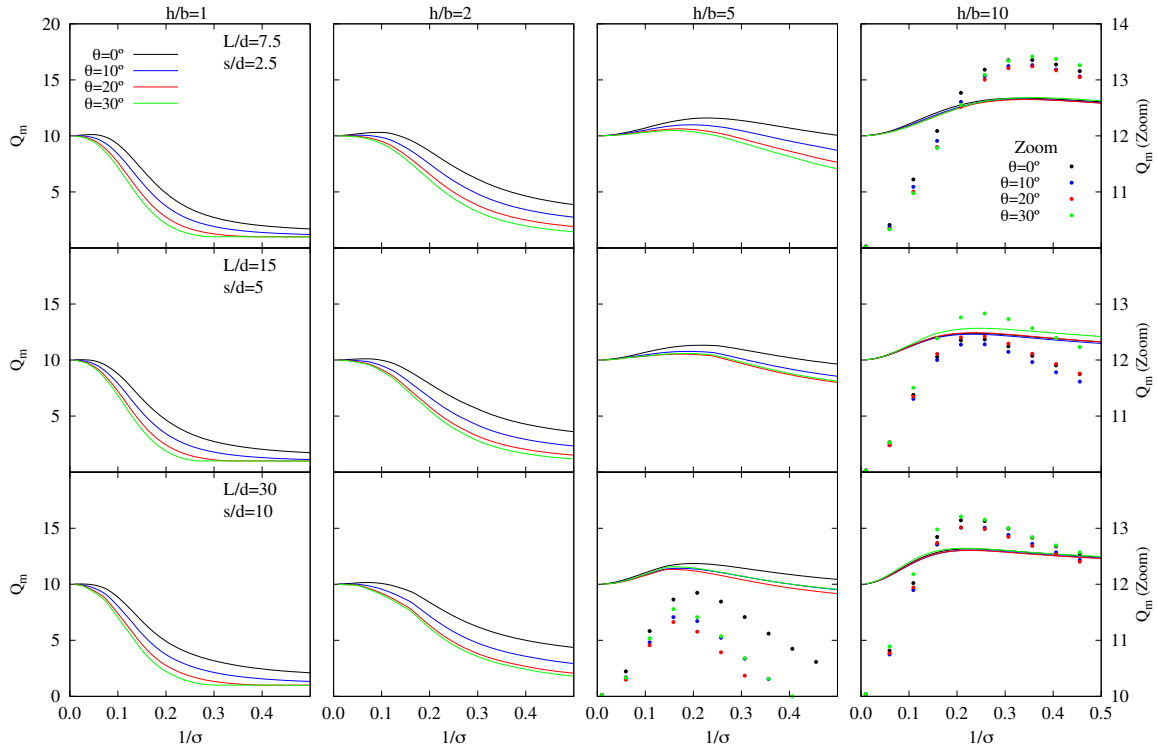


FIGURE 6.4: Maximum structural response value Q_m for different 3×3 pile groups. $E_p/E_s = 1000$ and $\xi_s = 0.05$. $L/d(s/d) = 7.5(2.5), 15(5), 30(10)$. $h/b = 1, 2, 5, 10$. Dotted lines to be read on right axis provide a zoomed view.

rake angles [54]. However, for small pile-to-pile separation ($L/d = 7.5$ and $s/d = 2.5$ or $s/d = 3.75$) the rotational kinematic interaction factor I_φ of inclined piles is smaller than the one corresponding to vertical piles for all rake angles within the range under study.

A minimum cap rotation can be achieved by inclining piles a small rake angle as $\theta = 1^\circ$ or $\theta = 3^\circ$ [54]. It might accordingly be inferred that a minimum value of the maximum shear force at the base of the structure Q_m could be reached for these rake angles. However, this does not occur (see figures 6.5 and 6.6) because even though the rotational kinematic interaction factor I_φ increases with the rake angle, as shown in figure 4.37, so does the horizontal damping c_{xx} (see figure 4.33) which leads to a reduction of Q_m as the rake angle θ increases.

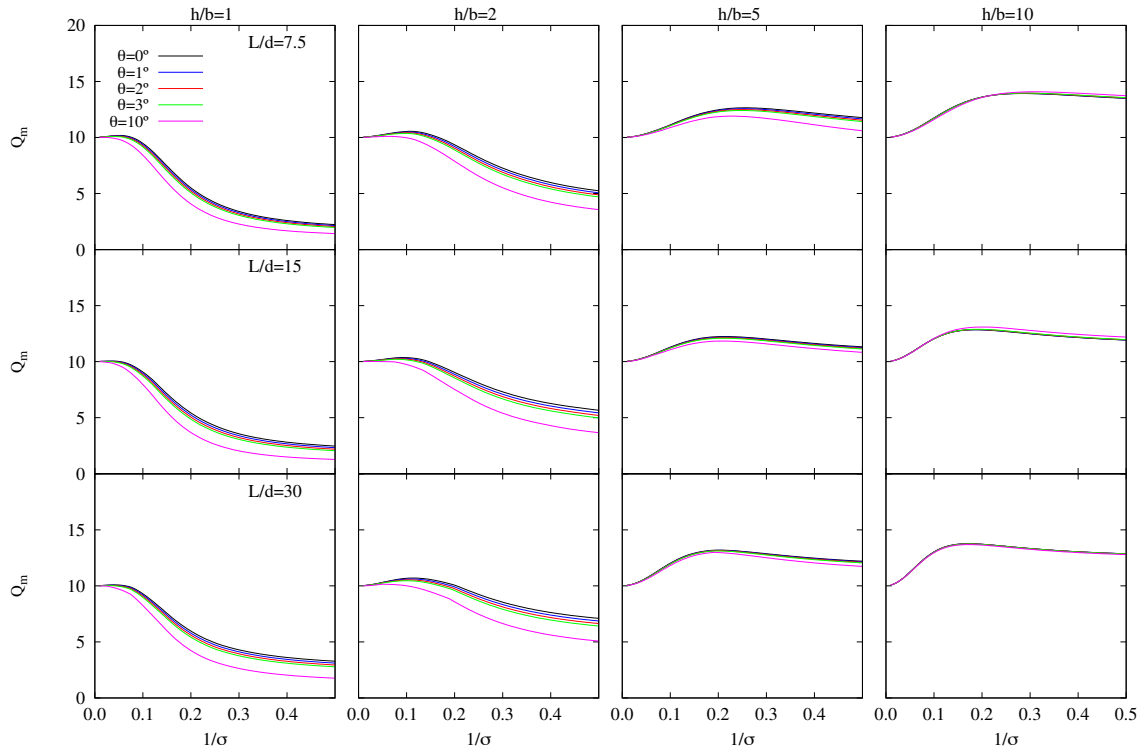


FIGURE 6.5: Maximum structural response value Q_m for different 2×2 pile groups. $E_p/E_s = 1000$ and $\xi_s = 0.05$. $L/d (s/d) = 7.5(3.75), 15(7.5), 30(15)$. $h/b = 1, 2, 5, 10$.

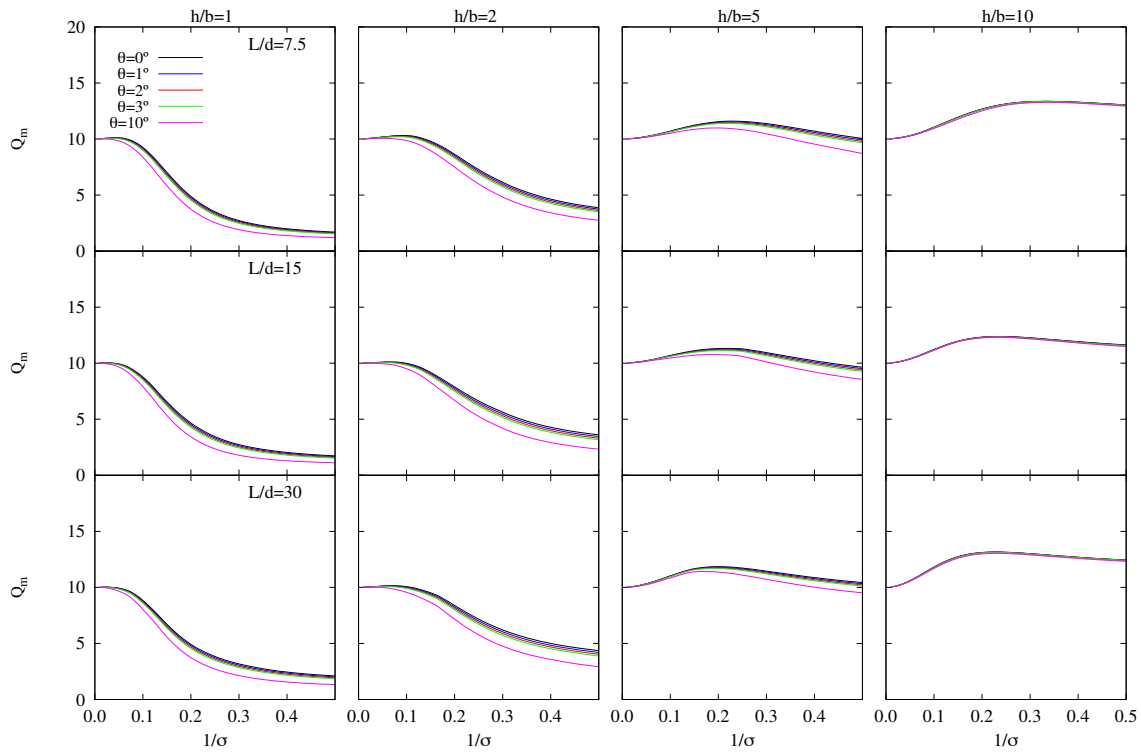


FIGURE 6.6: Maximum structural response value Q_m for different 3×3 pile groups. $E_p/E_s = 1000$ and $\xi_s = 0.05$. $L/d (s/d) = 7.5(2.5), 15(5), 30(10)$. $h/b = 1, 2, 5, 10$.

Regarding the relationship between the geometric and mechanic properties of the foundation, one could think that the geometric point where the extension of the raked pile axes meet above the cap $h_p = s/(2 \tan \theta)$ could be close to the center of stiffness of the pile group, computed as $\mathcal{D} = -Re[D] = -Re[-K_{\theta x}/K_{xx}]$ (see figure 6.7), in which case the seismic response of a structure should be closely related to the relationship h/h_p between the height of the center of mass of the building (or corresponding effective modal height h) and the height of the geometric point h_p . This would imply different structural behaviour for buildings with heights such that $h/h_p > 1$ and for those with heights such that $h/h_p < 1$. In order to test this hypothesis, figure 6.8 show h_p/d and \mathcal{D}/d for several configurations of 2×2 pile groups and rake angles θ between 0° and 30° . The values of \mathcal{D}/d have been obtained in two alternative ways: for $a_o = 0$ (left plot) as well as for those values of the dimensionless frequency a_o at which the maximum shear force at the base of the structure Q_m occurs (see right plot for $1/\sigma = 0.3$). The comparison between the left and right plots of figure 6.8 shows that there exist no significant differences between the computation of the centre of stiffness from the static stiffnesses (usual hypothesis) or from the resonant values. The same conclusions applies to all configurations analysed by the author.

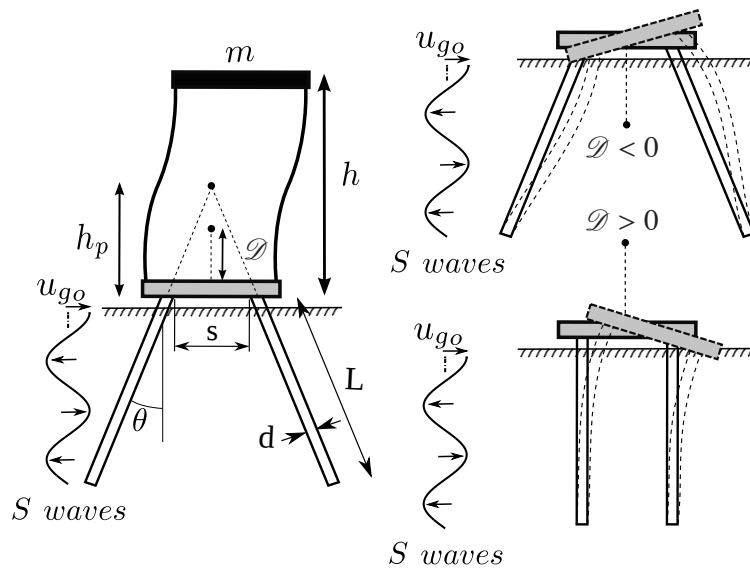


FIGURE 6.7: Center of stiffness \mathcal{D} and height of the geometric point h_p .

In the case of vertical piles ($\theta = 0^\circ$) the axes of both piles never meet above the cap so $h_p \rightarrow \infty$ whereas \mathcal{D}/d takes negative values. From this situation, and as the rake angle increases, h_p/d decreases while \mathcal{D}/d increases, even becoming positive. However, they do not cross each other in the range under study. In fact, \mathcal{D}/d and h_p/d could only coincide for rake angles over 30° and very low values of E_p/E_s , which would represent cases with no practical interest.

In order to confirm these observations and show that there is no significant influence on the seismic response in the transition between values of h/h_p smaller or greater than one, figure 6.9 shows the maximum response Q_m of a structure with $h/b = 2$ founded

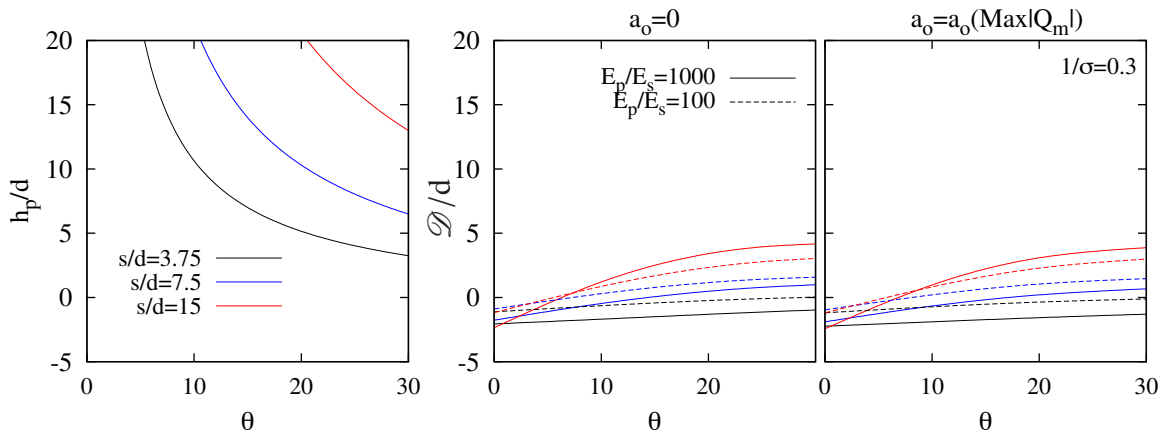


FIGURE 6.8: (a) Evolution of h_p/d (h_p : height above the cap of the geometric point where pile axes meet). (b) evolution of ratio \mathcal{D}/d (\mathcal{D} : center of stiffness) at $a_o = 0$ and $a_o = a_o(\text{Max}|Q_m|)$. All figures correspond to 2×2 pile groups ($b = s$) with different rake angles. ($h/b = 2$ and $\xi_s = 0.05$ in right plot.)

on a 2×2 pile group with inclined elements. In this case (being $b = s$), the relationship between the ratio h/h_p and the rake angle (also shown in figure 6.9) can be expressed as $h/h_p = 4 \tan \theta$, in such a way that rake angles θ between 0° and 25° imply ratios h/h_p from 0 to 1.865. Results for different values of $1/\sigma$ are depicted in this figure. Even though, for this configuration, a rake angle $\theta = 14^\circ$ makes the height h_p coincide with the height h of the vibrating mass ($h/h_p = 1$), no change of trend in the seismic shear forces is found for θ above or below 14° . Therefore, in the case of fixed pile-cap connections, this parameter h/h_p does not influence the behaviour of the system.

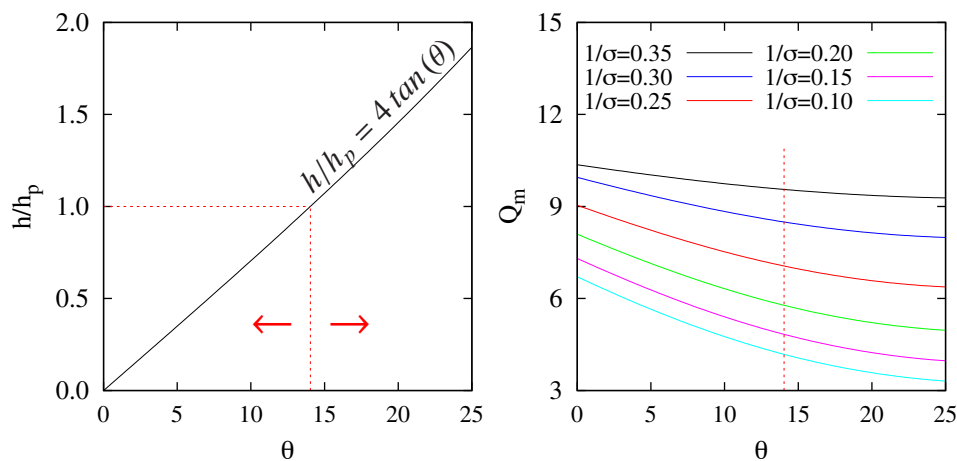


FIGURE 6.9: Evolution of the structural maximum response of a structure with $h/b = 2$ supported on 2×2 pile groups ($b = s$) with different rake angles when h/h_p varies from $h/h_p > 1$ to $h/h_p < 1$ (left or right to the vertical red line). $s/d = 7.5$, $E_p/E_s = 1000$ and $\xi_s = 0.05$.

6.5 Influence of rake angle on the elastic response spectra

In this section, for the purpose of illustrating the effects explained before, results in terms of effective system period \tilde{T}/T and damping $\tilde{\xi}$ are used to build modified response spectra that include the influence of pile rake angle θ . This way of representing the structural response has been previously used by other authors such as Veletsos and Meek [7] or Avilés *et al.* [14].

Firstly, and only in order to verify the validity of the approach of an equivalent SDOF system for the analysis of the seismic structural response, figure 6.10 compares the plots of peak acceleration at the vibrating mass for the 3DOF system against the peak pseudo-acceleration of the equivalent SDOF system, both as a function of its fixed-base fundamental period for the N-S component of the 1940 El Centro earthquake [114] and keeping $1/\sigma$ constant as by Veletsos and Meek [7]. In this figure, the vertical and the horizontal axes represent the structural pseudo-acceleration normalized to peak ground motion S_e/a_g and the fixed-base fundamental period T of the structure, respectively. The results represented in this figure correspond to superstructures with different slenderness ratios ($h/b = 1, 2, 5, 10$) supported on several 2×2 pile groups with pile spacing ratios $s/d = 3.75$ and $s/d = 15$. Three different values have been taken into account for the wave parameter: $1/\sigma = 0.1, 0.2, 0.3$. In this case, the rake angle is considered to be $\theta = 10^\circ$. For pile groups with $L/d = 7.5$ the results for the SDOF replacement oscillator reproduce very closely those obtained for the complete system. Nevertheless, minor discrepancies can be observed when $L/d = 30$ and $h/b = 1$ and 2 .

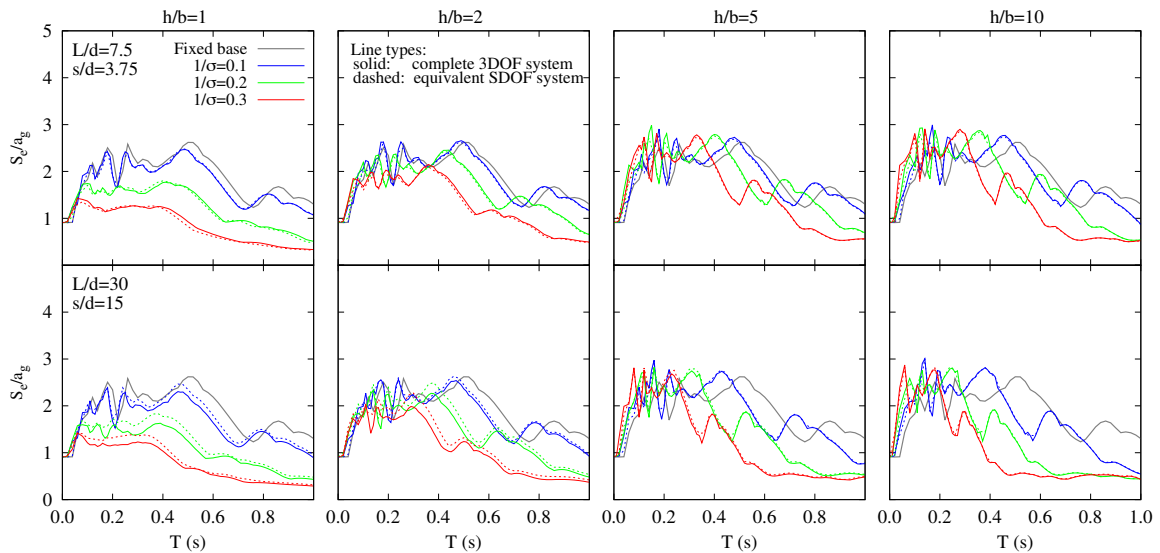


FIGURE 6.10: Elastic response spectra corresponding to the 1940 El Centro Earthquake for different 2×2 pile groups with piles inclined $\theta = 10^\circ$, $E_p/E_s = 1000$ and $\xi_s = 0.05$. $L/d(s/d) = 7.5(3.75), 30(15)$ and $h/b = 1, 2, 5, 10$. SDOF vs 3DOF.

Secondly, figure 6.11 presents elastic response spectra for different configurations of 2×2 pile groups with inclined elements. Foundation halfwidth b , pile slenderness ratio L/d and pile-to-pile separation ratio s/d are kept constant for all cases in the same row. The columns of the figure correspond to the cases with $h/b = 10 \cdot (1/\sigma) = 1, 2$ and 3 respec-

tively. These constraints imply that c_s is a common function of T in the three different spectra of a same row ($b = cte$, $L/d = cte$, $s/d = cte$), while growing fixed-base periods T convey softer soils, reason why the difference between response spectra of fixed- and flexible-base systems grow for increasing periods. It can be seen that, when $L/d = 7.5$, the influence of the rake angle increases with h/b . However, when $L/d = 30$ the influence of the rake angle becomes more appreciable as h/b decreases, while no clear trend is apparent for $L/d = 15$. On the other hand, the structural pseudo-acceleration tends to decrease for higher rake angles. This observation is rigorously true along the whole spectrum for $h/b = 10 \cdot (1/\sigma) = 1$ and $L/d = 7.5$ and 15 . In the other cases, however, there exist values of the fixed-base fundamental period of the structure for which pile inclination can be detrimental. As expected from the results shown in the previous sections, the more slender the superstructure, the less systematic and significant are the beneficial effects of rake angle on the structural response.

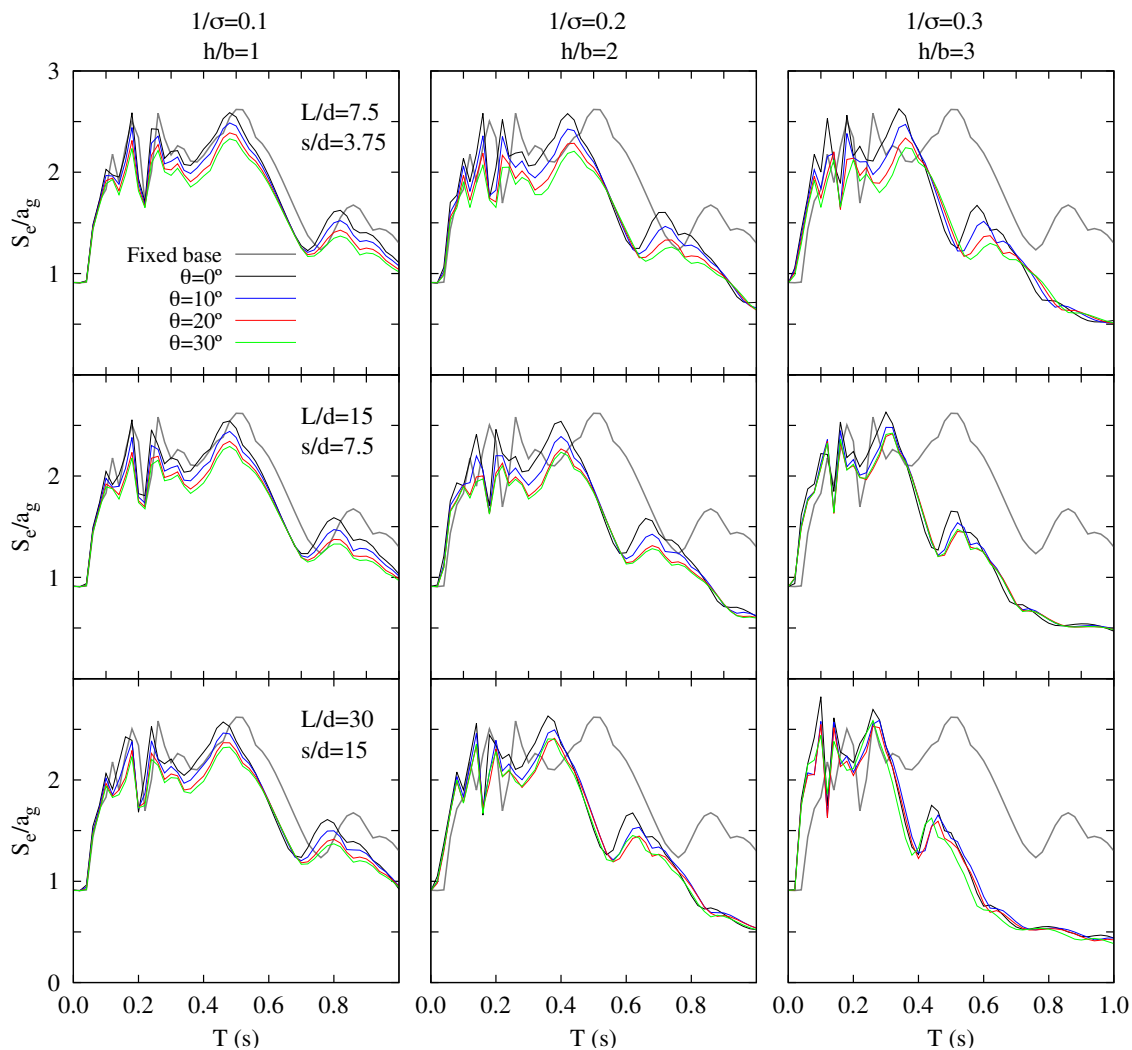


FIGURE 6.11: Elastic response spectra corresponding to the 1940 El Centro Earthquake for different 2×2 pile groups. $E_p/E_s = 1000$ and $\xi_s = 0.05$. $L/d(s/d) = 7.5(3.75)$, $15(7.5)$, $30(15)$ and $h/b = 1, 2, 3$.

Finally, in order to illustrate better the influence of structural height, figure 6.12 presents elastic response spectra of the motion of the vibrating mass of two superstructures with slenderness ratios $h/b = 1$ and 2 , respectively and the same fundamental period $T = 0.44$ s. A clear reduction of the spectral acceleration can be observed as the rake angle increases in both cases. These results are coherent with those provided by Giannakou *et al.* [48] for a case with less significant soil-structure interaction effects (smaller values of $1/\sigma$).

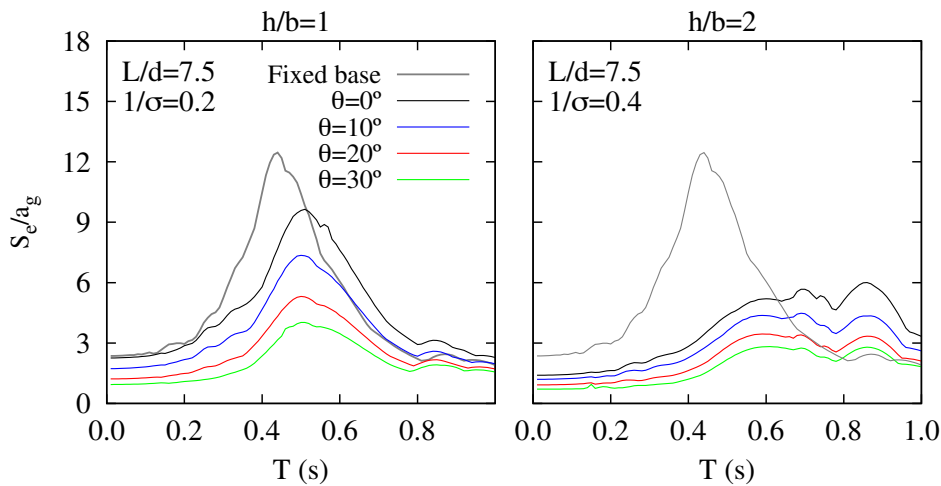


FIGURE 6.12: Elastic response spectra of the motion of the mass corresponding to the 1940 El Centro Earthquake a 2×2 pile group with $s/d = 3.75$ being $T = 0.44$ s. $E_p/E_s = 1000$ and $\xi_s = 0.05$.

6.6 Conclusions

This chapter addresses an analysis of the influence of the rake angle of piles on the dynamic response of pile-supported structures. To this end, a simple and accurate procedure, previously described and validated in chapter 2 as well as in [101], based on a substructuring model is used to obtain the maximum shear force at the base of the structure Q_m (paying particular attention to the differences among the values reached for Q_m in relation to θ) of an SDOF equivalent system which reproduces the coupled system response within the range where the peak response occurs. A BEM-FEM methodology is used to obtain the impedance functions and kinematic interaction factors of all configurations under investigation.

Results for 24 different cases are obtained. The main conclusions drawn from the analysis of the results obtained for the cases under investigation are summarised below:

- For short squat buildings, the effective period \tilde{T}/T is reduced as the rake angle increases due to the increment of the horizontal stiffness. However, for tall slender structures, \tilde{T}/T generally increases with the rake angle due to a reduction of the rocking impedance, except for close pile spacing.

- The increase of the rake angle leads to lower values of the maximum shear force at the base of the structure Q_m when $h/b = 1$ or $h/b = 2$. However, in the case of slender structures Q_m increases with the rake angle.
- The variation of the relationship h/h_p (h/h_p : ratio of the effective modal height h to the height of the geometric point where the extension of the raked pile axes meet above the cap h_p) above or below unity does not imply a change of trend in the structural response presented in terms of maximum shear force at the base of a structure when a fixed pile-cap connection exists. This is due to the fact that, in that case, the height \mathcal{D} of the centre of stiffness of the pile group is not related to h_p .
- In most cases, a reduction of the spectral acceleration can be observed as the rake angle increases. However, the more slender the superstructure, the less systematic and significant are the beneficial effects of rake angle on the structural response.

A decorative graphic consisting of several overlapping, dashed lines in a light grey color, forming a circular or semi-circular pattern on the left side of the page.

7. SUMMARY, CONCLUSIONS AND FUTURE RESEARCH DIRECTIONS

- 7.1 Summary and conclusions
- 7.2 Future research directions

7.1 Summary and conclusions

This dissertation proposes a simple and stable procedure for estimating the dynamic characteristics of a replacement oscillator able to accurately reproduce the dynamic behaviour of linear shear structures, when considering soil-structure interaction, within the range where the peak response occurs. The coupled-system response is obtained by using a substructuring model that includes the three-dimensional character of the foundations. In this model, the structure is considered as a SDOF in its fixed-base condition that represents, from a general point of view, one mode of vibration of multi-storey buildings. Both, dynamic and kinematic interaction effects are included in the analysis of this coupled system. Moreover, all the elements of the impedance matrix are considered. This procedure is applicable to shear structures supported on shallow, embedded or pile foundations.

A substructure approach, in which the system is subdivided into *building-cap* superstructure and *soil-foundation* stiffness and damping, is used herein to tackle this problem. As proposed by Kausel and Roësset [18], the solution is broken into three steps. The first two steps consist in determining the kinematic interaction factors and the impedance functions, being both complex-valued frequency-dependent functions. Once they are obtained, the response of the structure at each frequency is computed as it was supported on springs and dashpots, characterized by impedances, and subjected to the input motion defined in terms of kinematic interaction factors.

A procedure consisting in performing several basic algebraic operations has been applied in order to express the equations of motion of the coupled system in terms of a set of dimensionless parameters, covering the main features of SSI problems. This facilitates the performance of analyses that allow determining how the variations of these parameters affect the system dynamic response. Subsequently, the equivalence between the 3DOF system and a viscously damped SDOF oscillator is established in terms of the maximum shear force at the base of the structure per effective earthquake force unit. The usefulness of presenting the seismic response of the structure in these terms, lies in the fact that the product of this value with the structural mass and the corresponding free-field horizontal acceleration at ground surface level results in the amplitude of the shear force at the base of the structure.

The strategies used in the literature to estimate the dynamic properties of the SDOF equivalent system have been reviewed. This dissertation proposes a modified strategy that yields accurate results not only for shallow or embedded foundations but also for foundations consisting of piles. To this end, the loss of accuracy resulting from the simplifying assumptions extensively adopted by other authors is assessed for the case of pile foundations. In pioneering works the kinematic effects of the incident wave were not considered, using as base excitation a horizontal harmonic motion with constant amplitude. In this line, it has been found that the kinematic interaction can significantly affect the system effective damping and it should be considered to obtain accurate results both for the case of embedded and for pile foundations. Moreover, the influence of the coupled terms of the soil-impedance matrix is usually neglected in order to consider a diagonal impedance matrix which allows obtaining manageable approximated expressions for the dynamic response of the coupled system, as Avilés and Pérez-Rocha [14] do. However, neglecting the cross-coupled horizontal-rocking terms is not acceptable for pile foundations, not even for certain configurations of embedded foundations. In order to overcome



this drawback, in this work, the impedance matrix including the crossed-coupled terms is diagonalized by condensing the soil-foundation interaction to a point at a certain virtual depth, as some authors propose [27, 32].

Once the procedure has been formulated and implemented in a code, it has been validated through several comparisons against the results obtained by Veletsos and Meek [7] and those provided by Avilés and Pérez-Rocha [14] for shallow and embedded foundations, respectively. Negligible differences were obtained in all cases. Afterwards, the proposed procedure has been applied to the analysis of the SSI effects on the dynamic behaviour of linear shear structures founded on square pile groups embedded in homogeneous viscoelastic half-spaces subjected to vertically-incident S waves. In fulfilling this task, substructuring methodologies are of great interest due to their simplicity and affordable computational cost, which makes them particularly appropriate for conducting parametric analyses to determine the influence of the main parameters of the problem on the final response. The configurations of all the foundations under investigation consist of square regular groups of piles which are symmetrical with respect to planes xy and yz . All piles have identical material and geometrical properties. Both the foundations mass and the structural mass are assumed to be uniformly distributed over square areas. The columns of the structure are supposed to be massless and axially inextensible.

Impedances and kinematic interaction factors of the pile configurations under investigation, are calculated using the boundary element (BEM) - finite element (FEM) methodology previously developed by Padrón *et al.* [49, 71, 120]. The soil is modelled as a linear, isotropic, homogeneous, viscoelastic half-space by using boundary elements, while the piles are modelled by monodimensional finite elements as Euler-Bernoulli beams embedded in the soil. Coupling is performed by equilibrium and compatibility conditions. Welded boundary contact conditions at the pile-soil interfaces are assumed and the pile heads are constrained by a rigid pile-cap which is not in contact with the half-space. This formulation implies a reduction in terms of number of degrees of freedom in comparison with a pure multi-region boundary element method and provides accurate results at the same time.

Results for 21 different configurations of vertical pile groups have been obtained in order to accomplish an analysis of the influence of the main parameters of the SSI problem on the dynamic response of the structures supported on them. All the results obtained herein have a dimensionless character, thus their physical interpretation must be carefully done and requires a specific data processing taking into account the influence of every dimensionless parameter. Results in terms of period \tilde{T}/T and damping $\tilde{\xi}$ for different pile configurations are provided in ready-to-use graphs that can be used to build modified response spectra that include SSI effects. Maximum shear forces together with base displacement and rocking peak response are also depicted. Several interesting conclusions have been drawn from studying how the system dynamic behaviour is influenced by the variation of parameters such as the pile-soil Young's modulus ratio, the fixed-base structure damping ratio, the foundation-structure mass ratio, the mass density ratio, the structural slenderness ratio, the wave parameter, the pile slenderness ratio, the spacing between adjacent piles, the embedment ratio and the number of piles. These conclusions are consistent with those drawn in relevant literature for embedded foundations. The main conclusions are summarised below:

- Piles configurations which imply stiffer foundations yield a reduction on the effec-

tive period of the coupled system: larger number of piles (figure 5.12) or embedment ratio (figure 5.17), and lower pile slenderness ratio (figure 5.14). The obtained results show that this conclusion is not applicable for short and squat buildings, case in which the opposite occurs.

- The effective damping increases with the foundation stiffness (see figures 5.12, 5.14 and 5.17).
- Slender buildings as well as soft soils magnify the SSI effects for a particular configuration. This trend can be reversed for very stiff foundations or very short and squat buildings (see figure 5.9).
- The effective damping for slender buildings is close to that corresponding to fixed-base condition or lower. For short or medium-height buildings ($h/b < 5$), the effective damping increases as σ decreases and this effect becomes more relevant for stiffer piles configurations (see *e.g.* figures 5.12 and 5.17).
- As the influence of the SSI effects increases, the maximum shear force at the base of the structure remains lower than that corresponding to fixed-base condition for buildings with $h/b \leq 2$ in all configurations studied. For larger values of the structural slenderness ratio, the maximum shear force increases when these effects are considered (see *e.g.* figure 5.14). Stiffer foundations yield lower shear forces if $h/b < 5$ (see *e.g.* figure 5.12). However, for greater slenderness, the results show variations in the trend that depend on the parameter analysed.
- The foundation horizontal displacement and rocking increase for softer soils as well as for more flexible geometric configurations (see *e.g.* figures 5.14 or 5.17).
- Lower values of the pile-soil Young's modulus ratio E_p/E_s result in an increase of the foundation stiffness, which leads to lower values of the effective period and greater values of the effective damping.
- An increase of the mass density ratio δ implies greater values of the system effective period and damping.
- The effective period is not affected by variations of the fixed-base structure damping ratio ξ . However, the influence of this variation on the effective damping is more important as the wave parameter increases.
- In a significant number of cases, the system dynamic response is subestimated when neglecting the cross-coupled impedances.
- The results computed without considering the kinematic interaction effects are not on the side of safety, except for those corresponding to non-slender structures $h/b \leq 1$.

For the purpose of clarifying the beneficial or detrimental role of foundations including inclined piles, this dissertation shed light on two aspects that required further investigation: the kinematic interaction factors of pile foundations with inclined elements and the influence of pile rake angle on the seismic response of the superstructure.

This document provides kinematic interaction factors of single inclined piles, as well as of 2×2 and 3×3 pile groups including battered elements. The possibility of the development of large kinematic bending moments and shear forces when inclining the piles has resulted in a negative attitude towards batter piles (see [44]). In order to study the effect of rake angle on kinematic bending moments, maximum pile bending strain at pile heads has been also presented for some cases. Numerical results for different soil properties, rake angles and configurations have been obtained.

The relevance and main trends observed in the influence of the rake angle on the kinematic interaction factors of the analysed foundations have been inferred from the presented results. An important dependence of the kinematic interaction factors on the rake angle has been observed together with the existence of an inclination angle at which cap rotation and excitation become out of phase in the low-to-mid frequency range.

The main conclusions drawn from the analysis of the results obtained for the cases under study are summarised below:

- The ability of a deep foundation to filter the seismic input increases significantly if all or some of its members are inclined in the direction of shaking.
- The beneficial role of the pile inclination disappears at high frequencies.
- Both kinematic interaction factors strongly depends on the direction of inclination of piles. Deep foundations including piles inclined perpendicular to the direction of excitation generally have a detrimental role in terms of horizontal motion.
- The rotational kinematic interaction factor I_φ of battered single piles is almost independent of the rake angle.
- Cap rotation and horizontal free-field ground motion become out of phase when inclining piles parallel to the direction of excitation or symmetrically along the cap diagonals. This effect depend on the rake angle, as well as on the pile-soil Young's modulus ratio.
- There exists an optimum rake angle (usually small) for which a minimum rotational motion at the pile cap is obtained in the low-to-mid frequency range. This phenomenon could be used in order to minimize the seismic input of a structure submitted to seismic loads although, in some cases, the realization of the optimum small rake angles could not be feasible. A monotonic trend of increasing cap rotation for increasing rake angles is observed for larger angles.
- Higher stiffness ratios (softer soils) result in an increase of the rake angle at which cap rotation and horizontal free-field ground surface motion become out of phase at low-to-mid frequencies.
- The kinematic response of pile groups including battered piles is less sensitive to variations of the rake angle as the pile spacing ratio s/d or the number of piles increase.
- Lower stiffness ratios E_p/E_s (stiffer soils) lead to higher cap rocking motions.

- Contrary to what occurs for vertical piles, a reduction of the pile slenderness ratio L/d leads to decreasing values of the rocking motion at the pile cap, at least in a low frequency range, when considering configurations with piles inclined parallel to the direction of excitation.
- In the mid-to-low frequency range (usually the most important in the seismic design of deep foundations), maximum pile bending strains at pile heads tend to increase when piles are inclined parallel to the direction of the shaking; but tend to decrease when the piles are inclined perpendicular to such direction.

Furthermore, an analysis of the influence of the rake angle of piles on the dynamic response of pile-supported structures is accomplished. To this end, the dynamic response of slender and non-slender structures supported on several configurations of 2×2 and 3×3 pile groups including battered elements is studied considering soil-structure interaction.

Results corresponding to 24 different configurations are expressed in terms of flexible-base period and maximum shear force at the base of the structure. Moreover, modified response spectra considering soil-structure interaction effects are provided for different rake angles. The main conclusions drawn from the analysis of the results obtained for the cases under investigation are summarised below:

- It is shown that an increment of the rake angle can result in beneficial or detrimental effects depending on the structural slenderness ratio.
- For short squat buildings, the effective period \tilde{T}/T is reduced as the rake angle increases due to the increment of the horizontal stiffness. However, for tall slender structures, \tilde{T}/T generally increases with the rake angle due to a reduction of the rocking impedance, except for close pile spacing.
- The increase of the rake angle leads to lower values of the maximum shear force at the base of the structure Q_m when $h/b = 1$ or $h/b = 2$. However, in the case of slender structures Q_m increases with the rake angle.
- The variation of the relationship h/h_p (h/h_p : ratio of the effective modal height h to the height of the geometric point where the extension of the raked pile axes meet above the cap h_p) above or below unity does not imply a change of trend in the structural response presented in terms of maximum shear force at the base of a structure when a fixed pile-cap connection exists. This is due to the fact that, in that case, the height \mathcal{D} of the centre of stiffness of the pile group is not related to h_p .
- In most cases, a reduction of the spectral acceleration can be observed as the rake angle increases. However, the more slender the superstructure, the less systematic and significant are the beneficial effects of rake angle on the structural response.

7.2 Future research directions

The procedure and the model proposed in this dissertation have been used to perform several parametric analyses of the dynamic behaviour of linear shear structures supported on pile groups and subjected to vertically incident plane shear S waves. Moreover,

the BEM-FEM coupling formulation, previously developed by Padrón *et al.* [49, 71, 120], has been used to analyse the seismic response of several configurations of pile groups considering SSI. Some of the future developments of the presented work are:

- Parametric analysis including other foundation and superstructure configurations.
- Validation against experimental results such as those provided by Escoffier [51] or Goit and Masato [53].
- Parametric studies on the seismic behaviour of pile groups, including vertical or battered elements, subjected to different types of seismic waves (P, S and Rayleigh waves) and considering different directions of incidence.
- Search of the optimal configuration for a certain soil-structure system.
- Determining interpolated expressions for the equivalent SDOF system dynamic characteristics, which would allow obtaining more accurate design criteria for building structures.
- Developing a methodology that enables the consideration of SSI effects in the analysis of the dynamic response of multi-degree-of-freedom systems by superposition. This methodology would allow addressing the analysis of a system with n degrees of freedom by dividing it in n SDOF systems. Thus, the dynamic response associated with each mode of vibration could be obtained separately by substructuring, taking into account soil-structure interaction effects. The accuracy of the proposed methodology would be assessed by comparing its results against those obtained from the direct resolution of the multi-degree-of-freedom system by substructuring.
- Study of the influence of the configuration of the foundation, as well as that of the rake angle of piles, on the structural efforts in piles and cap.
- Analysis of the shear forces and bending moments induced by the earthquake in the piles as well as the sensitivity of these efforts to the variations of parameters as: superstructure slenderness ratio, soil-structure mass ratio, soil-structure stiffness ratio, pile foundation configuration, pile-soil stiffness ratio, pile slenderness ratio, stratigraphy of the soil, type of the incident waves and direction of incidence.
- Analysis of the influence on the system response of the contact between the foundation mat and the half-space, in the case of embedded foundations, as well as the influence of the foundation embedment ratio.
- Developing a compendium of maximum response spectra that could serve as a reference for designing structures considering the effects of soil-structure interaction.



Appendices



Contenidos



Contenidos	III
Índice de figuras	V
Índice de tablas	IX
A Summary of the dissertation in Spanish	191
A.1. Introducción y antecedentes	191
A.1.1. Introducción	191
A.1.2. Revisión bibliográfica	194
A.1.3. Alcance y objetivos	198
A.1.4. Publicaciones derivadas de esta tesis doctoral	199
A.1.5. Estructura del documento	200
A.2. Metodología de subestructuración	203
A.2.1. Introducción	203
A.2.2. Descripción del problema	203
A.2.3. Modelo de subestructuración	205
A.2.4. Parámetros que caracterizan el comportamiento dinámico de los pilotes	207
A.2.5. Influencia de la geometría de la sección transversal del pilote	211
A.2.6. Ecuaciones del sistema y parámetros adimensionales	222
A.2.7. Diagonalización de la matriz de impedancias	225
A.2.8. Periodo y amortiguamiento efectivos del sistema acoplado suelo-cimiento-estructura	231
A.2.9. Implementación	246
A.2.10. Validación del modelo	250
A.3. Comportamiento sísmico de estructuras sustentadas por pilotes verticales	262
A.3.1. Introducción	262
A.3.2. Configuraciones objeto de estudio	262
A.3.3. Impedancias y factores de interacción cinemática	266
A.3.4. Influencia de la relación entre la masa del encepado y la masa de la estructura	272
A.3.5. Influencia de las impedancias cruzadas	274
A.3.6. Influencia del ratio de esbeltez estructural y el parámetro de onda	278
A.3.7. Influencia de los factores de interacción cinemática	281
A.3.8. Influencia del ratio de esbeltez de los pilotes	283
A.3.9. Influencia del ratio de embebimiento	286
A.3.10. Influencia del número de pilotes	289
A.3.11. Influencia del ratio del módulo de Young pilote-suelo	290
A.3.12. Influencia del coeficiente de amortiguamiento de la estructura en base rígida	292
A.3.13. Influencia de la densidad de masa relativa estructura-suelo	293
A.3.14. Conclusiones	294
A.4. Resumen, conclusiones y desarrollos futuros	296
A.4.1. Resumen y conclusiones	296
A.4.2. Desarrollos futuros	302



Índice de figuras

A.1. Definición del problema.	204
A.2. Definición del problema y modelo de subestructuración.	205
A.3. El método de los tres pasos.	206
A.4. Modelo Winkler.	208
A.5. Sección transversal de los pilotes.	211
A.6. Geometría de la cimentación pilotada.	215
A.7. Influencia de la geometría de la sección transversal de los pilotes. Impedancias horizontales de distintos grupos de 2×2 y 3×3 pilotes con elementos verticales ($\theta = 0^\circ$) o inclinados ($\theta = 30^\circ$).	216
A.8. Influencia de la geometría de la sección transversal de los pilotes. Impedancias de balanceo de distintos grupos de 2×2 y 3×3 pilotes con elementos verticales ($\theta = 0^\circ$) o inclinados ($\theta = 30^\circ$).	217
A.9. Influencia de la geometría de la sección transversal de los pilotes. Impedancias cruzadas horizontal-balanceo de distintos grupos de 2×2 y 3×3 pilotes con elementos verticales ($\theta = 0^\circ$) o inclinados ($\theta = 30^\circ$).	218
A.10. Influencia de la geometría de la sección transversal de los pilotes. Factor de interacción cinemática traslacional I_u para distintos grupos de 2×2 y 3×3 pilotes con elementos verticales ($\theta = 0^\circ$) o inclinados ($\theta = 30^\circ$).	220
A.11. Influencia de la geometría de la sección transversal de los pilotes. Factor de interacción cinemática rotacional I_φ para distintos grupos de 2×2 y 3×3 pilotes con elementos verticales ($\theta = 0^\circ$) o inclinados ($\theta = 30^\circ$).	221
A.12. Modelo equivalente con matriz de impedancias diagonalizada.	226
A.13. Modelo de subestructuración de una estructura de una planta y oscilador equivalente de un grado de libertad.	232
A.14. Estrategia de búsqueda del valor máximo (MAX) para obtener la frecuencia natural y el amortiguamiento del sistema de 1GDL equivalente.	233
A.15. Estrategia del cálculo de la raíz (ROOT) para obtener la frecuencia natural y el amortiguamiento del sistema de 1GDL equivalente.	234
A.16. Aproximación mediante un oscilador de reemplazo de la respuesta de un sistema de 3GDL soportado por un grupo de 3×3 pilotes con $s/d = 5$ y $L/b = 1$. $E_p/E_s = 10^3$ y $\xi_s = 0.05$. Estrategia ROOT.	235
A.17. Aproximación mediante un oscilador de reemplazo de la respuesta de un sistema de 3GDL soportado por un grupo de 3×3 pilotes con $s/d = 5$ y $L/b = 4$. $E_p/E_s = 10^3$ y $\xi_s = 0.05$. Estrategia ROOT.	236
A.18. Aproximación mediante un oscilador de reemplazo de la respuesta de un sistema de 3GDL soportado por un grupo de 3×3 pilotes con $s/d = 5$ y $L/b = 2$. $E_p/E_s = 10^3$ y $\xi_s = 0.05$. Estrategia EIGEN-S.	238
A.19. Procedimiento propuesto (EIGEN) para obtener la frecuencia natural del sistema de 1GDL equivalente.	239
A.20. Aproximación mediante un oscilador de reemplazo de la respuesta de un sistema de 3GDL soportado por un grupo de 3×3 pilotes con $s/d = 5$ y $L/b = 4$. $E_p/E_s = 10^3$ y $\xi_s = 0.05$. EIGEN vs EIGEN-S.	240



A.21.Influencia de los términos de segundo orden del amortiguamiento. Periodo \tilde{T}/T y amortiguamiento $\tilde{\xi}$ efectivos para grupos de 2×2 pilotes con $L/b = 2$	241
A.22.Influencia de los términos de segundo orden del amortiguamiento. Periodo \tilde{T}/T y amortiguamiento $\tilde{\xi}$ efectivos para grupos de 4×4 pilotes con $s/d = 3.75$	242
A.23.Influencia de los términos de segundo orden del amortiguamiento. Periodo \tilde{T}/T y amortiguamiento $\tilde{\xi}$ efectivos para grupos de 2×2 , 3×3 y 4×4 pilotes con $L/b = 4$ y $L/d = 15$	243
A.24.Estrategias para obtener la frecuencia natural y el amortiguamiento del sistema de 1GDL equivalente.	244
A.25.Procedimiento del cálculo de la raíz (EIGEN) vs algoritmo de búsqueda del máximo (MAX). Periodo \tilde{T}/T y amortiguamiento efectivos $\tilde{\xi}$ para un grupo de 2×2 pilotes.	245
A.26.Aproximación mediante un oscilador de reemplazo de la respuesta de un sistema de 3GDL soportado por un grupo de 2×2 pilotes. $L/b = 1, 7.5$, y 15 . Funciones de transferencia, espectro de respuesta elástica correspondiente al terremoto de El Centro de 1940 y amortiguamiento efectivo ($\tilde{\xi}$) del oscilador equivalente de 1GDL.	246
A.27.Definición del problema.	251
A.28.Coeficientes adimensionales en las expresiones de la rigidez y el amortiguamiento del cimiento.	253
A.29.Comparación entre los resultados del modelo propuesto y los proporcionados por Veletsos y Meek.	255
A.30.Comparación entre los coeficientes proporcionados para las impedancias por Veletsos y Meek y aquellos propuestos por Veletsos y Verbic.	256
A.31.Definición del problema.	257
A.32.Comparación entre los resultados obtenidos mediante el modelo propuesto y aquellos proporcionados por Avilés y Pérez-Rocha.	260
A.33.Geometría de las cimentaciones con pilotes verticales.	264
A.34.Representación de las distintas configuraciones de pilotes verticales considerando el mismo diámetro $d = \text{cte}$ para todos los casos.	265
A.35.Rango de la frecuencia adimensional $\omega d/c_s$ para todos los casos analizados.	266
A.36.Impedancias para distintos grupos de 2×2 pilotes. $E_p/E_s = 10^3$ y $\xi_s = 0.05$	267
A.37.Impedancias para distintos grupos de 3×3 pilotes. $E_p/E_s = 10^3$ y $\xi_s = 0.05$	268
A.38.Impedancias para distintos grupos de 4×4 pilotes. $E_p/E_s = 10^3$ y $\xi_s = 0.05$	268
A.39.Factores de interacción cinemática para distintos grupos de pilotes embebidos en un suelo con $E_p/E_s = 10^3$ y $\xi_s = 0.05$	269
A.40.Factores de interacción cinemática para distintos grupos de 2×2 pilotes. $E_p/E_s = 10^3$ y $\xi_s = 0.05$	269
A.41.Factores de interacción cinemática para distintos grupos de 3×3 pilotes. $E_p/E_s = 10^3$ y $\xi_s = 0.05$	270
A.42.Factores de interacción cinemática para grupos de 4×4 pilotes. $E_p/E_s = 10^3$ y $\xi_s = 0.05$	270
A.43.Impedancias para distintos grupos de 2×2 pilotes. $E_p/E_s = 10^2$ y $\xi_s = 0.05$	271
A.44.Factores de interacción cinemática para distintos grupos de 2×2 pilotes. $E_p/E_s = 10^2$ y $\xi_s = 0.05$	271
A.45.Influencia de la relación de masas cimiento-estructura m_o/m . Respuesta máxima estructural para grupos de 4×4 pilotes. $L/b = 2$, $E_p/E_s = 10^3$ y $\xi_s = 0.05$	273



A.46.Representación esquemática de las distintas configuraciones analizadas en la figura A.45 considerando $d = \text{cte.}$	273
A.47.Influencia de las impedancias cruzadas. Periodo efectivo \tilde{T}/T , amortiguamiento $\tilde{\xi}$ y respuesta máxima estructural Q_m para un grupo de 2×2 pilotes con $L/b = 2$, $E_p/E_s = 10^3$ y $\xi_s = 0.05$	275
A.48.Representación esquemática de las configuraciones de grupos de pilotes analizadas en la figura A.47 considerando $d = \text{cte.}$	275
A.49.Influencia de las impedancias cruzadas. Periodo efectivo \tilde{T}/T , amortiguamiento $\tilde{\xi}$ y máxima respuesta estructural Q_m para un grupo de 2×2 pilotes con $L/d = 15$, $E_p/E_s = 10^3$ y $\xi_s = 0.05$	276
A.50.Representación esquemática de las configuraciones de grupos de pilotes analizadas en la figura A.49 considerando $d = \text{cte.}$	276
A.51.Influencia de las impedancias cruzadas. Periodo efectivo \tilde{T}/T , amortiguamiento $\tilde{\xi}$ y respuesta máxima estructural Q_m para grupos de pilotes con $L/d = 15, L/b = 2$, $E_p/E_s = 10^3$ y $\xi_s = 0.05$	277
A.52.Representación esquemática de las configuraciones de grupos de pilotes analizadas en la figura A.51 considerando $d = \text{cte.}$	277
A.53.Influencia del ratio de esbeltez de la estructura h/b . Periodo efectivo \tilde{T}/T para un grupo de 4×4 pilotes con $s/d = 3.75$ (columna izquierda) y para un grupo de pilotes con $L/b = 4$ y $L/d = 15$ (columna derecha). $E_p/E_s = 10^3$ y $\xi_s = 0.05$	279
A.54.Representación esquemática de las configuraciones de grupos de pilotes analizadas en la columna izquierda de la figura A.53 considerando $d = \text{cte.}$	280
A.55.Representación esquemática de las configuraciones de grupos de pilotes analizadas en la columna derecha de la figura A.53 considerando $d = \text{cte.}$	280
A.56.Influencia de la interacción cinemática y el número de pilotes. Periodo efectivo \tilde{T}/T , amortiguamiento $\tilde{\xi}$, respuesta máxima estructural Q_m y factor de interacción cinemática $ I_u + (h/b)I_\varphi $ para grupos de pilotes con $L/b = 4$, $L/d = 15$, $E_p/E_s = 10^3$ y $\xi_s = 0.05$	282
A.57.Representación esquemática de las configuraciones analizadas en la figura A.56 considerando $d = \text{cte.}$	282
A.58.Influencia del ratio de esbeltez de los pilotes L/d . Periodo efectivo \tilde{T}/T , amortiguamiento $\tilde{\xi}$, respuesta máxima estructural Q_m y valores relativos máximos del desplazamiento horizontal $ \omega_n^2 u_r^c / \ddot{u}_{g0} $ y el giro $ \omega_n^2 h \varphi_r^c / \ddot{u}_{g0} $ del cimiento para un grupo de 2×2 pilotes con $L/b = 2$, $E_p/E_s = 10^3$ y $\xi_s = 0.05$	284
A.59.Representación esquemática de las configuraciones de grupos de pilotes analizadas en las figuras A.58 y A.60 considerando $d = \text{cte.}$	285
A.60.Influencia del ratio de esbeltez de los pilotes L/d . Periodo efectivo \tilde{T}/T para grupos de 2×2 pilotes con $L/b = 2$, $E_p/E_s = 10^3$ y $\xi_s = 0.05$. $h/b = 0.6$	285
A.61.Influencia del ratio de embebimiento L/b . Periodo efectivo \tilde{T}/T , coeficiente de amortiguamiento $\tilde{\xi}$, respuesta máxima estructural Q_m y valores relativos máximos del desplazamiento horizontal $ \omega_n^2 u_r^c / \ddot{u}_{g0} $ y el giro $ \omega_n^2 h \varphi_r^c / \ddot{u}_{g0} $ del cimiento para un grupo de 4×4 pilotes con $s/d = 3.75$, $E_p/E_s = 10^3$ y $\xi_s = 0.05$	287
A.62.Representación esquemática de las configuraciones de grupos de pilotes analizadas en las figuras A.61 y A.63 considerando $d = \text{cte.}$	288
A.63.Influencia del ratio de embebimiento L/b . Periodo efectivo \tilde{T}/T para grupos de 4×4 pilotes con $s/d = 3.75$, $E_p/E_s = 10^3$ y $\xi_s = 0.05$. $h/b = 0.6$	288



A.64. Influencia del número de pilotes. Valores máximos relativos del desplazamiento horizontal $ \omega_n^2 u_r^c / \ddot{u}_{g0} $ y el giro $ \omega_n^2 h \varphi_r^c / \ddot{u}_{g0} $ del cimiento para grupos de pilotes con $L/b = 4$, $L/d = 15$, $E_p/E_s = 10^3$ y $\xi_s = 0.05$	289
A.65. Representación esquematizada de las configuraciones analizadas en la figura A.64 considerando $d = \text{cte}$	290
A.66. Influencia del ratio del módulo de Young pilote-suelo E_p/E_s . Periodo efectivo \tilde{T}/T , amortiguamiento $\tilde{\xi}$ y respuesta máxima estructural Q_m para grupos de 2×2 pilotes con $L/b = 2$ y $\xi_s = 0.05$	291
A.67. Representación esquemática de las configuraciones de grupos de pilotes analizadas en la figura A.66 considerando $d = \text{cte}$	291
A.68. Influencia del coeficiente de amortiguamiento de la estructura en base rígida ξ . Periodo efectivo \tilde{T}/T , amortiguamiento $\tilde{\xi}$ y máxima respuesta estructura Q_m para un grupo de 3×3 pilotes con $L/d = 30$, $L/b = 2$, $E_p/E_s = 10^3$ y $\xi_s = 0.05$	292
A.69. Influencia de la densidad de masa relativa entre la estructura y el suelo δ . Periodo efectivo \tilde{T}/T , amortiguamiento $\tilde{\xi}$ y respuesta máxima estructural Q_m para un grupo de 3×3 pilotes con $L/d = 15$, $L/b = 2$, $E_p/E_s = 10^3$ y $\xi_s = 0.05$	293



Índice de tablas

A.1. Valores de los parámetros adimensionales que caracterizan el problema de interacción suelo-estructura.	213
A.2. Geometría y propiedades equivalentes de la sección transversal circular del modelo.	213
A.3. Geometría y propiedades del material de la sección transversal real.	214
A.4. Error porcentual cometido en el cálculo de impedancias al usar un modelo de sección circular maciza para representar una sección anular con $\gamma = 0.9$	219
A.5. Error porcentual cometido en el cálculo de los factores de interacción cinemática al usar un modelo de sección circular maciza para representar una sección anular con $\gamma = 0.9$	222
A.6. Coeficientes numéricos de las ecuaciones de la (A.102) a la (A.105), según Veltsos y Verbic.	254
A.7. Configuraciones de grupos de pilotes verticales.	263



A. SUMMARY OF THE DISSERTATION IN SPANISH

- A.1. Introducción y antecedentes
- A.2. Metodología de subestructuración
- A.3. Comportamiento sísmico de estructuras sustentadas por pilotes verticales
- A.4. Resumen, conclusiones y desarrollos futuros

A.1. Introducción y antecedentes

A.1.1. Introducción

Las cimentaciones pilotadas son cimentaciones profundas que están constituidas por uno o varios elementos columnares largos y esbeltos cuyas cabezas suelen estar agrupadas mediante un bloque de hormigón al que se denomina encepado. Este encepado transfiere y distribuye las cargas desde la superestructura hasta la cimentación y además restringe el desplazamiento lateral en la parte superior de los pilotes cuando es preciso. Los pilotes suelen ser de acero, hormigón armado, hormigón pretensado y, en algunos casos, pueden ser de madera.

El uso de pilotes y cimentaciones pilotadas data de tiempos prehistóricos. Los habitantes de la región alpina, durante el Neolítico y la Era de Bronce, construían sus hogares sobre pilotes de madera hincados en los fondos blandos de lagos de escasa profundidad. Este tipo de construcción se utilizó también en distintos lugares alrededor del mundo como Oceanía, África y Sudamérica. Venecia se sustenta sobre pilotes de madera desde el siglo IX. En torno a un millón de pilotes de madera fueron hincados bajo el agua para la construcción de la Iglesia de Santa María de la Salud en Venecia en el siglo XVII. Los pilotes de acero comenzaron a utilizarse en el siglo XIX y fue en el siglo XX cuando empezaron a emplearse los pilotes de hormigón. Hoy en día, las cimentaciones pilotadas se utilizan con frecuencia para soportar estructuras con alturas elevadas, edificaciones que albergan reactores nucleares, pilares de puentes, plataformas en mar abierto y estructuras marinas.

Las cimentaciones pilotadas suelen utilizarse para transferir cargas desde una estructura sobre rasante, a través de un terreno subyacente blando y con poca capacidad portante o incluso a través de suelos expansivos o colapsables, hasta estratos más profundos con mayor estabilidad y capacidad de carga. Este tipo de cimentación también se emplea para transmitir cargas de forma gradual mediante rozamiento en aquellos casos en los que no se encuentra una capa de suelo competente dentro de un rango de profundidad aceptable. Asimismo, pueden utilizarse pilotes verticales sometidos a flexión y cortante o bien pilotes inclinados para soportar grandes cargas horizontales. Por otra parte, este tipo de cimentación también es una opción recomendable en aquellas situaciones en las que el suelo subyacente no reúne las condiciones necesarias para evitar un asentamiento excesivo. El uso de cimentaciones pilotadas puede mejorar la respuesta sísmica de las estructuras, ya que puede aumentar el amortiguamiento del sistema y reducir la magnitud de la sollicitación sísmica en la base de la estructura.

Los métodos convencionales para el análisis y el diseño de estructuras suelen asumir la condición de base rígida. Esto implica que el sistema cimentación-suelo que se encuentra bajo la estructura es rígido y no se tienen en cuenta los efectos de la interacción dinámica suelo-estructura. Dicha interacción se compone de la interacción inercial y la interacción cinemática. La interacción inercial surge como resultado de las fuerzas de inercia transmitidas por la masa de la superestructura al suelo portante. Por otra parte, la interacción cinemática aparece debido a que la presencia de la cimentación altera el movimiento del terreno generado por las ondas sísmicas incidentes. El estudio del comportamiento de las estructuras durante eventos sísmicos ha revelado que la interacción suelo-estructura puede afectar a la respuesta dinámica de edificios, especialmente en el caso de estructuras rígidas cimentadas sobre suelos relativamente blandos.

A la vista de lo anterior, un análisis adecuado de la respuesta dinámica de la estructura requiere del desarrollo de modelos que incorporen, de manera rigurosa, la interacción entre la estructura y el suelo sobre el que se encuentra. Las metodologías utilizadas para el análisis sísmico teniendo en cuenta la interacción suelo-estructura pueden clasificarse en dos categorías: métodos directos y métodos de subestructuración.

El método de los tres pasos es una metodología de subestructuración que suele utilizarse para analizar el comportamiento sísmico de estructuras considerando los efectos de interacción suelo-estructura que aparecen cuando no se asumen condiciones de base rígida para la estructura. Como su propio nombre indica, esta metodología consiste en dividir la resolución del problema en tres partes. La primera consiste en determinar el movimiento de la cimentación sometida a las ondas sísmicas y considerando que tanto la estructura como la cimentación carecen de masa. El siguiente paso aborda la obtención de las impedancias que representan la rigidez del cimiento y el amortiguamiento asociado a la interacción cimiento-suelo. Finalmente, el último paso es el cálculo, para cada valor de la frecuencia, de la respuesta de la estructura sustentada sobre resortes y amortiguadores caracterizados por la matriz de impedancias de la cimentación y sometidos en la base al movimiento calculado en el primer paso. Esta metodología arroja resultados suficientemente precisos para el tipo de problema que se aborda en esta tesis y su implementación es sencilla. Por otra parte, cabe señalar que se trata de una metodología especialmente apropiada para la realización de análisis paramétricos, encaminados a determinar la influencia de los principales parámetros del problema de interacción suelo-estructura sobre la respuesta del sistema, con un coste computacional asumible. Otra ventaja importante de esta metodología reside en el hecho de que las condiciones de simetría pueden aplicarse para reducir el tamaño del modelo, sin menoscabo de la precisión, si la cimentación cumple dichas condiciones incluso en los casos en los que la superestructura no las cumple.

Por otra parte, los métodos directos modelan en un único paso el suelo, la cimentación y la estructura, y consideran la interacción mutua de una forma más rigurosa. El principal inconveniente de estos métodos es su alto coste computacional, que deriva de la complejidad de los modelos que tienen un mayor número de grados de libertad. De hecho, normalmente se llevan a cabo menos estudios paramétricos utilizando métodos directos, puesto que cualquier variación en las propiedades de cualquier parte del sistema requieren de la realización un nuevo análisis completo. Sin embargo, estos métodos son especialmente competitivos en el análisis de los fenómenos de interacción entre estructuras cercanas y en problemas que involucran no linealidades.

El uso de metodologías de subestructuración aplicadas al análisis de la respuesta dinámica de estructuras soportadas por cimentaciones superficiales o embebidas ha sido objeto de numerosas investigaciones. Sin embargo, el estudio del comportamiento dinámico de estructuras soportadas por pilotes ha recibido menos atención por parte de los investigadores. Con el ánimo de contribuir a profundizar en este aspecto, este trabajo aprovecha las ventajas de la metodología de subestructuración para desarrollar un procedimiento simple y estable que permita la estimación de los periodos y ratios de amortiguamiento de estructuras a cortante soportadas por grupos de pilotes, teniendo en cuenta la interacción suelo-estructura. Para ello, se establece una equivalencia entre el sistema objeto de estudio y un oscilador de un solo grado de libertad que reproduce, con la mayor precisión posible, la respuesta del sistema acoplado dentro del rango donde se produce la respuesta máxima. La respuesta del sistema acoplado se obtiene mediante

el uso de un modelo de subestructuración en el que la estructura se considera como una estructura a cortante de un solo grado de libertad que representa, desde un punto de vista general, uno de los modos de vibración en el caso de edificios de varias plantas. En el análisis del sistema acoplado se tienen en cuenta los efectos de interacción cinemática y todos los elementos de la matriz de impedancias. Las impedancias y los factores de interacción cinemática, correspondientes a las distintas configuraciones de grupos de pilotes analizadas, se han obtenido utilizando una formulación acoplada de elementos finitos y elementos de contorno. La estructura se considera asentada sobre un semiespacio elástico y homogéneo y sometida a ondas S de incidencia vertical.

Una vez formulado, implementado y validado el modelo, este se aplicará al estudio de cimentaciones pilotadas constituidas por elementos verticales e inclinados. Los pilotes inclinados suelen emplearse en cimentaciones que deben soportar importantes cargas laterales. Los pilotes verticales transmiten estas cargas únicamente mediante flexión y cortante. Sin embargo, los pilotes inclinados tienen la capacidad de transmitir las cargas laterales principalmente mediante compresión y/o tracción, lo cual implica un aumento de su rigidez lateral. De este modo, cuando se encuentran sometidos a cargas laterales, los pilotes inclinados presentan generalmente menores deformaciones y proporcionan una mayor capacidad de carga que pilotes verticales del mismo material y con idénticas dimensiones.

Hasta los años 90, los pilotes inclinados fueron utilizados con frecuencia en el diseño sísmico de puentes, así como en el diseño de embarcaderos y otras estructuras portuarias. Sin embargo, después del comportamiento poco satisfactorio que las cimentaciones profundas con pilotes inclinados mostraron durante una serie de seísmos se desaconsejó su uso. De hecho, la elección de pilotes inclinados como sistema de cimentación suele evitarse en regiones sísmicamente activas debido, también, a la falta de comprensión en lo que respecta a la respuesta sísmica de pilotes inclinados y cimentaciones pilotadas con elementos inclinados. Asimismo, el epígrafe 5 del Eurocódigo 8 indica en una nota que, en la realización de diseños sismorresistentes, no se recomienda el uso de pilotes inclinados para transmitir cargas laterales al suelo. Dada la falta de información disponible en la literatura científica, así como en los distintos códigos de edificación, parece evidente la necesidad de una mayor investigación de todos los aspectos de este problema.

En los últimos años, los pilotes inclinados han recuperado su popularidad. De hecho, varios estudios han demostrado el papel beneficioso que estos tienen sobre la respuesta sísmica de la superestructura. Sin embargo, se requiere de una investigación más profunda para ser capaces de discernir en qué casos la presencia de pilotes inclinados es beneficiosa o perjudicial. Uno de los aspectos que no ha recibido suficiente atención por parte de los investigadores es la influencia del ángulo de inclinación de los pilotes sobre los factores de interacción cinemática de cimentaciones pilotadas. Asimismo, la influencia de dicho ángulo sobre la respuesta dinámica de la superestructura es otro aspecto que requiere de más investigación. Estos dos aspectos se abordan en esta tesis.

En este trabajo se lleva a cabo, mediante un procedimiento basado en un modelo de subestructuración, un análisis de la influencia de los efectos de interacción suelo-estructura sobre la respuesta dinámica de estructuras esbeltas y no esbeltas sustentadas sobre diversas configuraciones de grupos de 2×2 , 3×3 y 4×4 pilotes. Los resultados que se presentan han permitido extraer conclusiones acerca de la importancia y de las tendencias que se observan al analizar cómo influye la variación de los principales parámetros del problema sobre la respuesta dinámica de la estructura.

Este documento proporciona una serie de gráficos que permiten estimar el periodo y el amortiguamiento de la estructura en base flexible en términos de los valores correspondientes a la condición de base rígida y en función de la configuración del conjunto. Además, se representan los valores del cortante máximo en la base de la estructura, así como los valores máximos del desplazamiento y giro de la base. Por otra parte, se muestran los espectros de respuesta elástica modificados, que han sido obtenidos teniendo en cuenta los efectos de interacción suelo-estructura, para diferentes valores del ángulo de inclinación de los pilotes.

A.1.2. Revisión bibliográfica

El diseño sísmico de centrales nucleares en las décadas de los sesenta y los setenta trajeron consigo un interés creciente en los efectos de la interacción suelo-estructura sobre la respuesta sísmica de las edificaciones. Los trabajos de investigación llevados a cabo por Parmelee [1], Parmelee *et al.* [2], Perelman *et al.* [3] y Sarrazin *et al.* [4] fueron pioneros en la investigación de la influencia que tiene, sobre la respuesta dinámica de estructuras a cortante de una sola planta, la elasticidad del suelo sobre el que se sustentan. Una revisión de los trabajos desarrollados en las primeras etapas de la investigación de la interacción sísmica suelo-estructura puede encontrarse en [5].

Al analizar el comportamiento sísmico de estructuras, los efectos cinemáticos e inerciales asociados a la interacción suelo-estructura afectan a las características dinámicas del sistema e influyen en el movimiento del terreno en torno a la cimentación. Por ello, es importante evaluar las variaciones en el periodo del sistema asociadas a la rigidez del suelo, así como las variaciones del amortiguamiento modal asociadas al amortiguamiento del material en el suelo y especialmente a los efectos de radiación.

Los efectos de interacción suelo-estructura sobre las características dinámicas de sistemas suelo-estructura han sido ampliamente estudiados, tanto para cimentaciones superficiales [6–11] como para cimentaciones embebidas, utilizando modelos 3D [12–15] y modelos 2D [16, 17]. Los artículos de Jennings y Bielak [6], Veletsos y Meek [7], Luco [10], Wolf [11] o Bielak [12] introducen la analogía de un oscilador de reemplazo de un solo grado de libertad en base rígida cuyo periodo y amortiguamiento pueden representar el comportamiento dinámico del sistema estructura-cimiento. En estos trabajos pioneros se adoptaron algunas simplificaciones con el objetivo de obtener resultados o expresiones para el periodo y el amortiguamiento efectivos del sistema: se despreció la influencia de los términos cruzados de la matriz de impedancias del suelo y, en el caso de cimentaciones embebidas, no se consideraron los efectos cinemáticos de la onda incidente, utilizando como excitación en la base un movimiento horizontal armónico con amplitud constante. En cambio, Kausel y Roësset [18] y, más adelante, Kausel *et al.* [19] utilizaron una metodología de subestructuración que permite dividir la resolución del problema de interacción suelo-estructura en tres pasos considerando la interacción cinemática. Los efectos del embebimiento de la cimentación fueron estudiados, considerando tanto la interacción cinemática como inercial, por Avilés y Pérez-Rocha [14] (para cimentaciones rectangulares 3D), por Avilés y Suárez [20] (para cimentaciones axisimétricas embebidas en un estrato), y por Todorovska [16] y Todorovska y Trifunac [17, 21] quienes presentaron un modelo bidimensional con soluciones analíticas para impedancias y efectos cinemáticos para edificios muy largos sustentados sobre cimentaciones cilíndricas rígidas. Por otra parte, Todorovska y Trifunac [17, 21] y Avilés *et al.* [15] estudiaron los efectos del tipo

de ondas y su ángulo de incidencia sobre la frecuencia y el amortiguamiento del sistema para problemas con cimentaciones embebidas cuadradas.

En lo que respecta a edificios pilotados, existen pocos estudios en la literatura científica que analicen los efectos de interacción suelo-estructura sobre las características dinámicas de la estructura [22–30]. Rainer [22] emplea una metodología de subestructuración para analizar el amortiguamiento modal de una superestructura soportada por pilotes. Kaynia y Mahzooni [23] utilizan una formulación tridimensional basada en funciones de Green para la cimentación pilotada, y un modelo de un solo grado de libertad para la estructura, con el objetivo de calcular los esfuerzos cortantes sísmicos en los pilotes durante las fases de interacción cinemática e inercial para distintas cimentaciones pilotadas. Por otra parte, Aguilar y Avilés [26] analizan cimentaciones pilotadas ampliando el procedimiento propuesto por Avilés y Pérez-Rocha [14] para cimentaciones embebidas y estudian los efectos de interacción suelo-estructura sobre el periodo y el amortiguamiento del sistema para una configuración específica de 8×8 pilotes, sin tener en cuenta los efectos de interacción cinemática. Con el fin de obtener expresiones aproximadas manejables para el periodo y el amortiguamiento del sistema, Avilés y Pérez-Rocha [14] adoptan una simplificación que consiste en desprestigiar los términos cruzados de la matriz de impedancias y también los términos de amortiguamiento de alto orden. Tales simplificaciones han sido ampliamente utilizadas por muchos autores [6–13, 31]. Sin embargo, no es aceptable desprestigiar los términos cruzados de rigidez y amortiguamiento en el análisis de cimentaciones pilotadas, ni siquiera lo es en el caso de ciertas configuraciones de cimentaciones embebidas. Por lo tanto, con el fin de obtener expresiones manejables manteniendo al mismo tiempo las impedancias cruzadas, algunos autores [27, 32] proponen condensar la interacción suelo-cimentación en un punto a una cierta profundidad virtual tal que la matriz de impedancias sea diagonal. Maravas *et al.* [27] proponen una metodología sencilla para estudiar los efectos de interacción suelo-estructura, sobre estructuras a cortante de una planta soportadas por un pilote simple, mediante la obtención del periodo y amortiguamiento de las mismas. Sin embargo, no existen estudios paramétricos de esta naturaleza para cimentaciones pilotadas constituidas por un número variable de pilotes, con diferentes embebimientos y separación entre ellos.

En lo que respecta a grupos de pilotes que incluyen elementos inclinados, a día de hoy, no se ha esclarecido si el uso de pilotes inclinados tiene un efecto beneficioso o perjudicial sobre la respuesta de la superestructura o sobre la propia cimentación cuando están sometidas a cargas sísmicas. Se han llevado a cabo estudios relacionados con este asunto con el fin de identificar los inconvenientes y las ventajas del uso de pilotes inclinados. Los trabajos pioneros realizados por Banerjee y Driscoll [33], y Poulos y Davis [34] señalan la necesidad de desarrollar más investigaciones para comprender mejor el comportamiento de este tipo de cimentaciones. Algunos autores [35–37] desarrollaron análisis numéricos que señalaban al aumento de las cargas axiales a lo largo del fuste del pilote y al aumento del momento flector en la cabeza del mismo como argumentos para usar pilotes verticales en lugar de inclinados para soportar las cargas sísmicas. Otros resultados que desaconsejan el uso de pilotes inclinados en áreas sísmicas fueron proporcionados por Neely [38] y Ravazi *et al.* [39]. En cambio, se han hallado evidencias en la práctica [40, 41] del papel beneficioso que los pilotes inclinados pueden tener tanto para la estructura que sustentan como para los pilotes en sí mismos. Estas conclusiones están en la línea de aquellas extraídas de distintos análisis numéricos [42–44]. Estos ha-

llazgos explican por qué la investigación sobre este tema se ha relanzado en los últimos años ([36,39,43–55]). Sin embargo, sólo Gerolymos *et al.* [44] y Giannakou *et al.* [48] han analizado la influencia del uso de cimentaciones profundas con pilotes inclinados sobre la respuesta dinámica de las estructuras que soportan.

Las impedancias y los factores de interacción cinemática son aspectos clave del problema. Estos pueden utilizarse para analizar los efectos de interacción suelo-estructura sobre el comportamiento dinámico de estructuras haciendo uso de metodologías de subestructuración, tal y como se hace en [23,24,56] para el caso de estructuras pilotadas. En la literatura pueden encontrarse diversas expresiones y gráficos para algunas configuraciones. Sin embargo, en general, la obtención de valores precisos para un caso particular requiere del uso de modelos numéricos sofisticados que permitan incorporar la interacción cimiento-suelo de forma rigurosa.

Existe un gran número de trabajos que abordan la obtención de funciones de impedancia (rigidez dinámica) de pilotes y grupos de pilotes. Por ejemplo, Gazetas [57] proporciona expresiones analíticas para pilotes flotantes simples, mientras que Dobry y Gazetas [58] presentan expresiones para grupos de pilotes utilizando factores de grupo que son una extensión de aquellas obtenidas para problemas estáticos por Poulos [59]. Otras investigaciones relacionadas con expresiones de impedancias han sido llevadas a cabo por Konagai *et al.* [60], Taherzadeh *et al.* [61] o Dai y Roësset [62]. Diversas técnicas numéricas han sido utilizadas para determinar las impedancias de cimentaciones pilotadas. Por ejemplo, Wolf *et al.* [63] emplean un procedimiento computacional basado en un modelo de elementos finitos para obtener rigideces dinámicas dependientes de la frecuencia de pilotes simples y cimentaciones de 2×2 y 10×10 pilotes embebidos en suelos estratificados. Kaynia [64] obtuvo impedancias y factores de interacción cinemática para varias configuraciones de grupos de pilotes embebidos en un semiespacio homogéneo mediante la utilización de una formulación basada en funciones de Green. Velez *et al.* [65] utilizan una formulación de elementos finitos para calcular impedancias de pilotes simples. Asimismo, Miura *et al.* [66] emplean una formulación tridimensional basada en funciones de Green para determinar los valores de las impedancias correspondientes a grupos de 2×2 y 4×4 pilotes. Por otra parte, Kaynia y Mahzooni [23] utilizan la formulación previamente propuesta por Kaynia y Kausel [67] para obtener impedancias horizontales y de cabeceo para grupos de 5×5 pilotes. Vinciprova *et al.* [69] y Maeso *et al.* [70] emplearon un código de elementos de contorno desarrollado por Aznárez [68] para calcular impedancias de pilotes y grupos de pilotes embebidos en suelos viscoelásticos y poroelásticos. Padrón *et al.* [71] presentaron funciones de impedancia correspondientes a distintas configuraciones de grupos de pilotes obtenidas mediante el uso de un modelo tridimensional acoplado de elementos de contorno y elementos finitos.

En lo que respecta a pilotes inclinados, Mamoon *et al.* [72] presentaron rigideces dinámicas para una configuración específica de un grupo de 3×3 pilotes. Con posterioridad, Giannakou *et al.* [46] utilizaron un modelo tridimensional de elementos finitos para obtener funciones de impedancia de pilotes simples embebidos, tanto en un suelo homogéneo como en un suelo no homogéneo. Por otra parte, Padrón *et al.* [49] presentaron funciones de impedancia correspondientes a varias configuraciones de grupos de 2×2 y 3×3 pilotes con elementos inclinados.

En lo referente a factores de interacción cinemática, y con respecto a la investigación numérica, se han llevado a cabo diversos estudios para el caso de cimentaciones con pilotes verticales. Gazetas [73] obtuvo factores de interacción cinemática para pilotes

simples embebidos en distintos suelos y sometidos a ondas S de incidencia vertical. Mamoon y Ahmad [74] así como Mamoon y Benerjee [75] presentaron trabajos pioneros en los cuales se analiza, en términos de factores de interacción cinemática, la respuesta de pilotes simples y cimentaciones pilotadas sometidas tanto a ondas de incidencia vertical como a ondas con ángulo de incidencia variable. Este problema también fue estudiado por Makris y Badoni [76] para el caso de ondas de Rayleigh. Uno de los análisis más completos fue el llevado a cabo por Kaynia y Novak [77]. En él se presentan factores de interacción cinemática correspondientes a diversas configuraciones de grupos de pilotes sometidas tanto a ondas con ángulo de incidencia variable como a ondas de Rayleigh. Otros trabajos en los que se obtienen valores de los factores de interacción cinemática para cimentaciones pilotadas son, por ejemplo, aquellos presentados por Kaynia [64], Fan *et al.* [78], Gazetas *et al.* [79], Kavvadas y Gazetas [80] y Padrón [81].

Aunque otros autores han llevado a cabo análisis de la respuesta cinemática de pilotes inclinados (*e.g.* [37, 82]), en lo que respecta a la obtención de factores de interacción cinemática, sólo Giannakou [47] presenta resultados en estos términos correspondientes a grupos de 2×1 pilotes. Por lo tanto, parece evidente que este es un aspecto que requiere de un mayor esfuerzo investigador.

El trabajo que se presenta en esta tesis se enmarca en una línea de investigación que ha venido desarrollándose durante los últimos 20 años en el seno de la División de Mecánica de los Medios Continuos y Estructuras del Instituto Universitario de Sistemas Inteligentes y Aplicaciones Numéricas en Ingeniería (SIANI) en la Universidad de Las Palmas de Gran Canaria. Esta línea comenzó a finales de la década de los 70 en el grupo de investigación liderado por José Domínguez en la Universidad de Sevilla con los trabajos pioneros realizados por Domínguez [83] y Domínguez y Alarcón [84]. Dichos trabajos abordan la aplicación del método de elementos de contorno a problemas de elastodinámica. En los años posteriores este grupo llevó a cabo importantes trabajos en esta línea (véanse, por ejemplo, [85–88]). Un compendio detallado del trabajo realizado en el marco de esta línea de investigación en la Universidad de Sevilla hasta 1993 puede encontrarse en [89]. El desarrollo de un código multidominio tridimensional de elementos de contorno en el dominio de la frecuencia [90–92] fue llevado a cabo por Orlando Maeso y José Domínguez en el marco de una fructífera colaboración entre la Universidad de Las Palmas de Gran Canaria y la Universidad de Sevilla. Siguiendo esta línea, un código de elementos de contorno que permite analizar la respuesta sísmica de presas bóveda con sedimentos porosos [93–96], así como obtener impedancias de pilotes y grupos de pilotes embebidos en suelos viscoelásticos y poroelásticos [69, 70], se presentó en la tesis de Juan J. Aznárez [68]. Con el fin de simplificar esta metodología y también de reducir su coste computacional sin perder rigor, la tesis doctoral de Luis A. Padrón [81] aborda la formulación e implementación de un modelo en el cual los pilotes se modelan directamente utilizando elementos finitos tipo viga, de acuerdo a las hipótesis de Bernoulli, mientras que el suelo se modela utilizando elementos de contorno. Este modelo armónico acoplado tridimensional permite estudiar el comportamiento dinámico de cimentaciones pilotadas [71]. Posteriormente, dicho modelo ha sido ampliado para abordar el análisis dinámico de cimentaciones que incluyen pilotes inclinados [49] y también para llevar a cabo el estudio de la respuesta dinámica de la superestructura y analizar los fenómenos de interacción entre estructuras cercanas [97]. Por otra parte, este código ha permitido analizar cómo afectan el tipo de onda y su ángulo de incidencia a los momentos flectores a nivel del encepado de pilotes simples y grupos de 3×3 pilotes [98].

A.1.3. Alcance y objetivos

Este trabajo pretende utilizar el modelo acoplado de elementos finitos y elementos de contorno desarrollado por Padrón *et al.* para obtener las impedancias y los factores de interacción cinemática de diversas configuraciones de cimentaciones pilotadas, con la finalidad de realizar estudios paramétricos mediante técnicas de subestructuración. Si bien es cierto que pueden encontrarse en la literatura numerosas referencias que abordan el uso de metodologías de subestructuración para el análisis de la respuesta dinámica de estructuras sustentadas por cimentaciones superficiales o embebidas, también lo es que las referencias son escasas en lo que respecta al estudio del comportamiento dinámico de estructuras pilotadas. Por este motivo, siguiendo la línea de los trabajos de referencia para cimentaciones superficiales y embebidas, el principal objetivo de esta tesis doctoral es desarrollar un procedimiento basado en un modelo de subestructuración que permita evaluar la influencia de los efectos de interacción suelo-estructura sobre el comportamiento dinámico de estructuras a cortante cimentadas sobre grupos de pilotes.

El periodo y el amortiguamiento efectivos del sistema (\tilde{T} y $\tilde{\xi}$) [7, 12–14, 21] representan las características dinámicas de un sistema equivalente de un solo grado de libertad con amortiguamiento viscoso que es excitado por el movimiento en campo libre. Este oscilador de reemplazo debe reproducir, con tanta precisión como sea posible, la respuesta del sistema acoplado dentro del rango de frecuencias en el que se produce la respuesta máxima. El objetivo de este trabajo es desarrollar un procedimiento sencillo y estable, en el dominio de la frecuencia, para la estimación de periodos y amortiguamientos de edificios a cortante soportados por cimentaciones pilotadas, teniendo en cuenta los efectos de interacción cinemática e inercial. A tal efecto, es preciso realizar una revisión comparativa de las distintas estrategias empleadas en la literatura para establecer dicha equivalencia y calcular los valores de los parámetros de este sistema de un grado de libertad, con el objetivo de identificar aquella que mejor se adapta al problema objeto de estudio. Asimismo, las simplificaciones que muchos autores [6–13, 31] han adoptado en los casos de cimentaciones superficiales y embebidas deben ser analizadas a fin de determinar si estas son aplicables a cimentaciones pilotadas y cómo afectan a la precisión de los resultados. En esta línea, la influencia de considerar las impedancias cruzadas y los factores de interacción cinemática en el caso de configuraciones de grupos de pilotes también debe ser estudiada.

La exactitud del procedimiento propuesto será evaluada a partir de la comparación de sus resultados con aquellos obtenidos a partir de la resolución iterativa de un sistema de ecuaciones complejas que representa la ecuación de movimiento del sistema objeto de estudio.

Una vez que el modelo haya sido formulado y validado, el objetivo es realizar una serie de análisis paramétricos, considerando un conjunto de configuraciones de grupos de pilotes, con el propósito de analizar la influencia de la interacción suelo-estructura sobre la respuesta sísmica de la superestructura. La idea es expresar todas las ecuaciones en términos de los principales parámetros adimensionales del problema con el fin de facilitar el estudio de su influencia sobre la respuesta dinámica del sistema.

El alcance de este trabajo también abarca el estudio de cimentaciones profundas que incluyen pilotes inclinados. En este sentido, se llevará a cabo un análisis de la influencia del ángulo de inclinación de los pilotes sobre el comportamiento dinámico de la

superestructura, con el objetivo de esclarecer el papel beneficioso o perjudicial que juegan las cimentaciones que incluyen pilotes inclinados.

A.1.4. Publicaciones derivadas de esta tesis doctoral

El procedimiento que se desarrolla en esta tesis, así como parte de los resultados que se incluyen en este documento, han sido previamente publicados en diversas revistas científicas y congresos [54,55,99–105]. A continuación figuran las referencias completas de estos trabajos.

A.1.4.1. Publicaciones en revistas científicas JCR

- Medina, C., Aznárez, J. J., Padrón, L. A. y Maeso, O. (2013) Effects of soil-structure interaction on the dynamic properties and seismic response of piled structures. *Soil Dynamics and Earthquake Engineering*, **53**, 160–175.
- Medina, C., Padrón, L. A., Aznárez, J. J., Santana, A. y Maeso, O. (2014) Kinematic interaction factors of deep foundations with inclined piles. *Earthquake Engineering and Structural Dynamics*, **43**, 2035–2050.
- Medina, C., Padrón, L. A., Aznárez, J. J. y Maeso, O. (2015) Influence of pile inclination angle on the dynamic properties and seismic response of piled structures. *Soil Dynamics and Earthquake Engineering*, **69**, 196–206.

A.1.4.2. Contribuciones a congresos

- Medina, C., Padrón, L. A., Aznárez, J. J., y Maeso, O. (2011) Influencia de los fenómenos de interacción en las propiedades dinámicas de estructuras de edificación pilotadas. *Proceedings of the Congress on Numerical Methods in Engineering 2011*, Coimbra, Portugal, pp. 96–115.
- Medina, C., Aznárez, J. J., Padrón, L. A., y Maeso, O. (2013) A procedure for evaluating the soil-structure interaction effects on the system period and damping of pile-supported structures. *Proceedings of 4th ECCOMAS Thematic Conference on Computational Methods in Structural Dynamics and Earthquake Engineering, COMPDYN 2013*, Kos Island, Greece, pp. 4463–4487.
- Medina, C., Aznárez, J. J., Padrón, L. A., y Maeso, O. (2014) Influence of pile rake angle on the seismic response of pile foundations and piled structures. *Proceedings of the 9th International Conference on Structural Dynamics, EURO DYN 2014*, Porto, Portugal, pp. 733–740.
- Medina, C., Aznárez, J. J., Padrón, L. A., y Maeso, O. (2014) Seismic response of deep foundations and piled structures considering inclined piles. *Proceedings of the jointly organized 11th World Congress on Computational Mechanics (WCCM XI) and 5th European Congress on Computational Mechanics (ECCM V)*, Barcelona, Spain, pp. 453–463.

- Medina, C., Padrón, L. A., Aznárez, J. J., y Maeso, O. (2015) Respuesta sísmica de estructuras de edificación cimentadas sobre pilotes inclinados. *Proceedings of the Congress on Numerical Methods in Engineering*, Lisbon, Portugal, no. 237.
- Padrón, L. A., Medina, C., Álamo, G. M., Aznárez, J. J., Santana, A., Maeso, O., García, F., y Chirino, F. (2015) Pilotes inclinados: situación normativa y ventajas e inconvenientes de su uso en proyectos de edificación en zonas con riesgo sísmico. *Proceedings of the 19th International Congress on Project Management and Engineering*, Granada, Spain.

A.1.5. Estructura del documento

Esta tesis doctoral se ha redactado en inglés. Por ello, y de acuerdo con lo establecido en *reglamento para la elaboración, tribunal, defensa y evaluación de tesis doctorales de la Universidad de Las Palmas de Gran Canaria* de año 2007, este anexo, redactado en castellano, recoge los antecedentes y objetivos de la investigación, la metodología utilizada, las aportaciones originales, las conclusiones obtenidas y las futuras líneas de investigación.

Con el propósito de ofrecer al lector una visión completa de los temas tratados en esta tesis, se ha optado por exponer a continuación la estructura y contenidos de la parte principal del documento de tesis redactada en inglés, aunque este anexo en castellano sólo incluye una parte del material presentado.

Esta tesis doctoral se ha estructurado en siete capítulos. El núcleo de la misma se aborda en el capítulo 2 y consiste en el desarrollo de un procedimiento sencillo y estable para la estimación del periodo y amortiguamiento efectivos de estructuras a cortante cimentadas sobre pilotes. El capítulo comienza describiendo los conceptos básicos necesarios para la comprensión de la metodología de subestructuración empleada para modelar el problema en cuestión. Una vez definido en detalle el problema objeto de estudio, se escriben las correspondientes ecuaciones de movimiento. A continuación, se emplea un modelo semianalítico para identificar los principales parámetros adimensionales que caracterizan la respuesta dinámica de cimentaciones pilotadas. Posteriormente, se estima la precisión del modelo utilizado para la cimentación en el que se representan los pilotes huecos mediante pilotes macizos equivalentes. Después, se exponen los distintos pasos del procedimiento que se ha seguido para expresar el sistema de ecuaciones de movimiento en términos de un conjunto de parámetros adimensionales, que abarcan las principales características de los problemas de interacción suelo-estructura. Esto facilita de manera considerable el posterior análisis de la influencia de cada uno de dichos parámetros sobre la respuesta dinámica del sistema. Llegados a este punto, se aborda la estimación de las características dinámicas del oscilador equivalente que reproduce, con tanta precisión como sea posible, la respuesta del sistema acoplado dentro del rango de frecuencias en el que se produce la respuesta máxima. Con este propósito, se analizan y comparan las distintas estrategias propuestas con anterioridad por otros autores para establecer dicha equivalencia y determinar las características dinámicas del oscilador de reemplazo. En esta línea, los espectros de respuesta armónica correspondientes a los sistemas de un grado de libertad, obtenidos de la aplicación de cada una de dichas estrategias al caso de cimentaciones pilotadas, se comparan con el espectro de respuesta armónica del sistema objeto de estudio, con el propósito de determinar si las simplifica-

ciones adoptadas en cada una de las estrategias son apropiadas para el caso de estructuras pilotadas. Una vez hecho esto, se propone una estrategia modificada que proporciona resultados precisos para estructuras soportadas tanto por cimentaciones superficiales o embebidas como por cimentaciones pilotadas. La estrategia propuesta incorpora la interacción cinemática así como las impedancias cruzadas. Posteriormente, se explica la implementación del procedimiento propuesto en un código. Al final de este capítulo, la validación del modelo propuesto se completa mediante la comparación de los resultados obtenidos con aquellos proporcionados con anterioridad por otros autores para los casos de cimentaciones superficiales y embebidas.

Posteriormente, en el capítulo 3, se explica el modelo acoplado de elementos finitos y elementos de contorno utilizado para el cálculo de las impedancias y los factores de interacción cinemática de las cimentaciones pilotadas. Asimismo, se describe la formulación de elementos de contorno multidominio que se utiliza en un capítulo posterior para calcular la precisión del modelo mencionado anteriormente aplicado a la determinación de factores de interacción cinemática para cimentaciones pilotadas que incluyen elementos inclinados.

El análisis de la influencia de la interacción suelo-estructura sobre el comportamiento dinámico de la superestructura mediante un procedimiento basado en un modelo de subestructuración, como el que se explica en el capítulo 2, requiere del cálculo previo de impedancias y factores de interacción cinemática. En esta línea, el capítulo 4 aborda la obtención numérica de las impedancias y factores de interacción cinemática de cimentaciones pilotadas mediante la formulación descrita en el capítulo 3. Al comienzo de este capítulo se describe la configuración geométrica de los grupos de pilotes considerados en esta investigación, así como las propiedades de los materiales del suelo y los pilotes. Posteriormente, se define el conjunto de configuraciones de pilotes verticales analizadas en este estudio. Las impedancias y los factores de interacción cinemática de dichas configuraciones se presentan en diversos gráficos. Seguidamente, se exponen las impedancias y los factores de interacción cinemática de distintas configuraciones de grupos de pilotes que incluyen elementos inclinados. Estos valores se utilizan en un capítulo posterior para llevar a cabo diversos análisis que permiten determinar cómo las variaciones del ángulo de inclinación de los pilotes afectan a la respuesta dinámica de la superestructura cuando se tiene en cuenta la interacción suelo-estructura. Las principales tendencias que se observan en el comportamiento dinámico de sistema suelo-cimiento se han analizado tanto para grupos de pilotes verticales como para aquellos que contienen pilotes inclinados.

El capítulo 5 aborda el análisis de los efectos de interacción suelo-estructura sobre las propiedades dinámicas y la respuesta sísmica de estructuras soportadas por pilotes verticales. La configuración geométrica así como las propiedades de los materiales en los casos objeto de estudio se presentan al principio del capítulo. Los valores obtenidos en el capítulo 4 para las impedancias y los factores de interacción cinemática se utilizan aquí para realizar diversos análisis paramétricos empleando el procedimiento previamente desarrollado y validado en el capítulo 2. De este modo, se lleva a cabo un estudio de la influencia de los principales parámetros del problema de interacción suelo-estructura sobre la respuesta dinámica de la superestructura. Se presentan y analizan los resultados obtenidos para 21 configuraciones de grupos de 2×2 , 3×3 y 4×4 pilotes. Se proporcionan gráficos que permiten la estimación del periodo y el amortiguamiento de la estructura en base flexible en función de los valores correspondientes a la condición de base rígida

y de la configuración del sistema. Esto permite obtener con posterioridad espectros de respuesta elástica modificados que incluyen los efectos de interacción suelo-estructura. Por otra parte, se representan los valores del esfuerzo cortante máximo en la base de la estructura, así como los valores del desplazamiento y del giro del encepado para la frecuencia a la que se produce la respuesta máxima. Además, en este capítulo se evalúa la importancia de considerar las impedancias cruzadas y los factores de interacción cinemática en el cálculo de la respuesta dinámica del sistema. El capítulo finaliza con la exposición de las conclusiones extraídas de los resultados que se presentan.

El capítulo 6 pretende contribuir a esclarecer el efecto beneficioso o perjudicial que puede tener el uso de cimentaciones que incluyen pilotes inclinados, lo cual continúa siendo una cuestión abierta. En esta línea, la contribución de este capítulo se centra en la influencia del ángulo de inclinación de los pilotes sobre la respuesta sísmica de estructuras a cortante soportadas por grupos de pilotes. A tal efecto, se obtienen resultados para diversas configuraciones de grupos de 2×2 y 3×3 pilotes. Como se hizo en el capítulo 5, para el caso de pilotes verticales, en este capítulo se representan y analizan los resultados en términos del periodo y amortiguamiento efectivos, así como del cortante máximo en la base de la estructura para el caso de pilotes inclinados. Asimismo, se obtienen espectros de respuesta elástica modificados para distintos valores del ángulo de inclinación. Al final de este capítulo se resumen las principales conclusiones extraídas del análisis de los resultados expuestos.

Finalmente, las conclusiones más relevantes de este trabajo de investigación se resumen en el capítulo 7. El documento finaliza proponiendo desarrollos futuros que pueden dar continuidad a la línea de investigación de esta tesis doctoral.

A.2. Metodología de subestructuración

A.2.1. Introducción

La interacción suelo-estructura conlleva efectos cinemáticos e inerciales que afectan al comportamiento dinámico de las estructuras. Por lo tanto, una evaluación apropiada de su respuesta dinámica requiere del desarrollo de modelos que incorporen, de forma rigurosa, la interacción entre la estructura y el suelo sobre el que se sustenta. Estos fenómenos de interacción dependen de factores tales como, el tipo de cimentación, su geometría y profundidad de embebimiento, el tipo de suelo, así como las características de la estructura. En la línea de los estudios llevados a cabo por otros autores para cimentaciones superficiales [7] y embebidas [14], en esta sección se propone un modelo simple de la interacción suelo-estructura en el dominio de la frecuencia, basado en una metodología de subestructuración, que permite evaluar la influencia de estos factores en la respuesta dinámica de estructuras cimentadas sobre grupos de pilotes y sometidas a cargas sísmicas.

Esta sección comienza con la definición del problema objeto de estudio que se aborda en la sección A.2.2. Una vez hecho esto, en la sección A.2.3 se describe el modelo de subestructuración que se utiliza en este trabajo. En la sección A.2.4 se emplea un modelo semianalítico simple con el fin de determinar los principales parámetros adimensionales que caracterizan el comportamiento dinámico de los grupos de pilotes. Posteriormente, con el propósito de evaluar la validez de modelar pilotes huecos mediante pilotes macizos, la precisión de los resultados obtenidos adoptando esta simplificación se analiza en términos de impedancias y factores de interacción cinemática en la sección A.2.5. Las ecuaciones de movimiento del sistema se expresan en términos de una serie de parámetros adimensionales que caracterizan el problema de interacción suelo-estructura. Dichos parámetros se definen en la sección A.2.6. La sección A.2.7 aborda la diagonalización de la matriz de impedancias a fin de obtener expresiones manejables del cortante en la base de la estructura. Las estrategias propuestas con anterioridad por otros autores para establecer una equivalencia entre el sistema acoplado y un oscilador de reemplazo de un solo grado de libertad, así como para determinar sus características dinámicas, se analizan y comparan en la sección A.2.8. Una vez hecho esto, se propone un procedimiento simplificado y estable para la estimación del periodo y el amortiguamiento de edificios a cortante, teniendo en cuenta la interacción suelo-estructura y considerando las impedancias cruzadas. La sección A.2.9 aborda la implementación de dicho procedimiento. Por último, la validación del modelo propuesto se desarrolla en la sección A.2.10 mediante la comparación de los resultados obtenidos con aquellos aportados por otros autores para cimentaciones superficiales y embebidas.

A.2.2. Descripción del problema

En esta tesis se estudia la respuesta dinámica de estructuras a cortante, en el rango lineal, soportadas por cimentaciones pilotadas. Para ello se utiliza un sistema de un solo grado de libertad en su condición de base rígida, como el que se muestra en la figura A.1, que puede representar bien estructuras de una planta o bien un modo de vibración de edificios de varias plantas. La superestructura puede definirse mediante su periodo en base rígida T , su masa m , la rigidez estructural k , la altura h de la resultante de las

fuerzas de inercia para el modo de vibración analizado, el momento de inercia de la masa vibrante I , y el coeficiente de amortiguamiento viscoso ξ . La estructura se considera cimentada sobre un grupo de pilotes distribuidos en un área cuadrada, como el que se muestra en la figura A.1, embebidos en un semiespacio isotrópico, viscoelástico y homogéneo. Se ha supuesto que el movimiento de las cabezas de los pilotes está restringido por un encepado rígido, modelado como una placa rígida cuadrada de espesor despreciable, que no está en contacto con el semiespacio. El momento de inercia de este encepado se designa como I_o . Todos los pilotes tienen las mismas propiedades geométricas definidas por su longitud L y el diámetro de su sección d . En este estudio se analizan diversas configuraciones de grupos de pilotes. Cada una de ellas está definida por el número de pilotes, el semiancho del encepado b , la distancia entre centros de pilotes adyacentes s y el ángulo de inclinación de los pilotes θ . Los pilares de la estructura se han supuesto sin masa e inextensibles axialmente. Tanto la masa del cemento como la masa de la estructura se consideran uniformemente distribuidas en áreas cuadradas. Este modelo del sistema cemento-estructura es una evolución de aquel que parece haber sido empleado por primera vez por Parmelee [1] en 1967 para cimentaciones superficiales y que, según Veletsos y Meek [7], ha constituido la base de la mayoría de las investigaciones posteriores.

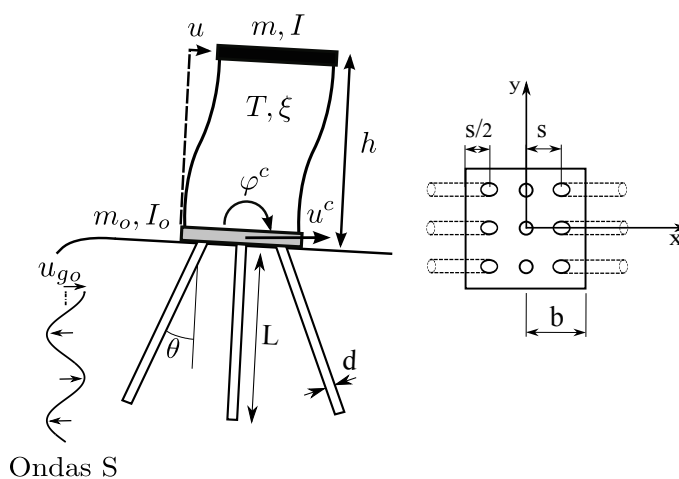


FIGURA A.1: Definición del problema. Estructura a cortante sustentada por una cimentación pilotada embebida en un semiespacio homogéneo y sometida a ondas S de incidencia vertical.

Si se tiene en cuenta la interacción suelo-estructura, el comportamiento del sistema puede aproximarse mediante el de un sistema de tres grados de libertad, definido por el desplazamiento horizontal u^c y el giro φ^c de la cimentación, unido al desplazamiento horizontal de la planta u . (Téngase en cuenta que el giro del encepado y el giro de la estructura son idénticos). El sistema es excitado por ondas S planas de incidencia vertical. Dadas las características del modelo estructural y la excitación, los movimientos verticales y de torsión se han despreciado en este trabajo.

A.2.3. Modelo de subestructuración

El problema descrito en la sección A.2.2 puede analizarse utilizando una metodología de subestructuración, en la cual el sistema se subdivide en el sistema *estructura-encepado*, y la rigidez y el amortiguamiento del sistema *suelo-cimiento*, representada por medio de resortes y amortiguadores, tal como se muestra en la Figura A.2(b).

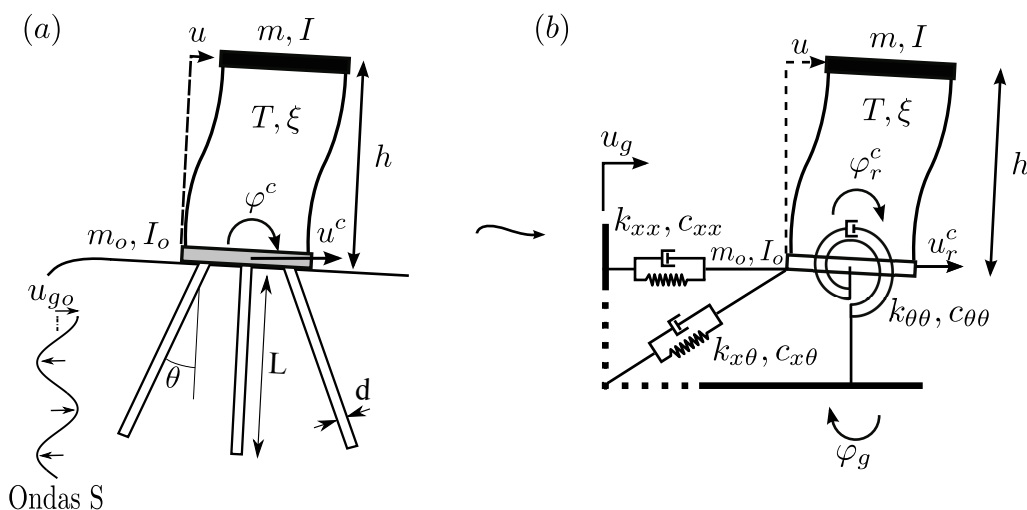


FIGURA A.2: (a) Definición del problema. (b) Modelo de subestructuración de una estructura de una planta.

Según Kausel y Roësset [18], la resolución de este problema puede dividirse en tres pasos, como se refleja en la figura A.3.

1. **Interacción cinemática.** En este caso, el primer paso consiste en determinar el movimiento de la cimentación rígida de masa despreciable cuando está sometida al mismo movimiento de excitación que el sistema completo. Incluso para ondas armónicas planas S de incidencia vertical (en cuyo caso el desplazamiento de campo libre en la superficie del suelo es exclusivamente horizontal), estos factores de interacción cinemática dependientes de la frecuencia se representan como el desplazamiento horizontal (u_g) y el giro (φ_g) en el encepado.
2. **Funciones de impedancia.** El segundo paso es la obtención de las impedancias, que son funciones complejas dependientes de la frecuencia (k_{xx}, c_{xx}), ($k_{\theta\theta}, c_{\theta\theta}$) y ($k_{x\theta}, c_{x\theta}$) que representan la rigidez y el amortiguamiento del suelo en los modos de vibración horizontal, de balanceo y modo de vibración cruzado horizontal-balanceo, respectivamente. La representación matemática de las funciones de impedancia es $K_{ij} = k_{ij} + ia_o c_{ij}$, donde $a_o = \omega b/c_s$; siendo i la unidad imaginaria $i = \sqrt{-1}$, ω la frecuencia circular de excitación, $c_s = \sqrt{\mu_s/\rho_s}$ la velocidad de propagación de las ondas de corte en el semiespacio, y μ_s y ρ_s el módulo de elasticidad transversal y la densidad del suelo, respectivamente.
3. **Interacción inercial.** Finalmente, el último paso consiste en el cálculo de la respuesta, para cada frecuencia, de la estructura soportada por los resortes y amorti-

guadores cuyas propiedades se han obtenido en el segundo paso y sujeta al movimiento obtenido en el primer paso.

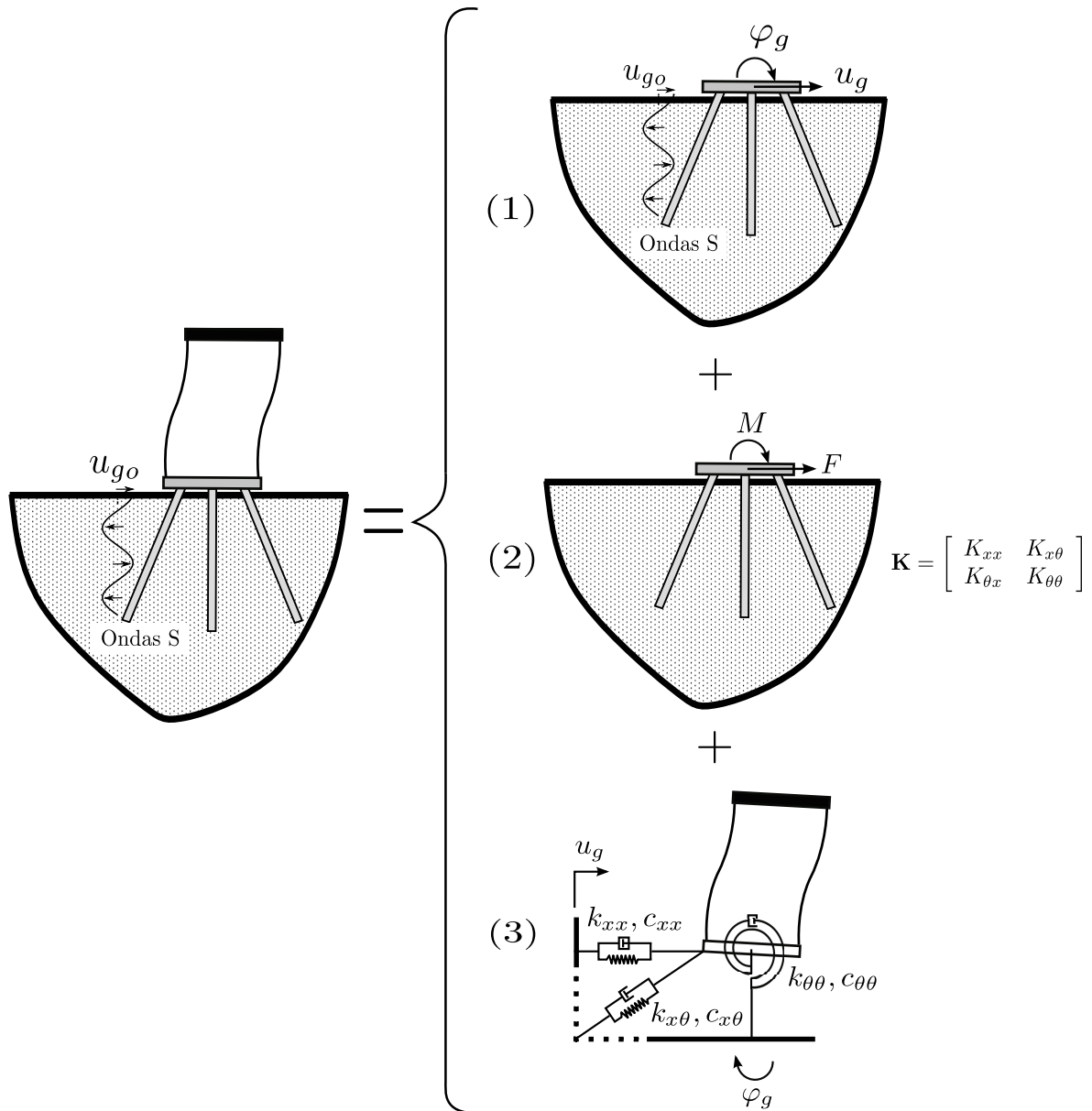


FIGURA A.3: El método de los tres pasos.

A.2.3.1. Ecuaciones de movimiento

Las ecuaciones de movimiento del sistema mostrado en la figura A.2(b), asumiendo pequeños desplazamientos, puede escribirse en términos de desplazamientos relativos, $u_r^c = u^c - u_g$ y $\varphi_r^c = \varphi^c - \varphi_g$, como

$$m \cdot [\ddot{u} + \ddot{u}_r^c + \ddot{u}_g + h(\ddot{\varphi}_r^c + \ddot{\varphi}_g)] + K \cdot u = 0 \quad (\text{A.1})$$

$$m_o \cdot [\ddot{u}_r^c + \ddot{u}_g] + K_{xx} \cdot u_r^c + K_{x\theta} \cdot \varphi_r^c - K \cdot u = 0 \quad (\text{A.2})$$

$$m \cdot h[\ddot{u} + \ddot{u}_r^c + \ddot{u}_g + h(\ddot{\varphi}_r^c + \ddot{\varphi}_g)] + I(\ddot{\varphi}_r^c + \ddot{\varphi}_g) + K_{\theta x} \cdot u_r^c + K_{\theta\theta} \cdot \varphi_r^c + I_o(\ddot{\varphi}_r^c + \ddot{\varphi}_g) = 0 \quad (\text{A.3})$$

donde la ecuación (A.1) representa el equilibrio de fuerzas horizontales de la masa vibrante; la ecuación (A.2), el equilibrio de fuerzas horizontales del sistema *suelo-cimiento* y la ecuación (A.3), el equilibrio de momentos en torno al centro de gravedad del encepado del sistema *estructura-cimiento*. En el dominio de la frecuencia (con dependencia temporal $e^{i\omega t}$), este conjunto de ecuaciones puede expresarse en forma matricial como

$$\left\{ \left[\begin{array}{ccc} K & 0 & 0 \\ -K & K_{xx} & K_{x\theta} \\ 0 & K_{\theta x} & K_{\theta\theta} \end{array} \right] - \omega^2 \left[\begin{array}{ccc} m & m & mh \\ 0 & m_o & 0 \\ mh & mh & I_T \end{array} \right] \right\} \cdot \left[\begin{array}{c} u \\ u_r^c \\ \varphi_r^c \end{array} \right] = \omega^2 \left\{ \left[\begin{array}{c} m \\ m_o \\ mh \end{array} \right] u_g + \left[\begin{array}{c} mh \\ 0 \\ I_T \end{array} \right] \varphi_g \right\} \quad (\text{A.4})$$

donde $I_T = m h^2 + I_o + I$ y $K = k + i2\omega_n m \xi \omega$, siendo $\omega_n = 2\pi/T$ la frecuencia natural de la superestructura en base rígida. Una vez obtenido el movimiento de excitación de la cimentación, así como el vector del lado derecho, y conocidos los coeficientes de la matriz, el desplazamiento de la planta y los movimientos relativos de la cimentación pueden calcularse en el rango de frecuencias de interés.

A.2.4. Parámetros que caracterizan el comportamiento dinámico de los pilotes

Esta sección explica el procedimiento que se ha seguido para identificar los principales parámetros dimensionales que caracterizan el comportamiento dinámico de un pilote simple cuando se tiene en cuenta la interacción suelo-estructura. Esto permite expresar las ecuaciones de movimiento del sistema, escritas en la ecuación (A.4), en función de dichos parámetros. A su vez, esto hace posible la realización de análisis paramétricos con el fin de determinar cómo afectan las variaciones de cada uno de estos parámetros a la respuesta dinámica del sistema.

La figura A.4 muestra un modelo simplificado basado en el método Winkler para vigas embebidas, que se emplea en esta sección con el fin de identificar los parámetros de los

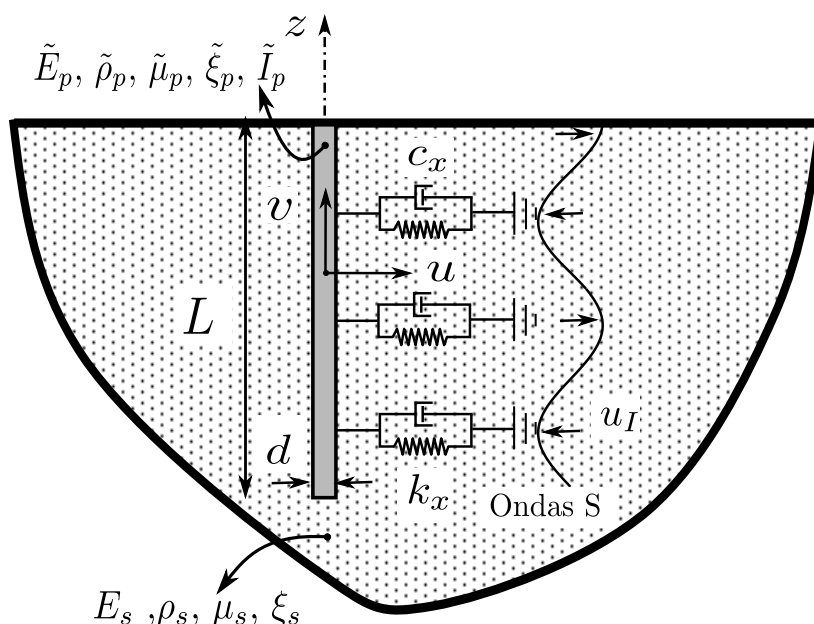


FIGURA A.4: Modelo Winkler.

que depende la respuesta dinámica de un pilote simple. Este tipo de modelos ha sido utilizado previamente por otros autores para obtener impedancias y factores de interacción cinemática de cimentaciones pilotadas [79, 80, 106–113]. En este modelo el suelo está representado por medio de resortes y amortiguadores distribuidos de forma continua a lo largo de la longitud del pilote, que se caracterizan mediante las impedancias que se oponen al desplazamiento horizontal $K_x = k_x + i\omega c_x$. k_x y c_x representan, respectivamente, la rigidez y el amortiguamiento del suelo, $i = \sqrt{-1}$ es la unidad imaginaria y ω es la frecuencia circular de la excitación. Las propiedades correspondientes al material del suelo son: módulo de Young E_s , densidad de masa ρ_s , módulo de elasticidad transversal μ_s y coeficiente de amortiguamiento ξ_s . Por otra parte, el pilote se modela como una viga Euler-Bernoulli sometida a un campo de ondas SH de incidencia vertical designado como u_I . La geometría del pilote está definida por su longitud L y su diámetro exterior d . Asimismo su sección transversal se caracteriza mediante su área \tilde{A}_p y su inercia rotacional \tilde{I}_p . Las propiedades del material del pilote son: módulo de Young \tilde{E}_p , densidad de masa $\tilde{\rho}_p$, módulo de elasticidad transversal $\tilde{\mu}_p$ y coeficiente de amortiguamiento $\tilde{\xi}_p$. Finalmente, $u = u(\omega, z)$ y $v = v(\omega, z)$ representan, respectivamente, los desplazamientos horizontales y verticales en cualquier punto del pilote.

Considerando como fuerzas externas que actúan sobre la sección, las fuerzas de inercia y aquellas causadas por un campo de ondas incidentes actuando sobre los resortes y amortiguadores, la ecuación de equilibrio dinámico para una porción diferencial de la viga sometida a flexión puede expresarse como

$$\tilde{E}_p \tilde{I}_p \frac{\partial^4 u}{\partial z^4} + (K_x - \tilde{\rho}_p \tilde{A}_p \omega^2) u = K_x u_I \quad (\text{A.5})$$

donde el campo de ondas SH con incidencia vertical u_I tiene la siguiente expresión:

$$u_I = \frac{1}{2} \left(e^{-i\kappa(z-z_s)} + e^{i\kappa(z-z_s)} \right) \quad (\text{A.6})$$

siendo $\kappa = \omega/c_s$ el número de onda y z_s la cota de la superficie libre.

Un pilote vertical, como el que se muestra en la figura A.4, está sometido a flexión. Sin embargo, cuanto más se inclina el pilote más trabaja de forma axial de acuerdo a la siguiente ecuación:

$$\tilde{\mu}_p \tilde{A}_p \frac{\partial^2 v}{\partial z^2} + \left(K_z - \tilde{\rho}_p \tilde{A}_p \omega^2 \right) v = K_z v_I \quad (\text{A.7})$$

donde $K_z = k_z + i\omega c_z$ representa la impedancia que se opone al desplazamiento y v_I es la componente del campo incidente en la dirección del eje longitudinal del pilote.

La solución de estas ecuaciones es la suma de la solución de la ecuación homogénea v_H y u_H , respectivamente, y cualquier solución particular v_P y u_P , en cada caso, que satisfaga la ecuación correspondiente. De este modo, $v = v_H + v_P$ y $u = u_H + u_P$.

Las respectivas soluciones homogéneas satisfacen las siguientes ecuaciones:

$$\frac{\partial^4 u}{\partial z^4} + \lambda_u^4 u = 0 \quad ; \quad \frac{\partial^2 v}{\partial x^2} + \lambda_v^2 v = 0 \quad (\text{A.8})$$

siendo

$$\lambda_u^4 = \frac{K_x - \tilde{\rho}_p \tilde{A}_p \omega^2}{\tilde{E}_p \tilde{I}_p} \quad ; \quad \lambda_v^2 = \frac{K_z - \tilde{\rho}_p \tilde{A}_p \omega^2}{\tilde{\mu}_p \tilde{A}_p} \quad (\text{A.9})$$

Dado que su solución es del tipo $e^{\alpha z}$, las ecuaciones características pueden escribirse, respectivamente, de la siguiente manera.

$$\alpha_u^4 + \lambda_u^4 = 0 \quad ; \quad \alpha_v^2 + \lambda_v^2 = 0 \quad (\text{A.10})$$

así

$$\alpha_u^4 = -\frac{K_x - \tilde{\rho}_p \tilde{A}_p \omega^2}{\tilde{E}_p \tilde{I}_p} \quad ; \quad \alpha_v^2 = -\frac{K_z - \tilde{\rho}_p \tilde{A}_p \omega^2}{\tilde{\mu}_p \tilde{A}_p} \quad (\text{A.11})$$

las cuales tienen soluciones complejas que pueden escribirse, respectivamente, como

$$\alpha_u^j = \sqrt[4]{M_u} e^{i(\theta_u/4 + (j-1)\pi/2)} \quad \text{siendo} \quad j = 1, 2, 3, 4 \quad (\text{A.12})$$

$$\alpha_v^j = \sqrt{M_v} e^{i(\theta_v/2 + (j-1)\pi)} \quad \text{siendo} \quad j = 1, 2 \quad (\text{A.13})$$

donde M_u y M_v son los módulos y θ_u y θ_v son las fases de los números complejos α_u^4 y α_v^2 , respectivamente. De esta forma,

$$u_H = \sum_{j=1}^{j=4} D_j e^{\alpha_u^j z} \quad \text{y} \quad v_H = \sum_{j=1}^{j=2} \tilde{D}_j e^{\alpha_v^j z} \quad (\text{A.14})$$

La solución homogénea en la cabeza del pilote depende entonces de los siguientes parámetros

$$(\alpha_u L)^4 = \frac{K_x L^4}{\tilde{E}_p \tilde{I}_p} \left(1 - \frac{\tilde{\rho}_p \tilde{A}_p \omega^2}{K_x} \right) \quad (\text{A.15})$$

$$(\alpha_v L)^2 = \frac{K_z L^2}{\tilde{\mu}_p \tilde{A}_p} \left(1 - \frac{\tilde{\rho}_p \tilde{A}_p \omega^2}{K_z} \right) \quad (\text{A.16})$$

donde K_x puede expresarse como $n_x E_s$ y K_z como $n_z E_s$, siendo n_x y n_z constantes de proporcionalidad, y $E_s = 2(1 + \nu_s) c_s^2 \rho_s$. Esto conduce a las siguientes expresiones.

$$(\alpha_u L)^4 = n_x \frac{E_s L^4}{\tilde{E}_p \tilde{I}_p} \left(1 - \frac{\tilde{\rho}_p \tilde{A}_p \omega^2}{\rho_s c_s^2} \frac{1}{n_x 2(1 + \nu_s)} \right) \quad (\text{A.17})$$

$$(\alpha_v L)^2 = n_z \frac{E_s L^2}{\tilde{E}_p \tilde{A}_p} \left(1 - \frac{\tilde{\rho}_p \tilde{A}_p \omega^2}{\rho_s c_s^2} \frac{1}{n_z 2(1 + \nu_s)} \right) \quad (\text{A.18})$$

Por otra parte, cuando se introduce el campo incidente, las soluciones particulares en la cabeza del pilote dependen también del parámetro κL , donde $\kappa = \omega/c_s$ es el número de onda.

En este punto, los parámetros adimensionales que caracterizan el comportamiento dinámico de los pilotes pueden identificarse a partir de las Ecuaciones (A.17) y (A.18). Por una parte, puede observarse que ambas expresiones dependen de

$$\frac{\tilde{\rho}_p \tilde{A}_p \omega^2}{\rho_s c_s^2} \quad (\text{A.19})$$

Por otra parte, las ecuaciones (A.17) y (A.18) dependen, respectivamente, de

$$\frac{\tilde{E}_p \tilde{I}_p}{E_s L^4} \quad (\text{A.20})$$

y

$$\frac{\tilde{E}_p \tilde{A}_p}{E_s L^2} \quad (\text{A.21})$$

Realizando algunas operaciones algebraicas básicas, partiendo de la ecuación (A.20) se obtiene

$$\frac{\tilde{E}_p \tilde{I}_p}{E_s L^4} = \frac{\tilde{E}_p \tilde{I}_p I_p}{E_s I_p L^4} = \frac{E_p \pi}{E_s 64} \left(\frac{d}{L} \right)^4 \quad (\text{A.22})$$

donde $I_p = \pi d^4/64$ es la inercia rotacional correspondiente a una sección transversal circular maciza cuyo diámetro coincide con el diámetro exterior de la sección transversal anular real del pilote. Por otra parte, $E_p = \tilde{E}_p \tilde{I}_p / I_p$ representa el módulo de Young de un pilote sólido equivalente que podría modelar el comportamiento dinámico del pilote hueco real.

De forma similar, partiendo de la ecuación (A.21)

$$\frac{\tilde{E}_p \tilde{A}_p}{E_s L^2} = \frac{\tilde{E}_p \tilde{I}_p I_p \tilde{A}_p}{E_s I_p \tilde{I}_p L^2} = \frac{E_p I_p L^2}{E_s L^4 \tilde{i}_p^2} = \frac{E_p \pi}{E_s 64} \left(\frac{d}{L} \right)^4 \left(\frac{L}{\tilde{i}_p} \right)^2 \quad (\text{A.23})$$

siendo $A_p = \pi d^2/4$ el área de una sección transversal circular maciza de diámetro d .

Finalmente, partiendo de la ecuación (A.19)

$$\frac{\tilde{\rho}_p \tilde{A}_p \omega^2}{\rho_s c_s^2} = \frac{\tilde{A}_p \tilde{\rho}_p A_p \omega^2}{A_p \rho_s c_s^2} = \frac{\rho_p}{\rho_s} \left(\frac{\omega d}{c_s} \right)^2 \frac{\pi}{4} \quad (\text{A.24})$$

siendo $\rho_p = \tilde{\rho}_p \tilde{A}_p / A_p$ la densidad de masa correspondiente a un pilote sólido equivalente mencionado con anterioridad y $\tilde{i}_p^2 = \tilde{I}_p / \tilde{A}_p$ el radio de giro de la sección transversal real del pilote.

Por lo tanto, los principales parámetros del problema pueden escribirse del siguiente modo:

$$\frac{E_p}{E_s} ; \frac{L}{d} ; \frac{L}{\tilde{i}_p} ; \frac{\rho_p}{\rho_s} ; \frac{\omega d}{c_s} ; \nu_s ; \frac{s}{d} \quad (\text{A.25})$$

donde s/d representa la distancia entre pilotes para el caso de grupos de pilotes.

El mismo comportamiento dinámico es de esperar en todos los casos en los que estos parámetros adimensionales tengan los mismos valores. Con el fin de comprobar esta hipótesis, en la sección A.2.5, se analiza la respuesta dinámica de un conjunto de diferentes configuraciones de grupos de pilotes con los mismos valores de estos parámetros.

A.2.5. Influencia de la geometría de la sección transversal del pilote

En la sección A.2.4 se ha identificado el conjunto de parámetros adimensionales que caracterizan el comportamiento dinámico de los pilotes cuando se tiene en cuenta la interacción suelo-estructura. Para la mayor parte de los resultados que se presentan en este trabajo, se ha considerado que $E_p/E_s = 10^3$ y $\rho_s/\rho_p = 0.7$. Cuando se utilizan pilotes de acero, una sección transversal anular, como la que se muestra en el lado derecho de la figura A.5, es la geometría de la sección transversal del pilote que se correspondería con la realidad para dichos valores del ratio entre los módulos de Young del material del pilote y del suelo E_p/E_s y la relación de densidades suelo-pilote ρ_s/ρ_p .

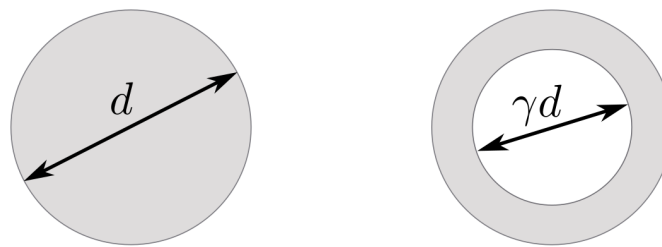


FIGURA A.5: Sección transversal de los pilotes.

En esta figura, el valor del parámetro γ representa la relación entre los diámetros interno y externo de la sección del pilote, y toma valores dentro del rango $0 \leq \gamma < 1$. Así, el área de la sección transversal anular puede expresarse como

$$\tilde{A}_p = \frac{\pi d^2}{4} (1 - \gamma^2) \quad (\text{A.26})$$

Asimismo, su inercia rotacional puede escribirse como

$$\tilde{I}_p = \frac{\pi d^4}{64}(1 - \gamma^4) \quad (\text{A.27})$$

Sin embargo, las funciones de impedancia y los factores de interacción cinemática se han obtenido suponiendo una sección transversal circular maciza para los pilotes, como la que se muestra en la parte izquierda de la figura A.5. El área y la inercia rotacional de una sección transversal circular maciza ($\gamma = 0$) se han definido como A_p e I_p , respectivamente. De acuerdo con las ecuaciones (A.26) y (A.27), cuando $\gamma = 0$

$$A_p = \tilde{A}_p(\gamma = 0) = \frac{\pi d^2}{4} \quad (\text{A.28})$$

y

$$I_p = \tilde{I}_p(\gamma = 0) = \frac{\pi d^4}{64} \quad (\text{A.29})$$

Así, el ratio de giro de una sección transversal circular maciza i_p puede definirse como

$$i_p = \tilde{i}_p(\gamma = 0) = \sqrt{\frac{I_p}{A_p}} = \frac{d}{4} \quad (\text{A.30})$$

Por lo tanto, cuando se considera una sección circular maciza, el parámetro adimensional L/\tilde{i}_p depende únicamente del ratio de esbeltez del pilote L/d . Esto implica que el comportamiento dinámico de los pilotes puede caracterizarse mediante los siguientes seis parámetros:

$$\frac{E_p}{E_s} \quad ; \quad \frac{L}{d} \quad ; \quad \frac{\rho_p}{\rho_s} \quad ; \quad \frac{\omega d}{c_s} \quad ; \quad \nu_s \quad ; \quad \frac{s}{d} \quad (\text{A.31})$$

En primer lugar, esta sección pretende verificar que se obtienen los mismos resultados, en términos de impedancias y factores de interacción cinemática, para todos los casos en los que los parámetros adimensionales que caracterizan el problema de interacción suelo-estructura adoptan los mismos valores. Con este propósito, se ha empleado un modelo de pilote con la misma sección circular maciza ($\tilde{A}_p = A_p = \text{cte}$ y $\tilde{I}_p = I_p = \text{cte}$) para representar pilotes con diversas secciones anulares de distinto espesor, según el valor de γ en cada caso. Los valores de las propiedades asignadas a la sección maciza a fin de modelar la sección anular real, E_p y ρ_p , varían con γ de acuerdo a las ecuaciones (A.32) y (A.33).

$$E_p = \tilde{E}_p \frac{\tilde{I}_p}{I_p} = \tilde{E}_p(1 - \gamma^4) \quad (\text{A.32})$$

$$\rho_p = \tilde{\rho}_p \frac{\tilde{A}_p}{A_p} = \tilde{\rho}_p(1 - \gamma^2) \quad (\text{A.33})$$

donde el módulo de Young y la densidad del material de los pilotes se han designado como \tilde{E}_p y $\tilde{\rho}_p$, respectivamente.

En este estudio, se han adoptado los siguientes valores para las propiedades del material del pilote: $\tilde{E}_p = 2.8 \cdot 10^3 \text{ Pa}$ y $\tilde{\rho}_p = 1 \text{ kg/m}^3$. Se ha considerado un diámetro exterior

$d = 2$ y una longitud del pilote $L = 30$. Los valores que se han supuesto para los parámetros adimensionales que caracterizan el comportamiento dinámico de los grupos de pilotes figuran en la tabla A.1. Cada columna de la tabla A.2 recoge las propiedades correspondientes al modelo de cada sección anular objeto de estudio. Puede observarse que el parámetro L/\tilde{i}_p se mantiene constante para todos los valores de γ dado que este depende únicamente de L/d cuando la sección transversal del pilote tiene una geometría circular maciza.

TABLA A.1: Valores de los parámetros adimensionales que caracterizan el problema de interacción suelo-estructura.

E_p/E_s	L/d	ρ_s/ρ_p	$\omega d/c_s$	ν_s	s/d
10^3	15	0.7	0 – 1	0.4	5, 10

TABLA A.2: Geometría y propiedades equivalentes de la sección transversal circular del modelo.

γ	A_p	I_p	L/\tilde{i}_p	E_p	E_s	ρ_p	ρ_s
0.00	3.1416	0.7854	60.00	$2.800 \cdot 10^3$	2.800	1.000	0.700
0.50	3.1416	0.7854	60.00	$2.625 \cdot 10^3$	2.625	0.750	0.525
0.80	3.1416	0.7854	60.00	$1.653 \cdot 10^3$	1.653	0.360	0.252
0.90	3.1416	0.7854	60.00	$0.962 \cdot 10^3$	0.962	0.190	0.133
0.95	3.1416	0.7854	60.00	$0.519 \cdot 10^3$	0.519	0.098	0.068

Por otra parte, se ha evaluado la precisión de los resultados obtenidos, en términos de impedancias y factores de interacción cinemática, cuando se modelan pilotes huecos mediante pilotes macizos de sección circular. Para ello, se han obtenido resultados considerando la geometría real de la sección transversal del pilote en cada caso. La tabla A.3 recoge las propiedades correspondientes a cada sección anular analizada. Para todos los casos recogidos en dicha tabla, se han considerado los mismos valores de los parámetros adimensionales adoptados para los casos que figuran en la tabla A.2. En este punto, el objetivo es comparar los resultados correspondientes a cada fila de la tabla A.3, que representa la geometría real de la sección transversal, con aquellos obtenidos para la misma fila de la tabla A.2, que corresponde a una sección circular equivalente en cada caso. Esto permite dilucidar si la simplificación que consiste en modelar pilotes huecos como pilotes macizos arroja o no resultados suficientemente precisos.

El radio de giro de la sección transversal anular \tilde{i}_p puede expresarse como una función del radio de giro de la sección circular i_p de la siguiente manera:

$$\tilde{i}_p = \sqrt{\frac{\tilde{I}_p}{\tilde{A}_p}} = i_p \sqrt{\frac{1 - \gamma^4}{1 - \gamma^2}} \quad (\text{A.34})$$

Así, el parámetro L/\tilde{i}_p puede escribirse como

$$\frac{L}{\tilde{i}_p} = 4 \frac{L}{d} \frac{i_p}{\tilde{i}_p} \quad (\text{A.35})$$

Tabla A.3: Geometría y propiedades del material de la sección transversal real.

γ	\tilde{A}_p	\tilde{I}_p	L/\tilde{i}_p	\tilde{E}_p	E_s	$\tilde{\rho}_p$	ρ_s	$\frac{\tilde{E}_p \tilde{I}_p}{E_s L^4} \cdot 10^4$	$\frac{\tilde{E}_p \tilde{A}_p}{E_s L^2}$
0.00	3.1416	0.7854	60.00	$2.8 \cdot 10^3$	2.800	1.000	0.700	9.6963	3.4907
0.50	2.3562	0.7363	53.67	$2.8 \cdot 10^3$	2.625	1.000	0.525	9.6963	2.7929
0.80	1.1310	0.4637	46.85	$2.8 \cdot 10^3$	1.653	1.000	0.252	9.6963	2.1283
0.90	0.5969	0.2701	44.60	$2.8 \cdot 10^3$	0.962	1.000	0.133	9.6963	1.9287
0.95	0.3063	0.1457	43.50	$2.8 \cdot 10^3$	0.519	1.000	0.068	9.6963	1.8347

Por lo tanto, la columna correspondiente a L/\tilde{i}_p en la tabla A.3 muestra la relación entre el radio de giro de la sección real \tilde{i}_p y el de la sección circular equivalente i_p utilizada en el modelo al que corresponde la tabla A.2.

Cabe mencionar que la novena columna de la tabla A.3 contiene los valores de un parámetro que gobierna el comportamiento de los pilotes cuando están sometidos a flexión (véase la ecuación (A.17)). Asimismo, la décima columna de la tabla A.3 refleja los valores de un parámetro que afecta a la respuesta de los pilotes cuando trabajan a axil (véase la ecuación (A.18)). Puede observarse que las variaciones de L/\tilde{i}_p sólo afectan a la última columna, asociada con el axil. De hecho, este parámetro no tiene influencia cuando el pilote está sometido únicamente a flexión (véanse las ecuaciones (A.22) y (A.23)) y sólo aparece cuando el pilote trabaja a axil. Así, la novena columna de la tabla A.3, que está asociada a la flexión, permanece constante. El pilote trabaja más a axil cuanto más inclinado se encuentra. Por lo tanto, modelar pilotes huecos como pilotes macizos arroja resultados menos precisos a medida que el ángulo de inclinación aumenta.

Con el fin de ilustrar la precisión de esta metodología, se han calculado las impedancias y los factores de interacción cinemática correspondientes a varias configuraciones de grupos de pilotes que contienen tanto pilotes verticales como inclinados. A su vez, se han obtenido resultados para las distintas secciones transversales anulares recogidas en la tabla A.3, así como para las secciones circulares equivalentes correspondientes que figuran en la tabla A.2. La obtención numérica de estos valores se ha llevado a cabo mediante el uso de una metodología de elementos finitos y elementos de contorno desarrollada por Padrón *et al.* [71].

Se han analizado distintas configuraciones de grupos de 2×2 y 3×3 pilotes con ratios de separación entre pilotes adyacentes $s/d = 5$ y 10 . Todas ellas siguen el patrón representado en la figura A.6. Se han considerado configuraciones que contienen pilotes verticales e inclinados en la dirección de la excitación con tres ángulos de inclinación diferentes $\theta = 10^\circ, 20^\circ$ y 30° .

La hipótesis de la primera parte del análisis que se aborda en esta sección se ha verificado dado que todas las filas de la tabla A.2, que corresponden a la misma sección circular ($\tilde{A}_p = A_p = cte$ y $\tilde{I}_p = I_p = cte$) con distintos valores de E_p y ρ_p pero con los mismos valores de los principales parámetros del problema ($E_p/E_s, L/d, L/\tilde{i}_p, \rho_p/\rho_s, \nu_s$), arrojan resultados idénticos para todas las configuraciones de grupos de pilotes objeto de estudio. De este modo, la línea de color negro que corresponde a $\gamma = 0$ en todas las figuras de las secciones A.2.5.1 y A.2.5.2 representa, al mismo tiempo, los resultados correspondientes a todas las filas de la tabla A.2.

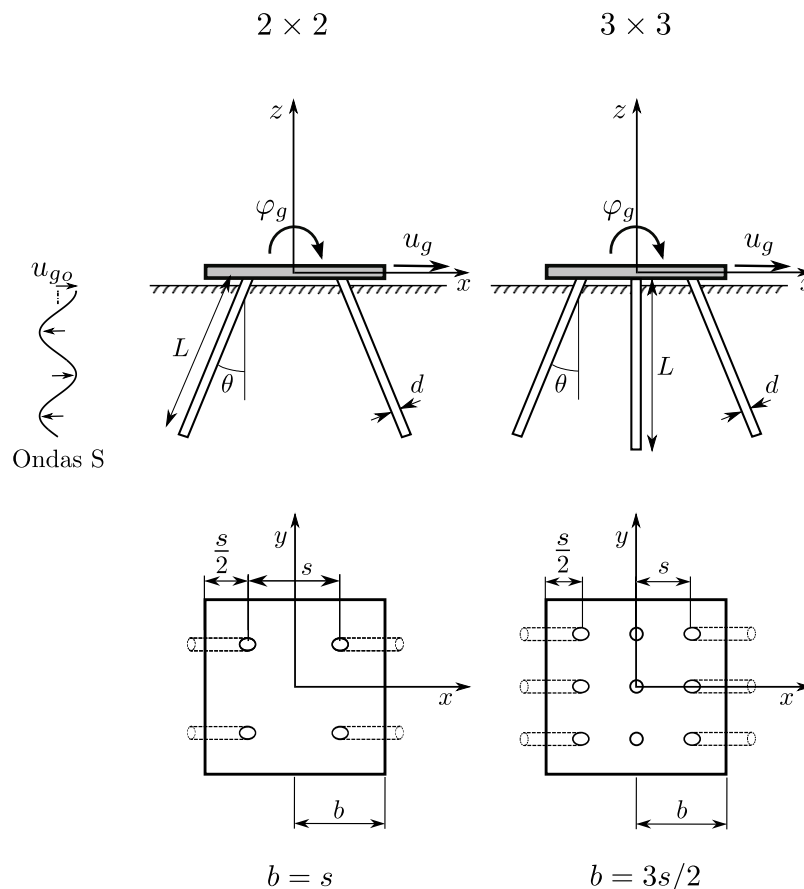


FIGURA A.6: Geometría de la cimentación pilotada.

En las siguientes subsecciones se evalúa la precisión de los resultados, en términos de impedancias y factores de interacción cinemática, obtenidos cuando se modelan pilotes huecos mediante pilotes macizos equivalentes.

A.2.5.1. Impedancias

Las figuras que van de la A.7 a la A.9 muestran impedancias, correspondientes a los modos de vibración horizontal, de balanceo y modo de vibración cruzado horizontal-balanceo, respectivamente, para todas las configuraciones analizadas. Con el ánimo de proporcionar al lector información concisa que pueda ser interpretada con facilidad, aunque se han considerado cuatro valores distintos del ángulo de inclinación, sólo se muestran los resultados correspondientes a los ángulos de inclinación $\theta = 0^\circ$ (pilotes verticales) y $\theta = 30^\circ$ para ilustrar las conclusiones de este análisis. En dichas figuras, cada columna corresponde a una configuración concreta de grupo de pilotes.

Puede observarse que la variación de γ no conduce a grandes diferencias en términos de impedancias, lo cual implica que modelar la sección transversal anular de los pilotes ($\gamma > 0$) como una sección circular maciza ($\gamma = 0$) permite obtener resultados suficientemente precisos para representar la rigidez y el amortiguamiento del sistema *suelo-cimiento*.

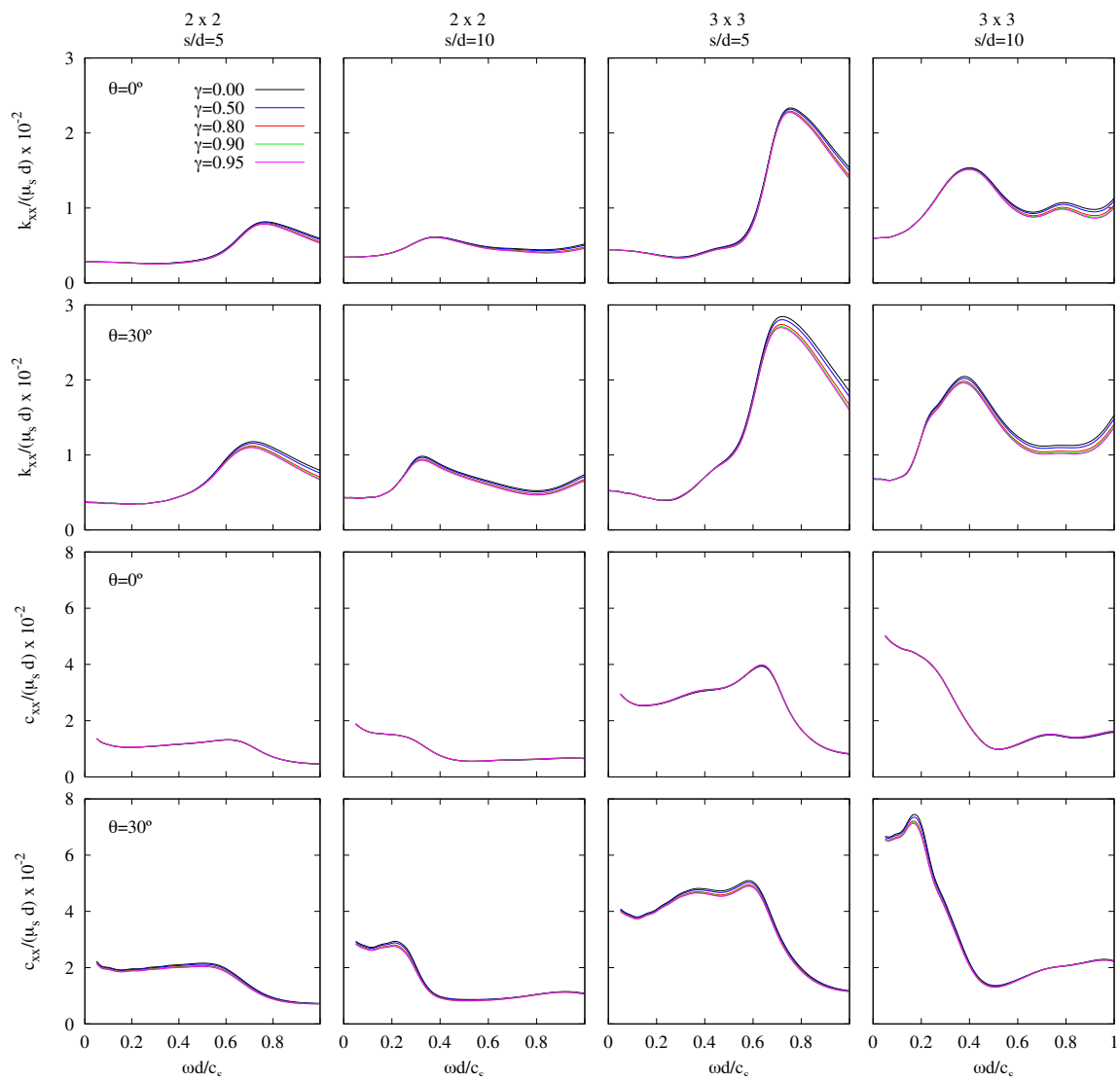


FIGURA A.7: Influencia de la geometría de la sección transversal de los pilotes. Impedancias horizontales de distintos grupos de 2×2 y 3×3 pilotes con elementos verticales ($\theta = 0^\circ$) o inclinados ($\theta = 30^\circ$). $E_p/E_s = 1000$ y $\xi_s = 0.05$.

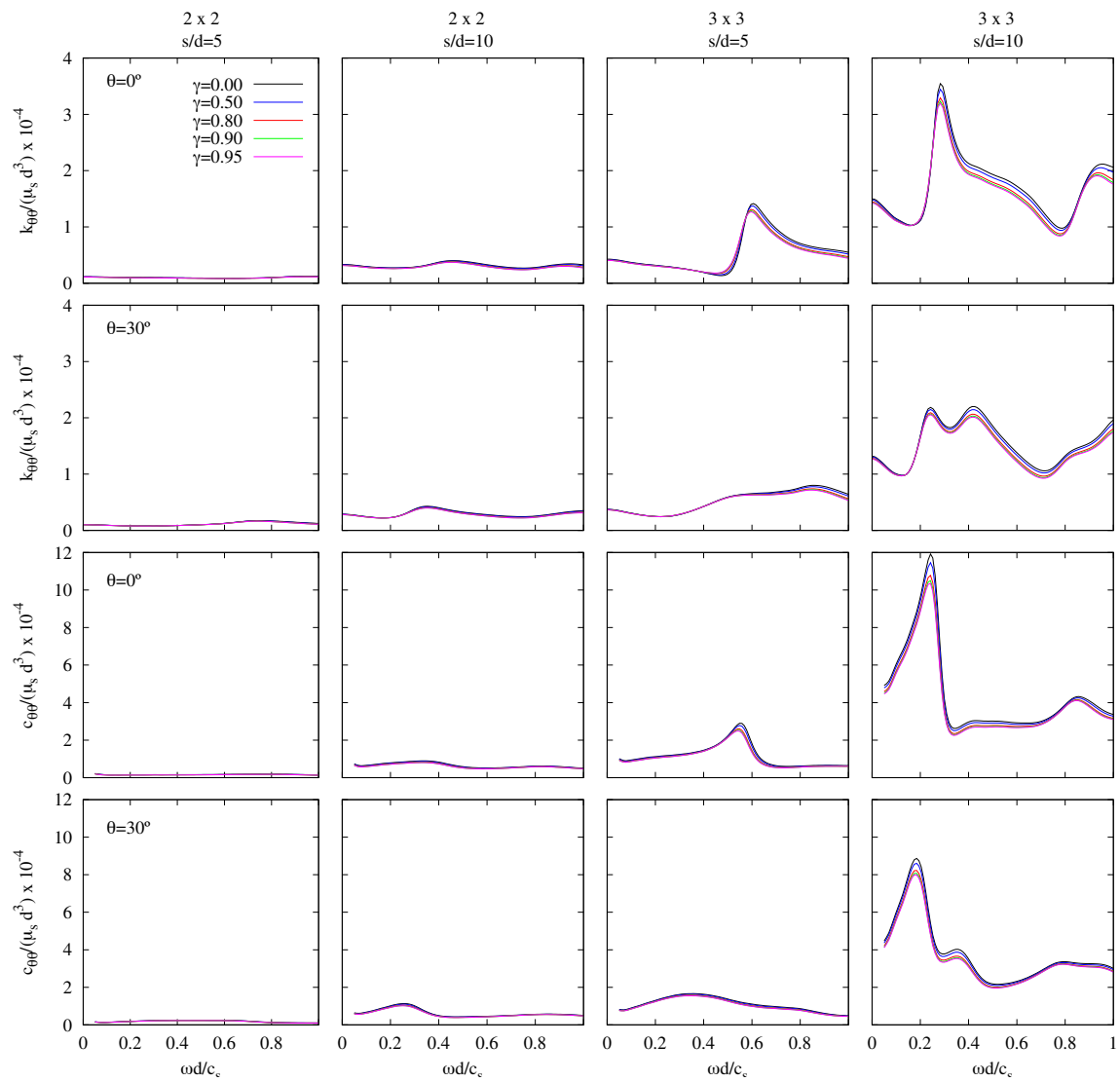


FIGURA A.8: Influencia de la geometría de la sección transversal de los pilotes. Impedancias de balanceo de distintos grupos de 2×2 y 3×3 pilotes con elementos verticales ($\theta = 0^\circ$) o inclinados ($\theta = 30^\circ$). $E_p/E_s = 1000$ y $\xi_s = 0.05$.

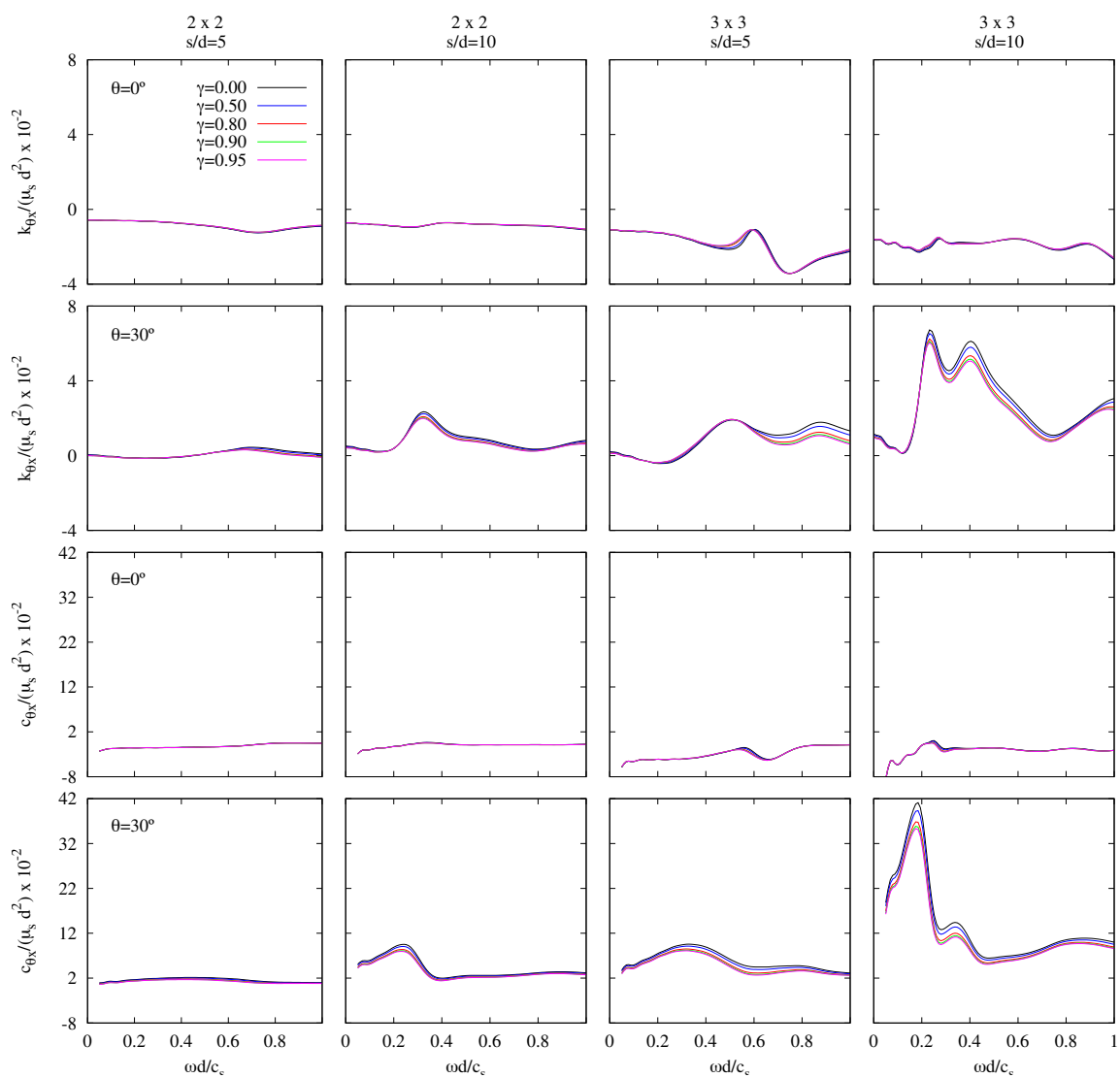


FIGURA A.9: Influencia de la geometría de la sección transversal de los pilotes. Impedancias cruzadas horizontal-balanceo de distintos grupos de 2×2 y 3×3 pilotes con elementos verticales ($\theta = 0^\circ$) o inclinados ($\theta = 30^\circ$). $E_p/E_s = 1000$ y $\xi_s = 0.05$.

Con el objetivo de evaluar de forma más precisa la exactitud de esta simplificación relacionada con la geometría de la sección transversal de los pilotes, se ha calculado el error porcentual que se comente al suponer una sección transversal maciza para modelar una sección anular con $\gamma = 0.9$. En este caso, dicho error porcentual se ha cuantificado en términos del área bajo las curvas de rigidez y amortiguamiento en el rango de frecuencias de interés para carga sísmica ($0 \leq \omega d/c_s \leq 0.5$) según Gazetas *et al.* [79]. En esta línea, la tabla A.4 recoge los resultados obtenidos para diversas configuraciones de pilotes con elementos verticales o inclinados con un ángulo de $\theta = 30^\circ$.

TABLA A.4: Error porcentual cometido en el cálculo de impedancias al usar un modelo de sección circular maciza para representar una sección anular con $\gamma = 0.9$.

s/d	2×2				3×3			
	5		10		5		10	
θ	0°	30°	0°	30°	0°	30°	0°	30°
$k_{xx}/(\mu_s d)$	1.88	1.06	1.11	3.51	2.57	0.14	1.07	2.88
$c_{xx}/(\mu_s d)$	0.49	3.93	0.23	5.05	0.59	2.53	0.21	3.50
$k_{\theta\theta}/(\mu_s d^3)$	5.71	1.40	5.55	4.73	0.45	0.80	6.42	5.34
$c_{\theta\theta}/(\mu_s d^3)$	10.71	6.12	11.28	9.13	6.65	6.38	10.92	9.39
$k_{\theta x}/(\mu_s d^2)$	2.02	0.06	1.42	16.36	4.06	2.25	1.46	14.04
$c_{\theta x}/(\mu_s d^2)$	0.19	27.43	0.90	20.42	1.96	19.11	0.38	18.45

A.2.5.2. Factores de interacción cinemática

Esta sección pretende ilustrar hasta qué punto los factores de interacción cinemática de grupos de pilotes constituidos por pilotes con sección transversal anular ($\gamma > 0$) pueden aproximarse mediante aquellos que corresponden a un grupo de pilotes equivalentes con sección transversal maciza ($\gamma = 0$). Con este propósito, las figuras A.10 y A.11 presentan, respectivamente, factores de interacción cinemática traslacionales y rotacionales para distintas configuraciones de grupos de 2×2 y 3×3 pilotes. La primera y la tercera fila corresponden a grupos de pilotes verticales, mientras que la segunda y la cuarta fila corresponden a grupos de pilotes que incluyen elementos inclinados con un ángulo de inclinación $\theta = 30^\circ$. Tal y como se ha mencionado con anterioridad, los resultados obtenidos para ángulos de inclinación $\theta = 10^\circ$ y 20° no se muestran en estas figuras, a fin de proporcionar al lector una información que pueda interpretarse con facilidad. Puede observarse que la variación de γ no implica grandes diferencias en términos de los factores de interacción cinemática. Esto permite afirmar que la simplificación adoptada, en cuanto a la geometría de la sección transversal del pilote, permite obtener resultados suficientemente precisos.

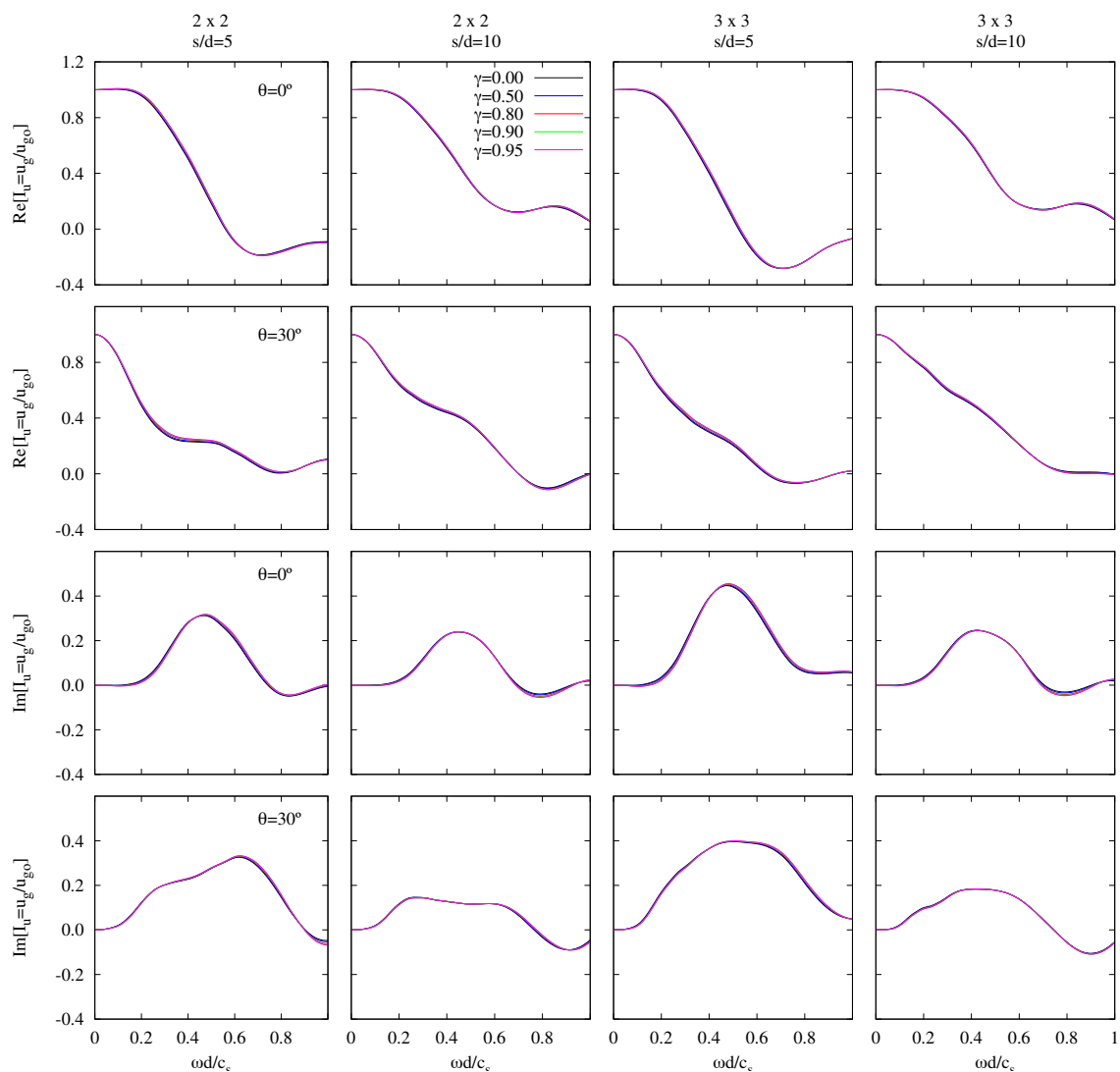


FIGURA A.10: Influencia de la geometría de la sección transversal de los pilotes. Factor de interacción cinemática traslacional I_u para distintos grupos de 2×2 y 3×3 pilotes con elementos verticales ($\theta = 0^\circ$) o inclinados ($\theta = 30^\circ$). $E_p/E_s = 1000$ y $\xi_s = 0.05$.

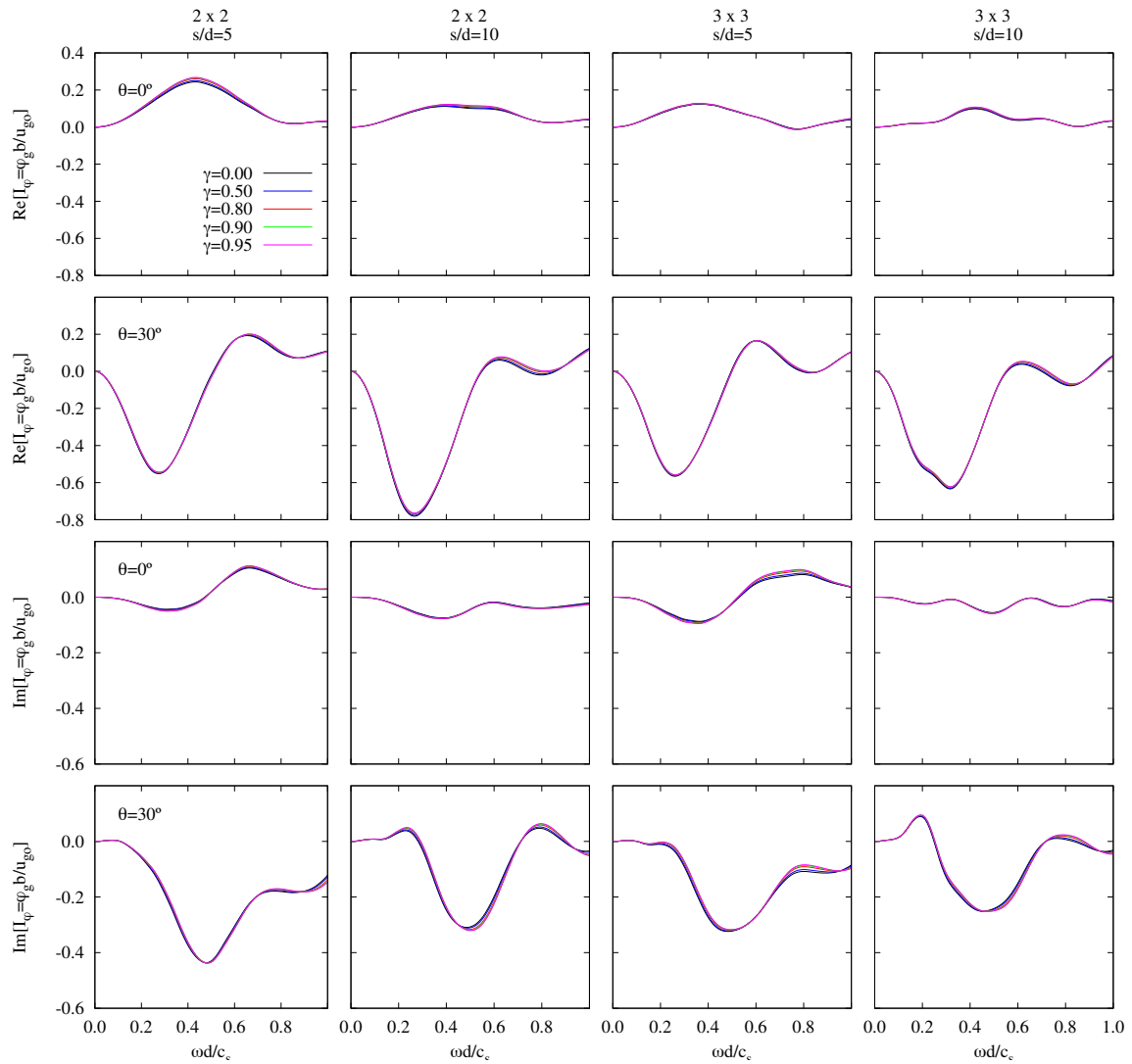


FIGURA A.11: Influencia de la geometría de la sección transversal de los pilotes. Factor de interacción cinemática rotacional I_φ para distintos grupos de 2×2 y 3×3 pilotes con elementos verticales ($\theta = 0^\circ$) o inclinados ($\theta = 30^\circ$). $E_p/E_s = 1000$ y $\xi_s = 0.05$.

TABLA A.5: Error porcentual cometido en el cálculo de los factores de interacción cinemática al usar un modelo de sección circular maciza para representar una sección anular con $\gamma = 0.9$.

s/d	2×2				3×3			
	5		10		5		10	
θ	0°	30°	0°	30°	0°	30°	0°	30°
$\text{Re}[I_u]$	1.91	3.13	0.93	1.73	1.99	2.82	0.80	1.34
$\text{Im}[I_u]$	2.92	0.03	2.78	1.47	2.87	1.58	3.02	2.19
$\text{Re}[I_\varphi]$	7.70	0.67	7.65	2.00	3.60	0.51	7.37	1.86
$\text{Im}[I_\varphi]$	11.03	3.22	4.75	0.27	6.83	8.51	4.67	2.21

Con el fin de evaluar de una forma más precisa la exactitud de esta simplificación de la geometría de los pilotes, se ha calculado el error porcentual derivado de considerar una sección transversal maciza para representar la sección real con una geometría anular con $\gamma = 0.9$. En este caso, dicho error se ha cuantificado en términos del área bajo las curvas de los factores de interacción cinemática. En este sentido, la tabla A.5 recoge los valores obtenidos para distintas configuraciones de pilotes con elementos verticales o inclinados con un ángulo de inclinación $\theta = 30^\circ$.

A.2.6. Ecuaciones del sistema y parámetros adimensionales

Un conjunto de parámetros adimensionales, que abarcan las principales características de los problemas de interacción suelo-estructura, ha sido empleado repetidamente en la literatura relacionada para llevar a cabo análisis paramétricos [7,8,13,14]. Siguiendo la línea de estos autores, los parámetros utilizados en este trabajo para caracterizar el sistema *suelo-cimiento-estructura* son:

1. Parámetro de onda $\sigma = c_s T/h$, que mide la rigidez relativa suelo-estructura.
2. Ratio de esbeltez h/b , que mide la relación entre la altura de la estructura y el semiancho del cimiento.
3. Densidad de masa relativa entre la estructura y el suelo $\delta = m/(\rho_s A_b h)$, donde A_b es el área de la base de la estructura. Así, en el caso de cimentaciones cuadradas $A_b = 4b^2$ y, por lo tanto, $\delta = m/(4\rho_s b^2 h)$.
4. Ratio de masa cimiento-estructura m_o/m .
5. Coeficiente de amortiguamiento de la estructura en base rígida ξ .
6. Frecuencia adimensional de la estructura en base rígida $\lambda = \omega_n/\omega$.
7. Frecuencia de excitación adimensional $a_o = \omega b/c_s = (b/d)(\omega d/c_s)$.

En este trabajo se ha considerado un modelo de amortiguamiento histerético del tipo $\mu_s = \text{Re}[\mu_s](1 + 2i\xi_s)$ para el material del suelo, siendo ξ_s el coeficiente de amortiguamiento correspondiente.

En lo que se refiere a la cimentación pilotada, se han considerado los principales parámetros adimensionales que caracterizan su comportamiento dinámico, previamente identificados en la sección A.2.4, que son:

1. Ratio de separación entre pilotes s/d .
2. Ratio de embebimiento L/b .
3. Ratio del módulo de Young pilote-suelo E_p/E_s .
4. Frecuencia adimensional a_o .
5. Relación de densidades suelo-pilote ρ_s/ρ_p .
6. Ratio de esbeltez de los pilotes L/d .
7. Ángulo de inclinación de los pilotes θ .
8. Coeficiente de Poisson del suelo ν_s .

La ecuación de movimiento del sistema (ec. (A.4)) puede expresarse en función de los parámetros adimensionales definidos anteriormente, con el fin de facilitar el análisis de la influencia de cada uno de ellos en la respuesta dinámica del sistema, realizando operaciones algebraicas básicas. Tales operaciones se describen a continuación:

1. Tras sumar las dos primeras filas, la segunda ecuación representa el equilibrio horizontal de fuerzas en el conjunto.

$$\left\{ \left[\begin{array}{ccc} K & 0 & 0 \\ 0 & K_{xx} & K_{x\theta} \\ 0 & K_{\theta x} & K_{\theta\theta} \end{array} \right] - \omega^2 \left[\begin{array}{ccc} m & m & mh \\ m & m + m_o & mh \\ mh & mh & I_T \end{array} \right] \right\} \cdot \left[\begin{array}{c} u \\ u_r^c \\ \varphi_r^c \end{array} \right] = \omega^2 \left\{ \left[\begin{array}{c} m \\ m + m_o \\ mh \end{array} \right] u_g + \left[\begin{array}{c} mh \\ mh \\ I_T \end{array} \right] \varphi_g \right\} \quad (\text{A.36})$$

2. Introduciendo las expresiones de la rigidez y el amortiguamiento estructural, $k = \omega_n^2 m$ y $c = 2m\omega_n \xi \omega / a_o$, en la ecuación (A.36), y dividiendo la ecuación completa por el movimiento de campo libre en la superficie \ddot{u}_{g_o} se llega a la ecuación (A.37).

$$\left\{ \begin{bmatrix} \omega_n^2 m + i2\omega_n m \xi \omega & 0 & 0 \\ 0 & K_{xx} & K_{x\theta} \\ 0 & K_{\theta x} & K_{\theta\theta} \end{bmatrix} - \omega^2 \begin{bmatrix} m & m & mh \\ m & m+m_o & mh \\ mh & mh & I_T \end{bmatrix} \right\} \cdot \begin{bmatrix} u/\ddot{u}_{g_o} \\ u_r^c/\ddot{u}_{g_o} \\ \varphi_r^c/\ddot{u}_{g_o} \end{bmatrix} = - \left\{ \begin{bmatrix} m \\ m+m_o \\ mh \end{bmatrix} I_u + \frac{1}{b} \begin{bmatrix} mh \\ mh \\ I_T \end{bmatrix} I_\varphi \right\} \quad (\text{A.37})$$

donde $I_u = u_g/u_{g_o}$ e $I_\varphi = \varphi_g b/u_{g_o}$ son los factores de interacción cinemática normalizados, siendo ambos funciones de la frecuencia adimensional a_o .

3. El ratio ω^2/ω_n^2 puede extraerse como factor común del primer término de la ecuación (A.37). Por otra parte, la masa estructural m puede extraerse como factor común de ambos lados de dicha ecuación, lo cual conduce a la ecuación (A.38).

$$\frac{1}{\lambda^2} \cdot \left\{ \begin{bmatrix} \lambda^2 + 2\lambda \xi i & 0 & 0 \\ 0 & \frac{K_{xx}}{\omega^2 m} & \frac{K_{x\theta}}{\omega^2 m} \\ 0 & \frac{K_{\theta x}}{\omega^2 m} & \frac{K_{\theta\theta}}{\omega^2 m} \end{bmatrix} - \begin{bmatrix} 1 & 1 & h \\ 1 & 1 + \frac{m_o}{m} & h \\ h & h & \frac{I_T}{m} \end{bmatrix} \right\} \cdot \begin{bmatrix} \omega_n^2 u/\ddot{u}_{g_o} \\ \omega_n^2 u_r^c/\ddot{u}_{g_o} \\ \omega_n^2 \varphi_r^c/\ddot{u}_{g_o} \end{bmatrix} = - \left\{ \begin{bmatrix} 1 \\ 1 + \frac{m_o}{m} \\ h \end{bmatrix} I_u + \frac{1}{b} \begin{bmatrix} h \\ h \\ \frac{I_T}{m} \end{bmatrix} I_\varphi \right\} \quad (\text{A.38})$$

4. Dividiendo entre h la tercera fila de la ecuación y la tercera columna de la matriz del sistema y sustituyendo las inercias rotacionales I_o e I por sus expresiones $I_o = m_o b^2/3$ e $I = m b^2/3$, respectivamente, la ecuación (A.38) se transforma en la ecuación (A.39).

$$\frac{1}{\lambda^2} \cdot \left\{ \begin{bmatrix} \lambda^2 + 2\lambda \xi i & 0 & 0 \\ 0 & \frac{K_{xx}}{\omega^2 m} & \frac{K_{x\theta}}{\omega^2 mh} \\ 0 & \frac{K_{\theta x}}{\omega^2 mh} & \frac{K_{\theta\theta}}{\omega^2 mh} \end{bmatrix} - \begin{bmatrix} 1 & 1 & 1 \\ 1 & 1 + \frac{m_o}{m} & 1 \\ 1 & 1 & 1 + \frac{b^2}{3h^2} \left(1 + \frac{m_o}{m}\right) \end{bmatrix} \right\} \cdot \begin{bmatrix} \omega_n^2 u/\ddot{u}_{g_o} \\ \omega_n^2 u_r^c/\ddot{u}_{g_o} \\ \omega_n^2 \varphi_r^c/\ddot{u}_{g_o} \end{bmatrix} = - \left\{ \begin{bmatrix} 1 \\ 1 + \frac{m_o}{m} \\ 1 \end{bmatrix} I_u + \frac{1}{b} \begin{bmatrix} h \\ h \\ h + \frac{b^2}{3h} \left(1 + \frac{m_o}{m}\right) \end{bmatrix} I_\varphi \right\} \quad (\text{A.39})$$

5. Los términos del sistema de ecuaciones de movimiento que dependen de las impedancias pueden expresarse también como una función de los parámetros adimensionales ya definidos, tal y como se indica a continuación. Cabe mencionar que $K_{\theta x} = K_{x\theta}$ como consecuencia de los teoremas de reciprocidad.

$$\frac{K_{xx}}{\omega^2 m} = \frac{\mu_s b \tilde{K}_{xx}}{\omega^2 m} = \frac{(c_s^2 \rho_s) b \tilde{K}_{xx}}{\omega^2 m} = \left(\frac{\sigma h}{T} \right)^2 \frac{m}{4 \delta b^2 h} \frac{b \tilde{K}_{xx}}{\omega^2 m} = \frac{\lambda^2 \sigma^2 h}{16 \pi^2 b} \frac{1}{\delta} \tilde{K}_{xx} \quad (\text{A.40})$$

$$\frac{K_{x\theta}}{\omega^2 m h} = \frac{\mu_s b^2 \tilde{K}_{x\theta}}{\omega^2 m h} = \frac{(c_s^2 \rho_s) b^2 \tilde{K}_{x\theta}}{\omega^2 m h} = \left(\frac{\sigma h}{T} \right)^2 \frac{m}{4 \delta b^2 h} \frac{b^2 \tilde{K}_{x\theta}}{m h \omega^2} = \frac{\lambda^2 \sigma^2}{16 \pi^2} \frac{1}{\delta} \tilde{K}_{x\theta} \quad (\text{A.41})$$

$$\frac{K_{\theta\theta}}{\omega^2 m h^2} = \frac{\mu_s b^3 \tilde{K}_{\theta\theta}}{\omega^2 m h^2} = \frac{(c_s^2 \rho_s) b^3 \tilde{K}_{\theta\theta}}{\omega^2 m h^2} = \left(\frac{\sigma h}{T} \right)^2 \frac{m}{4 \delta b^2 h} \frac{b^3 \tilde{K}_{\theta\theta}}{m h^2 \omega^2} = \frac{\lambda^2 \sigma^2}{16 \pi^2} \frac{1}{\delta} \frac{b}{h} \tilde{K}_{\theta\theta} \quad (\text{A.42})$$

De este modo, la ecuación de movimiento del sistema puede escribirse de la siguiente forma:

$$\left\{ \begin{array}{ccc} \lambda^2 + 2\lambda \xi_i & 0 & 0 \\ 0 & \lambda^2 \sigma^2 \frac{1}{16 \pi^2} \frac{h}{b} \frac{1}{\delta} \tilde{K}_{xx} & \lambda^2 \sigma^2 \frac{1}{\delta} \frac{1}{16 \pi^2} \tilde{K}_{x\theta} \\ 0 & \lambda^2 \sigma^2 \frac{1}{\delta} \frac{1}{16 \pi^2} \tilde{K}_{\theta x} & \lambda^2 \sigma^2 \frac{1}{16 \pi^2} \frac{b}{h} \frac{1}{\delta} \tilde{K}_{\theta\theta} \end{array} \right\} - \left[\begin{array}{ccc} 1 & 1 & 1 \\ 1 & 1 + \frac{m_o}{m} & 1 \\ 1 & 1 & 1 + \frac{b^2}{3h^2} \left(1 + \frac{m_o}{m} \right) \end{array} \right] \left[\begin{array}{c} \omega_n^2 u / \ddot{u}_{g_o} \\ \omega_n^2 u_r^c / \ddot{u}_{g_o} \\ \omega_n^2 h \varphi_r^c / \ddot{u}_{g_o} \end{array} \right] = \quad (\text{A.43})$$

$$- \lambda^2 \left\{ \left[\begin{array}{c} 1 \\ 1 + \frac{m_o}{m} \\ 1 \end{array} \right] I_u + \frac{h}{b} \left[\begin{array}{c} 1 \\ 1 \\ 1 + \frac{b^2}{3h^2} \left(1 + \frac{m_o}{m} \right) \end{array} \right] I_\varphi \right\}$$

donde las inercias rotacionales han sido reemplazadas por las expresiones $I = mb^2/3$ e $I_o = m_o b^2/3$, respectivamente, estando tanto la masa de la estructura como la del encepado uniformemente distribuida en áreas cuadradas. Las funciones de impedancia se han normalizado de la siguiente manera: $\tilde{K}_{xx} = K_{xx}/(\mu_s b)$, $\tilde{K}_{\theta\theta} = K_{\theta\theta}/(\mu_s b^3)$ y $\tilde{K}_{x\theta} = K_{x\theta}/(\mu_s b^2)$, y los factores de interacción cinemática se han normalizado con el movimiento de campo libre en la superficie u_{g_o} , siendo $I_u = u_g/u_{g_o}$ e $I_\varphi = \varphi_g b/u_{g_o}$, ambos funciones de la frecuencia adimensional a_o .

A.2.7. Diagonalización de la matriz de impedancias

La respuesta dinámica del sistema acoplado puede expresarse en términos del constante en la base de la estructura por unidad de fuerza sísmica efectiva [7, 114] definido como

$$Q = \left| \frac{\omega_n^2 u}{\ddot{u}_{g_o}} \right| \quad (\text{A.44})$$

Así, Q puede obtenerse para cada frecuencia resolviendo el sistema complejo de ecuaciones algebraicas de la ecuación (A.43) para $\omega_n^2 u / \ddot{u}_{g_o}$.

La utilidad que tiene expresar la respuesta sísmica de la estructura en estos términos, reside en el hecho de que el producto de este valor por la masa estructural y la

correspondiente aceleración horizontal de campo libre a nivel de la superficie conduce a la amplitud del cortante en la base de la estructura.

Con el fin de obtener expresiones aproximadas manejables para Q , manteniendo las impedancias cruzadas, es necesario condensar la interacción suelo-cimentación en un punto situado a una cierta profundidad virtual $D(\omega) = -K_{x\theta}/K_{xx}$ (véase la figura A.12) tal que la matriz de impedancias sea diagonal, tal y como algunos autores proponen [27, 32].

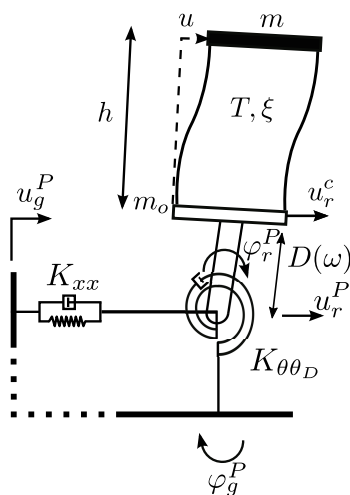


FIGURA A.12: Modelo equivalente con matriz de impedancias diagonalizada.

Si se considera el sistema mostrado en la figura A.12, la ecuación de movimiento de la cimentación puede escribirse como sigue:

$$\begin{bmatrix} F \\ M \end{bmatrix} = \begin{bmatrix} K_{xx} & K_{x\theta} \\ K_{\theta x} & K_{\theta\theta} \end{bmatrix} \cdot \begin{bmatrix} u_r^c \\ \varphi_r^c \end{bmatrix} \quad (\text{A.45})$$

Condensando la interacción suelo-cimentación en un punto situado a una profundidad virtual $D(\omega)$, la ecuación de movimiento de la cimentación puede expresarse como

$$\begin{bmatrix} F^P \\ M^P - F^P D \end{bmatrix} = \begin{bmatrix} K_{xx} & K_{x\theta} \\ K_{\theta x} & K_{\theta\theta} \end{bmatrix} \cdot \begin{bmatrix} u_r^P + \varphi_r^P D \\ \varphi_r^P \end{bmatrix} \quad (\text{A.46})$$

donde $F^P = F$, $M^P - F^P D = M$, $u_r^P = u_r^c - \varphi_r^P D$ y $\varphi_r^P = \varphi_r^c$.

De este modo, la ecuación (A.46) puede escribirse también como

$$\begin{bmatrix} F^P \\ M^P \end{bmatrix} = \begin{bmatrix} K_{xx} & K_{x\theta} + K_{xx} D \\ K_{\theta x} + K_{xx} D & K_{\theta\theta} + 2K_{x\theta} D + K_{xx} D^2 \end{bmatrix} \cdot \begin{bmatrix} u_r^P \\ \varphi_r^P \end{bmatrix} \quad (\text{A.47})$$

Puede observarse que para obtener una matriz de impedancias diagonal, el polo del encepado debe desplazarse una distancia $D(\omega) = -K_{\theta x}/K_{xx}$, lo cual conduce a la ecuación

ción A.48. Téngase en cuenta que, como se mencionó anteriormente, $K_{\theta x} = K_{x\theta}$ como consecuencia de los teoremas de reciprocidad.

$$\begin{bmatrix} F^P \\ M^P \end{bmatrix} = \begin{bmatrix} K_{xx} & 0 \\ 0 & K_{\theta\theta} - \frac{K_{\theta x}^2}{K_{xx}} \end{bmatrix} \cdot \begin{bmatrix} u_r^P \\ \varphi_r^P \end{bmatrix} \quad (\text{A.48})$$

siendo $K_{\theta\theta} - K_{\theta x}^2/K_{xx} = K_{\theta\theta D}$.

Por lo tanto, las ecuaciones de movimiento del sistema ((A.1),(A.2) y (A.3) pueden expresarse ahora, referidas a dicho punto situado a una profundidad virtual D , como

$$m \cdot [\ddot{u} + \ddot{u}_r^P + \ddot{u}_g^P + (h + D) \cdot (\ddot{\varphi}_r^P + \ddot{\varphi}_g^P)] + K \cdot u = 0 \quad (\text{A.49})$$

$$m_o \cdot [\ddot{u}_r^P + \ddot{u}_g^P + (\ddot{\varphi}_r^P + \ddot{\varphi}_g^P) \cdot D] + K_{xx} \cdot u_r^P - K \cdot u = 0 \quad (\text{A.50})$$

$$\begin{aligned} m \cdot (h + D) [\ddot{u} + \ddot{u}_r^P + \ddot{u}_g^P + (h + D) \cdot (\ddot{\varphi}_r^P + \ddot{\varphi}_g^P)] + I \cdot (\ddot{\varphi}_r^P + \ddot{\varphi}_g^P) + \\ m_o \cdot D [\ddot{u}_r^P + \ddot{u}_g^P + (\ddot{\varphi}_r^P + \ddot{\varphi}_g^P) \cdot D] + I_o \cdot (\ddot{\varphi}_r^P + \ddot{\varphi}_g^P) + K_{\theta\theta D} \cdot \varphi_r^P = 0 \end{aligned} \quad (\text{A.51})$$

donde la ecuación (A.49) representa el equilibrio de fuerzas horizontales en la estructura; la ecuación (A.50), el equilibrio de fuerzas horizontales del sistema estructura-cimiento y la ecuación (A.51), el equilibrio de momentos del sistema *estructura-cimiento* entorno al punto situado a una profundidad virtual D en el que se ha condensado la interacción suelo-cimiento.

En el dominio de la frecuencia (con dependencia temporal $e^{i\omega t}$) este conjunto de ecuaciones puede escribirse en forma matricial como

$$\begin{aligned} & \left\{ \begin{bmatrix} K & 0 & 0 \\ -K & K_{xx} & 0 \\ 0 & 0 & K_{\theta\theta D} \end{bmatrix} \right. \\ & -\omega^2 \left. \begin{bmatrix} m & m & m(h+D) \\ 0 & m_o & m_o D \\ m(h+D) & m(h+D) + m_o D & I_T \end{bmatrix} \right\} \cdot \begin{bmatrix} u \\ u_r^P \\ \varphi_r^P \end{bmatrix} = \\ & \omega^2 \left\{ \begin{bmatrix} m \\ m_o \\ m(h+D) + m_o D \end{bmatrix} u_g^P + \begin{bmatrix} m(h+D) \\ m_o D \\ I_T \end{bmatrix} \varphi_g^P \right\} \end{aligned} \quad (\text{A.52})$$

donde $I_T = m(h+D)^2 + m_o D^2 + I_o + I$, $K = k + ia_o c$; y los movimientos se han considerado del tipo $u(t) = u e^{i\omega t}$.

Debe tenerse en cuenta que, tras la transformación expuesta anteriormente, las ecuaciones de movimiento del sistema están escritas en términos de los movimientos de entrada horizontal y de giro en el punto en que se ha condensado la interacción suelo-cimiento,

u_g^P y φ_g^P , mientras que la ecuación (A.4) estaba expresada en términos de los movimientos de entrada horizontal y de giro en el encepado u_g y φ_g . Además, la ecuación (A.52) está escrita en términos del desplazamiento horizontal y el giro relativos en el citado punto, u_r^P y φ_r^P , en lugar de estar expresadas en términos del desplazamiento horizontal y el giro relativos en el cimienta a nivel del encepado, u_r^c y φ_r^c .

Con el fin de expresar el sistema de ecuaciones de movimiento como una función de los parámetros adimensionales definidos con anterioridad, se ha seguido un procedimiento similar al descrito en la sección A.2.6. En esta línea, las operaciones algebraicas realizadas con este propósito se explican con detalle a continuación:

1. El primer paso consiste en sumar las dos primeras filas de la ecuación. De este modo, la segunda ecuación representará el equilibrio horizontal del conjunto.
2. Luego, al introducir las expresiones de la rigidez y el amortiguamiento de la estructura, $k = \omega_n^2 m$ y $c = 2m\omega_n \xi \omega / a_o$, en la ecuación (A.52), y dividiendo la ecuación entre el movimiento de campo libre a nivel de la superficie \ddot{u}_{g_o} se llega a la ecuación (A.53).

$$\begin{aligned} & \left\{ \begin{bmatrix} \omega_n^2 m + i2\omega_n m \xi \omega & 0 & 0 \\ 0 & K_{xx} & 0 \\ 0 & 0 & K_{\theta\theta D} \end{bmatrix} - \right. \\ & \left. \omega^2 \begin{bmatrix} m & m & m(h+D) \\ m & m+m_o & m(h+D) + m_o D \\ m(h+D) & m(h+D) + m_o D & I_T \end{bmatrix} \right\} \begin{bmatrix} u/\ddot{u}_{g_o} \\ u_r^P/\ddot{u}_{g_o} \\ \varphi_r^P/\ddot{u}_{g_o} \end{bmatrix} \\ & = \omega^2 \left\{ \begin{bmatrix} m \\ m+m_o \\ m(h+D) + m_o D \end{bmatrix} \frac{u_g^P}{\ddot{u}_{g_o}} + \begin{bmatrix} m(h+D) \\ m(h+D) + m_o D \\ I_T \end{bmatrix} \frac{\varphi_g^P}{\ddot{u}_{g_o}} \right\} \end{aligned} \quad (A.53)$$

3. El ratio ω^2/ω_n^2 puede extraerse como factor común del primer término de la ecuación anterior. Por otra parte, la masa estructural m puede extraerse como factor común de ambos lados de dicha ecuación. Esto conduce a la siguiente ecuación:

$$\begin{aligned} & \frac{1}{\lambda^2} \left\{ \begin{bmatrix} \lambda^2 + 2\lambda \xi i & 0 & 0 \\ 0 & \frac{K_{xx}}{\omega^2 m} & 0 \\ 0 & 0 & \frac{K_{\theta\theta D}}{\omega^2 m} \end{bmatrix} - \right. \\ & \left. \begin{bmatrix} 1 & 1 & h+D \\ 1 & 1 + \frac{m_o}{m} & h+D + \frac{m_o}{m} D \\ h+D & h+D + \frac{m_o}{m} D & \frac{I_T}{m} \end{bmatrix} \right\} \begin{bmatrix} \omega_n^2 u/\ddot{u}_{g_o} \\ \omega_n^2 u_r^P/\ddot{u}_{g_o} \\ \omega_n^2 \varphi_r^P/\ddot{u}_{g_o} \end{bmatrix} \\ & = \omega^2 \left\{ \begin{bmatrix} 1 \\ 1 + \frac{m_o}{m} \\ h+D + \frac{m_o}{m} D \end{bmatrix} \frac{u_g^P}{\ddot{u}_{g_o}} + \begin{bmatrix} h+D \\ h+D + \frac{m_o}{m} D \\ \frac{I_T}{m} \end{bmatrix} \frac{\varphi_g^P}{\ddot{u}_{g_o}} \right\} \end{aligned} \quad (A.54)$$

4. Dividiendo entre $(h + D)$ la tercera fila de la ecuación y la tercera columna de la matriz del sistema, la ecuación (A.54) puede escribirse como sigue:

$$\begin{aligned}
 & \frac{1}{\lambda^2} \left\{ \begin{bmatrix} \lambda^2 + 2\lambda\xi i & 0 & 0 \\ 0 & \frac{K_{xx}}{\omega^2 m} & 0 \\ 0 & 0 & \frac{K_{\theta\theta D}}{\omega^2 m (h+D)^2} \end{bmatrix} \right. \\
 & - \left. \begin{bmatrix} 1 & 1 & 1 \\ 1 & 1 + \frac{m_o}{m} & 1 + \frac{m_o}{m} \frac{D}{h+D} \\ 1 & 1 + \frac{m_o}{m} \frac{D}{h+D} & 1 + \frac{b^2}{3(h+D)^2} \left(1 + \frac{m_o}{m}\right) + \frac{m_o}{m} \frac{D^2}{(h+D)^2} \end{bmatrix} \right\} \begin{bmatrix} \omega_n^2 u / \ddot{u}_{g_o} \\ \omega_n^2 u_r^P / \ddot{u}_{g_o} \\ \omega_n^2 (h+D) \varphi_r^P / \ddot{u}_{g_o} \end{bmatrix} \quad (\text{A.55}) \\
 & = \omega^2 \left\{ \begin{bmatrix} 1 \\ 1 + \frac{m_o}{m} \\ 1 + \frac{m_o}{m} \frac{D}{h+D} \end{bmatrix} \frac{u_g^P}{\ddot{u}_{g_o}} + \begin{bmatrix} h+D \\ h+D + \frac{m_o}{m} D \\ h+D + \frac{b^2}{3(h+D)} \left(1 + \frac{m_o}{m}\right) + \frac{m_o}{m} \frac{D^2}{(h+D)} \end{bmatrix} \frac{\varphi_g^P}{\ddot{u}_{g_o}} \right\}
 \end{aligned}$$

5. Los términos de la matriz del sistema donde hay expresiones que dependen de las impedancias también pueden expresarse en función de los parámetros adimensionales definidos con anterioridad, como se indica a continuación:

$$\frac{K_{xx}}{\omega^2 m} = \frac{\mu_s b \tilde{K}_{xx}}{\omega^2 m} = \frac{(c_s^2 \rho_s) b \tilde{K}_{xx}}{\omega^2 m} = \left(\frac{\sigma h}{T}\right)^2 \frac{m}{4\delta b^2 h} \frac{b \tilde{K}_{xx}}{\omega^2 m} = \frac{\lambda^2 \sigma^2 h}{16\pi^2 b \delta} \tilde{K}_{xx} \quad (\text{A.56})$$

$$\begin{aligned}
 \frac{K_{\theta\theta D}}{\omega^2 m (h+D)^2} &= \frac{\mu_s b^3 \tilde{K}_{\theta\theta D}}{\omega^2 m (h+D)^2} = \frac{(c_s^2 \rho_s) b^3 \tilde{K}_{\theta\theta D}}{\omega^2 m (h+D)^2} \\
 &= \left(\frac{\sigma h}{T}\right)^2 \frac{m}{4\delta b^2 h} \frac{b^3 \tilde{K}_{\theta\theta D}}{m (h+D)^2 \omega^2} = \frac{\lambda^2 \sigma^2}{16\pi^2} \frac{1}{\delta} \frac{h}{b} \frac{b^2}{(h+D)^2} \tilde{K}_{\theta\theta D} \quad (\text{A.57})
 \end{aligned}$$

Cabe mencionar que el movimiento de giro de la sollicitación en el punto en el que se ha condensado la interacción suelo-cimiento coincide con el giro en el encepado ($\varphi_g^P = \varphi_g$). Asimismo, el movimiento de giro relativo en dicho punto coincide con el giro relativo del cimiento ($\varphi_r^P = \varphi_r^c$). Considerando estas equivalencias y dado que $u_g^P = u_g - \varphi_g D$, la ecuación (A.55) puede escribirse como

$$\begin{aligned}
 & \left\{ \begin{bmatrix} \lambda^2 + 2\lambda\xi i & 0 & 0 \\ 0 & \lambda^2 \sigma^2 \frac{1}{16\pi^2} \frac{h}{b} \frac{1}{\delta} \tilde{K}_{xx} & 0 \\ 0 & 0 & \lambda^2 \sigma^2 \frac{1}{16\pi^2} \frac{1}{\delta} \frac{h}{b} \frac{b^2}{(h+D)^2} \tilde{K}_{\theta\theta D} \end{bmatrix} \right. \\
 & - \left. \begin{bmatrix} 1 & 1 & 1 \\ 1 & 1 + \frac{m_o}{m} & 1 + \frac{m_o}{m} \frac{D}{h+D} \\ 1 & 1 + \frac{m_o}{m} \frac{D}{h+D} & 1 + \frac{1}{3} \frac{b^2}{(h+D)^2} \left(1 + \frac{m_o}{m}\right) + \frac{m_o}{m} \frac{D^2}{(h+D)^2} \end{bmatrix} \right\} \cdot \begin{bmatrix} \omega_n^2 u / \ddot{u}_{g_o} \\ \omega_n^2 u_r^P / \ddot{u}_{g_o} \\ \omega_n^2 (h+D) \varphi_r^c / \ddot{u}_{g_o} \end{bmatrix} \quad (\text{A.58}) \\
 & = -\lambda^2 \left\{ \begin{bmatrix} 1 \\ 1 + \frac{m_o}{m} \\ 1 + \frac{m_o}{m} \frac{D}{h+D} \end{bmatrix} I_u + \frac{h}{b} \begin{bmatrix} 1 \\ 1 \\ 1 + \frac{1}{3} \frac{b}{h} \frac{b}{3(h+D)} \left(1 + \frac{m_o}{m}\right) \end{bmatrix} I_\varphi \right\}
 \end{aligned}$$

o, de forma alternativa, como

$$\left\{ \lambda^2 \begin{bmatrix} (1+i2\xi') & 0 & 0 \\ 0 & \alpha_{xx}^2(1+i2\xi_{xx}) & 0 \\ 0 & 0 & \alpha_{\theta\theta}^2(1+i2\xi_{\theta\theta}) \end{bmatrix} - \begin{bmatrix} 1 & 1 & 1 \\ 1 & 1+\frac{m_o}{m} & 1+\frac{m_o}{m}\frac{D}{h+D} \\ 1 & 1+\frac{m_o}{m}\frac{D}{h+D} & 1+\frac{1}{3}\frac{b^2}{(h+D)^2}\left(1+\frac{m_o}{m}\right)+\frac{m_o}{m}\frac{D^2}{(h+D)^2} \end{bmatrix} \right\} \cdot \begin{bmatrix} \omega_n^2 u / \ddot{u}_{g_o} \\ \omega_n^2 u_r^P / \ddot{u}_{g_o} \\ \omega_n^2 (h+D) \varphi_r^c / \ddot{u}_{g_o} \end{bmatrix} \quad (\text{A.59})$$

$$= -\lambda^2 \left\{ \begin{bmatrix} 1 \\ 1+\frac{m_o}{m} \\ 1+\frac{m_o}{m}\frac{D}{h+D} \end{bmatrix} I_u + \frac{h}{b} \begin{bmatrix} 1 \\ 1 \\ 1+\frac{1}{3}\frac{b}{h}\frac{b}{(h+D)}\left(1+\frac{m_o}{m}\right) \end{bmatrix} I_\varphi \right\}$$

donde,

$$\xi' = \frac{1}{\lambda} \xi \quad (\text{A.60})$$

$$\alpha_{xx}^2 = \sigma^2 \frac{1}{16\pi^2} \frac{h}{b} \frac{1}{\delta} \tilde{k}_{xx} \quad (\text{A.61})$$

$$\xi_{xx} = \frac{\tilde{c}_{xx}}{2\tilde{k}_{xx}} \quad (\text{A.62})$$

$$\alpha_{\theta\theta}^2 = \sigma^2 \frac{1}{16\pi^2} \frac{h}{b} \frac{1}{\delta} \operatorname{Re} \left[\frac{b^2}{(h+D)^2} \tilde{K}_{\theta\theta D} \right] \quad (\text{A.63})$$

$$\xi_{\theta\theta} = \frac{\operatorname{Im} \left[\frac{b^2}{(h+D)^2} \tilde{K}_{\theta\theta D} \right]}{2\operatorname{Re} \left[\frac{b^2}{(h+D)^2} \tilde{K}_{\theta\theta D} \right]} \quad (\text{A.64})$$

siendo $\tilde{K}_{xx} = \tilde{k}_{xx} + i\tilde{c}_{xx}$ y

$$\tilde{K}_{\theta\theta D} = \frac{1}{\mu_s b^3} \left(K_{\theta\theta} - \frac{K_{\theta x}^2}{K_{xx}} \right) \quad (\text{A.65})$$

$$\frac{b^2}{(h+D)^2} = \left(\left(\frac{h}{b} \right)^2 - 2 \left(\frac{h}{b} \right) \frac{\tilde{K}_{\theta x}}{\tilde{K}_{xx}} + \left(\frac{\tilde{K}_{\theta x}}{\tilde{K}_{xx}} \right)^2 \right)^{-1} \quad (\text{A.66})$$

$$\frac{D}{h+D} = \frac{\tilde{K}_{\theta x}}{\tilde{K}_{xx}} \left(\frac{\tilde{K}_{\theta x}}{\tilde{K}_{xx}} - \frac{h}{b} \right)^{-1} \quad (\text{A.67})$$

Finalmente, anulando m_o , I y I_o , como suele hacerse (véase, por ejemplo [6, 12, 14]), se obtiene

$$\left\{ \lambda^2 \begin{bmatrix} (1+i2\xi') & 0 & 0 \\ 0 & \alpha_{xx}^2(1+i2\xi_{xx}) & 0 \\ 0 & 0 & \alpha_{\theta\theta}^2(1+i2\xi_{\theta\theta}) \end{bmatrix} - \begin{bmatrix} 1 & 1 & 1 \\ 1 & 1 & 1 \\ 1 & 1 & 1 \end{bmatrix} \right\} \cdot \begin{bmatrix} \omega_n^2 u / \ddot{u}_{g_o} \\ \omega_n^2 u_r^P / \ddot{u}_{g_o} \\ \omega_n^2 (h + D) \varphi_r^c / \ddot{u}_{g_o} \end{bmatrix} = -\lambda^2 \left(I_u + \frac{h}{b} I_\varphi \right) \begin{bmatrix} 1 \\ 1 \\ 1 \end{bmatrix} \quad (\text{A.68})$$

Resolviendo el sistema complejo de ecuaciones algebraicas de la ecuación (A.68) para $\omega_n^2 u / \ddot{u}_{g_o}$ se obtiene la siguiente expresión para el cortante en la base de la estructura por unidad de fuerza sísmica efectiva Q :

$$\left| \frac{\omega_n^2 u}{\ddot{u}_{g_o}} \right| = Q(\lambda) = \left| \frac{I_u(\lambda) + \frac{h}{b} I_\varphi(\lambda)}{A(\lambda) + i B(\lambda)} \right| \quad (\text{A.69})$$

donde

$$A(\lambda) = 1 - \frac{1}{\lambda^2} - \frac{1 + 4\xi_{xx}\xi'}{\lambda^2 \alpha_{xx}^2 (1 + 4\xi_{xx}^2)} - \frac{1 + 4\xi_{\theta\theta}\xi'}{\lambda^2 \alpha_{\theta\theta}^2 (1 + 4\xi_{\theta\theta}^2)} \quad (\text{A.70})$$

$$B(\lambda) = 2 \left[\xi' - \frac{\xi' - \xi_{xx}}{\lambda^2 \alpha_{xx}^2 (1 + 4\xi_{xx}^2)} - \frac{\xi' - \xi_{\theta\theta}}{\lambda^2 \alpha_{\theta\theta}^2 (1 + 4\xi_{\theta\theta}^2)} \right] \quad (\text{A.71})$$

A.2.8. Periodo y amortiguamiento efectivos del sistema acoplado suelo-cimiento-estructura

El objetivo de esta sección es determinar las características dinámicas de un oscilador de un grado de libertad (1GDL) con amortiguamiento viscoso (figura A.13b) capaz de reproducir, de la forma más precisa posible, la respuesta del sistema acoplado de tres grados de libertad (3GDL) que se muestra en la figura A.13a.

Este sistema equivalente de un grado de libertad puede definirse mediante el periodo natural del sistema no amortiguado \tilde{T} y el amortiguamiento del sistema $\tilde{\xi}$, de manera que su ecuación de movimiento puede escribirse como

$$\frac{\tilde{\omega}_n^2 u}{\ddot{u}_{g_o}} = \frac{1}{\left(\frac{\omega^2}{\tilde{\omega}_n^2} - 1 \right) - i 2 \tilde{\xi} \frac{\omega}{\tilde{\omega}_n}} \quad (\text{A.72})$$

siendo $\tilde{\omega}_n = 2\pi/\tilde{T}$ y

$$\tilde{Q} = \left| \frac{\tilde{\omega}_n^2 u}{\ddot{u}_{g_o}} \right| \quad (\text{A.73})$$

la función de transferencia utilizada para establecer dicha equivalencia, siendo esta la más apropiada desde un punto de vista operativo dado que representa la relación entre el cortante en la base de la estructura y la fuerza sísmica efectiva [114].

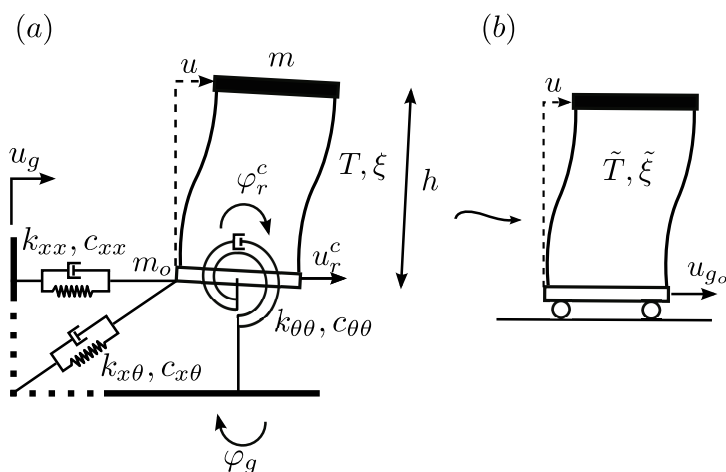


FIGURA A.13: (a) Modelo de subestructuración de una estructura de una planta. (b) Oscilador equivalente de un grado de libertad.

No es posible encontrar un sistema de un grado de libertad con impedancias constantes que reproduzca con exactitud la curva de respuesta armónica de un sistema de tres grados de libertad (véase 3DOF en la figura A.14), ya sea con impedancias constantes o dependientes de la frecuencia. Por lo tanto, el objetivo es reproducir la respuesta del sistema de tres grados de libertad dentro del rango de frecuencias en el que se produce la respuesta máxima. Dado que la definición de un sistema de un grado de libertad requiere únicamente de dos parámetros, las estrategias empleadas para determinar sus características dinámicas están basadas en tomar un punto común entre la curva de respuesta del sistema de tres grados de libertad y la curva de respuesta de un sistema de un grado de libertad que se aproxime lo más posible a ella.

Desde un punto de vista ingenieril, la estrategia más intuitiva consiste en tomar como punto común aquel correspondiente al valor máximo Q_m del espectro de respuesta (véase MAX en la figura A.14) tal y como hacen algunos autores como Todorovska [16] o Avilés y Pérez-Rocha [14]. Este punto puede determinarse, en este caso, mediante la resolución iterativa del sistema de ecuaciones (A.43), lo cual permite hallar el periodo de respuesta máxima T_m y el valor máximo correspondiente Q_m . Posteriormente, asumiendo que el mecanismo de amortiguamiento del oscilador equivalente de un grado de libertad es de naturaleza viscosa, es bien sabido [115] que su coeficiente de amortiguamiento puede hallarse como

$$\tilde{\xi} = \frac{1}{\sqrt{2}} \left(1 - \sqrt{\frac{Q_m^2 - 1}{Q_m^2}} \right)^{\frac{1}{2}} \quad (\text{A.74})$$

que se obtiene de la expresión de Q_m que aparece en la figura A.14. Ahora, el periodo

natural del oscilador equivalente \tilde{T} puede obtenerse como

$$\tilde{T} = \sqrt{1 - 2\tilde{\xi}^2} T_m \quad (\text{A.75})$$

lo cual es aplicable sólo para valores de amortiguamiento inferiores a $1/\sqrt{2}$ [115].

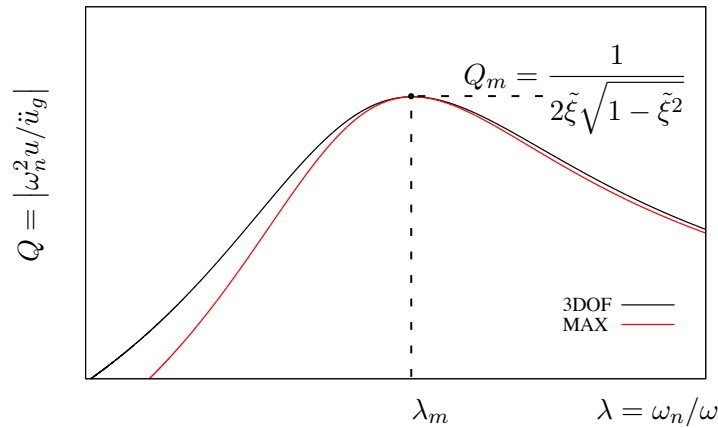


FIGURA A.14: Estrategia de búsqueda del valor máximo (MAX) para obtener la frecuencia natural y el amortiguamiento del sistema de 1GDL equivalente al sistema acoplado (3DOF) en el rango de frecuencias en el que se produce la respuesta máxima.

Sin embargo, esta estrategia conduce a valores de la frecuencia natural poco fiables en el caso de sistemas muy amortiguados, en los cuales la frecuencia a la que se produce la respuesta máxima se vuelve bastante indefinida. En estos casos, el espectro de respuesta armónica se hace más plano lo cual hace más difícil hallar el valor de la frecuencia asociado con el valor máximo de la respuesta. Con el fin de evitar este inconveniente, puede emplearse otra aproximación basada en hallar el autovalor $\tilde{\lambda}$ del sistema de tres grados de libertad.

Igualar las ecuaciones de movimiento del sistema acoplado ((A.69), (A.70), (A.71)), obtenidas tras la diagonalación de la matriz de impedancias llevada a cabo en la sección A.2.7, y aquellas correspondientes al sistema de un grado de libertad (A.73) en resonancia permite obtener el periodo efectivo hallando la raíz de la ecuación (A.70). Obviamente, el sistema de 3GDL tiene más de un modo de vibración y, por tanto, la ecuación (A.70) tiene más de una raíz. Sin embargo, en la mayoría de los casos de interés, la respuesta máxima corresponde al primer modo. Por este motivo, en adelante, el procedimiento se centra en esta primera solución λ' , pese a ser conscientes de que existen más raíces. Así, el coeficiente de amortiguamiento del sistema puede determinarse como $\tilde{\xi} = 1/(2Q(\lambda'))$.

Utilizar la raíz λ' de la ecuación (A.70) conduce a un sistema de un grado de libertad cuya respuesta máxima no siempre representa una aproximación aceptable de la respuesta máxima del sistema de 3GDL (véase ROOT en la figura A.15). De hecho, esta aproximación pierde precisión a medida que $1/\sigma$ o L/b aumentan, así como para valores

decrecientes del ratio de esbeltez de la estructura h/b . Con el fin de ilustrar estos efectos, las figuras A.16 y A.17 muestran una representación superpuesta de la respuesta del sistema acoplado (3DOF) y la respuesta de un sistema equivalente de un grado de libertad cuyas características dinámicas se han calculado utilizando esta estrategia. Los resultados que se exponen en dichas figuras corresponden a estructuras con $h/b = 1, 2$ y 5 sustentadas por grupos de 3×3 pilotes con $s/d = 5$ y $L/b = 1$ y 4 .

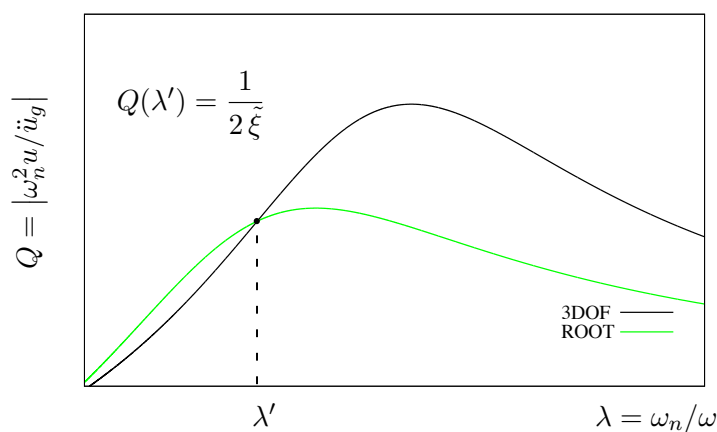


FIGURA A.15: Estrategia del cálculo de la raíz (ROOT) para obtener la frecuencia natural y el amortiguamiento del sistema de 1GDL equivalente al sistema acoplado (3DOF), en el rango de frecuencias en el que se produce la respuesta máxima, sin anular los términos de amortiguamiento de segundo orden.

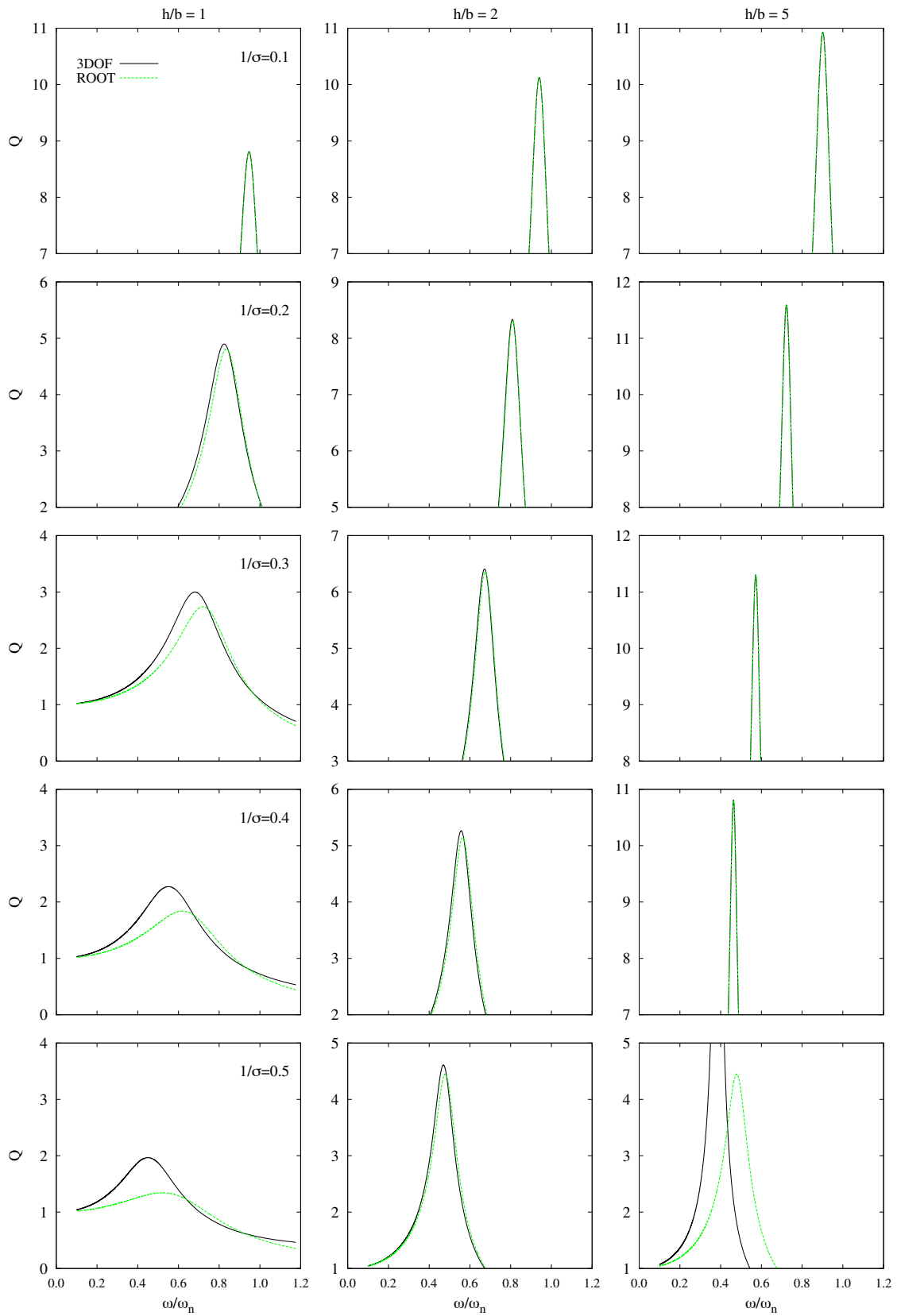


FIGURA A.16: Aproximación mediante un oscilador de reemplazo de la respuesta de un sistema de 3GDL (3DOF) soportado por un grupo de 3×3 pilotes con $s/d = 5$ y $L/b = 1$. $E_p/E_s = 10^3$ y $\xi_s = 0.05$. Estrategia ROOT.

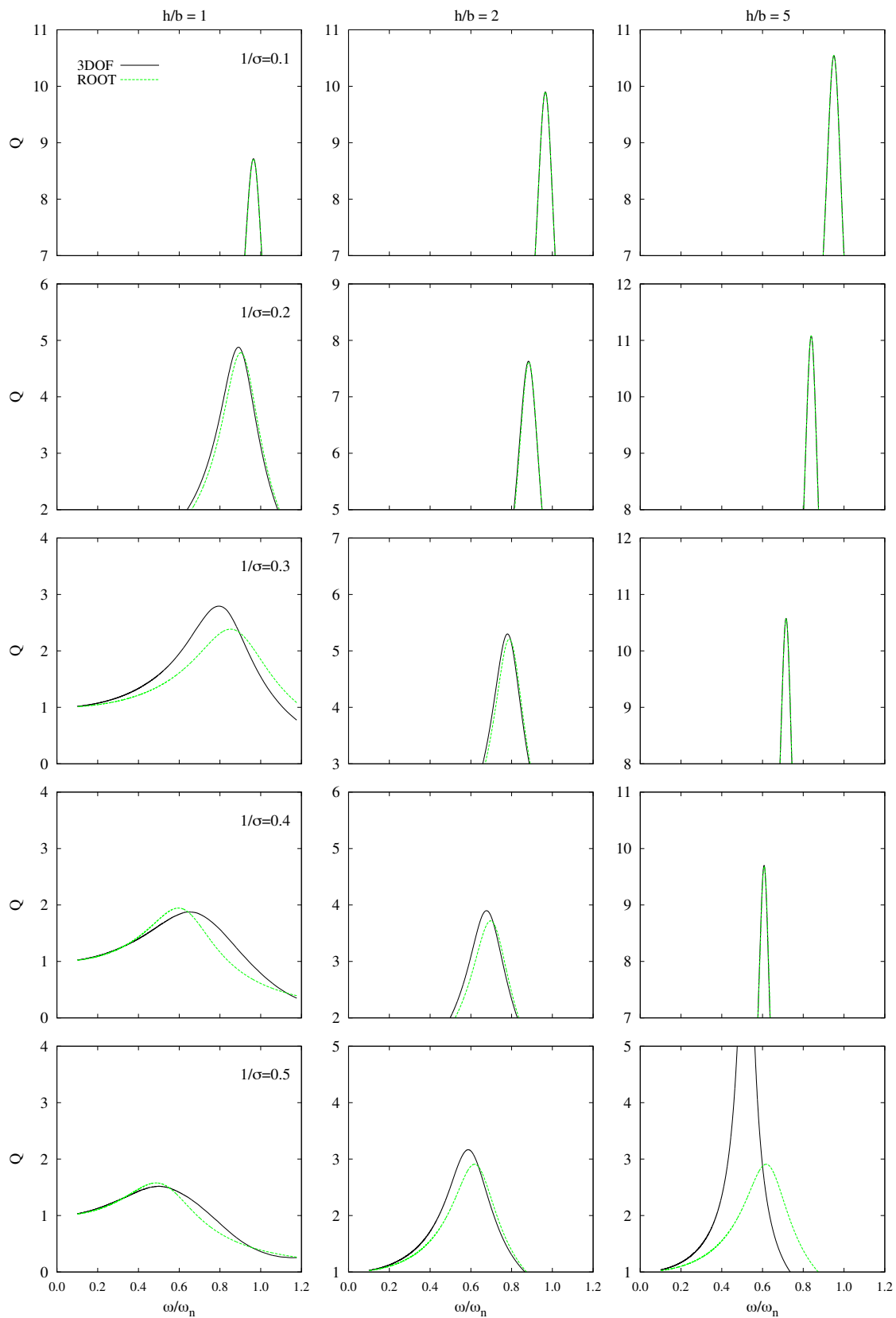


FIGURA A.17: Aproximación mediante un oscilador de reemplazo de la respuesta de un sistema de 3GDL (3DOF) soportado por un grupo de 3×3 pilotes con $s/d = 5$ y $L/b = 4$. $E_p/E_s = 10^3$ y $\xi_s = 0.05$. Estrategia ROOT.

Por otra parte, se obtienen mejores resultados anulando todos los términos de amortiguamiento de segundo orden, como hacen Avilés y Pérez-Rocha [14]. Esto conduce a las siguientes expresiones aproximadas de A y B :

$$A(\lambda) = 1 - \frac{1}{\lambda^2} - \frac{1}{\lambda^2 \alpha_{xx}^2} - \frac{1}{\lambda^2 \alpha_{\theta\theta}^2} \quad (\text{A.76})$$

$$B(\lambda) = 2 \left[\xi' - \frac{\xi' - \xi_{xx}}{\lambda^2 \alpha_{xx}^2} - \frac{\xi' - \xi_{\theta\theta}}{\lambda^2 \alpha_{\theta\theta}^2} \right] \quad (\text{A.77})$$

La frecuencia natural adimensional del sistema de 1GDL no amortiguado $\tilde{\lambda} = \omega_n / \tilde{\omega}_n$ puede hallarse como la raíz de la ecuación (A.76). Esto equivale a la resolución del problema de autovalores de la ecuación (A.68), sin considerar el amortiguamiento.

Como, en este caso, $\tilde{\xi} = 1/(2Q(\tilde{\lambda}))$ y tomando la expresión aproximada de $Q(\tilde{\lambda})$ obtenida considerando los valores de A y B calculados a partir de las ecuaciones (A.76) y (A.77), puede escribirse el coeficiente de amortiguamiento del sistema como

$$\tilde{\xi} = \left| \left(I_u + \frac{h}{b} I_\varphi \right)^{-1} \frac{1}{\tilde{\lambda}^2} \left(\xi' + \frac{\xi_{xx}}{\alpha_{xx}^2} + \frac{\xi_{\theta\theta}}{\alpha_{\theta\theta}^2} \right) \right| \quad (\text{A.78})$$

Sin embargo, esta metodología no siempre proporciona una buena aproximación de la respuesta máxima del sistema de 3GDL, tal y como se observa en la figura A.18. En ella se han representado los resultados obtenidos mediante esta metodología (EIGEN-S) para estructuras sustentadas sobre un grupo de 3×3 pilotes con $s/d = 5$ y $L/b = 2$.

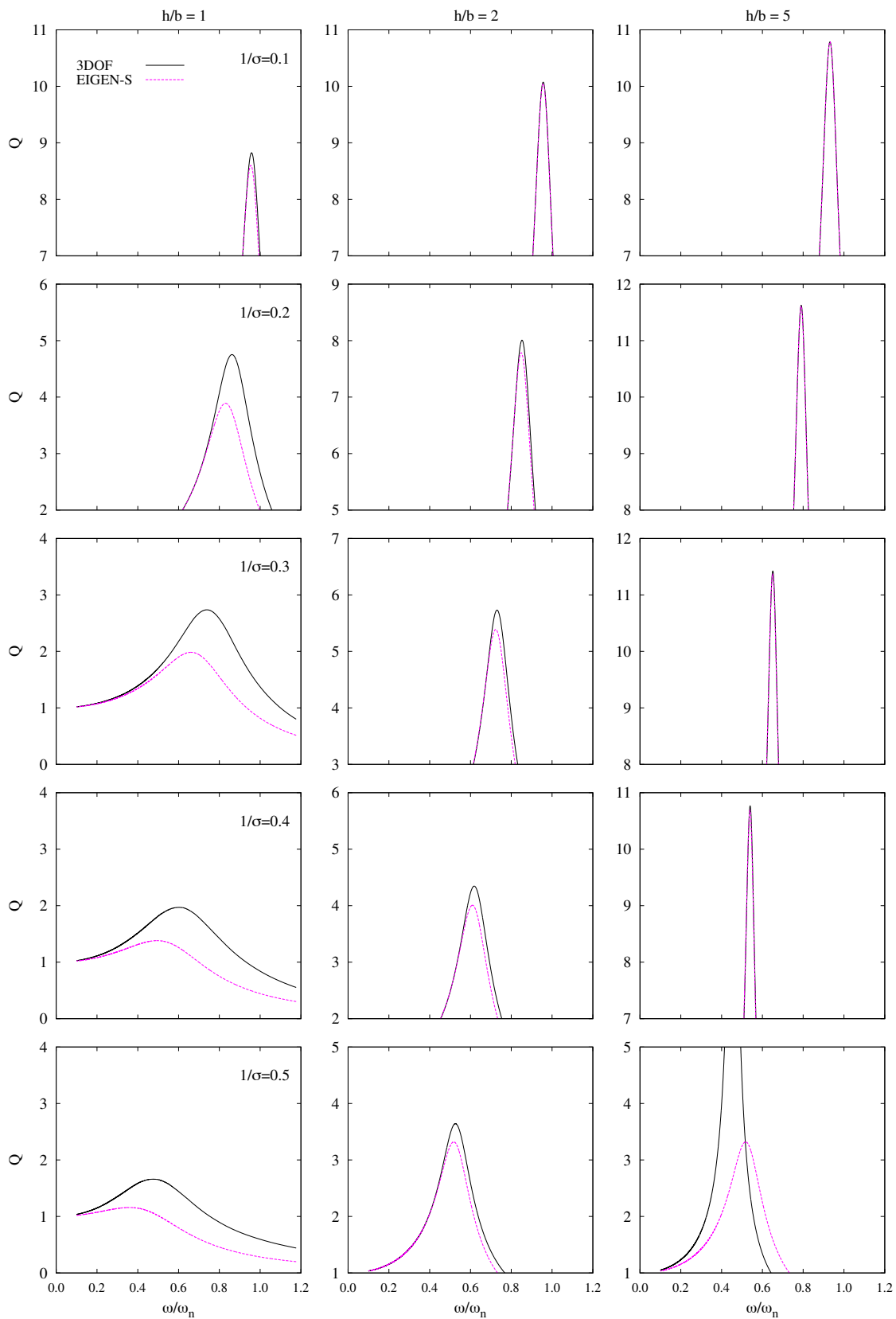


FIGURA A.18: Aproximación mediante un oscilador de reemplazo de la respuesta de un sistema de 3GDL (3DOF) soportado por un grupo de 3×3 pilotes con $s/d = 5$ y $L/b = 2$. $E_p/E_s = 10^3$ y $\xi_s = 0.05$. Estrategia EIGEN-S.

Por consiguiente, el procedimiento que se propone en esta tesis doctoral (EIGEN en la figura A.19) calcula la frecuencia natural adimensional del sistema no amortiguado $\tilde{\lambda}$ como la raíz de la ecuación (A.76) pero, al contrario de lo que hacen Avilés y Pérez-Rocha [14], este procedimiento calcula $\tilde{\xi}$ empleando las ecuaciones (A.70) y (A.71) para obtener los valores de A y B , en lugar de las ecuaciones (A.76) y (A.77). Esto conduce a la siguiente expresión:

$$\tilde{\xi} = \left| \left(I_u + \frac{h}{b} I_\varphi \right)^{-1} \left[\frac{\xi'}{\tilde{\lambda}^2} + \frac{1}{\tilde{\lambda}^2} \left(\frac{\xi_{xx}}{\alpha_{xx}^2 (1 + i2\xi_{xx})} + \frac{\xi_{\theta\theta}}{\alpha_{\theta\theta}^2 (1 + i2\xi_{\theta\theta})} \right) \right] \right| \quad (\text{A.79})$$

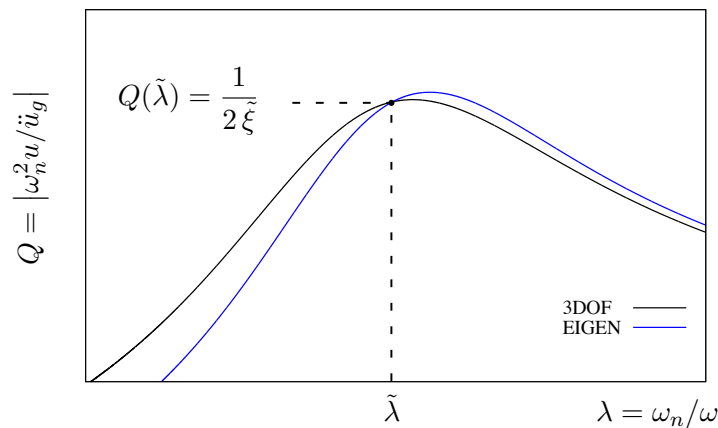


FIGURA A.19: Procedimiento propuesto (EIGEN) para obtener la frecuencia natural del sistema de 1GDL equivalente al sistema acoplado (3DOF), en el rango de frecuencias en el que se produce la respuesta máxima, anulando los términos de amortiguamiento de segundo orden y calcular el amortiguamiento del sistema teniéndolos en cuenta.

En la figura A.20 puede observarse que considerando los términos de amortiguamiento de segundo orden, para el cálculo del amortiguamiento efectivo del sistema equivalente $\tilde{\xi}$ (EIGEN), se logra una mejor aproximación de la respuesta máxima del sistema de tres grados de libertad (3DOF) que la que se obtiene despreciando dichos términos (EIGEN-S). Con el fin de ilustrar este efecto, se ha representado de forma superpuesta la respuesta de los sistemas equivalentes obtenidos mediante ambas estrategias y la respuesta dinámica del sistema acoplado para estructuras sustentadas sobre grupos de 3×3 pilotes con $s/d = 5$ y $L/b = 4$.

Las figuras A.21, A.22 y A.23 permiten analizar la influencia que tiene despreciar los términos de amortiguamiento de segundo orden sobre la características dinámicas del sistema equivalente, en función de la configuración del grupo de pilotes. Para ello, en estas figuras se han representado resultados en términos de periodo \tilde{T}/T y amortiguamiento $\tilde{\xi}$ para diversas configuraciones de grupos de pilotes. La influencia que tiene adoptar esta simplificación aumenta a medida que disminuye el ratio de esbeltez de los pilotes L/d (véase la figura A.21), el ratio de esbeltez de la estructura h/b y el parámetro de onda σ , así como para valores crecientes del ratio de embebimiento L/b (véase la figura A.22) y el número de pilotes (véase la figura A.23). De hecho, adoptar dicha simplificación puede conducir a diferencias significativas en términos del periodo y el amortiguamiento efectivos del sistema cuando $h/b \leq 2$.

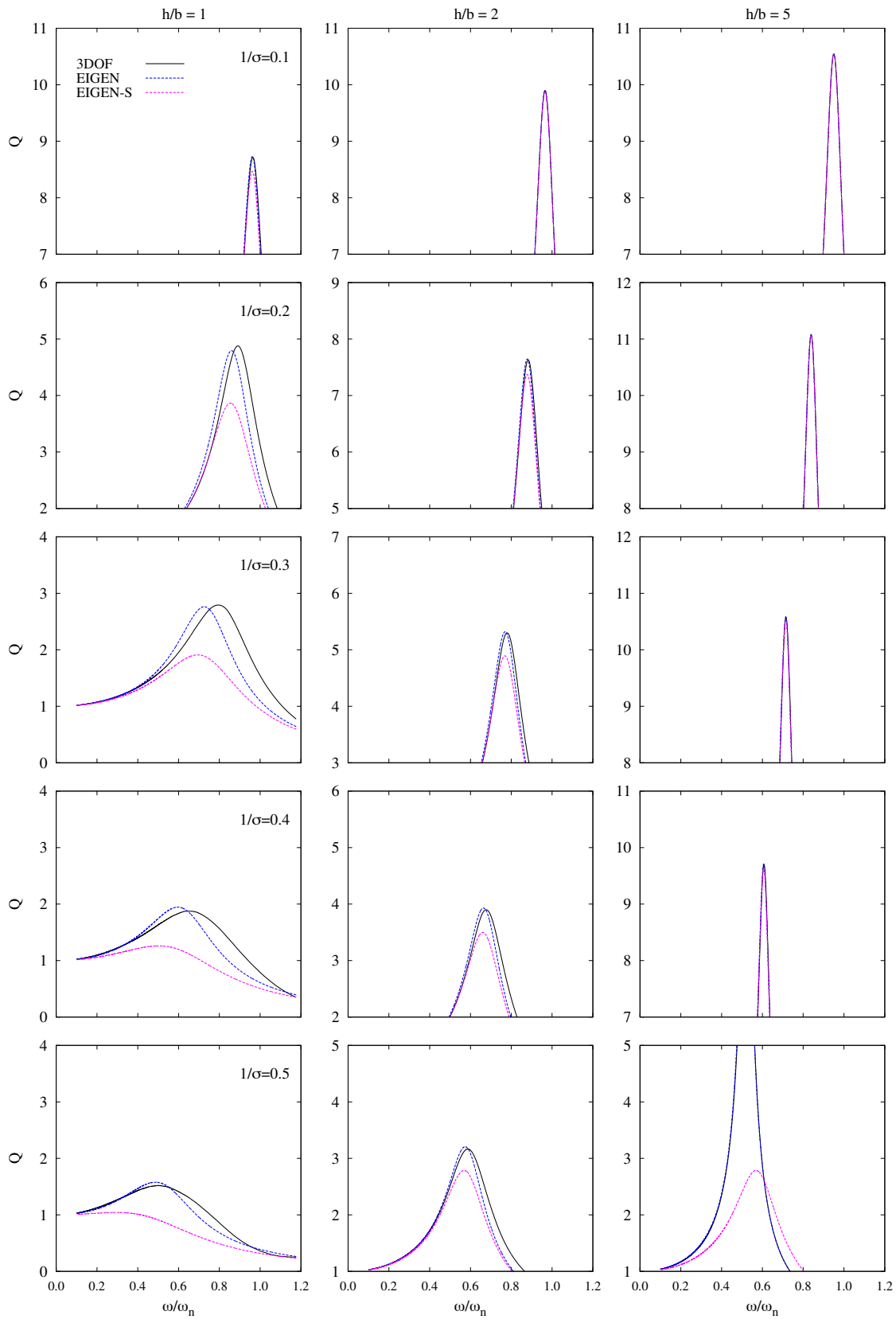


FIGURA A.20: Aproximación mediante un oscilador de reemplazo de la respuesta de un sistema de 3GDL (3DOF) soportado por un grupo de 3×3 pilotes con $s/d = 5$ y $L/b = 4$. $E_p/E_s = 10^3$ y $\xi_s = 0.05$. EIGEN vs EIGEN-S.

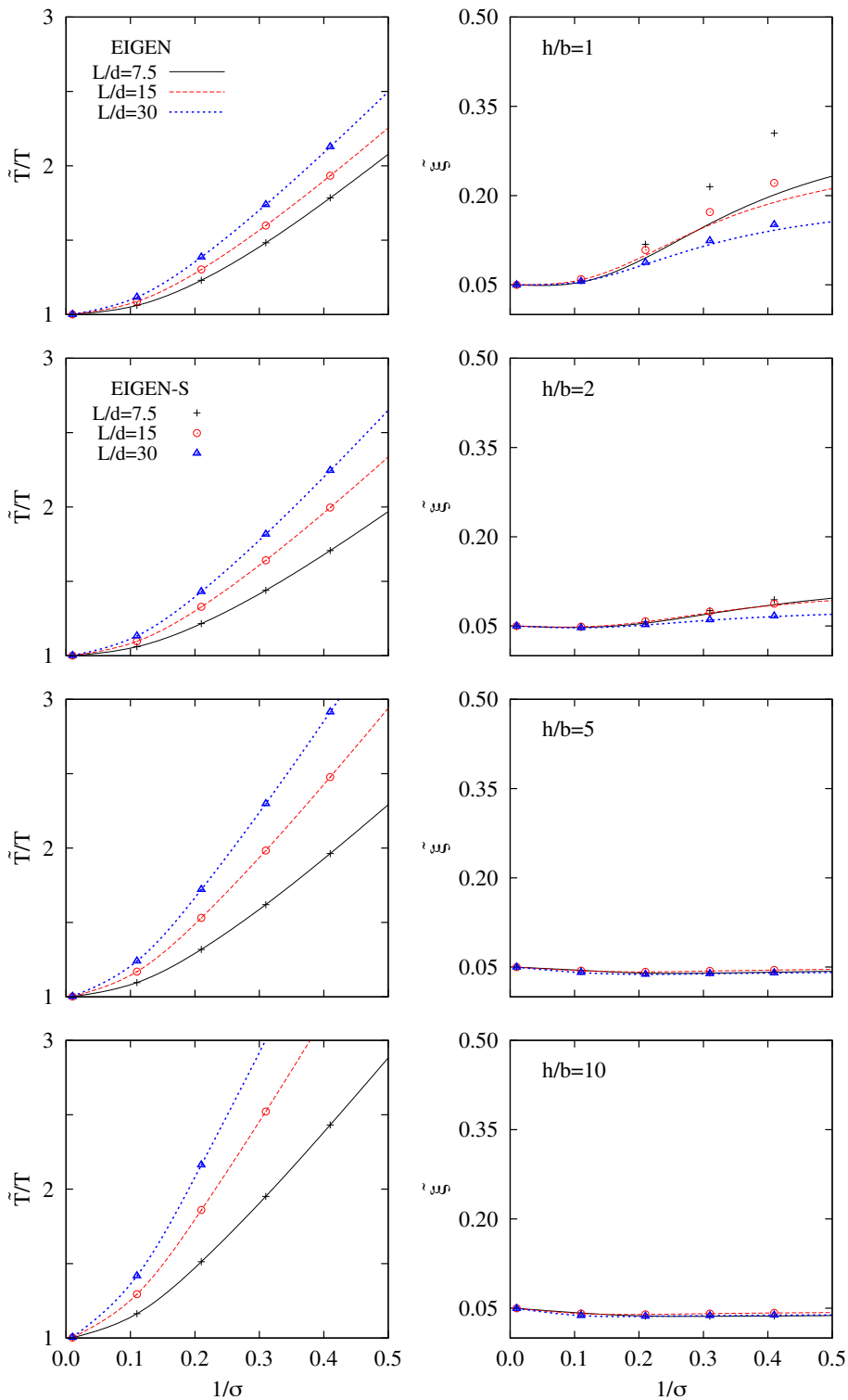


FIGURA A.21: Influencia de los términos de segundo orden del amortiguamiento. EIGEN vs EIGEN-S. Periodo \tilde{T}/T y amortiguamiento $\tilde{\xi}$ efectivos para grupos de 2×2 pilotes con $L/b = 2$, $E_p/E_s = 10^3$ y $\xi_s = 0.05$.

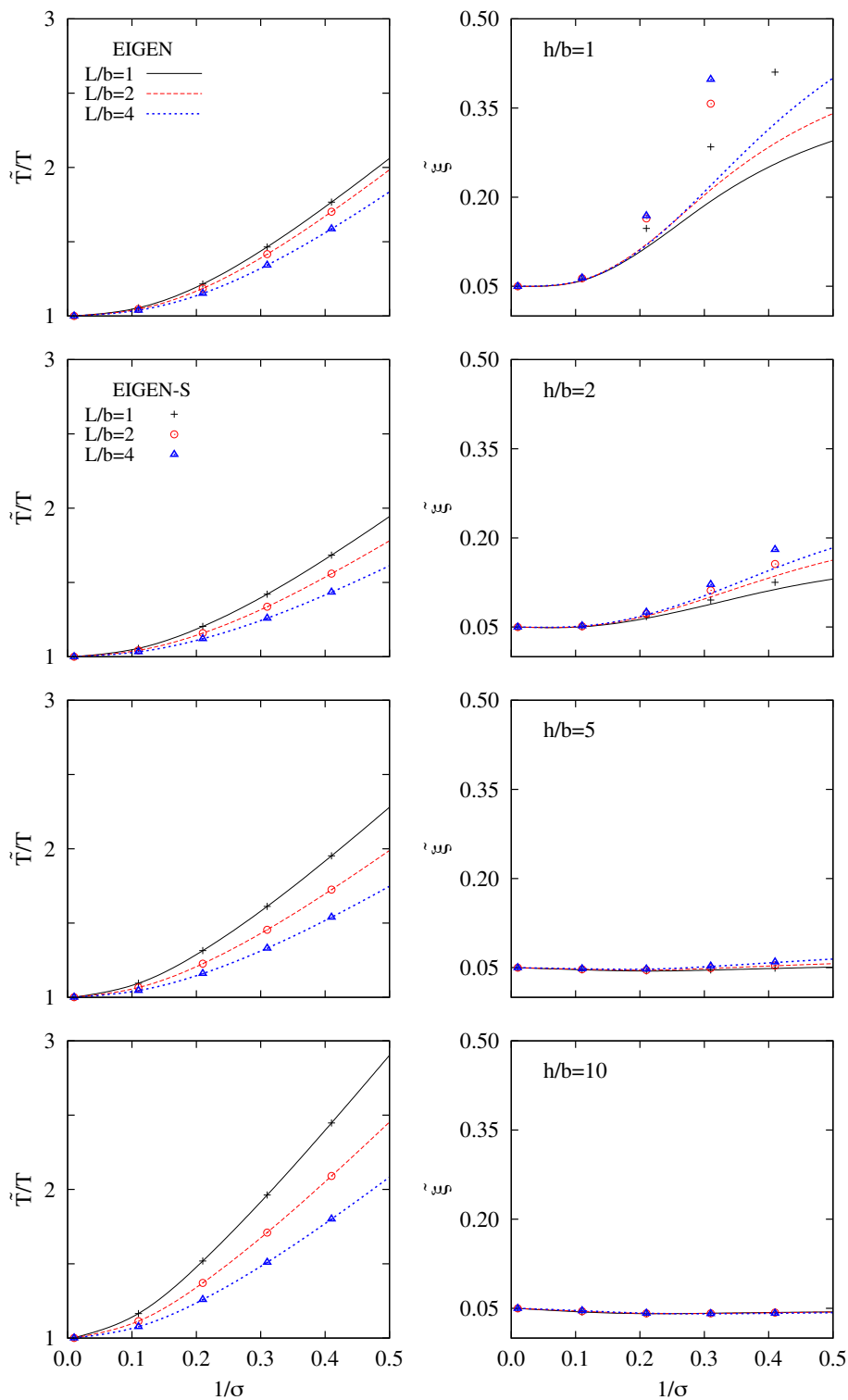


FIGURA A.22: Influencia de los términos de segundo orden del amortiguamiento. EIGEN vs EIGEN-S. Periodo \tilde{T}/T y amortiguamiento $\tilde{\xi}$ efectivos para grupos de 4×4 pilotes con $s/d = 3.75$, $E_p/E_s = 10^3$ y $\xi_s = 0.05$.

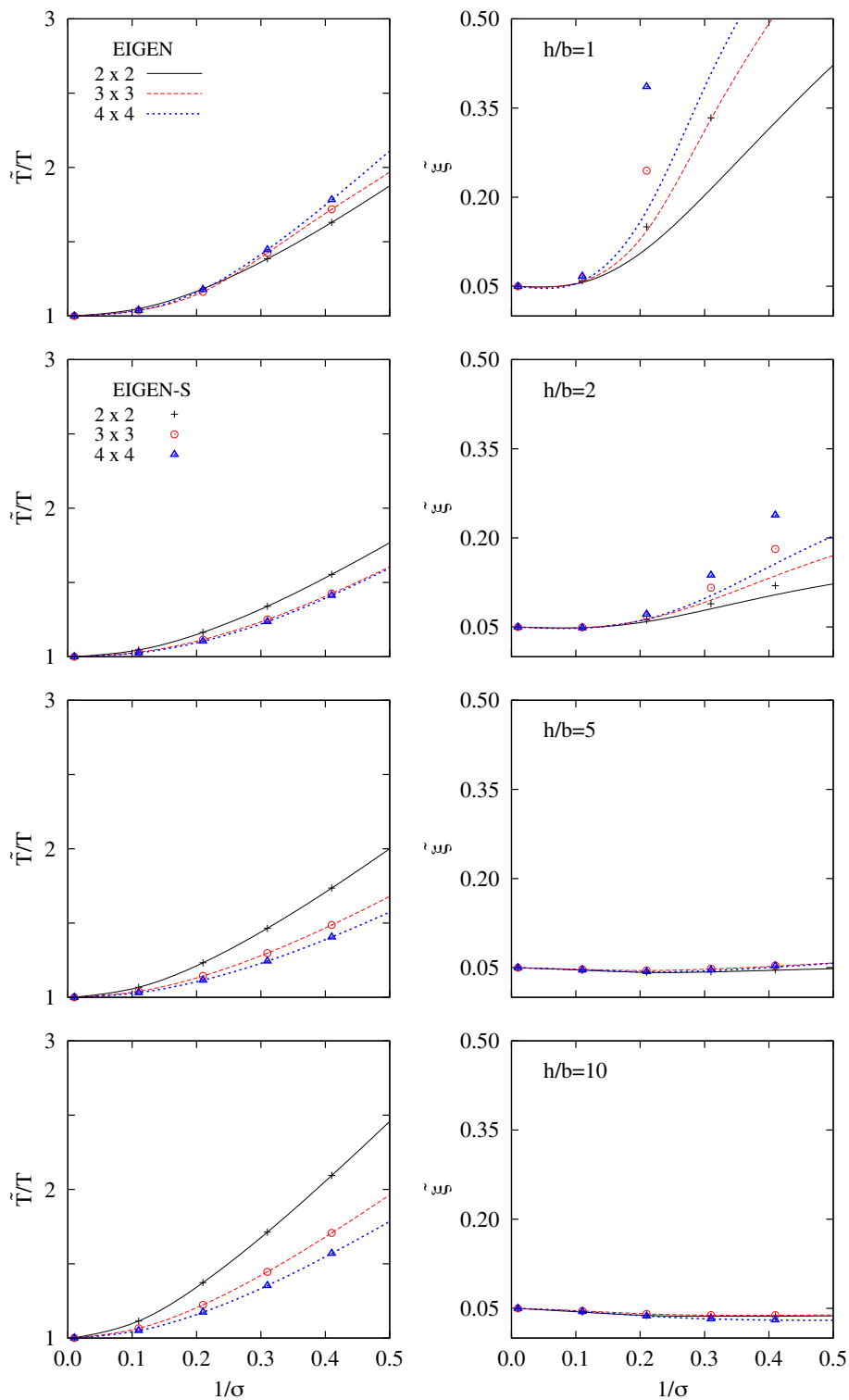


FIGURA A.23: Influencia de los términos de segundo orden del amortiguamiento. EIGEN vs EIGEN-S. Periodo \tilde{T}/T y amortiguamiento $\tilde{\xi}$ efectivos para grupos de 2×2 , 3×3 y 4×4 pilotes con $L/b = 4$, $L/d = 15$, $E_p/E_s = 10^3$ y $\xi_s = 0.05$.

Con el fin de mostrar las distintas estrategias empleadas para determinar las características dinámicas de un sistema equivalente de un grado de libertad, la figura A.24 muestra una representación esquemática superpuesta de la respuesta del sistema acoplado de tres grados de libertad objeto de estudio (3DOF) y las curvas de respuesta de los distintos modelos de sistemas de un grado de libertad descritos a lo largo de esta sección. Las diferencias se han exagerado en la figura con el propósito de resaltar las características de dichas estrategias y mostrar que ninguna de estas aproximaciones reproduce de forma exacta la respuesta del sistema acoplado, teniendo cada una de ellas sus ventajas e inconvenientes asociados.

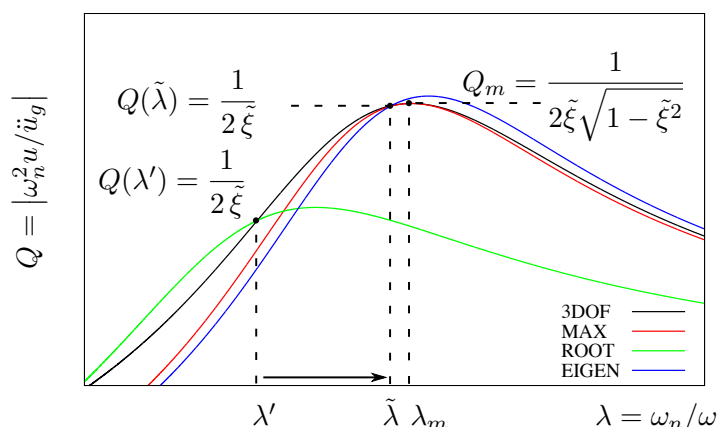


FIGURA A.24: Estrategias para obtener la frecuencia natural y el amortiguamiento del sistema de 1GDL equivalente al sistema acoplado (3DOF), en el rango de frecuencias en el que se produce la respuesta máxima.

Cuando $\tilde{\xi} < 0.2$, los resultados obtenidos, tanto para el periodo como para el amortiguamiento efectivos, utilizando el procedimiento propuesto en esta tesis basado en el cálculo de la raíz (EIGEN) o llevando a cabo una resolución iterativa del sistema de ecuaciones que figura en la ecuación (A.43) para encontrar el valor de la respuesta máxima (MAX), son casi idénticos. La figura A.25 ilustra este hecho para un caso particular. Sin embargo, a pesar de que ambos procedimientos proporcionan buenos resultados en la mayoría de los casos, es importante señalar que, al contrario de lo que ocurre con el algoritmo de búsqueda del máximo (MAX), el procedimiento del cálculo de la raíz (EIGEN) muestra, en todos los casos, un comportamiento estable cuya fiabilidad no se ve afectada por el incremento del amortiguamiento efectivo del sistema equivalente ($\tilde{\xi} > 0.2$). Por este motivo, el procedimiento simplificado (EIGEN) es la estrategia que se emplea en adelante en este trabajo, siendo cierto también que, como se comenta más adelante, la búsqueda de un sistema equivalente de 1GDL no siempre es aplicable como metodología simplificada para sistemas altamente amortiguados.

Finalmente, habiendo descrito el procedimiento numérico a emplear para definir los parámetros del sistema equivalente de 1GDL, y teniendo presente que la respuesta de dicho oscilador de reemplazo de 1GDL no coincide exactamente con la respuesta del sistema completo de 3GDL, es preciso establecer un rango de validez práctico que dependerá de las características del problema. Avilés y Suárez [20] llegaron a la conclusión de que la solución del sistema equivalente de 1GDL no es adecuada para sistemas muy amor-

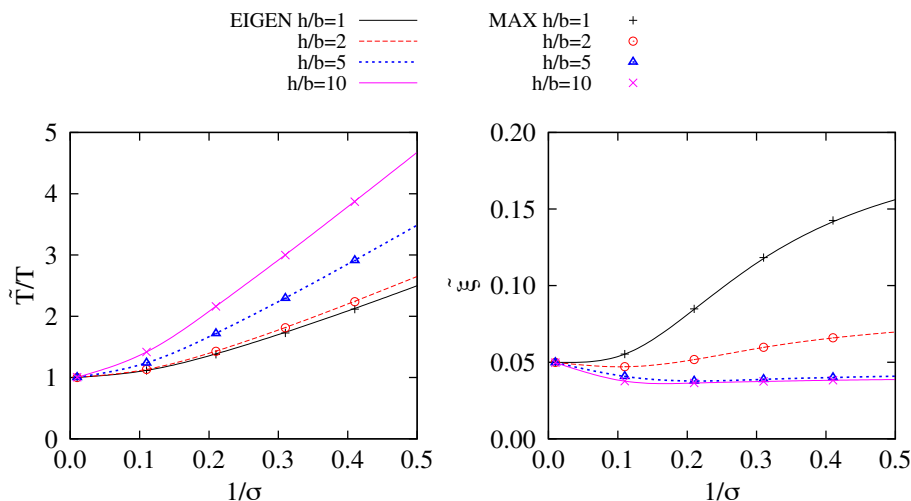


FIGURA A.25: Procedimiento del cálculo de la raíz (EIGEN) vs algoritmo de búsqueda del máximo (MAX). Periodo \tilde{T}/T y amortiguamiento efectivos $\tilde{\xi}$ para un grupo de 2×2 pilotes. $E_p/E_s = 10^3$, $s/d = 15$, $h/b = 2, 5, 10$, $L/b = 2$, $L/d = 30$ y $\xi_s = 0.05$.

tiguados ($\tilde{\xi} > 0.2$), lo que normalmente corresponde a estructuras muy poco esbeltas ($h/b \leq 1$) sobre suelos blandos ($1/\sigma > 0.2$). Los resultados obtenidos para un número significativo de configuraciones analizadas en este trabajo concuerdan con dicha conclusión y sugieren un valor límite del parámetro $1/\sigma$ entre 0.2 y 0.3, dependiendo de la configuración. Sin embargo, en otros muchos casos, el oscilador de reemplazo de 1GDL arroja excelentes resultados, incluso para valores altos del amortiguamiento efectivo ($\tilde{\xi} > 0.2$). Por otra parte, la configuración del grupo de pilotes es otro factor importante a la hora de establecer el rango de validez del método. Con el fin de ilustrar este hecho, la figura A.26 muestra funciones de respuesta en frecuencia y espectros de respuesta elástica (correspondientes a la componente N-S del terremoto de El Centro de 1940 [114]), ambos obtenidos manteniendo $1/\sigma$ constante como en [7], para el caso de un grupo de 2×2 pilotes con ratios de embebimiento y de esbeltez de $L/b = 2$ y $L/d = 7.5$ y 15 , respectivamente. En ambos casos, para $h/b = 1$, el amortiguamiento efectivo del sistema equivalente $\tilde{\xi}$ es muy similar (véanse las gráficas de la derecha la figura A.26). Sin embargo, mientras que el oscilador equivalente de 1GDL es capaz de aproximar con bastante exactitud las funciones de respuesta en frecuencia del sistema completo cuando $L/d = 15$, no sucede lo mismo cuando $L/d = 7.5$. Como consecuencia, los espectros de respuesta elástica obtenidos a partir del sistema equivalente de 1GDL son muy próximos a aquellos obtenidos empleando la respuesta del sistema completo de 3GDL para todos los valores de $1/\sigma$ cuando $L/d = 15$. Sin embargo, las discrepancias son muy significativas cuando $L/d = 7.5$, incluso para $1/\sigma = 0.1$. Por lo tanto, es importante señalar que el método del sistema equivalente de 1GDL presenta un rango de validez finito que debe ser tenido en cuenta con carácter previo a su aplicación práctica.

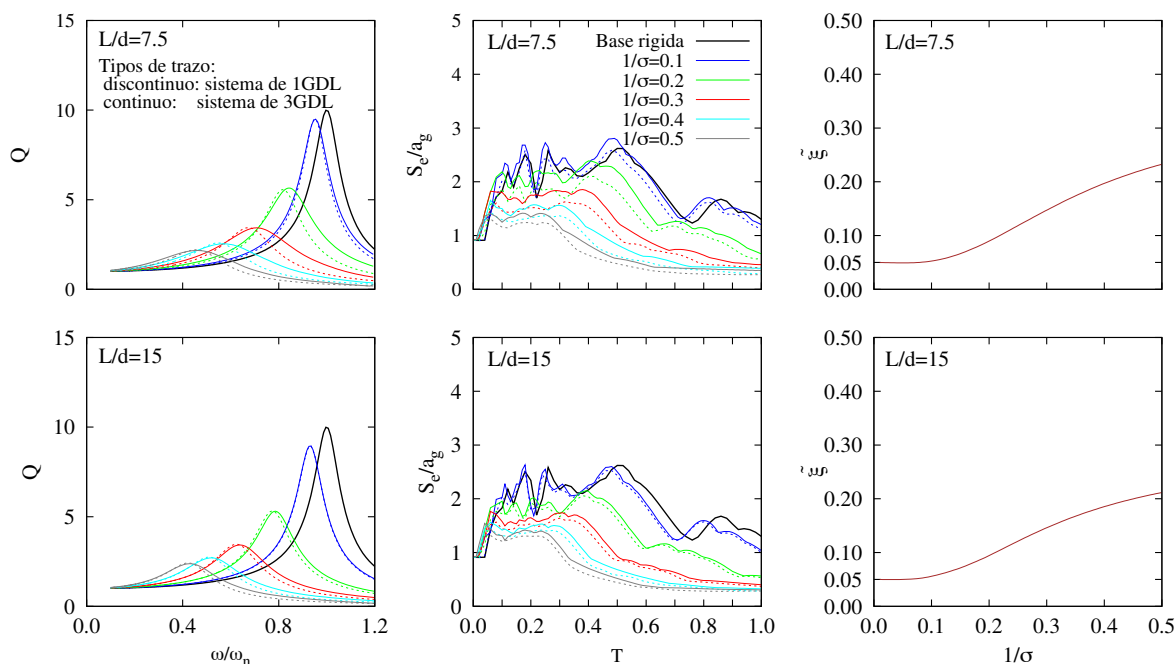


FIGURA A.26: Aproximación mediante un oscilador de reemplazo de la respuesta de un sistema de 3GDL soportado por un grupo de 2×2 pilotes. $L/b = 1$, $L/d = 7.5$ (arriba) y $L/d = 15$ (abajo). Funciones de transferencia (columna izquierda), espectro de respuesta elástica correspondiente al terremoto de El Centro de 1940 (columna central), y amortiguamiento efectivo (ξ) del oscilador equivalente de 1GDL (columna derecha).

A.2.9. Implementación

Con el fin de ilustrar la implementación práctica de las estrategias descritas en la sección A.2.8 en un código, los algoritmos A.1 y A.2 muestran los pseudocódigos correspondientes para el cálculo del periodo \tilde{T}/T y el amortiguamiento $\tilde{\xi}$ efectivos del sistema objeto de estudio. El algoritmo A.1 muestra la implementación de una estrategia de búsqueda del máximo (MAX), mientras que el algoritmo A.2 presenta aquella que corresponde a procedimientos basados en el cálculo de raíces (ROOT, EIGEN or EIGEN-S).

El algoritmo de búsqueda del máximo (MAX) consiste en un procedimiento iterativo que busca el valor máximo del espectro de respuesta armónica para distintos valores del parámetro de onda σ . Tal y como se muestra en el algoritmo A.1, en la primera iteración $\sigma = \sigma_{max}$, donde $1/\sigma_{max}$ toma un valor próximo a cero que corresponde a estructuras muy flexibles o suelos muy rígidos. Esto implica que el periodo del sistema en base flexible tiende al valor correspondiente a la condición de base rígida $\tilde{T} \rightarrow T$ y, por consiguiente, el periodo efectivo del sistema \tilde{T}/T tiende a la unidad $\tilde{T}/T \rightarrow 1$. Así, suponiendo que $\lambda^{(i)} = 1$, se calculan los valores del cortante en la base de la estructura por unidad de fuerza sísmica efectiva Q para $\lambda^{(i)} - \Delta\lambda$, $\lambda^{(i)}$ y $\lambda^{(i)} + \Delta\lambda$, siendo $\Delta\lambda \rightarrow 0$. Dichos valores se obtienen utilizando la ecuación (A.69), donde $A^{(i)}$ y $B^{(i)}$ se calculan a partir de las ecuaciones (A.70) y (A.71), respectivamente. Dado que se sabe que estas curvas son suaves, el punto de búsqueda se desplaza en la dirección de valores crecientes de Q hasta que se al-

canza un máximo, momento en el cual el valor de $\lambda^{(i)}$ correspondiente se almacena como el periodo $(T_m/T)^{(i)}$ asociado a la respuesta máxima Q_m para el valor de σ considerado. Seguidamente, el coeficiente de amortiguamiento efectivo $\tilde{\xi}^{(i)}$ se calcula introduciendo el valor obtenido para $Q_m^{(i)}$ en la ecuación (A.74). Por último, el periodo efectivo del oscilador equivalente $(\tilde{T}/T)^{(i)}$ se obtiene a partir de la ecuación (A.75). El proceso iterativo se repite para valores decrecientes de σ hasta que $\sigma = \sigma_{min}$, esta vez empezando por el último valor obtenido para λ , siendo $\lambda^{(i)} = \lambda^{(i-1)}$.

Por otra parte, el algoritmo A.2 describe la implementación del procedimiento que se propone en este trabajo (EIGEN), así como la de otras estrategias (ROOT y EIGEN-S), basadas también en algoritmos de búsqueda de raíces. Cabe mencionar que el mismo algoritmo puede utilizarse para obtener los resultados correspondientes a cada una de estas estrategias, modificando únicamente las expresiones utilizadas para calcular la parte real (A) e imaginaria (B) del denominador de la expresión del cortante en la base de la estructura por unidad de fuerza sísmica efectiva Q_2 , así como la expresión utilizada para obtener el amortiguamiento efectivo del sistema ξ . Este algoritmo corresponde a un procedimiento iterativo que busca la raíz de la parte real A del denominador de la expresión de Q . En el caso del procedimiento denominado ROOT, A viene definida por la ecuación (A.70). Sin embargo, en las estrategias EIGEN y EIGEN-S todos los términos de amortiguamiento de segundo orden se desprecian y, por lo tanto, A se calcula a partir de la ecuación (A.76). En la primera iteración $\sigma = \sigma_{max}$, donde $1/\sigma_{max} \rightarrow 0$ lo cual implica que $\tilde{T}/T \rightarrow 1$, como se explicó anteriormente. Así, suponiendo que $\lambda^{(i)} = 1$, se calculan los valores de A para $\lambda^{(i)}$ y $\lambda^{(i)} + \Delta\lambda$, siendo $\Delta\lambda \rightarrow 0$. Estos dos puntos se desplazan hasta que el valor de A experimenta un cambio de signo, momento en el cual el valor de λ que se corresponde con el menor valor absoluto de $A^{(i)}$ se almacena como el periodo efectivo del sistema $(\tilde{T}/T)^{(i)}$. A continuación, $Q^{(i)}$ se calcula a partir de la ecuación (A.69). Los valores de $A^{(i)}$ y $B^{(i)}$ se calculan bien a partir de las ecuaciones (A.70) y (A.71), cuando los términos de amortiguamiento de segundo orden se tienen en cuenta (ROOT y EIGEN), o bien a partir de las ecuaciones (A.76) y (A.77), cuando dichos términos se desprecian (EIGEN-S). Finalmente, el amortiguamiento efectivo del sistema $\tilde{\xi}^{(i)}$ se determina bien a partir de la ecuación (A.79) (ROOT y EIGEN), o bien a partir de la expresión aproximada que figura en la ecuación (A.78) (EIGEN-S). El procedimiento iterativo se repite para valores decrecientes de σ hasta que $\sigma = \sigma_{min}$, esta vez comenzando por el último valor obtenido para λ , siendo $\lambda^{(i)} = \lambda^{(i-1)}$.

Algoritmo A.1 Pseudocódigo para el cálculo de $\tilde{T}/T = \mathcal{F}(\sigma)$ y $\tilde{\xi} = \mathcal{G}(\sigma)$ mediante el algoritmo de búsqueda del máximo (MAX)

ENTRADA: Conjunto de parámetros que definen el sistema: h/b , δ , ξ , impedancias (\tilde{K}_{xx} , $\tilde{K}_{\theta x}$ y $\tilde{K}_{\theta\theta}$) y factores de interacción cinemática (I_u y I_φ); y parámetros del algoritmo σ_{min} , σ_{max} , $\Delta\sigma$, y $\Delta\lambda$.

$Q^{(i)}$ se obtiene de la ecuación (A.69) calculando $A^{(i)}$ y $B^{(i)}$, respectivamente, a partir de las ecuaciones (A.70) y (A.71).

para $\sigma^{(i)} = \sigma_{max}$ a σ_{min} , con un incremento $\Delta\sigma$

si $\sigma^{(i)} = \sigma_{max}$ **entonces**

$\lambda^{(i)} \leftarrow 1$

si no

$\lambda^{(i)} \leftarrow \lambda^{(i-1)}$

fin si

$Q_1^{(i)} = Q(\lambda^{(i)} - \Delta\lambda)$

$Q_2^{(i)} = Q(\lambda^{(i)})$

$Q_3^{(i)} = Q(\lambda^{(i)} + \Delta\lambda)$

repite

si $Q_3^{(i)} \geq Q_2^{(i)}$ **entonces**

$\lambda^{(i)} \leftarrow \lambda^{(i)} + \Delta\lambda$

$Q_1^{(i)} \leftarrow Q_2^{(i)}$

$Q_2^{(i)} \leftarrow Q_3^{(i)}$

$Q_3^{(i)} = Q(\lambda^{(i)} + \Delta\lambda)$

si no

si $Q_1^{(i)} \geq Q_2^{(i)}$ **entonces**

$\lambda^{(i)} \leftarrow \lambda^{(i)} - \Delta\lambda$

$Q_3^{(i)} \leftarrow Q_2^{(i)}$

$Q_2^{(i)} \leftarrow Q_1^{(i)}$

$Q_1^{(i)} = Q(\lambda^{(i)} - \Delta\lambda)$

fin si

fin si

mientras $(Q_1^{(i)} \geq Q_2^{(i)}) \cdot \text{O} \cdot (Q_3^{(i)} \geq Q_2^{(i)})$

$(T_m/T)^{(i)} \leftarrow \lambda^{(i)}$

$Q^{(i)} \leftarrow Q_2^{(i)}$

calcula $\xi^{(i)}$ a partir de la ecuación (A.74)

calcula $(\tilde{T}/T)^{(i)}$ a partir de la ecuación (A.75)

fin para

SALIDA: $\sigma^{(i)}$, $(\tilde{T}/T)^{(i)}$, $\tilde{\xi}^{(i)}$

Algoritmo A.2 Pseudocódigo para el cálculo de $\tilde{T}/T = \mathcal{F}(\sigma)$ y $\tilde{\xi} = \mathcal{G}(\sigma)$ mediante algoritmos basados en la búsqueda de la raíz (ROOT, EIGEN o EIGEN-S)

ENTRADA: Conjunto de parámetros que definen el sistema: h/b , δ , ξ , impedancias (\tilde{K}_{xx} , $\tilde{K}_{\theta x}$ y $\tilde{K}_{\theta\theta}$) y factores de interacción cinemática (I_u y I_φ); y parámetros del algoritmo σ_{min} , σ_{max} , $\Delta\sigma$, y $\Delta\lambda$.

$A^{(i)}$ se obtiene a partir de la ecuación (A.70) (ROOT) o a partir de la ecuación (A.76) (EIGEN y EIGEN-S).

para $\sigma^{(i)} = \sigma_{max}$ a σ_{min} , con un incremento $\Delta\sigma$

si $\sigma^{(i)} = \sigma_{max}$ **entonces**

$\lambda^{(i)} \leftarrow 1$

si no

$\lambda^{(i)} \leftarrow (\tilde{T}/T)^{(i-1)}$

fin si

$A_1^{(i)} = A(\lambda^{(i)})$

$A_2^{(i)} = A(\lambda^{(i)} + \Delta\lambda)$

repite

si ($A_1^{(i)} > 0$.Y. $A_2^{(i)} > 0$) .O. ($A_1^{(i)} < 0$.Y. $A_2^{(i)} < 0$) **entonces**

$\lambda^{(i)} \leftarrow \lambda^{(i)} + \Delta\lambda$

$A_1^{(i)} \leftarrow A_2^{(i)}$

$A_2^{(i)} = A(\lambda^{(i)} + \Delta\lambda)$

si no

si $|A_1^{(i)}| > |A_2^{(i)}|$ **entonces**

$(\tilde{T}/T)^{(i)} \leftarrow \lambda^{(i)} - \Delta\lambda$

si no

$(\tilde{T}/T)^{(i)} \leftarrow \lambda^{(i)}$

fin si

fin si

mientras ($A_1^{(i)} > 0$.Y. $A_2^{(i)} > 0$) .O. ($A_1^{(i)} < 0$.Y. $A_2^{(i)} < 0$)

calcula $Q^{(i)}$ a partir de la ecuación (A.69) obteniendo $A^{(i)}$ y $B^{(i)}$, respectivamente, bien a partir de las ecuaciones (A.70) y (A.71) (ROOT y EIGEN), o bien a partir de las ecuaciones (A.76) y (A.77) (EIGEN-S).

calcula $\tilde{\xi}^{(i)}$ a partir de la ecuación (A.79) (ROOT y EIGEN) o a partir de la ecuación (A.78) (EIGEN-S).

fin para

SALIDA: $\sigma^{(i)}$, $(\tilde{T}/T)^{(i)}$, $\tilde{\xi}^{(i)}$

A.2.10. Validación del modelo

A fin de completar la validación del modelo propuesto, los resultados obtenidos a partir de las ecuaciones adimensionales de movimiento del sistema se han validado en esta sección comparándolos con los resultados proporcionados por Veletsos y Meek [7] para cimentaciones superficiales. En el citado artículo las impedancias se toman de un trabajo de Bielak [12], así como de un trabajo previo de Verbic y Veletsos [116]. Por otra parte, los resultados obtenidos para cimentaciones embebidas se han comparado con aquellos presentados por Avilés y Pérez-Rocha [14].

A.2.10.1. Cimentaciones superficiales. Comparación con Veletsos y Meek [7]

Las ecuaciones de movimiento del sistema (ecuación (A.59)) obtenidas en la sección A.2.7 para cimentaciones pilotadas son aplicables también a cimentaciones superficiales. Sin embargo, en el caso de estas últimas, las impedancias cruzadas se anulan ($K_{\theta x} = 0$), haciendo que $D = 0$ lo que implica que $u_r^P = u_r^c$. Por otra parte, el movimiento de solicitación en el cimienta concide con el movimiento de campo libre a nivel de la superficie, que es exclusivamente horizontal ($u_g = u_{g_o}$ y $\varphi_g = 0$). Por lo tanto, el factor de interacción cinemática asociado al giro se anula $I_\varphi = 0$, mientras que el asociado a la traslación es igual a la unidad $I_u = 1$. De este modo, la ecuación (A.59) puede escribirse para cimentaciones superficiales como

$$\left\{ \lambda^2 \begin{bmatrix} (1+i2\xi') & 0 & 0 \\ 0 & \alpha_{xx}^2(1+i2\xi_{xx}) & 0 \\ 0 & 0 & \alpha_{\theta\theta}^2(1+i2\xi_{\theta\theta}) \end{bmatrix} - \begin{bmatrix} 1 & 1 & 1 \\ 1 & 1+\frac{m_o}{m} & 1 \\ 1 & 1 & 1+\frac{b^2}{3h^2} \left(1+\frac{m_o}{m}\right) \end{bmatrix} \right\} \cdot \begin{bmatrix} \omega_n^2 u / \ddot{u}_{g_o} \\ \omega_n^2 u_r^c / \ddot{u}_{g_o} \\ \omega_n^2 h \varphi_r^c / \ddot{u}_{g_o} \end{bmatrix} = -\lambda^2 \begin{bmatrix} 1 \\ 1+\frac{m_o}{m} \\ 1 \end{bmatrix} \quad (\text{A.80})$$

donde,

$$\xi' = \frac{1}{\lambda} \xi \quad (\text{A.81})$$

$$\alpha_{xx}^2 = \sigma^2 \frac{1}{16\pi^2} \frac{h}{b} \frac{1}{\delta} \tilde{k}_{xx} \quad (\text{A.82})$$

$$\xi_{xx} = \frac{\tilde{c}_{xx}}{2\tilde{k}_{xx}} \quad (\text{A.83})$$

$$\alpha_{\theta\theta}^2 = \sigma^2 \frac{1}{16\pi^2} \frac{b}{h} \frac{1}{\delta} \tilde{k}_{\theta\theta} \quad (\text{A.84})$$

$$\xi_{\theta\theta} = \frac{\tilde{c}_{\theta\theta}}{2\tilde{k}_{\theta\theta}} \quad (\text{A.85})$$

siendo $\tilde{K}_{xx} = \tilde{k}_{xx} + i\tilde{c}_{xx}$ y $\tilde{K}_{\theta\theta} = \tilde{k}_{\theta\theta} + i\tilde{c}_{\theta\theta}$.

En el caso de estructuras a cortante soportadas por cimentaciones superficiales que consisten en una placa rígida circular de espesor despreciable, como las estudiadas por Veletsos y Meek [7], el problema objeto de estudio se corresponde con el esquema dibujado en la figura A.27. En dicha figura, los parámetros que definen la superestructura son los mismos que los expuestos en la sección A.2.2 para el caso de cimentaciones pilotadas. Sin embargo, en dicha sección la masa del cemento m_o y la masa de la estructura m se suponen distribuidas uniformemente en áreas cuadradas, mientras que Veletsos y Meek las suponen distribuidas uniformemente en áreas circulares. En este último caso, las inercias rotacionales tienen las expresiones $I_o = m_o r^2/4$ y $I = m r^2/4$, respectivamente, siendo r el radio de dichas áreas circulares. Asimismo, el ratio de esbeltez de la estructura se define como h/r . Además, este cambio en la geometría del cemento también conlleva una variación en la expresión que relaciona la densidad de masa relativa entre la estructura y el suelo δ y la densidad del suelo ρ_s . Esta relación puede escribirse, para cimentaciones circulares, como $\delta = m/(\rho_s \pi r^2)h$. Por otra parte, las impedancias se normalizan, en este caso, con respecto a r de la siguiente manera: $\tilde{K}_{xx} = K_{xx}/(\mu_s r)$ y $\tilde{K}_{\theta\theta} = K_{\theta\theta}/(\mu_s r^3)$. Por último, la frecuencia adimensional se define aquí como $a_o = \omega r/c_s$.

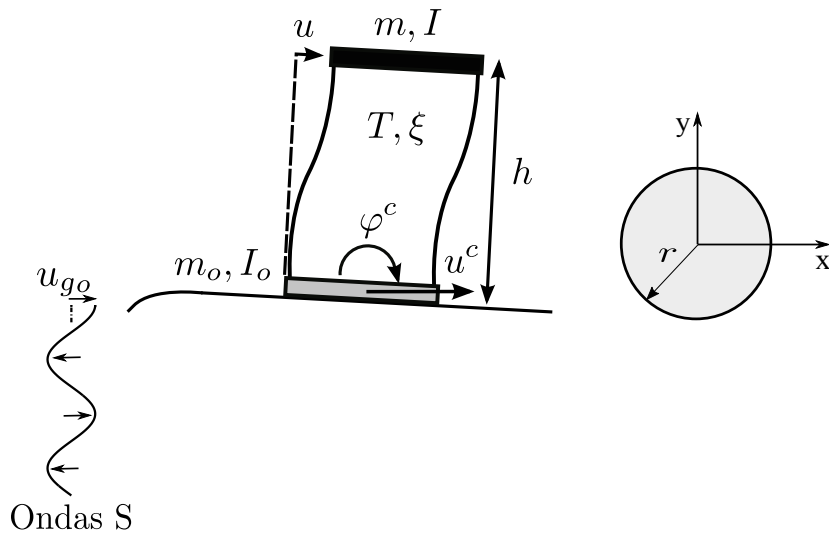


FIGURA A.27: Definición del problema. Estructura a cortante soportada por una cimentación superficial sobre un semiespacio homogéneo sometido a ondas S de incidencia vertical.

La ecuación adimensional de movimiento del sistema, análoga a la proporcionada anteriormente para cimentaciones cuadradas (ecuación (A.80)), puede obtenerse para cimentaciones circulares a partir de la ecuación (A.4), teniendo en cuenta los cambios mencionados durante la aplicación del procedimiento descrito en la sección A.2.6, lo cual conduce a la siguiente expresión:

$$\begin{aligned}
 & \left\{ \lambda^2 \begin{bmatrix} (1+i2\xi') & 0 & 0 \\ 0 & \alpha_{xx}^2(1+i2\xi_{xx}) & 0 \\ 0 & 0 & \alpha_{\theta\theta}^2(1+i2\xi_{\theta\theta}) \end{bmatrix} - \right. \\
 & \left. \begin{bmatrix} 1 & 1 & 1 \\ 1 & 1+\frac{m_o}{m} & 1 \\ 1 & 1 & 1+\frac{r^2}{4h^2} \left(1+\frac{m_o}{m}\right) \end{bmatrix} \right\} \cdot \begin{bmatrix} \omega_n^2 u / \ddot{u}_{g_o} \\ \omega_n^2 u_r^c / \ddot{u}_{g_o} \\ \omega_n^2 h \varphi_r^c / \ddot{u}_{g_o} \end{bmatrix} \\
 & = -\lambda^2 \begin{bmatrix} 1 \\ 1+\frac{m_o}{m} \\ 1 \end{bmatrix}
 \end{aligned} \tag{A.86}$$

donde,

$$\xi' = \frac{1}{\lambda} \xi \tag{A.87}$$

$$\alpha_{xx}^2 = \sigma^2 \frac{1}{4\pi^3} \frac{h}{r} \frac{1}{\delta} \tilde{k}_{xx} \tag{A.88}$$

$$\xi_{xx} = \frac{\tilde{c}_{xx}}{2\tilde{k}_{xx}} \tag{A.89}$$

$$\alpha_{\theta\theta}^2 = \sigma^2 \frac{1}{4\pi^3} \frac{r}{h} \frac{1}{\delta} \tilde{k}_{\theta\theta} \tag{A.90}$$

$$\xi_{\theta\theta} = \frac{\tilde{c}_{\theta\theta}}{2\tilde{k}_{\theta\theta}} \tag{A.91}$$

siendo $\tilde{K}_{xx} = \tilde{k}_{xx} + i\tilde{c}_{xx}$ y $\tilde{K}_{\theta\theta} = \tilde{k}_{\theta\theta} + i\tilde{c}_{\theta\theta}$.

Debe tenerse en cuenta que los resultados que aquí se presentan se han obtenido considerando los siguientes valores: $m_o/m = 0$, $I_o = 0$, $\nu_s = 0.45$, $\xi = 0.02$ y $\delta = 0.15$, tal y como hacen Veletsos y Meek.

Con respecto a las impedancias de la cimentación, Veletsos y Meek [7] proporcionan un conjunto de expresiones sencillas para las impedancias horizontales y de balanceo, que dependen de una serie de parámetros adimensionales (α_x , α_θ , β_x y β_θ). Dichas expresiones pueden escribirse de la siguiente forma:

$$K_{xx} = k_{xx}^s \left(\hat{k}_{xx} + i a_o \hat{c}_{xx} \right) \tag{A.92}$$

$$K_{\theta\theta} = k_{\theta\theta}^s \left(\hat{k}_{\theta\theta} + i a_o \hat{c}_{\theta\theta} \right) \tag{A.93}$$

donde

$$k_{xx}^s = \frac{8}{2 - \nu_s} \mu_s r \tag{A.94}$$

$$\hat{k}_{xx} = \alpha_x \quad (\text{A.95})$$

$$\hat{c}_{xx} = \beta_x \quad (\text{A.96})$$

$$k_{\theta\theta}^s = \frac{8}{2 - \nu_s} \mu_s r \quad (\text{A.97})$$

$$\hat{k}_{\theta\theta} = \alpha_\theta \quad (\text{A.98})$$

$$\hat{c}_{\theta\theta} = \beta_\theta \quad (\text{A.99})$$

Los valores de los parámetros adimensionales α_x , α_θ , β_x y β_θ que corresponden a un suelo con un coeficiente de Poisson $\nu_s = 0.45$ han sido digitalizados a partir del citado artículo y se han representado en la figura A.28. Pueden encontrarse curvas para otros valores de ν_s en [117].

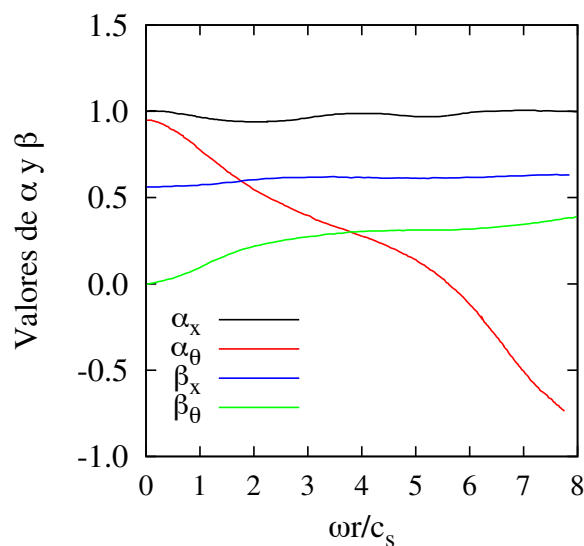


FIGURA A.28: Coeficientes adimensionales en las expresiones de la rigidez y el amortiguamiento del cimientto (según Veletsos y Meek [7]).

Cabe destacar que la expresión propuesta para la rigidez estática en el modo de vibración de balanceo (ecuación (A.97)) no permite expresar la ecuación de movimiento del sistema en términos de los parámetros adimensionales definidos en la sección A.2.6. De hecho, puede detectarse una diferencia con respecto a la que figura en un artículo de Veletsos y Verbic [118] y que, a su vez, fue tomada de un trabajo previo de Verbic y

Veletsos [116]. Con el fin de esclarecer este punto, las expresiones aproximadas proporcionadas en [116] para las impedancias se escriben a continuación, utilizando la misma representación matemática que figura en las ecuaciones (A.92) y (A.93).

$$k_{xx}^s = \frac{8}{2 - \nu_s} \mu_s r \quad (\text{A.100})$$

$$\hat{k}_{xx} = 1 \quad (\text{A.101})$$

$$\hat{c}_{xx} = a_1 \quad (\text{A.102})$$

$$k_{\theta\theta}^s = \frac{8}{3(1 - \nu_s)} \mu_s r^3 \quad (\text{A.103})$$

$$\hat{k}_{\theta\theta} = 1 - \frac{b_1(b_2 a_o)^2}{1 + (b_2 a_o)^2} - b_3 a_o^2 \quad (\text{A.104})$$

$$\hat{c}_{\theta\theta} = \frac{b_1 b_2 (b_2 a_o)^2}{1 + (b_2 a_o)^2} \quad (\text{A.105})$$

donde a_1 , b_1 , b_2 y b_3 son coeficientes numéricos que dependen de ν_s , como se muestra en la tabla A.6.

TABLA A.6: Coeficientes numéricos de las ecuaciones de la (A.102) a la (A.105), según Veletsos y Verbic [118].

Valor	ν_s			
	0	1/3	0.45	0.5
a_1	0.775	0.65	0.60	0.60
b_1	0.525	0.5	0.45	0.4
b_2	0.8	0.8	0.8	0.8
b_3	0	0	0.023	0.027

Por otra parte, los resultados obtenidos en términos del espectro de respuesta armónica empleando para las impedancias las expresiones propuestas por Veletsos y Meek no coinciden con aquellos que se extraen de las gráficas que se exponen en dicho trabajo. Por el contrario, las expresiones propuestas por Veletsos y Verbic, permiten obtener dichas curvas. Por lo tanto, para obtener los resultados que se muestran en esta sección se han tomado las impedancias propuestas en el artículo de Veletsos y Verbic.

Con el fin de validar el modelo propuesto, la figura A.29 permite comparar los resultados obtenidos mediante dicho modelo con los proporcionados por Veletsos y Meek en términos de frecuencia T/\tilde{T} y amortiguamiento ξ efectivos del sistema, para valores del ratio de esbeltez estructural $h/r = 1, 2$ y 5 . Tal y como señalan Veletsos y Meek, pueden extraerse algunas conclusiones relevantes del análisis de estos resultados:

- La frecuencia efectiva del sistema T/\tilde{T} disminuye con el parámetro de onda σ , así como para valores crecientes del ratio de esbeltez de la estructura h/r .

- La influencia de la interacción suelo-estructura sobre el amortiguamiento efectivo del sistema $\tilde{\xi}$ aumenta para valores decrecientes de σ y puede tomar valores por encima o por debajo del correspondiente a la condición de base rígida en función del valor de h/r . Veletsos y Meek explican este hecho como el resultado de dos efectos opuestos: a medida que la rigidez relativa suelo-estructura σ disminuye, el amortiguamiento efectivo $\tilde{\xi}$ tiende a aumentar como consecuencia de un incremento de la energía disipada en el suelo; sin embargo, una disminución de σ conduce también a un aumento del giro del cimiento lo cual conlleva mayores fuerzas de inercia en la masa de la estructura m , lo que a su vez conduce a un incremento en la respuesta de la estructura. Este último efecto es más relevante a medida que aumenta el ratio de esbeltez h/r haciendo que disminuya el amortiguamiento efectivo $\tilde{\xi}$. Por el contrario, el primer efecto es el que predomina en el caso de estructuras no esbeltas, lo cual explica un aumento de $\tilde{\xi}$ a medida que h/r disminuye.

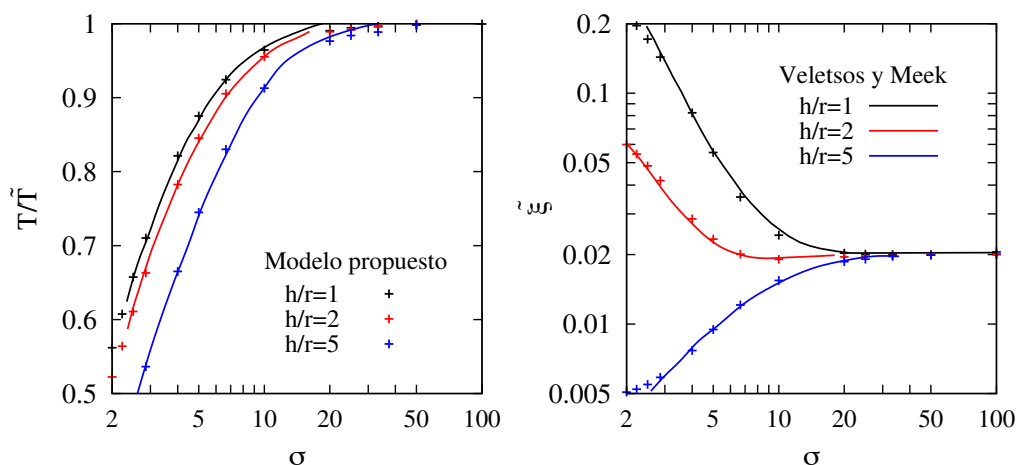


FIGURA A.29: Comparación entre los resultados del modelo propuesto y los proporcionados por Veletsos y Meek, digitalizados a partir del artículo original [7].

Las diferencias que se detectan al comparar los resultados calculados mediante el procedimiento propuesto y aquellos proporcionados por Veletsos y Meek son despreciables. Cabe mencionar que las ligeras diferencias que aparecen en las curvas de amortiguamiento efectivo se deben a pequeñas discrepancias entre las expresiones que proporcionan Veletsos y Verbic y aquellas que proponen Veletsos y Meek para las impedancias. Dichas diferencias pueden observarse en la figura A.30.

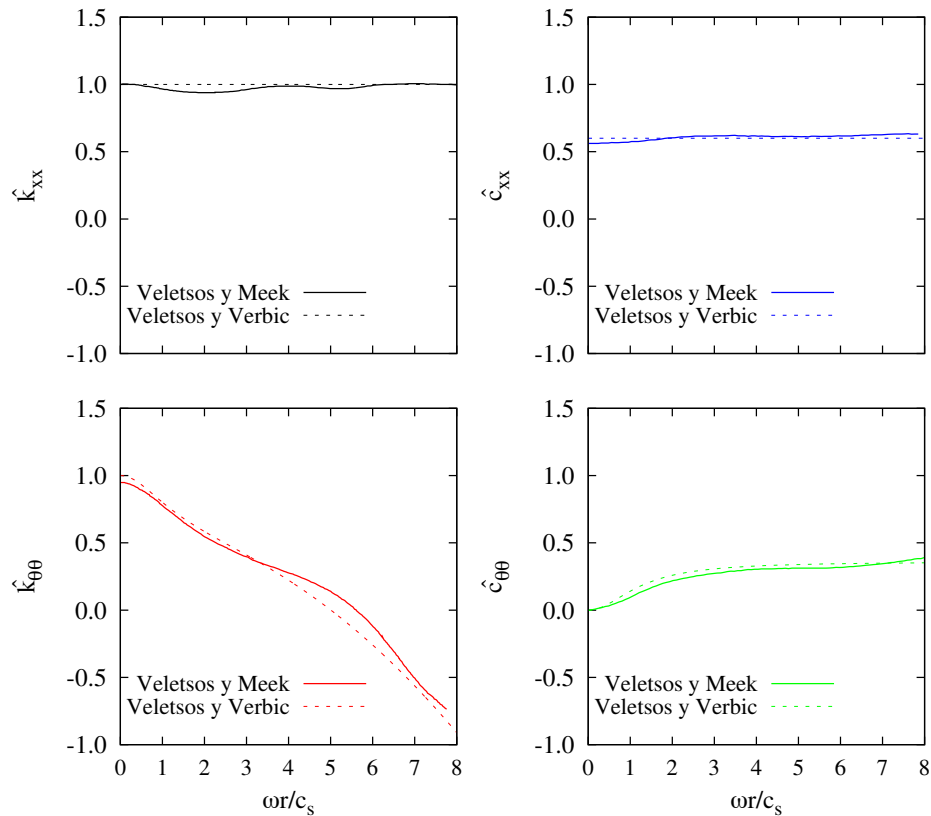


FIGURA A.30: Comparación entre los coeficientes proporcionados para las impedancias por Veletsos and Meek [7] y aquellos propuestos por Veletsos y Verbic [118].

A.2.10.2. Cimentaciones embebidas. Comparación con Avilés y Pérez-Rocha [14]

El modelo que se propone en esta tesis también puede aplicarse a cimentaciones embebidas como la que se muestra en la figura A.31. En dicha figura, los parámetros que caracterizan la superestructura son los mismos que los que se definen en la sección A.2.2 para el caso de cimentaciones pilotadas. Sin embargo, cabe mencionar que, en el caso de cimentaciones embebidas, D_e representa la profundidad de embetimiento. El desplazamiento horizontal u^c y el giro φ^c del cimientto, así como los movimientos de excitación horizontal u_g y de giro φ_g están definidos, en este caso, en la base de la cimentación. Por otra parte, la masa del cimientto m_o se supone ubicada a la mitad de la profundidad de embetimiento.

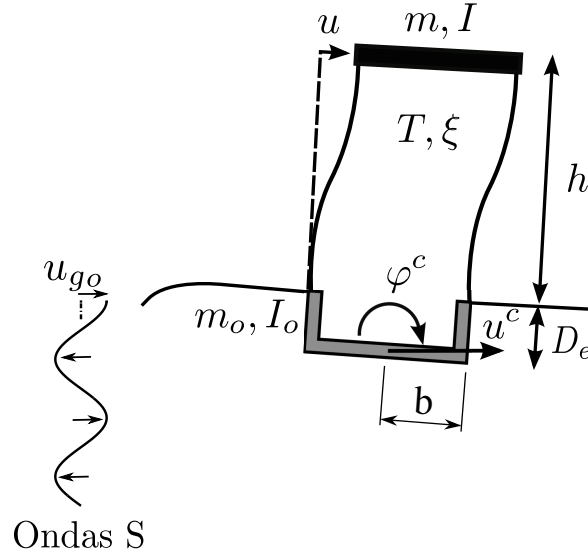


FIGURA A.31: Definición del problema. Estructura a cortante soportada por una cimentación embebida en un semiespacio homogéneo sometida a ondas S de incidencia vertical.

De este modo, las ecuaciones de movimiento del sistema representado en la figura A.31, pueden escribirse, en términos de desplazamientos relativos $u_r^c = u^c - u_g$ y $\varphi_r^c = \varphi^c - \varphi_g$, como

$$m \cdot [\ddot{u} + \ddot{u}_r^c + \ddot{u}_g + (h + D_e)(\ddot{\varphi}_r^c + \ddot{\varphi}_g)] + K \cdot u = 0 \quad (\text{A.106})$$

$$m_o \cdot [\ddot{u}_r^c + \ddot{u}_g + \frac{D_e}{2}(\ddot{\varphi}_r^c + \ddot{\varphi}_g)] + K_{xx} \cdot u_r^c + K_{x\theta} \cdot \varphi_r^c - K \cdot u = 0 \quad (\text{A.107})$$

$$m \cdot (h + D_e)[\ddot{u} + \ddot{u}_r^c + \ddot{u}_g + (h + D_e)(\ddot{\varphi}_r^c + \ddot{\varphi}_g)] + I(\ddot{\varphi}_r^c + \ddot{\varphi}_g) + K_{\theta x} \cdot u_r^c + K_{\theta\theta} \cdot \varphi_r^c + m_o \frac{D_e}{2}[\ddot{u}_r^c + \ddot{u}_g + \frac{D_e}{2}(\ddot{\varphi}_r^c + \ddot{\varphi}_g)] + I_o(\ddot{\varphi}_r^c + \ddot{\varphi}_g) = 0 \quad (\text{A.108})$$

donde la ecuación (A.106) representa el equilibrio de fuerzas sobre la estructura; la ecuación (A.107), el equilibrio de fuerzas horizontales del sistema suelo-cimiento, y la ecuación (A.108), el equilibrio de momentos del sistema estructura-cimiento en torno al centro de la base.

Puede observarse que para $D_e = 0$ las ecuaciones (A.106), (A.107) y (A.108) coinciden, respectivamente, con las escritas en la sección A.2.3.1 para cimentaciones pilotadas (ecuaciones (A.1), (A.2) y (A.3)). Asimismo, siguiendo un procedimiento análogo al descrito en la sección A.2.6, estas ecuaciones pueden escribirse en el dominio de la frecuencia, en términos de los parámetros adimensionales definidos en dicha sección. Por otra parte, tal y como se explica en la sección A.2.7, la interacción suelo-cimiento se ha condensado en un punto a una cierta profundidad virtual $D(\omega) = -K_{x\theta}/K_{xx}$, con el fin de diagonalizar la matriz de impedancias. De este modo, las ecuaciones de movimiento del sistema pueden expresarse como

$$\left\{ \lambda^2 \begin{bmatrix} (1+i2\xi') & 0 & 0 \\ 0 & \alpha_{xx}^2(1+i2\xi_{xx}) & 0 \\ 0 & 0 & \alpha_{\theta\theta}^2(1+i2\xi_{\theta\theta}) \end{bmatrix} - \begin{bmatrix} 1 & 1 & 1 \\ 1 & 1 + \frac{m_o}{m} & 1 + \frac{m_o}{m} \frac{D_e+2D}{2(h+D+D_e)} \\ 1 & 1 + \frac{m_o}{m} \frac{D_e+2D}{2(h+D+D_e)} & 1 + \frac{b^2}{3(h+D+D_e)^2} \left(1 + \frac{m_o}{m}\right) + \frac{m_o}{m} \frac{(D_e+2D)^2}{4(h+D+D_e)^2} \end{bmatrix} \right\} \quad (\text{A.109})$$

$$\begin{bmatrix} \omega_n^2 u / \ddot{u}_{g_o} \\ \omega_n^2 u_r^P / \ddot{u}_{g_o} \\ \omega_n^2 (h+D+D_e) \varphi_r^c / \ddot{u}_{g_o} \end{bmatrix} = -\lambda^2 \left\{ \begin{bmatrix} 1 \\ 1 + \frac{m_o}{m} \\ 1 + \frac{m_o}{m} \frac{D_e+2D}{2(h+D+D_e)} \end{bmatrix} I_u + \left(\frac{h}{b} + \frac{D_e}{b} \right) \begin{bmatrix} 1 \\ 1 + \frac{m_o}{m} \frac{D_e}{2(h+D_e)} \\ 1 + \frac{b^2}{3(h+D_e)(h+D+D_e)} \left(1 + \frac{m_o}{m}\right) + \frac{m_o}{m} \frac{D_e(D_e+2D)}{4(h+D_e)(h+D+D_e)} \end{bmatrix} I_\varphi \right\}$$

donde $u_g^P = u_g - \varphi_g D$ y

$$\xi' = \frac{1}{\lambda} \xi \quad (\text{A.110})$$

$$\alpha_{xx}^2 = \sigma^2 \frac{1}{16\pi^2} \frac{h}{b} \frac{1}{\delta} \tilde{k}_{xx} \quad (\text{A.111})$$

$$\xi_{xx} = \frac{\tilde{c}_{xx}}{2\tilde{k}_{xx}} \quad (\text{A.112})$$

$$\alpha_{\theta\theta}^2 = \sigma^2 \frac{1}{16\pi^2} \frac{h}{b} \frac{1}{\delta} \text{Re} \left[\frac{b^2}{(h+D+D_e)^2} \tilde{K}_{\theta\theta D} \right] \quad (\text{A.113})$$

$$\xi_{\theta\theta} = \frac{\text{Im} \left[\frac{b^2}{(h+D+D_e)^2} \tilde{K}_{\theta\theta D} \right]}{2\text{Re} \left[\frac{b^2}{(h+D+D_e)^2} \tilde{K}_{\theta\theta D} \right]} \quad (\text{A.114})$$

siendo $\tilde{K}_{xx} = \tilde{k}_{xx} + i\tilde{c}_{xx}$ y

$$\tilde{K}_{\theta\theta D} = \frac{1}{\mu_s b^3} \left(K_{\theta\theta} - \frac{K_{\theta x}^2}{K_{xx}} \right) \quad (\text{A.115})$$

$$\frac{b^2}{(h+D+D_e)^2} = \left(\frac{h}{b} + \frac{D_e}{b} - \frac{\tilde{K}_{\theta x}}{\tilde{K}_{xx}} \right)^{-2} \quad (\text{A.116})$$

$$\frac{D_e+2D}{h+D+D_e} = \left(\frac{D_e}{b} - 2 \frac{\tilde{K}_{\theta x}}{\tilde{K}_{xx}} \right) \left(\frac{h}{b} + \frac{D_e}{b} - \frac{\tilde{K}_{\theta x}}{\tilde{K}_{xx}} \right)^{-1} \quad (\text{A.117})$$

$$\frac{b}{h + D_e} = \left(\frac{h}{b} + \frac{D_e}{b} \right)^{-1} \quad (\text{A.118})$$

$$\frac{D_e}{h + D_e} = \frac{D_e}{b} \left(\frac{h}{b} + \frac{D_e}{b} \right)^{-1} \quad (\text{A.119})$$

Finalmente, despreciando m_o , I e I_o , como suele hacerse (véase, por ejemplo [6, 12, 14]), se obtiene

$$\left\{ \lambda^2 \begin{bmatrix} (1+i2\xi') & 0 & 0 \\ 0 & \alpha_{xx}^2(1+i2\xi_{xx}) & 0 \\ 0 & 0 & \alpha_{\theta\theta}^2(1+i2\xi_{\theta\theta}) \end{bmatrix} - \begin{bmatrix} 1 & 1 & 1 \\ 1 & 1 & 1 \\ 1 & 1 & 1 \end{bmatrix} \right\} \begin{bmatrix} \omega_n^2 u / \ddot{u}_{g_o} \\ \omega_n^2 u_r^P / \ddot{u}_{g_o} \\ \omega_n^2 (h + D + D_e) \varphi_r^c / \ddot{u}_{g_o} \end{bmatrix} = -\lambda^2 \left(I_u + \left(\frac{h}{b} + \frac{D_e}{b} \right) I_\varphi \right) \begin{bmatrix} 1 \\ 1 \\ 1 \end{bmatrix} \quad (\text{A.120})$$

Resolviendo el sistema complejo de ecuaciones algebraicas que figura en la ecuación (A.120) para $\omega_n^2 u / \ddot{u}_{g_o}$, se obtiene la siguiente expresión del cortante en la base de la estructura por unidad de fuerza sísmica efectiva Q :

$$\left| \frac{\omega_n^2 u}{\ddot{u}_{g_o}} \right| = Q(\lambda) = \left| \frac{I_u(\lambda) + \left(\frac{h}{b} + \frac{D_e}{b} \right) I_\varphi(\lambda)}{A(\lambda) + iB(\lambda)} \right| \quad (\text{A.121})$$

donde

$$A(\lambda) = 1 - \frac{1}{\lambda^2} - \frac{1 + 4\xi_{xx}\xi'}{\lambda^2 \alpha_{xx}^2 (1 + 4\xi_{xx}^2)} - \frac{1 + 4\xi_{\theta\theta}\xi'}{\lambda^2 \alpha_{\theta\theta}^2 (1 + 4\xi_{\theta\theta}^2)} \quad (\text{A.122})$$

$$B(\lambda) = 2 \left[\xi' - \frac{\xi' - \xi_{xx}}{\lambda^2 \alpha_{xx}^2 (1 + 4\xi_{xx}^2)} - \frac{\xi' - \xi_{\theta\theta}}{\lambda^2 \alpha_{\theta\theta}^2 (1 + 4\xi_{\theta\theta}^2)} \right] \quad (\text{A.123})$$

Cabe mencionar que, cuando se anula la profundidad de embebimiento $D_e = 0$, las ecuaciones (A.109) y (A.120) coinciden con las escritas para cimentaciones pilotadas en las ecuaciones (A.59) y (A.68), respectivamente. Asimismo, la expresión del cortante en la base de la estructura por unidad de fuerza sísmica efectiva Q para cimentaciones embebidas (ecuación (A.121)) coincide con la obtenida para cimentaciones pilotadas (ecuación (A.69)) cuando $D_e = 0$.

Con el propósito de validar el modelo propuesto, en la figura A.32 se representan, de forma superpuesta, los resultados presentados por Avilés y Pérez-Rocha [14] para cimentaciones embebidas, en términos de periodo \tilde{T}/T y amortiguamiento $\tilde{\xi}$ efectivos del sistema, y aquellos obtenidos utilizando el modelo propuesto en esta tesis. En esta figura, cada columna muestra resultados correspondientes a distintos ratios de embebimiento: $D_e/b = 0$ (columna izquierda), 0.5 (columna central) y 1.5 (columna derecha). Asimismo, cada área gráfica proporciona resultados para dos valores del ratio de esbeltez de la estructura: $h/b = 1$, que corresponde a estructuras no esbeltas, y $h/b = 3$, que corresponde

a estructuras esbeltas. Además se han representado de forma conjunta resultados que se han obtenido teniendo en cuenta la interacción cinemática e inercial y aquellos calculados sin considerar la interacción cinemática. Todos estos resultados se han obtenido haciendo uso de las impedancias y los factores de interacción cinemática proporcionados, en forma de tabla, por Mita y Luco [119] para valores de los coeficientes de amortiguamiento histerético del suelo para ondas S y P, $\xi_S = 0.001$ y $\xi_P = 0.0005$, respectivamente. Además, se ha considerado que $\nu_s = 1/3$, $\xi = 0.05$ y $\delta = 0.15$. Cabe mencionar que las impedancias cruzadas y todos los términos de amortiguamiento de segundo orden se han tenido en cuenta.

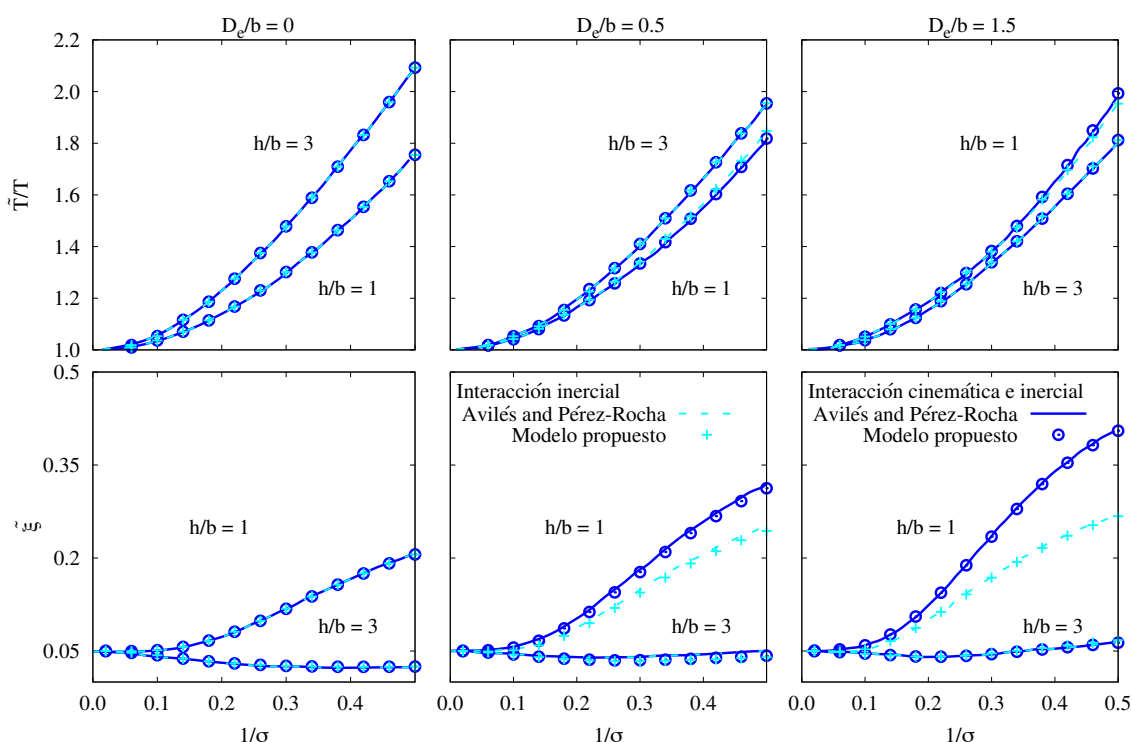


FIGURA A.32: Comparación entre los resultados obtenidos mediante el modelo propuesto y aquellos proporcionados por Avilés y Pérez-Rocha, digitalizados a partir del artículo original [14].

Tal y como señalaron Avilés y Pérez-Rocha, en la figura A.32 pueden observarse las siguientes tendencias:

- El periodo efectivo del sistema \tilde{T}/T aumenta a medida que el parámetro de onda σ disminuye. Para el caso de estructuras no esbeltas ($h/b = 1$), este aumenta con el ratio de embebimiento D_e/b . Por el contrario, en el caso de estructuras esbeltas ($h/b = 3$), \tilde{T}/T experimenta una disminución a medida que D_e/b aumenta. Debe tenerse en cuenta que el periodo efectivo del sistema aumenta con el ratio de esbeltez estructural h/b , salvo para $D_e/b = 1.5$. Por otra parte, puede observarse que el periodo del sistema no se ve afectado al considerar la interacción cinemática.

- Con respecto al amortiguamiento efectivo del sistema $\tilde{\xi}$, puede observarse que este experimenta una reducción a medida que h/b aumenta. En el caso de estructuras no esbeltas ($h/b = 1$), $\tilde{\xi}$ siempre toma valores superiores al correspondiente a la condición de base rígida y aumenta para valores decrecientes de σ , mientras que en el caso de estructuras esbeltas ($h/b = 3$), los efectos de la interacción suelo-estructura sobre $\tilde{\xi}$ dependen del valor de σ . Por otra parte, cuando se tiene en cuenta la interacción cinemática, se observa un incremento significativo del amortiguamiento efectivo en el caso de estructuras no esbeltas ($h/b = 1$). Sin embargo, para estructuras esbeltas ($h/b = 3$), sólo se observan ligeras reducciones o incrementos de $\tilde{\xi}$ como consecuencia de considerar la interacción cinemática.

Por último, cabe mencionar que los resultados obtenidos mediante el procedimiento propuesto en este trabajo coinciden con los extraídos del citado artículo de Avilés y Pérez-Rocha.

A.3. Comportamiento sísmico de estructuras sustentadas por pilotes verticales

A.3.1. Introducción

Esta sección aborda el análisis de la respuesta dinámica de estructuras a cortante sustentadas sobre grupos de pilotes verticales embebidos en un semiespacio homogéneo, viscoelástico e isotrópico y sometidos a ondas S de incidencia vertical. En la sección A.2.2 se expone una descripción detallada del problema objeto de estudio. El procedimiento propuesto en la sección A.2 se emplea en esta sección para estudiar la influencia de la interacción suelo-estructura sobre la respuesta de estructuras pilotadas, expresada en términos del cortante máximo en la base de la estructura por unidad de fuerza sísmica efectiva Q_m , así como en términos del periodo \tilde{T}/T y el amortiguamiento $\tilde{\xi}$ efectivos del sistema. Estos dos últimos parámetros caracterizan el comportamiento dinámico de un sistema equivalente con amortiguamiento viscoso de un solo grado de libertad [7, 12–14, 21]. Dicho sistema reproduce, de la forma más precisa posible, la respuesta del sistema acoplado dentro del rango de frecuencias en el que se produce la respuesta máxima. El desplazamiento horizontal y el giro del encepado, así como los factores de interacción cinemática correspondientes, se muestran también para distintos casos. Aunque este no es un análisis exhaustivo, pueden extraerse varias conclusiones relevantes acerca de cómo los efectos de interacción suelo-estructura, que afectan al comportamiento dinámico del sistema, están influenciados por la variación de parámetros tales como: la relación entre la masa del encepado y la masa de la estructura m_o/m , el ratio de esbeltez de la superestructura h/b , el parámetro de onda σ , la separación entre pilotes adyacentes s/d , la relación entre los módulos de elasticidad de los pilotes y el suelo E_p/E_s , el amortiguamiento de la estructura en base rígida ξ y la densidad de masa relativa entre la estructura y el suelo δ . En esta sección se estudia también la importancia de considerar las impedancias cruzadas y los factores de interacción cinemática en el cálculo de la respuesta dinámica de las configuraciones de cimentaciones pilotadas analizadas en este trabajo.

Inicialmente, en la sección A.3.2 se definen las configuraciones objeto de estudio. Posteriormente, en las secciones que van de la A.3.4 a la A.3.13 se presentan diversos estudios paramétricos, a fin de determinar la influencia de los principales parámetros del problema sobre la respuesta dinámica del sistema. En este sentido, se muestran diversas figuras que permiten comparar los resultados obtenidos para distintas configuraciones de grupos de pilotes. Con el propósito de facilitar la comprensión de estos resultados, cada una de estas figuras se presenta acompañada de dibujos que representan, de forma esquemática, las configuraciones consideradas en cada caso. Finalmente, las conclusiones que pueden extraerse de estos resultados se recogen en la sección A.3.14.

A.3.2. Configuraciones objeto de estudio

En esta sección se analiza la respuesta dinámica de estructuras soportadas por distintos grupos de 2×2 , 3×3 y 4×4 pilotes. Se han considerado cuatro valores diferentes del ratio de esbeltez estructural ($h/b = 1, 2, 5, 10$).

La figura A.33 muestra los parámetros que definen la geometría de la cimentación: longitud (L) y diámetro (d) de los pilotes y distancia entre los centros de las cabezas de pilotes adyacentes (s). El semiancho del encepado se define como $b = d$ para pilotes

simples, $b = s$ para grupos de 2×2 pilotes, $b = 3s/2$ para grupos de 3×3 pilotes y $b = 2s$ para grupos de 4×4 pilotes.

Los valores de los parámetros adimensionales que definen la geometría de dichas configuraciones están recogidos en la tabla A.7.

TABLA A.7: Configuraciones de grupos de pilotes verticales.

L/b	L/d	s/d		
		2×2	3×3	4×4
1	7.5	7.5	5	3.75
	15	15	10	7.5
2	7.5	3.75	2.5	1.875
	15	7.5	5	3.75
	30	15	10	7.5
4	15	3.75	2.5	1.875
	30	7.5	5	3.75

Los valores que se han considerado para el ratio de separación entre pilotes adyacentes s/d se han escogido de forma que se mantiene constante el semiancho del encepado b para configuraciones con distinto número de pilotes. Esto hace que los resultados sean comparables entre sí. Con el propósito de facilitar la interpretación de los resultados, la figura A.34 muestra una representación de las distintas configuraciones considerando el mismo diámetro de los pilotes ($d = \text{cte}$) para todos los casos. Así, puede observarse que todas las configuraciones de una misma fila comparten el mismo valor de b . A su vez, se han considerado tres valores diferentes del ratio de esbeltez de los pilotes ($L/d = 7.5, 15, \text{ y } 30$), así como del ratio de embebimiento ($L/b = 1, 2, \text{ y } 4$), con el fin de analizar los efectos que tiene la variación de estos parámetros sobre el comportamiento dinámico de la superestructura.

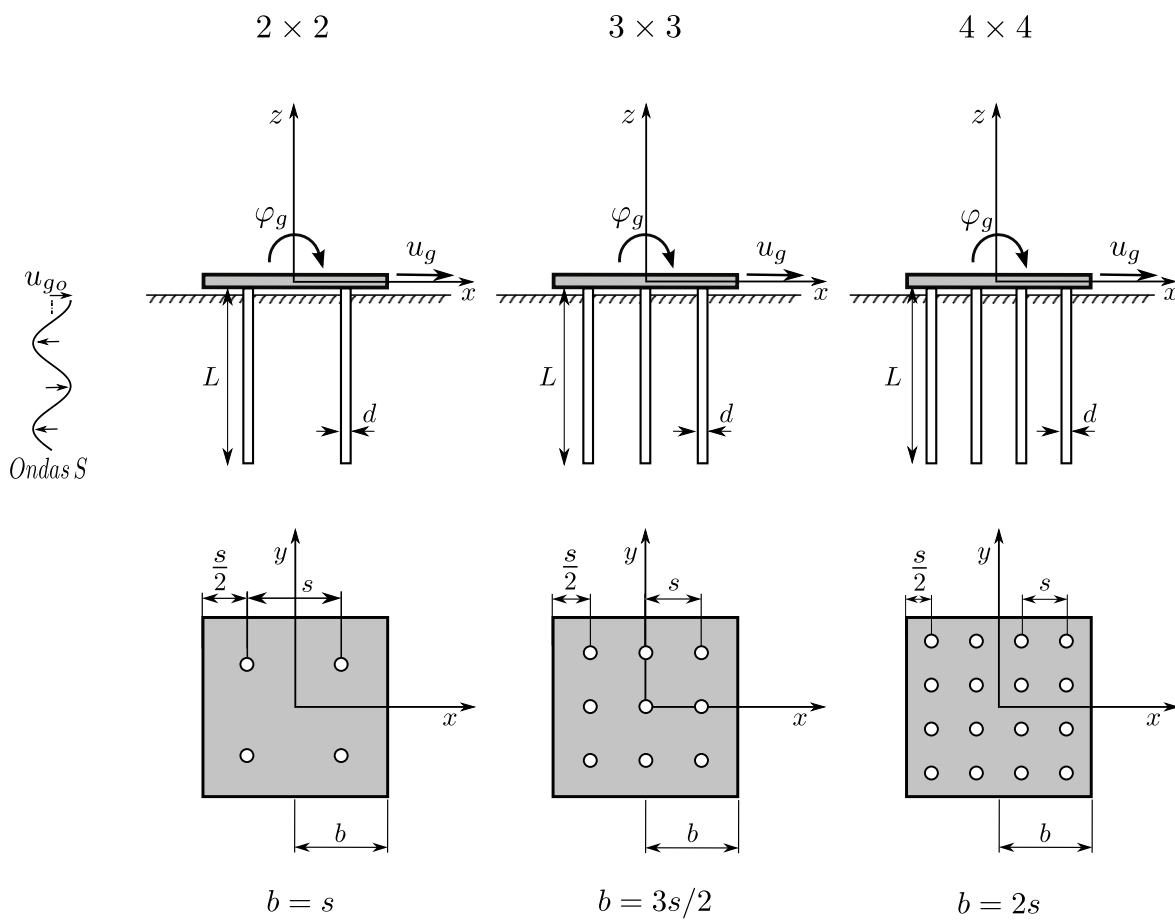


FIGURA A.33: Geometría de las cimentaciones con pilotes verticales.

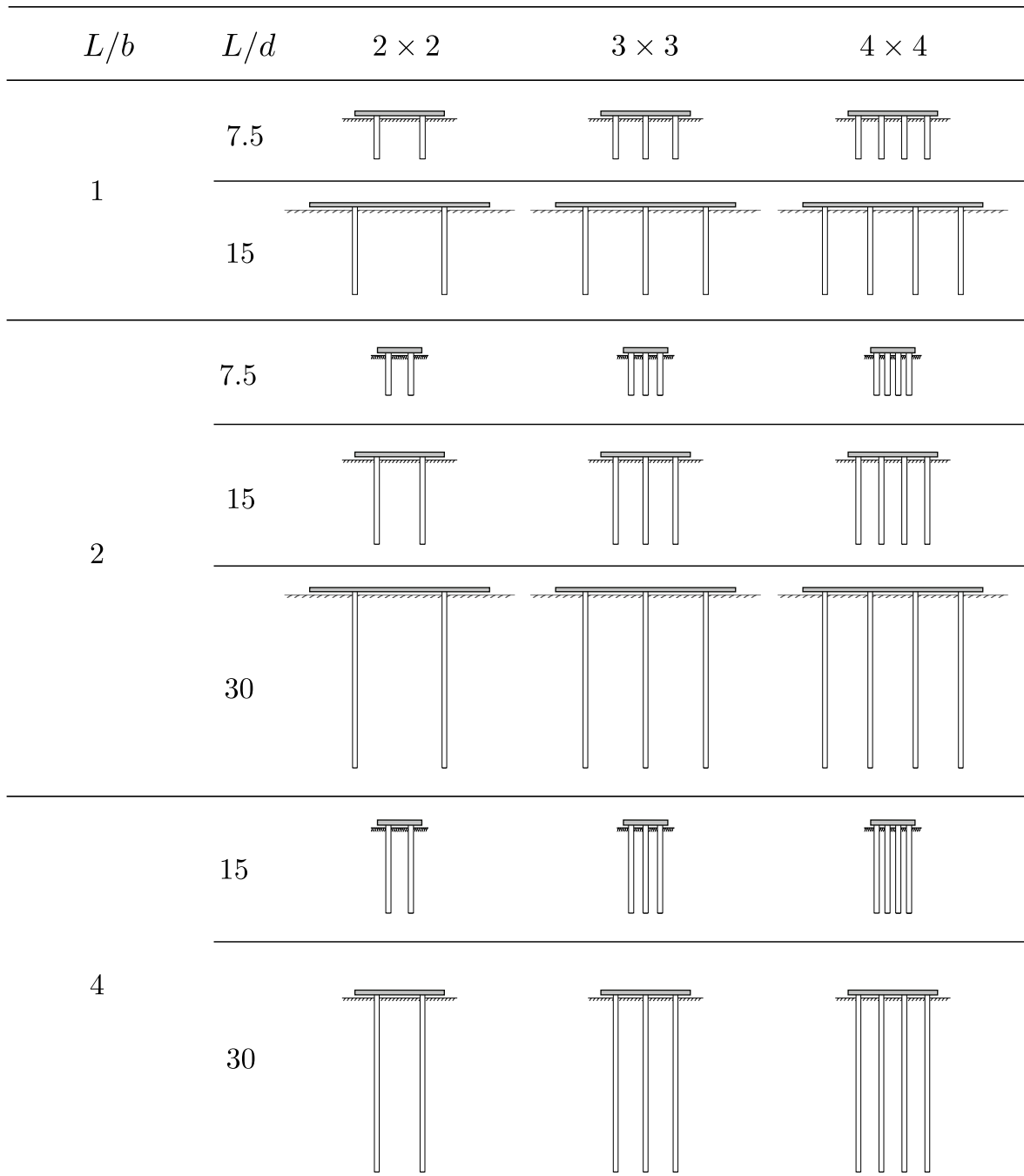


FIGURA A.34: Representación de las distintas configuraciones de pilotes verticales considerando el mismo diámetro $d = cte$ para todos los casos.

Las distintas configuraciones de grupos de pilotes se han analizado en el rango de frecuencias de interés para carga sísmica ($\omega d/c_s < 0.5$, según Gazetas *et al.* [79]). La figura A.35 muestra que, en todos los casos estudiados, el valor de a_o que corresponde al periodo efectivo para cada valor de σ , siendo $1/\sigma \leq 0.5$, es siempre inferior a 0.5.

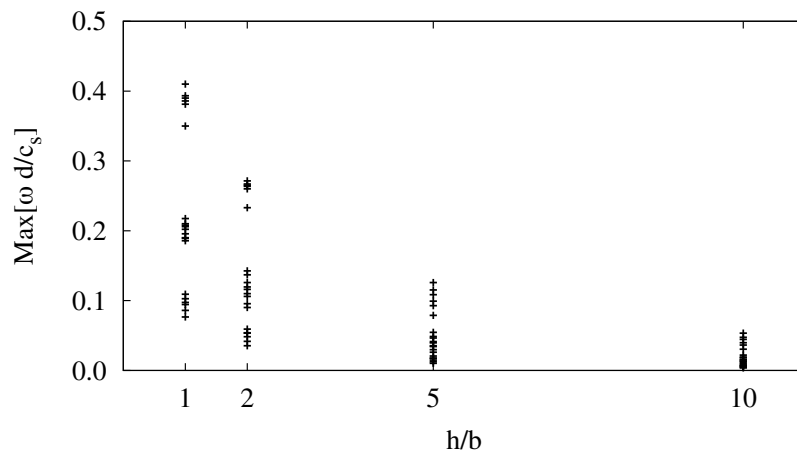


FIGURA A.35: Rango de la frecuencia adimensional $\omega d/c_s$ para todos los casos analizados.

Salvo que se especifique lo contrario, para la obtención de los resultados que se presentan en esta sección se ha considerado: $\delta = 0.15$, $m_o/m = 0$, $0 < 1/\sigma < 0.5$, $\xi = 0.05$, $\xi_s = 0.05$ y $\nu_s = 0.4$. Estos valores son representativos de edificios y suelos reales [14, 122]. Asimismo, $E_p/E_s = 10^3$ ó 10^2 y $\rho_s/\rho_p = 0.7$.

La elección del rango de valores considerado para el parámetro $1/\sigma$ se ha realizado teniendo en cuenta los resultados empíricos presentados por Stewart *et al.* [122]. Dichos resultados muestran los efectos de interacción suelo-estructura para 57 edificaciones que cubren un amplio rango de condiciones geotécnicas y estructurales representativas de la realidad. La mayor parte de estos casos muestran valores de $1/\sigma$ entre 0 y 0.3.

Las impedancias y los factores de interacción cinemática, correspondientes a todas las configuraciones de grupos de pilotes consideradas en este estudio, se han calculado empleando la formulación acoplada de elementos finitos y elementos de contorno desarrollada por Padrón *et al.* [71, 81, 120].

A.3.3. Impedancias y factores de interacción cinemática

Las figuras desde la A.36 a la A.38 muestran las impedancias de los grupos de pilotes que se analizan, en el rango de a_o que se precisa para obtener todos los resultados que figuran en las secciones posteriores. Por otra parte, la figura A.39 presenta los correspondientes factores de interacción cinemática, en términos de una curva general idealizada [79] para cada L/d . Esta curva es la línea central de una banda que contiene todas las curvas obtenidas para las distintas configuraciones estudiadas con un valor determinado de L/d . Se ha demostrado que el factor de interacción cinemática asociado a la traslación I_u depende fundamentalmente de L/d y no se ve afectado de forma significativa por el número de pilotes del grupo. Sin embargo, esta conclusión no es tan válida

para I_φ [78, 79]. El error relativo medio en términos de Q_m , que se deriva del uso de los factores de interacción cinemática idealizados para un valor concreto de L/d (véase la figura A.39), tomando como referencia los resultados obtenidos con sus valores exactos, es inferior al 14 % para todos los casos estudiados. Cabe señalar que este efecto disminuye para valores crecientes de h/b . Así, cuando $h/b = 10$ el error relativo alcanza el 4 % en el caso más desfavorable. Sin embargo, aunque se incluyen en este documento las curvas idealizadas de I_u e I_φ para cada valor de L/d , todos los resultados que se muestran en adelante han sido obtenidos utilizando los valores exactos de los factores de interacción cinemática representados en las figuras de la A.40 a la A.42.

Con el propósito de determinar la influencia que tiene el ratio del módulo de Young pilote-suelo sobre el comportamiento dinámico de la estructura, se ha considerado un valor adicional para E_p/E_s . En esta línea, las figuras A.43 y A.44 muestran, respectivamente, impedancias y factores de interacción cinemática para grupos de 2×2 pilotes embebidos en un suelo homogéneo tal que $E_p/E_s = 10^2$. En dichas figuras se representan resultados para tres valores diferentes del ratio de esbeltez de los pilotes $L/d = 7.5, 15$ y 30 .

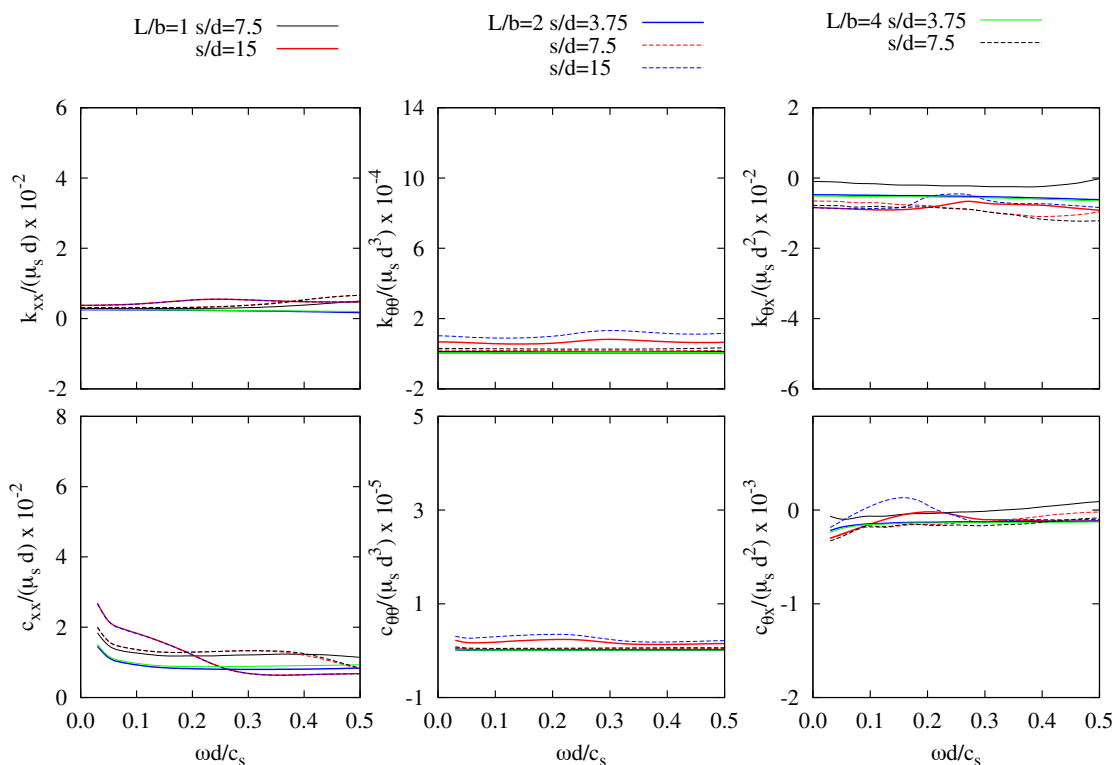


FIGURA A.36: Impedancias para distintos grupos de 2×2 pilotes. $E_p/E_s = 10^3$ y $\xi_s = 0.05$.

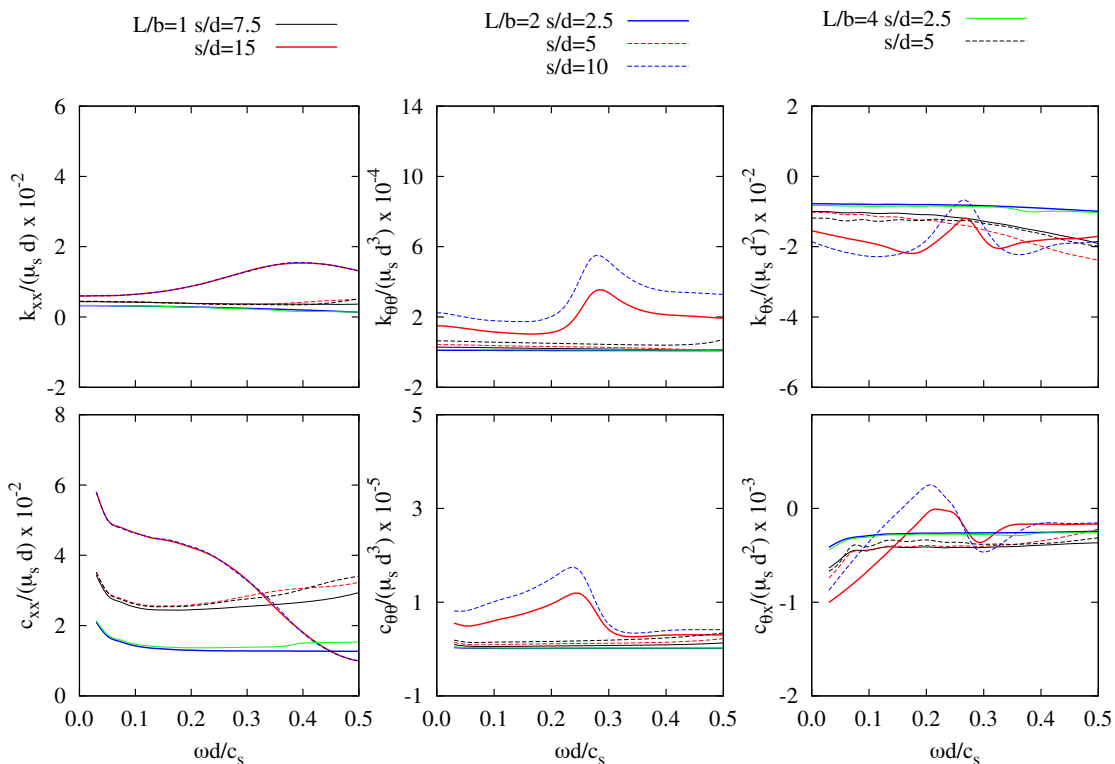


FIGURA A.37: Impedancias para distintos grupos de 3×3 pilotes. $E_p/E_s = 10^3$ y $\xi_s = 0.05$.

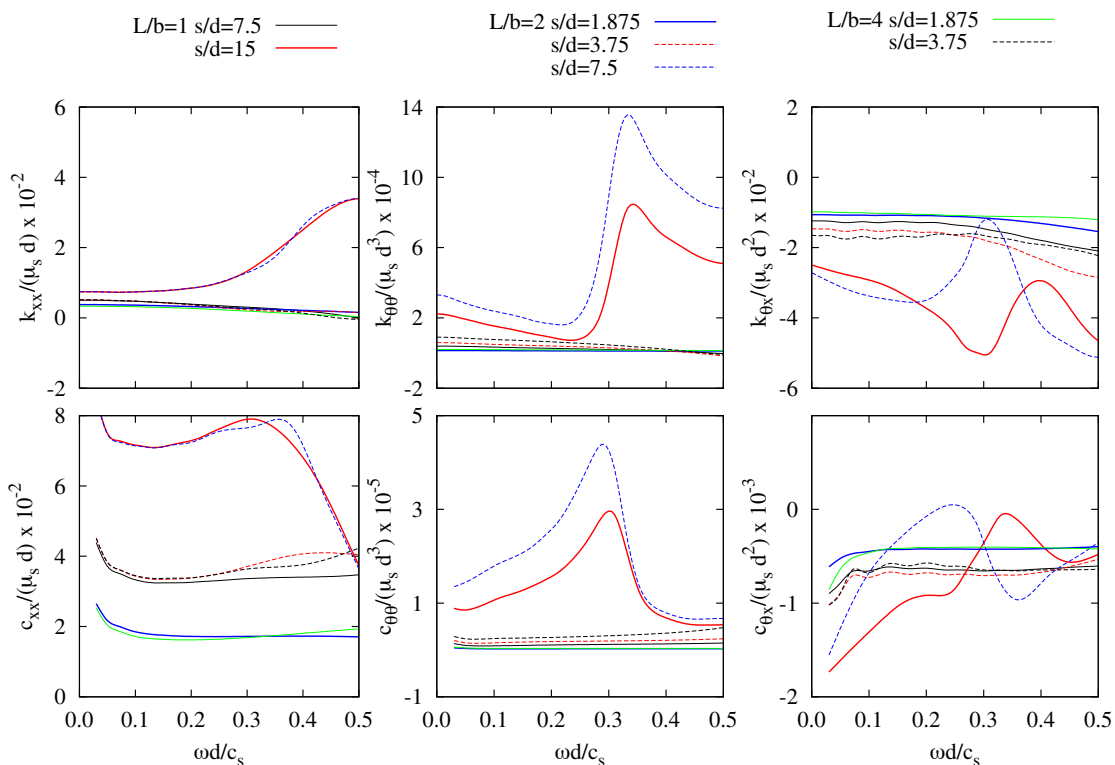


FIGURA A.38: Impedancias para distintos grupos de 4×4 pilotes. $E_p/E_s = 10^3$ y $\xi_s = 0.05$.

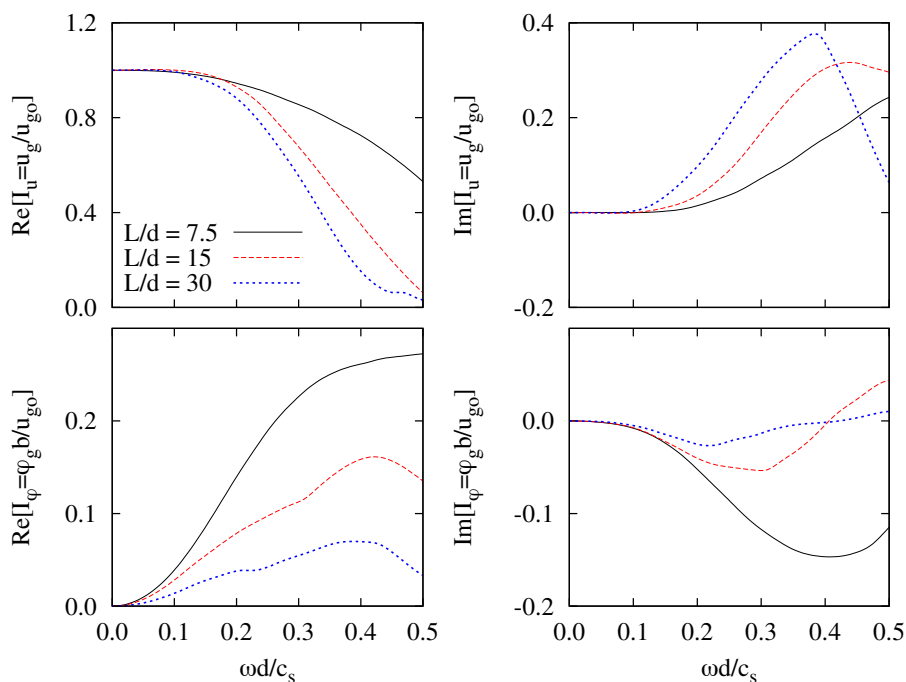


FIGURA A.39: Factores de interacción cinemática para distintos grupos de pilotes embebidos en un suelo con $E_p/E_s = 10^3$ y $\xi_s = 0.05$.

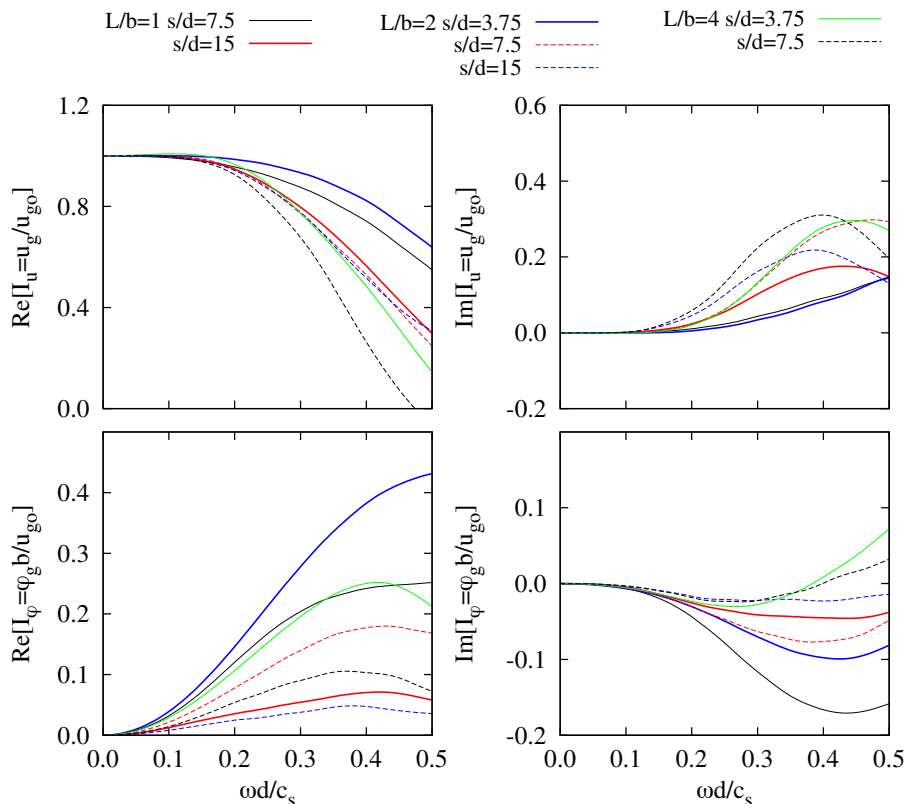


FIGURA A.40: Factores de interacción cinemática para distintos grupos de 2×2 pilotes. $E_p/E_s = 10^3$ y $\xi_s = 0.05$.

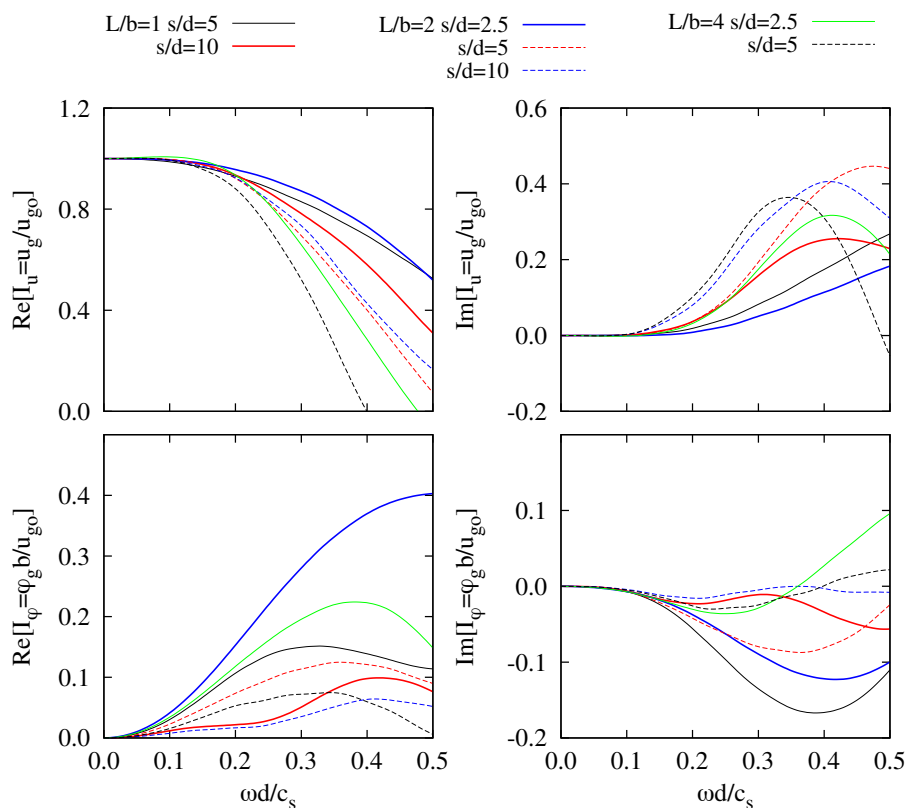


FIGURA A.41: Factores de interacción cinemática para distintos grupos de 3×3 pilotes. $E_p/E_s = 10^3$ y $\xi_s = 0.05$.

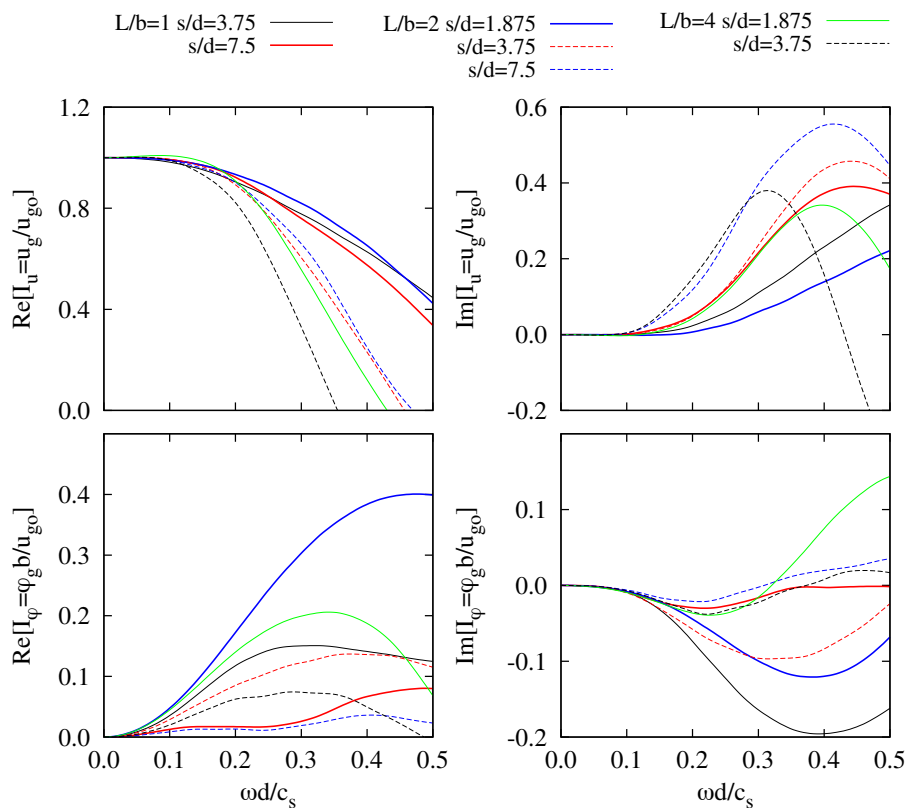


FIGURA A.42: Factores de interacción cinemática para grupos de 4×4 pilotes. $E_p/E_s = 10^3$ y $\xi_s = 0.05$.

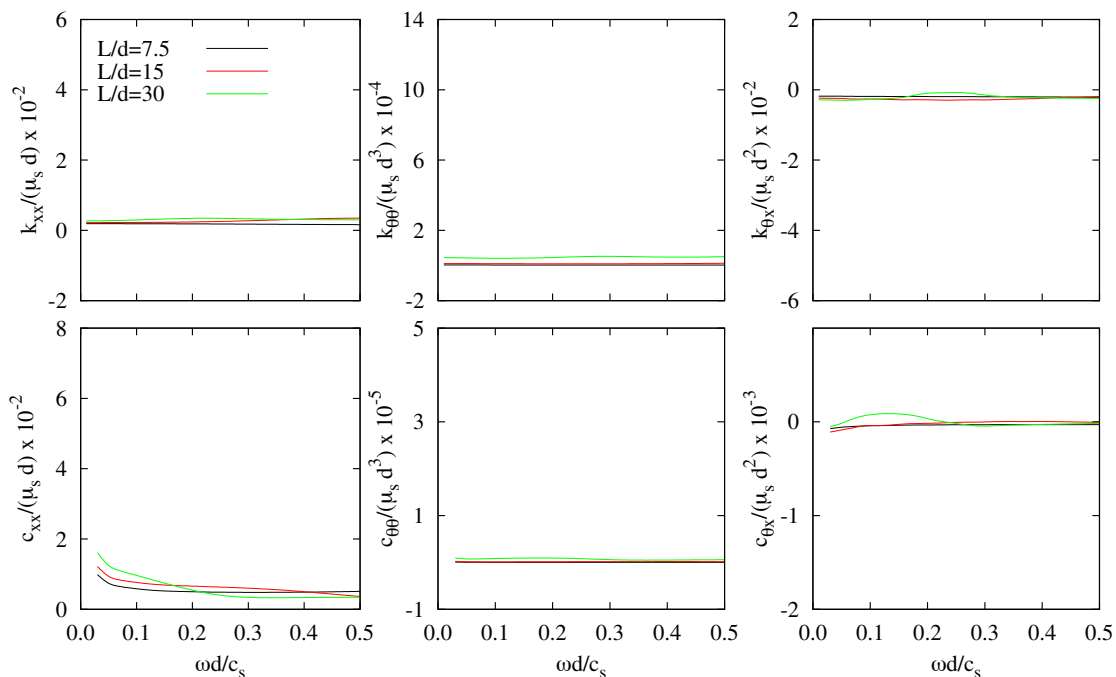


FIGURA A.43: Impedancias para distintos grupos de 2×2 pilotes. $E_p/E_s = 10^2$ y $\xi_s = 0.05$.

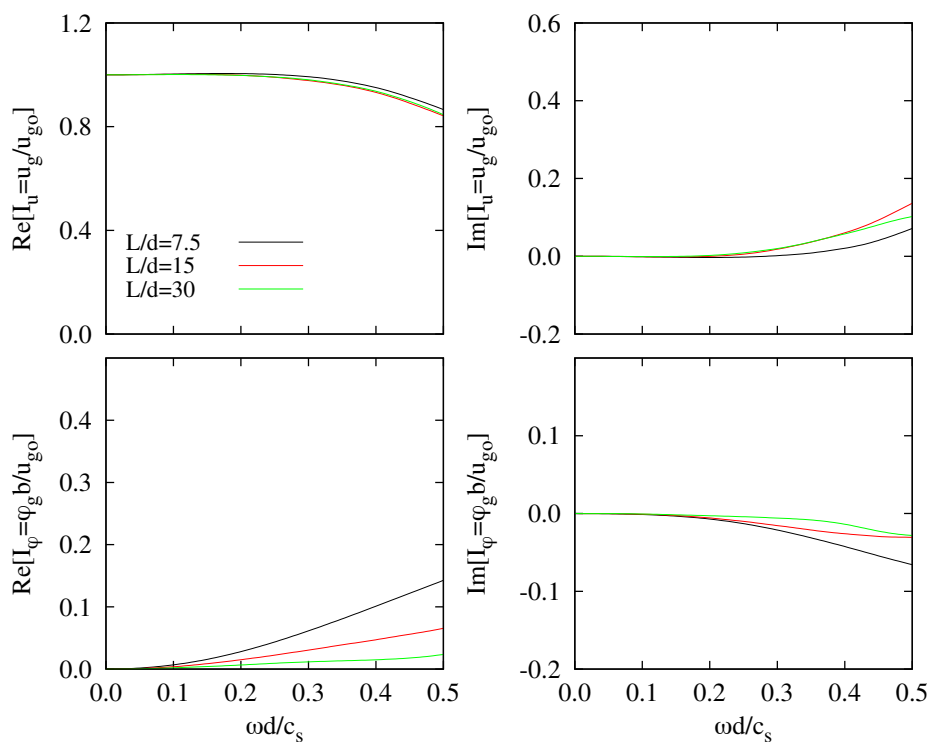


FIGURA A.44: Factores de interacción cinemática para distintos grupos de 2×2 pilotes. $E_p/E_s = 10^2$ y $\xi_s = 0.05$.

A.3.4. Influencia de la relación entre la masa del encepado y la masa de la estructura

La simplificación que consiste en anular la masa del encepado m_o ha sido adoptada por muchos autores (véase, por ejemplo, [6, 7, 9, 11, 13, 14]). Con el fin de evaluar cómo afecta esta simplificación a la respuesta dinámica de la superestructura, la figura A.45 muestra, para cinco valores diferentes de la relación entre la masa del encepado y la masa de la estructura ($m_o/m = 0, 0.25, 0.50, 0.75$ y 1), el cortante máximo en la base de la estructura por unidad de fuerza sísmica efectiva Q_m , para superestructuras con distintos valores de esbeltez sustentadas sobre grupos de 4×4 pilotes con un ratio de embebimiento $L/b = 2$. En cada fila se han representado los resultados correspondientes a distintos valores del ratio de esbeltez de los pilotes ($L/d = 7.5, 15$ y 30). En la figura A.46 se han representado, de forma esquematizada, dichas configuraciones de grupos de pilotes considerando $d = \text{cte}$. Todas las gráficas se presentan en función de $1/\sigma$, siendo σ el parámetro de onda.

En todas las configuraciones estudiadas en este trabajo, el error relativo, en términos de Q_m , que supone considerar $m_o/m = 0$ cuando $m_o/m = 0.5$, alcanza un valor máximo del 8%. Sin embargo, el error relativo medio es inferior al 5% en todos los casos. Siendo así, puede concluirse que las variaciones de la relación entre la masa del encepado y la masa de la estructura m_o/m , en el rango entre 0 y 0.5, no conduce a diferencias significativas en términos de Q_m . Estas conclusiones respaldan la simplificación adoptada con frecuencia y que consiste en despreciar m_o .

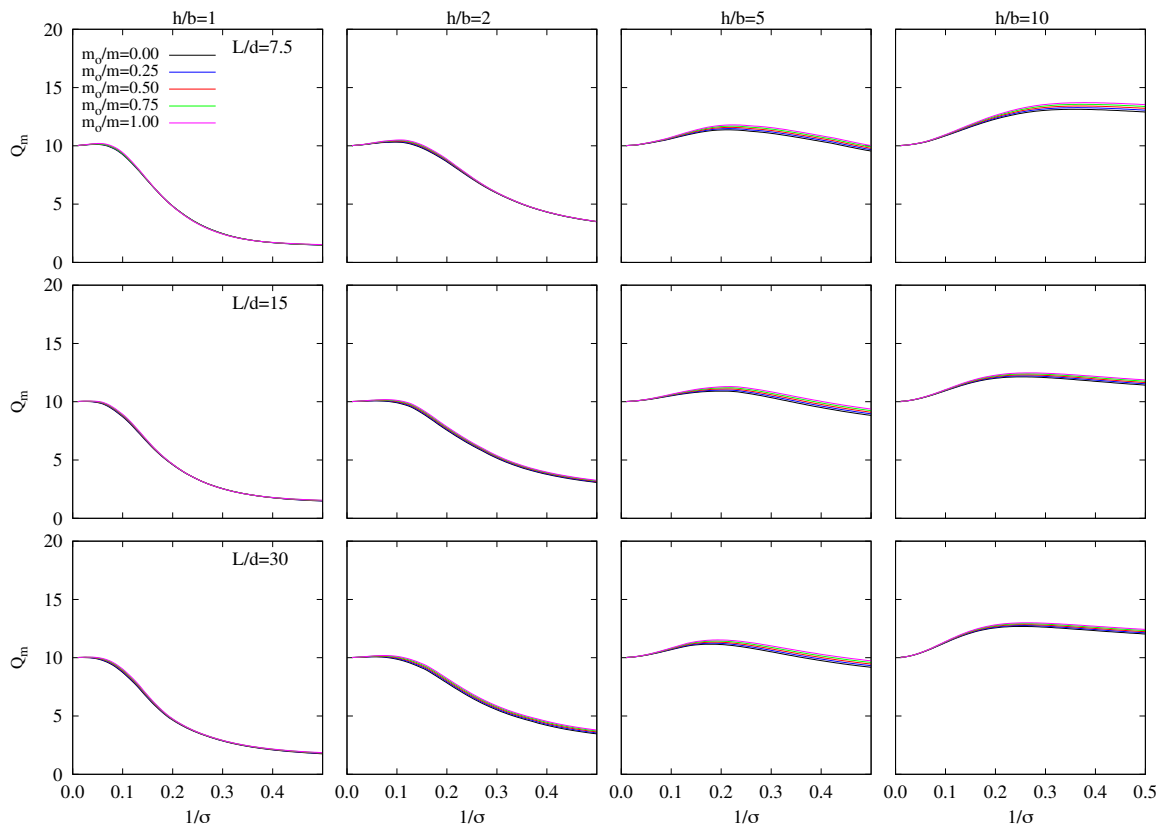


FIGURA A.45: Influencia de la relación de masas cemento-estructura m_o/m . Respuesta máxima estructural Q_m para grupos de 4×4 pilotes con $L/b = 2$, $E_p/E_s = 10^3$ y $\xi_s = 0.05$.

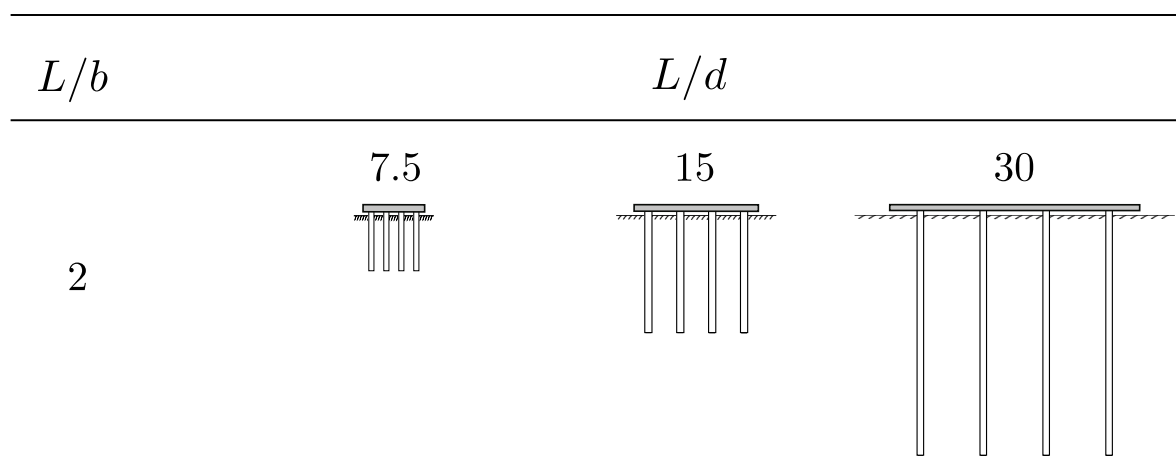


FIGURA A.46: Representación esquemática de las distintas configuraciones analizadas en la figura A.45 considerando $d = cte$.

A.3.5. Influencia de las impedancias cruzadas

Todos los resultados que se presentan en esta tesis se han obtenido teniendo en cuenta todos los elementos de la matriz de impedancias. A pesar de que muchos autores desprecian los términos de rigidez y amortiguamiento asociados al modo de vibración cruzado horizontal-balanceo [7, 8, 12, 13], esto no es aceptable para cimentaciones pilotadas, ni siquiera lo es para ciertas configuraciones de cimentaciones embebidas. Por este motivo, se ha llevado cabo un análisis comparativo que permite determinar la influencia de las impedancias cruzadas sobre la respuesta dinámica del sistema.

Las figuras A.47, A.49 y A.51 muestran hasta qué punto influye el hecho de anular las impedancias cruzadas sobre la respuesta dinámica del sistema y, al mismo tiempo, dichas figuras permiten identificar cómo esta influencia se ve afectada por la variación de los principales parámetros del problema. Asimismo, las figuras A.48, A.50 y A.52 proporcionan, respectivamente, representaciones esquemáticas de las configuraciones de grupos de pilotes consideradas en cada caso. Se han representado, de forma superpuesta y en términos de \tilde{T} , $\tilde{\xi}$ y Q_m , los resultados obtenidos anulando las impedancias cruzadas y aquellos calculados teniendo en cuenta dichas impedancias. Dichas figuras ponen de manifiesto que la influencia de considerar las impedancias cruzadas disminuye, por lo general, para valores crecientes de σ y h/b . Asimismo, tal y como puede observarse en la figura A.47, esta influencia se vuelve más apreciable a medida que L/d disminuye. Por otra parte, en la figura A.49, se observa una influencia mayor de las impedancias cruzadas a medida que aumenta L/b . Por último, la figura A.51 muestra cómo el número de pilotes del grupo modifica la influencia de las impedancias cruzadas sobre la respuesta dinámica del sistema. Puede observarse que esta influencia disminuye ligeramente para aquellas configuraciones con un mayor número de pilotes.

En un número significativo de casos, el amortiguamiento del sistema $\tilde{\xi}$ disminuye cuando se tienen en cuenta en el cálculo las impedancias cruzadas, lo cual implica que la respuesta dinámica del sistema se subestima cuando estas se desprecian. Por otra parte, el periodo natural del sistema \tilde{T} aumenta en todos los casos cuando se consideran las impedancias cruzadas.

Para las configuraciones analizadas en este trabajo, el error relativo en términos de Q_m , que supone anular las impedancias cruzadas, alcanza un valor máximo del 40 %. Sin embargo, el error relativo medio es inferior al 16 %.

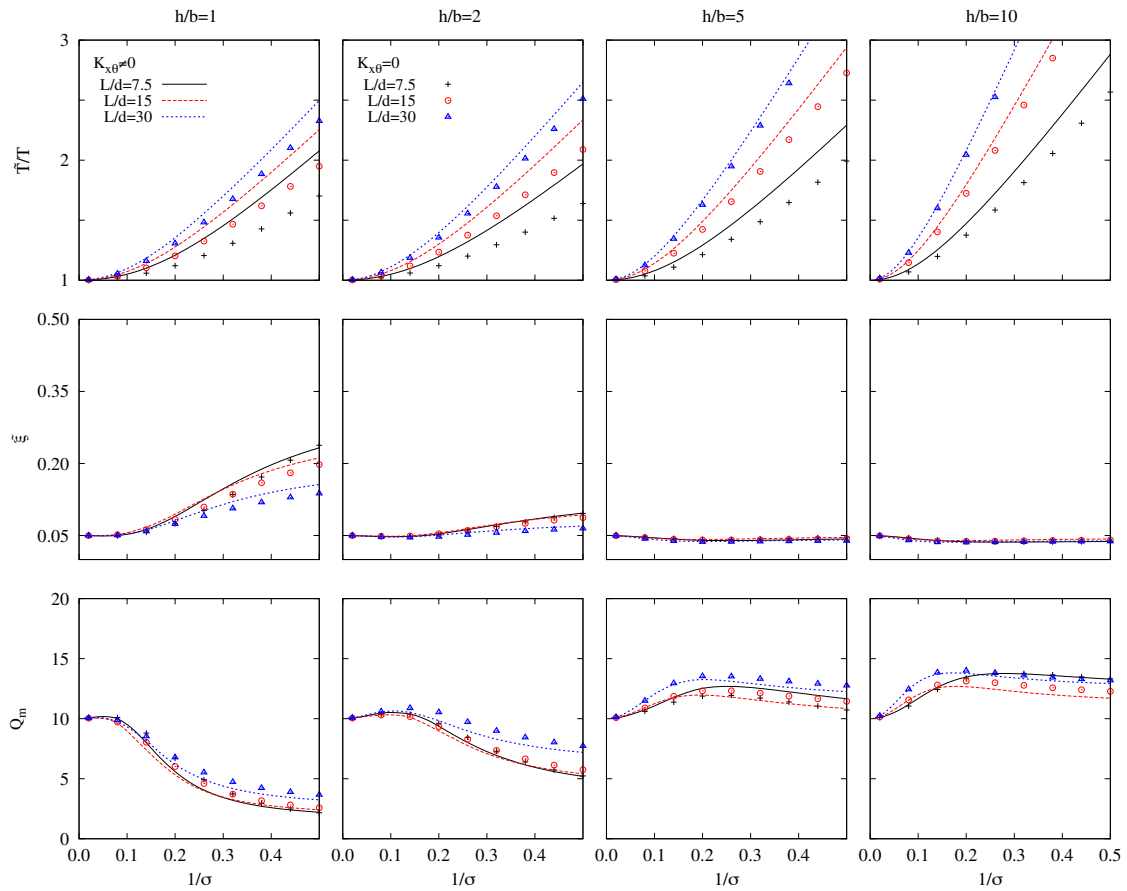


FIGURA A.47: Influencia de las impedancias cruzadas. Periodo efectivo \tilde{T}/T , amortiguamiento $\tilde{\xi}$ y respuesta máxima estructural Q_m para un grupo de 2×2 pilotes con $L/b = 2$, $E_p/E_s = 10^3$ y $\xi_s = 0.05$.

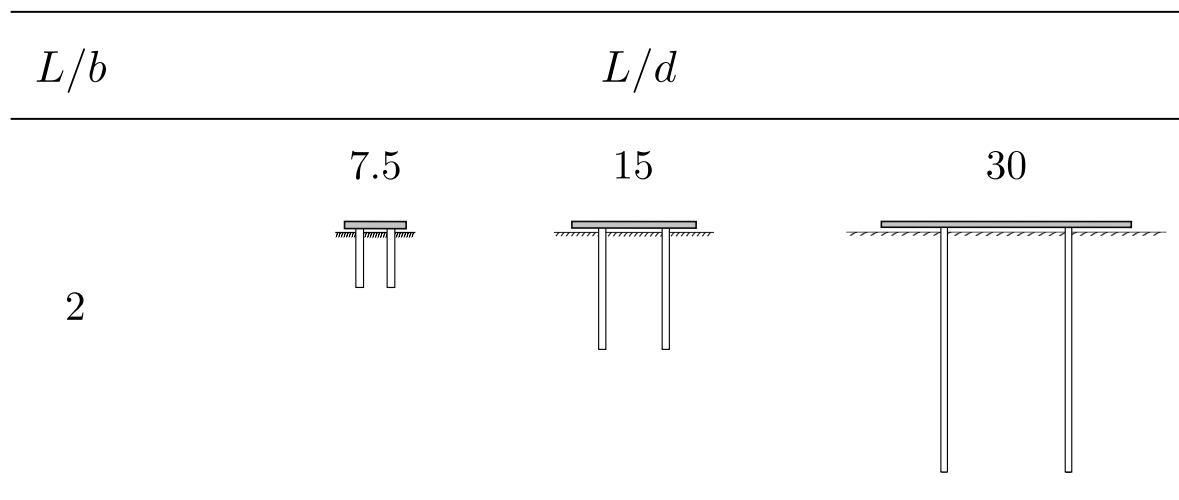


FIGURA A.48: Representación esquemática de las configuraciones de grupos de pilotes analizadas en la figura A.47 considerando $d = cte$.

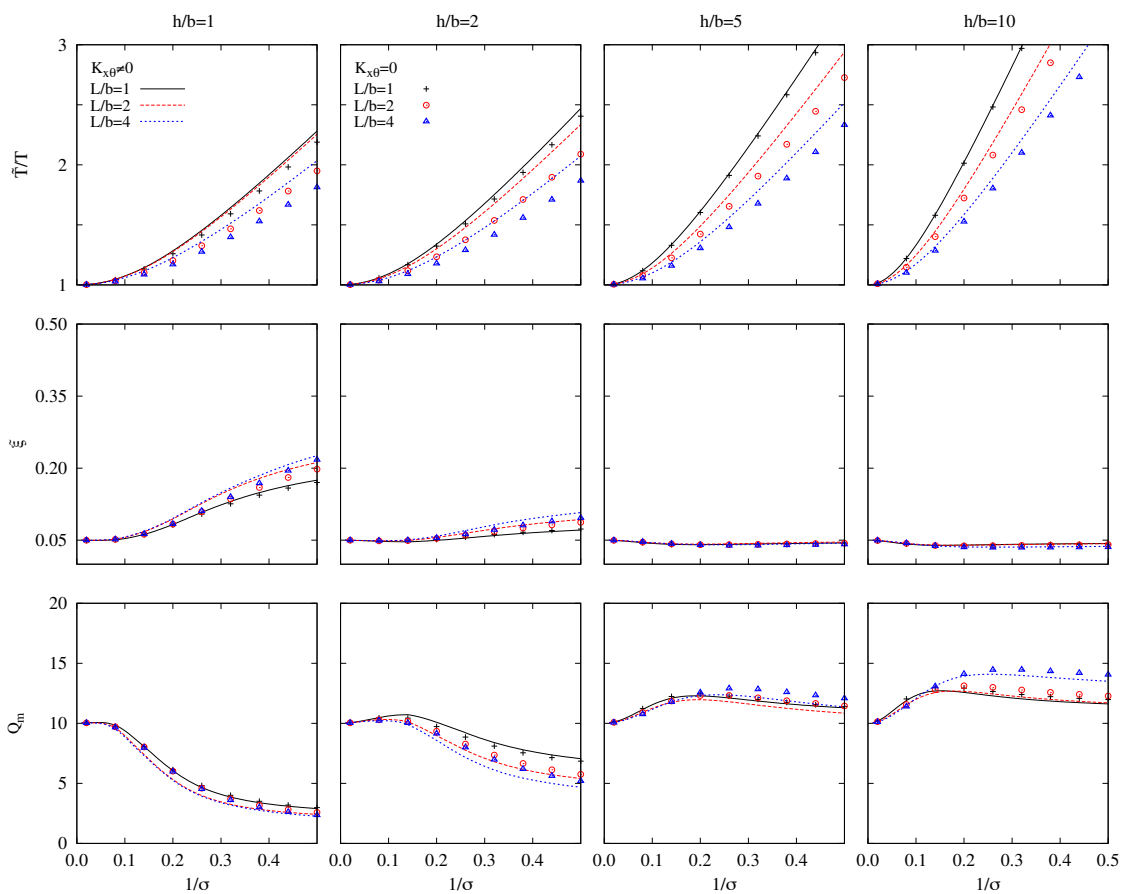


FIGURA A.49: Influencia de las impedancias cruzadas. Periodo efectivo \tilde{T}/T , amortiguamiento ξ y máxima respuesta estructural Q_m para un grupo de 2×2 pilotes con $L/d = 15$, $E_p/E_s = 10^3$ y $\xi_s = 0.05$.

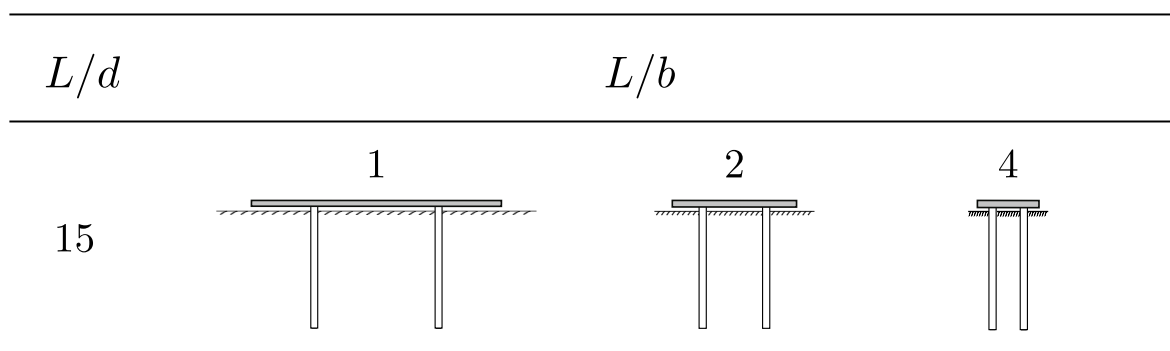


FIGURA A.50: Representación esquemática de las configuraciones de grupos de pilotes analizadas en la figura A.49 considerando $d = \text{cte}$.

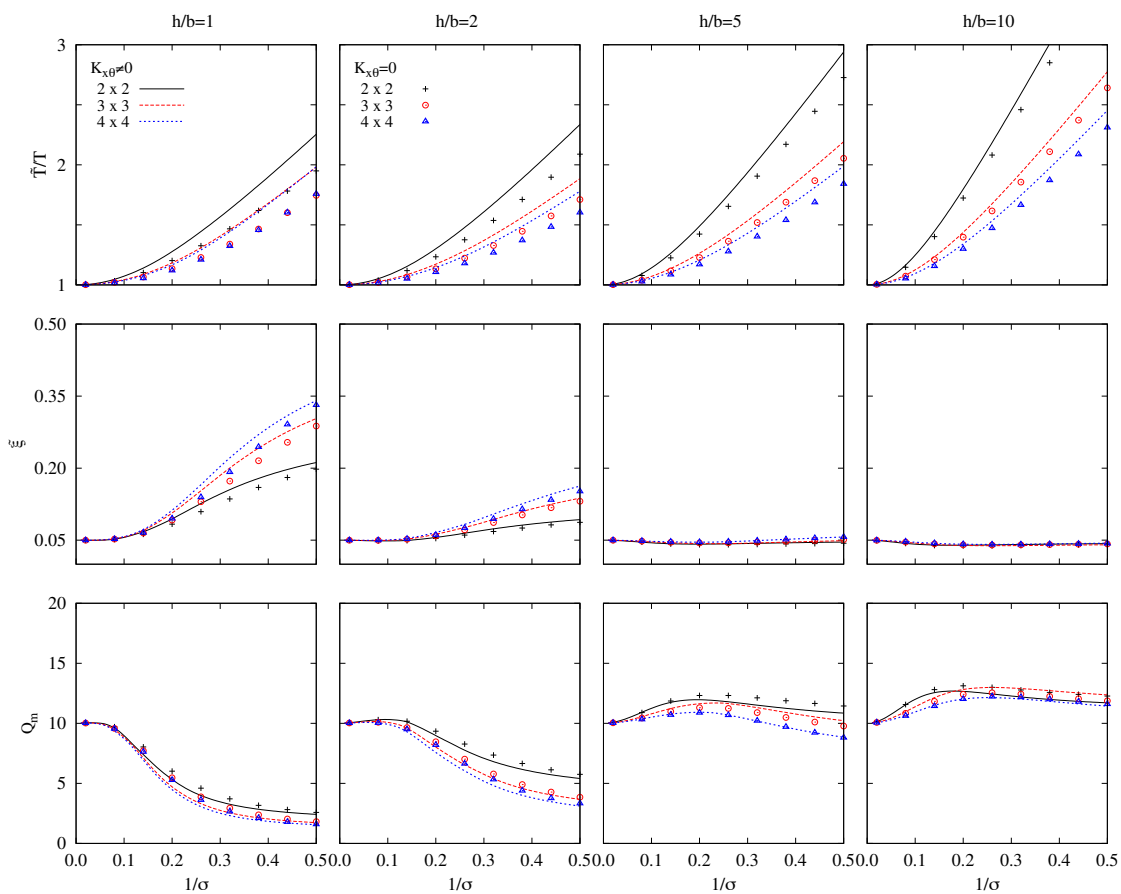


FIGURA A.51: Influencia de las impedancias cruzadas. Periodo efectivo \tilde{T}/T , amortiguamiento $\tilde{\xi}$ y respuesta máxima estructural Q_m para grupos de pilotes con $L/d = 15, L/b = 2, E_p/E_s = 10^3$ y $\xi_s = 0.05$.

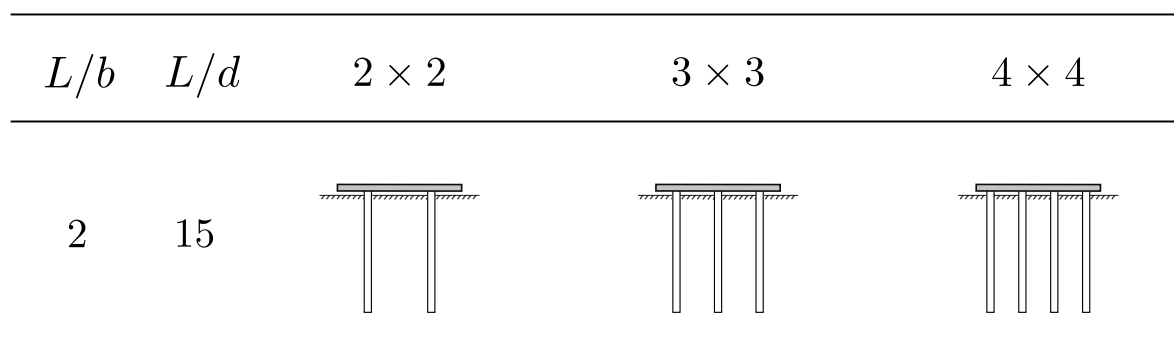


FIGURA A.52: Representación esquemática de las configuraciones de grupos de pilotes analizadas en la figura A.51 considerando $d = cte$.

A.3.6. Influencia del ratio de esbeltez estructural y el parámetro de onda

La influencia del ratio de esbeltez estructural h/b y el parámetro de onda σ puede analizarse a partir de las figuras A.53, A.56, A.58 y A.61. Las figuras que van de la A.56 a la A.61 se emplean también para abordar análisis comparativos en secciones posteriores. En la figura A.53 se representa el periodo efectivo del sistema \tilde{T}/T para estructuras con $h/b = 1, 2, 5$ y 10 , soportadas por varias configuraciones de grupos de pilotes. Las representaciones esquemáticas de las configuraciones a las que corresponden los resultados representados en la columna de la izquierda se muestran en la figura A.54. A su vez, la figura A.55 proporciona las representaciones correspondientes a los resultados que figuran en la columna de la derecha. Por otra parte, las figuras A.56, A.58 y A.61 proporcionan resultados en términos del periodo \tilde{T}/T y el amortiguamiento $\tilde{\xi}$ efectivos, así como del cortante máximo en la base de la estructura por unidad de fuerza sísmica efectiva Q_m , para diversas configuraciones de grupos de pilotes cuya representación esquemática se muestra en las figuras A.57, A.59 y A.62, respectivamente. Todas las gráficas se presentan en función de $1/\sigma$, siendo σ el parámetro de onda.

Como era de esperar, el periodo efectivo del sistema \tilde{T}/T aumenta para valores decrecientes de σ , lo cual implica una menor rigidez del suelo. Por lo general, valores menores de h/b conducen a una reducción de \tilde{T}/T . Sin embargo, esta tendencia puede cambiar para $h/b \leq 1$ (véase la figura A.53). En todos los casos, la interacción suelo-estructura implica un aumento del periodo del sistema ($\tilde{T} > T$). Por el contrario, el valor del coeficiente de amortiguamiento efectivo $\tilde{\xi}$ puede ser mayor o menor que el correspondiente a la estructura en base rígida, dependiendo principalmente de h/b (véanse las figuras A.56, A.58 ó A.61). Para edificios con $h/b < 5$, el amortiguamiento efectivo aumenta con $1/\sigma$ y muestra valores por encima del coeficiente de amortiguamiento de la estructura en base rígida. En cambio, para edificios con $h/b \geq 5$ el amortiguamiento efectivo es casi independiente de $1/\sigma$, de manera que permanece en el entorno del coeficiente de amortiguamiento de la estructura en base rígida. Estudios realizados en la misma línea para estructuras con cimentaciones superficiales [7] y cimentaciones embebidas [14] arrojaron conclusiones similares.

Observando nuevamente las figuras A.56, A.58 o A.61, puede notarse que, para edificios poco esbeltos con $h/b \leq 2$, el valor de Q_m disminuye a medida que aumenta $1/\sigma$. Sin embargo, para edificios esbeltos con $h/b \geq 3$, Q_m muestra una dependencia moderada de $1/\sigma$ y puede alcanzar valores por encima de los correspondientes a la condición de base rígida. Por otra parte, a medida que aumenta h/b , el valor máximo de Q_m tiene lugar a valores mayores de $1/\sigma$ (en la mayoría de los casos entre 0.1 y 0.3). En efecto, en los casos analizados en este trabajo, el valor máximo obtenido para Q_m , teniendo en cuenta los efectos de interacción suelo-estructura, es un 67% mayor que el correspondiente a la condición de base rígida. Este es el caso del valor máximo de Q_m alcanzado para una superestructura con $h/b = 10$ sustentada por un grupo de 4×4 pilotes con ratio de embebimiento $L/b = 4$ y ratio de esbeltez de los pilotes $L/d = 15$ (véase la figura A.56).

El desplazamiento horizontal del cimiento $|\omega_n^2 u_r^c / \ddot{u}_{g0}|$ (véanse las figuras A.58 y A.61) aumenta con $1/\sigma$ para todos los casos estudiados. Su dependencia del ratio de esbeltez de la estructura h/b está asociada a la configuración correspondiente a cada caso particular. Por otra parte, el giro del cimiento $|\omega_n^2 h \varphi_r^c / \ddot{u}_{g0}|$ aumenta con $1/\sigma$, siendo este efecto más pronunciado para valores más altos del ratio h/b .

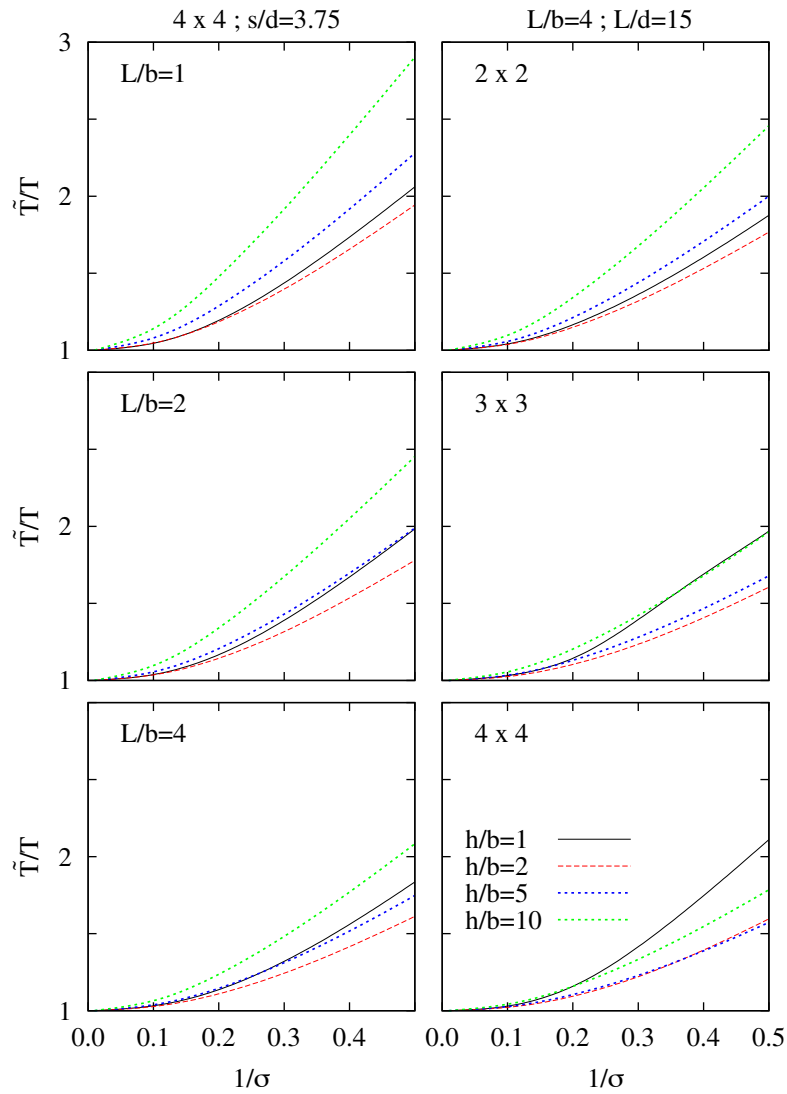


FIGURA A.53: Influencia del ratio de esbeltez de la estructura h/b . Periodo efectivo \tilde{T}/T para un grupo de 4×4 pilotes con $s/d = 3.75$ (columna izquierda) y para un grupo de pilotes con $L/b = 4$ y $L/d = 15$ (columna derecha). $E_p/E_s = 10^3$ y $\xi_s = 0.05$.

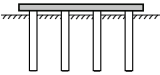
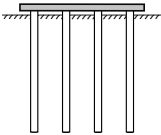
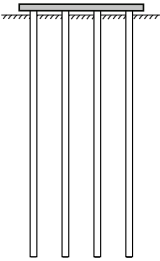
L/b	1	2	4
L/d	7.5	15	30
			

FIGURA A.54: Representación esquemática de las configuraciones de grupos de pilotes analizadas en la columna izquierda de la figura A.53 considerando $d = cte.$

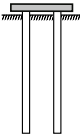
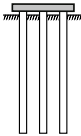
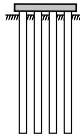
L/b	L/d	2×2	3×3	4×4
4	15			

FIGURA A.55: Representación esquemática de las configuraciones de grupos de pilotes analizadas en la columna derecha de la figura A.53 considerando $d = cte.$

A.3.7. Influencia de los factores de interacción cinemática

La figura A.56 permite observar hasta qué punto la interacción cinemática influye sobre las características dinámicas del sistema. A tal fin, en dicha figura se representan, de forma superpuesta, las curvas de \tilde{T} , $\tilde{\xi}$ y Q_m que se han obtenido considerando la interacción suelo-estructura completa (tanto interacción cinemática como inercial), o teniendo en cuenta únicamente la interacción inercial. Dichos resultados corresponden a distintos grupos de pilotes (2×2 , 3×3 y 4×4) con el mismo ratio de esbeltez (L/d) y las mismas propiedades mecánicas (E_p/E_s). En la figura A.57 se representan de forma esquemática las configuraciones analizadas. La interacción cinemática también se ha evaluado en este caso mediante la función $|I_u + (h/b)I_\varphi|$.

Obviamente, dado que la frecuencia natural de un sistema no depende de la excitación, el periodo efectivo del sistema no se ve afectado por la interacción cinemática. Sin embargo, en la mayoría de los casos, el amortiguamiento efectivo disminuye cuando estos factores se tienen en cuenta ($|I_u + (h/b)I_\varphi| > 1$). En cambio, esta tendencia puede invertirse para estructuras no esbeltas ($h/b \leq 1$) sobre suelos blandos ($1/\sigma \geq 0.2$) (i.e. $|I_u + (h/b)I_\varphi| < 1$), lo que implica que pueden alcanzarse mayores valores de $\tilde{\xi}$ cuando se considera la interacción cinemática. Este efecto se vuelve más pronunciado a medida que aumenta el número de pilotes del grupo (cimentación más rígida). Por lo tanto, los resultados obtenidos sin considerar los efectos de la interacción cinemática no se encuentran del lado de la seguridad, excepto en el caso de estructuras no esbeltas $h/b \leq 1$. Estas conclusiones son similares a las alcanzadas por Avilés y Pérez-Rocha [14] para el caso de cimentaciones embebidas.

Cabe mencionar que, en aquellos casos en que los efectos de la interacción cinemática son relevantes, su influencia se hace más apreciable a medida que el parámetro σ disminuye. Con respecto al coeficiente de amortiguamiento, la influencia de los efectos de interacción cinemática disminuye e incluso desaparece para valores decrecientes de la rigidez del cimiento, y lo mismo ocurre para valores crecientes del ratio de esbeltez de la estructura h/b .

El error relativo que supone ignorar los factores de interacción cinemática, en términos de cortante máximo en la base de la estructura Q_m , alcanza un 55% para la configuración más desfavorable de entre todas las que se han analizado. Esto ocurre para estructuras no esbeltas $h/b = 1$, para las cuales el valor máximo de la respuesta estructural es inferior al correspondiente a la condición de base rígida. Sin embargo, el error relativo es inferior al 10% en el caso de edificios con $h/b = 10$.

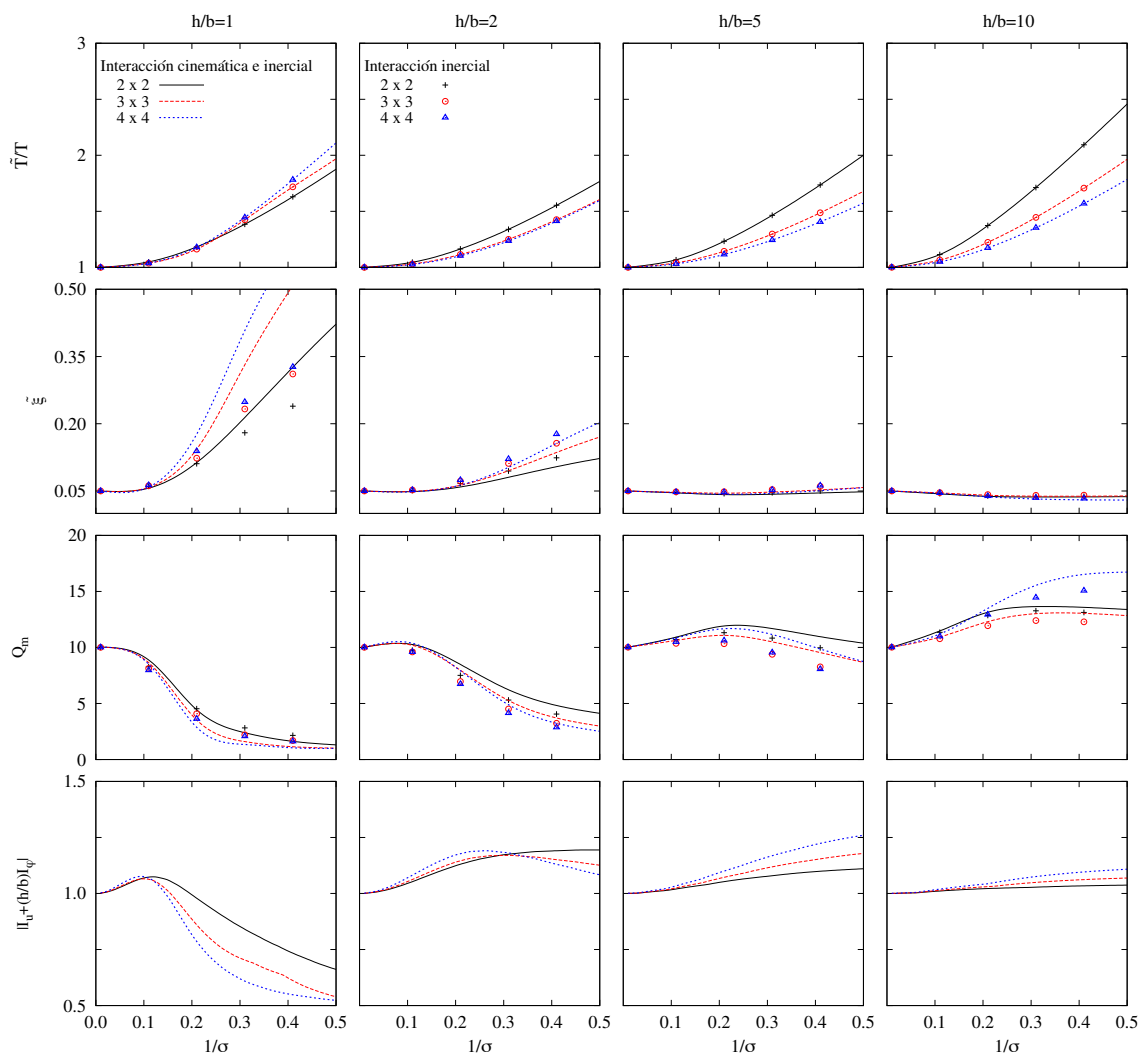


FIGURA A.56: Influencia de la interacción cinemática y el número de pilotes. Periodo efectivo \tilde{T}/T , amortiguamiento $\tilde{\xi}$, respuesta máxima estructural Q_m y factor de interacción cinemática $|I_u + (h/b)I_\varphi|$ para grupos de pilotes con $L/b = 4$, $L/d = 15$, $E_p/E_s = 10^3$ y $\xi_s = 0.05$.

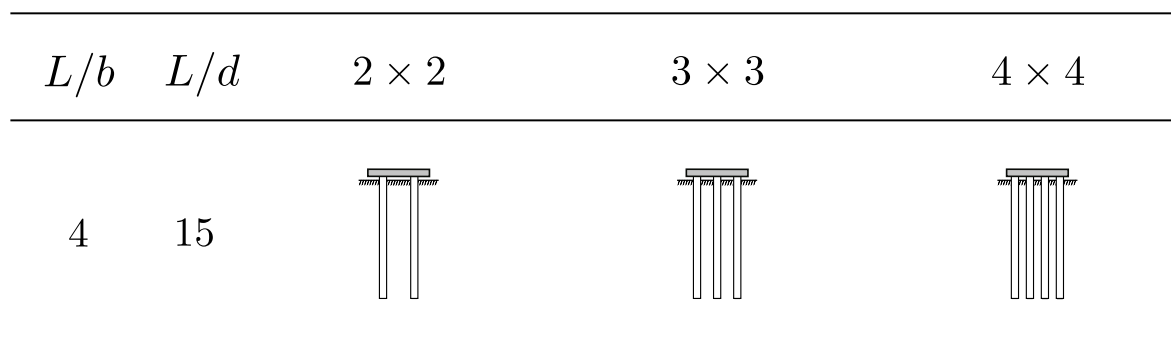


FIGURA A.57: Representación esquemática de las configuraciones analizadas en la figura A.56 considerando $d = cte$.

A.3.8. Influencia del ratio de esbeltez de los pilotes

Como se muestra en la figura A.58, para el caso de cimentaciones pilotadas con el mismo coeficiente de embebimiento L/b , valores crecientes de L/d (pilotes más esbeltos) implican una reducción de la longitud efectiva de los pilotes, y consecuentemente una disminución de la rigidez del sistema, lo cual conduce a un aumento del periodo efectivo. Este efecto aumenta a medida que disminuye la rigidez del suelo (valores menores de σ). Estas diferencias son menores en el caso de estructuras no esbeltas (menores valores h/b); aunque esta tendencia llega incluso a invertirse para valores muy bajos de dicho parámetro. A fin de ilustrar este efecto, la figura A.60 muestra resultados en términos del periodo efectivo \tilde{T}/T para las mismas configuraciones de grupos de pilotes consideradas en la figura A.58, pero suponiendo una superestructura con ratio de esbeltez $h/b = 0.6$. En este caso, puede observarse que para valores del parámetro de onda tales que $1/\sigma > 0.25$, los valores que alcanza \tilde{T}/T para $L/d = 7.5$ son superiores a aquellos obtenidos para $L/d = 15$.

En lo que respecta al coeficiente de amortiguamiento, por lo general, este disminuye a medida que aumenta L/d . Este efecto se vuelve menos apreciable para estructuras esbeltas (valores más altos de h/b). Cabe mencionar que cuando $h/b \geq 5$ el amortiguamiento del sistema $\tilde{\xi}$ se aproxima al amortiguamiento estructural en base rígida ξ y no es demasiado sensible a las variaciones de L/d . Por otra parte, puede observarse que no existen diferencias significativas entre los resultados obtenidos en términos del coeficiente de amortiguamiento cuando $L/d = 7.5$ y $L/d = 15$, respectivamente.

Los resultados en términos de la respuesta máxima del sistema Q_m se ven afectados por las tendencias explicadas anteriormente para el coeficiente de amortiguamiento $\tilde{\xi}$. Así, cabe señalar que cuando $h/b \leq 2$, Q_m alcanza mayores valores para $L/d = 30$ que para valores inferiores de L/d ; y no existen diferencias significativas entre los resultados obtenidos para $L/d = 7.5$ y $L/d = 15$, respectivamente. Sin embargo, puede observarse un cambio de tendencia cuando $h/b \geq 5$, lo que implica un incremento de la respuesta máxima del sistema correspondiente a la configuración con $L/d = 7.5$ con respecto a la obtenida cuando se considera $L/b = 15$ ó incluso $L/b = 30$. Este es el caso de estructuras esbeltas con $h/b = 10$ cuando se consideran valores del parámetro de onda tales que $1/\sigma > 0.2$.

En lo que se refiere al desplazamiento horizontal y al giro del cimiento, puede observarse que ambos aumentan con el ratio de esbeltez de los pilotes L/d .

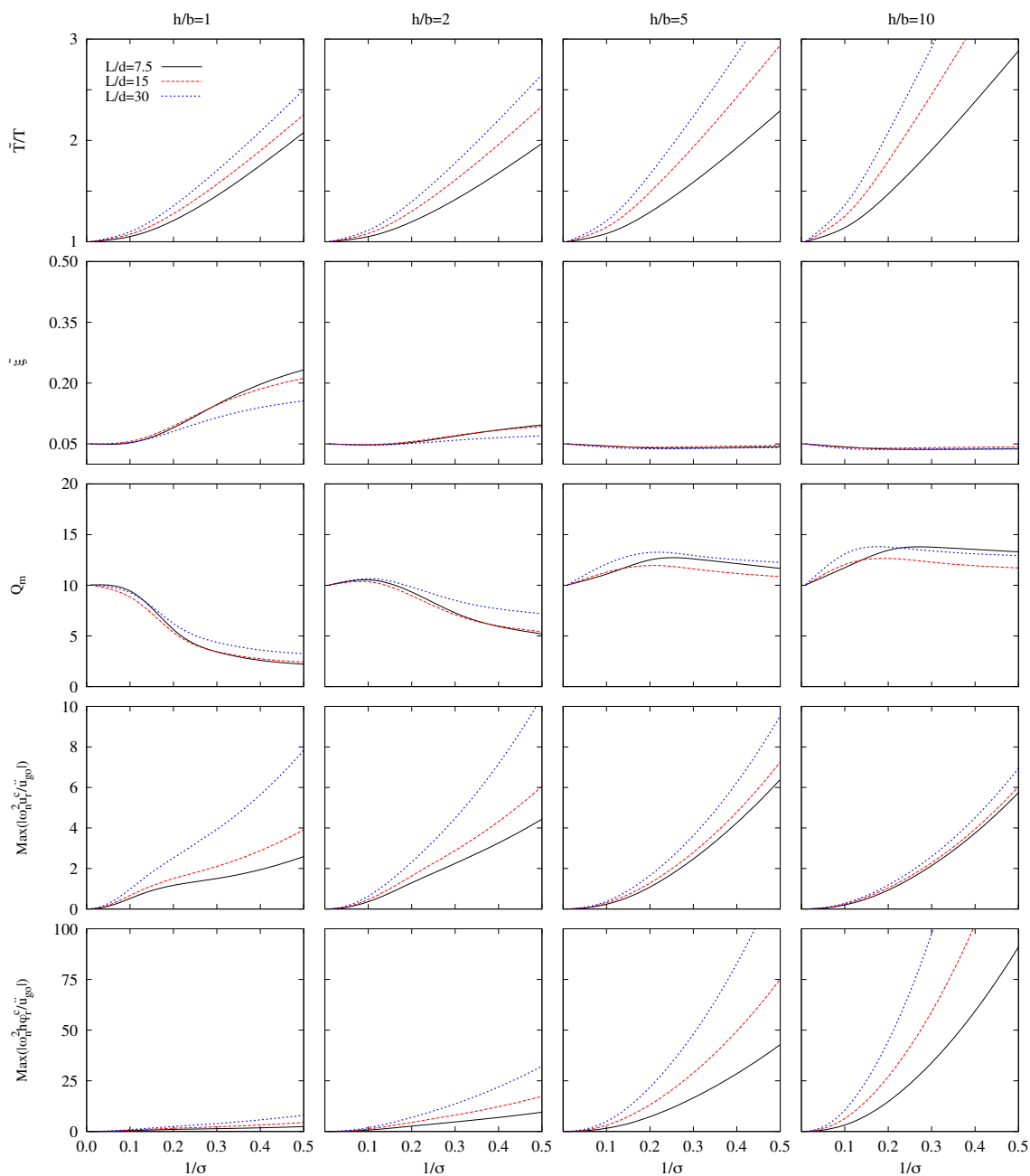


FIGURA A.58: Influencia del ratio de esbeltez de los pilotes L/d . Periodo efectivo \tilde{T}/T , amortiguamiento $\tilde{\xi}$, respuesta máxima estructural Q_m y valores relativos máximos del desplazamiento horizontal $|\omega_n^2 u_r^c / \ddot{u}_{go}|$ y el giro $|\omega_n^2 h \varphi_r^c / \ddot{u}_{go}|$ del cimienta para un grupo de 2×2 pilotes con $L/b = 2$, $E_p/E_s = 10^3$ y $\xi_s = 0.05$.

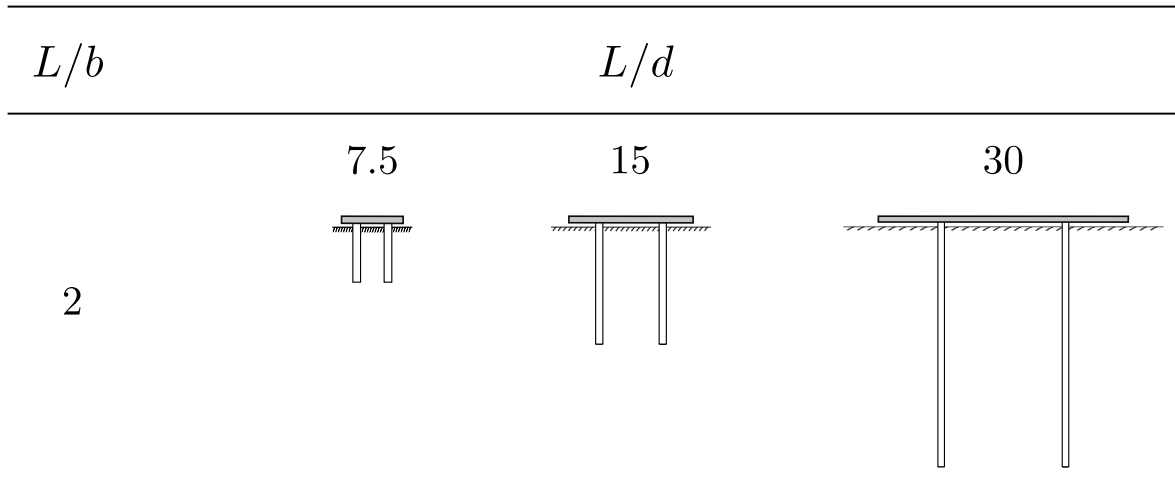


FIGURA A.59: Representación esquemática de las configuraciones de grupos de pilotes analizadas en las figuras A.58 y A.60 considerando $d = \text{cte}$.

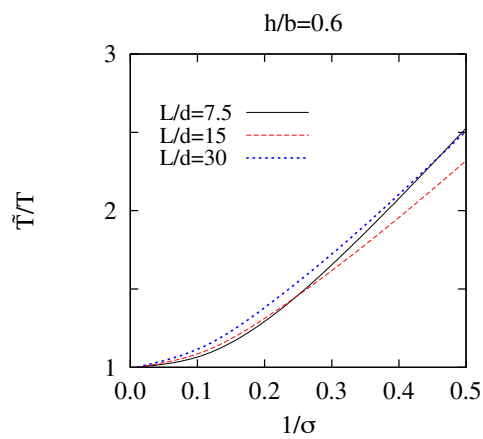


FIGURA A.60: Influencia del ratio de esbeltez de los pilotes L/d . Periodo efectivo \tilde{T}/T para grupos de 2×2 pilotes con $L/b = 2$, $E_p/E_s = 10^3$ y $\xi_s = 0.05$. $h/b = 0.6$.

A.3.9. Influencia del ratio de embebimiento

Como se muestra en la figura A.61, en el caso de cimentaciones pilotadas con la misma separación entre pilotes adyacentes s/d y manteniendo constante el semiancho del encepado b , la disminución de L/b supone una reducción de la longitud de los pilotes L (véase la figura A.62), y consecuentemente de la rigidez del sistema, lo cual conduce a un aumento del periodo efectivo. Este efecto es menos apreciable para edificios menos esbeltos (valores menores de h/b); y esta tendencia se invierte para valores muy bajos de dicho parámetro. Con el propósito de ilustrar este efecto, la figura A.63 recoge resultados en términos del periodo efectivo \tilde{T}/T para las mismas configuraciones de grupos de pilotes consideradas en la figura A.61, pero suponiendo una superestructura con ratio de esbeltez $h/b = 0.6$. En este caso, puede observarse que \tilde{T}/T alcanza mayores valores para $L/b = 2$ que para $L/b = 1$.

En lo que se refiere al coeficiente de amortiguamiento efectivo, aunque este no se ve afectado por las variaciones de L/b en aquellos casos en que $1/\sigma < 0.2$, en todos los casos la disminución de L/b conduce a una reducción del amortiguamiento del sistema para valores más altos de $1/\sigma$. Este efecto disminuye para valores crecientes de h/b . Cabe señalar que en los casos en que $h/b \geq 5$ el amortiguamiento del sistema $\tilde{\xi}$ se aproxima al amortiguamiento estructural ξ y no es sensible a variaciones de L/b .

En lo que respecta al efecto del coeficiente de embebimiento sobre la respuesta máxima estructural Q_m , la misma figura muestra que este factor aumenta para valores decrecientes del ratio de embebimiento L/b . Generalmente, este efecto es más apreciable en aquellos casos en que $h/b = 2$ y 5 ; sin embargo, puede observarse un cambio de tendencia entre los resultados correspondientes a $h/b = 5$ y $h/b = 10$, respectivamente, donde este efecto no es tan apreciable. Algo similar sucede con el desplazamiento horizontal del cimiento expresado como $|\omega_n^2 u_r^c / \ddot{u}_{g0}|$. El giro del cimiento $|\omega_n^2 h \varphi_r^c / \ddot{u}_{g0}|$, por otra parte, aumenta a medida que disminuye L/b , siendo este efecto más pronunciado a medida que h/b aumenta.

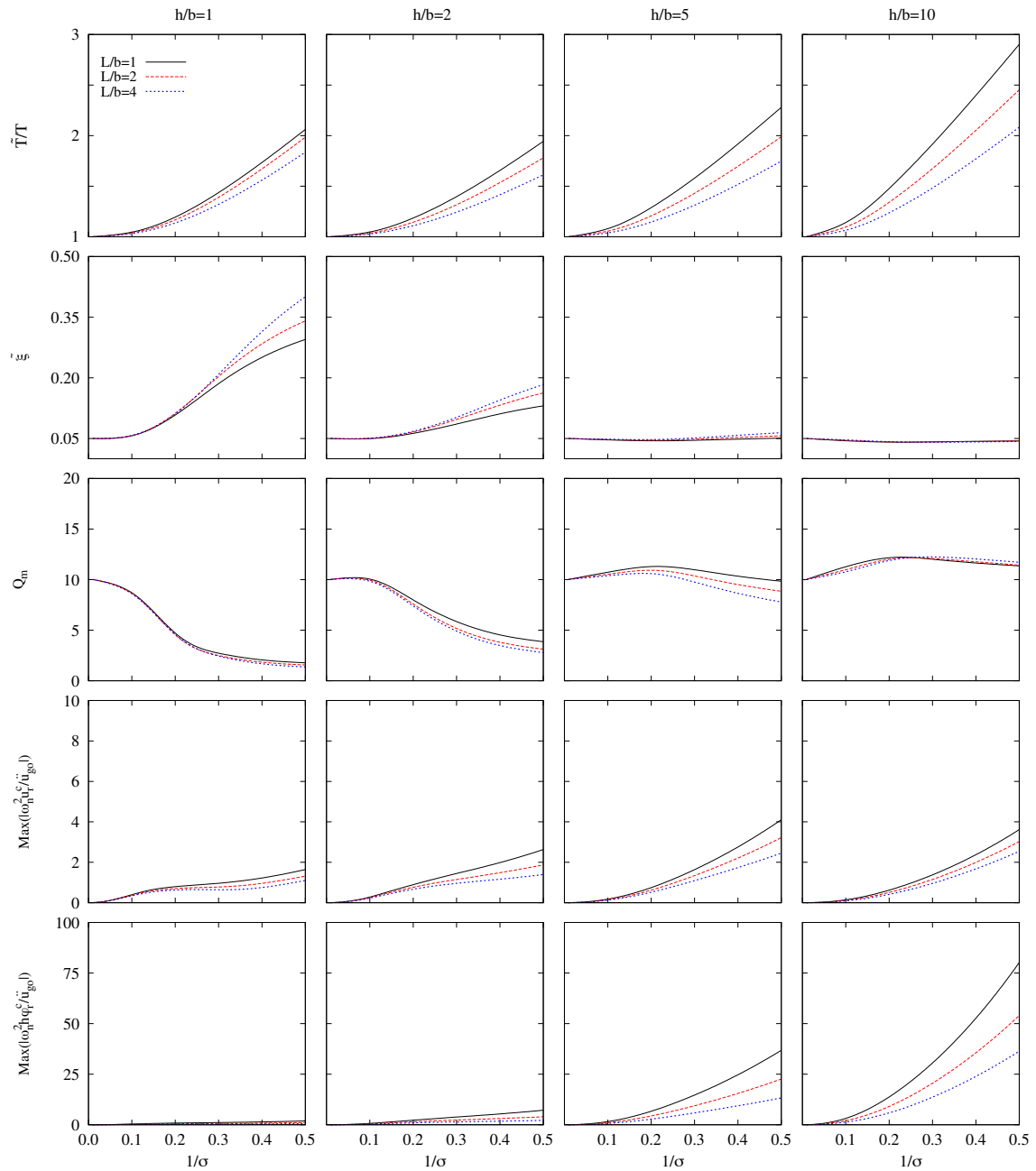


FIGURA A.61: Influencia del ratio de embebimiento L/b . Periodo efectivo \tilde{T}/T , coeficiente de amortiguamiento $\tilde{\xi}$, respuesta máxima estructural Q_m y valores relativos máximos del desplazamiento horizontal $|\omega_n^2 u_r^c / \ddot{u}_{go}|$ y el giro $|\omega_n^2 h \varphi_r^c / \ddot{u}_{go}|$ del cimiento para un grupo de 4×4 pilotes con $s/d = 3.75$, $E_p/E_s = 10^3$ y $\xi_s = 0.05$.

L/b	1	2	4
L/d	7.5	15	30

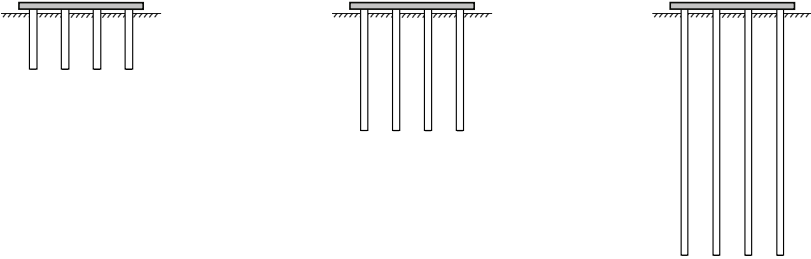


FIGURA A.62: Representación esquemática de las configuraciones de grupos de pilotes analizadas en las figuras A.61 y A.63 considerando $d = cte$.

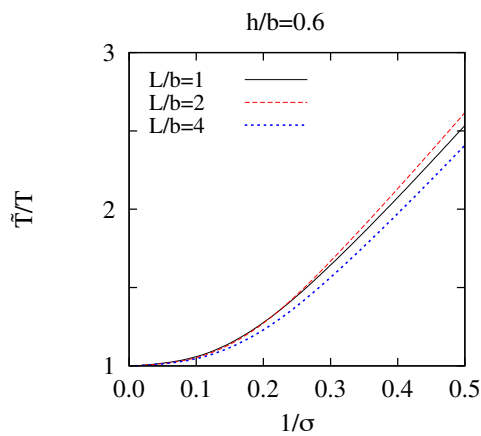


FIGURA A.63: Influencia del ratio de embebimiento L/b . Periodo efectivo \tilde{T}/T para grupos de 4×4 pilotes con $s/d = 3.75$, $E_p/E_s = 10^3$ y $\xi_s = 0.05$. $h/b = 0.6$.

A.3.10. Influencia del número de pilotes

Como se observa en la figura A.56, en el caso de cimentaciones pilotadas con valores altos de h/b e igual coeficiente de embebimiento L/b y ratio de esbeltez de los pilotes L/d , una reducción del número de pilotes implica una disminución de la rigidez del sistema, lo cual conduce a un aumento del periodo efectivo. Sin embargo, la magnitud de esta tendencia disminuye a medida que lo hace h/b , y tiende a invertirse en el caso de estructuras no esbeltas. Por otra parte, un aumento del número de pilotes del grupo conduce a un incremento del amortiguamiento efectivo del sistema y, consecuentemente, a menores valores de la respuesta máxima de la estructura Q_m , cuando $h/b < 5$, mientras que no se observan tendencias claras para esbelteces mayores. En el caso de edificios esbeltos ($h/b = 5$ y 10), el valor de Q_m obtenido teniendo en cuenta la interacción suelo-estructura supera a aquel correspondiente a la condición de base rígida. Además, el valor máximo de Q_m tiene lugar para $1/\sigma = 0.2$ cuando $h/b = 5$ y aumenta con $1/\sigma$ para $h/b = 10$, aproximándose (en el rango representado) a un valor asintótico que aumenta con el número de pilotes.

En lo que respecta al desplazamiento horizontal y el giro de la cimentación, ambos aumentan a medida que disminuye el número de pilotes, siendo este efecto más apreciable en el caso de estructuras esbeltas, como se muestra en la figura A.64.

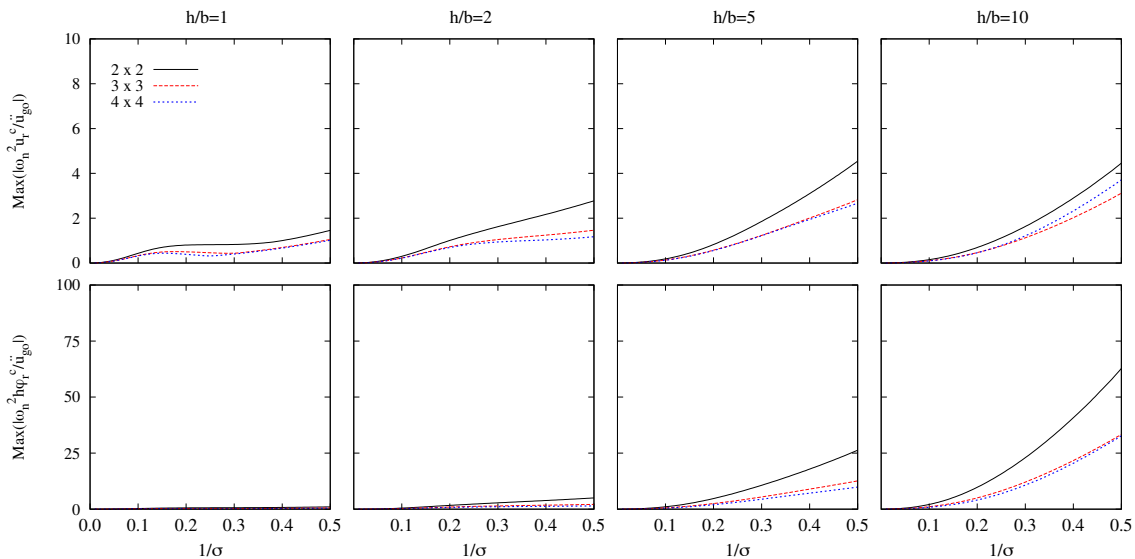


FIGURA A.64: Influencia del número de pilotes. Valores máximos relativos del desplazamiento horizontal $|\omega_n^2 u_r^c / \ddot{u}_{go}|$ y el giro $|\omega_n^2 h \varphi_r^c / \ddot{u}_{go}|$ del cimiento para grupos de pilotes con $L/b = 4$, $L/d = 15$, $E_p/E_s = 10^3$ y $\xi_s = 0.05$.

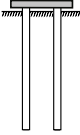
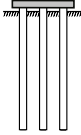
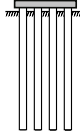
L/b	L/d	2×2	3×3	4×4
4	15			

FIGURA A.65: Representación esquematizada de las configuraciones analizadas en la figura A.64 considerando $d = \text{cte}$.

A.3.11. Influencia del ratio del módulo de Young pilote-suelo

La variación del ratio entre los módulos de Young de los pilotes y el suelo E_p/E_s afecta a las funciones de impedancia y a los factores de interacción cinemática del sistema suelo-cimiento. Por consiguiente, los efectos de interacción suelo-estructura sobre la respuesta dinámica del sistema también se ven influenciados por dichas variaciones. A fin de analizar dicha influencia, la figura A.66 muestra, en las distintas columnas, la respuesta dinámica de estructuras con ratios de esbeltez $h/b = 1, 2, 5$ y 10 , respectivamente, soportadas por grupos de 2×2 pilotes verticales embebidos en un semiespacio homogéneo, viscoelástico e isotrópico tal que $E_p/E_s = 10^2$ ó 10^3 . Cada área gráfica muestra resultados para tres valores diferentes del ratio de esbeltez de los pilotes: $L/d = 7.5, 15$ y 30 . Todos las gráficas se presentan en función de $1/\sigma$, siendo σ el parámetro de onda. En la parte superior, central e inferior de la figura se han representado, respectivamente, resultados en términos de periodo efectivo \tilde{T}/T , amortiguamiento efectivo $\tilde{\xi}$ y cortante máximo en la base de la estructura por unidad de fuerza sísmica efectiva Q_m . A su vez, la figura A.67 proporciona una representación esquemática de las distintas configuraciones de grupos de pilotes consideradas en la figura A.66.

Suponiendo propiedades constantes para el material de los pilotes, valores menores de E_p/E_s implican un aumento de la rigidez del suelo, lo cual conduce a un incremento del periodo efectivo del sistema \tilde{T}/T y una disminución del amortiguamiento efectivo $\tilde{\xi}$. Por lo tanto, se alcanzan valores más altos de Q_m . Este efecto es más notable para valores mayores del ratio de esbeltez de los pilotes L/d y a medida que $1/\sigma$ aumenta.

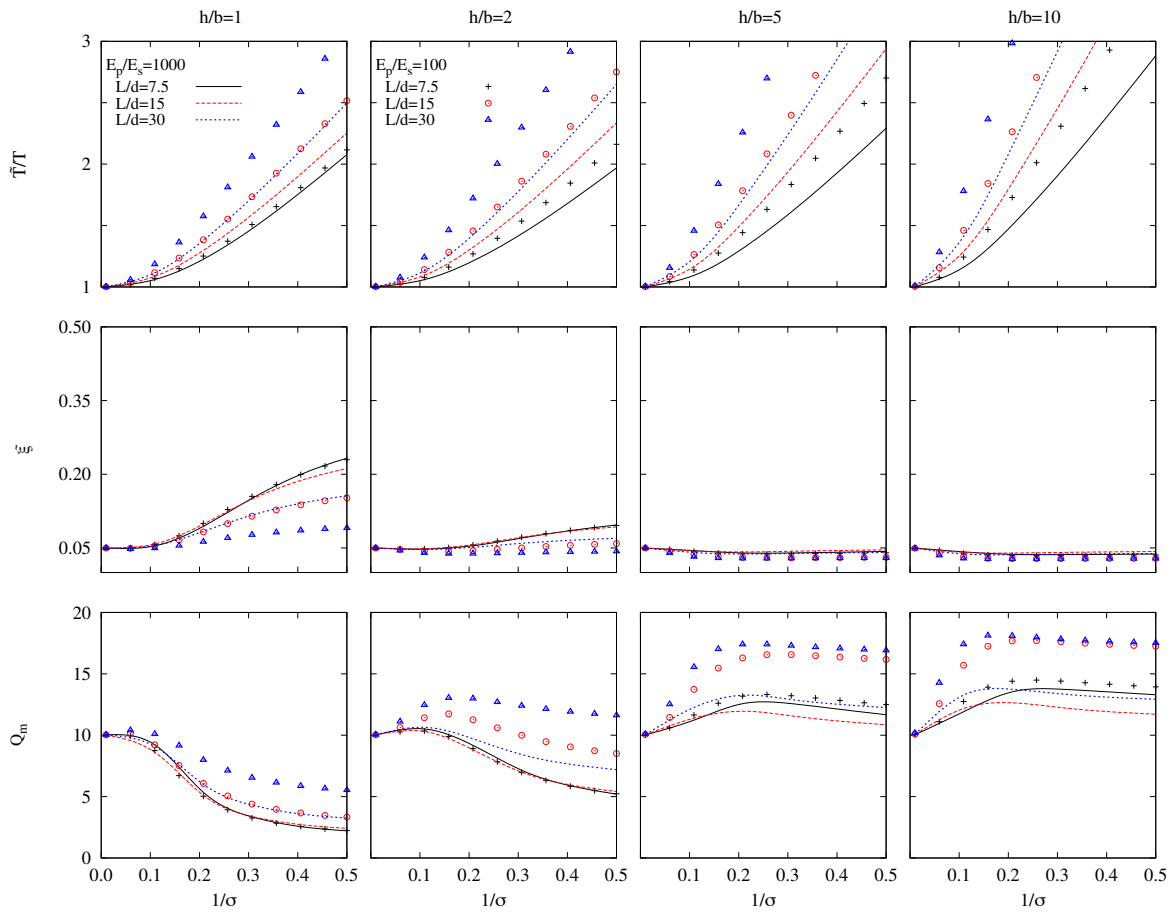


FIGURA A.66: Influencia del ratio del módulo de Young pilote-suelo E_p/E_s . Periodo efectivo \tilde{T}/T , amortiguamiento $\tilde{\xi}$ y respuesta máxima estructural Q_m para grupos de 2×2 pilotes con $L/b = 2$ y $\xi_s = 0.05$.

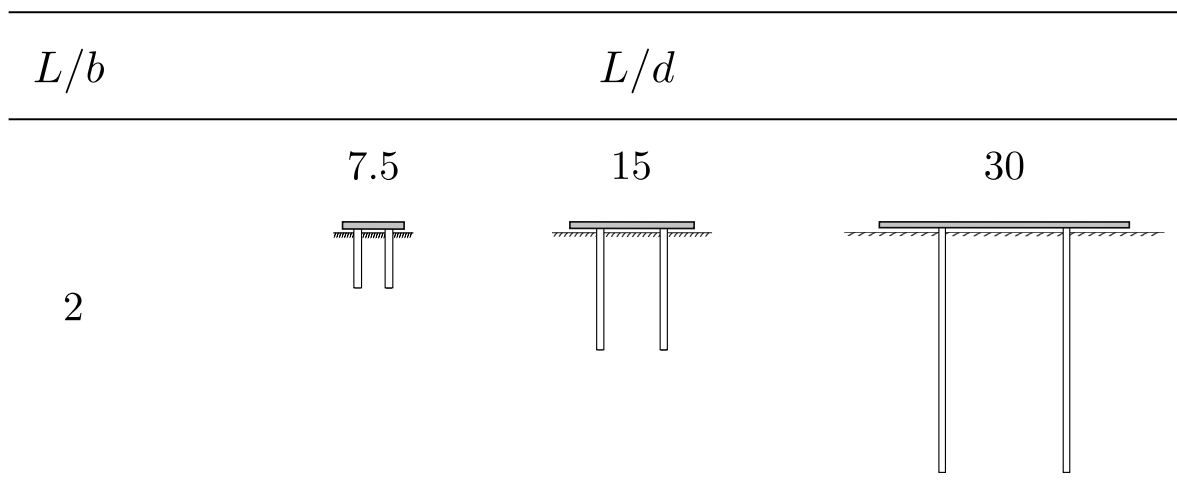


FIGURA A.67: Representación esquemática de las configuraciones de grupos de pilotes analizadas en la figura A.66 considerando $d = cte$.

A.3.12. Influencia del coeficiente de amortiguamiento de la estructura en base rígida

La figura A.68 muestra cómo los efectos de interacción suelo-estructura, sobre la respuesta dinámica del sistema, se ven afectados por la variación del coeficiente de amortiguamiento de la estructura en base rígida. Puede observarse que este parámetro no tiene influencia alguna sobre el periodo efectivo del sistema \tilde{T}/T . Sin embargo, como es de esperar, afecta al amortiguamiento efectivo del mismo $\tilde{\xi}$ que alcanza mayores valores a medida que ξ aumenta. Este efecto se hace más notable para valores mayores del parámetro de onda σ . Por el contrario, su influencia es despreciable cuando $1/\sigma \geq 0.4$. Estas variaciones del amortiguamiento efectivo del sistema conducen a un aumento de Q_m a medida que disminuye el coeficiente de amortiguamiento de la estructura en base rígida ξ . Por otra parte, el rango de valores del parámetro σ dentro del cual la variación de ξ tiene una influencia significativa, se amplía a medida que aumenta el ratio de esbeltez de la estructura h/b .

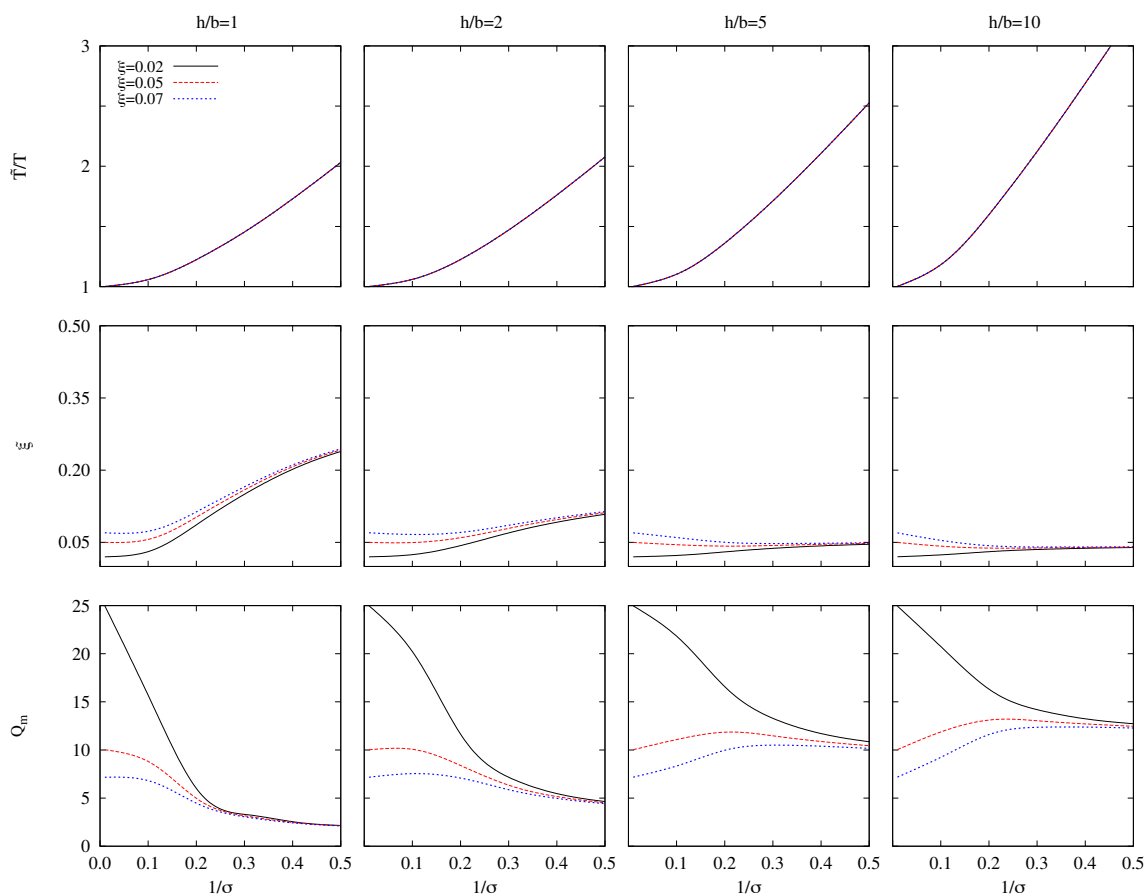


FIGURA A.68: Influencia del coeficiente de amortiguamiento de la estructura en base rígida ξ . Periodo efectivo \tilde{T}/T , amortiguamiento $\tilde{\xi}$ y máxima respuesta estructura Q_m para un grupo de 3×3 pilotes con $L/d = 30$, $L/b = 2$, $E_p/E_s = 10^3$ y $\xi_s = 0.05$.

A.3.13. Influencia de la densidad de masa relativa estructura-suelo

En lo que respecta a la densidad de masa relativa entre la estructura y el suelo δ , cabe mencionar que se trata de un parámetro que tiene una influencia relevante en la respuesta del sistema. En la figura A.69 puede observarse que la disminución de δ implica un aumento de la rigidez del sistema, lo cual conduce a menores valores del periodo \tilde{T}/T y el amortiguamiento $\tilde{\xi}$ efectivos y, consecuentemente, valores más altos de Q_m . Los efectos asociados a la interacción suelo-estructura se hacen más notables a medida que aumenta el ratio de esbeltez de la estructura h/b . No obstante, como se ha mencionado con anterioridad, el valor de este parámetro que se ha considerado en este trabajo ($\delta = 0.15$) es un valor representativo para edificios y suelos reales y se ha venido utilizando en trabajos realizados previamente por otros autores tales como Avilés y Pérez-Rocha [14] o Veletsos y Meek [7].

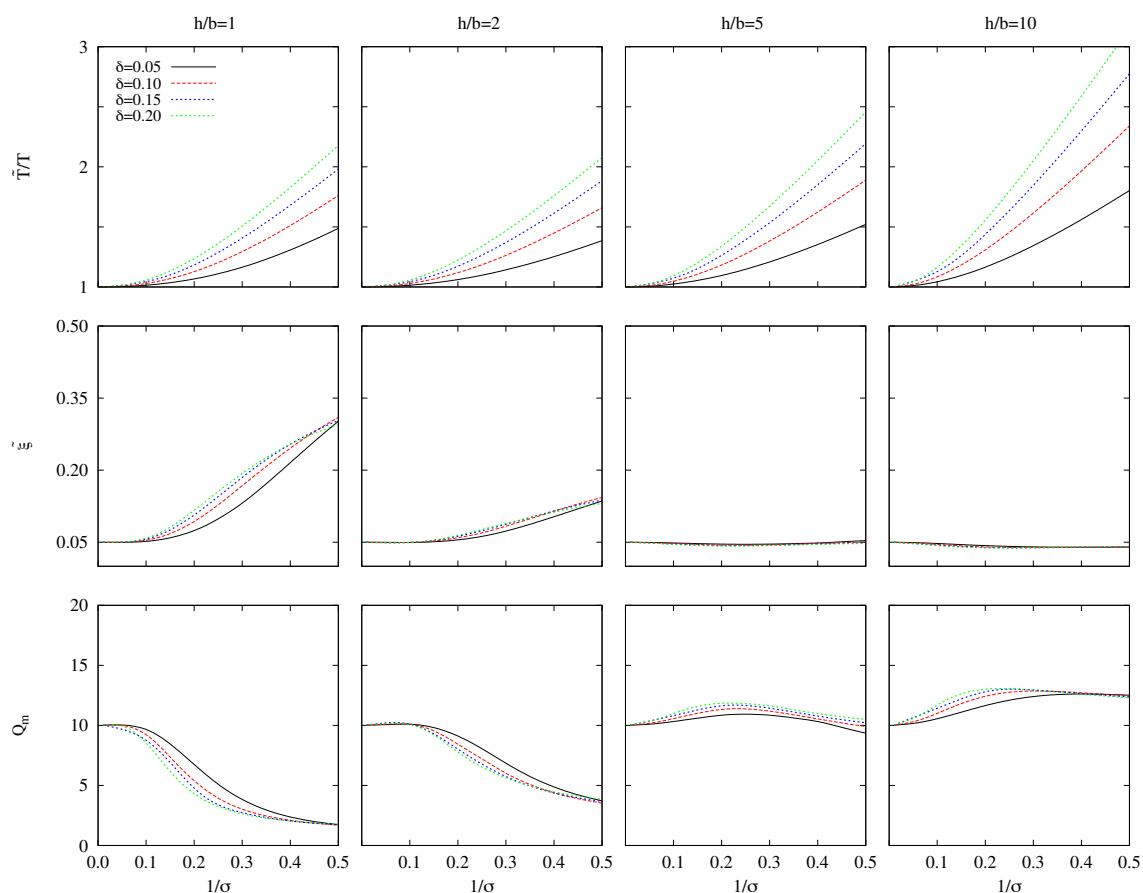


FIGURA A.69: Influencia de la densidad de masa relativa entre la estructura y el suelo δ . Periodo efectivo \tilde{T}/T , amortiguamiento $\tilde{\xi}$ y respuesta máxima estructural Q_m para un grupo de 3×3 pilotes con $L/d = 15$, $L/b = 2$, $E_p/E_s = 10^3$ y $\xi_s = 0.05$.

A.3.14. Conclusiones

En esta sección, se ha llevado a cabo un análisis de los efectos de la interacción suelo-estructura sobre el periodo y el amortiguamiento de estructuras pilotadas. A tal fin, se ha utilizado el procedimiento simplificado y estable propuesto en la sección A.2 para determinar las propiedades dinámicas de un sistema de un grado de libertad que reproduce, de la forma más precisa posible, la respuesta del sistema acoplado dentro del rango de frecuencias donde se produce la respuesta máxima. La respuesta del sistema acoplado se obtiene mediante el uso de un modelo de subestructuración en el cual la estructura se considera como una estructura a cortante de 1GDL que representa, desde un punto de vista general, un modo de vibración de edificios de varias plantas. En el análisis del sistema acoplado se han tenido en cuenta los efectos de interacción inercial y cinemática. Las impedancias y los factores de interacción cinemática de las configuraciones de grupos de pilotes estudiadas en esta sección se han calculado mediante la metodología acoplada de elementos finitos y elementos de contorno desarrollada por Padrón *et al.* [71, 81, 120].

Se han obtenido resultados para 21 configuraciones diferentes, con el fin de realizar un análisis de la influencia de los principales parámetros del problema para cada uno de los casos. Todos los resultados que se presentan tienen un carácter adimensional, por tanto su interpretación física debe realizarse con precaución y requiere de un procesamiento específico de los datos, teniendo en cuenta la influencia de cada uno de los parámetros adimensionales.

Las conclusiones extraídas de este análisis se han explicado de forma detallada en las secciones de la A.3.5 a la A.3.13 y son coherentes con aquellas que figuran en la bibliografía para el caso de cimentaciones embebidas. Las principales conclusiones se resumen a continuación:

- Las configuraciones de pilotes que implican cimentaciones más rígidas suponen una reducción del periodo efectivo del sistema acoplado. Este es el caso de cimentaciones con mayor número de pilotes (figura A.56) ó mayor ratio de embebimiento (figura A.61), y menores ratios de esbeltez de los pilotes (figura A.58). Los resultados obtenidos muestran que esta conclusión no es aplicable a estructuras no esbeltas, en cuyo caso sucede lo contrario.
- El amortiguamiento efectivo aumenta con la rigidez de la cimentación (véanse las figuras A.56, A.58 y A.61).
- Los edificios esbeltas así como los suelos blandos amplifican los efectos de la interacción suelo-estructura para una configuración determinada. Esta tendencia puede invertirse para cimentaciones muy rígidas o edificios muy poco esbeltas (véase la figura A.53).
- El amortiguamiento efectivo en el caso de edificios esbeltas se aproxima al correspondiente a la condición de base rígida o es inferior al mismo. En el caso de edificios bajos y de media altura ($h/b < 5$), el amortiguamiento efectivo aumenta a medida que disminuye σ y este efecto se hace más pronunciado para configuraciones de pilotes más rígidas (véanse *e.g.* figuras A.56 y A.61).
- A medida que aumenta la influencia de los efectos de interacción suelo-estructura, el cortante máximo en la base de la estructura se mantiene por debajo del corres-

pendiente a la condición de base rígida para edificios con $h/b \leq 2$ en todas las configuraciones estudiadas. En los casos con valores mayores del ratio de esbeltez de la estructura, el cortante máximo aumenta cuando se consideran dichos efectos (véase *e.g.* figura A.58). Cimentaciones más rígidas conducen a menores valores del cortante en los casos en que $h/b < 5$ (véase *e.g.* figura A.56). Sin embargo, para esbelteces mayores, los resultados muestran cambios de tendencia que dependen del parámetro analizado.

- El desplazamiento horizontal y el giro del cimiento aumentan en el caso de suelos más blandos así como para configuraciones geométricas más flexibles (véanse *e.g.* figuras A.58 ó A.61).
- Valores inferiores del ratio del módulo de Young pilote-suelo E_p/E_s suponen un aumento de la rigidez de la cimentación, lo cual conduce a menores valores del periodo efectivo y mayores valores del amortiguamiento efectivo.
- Un aumento de la densidad de masa relativa δ implica mayores valores del periodo y el amortiguamiento efectivos del sistema.
- El periodo efectivo no se ve afectado por las variaciones del coeficiente de amortiguamiento de la estructura en base rígida ξ . Sin embargo, la influencia de dicha variación sobre el amortiguamiento efectivo gana importancia a medida que aumenta el parámetro de onda.
- En un número significativo de casos, la respuesta dinámica del sistema se subestima cuando se desprecian las impedancias cruzadas.
- Los resultados obtenidos sin tener en cuenta los efectos de interacción cinemática no están del lado de la seguridad, salvo en el caso de estructuras no esbeltas ($h/b \leq 1$).

En esta sección se han presentado resultados para distintas configuraciones de grupos de pilotes en términos del periodo \tilde{T}/T y el amortiguamiento $\tilde{\xi}$. Estos resultados se han representado en gráficos que pueden emplearse de forma directa para obtener espectros de respuesta elástica modificados que contemplen los efectos de la interacción suelo-estructura.

A.4. Resumen, conclusiones y desarrollos futuros

A.4.1. Resumen y conclusiones

Esta tesis propone un procedimiento simple y estable para la estimación de las características dinámicas de un oscilador de reemplazo capaz de reproducir, con la mayor precisión posible, el comportamiento dinámico de estructuras lineales a cortante dentro del rango en el que se produce la respuesta máxima, teniendo en cuenta la interacción suelo-estructura. La respuesta del sistema acoplado se obtiene a partir de un modelo de subestructuración que contempla el carácter tridimensional de las cimentaciones. En dicho modelo, se considera una estructura a cortante de un grado de libertad que representa, desde un punto de vista general, uno de los modos de vibración de edificios de varias plantas. En el análisis del sistema acoplado se han tenido en cuenta tanto los efectos de interacción inercial como los de interacción cinemática. Todos los elementos de la matriz de impedancias se tienen en cuenta en el cálculo. Este procedimiento es aplicable a estructuras a cortante sustentadas sobre cimentaciones superficiales, embebidas o pilotadas.

El problema se ha abordado mediante el uso de una metodología de subestructuración que permite subdividir el sistema en los sistemas *estructura-encepado* y *suelo-cimiento*. La rigidez y el amortiguamiento de este último se representa mediante resortes y amortiguadores, respectivamente. Tal y como proponen Kausel y Roësset [18], la resolución del problema puede dividirse en tres pasos. Los dos primeros consisten en determinar los factores de interacción cinemática y las impedancias, siendo ambas funciones complejas dependientes de la frecuencia. Una vez que se han obtenido sus valores para rango de frecuencias objeto de estudio, la respuesta de la superestructura se calcula, para cada valor de la frecuencia, considerando que se encuentra sustentada sobre los resortes y amortiguadores caracterizados por las impedancias, y sometida al movimiento definido por los factores de interacción cinemática.

Tras realizar una serie de operaciones algebraicas básicas, las ecuaciones de movimiento del sistema acoplado se han expresado en términos de un conjunto de parámetros adimensionales que abarcan las principales características de los problemas de interacción suelo-estructura. Esto facilita la realización de análisis encaminados a determinar cómo afectan las variaciones de dichos parámetros a la respuesta dinámica del sistema. Posteriormente, se ha establecido una equivalencia entre el sistema objeto de estudio y un oscilador de un solo grado de libertad con amortiguamiento viscoso en términos del cortante máximo en la base de la estructura por unidad de fuerza sísmica efectiva. La ventaja de presentar la respuesta sísmica de la estructura en estos términos reside en el hecho de que el producto de este valor por la masa estructural y la correspondiente aceleración horizontal de campo libre a nivel de la superficie da como resultado la amplitud del cortante en la base de la estructura.

Se ha llevado a cabo una revisión de las estrategias utilizadas en la literatura científica para estimar las características dinámicas del sistema equivalente de un grado de libertad. Esta tesis propone una estrategia modificada que arroja resultados precisos, no sólo para los casos de cimentaciones superficiales y embebidas, sino también para cimentaciones pilotadas. A tal efecto, se ha cuantificado la pérdida de precisión que resulta de aplicar las simplificaciones adoptadas con frecuencia por otros autores al caso de cimentaciones constituidas por pilotes. En los trabajos pioneros relacionados

con el tema, los efectos de interacción cinemática de la onda incidente no se consideraban, usando como excitación en la base un movimiento horizontal armónico de amplitud constante. En esta línea, se ha demostrado que la interacción cinemática puede afectar de forma significativa al amortiguamiento efectivo del sistema y, por lo tanto, debería tenerse en cuenta si se desean obtener resultados precisos, tanto para cimentaciones embebidas como pilotadas. Por otra parte, la influencia de los términos cruzados de la matriz de impedancias suele despreciarse con el propósito de considerar una matriz de impedancias diagonal que permita obtener expresiones aproximadas manejables para la respuesta dinámica del sistema acoplado, tal y como hacen Avilés y Pérez-Rocha [14]. Sin embargo, anular los términos cruzados, correspondientes al modo de vibración acoplado horizontal-cabeceo, no es aceptable en el caso de cimentaciones pilotadas, y tampoco lo es para ciertas configuraciones de cimentaciones embebidas. Con el fin de superar este inconveniente, en esta tesis se ha diagonalizado la matriz de impedancias condensando la interacción suelo-estructura en un punto situado a una cierta profundidad virtual, tal y como proponen algunos autores [27,32]. De este modo, se tienen en cuenta los términos cruzados de la matriz de impedancias.

Una vez que el procedimiento se ha formulado e implementado en un código, este se ha validado mediante la realización de estudios comparativos con los resultados obtenidos por Veletsos y Meek [7] y Avilés y Pérez-Rocha [14] para cimentaciones superficiales y embebidas, respectivamente. En ninguno de los casos se encontraron diferencias significativas. Posteriormente, el procedimiento propuesto se ha utilizado para analizar los efectos de interacción suelo-estructura sobre el comportamiento dinámico de estructuras lineales a cortante soportadas por grupos de pilotes embebidos en un semiespacio homogéneo y viscoelástico y sometidos a ondas S de incidencia vertical. Las metodologías de subestructuración constituyen una herramienta muy útil para acometer esta tarea debido a su simplicidad y a que tienen un coste computacional asumible; esto las hace especialmente apropiadas para llevar a cabo análisis paramétricos que permitan determinar la influencia de los principales parámetros del problema sobre la respuesta final. Las configuraciones de todas las cimentaciones que se han analizado consisten en grupos de pilotes dispuestos de forma regular en áreas cuadradas. Dichos grupos de pilotes son simétricos respecto a los planos xy e yz . Todos los pilotes son del mismo material y tienen idénticas propiedades geométricas. Tanto la masa del encepado como la masa de la estructura se consideran uniformemente distribuidas sobre áreas cuadradas. Los pilares de la estructura se han supuesto sin masa e inextensibles axialmente.

Las impedancias y los factores de interacción cinemática de las configuraciones de grupos de pilotes objeto de estudio, se han calculado mediante una metodología de elementos de contorno y elementos finitos desarrollada por Padrón *et al.* [49, 71, 120]. El suelo se ha modelado como un semiespacio lineal, isotrópico, homogéneo y viscoelástico utilizando elementos de contorno, mientras que los pilotes se han modelado mediante elementos finitos monodimensionales como vigas Euler-Bernoulli embebidas en el suelo. El acoplamiento se realiza mediante la aplicación de las condiciones de equilibrio y compatibilidad correspondientes. Por otra parte, el movimiento de las cabezas de los pilotes está restringido por un encepado rígido que no está en contacto con el suelo. Esta formulación implica una reducción del número de grados de libertad con respecto a una metodología multidominio de elementos de contorno y proporciona, al mismo tiempo, resultados suficientemente precisos para el problema analizado.

Con el fin de analizar la influencia que tienen los principales parámetros del problema de interacción suelo-estructura sobre la respuesta dinámica de las estructuras que sustentan, se han obtenido resultados correspondientes a 21 configuraciones diferentes de grupos de pilotes verticales. Todos los resultados que se presentan en este documento tienen un carácter adimensional, por lo que su interpretación física debe realizarse cuidadosamente y requiere de un procesamiento específico de los datos, teniendo en cuenta la influencia de cada parámetro adimensional. Se proporcionan resultados, en términos de periodo \tilde{T}/T y amortiguamiento $\tilde{\xi}$, para diversas configuraciones de pilotes en gráficos que pueden utilizarse de forma inmediata para obtener espectros de respuesta modificados, que contemplan los efectos de interacción suelo-estructura. Por otra parte, se exponen también resultados en términos del cortante máximo en la base de la estructura, así como del desplazamiento y el giro del encepado. Se han extraído diversas conclusiones de interés a partir del estudio acerca de cómo afecta al comportamiento dinámico del sistema la variación de parámetros tales como: la relación entre los módulos de elasticidad de los pilotes y el suelo, el coeficiente de amortiguamiento de la estructura en base rígida, la relación entre la masa del encepado y la masa de la estructura, la densidad de masa relativa entre la estructura y el suelo, el ratio de esbeltez de la superestructura, el parámetro de onda, el ratio de esbeltez del pilote, la separación entre pilotes adyacentes, el ratio de embebimiento y el número de pilotes. Dichas conclusiones son coherentes con aquellas alcanzadas por otros autores para cimentaciones embebidas. Por otra parte, se expone también el análisis de la importancia de considerar las impedancias cruzadas, así como los factores de interacción cinemática. A continuación se recogen de forma resumida las principales conclusiones:

- Se ha demostrado que las impedancias cruzadas y los factores de interacción cinemática deben ser considerados para obtener resultados precisos en el caso de edificios pilotados.
- Las configuraciones de grupos de pilotes que implican cimentaciones más rígidas (mayor número de pilotes (figura A.56) o mayor coeficiente de embebimiento (figura A.61), y menor ratio de esbeltez de los pilotes (figura A.58)) suponen una reducción del periodo efectivo del sistema acoplado. Los resultados obtenidos muestran que esta conclusión no es aplicable a edificios no esbeltos, en cuyo caso sucede lo contrario.
- El amortiguamiento efectivo aumenta con la rigidez de la cimentación (véanse las figuras A.56, A.58 y A.61).
- Los edificios esbeltos, así como los suelos blandos, magnifican los efectos de interacción suelo-estructura para una configuración determinada. Esta tendencia puede invertirse para cimentaciones muy rígidas o edificios muy bajos (véase la figura A.53).
- El amortiguamiento efectivo para edificios esbeltos se aproxima al valor correspondiente a la condición de base rígida o se mantiene por debajo del mismo. En el caso de estructuras bajas o de media altura ($h/b < 5$), el amortiguamiento efectivo aumenta a medida que disminuye σ y este efecto se hace más relevante para configuraciones de pilotes más rígidas (véanse *e.g.* las figuras A.56 y A.61).

- A medida que aumenta la influencia de los efectos de interacción suelo-estructura, el cortante máximo en la base de la estructura permanece por debajo de aquel correspondiente a la condición de base rígida para edificios con $h/b \leq 2$ en todas las configuraciones estudiadas. Para valores mayores del ratio de esbeltez estructural, el cortante máximo aumenta cuando se consideran estos efectos (véase *e.g.* la figura A.58). Cimentaciones más rígidas conducen a valores más bajos del cortante si $h/b < 5$ (véase *e.g.* la figura A.56). Sin embargo, para esbelteces mayores, los resultados muestran variaciones de tendencia que dependen del parámetro analizado.
- El desplazamiento horizontal y el giro del cimiento aumentan para suelos más blandos, así como para configuraciones geométricas más flexibles (véanse *e.g.* las figuras A.58 ó A.61).
- Valores inferiores del ratio del módulo de Young pilote-suelo E_p/E_s suponen un aumento de la rigidez de la cimentación, lo cual conduce a menores valores del periodo efectivo y a mayores valores del amortiguamiento efectivo.
- Un aumento de la densidad de masa relativa δ implica mayores valores del periodo y el amortiguamiento efectivos del sistema.
- El periodo efectivo no se ve afectado por las variaciones del coeficiente de amortiguamiento de la estructura en base rígida ξ . Sin embargo, la influencia de dicha variación sobre el amortiguamiento efectivo gana importancia a medida que aumenta el parámetro de onda.
- En un número significativo de casos, la respuesta dinámica del sistema se subestima cuando se desprecian las impedancias cruzadas.
- Los resultados obtenidos sin tener en cuenta los efectos de interacción cinemática no están del lado de la seguridad, excepto en el caso de estructuras no esbeltas $h/b \leq 1$.

Con el propósito de esclarecer el papel beneficioso o perjudicial de las cimentaciones que contienen pilotes inclinados, esta tesis arroja luz sobre dos aspectos que requerían de una investigación más profunda: los factores de interacción cinemática de cimentaciones pilotadas con elementos inclinados y la influencia del ángulo de inclinación sobre la respuesta sísmica de la superestructura.

En esta tesis se presentan también factores de interacción cinemática de pilotes simples inclinados, así como de grupos de 2×2 y 3×3 pilotes que incluyen elementos inclinados. La posibilidad de que se desarrollen grandes momentos flectores y esfuerzos cortantes cinemáticos al inclinar los pilotes ha propiciado una actitud negativa hacia el uso de pilotes inclinados (véase [44]). A fin de estudiar el efecto del ángulo de inclinación sobre los momentos flectores cinemáticos, también se ha representado la deformación máxima a flexión en la cabeza de los pilotes para algunos casos. En este documento se recogen resultados obtenidos para diversas configuraciones considerando distintos valores para las propiedades del suelo y el ángulo de inclinación de los pilotes.

A partir de los resultados obtenidos se ha evaluado la importancia de la influencia del ángulo de inclinación sobre los factores de interacción cinemática de las cimentaciones

analizadas y se comentan las principales tendencias. Los factores de interacción cinemática muestran una importante dependencia del ángulo de inclinación de los pilotes. Por otra parte, se ha detectado la existencia de un ángulo de inclinación para el cual el giro del encepado y la excitación entran en desfase en el rango de bajas y medias frecuencias.

A continuación se presenta una síntesis de las principales conclusiones extraídas del análisis de los resultados obtenidos para los casos analizados:

- La capacidad de una cimentación profunda para filtrar la excitación sísmica aumenta de forma significativa si todos o algunos de los pilotes están inclinados en la dirección de la excitación.
- El papel beneficioso de la inclinación de los pilotes desaparece a frecuencias altas.
- Los factores de interacción cinemática dependen enormemente de la dirección de inclinación de los pilotes. Las cimentaciones profundas que incluyen pilotes inclinados en dirección perpendicular a la dirección de la excitación tienen, generalmente, un peor comportamiento en términos de movimiento horizontal.
- El factor de interacción cinemática rotacional I_φ , en el caso de pilotes simples inclinados, es casi independiente del ángulo de inclinación.
- El giro del encepado y el movimiento horizontal del terreno en campo libre entran en desfase cuando los pilotes se inclinan en paralelo a la dirección de la excitación, o de forma simétrica a lo largo de las diagonales del encepado. Este efecto depende del ángulo de inclinación, así como del valor del ratio del módulo de Young pilote-suelo.
- Existe un ángulo de inclinación óptimo (normalmente pequeño) para el cual se obtiene un giro mínimo del encepado en el rango de frecuencias bajas y medias. Este fenómeno podría aprovecharse para minimizar la sollicitación sobre una estructura sometida a cargas sísmicas aunque, en algunos casos, la ejecución en la práctica de ángulos de inclinación óptimos muy pequeños no sería factible. Se observa una tendencia monótona creciente del giro del encepado con el ángulo de inclinación para valores altos de este último.
- Valores más altos del ratio de rigideces (suelos más blandos) implican un aumento del ángulo de inclinación para el cual el giro del encepado y el movimiento horizontal en campo libre en la superficie del terreno entran en desfase en el rango de frecuencias bajas o medias.
- La respuesta cinemática de grupos de pilotes que incluyen pilotes inclinados es menos sensible a variaciones del ángulo de inclinación a medida que el ratio de separación entre pilotes s/d o el número de pilotes aumentan.
- Ratios de rigidez E_p/E_s más bajos (suelos más rígidos) suponen mayores giros del encepado.
- Al contrario de lo que sucede para pilotes verticales, una reducción del ratio de esbeltez de los pilotes L/d conduce a valores decrecientes del giro en el encepado, al menos en el rango de frecuencias bajas, cuando se consideran configuraciones con pilotes inclinados en paralelo a la dirección de la excitación.

- En el rango de medias a bajas frecuencias (normalmente el más importante en el diseño sísmico de cimentaciones profundas), las deformaciones máximas a flexión en la cabeza de los pilotes tienden a aumentar cuando estos se inclinan en paralelo a la dirección de la excitación, pero tienden a disminuir cuando se inclinan en perpendicular a dicha dirección.

Por otra parte, se ha llevado a cabo un análisis de la influencia del ángulo de inclinación de los pilotes sobre la respuesta dinámica de estructuras pilotadas. A tal efecto, se ha estudiado la respuesta dinámica, considerando la interacción suelo-estructura, de estructuras esbeltas y no esbeltas sustentadas por diversas configuraciones de grupos de 2×2 y 3×3 pilotes, entre los que se incluyen elementos inclinados.

Se han representado resultados en términos del periodo en base flexible y el cortante máximo en la base de la estructura para 24 configuraciones diferentes. Además, se han obtenido espectros de respuesta modificados, considerando los efectos de interacción suelo-estructura, para diferentes ángulos de inclinación de los pilotes. Las principales conclusiones extraídas del análisis de los resultados para los casos estudiados se resumen a continuación:

- Se ha demostrado que un incremento del ángulo de inclinación puede tener un efecto beneficioso o perjudicial sobre la respuesta dinámica de la estructura, dependiendo del ratio de esbeltez de la misma.
- En el caso de edificios no esbeltos, el periodo efectivo \tilde{T}/T disminuye a medida que aumenta el ángulo de inclinación, debido al incremento de la rigidez horizontal. Sin embargo, en el caso de estructuras altas y esbeltas, \tilde{T}/T aumenta generalmente con el ángulo de inclinación, debido a una reducción de la impedancia de cabeceo, excepto para aquellos casos en los que la separación entre pilotes es pequeña.
- El aumento del ángulo de inclinación conduce a valores menores del cortante máximo en la base de la estructura Q_m cuando $h/b = 1$ o $h/b = 2$. Sin embargo, en el caso de estructuras esbeltas, Q_m aumenta con el ángulo de inclinación.
- La variación de la relación h/h_p (h/h_p : relación entre la altura modal efectiva h y la altura del punto geométrico de intersección, por encima del encepado, entre las extensiones de los ejes de los pilotes inclinados h_p) por encima o por debajo de la unidad no implica un cambio de tendencia en la respuesta estructural presentada en términos del cortante máximo en la base de la estructura cuando existe una conexión empotrada de los pilotes al encepado. Esto se debe al hecho de que, en este caso, la altura \mathcal{D} del centro de rigidez del grupo de pilotes no está relacionada con h_p .
- En la mayoría de los casos, puede observarse una reducción de la aceleración espectral a medida que el ángulo de inclinación aumenta. Sin embargo, cuanto más esbelta es la estructura, los efectos beneficiosos del uso de pilotes inclinados sobre la respuesta estructural son menos sistemáticos y menos significativos.

A.4.2. Desarrollos futuros

El procedimiento y el modelo propuestos en esta tesis han sido utilizados para acometer varios análisis paramétricos que han permitido estudiar el comportamiento dinámico de estructuras lineales a cortante sustentadas sobre grupos de pilotes y sometidas a ondas planas de corte S con incidencia vertical. Por otra parte, se ha empleado una formulación acoplada de elementos finitos y elementos de contorno, desarrollada por Padrón *et al.* [49, 71, 120], para analizar la respuesta sísmica de diversas configuraciones de grupos de pilotes, teniendo en cuenta la interacción suelo-estructura. Algunos de los desarrollos futuros del trabajo de investigación que se presenta son:

- Análisis paramétricos incluyendo otras configuraciones de cimentaciones y de superestructuras.
- Validación mediante comparación con resultados experimentales, tales como los proporcionados por Escoffier [51] o Goit y Masato [53].
- Estudios paramétricos acerca del comportamiento sísmico de grupos de pilotes, incluyendo elementos verticales o inclinados, sujetos a distintos tipos de ondas sísmicas (P, S y ondas de Rayleigh) y considerando distintas direcciones de incidencia.
- Búsqueda de la configuración óptima para un determinado sistema suelo-estructura.
- Obtención de expresiones interpoladas para las características dinámicas del sistema de un grado de libertad equivalente que permitan obtener un criterio de diseño más preciso para estructuras de edificación.
- Desarrollo de una metodología que permita tener en cuenta los efectos de la interacción suelo-estructura en el análisis de la respuesta dinámica de sistemas de varios grados de libertad mediante superposición. Esta metodología permitiría abordar el análisis de un sistema con n grados de libertad dividiéndolo en n sistemas de un grado de libertad. Así, la respuesta dinámica asociada con cada modo de vibración podría obtenerse de forma separada mediante subestructuración, teniendo en cuenta los efectos de interacción suelo-estructura. La precisión de la metodología propuesta se evaluaría mediante comparación con los resultados obtenidos a partir de la resolución directa del sistema de varios grados de libertad por subestructuración.
- Estudio de la influencia de la configuración de la cimentación, así como del ángulo de inclinación de los pilotes, sobre los esfuerzos estructurales en pilotes y encepado.
- Análisis de los esfuerzos cortantes y los momentos flectores inducidos por el terremoto en los pilotes, así como la sensibilidad de estos esfuerzos a las variaciones de parámetros como: ratio de esbeltez estructural, relación de masas cimiento-estructura, ratio de rigidez suelo-estructura, configuración de la cimentación pilotada, ratio de rigidez pilote-suelo, ratio de esbeltez de los pilotes, estratigrafía del suelo, tipo de ondas incidentes y dirección de las mismas.
- Análisis de la influencia del contacto entre el encepado y el semiespacio sobre la respuesta del sistema, en el caso de cimentaciones embebidas, así como de la influencia del coeficiente de embebimiento de la cimentación.



- Desarrollo de un compendio de espectros de respuesta máxima que pudieran servir como referencia para el diseño de estructuras, considerando los efectos de interacción suelo-estructura.



Bibliography



- [1] Parmelee, R. A. (1967) Building-foundation interaction effects. *Journal of the Engineering Mechanics Division, ASCE*, **93**, 131–162.
- [2] Parmelee, R. A., Perelman, D. S., and Lee, S. L. (1969) Seismic response of multiple-storey structures on flexible foundation. *Bulletin of the Seismological Society of America*, **59**, 1061–1070.
- [3] Perelman, D. S., Parmelee, R. A., and Lee, S. L. (1968) Seismic response of single-storey interaction systems. *Journal of the Structural Division, ASCE*, **94**, 2597–2608.
- [4] Sarrazin, M. A., Roesset, J. M., and Whitman, R. V. (1972) Dynamic soil-structure interaction. *Journal of the Structural Division, ASCE*, **98**, 1525–1544.
- [5] Roësset, J. M. (2013) Soil structure interaction. The early stages. *Journal of Applied Science and Engineering*, **16** (1), 1–8.
- [6] Jennings, P. C. and Bielak, J. (1973) Dynamics of building-soil interaction. *Bulletin of the Seismological Society of America*, **63**, 9–48.
- [7] Veletsos, A. S. and Meek, J. W. (1974) Dynamic behaviour of building-foundation systems. *Earthquake Engineering and Structural Dynamics*, **3**, 121–138.
- [8] Veletsos, A. S. and Nair, V. V. D. (1975) Seismic interaction of structures on hysteretic foundations. *Journal of the Structural Division, ASCE*, **101**, 109–129.
- [9] Bielak, J. (1976) Modal analysis for building-soil interaction. *Journal of the Engineering Mechanics Division, ASCE*, **102**, 771–786.
- [10] Luco, J. E. (1980) Linear soil-structure interaction. Report UCRL15272, Lawrence Livermore National Laboratory, Livermore, California.
- [11] Wolf, J. P. (1985) *Dynamic soil-structure interaction*. Englewood Cliffs, (NJ); Prentice-Hall.
- [12] Bielak, J. (1975) Dynamic behaviour of structures with embedded foundations. *Earthquake Engineering and Structural Dynamics*, **3**, 259–274.
- [13] Avilés, J. and Pérez-Rocha, L. E. (1996) Evaluation of interaction effects on the system period and the system damping due to foundation embedment and layer depth. *Soil Dynamics and Earthquake Engineering*, **15**, 11–27.
- [14] Avilés, J. and Pérez-Rocha, L. E. (1998) Effects of foundation embedment during building-soil interaction. *Earthquake Engineering and Structural Dynamics*, **27**, 1523–1540.
- [15] Avilés, J., Suárez, M., and Sánchez-Sesma, F. J. (2002) Effects of wave passage on the relevant dynamic properties of structures with flexible foundations. *Earthquake Engineering and Structural Dynamics*, **31**, 139–159.
- [16] Todorovska, M. I. (1992) Effects of the depth of the embedment on the system response during building-soil interaction. *Soil Dynamics and Earthquake Engineering*, **11**, 111–123.



- [17] Todorovska, M. I. and Trifunac, M. D. (1992) The system damping, the system frequency and the system response peak amplitudes during in-plane building-soil interaction. *Earthquake Engineering and Structural Dynamics*, **21**, 127–144.
- [18] Kausel, E. and Roësset, J. M. (1974) Soil-structure interaction for nuclear containment. *Power division specialty conference on electric power and civil engineer*, Boulder, Colorado, pp. 469–498.
- [19] Kausel, E., Whitman, R. V., Morray, J. O., and Elsabee, F. (1978) The spring method for the embedded foundations. *Nuclear Engineering and Design*, **48**, 377–392.
- [20] Avilés, J. and Suárez, M. (2002) Effective periods and dampings of building-foundation systems including seismic wave effects. *Engineering Structures*, **24**, 553–562.
- [21] Todorovska, M. I. and Trifunac, M. D. (1991) Radiation damping during two-dimensional in-plane building-soil interaction. Report 91-01, Department of Civil Engineering. University of Southern California.
- [22] Rainer, J. H. (1975) Simplified analysis of dynamic structure-ground interaction. *Canadian Journal of Civil Engineering*, **2** (3), 345–356.
- [23] Kaynia, A. M. and Mahzooni, S. (1996) Forces in pile foundations under seismic loading. *Journal of Engineering Mechanics*, **122** (1), 46–53.
- [24] Mylonakis, G., Nikolaou, A., and Gazetas, G. (1997) Soil-pile-bridge seismic interaction: kinematic and inertial effects. Part I: soft soil. *Earthquake Engineering and Structural Dynamics*, **26** (3), 337–359.
- [25] Guin, J. and Banerjee, P. K. (1998) Coupled soil-pile-structure interaction analysis under seismic excitation. *Journal of Structural Engineering, ASCE*, **124**, 434–444.
- [26] Aguilar, H. and Avilés, J. (2003) Influencia de pilotes de fricción en la interacción dinámica suelo-estructura. *Revista Internacional de Métodos Numéricos para Cálculo y Diseño en Ingeniería*, **19** (1), 3–18.
- [27] Maravas, A., Mylonakis, G., and Karabalis, D. L. (2007) Dynamic characteristics of simple structures on piles and footings. *Proceedings of 4th International Conference on earthquake geotechnical engineering*, Thessaloniki, Greece, no. 1672.
- [28] Rovithis, E. N., Pitilakis, K. D., and Mylonakis, G. (2009) Seismic analysis of coupled soil-pile-structure systems leading to the definition of a pseudo-natural SSI frequency. *Soil Dynamics and Earthquake Engineering*, **29**, 1005–1015.
- [29] Rovithis, E. N., Pitilakis, K. D., and Mylonakis, G. (2011) A note on a pseudo-natural SSI frequency for coupled soil-pile-structure systems. *Soil Dynamics and Earthquake Engineering*, **31**, 873–878.
- [30] Carbonari, S., Dezi, F., and Leoni, G. (2011) Seismic soil-structure interaction in multi-span bridges: Application to a railway bridge. *Earthquake Engineering and Structural Dynamics*, **40**, 1219–1239.



- [31] Luco, J. E. (1980) Soil-structure interaction and identification of structural models. *Proceedings of the ASCE Speciality Conference in Civil Engineering and Nuclear Power*, Knoxville, Tennessee.
- [32] Kausel, E. (1984) Structures in seismic regions. Report, Technische universität Berlin and MIT.
- [33] Banerjee, P. K. and Driscoll, R. M. (1976) Three-dimensional analysis of raked pile groups. *Proceedings of the Institution of Civil Engineers, Part 2*, vol. 61 (4), pp. 653–671.
- [34] Poulos, H. G. and Davis, E. H. (1980) *Pile Foundation Analysis and Design*. John Wiley & Sons.
- [35] Poulos, H. G. (1999) Approximate computer analysis of pile groups subjected to loads and ground movements. *International Journal for Numerical and Analytical Methods in Geomechanics*, **23**, 1021–1041.
- [36] Poulos, H. G. (2006) Raked piles-Virtues and drawbacks. *Journal of Geotechnical and Geoenvironmental Engineering*, **132** (6), 795–803.
- [37] Deng, N., Kulesza, R., and Ostadan, F. (2007) Seismic soil-pile group interaction analysis of a battered pile group. *Proceedings of the 4th International Conference on Earthquake Geotechnical Engineering*, Thessaloniki.
- [38] Neely, W. J. (2007) Discussion of "Raked piles - Virtues and drawbacks" by Harry G. Poulos. *Journal of Geotechnical and Geoenvironmental Engineering*, **133** (11), 1474–1477.
- [39] Ravazi, S. A., Fakher, A., and Mirghaderi, S. R. (2007) An insight into the bad reputation of batter piles in seismic performance of wharves. *Proceedings of the 4th International Conference on Earthquake Geotechnical Engineering*, Thessaloniki, Greece., no. 1423.
- [40] Gazetas, G. and Mylonakis, G. (1998) Seismic soil-structure interaction: new evidence and emerging issues. *Geotechnical Earthquake Engineering and Soil Dynamics III ASCE, Geotechnical Special Publication II*, pp. 1119–1174.
- [41] Berrill, J. B., Christensen, S. A., Keenan, R. P., Okada, W., and Pettinga, J. R. (2001) Case study of lateral spreading forces on a piled foundation. *Géotechnique*, **51** (6), 501–517.
- [42] Guin, J. (1997) *Advances in soil-pile-structure interaction and non-linear pile behavior*. Ph.D. thesis, State University of New York at Buffalo.
- [43] Sadek, M. and Shahrour, I. (2004) Three-dimensional finite element analysis of the seismic behavior of inclined micropiles. *Soil Dynamics and Earthquake Engineering*, **24** (6), 473–485.
- [44] Gerolymos, N., Giannakou, A., Anastasopoulos, I., and Gazetas, G. (2008) Evidence of beneficial role of inclined piles: observations and summary of numerical analyses. *Bulletin of Earthquake Engineering*, **6** (4), 705–722.



- [45] Juran, I., Bensimane, A., and Hanna, S. (2001) Engineering analysis of dynamic behavior of micropile systems. *Transportation Research Record*, **1772**, 91–106.
- [46] Giannakou, A., Gerolymos, N., and Gazetas, G. (2006) On the dynamics of inclined piles. *Proceedings of the 10th International Conference on Piling and Deep Foundations*, Amsterdam, The Netherlands, pp. 286–295.
- [47] Giannakou, A. (2007) *Seismic behavior of inclined piles*. Ph.D. thesis, National Technical University of Athens.
- [48] Giannakou, A., Gerolymos, N., Gazetas, G., Tazoh, T., and Anastasopoulos, I. (2010) Seismic behaviour of batter piles: elastic response. *Journal of Geotechnical and Geoenvironmental Engineering, ASCE*, **136 (9)**, 1187–1199.
- [49] Padrón, L. A., Aznárez, J. J., Maeso, O., and Santana, A. (2010) Dynamic stiffness of deep foundations with inclined piles. *Earthquake Engineering and Structural Dynamics*, **39 (12)**, 1343–1367.
- [50] Padrón, L. A., Aznárez, J. J., Maeso, O., and Saitoh, M. (2012) Impedance functions of end-bearing inclined piles. *Soil Dynamics and Earthquake Engineering*, **38**, 97–108.
- [51] Escoffier, S. (2012) Experimental study of the effect of inclined pile on the seismic behavior of pile group. *Soil Dynamics and Earthquake Engineering*, **42**, 275–291.
- [52] Shahrour, I., Alsaleh, H., and Souli, M. (2012) 3D elastoplastic analysis of the seismic performance of inclined micropiles. *Computers and Geotechnics*, **39**, 1–7.
- [53] Goit, C. S. and Saitoh, M. (2013) Model tests and numerical analyses on horizontal impedance functions of inclined single piles embedded in cohesionless soil. *Earthquake Engineering and Engineering Vibration*, **13**, 143–154.
- [54] Medina, C., Padrón, L. A., Aznárez, J. J., Santana, A., and Maeso, O. (2014) Kinematic interaction factors of deep foundations with inclined piles. *Earthquake Engineering and Structural Dynamics*, **43**, 2035–2050.
- [55] Medina, C., Padrón, L. A., Aznárez, J. J., and Maeso, O. (2015) Influence of pile inclination angle on the dynamic properties and seismic response of piled structures. *Soil Dynamics and Earthquake Engineering*, **69**, 196–206.
- [56] Wolf, J. P., von Arx, G. A., de Barros, F. C. P., and M, K. (1981) Seismic analysis of the pile foundation of the reactor building of the NPP Angra 2. *Nuclear Engineering and Design*, **65**, 329–341.
- [57] Gazetas, G. (1991) *Foundation Vibrations. Foundation Engineering Handbook*. Van Nostrand Reinhold, NY.
- [58] Dobry, R. and Gazetas, G. (1988) Simple method for dynamic stiffness and damping of floating pile groups. *Géotechnique*, **38**, 557–574.



- [59] Poulos, H. G. (1971) Analysis of displacements of laterally loaded piles II - Pile groups. *Journal of the Soil Mechanics and Foundations Division, ASCE*, **97** (5), 733–751.
- [60] Konagai, K., Ashan, R., and Maruyama, D. (2000) Simple expression of the dynamic stiffness of grouped piles in sway motion. *Journal of Earthquake Engineering*, **4** (3), 355–376.
- [61] Taherzadeh, R., Clouteau, D., and Cottureau, R. (2009) Simple formulas for the dynamic stiffness of pile groups. *Earthquake Engineering and Structural Dynamics*, **38**, 1665–1685.
- [62] Dai, W. and Roësset, J. M. (2010) Horizontal dynamic stiffness of pile groups: Approximate expression. *Soil Dynamics and Earthquake Engineering*, **30**, 844–850.
- [63] Wolf, J. P. and von Arx, G. A. (1978) Impedance function of a group of vertical piles. *Proceedings of the Conference on Structural Analysis, Design & Construction in Nuclear Power Plants*, Porto Alegre, Brasil, pp. 1–22, no. 1.
- [64] Kaynia, A. M. (1982) Dynamic stiffness and seismic response of pile groups. Report R83-03, Massachusetts Institute of Technology, Cambridge, MA.
- [65] Velez, A., Gazetas, G., and Krishnan, R. (1983) Lateral dynamic response of constrained-head piles. *Journal of Geotechnical Engineering, ASCE*, **109**, 1063–1081.
- [66] Miura, K., Kaynia, A. M., Masuda, K., Kitamura, E., and Seto, Y. (1994) Dynamic behaviour of pile foundations in homogeneous and non-homogeneous media. *Earthquake Engineering and Structural Dynamics*, **23**, 183–192.
- [67] Kaynia, A. M. and Kausel, E. (1991) Dynamics of piles and pile groups in layered soil media. *Soil Dynamics and Earthquake Engineering*, **10**, 386–401.
- [68] Aznárez, J. J. (2002) *Efectos de los fenómenos de interacción incluyendo los factores espaciales y sedimentos de fondo en la respuesta sísmica de presas bóveda*. Ph. d. thesis, University of Las Palmas de Gran Canaria, Las Palmas de G.C., Spain.
- [69] Vinciprova, F., Maeso, O., Aznárez, J. J., and Oliveto, G. (2003) *Problems in structural identification and diagnostic: General aspects and applications*, chap. Interaction of BEM analysis and experimental testing on pile-soil systems, pp. 195–227. Springer-Verlag.
- [70] Maeso, O., Aznárez, J. J., and García, F. (2005) Dynamic impedances of piles and groups of piles in saturated soils. *Computers and Structures*, **83**, 769–782.
- [71] Padrón, L. A., Aznárez, J. J., and Maeso, O. (2007) BEM-FEM coupling model for the dynamic analysis of piles and pile groups. *Engineering Analysis with Boundary Elements*, **31**, 473–484.
- [72] Mamoon, S. M., Kaynia, A. M., and Banerjee, P. K. (1990) Frequency domain dynamic analysis of piles and pile groups. *Journal of Engineering Mechanics, ASCE*, **116**, 2237–2257.



- [73] Gazetas, G. (1984) Seismic response of end-bearing single piles. *Soil Dynamics and Earthquake Engineering*, **3** (2), 82–93.
- [74] Mamoon, S. M. and Ahmad, S. (1990) Seismic response of pile to obliquely incident SH, SV and P waves. *Journal of Geotechnical Engineering*, **116**, 186–204.
- [75] Mamoon, S. M. and Banerjee, P. K. (1990) Response of piles and pile groups to travelling SH-waves. *Earthquake Engineering and Structural Dynamics*, **19**, 597–610.
- [76] Makris, N. and Badoni, D. (1995) Seismic response of pile groups under oblique-shear and Rayleigh waves. *Earthquake Engineering and Structural Dynamics*, **24** (4), 517–532.
- [77] Kaynia, A. M. and Novak, M. (1992) Response of pile foundations to Rayleigh waves and obliquely incident body waves. *Earthquake Engineering and Structural Dynamics*, **21**, 303–318.
- [78] K Fan, K., Gazetas, G., Kaynia, A. M., Kausel, E., and Ahmad, S. (1991) Kinematic seismic response of single piles and pile groups. *Journal of the Geotechnical Engineering Division, ASCE*, **117** (12), 1860–1879.
- [79] Gazetas, G., Fan, K., Tazoh, T., Shimizu, K., Kavvadas, M., and Makris, N. (1992) Seismic pile-group-structure interaction. *Geotechnical Specialty Publication, ASCE*, **34**, 56–93.
- [80] Kavvadas, M. and Gazetas, G. (1993) Kinematic seismic response and bending of free-head piles in layered soil. *Geothéchnique*, **43**, 207–222.
- [81] Padrón, L. A. (2008) *Numerical model for the dynamic analysis of pile foundations*. Ph.d. thesis, University of Las Palmas de Gran Canaria, Las Palmas de G. C., Spain.
- [82] Sadek, M. and Shahrour, I. (2006) Influence of the head and tip connection on the seismic performance of micropiles. *Soil Dynamics and Earthquake Engineering*, **26** (6), 461–468.
- [83] Domínguez, J. and Roësset, J. M. (1978) Dynamic stiffness of rectangular foundations. Research Report R78-20, Department of Civil Engineering, Massachusetts Institute of Technology, Cambridge, Massachusetts.
- [84] Domínguez, J. and Alarcón, E. (1981) *Progress in Boundary Element Methods*, chap. Elastodynamics. Pentech Press Ltd.
- [85] Abascal, R. and Domínguez, J. (1986) Vibrations on footings on zoned viscoelastic soils. *Journal of Engineering Mechanics, ASCE*, **112**, 433–447.
- [86] Medina, F. and Domínguez, J. (1989) Boundary elements for the analysis of the seismic response of dams including dam-water-foundation interaction effects I. *Engineering Analysis with Boundary Elements*, **6** (3), 152–157.



- [87] Domínguez, J. and Medina, F. (1989) Boundary elements for the analysis of the seismic response of dams including dam-water-foundation interaction effects II. *Engineering Analysis with Boundary Elements*, **6** (3), 158–163.
- [88] Alarcón, E., Cano, J. J., and Domínguez, J. (1989) Boundary element approach to the dynamic stiffness functions of circular foundations. *International Journal for Numerical and Analytical Methods in Geomechanics*, **13**, 645–664.
- [89] Domínguez, J. (1993) *Boundary elements in dynamics*. Computational Mechanics Publications & Elsevier Applied Science, Southampton, NY.
- [90] Maeso, O. (1992) *Modelo para el análisis sísmico de presas bóveda incluyendo los efectos de interacción suelo-agua-estructura*. Ph.d. thesis, University of Las Palmas de Gran Canaria, Las Palmas de G.C., Spain.
- [91] Maeso, O. and Domínguez, J. (1993) Earthquake analysis of arch dams. I: Dam-foundation interaction. *Journal of Engineering Mechanics, ASCE*, **119** (3), 496–512.
- [92] Domínguez, J. and Maeso, O. (1993) Earthquake analysis of arch dams. II: Dam-water-foundation interaction. *Journal of Engineering Mechanics, ASCE*, **119** (3), 513–530.
- [93] Aznárez, J. J., Maeso, O., and Domínguez, J. (2001) A 3-D boundary element model for the dynamic analysis of arch dams with porous sediments. *Earthquake Resistant Engineering Structures III. Series: Advances in Earthquake Engineering*, **9**, 713–722.
- [94] Maeso, O., Aznárez, J. J., and Domínguez, J. (2002) Effects of space distribution of excitation on seismic response of arch dams. *Journal of Engineering Mechanics, ASCE*, **128**, 759–768.
- [95] Maeso, O., Aznárez, J. J., and Domínguez, J. (2004) Three-dimensional models of reservoir sediment and effects on the seismic response of arch dams. *Earthquake Engineering and Structural Dynamics*, **33**, 1103–1123.
- [96] Aznárez, J. J., Maeso, O., and Domínguez, J. (2006) BE analysis of bottom sediments in dynamic fluid-structure interaction problems. *Engineering Analysis with Boundary Elements*, **30**, 124–136.
- [97] Padrón, L. A., Aznárez, J. J., and Maeso, O. (2009) Dynamic structure-soil-structure interaction between nearby piled buildings under seismic excitation by BEM-FEM model. *Soil Dynamics and Earthquake Engineering*, **29**, 1084–1096.
- [98] Zarzalejos, J. M., Aznárez, J. J., Padrón, L. A., and Maeso, O. (2014) Influence of type of wave and angle of incidence on seismic bending moments in pile foundations. *Earthquake Engineering and Structural Dynamics*, **43**, 41–59.
- [99] Medina, C., Padrón, L. A., Aznárez, J. J., and Maeso, O. (2011) Influencia de los fenómenos de interacción en las propiedades dinámicas de estructuras de edificación pilotadas. Tadeu, A., Narra Figueiredo, I., Menezes, L. F., Mendes,



- P. A., Rodríguez-Ferrán, A., Arias, I., and Blanco, J. M. (eds.), *Proceedings of the Congress on Numerical Methods in Engineering 2011*, Coimbra, Portugal, pp. 96–115.
- [100] Medina, C., Aznárez, J. J., Padrón, L. A., and Maeso, O. (2013) A procedure for evaluating the soil-structure-interaction effects on the system period and damping of pile-supported structures. Papadrakakis, M., Lagaros, N. D., and Plevris, V. (eds.), *Proceedings of 4th ECCOMAS Thematic Conference on Computational Methods in Structural Dynamics and Earthquake Engineering, COMPDYN 2013*, Kos Island, Greece, pp. 4463–4487.
- [101] Medina, C., Aznárez, J. J., Padrón, L. A., and Maeso, O. (2013) Effects of soil-structure interaction on the dynamic properties and seismic response of piled structures. *Soil Dynamics and Earthquake Engineering*, **53**, 160–175.
- [102] Medina, C., Aznárez, J. J., Padrón, L. A., and Maeso, O. (2014) Influence of pile rake angle on the seismic response of pile foundations and piled structures. Cunha, A., Caetano, E., Ribeiro, P., and Müller, G. (eds.), *Proceedings of the 9th International Conference on Structural Dynamics, EURODYN 2014*, Porto, Portugal, pp. 733–740.
- [103] Medina, C., Aznárez, J. J., Padrón, L. A., and Maeso, O. (2014) Seismic response of deep foundations and piled structures considering inclined piles. Oñate, E., Oliver, X., and Huerta, A. (eds.), *Proceedings of the jointly organized 11th. World Congress on Computational Mechanics (WCCM XI) and 5th. European Congress on Computational Mechanics (ECCM V)*, Barcelona, Spain, pp. 453–463.
- [104] Medina, C., Padrón, L. A., Aznárez, J. J., and Maeso, O. (2015) Respuesta sísmica de estructuras de edificación cimentadas sobre pilotes inclinados. *Proceedings of Congreso de Métodos Numéricos en Ingeniería*, Lisbon, Portugal, no. 237.
- [105] Padrón, L. A., Medina, C., Álamo, G. M., Aznárez, J. J., Santana, A., Maeso, O., García, F., and Chirino, F. (2015) Pilotes inclinados: situación normativa y ventajas e inconvenientes de su uso en proyectos de edificación en zonas con riesgo sísmico. *Proceedings of the 19th International Congress on Project Management and Engineering*, Granada, Spain.
- [106] Novak, M. (1974) Dynamic stiffness and damping of piles. *Canadian Geotechnical Journal*, **11**, 574–591.
- [107] Berger, E. and Pyke, R. (1977) Simplified method for evaluating soil-pile-structure interaction effects. *Proceedings of the 9th Offshore Technology Conference*, Houston, TX, pp. 589–598.
- [108] Dobry, R., Vincente, E., O'Rourke, M. J., and Roesset, J. M. (1982) Horizontal stiffness and damping of single piles. *Journal of Geotechnical Engineering, ASCE*, **108** (3), 439–459.
- [109] Flores-Berrones, R. and Whitman, R. V. (1982) Seismic response of end-bearing piles. *Journal of Geotechnical Engineering, ASCE*, **108** (4), 554–569.



- [110] Gazetas, G. and Dobry, R. (1984) Horizontal response of piles in layered soils. *Journal of Geotechnical Engineering, ASCE*, **110** (1), 20–40.
- [111] Barghouthi, A. F. (1984) *Pile response to seismic waves*. Ph.D. thesis, Department of Civil and Environmental Engineering. University of Wisconsin-Madison.
- [112] Makris, N. and Gazetas, G. (1992) Dynamic pile-soil-pile interaction. Part II: Lateral and seismic response. *Earthquake Engineering and Structural Dynamics*, **21**, 145–162.
- [113] Dezi, F., Carbonari, S., and Morici, M. (2015) A numerical model for the dynamic analysis of inclined pile groups. *Earthquake Engineering and Structural Dynamics*, published online in Wiley Online Library (wileyonlinelibrary.com). DOI: 10.1002/eqe.2615.
- [114] Chopra, A. K. (2001) *Dynamics of structures. Theory and applications to earthquake engineering*. Prentice-Hall (NJ).
- [115] Clough, R. W. and Penzien, J. (1982) *Dynamics of Structures*. McGraw-Hill.
- [116] Verbic, B. and Veletsos, A. S. (1972) Impulse response functions for elastic foundations. Report SRR 15, Department of Civil Engineering, Rice University, Houston, Texas.
- [117] Veletsos, A. S. and Wei, Y. T. (1971) Lateral and rocking vibration of footings. *Journal of the Soil Mechanics and Foundations Division, ASCE*, **97** (9), 1227–1248.
- [118] Veletsos, A. S. and Verbic, B. (1973) Vibration of viscoelastic foundations. *Earthquake Engineering and Structural Dynamics*, **2**, 87–102.
- [119] Mita, A. and Luco, J. E. (1989) Impedance functions and input motions for embedded square foundations. *Journal of Geotechnical Engineering, ASCE*, **115**, 491–503.
- [120] Padrón, L. A., Aznárez, J. J., and Maeso, O. (2008) Dynamic analysis of piled foundations in stratified soils by a BEM-FEM model. *Soil Dynamics and Earthquake Engineering*, **28**, 333–346.
- [121] Mylonakis, G. (2001) Simplified model for seismic pile bending at soil layer interfaces. *Soils and foundations*, **41** (4), 47–58.
- [122] Stewart, J. P., Seed, R. B., and Fenves, G. L. (1999) Seismic soil-structure interaction in buildings. II: Empirical findings. *Journal of Geotechnical and Geoenvironmental Engineering, ASCE*, **125**, 38–48.



INSTITUTO UNIVERSITARIO
SIANI
INGENIERIA COMPUTACIONAL

Edificio Central del Parque Tecnológico
Campus Universitario de Tafira
35017 Las Palmas de Gran Canaria
e-mail: info@siani.es · www.siani.es



UNIVERSIDAD DE LAS PALMAS
DE GRAN CANARIA